

# AGARD

ADVISORY GROUP FOR AEROSPACE RESEARCH & DEVELOPMENT

7 RUE ANCELLE 92200 NEUILLY SUR SEINE FRANCE

AD-A245 302



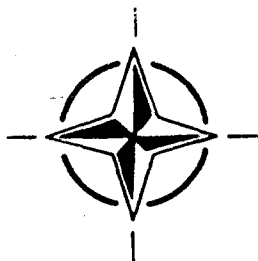
AGARD CONFERENCE PROCEEDINGS 497

## Manoeuvring Aerodynamics

(La Manoeuvrabilité par l'Aérodynamique)



*Papers presented and discussions held at the Fluid Dynamics Panel  
Specialists' Meeting held in Toulouse, France, 1st-2nd May 1991.*



NORTH ATLANTIC TREATY ORGANIZATION

This document has been approved  
for public release and sale; its  
distribution is unlimited.

Published November 1991

Distribution and Availability on Back Cover

AGARD-CP-497

# AGARD

ADVISORY GROUP FOR AEROSPACE RESEARCH & DEVELOPMENT

7 RUE ANCELLE 92200 NEUILLY SUR SEINE FRANCE

## AGARD CONFERENCE PROCEEDINGS 497

### Manoeuvring Aerodynamics

(La Manoeuvrabilité par l'Aérodynamique)



Accession For	
NTIS CRA&I	<input checked="" type="checkbox"/>
DTIC TAB	<input type="checkbox"/>
Unannounced	<input type="checkbox"/>
Justification	
By	
Distribution /	
Availability Codes	
Dist	Avail and/or Special
A-1	

Papers presented and discussions held at the Fluid Dynamics Panel  
Specialists' Meeting held in Toulouse, France, 1st-2nd May 1991.



North Atlantic Treaty Organization  
*Organisation du Traité de l'Atlantique Nord*

92 1 22 051

92-01817  
■■■■■■■■■■

## The Mission of AGARD

According to its Charter, the mission of AGARD is to bring together the leading personalities of the NATO nations in the fields of science and technology relating to aerospace for the following purposes:

- Recommending effective ways for the member nations to use their research and development capabilities for the common benefit of the NATO community;
- Providing scientific and technical advice and assistance to the Military Committee in the field of aerospace research and development (with particular regard to its military application);
- Continuously stimulating advances in the aerospace sciences relevant to strengthening the common defence posture;
- Improving the co-operation among member nations in aerospace research and development;
- Exchange of scientific and technical information;
- Providing assistance to member nations for the purpose of increasing their scientific and technical potential;
- Rendering scientific and technical assistance, as requested, to other NATO bodies and to member nations in connection with research and development problems in the aerospace field.

The highest authority within AGARD is the National Delegates Board consisting of officially appointed senior representatives from each member nation. The mission of AGARD is carried out through the Panels which are composed of experts appointed by the National Delegates, the Consultant and Exchange Programme and the Aerospace Applications Studies Programme. The results of AGARD work are reported to the member nations and the NATO Authorities through the AGARD series of publications of which this is one.

Participation in AGARD activities is by invitation only and is normally limited to citizens of the NATO nations.

The content of this publication has been reproduced directly from material supplied by AGARD or the authors.

Published November 1991

Copyright © AGARD 1991  
All Rights Reserved

ISBN 92-835-0643-X



Printed by Specialised Printing Services Limited  
40 Chigwell Lane, Loughton, Essex IG10 3TZ

# Recent Publications of the Fluid Dynamics Panel

## AGARDOGRAPHS (AG)

### Experimental Techniques in the Field of Low Density Aerodynamics

AGARD AG-318 (E), April 1991

### Techniques Expérimentales Liées à l'Aérodynamique à Basse Densité

AGARD AG-318 (FR), April 1990

### A Survey of Measurements and Measuring Techniques in Rapidly Distorted Compressible Turbulent Boundary Layers

AGARD AG-315, May 1989

### Reynolds Number Effects in Transonic Flows

AGARD AG-303, December 1988

### Three Dimensional Grid Generation for Complex Configurations — Recent Progress

AGARD AG-309, March 1988

## REPORTS (R)

### Aircraft Dynamics at High Angles of Attack: Experiments and Modelling

AGARD R-776, Special Course Notes, March 1991

### Inverse Methods in Airfoil Design for Aeronautical and Turbomachinery Applications

AGARD R-780, Special Course Notes, November 1990

### Aerodynamics of Rotorcraft

AGARD R-781, Special Course Notes, November 1990

### Three-Dimensional Supersonic/Hypersonic Flows Including Separation

AGARD R-764, Special Course Notes, January 1990

### Advances in Cryogenic Wind Tunnel Technology

AGARD R-774, Special Course Notes, November 1989

## ADVISORY REPORTS (AR)

### Appraisal of the Suitability of Turbulence Models in Flow Calculations

AGARD AR-291, Technical Status Review, July 1991

### Rotary-Balance Testing for Aircraft Dynamics

AGARD AR-265, Report of WG 11, December 1990

### Calculation of 3D Separated Turbulent Flows in Boundary Layer Limit

AGARD AR-255, Report of WG10, May 1990

### Adaptive Wind Tunnel Walls: Technology and Applications

AGARD AR-269, Report of WG12, April 1990

## CONFERENCE PROCEEDINGS (CP)

### Vortex Flow Aerodynamics

AGARD CP-494, July 1991

### Missile Aerodynamics

AGARD CP-493, October 1990

### Aerodynamics of Combat Aircraft Controls and of Ground Effects

AGARD CP-465, April 1990

### Computational Methods for Aerodynamic Design (Inverse) and Optimization

AGARD CP-463, March 1990

### Applications of Mesh Generation to Complex 3-D Configurations

AGARD CP-464, March 1990



**Fluid Dynamics of Three-Dimensional Turbulent Shear Flows and Transition**  
AGARD CP-438, April 1989

**Validation of Computational Fluid Dynamics**  
AGARD CP-437, December 1988

**Aerodynamic Data Accuracy and Quality: Requirements and Capabilities in Wind Tunnel Testing**  
AGARD CP-429, July 1988

**Aerodynamics of Hypersonic Lifting Vehicles**  
AGARD CP-428, November 1987

**Aerodynamic and Related Hydrodynamic Studies Using Water Facilities**  
AGARD CP-413, June 1987

**Applications of Computational Fluid Dynamics in Aeronautics**  
AGARD CP-412, November 1986

**Store Airframe Aerodynamics**  
AGARD CP-389, August 1986

**Unsteady Aerodynamics - Fundamentals and Applications to Aircraft Dynamics**  
AGARD CP-386, November 1985

**Aerodynamics and Acoustics of Propellers**  
AGARD CP-366, February 1985

**Improvement of Aerodynamic Performance through Boundary Layer Control and High Lift Systems**  
AGARD CP-365, August 1984

**Wind Tunnels and Testing Techniques**  
AGARD CP-348, February 1984

**Aerodynamics of Vortical Type Flows in Three Dimensions**  
AGARD CP-342, July 1983

**Missile Aerodynamics**  
AGARD CP-336, February 1983

**Prediction of Aerodynamic Loads on Rotorcraft**  
AGARD CP-334, September 1982

**Wall Interference in Wind Tunnels**  
AGARD CP-335, September 1982

**Fluid Dynamics of Jets with Applications to V/STOL**  
AGARD CP-308, January 1982

**Aerodynamics of Power Plant Installation**  
AGARD CP-301, September 1981

**Computation of Viscous-Inviscid Interactions**  
AGARD CP-291, February 1981

**Subsonic/Transonic Configuration Aerodynamics**  
AGARD CP-285, September 1980

**Turbulent Boundary Layers Experiments, Theory and Modelling**  
AGARD CP-271, January 1980

**Aerodynamic Characteristics of Controls**  
AGARD CP-262, September 1979

**High Angle of Attack Aerodynamics**  
AGARD CP-247, January 1979

**Dynamic Stability Parameters**  
AGARD CP-235, November 1978

**Unsteady Aerodynamics**  
AGARD CP-227, February 1978

**Laminar-Turbulent Transition**  
AGARD CP-224, October 1977

## Foreword

This is the third FDP meeting in the general area of Aerodynamics for Aircraft Dynamics, following the successful meetings in Göttingen, Germany, in May 1985 (AGARD CP 386) and in Athens, Greece, in May 1978 (AGARD CP 235). The theme reflects the growing interest in rapid, large-amplitude maneuvers of agile combat aircraft at high angles of attack and treats the unsteady, separated, vortical and often non-linear flows representative of such conditions. Developments in the pertinent analytical, computational and experimental design and prediction methods, techniques for vortex flow control, importance of time-dependent phenomena and the need for advanced dynamic experiments in wind tunnels are all reported on and the relevant aerodynamic data are presented. It is hoped that this information will significantly improve our understanding of the basic unsteady aerodynamics required for better prediction of the dynamic behavior of aircraft maneuvering at high angles of attack.

This conference is technically associated with two other recent activities of the Fluid Dynamics Panel, a Special Course on "Aircraft Dynamics at High Angles of Attack — Experiments and Modelling" given at NASA Langley Research Center, United States, and at the von Kármán Institute for Fluid Dynamics, Belgium, in April 1991 (AGARD R 776), and the recently completed FDP Working Group 11 on Rotary-Balance Testing for Aircraft Dynamics (AGARD AR 265); the reader may wish to consult the appropriate publications for more information in the general area of the conference.

All papers for this symposium were obtained by invitation. There was no general call for papers. Unfortunately, because of travel restrictions imposed during the Persian Gulf War, one of the organizations most active in the Maneuvering Aerodynamics technical area, NASA, was not able to be represented. Therefore, of the 19 invited papers, the two NASA papers (Papers No. 1 and 4) were withdrawn. In the place of Paper No. 1, opening comments by the chairman of the meeting were expanded, and for Paper No. 4, a video was presented showing recent flight tests of the X-31A experimental airplane. The original numbering system for the papers in the symposium program has been retained to avoid any confusion.

The organization of this volume warrants a brief comment. Usually, the symposium proceedings are published as soon after the symposium as possible, and at a later date, a Technical Evaluation Report on the meetings published as a stand-alone report. In the present case, we were fortunate to have a Technical Evaluator who not only did a superb job but also did it very quickly, and so, it is possible to include his report with the conference proceedings. It is hoped that this combination will make the present volume even more valuable and, for those who want an abbreviated review of the meeting and the related discussions, the Technical Evaluation Report (TER) can be used as a condensed version of the symposium. It may also serve as a guide to help the reader focus on specific papers he may be interested in reading in more detail.

The TER includes an Executive Summary which is an assessment of the meeting as a whole, a review of the individual papers that were presented, and finally, a summary of the Round Table Discussion that followed the presentation of the papers. Following the Technical Evaluation Report are the presented papers in their entirety and a manuscript of the Round Table Discussion.

Dr K.J. Orlik-Rückemann  
Program Chairman

## Avant-Propos

Ce symposium est la troisième réunion organisée par le Panel AGARD de la Dynamique des Fluides dans le domaine de l'aérodynamique pour la dynamique de vol des aéronefs. Elle fait suite aux réunions très fructueuses qui ont eu lieu à Göttingen en Allemagne au mois de mai 1985 (AGARD CP 386) et à Athènes en Grèce au mois de mai 1978 (AGARD CP 235). Le thème témoigne de l'intérêt croissant qui est porté aux manoeuvres rapides et de grande amplitude effectuées par les avions de combat à grande manoeuvrabilité à grands angles d'attaque. Il traite des écoulements instationnaires, décollés, tourbillonnaires et souvent non-linéaires qui sont représentatifs de telles conditions. Ce volume rend compte des développements récents en ce qui concerne les méthodes pertinentes d'analyse, de calcul, de concepts expérimentaux et de prédiction, ainsi que des techniques de contrôle des écoulements tourbillonnaires, l'importance des phénomènes diachroniques et le besoin d'essais dynamiques en soufflerie de niveau avancé, avec présentation des données aérodynamiques appropriées. Ces informations devraient permettre une meilleure compréhension des éléments de base de l'aérodynamique instationnaire nécessaires à l'amélioration de la prédiction du comportement dynamique des aéronefs manoeuvrant aux grands angles d'attaque.

La conférence est associée du point de vue technique à deux autres activités récentes du Panel, un cours spécial sur "La dynamique de vol des aéronefs aux grands angles d'attaque — expérimentation et modélisation" organisée au NASA Langley research center, USA, et à l'Institut von Kármán de la Dynamique des Fluides en Belgique au mois d'Avril 1991 (AGARD R776), et les travaux récents du groupe de travail 11 sur "Les essais à la balance rotative pour la dynamique de vol" (AGARD AR 265). Le lecteur souhaitant obtenir de plus amples informations concernant ces domaines devrait consulter les publications appropriées.

Toutes les communications présentées lors du symposium ont été remises sur invitation. Il n'a pas été lancé d'appel à publications. Malheureusement, en raison des restrictions de déplacement imposées lors de la guerre du Golfe, l'une des organisations les plus actives dans le domaine de la manoeuvrabilité par l'aérodynamique, la NASA, n'a pas pu envoyer de représentant à la réunion. Par conséquent, les 2 communications de la NASA sur les 19 appelées (les présentations Nos. 1 et 4) ont dû être retirées. Les observations préliminaires du Président ont été développées pour combler la lacune de la première présentation et en ce qui concerne la présentation No. 4, un film vidéo sur les essais en vol récents de l'avion expérimental X-31A a été projeté. Le système de numérotation des présentations adopté pour le programme du symposium a été retenu pour éviter toute possibilité de confusion.

Le plan de ce volume mérite une explication brève. Normalement, le compte-rendu d'un symposium est publié dans les plus brefs délais, suivi, à une date ultérieure et de façon indépendante, d'un rapport d'évaluation technique. Dans le cas présent, et à notre grand bonheur, ce rapport a été rédigé par un évaluateur technique qui a non seulement fait un excellent travail, mais qui l'a fait très rapidement, ce qui nous a permis de l'inclure au compte rendu du symposium. Nous espérons que cette présentation double ajoutera à la valeur du présent volume et que le rapport d'évaluation technique (TER) répondra aux attentes de ceux qui cherchent une revue abrégée du symposium et des discussions s'y rattachant, en tant que version condensée de la conférence. Il pourra aussi servir de guide au lecteur, en l'aidant à identifier certaines communications qui mériteraient une attention particulière de sa part.

Le TER comprend un résumé qui sert à la fois, d'évaluation globale de la réunion, de revue des présentations individuelles et, enfin, de sommaire des discussions qui ont eu lieu lors de la table ronde qui a clôturé cette manifestation. Le rapport d'évaluation technique est suivi des communications présentées en version intégrale et le manuscrit des discussions de la table ronde.

Dr K.J. Orlik-Rückemann

## Fluid Dynamics Panel

**Chairman:** Dr W.J. McCroskey  
Senior Staff Scientist  
US Army Aeroflightdynamics Directorate  
Mail Stop N 258-1  
NASA Ames Research Center  
Moffett Field, CA 94035-1099  
United States

**Deputy Chairman:** Professor Ir J.W. Slooff  
National Aerospace Laboratory NLR  
Anthony Fokkerweg 2  
1059 CM Amsterdam  
The Netherlands

### PROGRAMME COMMITTEE

Dr K.J. Orlik-Rückemann (Chairman)  
Applied Aerodynamics Laboratory  
Institute for Aerospace Research  
NRC, Bldg M-10  
Montreal Road  
Ottawa K1A 0R6  
Canada

Prof. R. Decuypere  
Ecole Royale Militaire  
Chaire de Mécanique Appliquée  
Avenue de la Renaissance 30  
1040 Brussels  
Belgium

M. l'Ing. en Chef B. Masure  
STCAN/BA  
8 Bd Victor  
00303 Paris Armées  
France

Dipl. Ing. P.W. Sacher  
Messerschmitt-Bölkow-Blohm GmbH  
FE11  
Postfach 80 11 60  
8000 München 80  
Germany

Dr Ing. G. Bucciattini  
Alenia-Aeritalia & Selenia S.p.A.  
Settore Aeronautica  
Gruppo Aerei Difesa  
C.P. 432  
10100 Torino  
Italy

Professor Dr T. Ytrehus  
Division of Applied Mechanics  
The University of Trondheim  
The Norwegian Inst. of Technology  
N-7034 Trondheim — NTH  
Norway

Professor Dr C. Çiray  
Aeronautical Eng. Department  
Middle East Technical University  
Inönü Bulvarı PK: 06531  
Ankara  
Turkey

Dr D. Woodward  
Superintendent AE2  
Experimental Aerodynamics and  
Applications Div. (F)  
X80 Building  
Royal Aerospace Establishment  
Farnborough, Hants GU14 6TD  
United Kingdom

Dr K.L. Kushman  
Director of Technology  
AEDC/DOT  
Arnold AFB, TN 37389-5000  
United States

Dr W.J. McCroskey  
Senior Staff Scientist  
US Army Aeroflightdynamics Directorate  
Mail Stop N258-1  
NASA Ames Research Center  
Moffett Field, CA 94035-1099  
United States

### PANEL EXECUTIVE

Dr W. Goodrich

**Mail from Europe:**  
AGARD—OTAN  
Attn: FDP Executive  
7, rue Ancelle  
92200 Neuilly-sur-Seine  
France

**Mail from US and Canada:**  
AGARD—NATO  
Attn: FDP Executive  
Unit 21551  
APO AE 09777

Tel: 33 (1) 47 38 57 75  
Telex: 610176 (France)  
Telefax: 33 (1) 47 38 57 99

# Contents

	<b>Page</b>
<b>Recent Publications of the Fluid Dynamics Panel</b>	iii
<b>Foreword</b>	v
<b>Avant-Propos</b>	vi
<b>Fluid Dynamics Panel</b>	vii
	<b>Reference</b>
<b>Technical Evaluation Report</b> by G.N. Malcolm	<b>TER</b>
 <b>SESSION I – HIGH ANGLE-OF-ATTACK AERODYNAMICS – I</b> Chairman: K.J. Orlik-Rückemann	
<b>Paper 1 withdrawn</b>	
<b>X-31 Enhancement of Aerodynamics for Maneuvering beyond Stall</b> by H. Ross	2
<b>Aerodynamic and Flowfield Hysteresis of Slender Wing Aircraft Undergoing Large-Amplitude Motions</b> by R.C. Nelson, A.S. Arena, Jr and S.A. Thompson	3
 <b>SESSION II – HIGH ANGLE-OF-ATTACK AERODYNAMICS – II</b> Chairman: P.W. Sacher	
<b>Paper 4 withdrawn</b>	
<b>Prediction of Aerodynamic Phenomena Limiting Aircraft Manoeuvrability</b> by A. Ferretti, A. Bartoli and A. Salvatore	5
<b>Parametric Effects of some Aircraft Components on High-Alpha Aerodynamic Characteristics</b> by L. Visintini, R. Pertile and A. Mentasti	6
 <b>SESSION III – DYNAMIC EXPERIMENTS – I</b> Chairman: M.E. Beyers	
<b>Non-Linear Airloads Hypersurface Representation – a Time Domain Perspective</b> by J.E. Jenkins and E.S. Hanff	7
<b>Analysis of Unsteady Force, Pressure and Flow-Visualization Data for a Pitching Straked Wing Model at High Angles of Attack</b> by A.M. Cunningham, Jr and R.G. den Boer	8
<b>Measurement of Derivatives due to Acceleration in Heave and Sideslip</b> by C.O. O'Leary, B. Weir and J.M. Walker	9

Reference

**SESSION IV – DYNAMIC EXPERIMENTS – II**

Chairman: R.A. Verbrugge

<b>Wind Tunnel Force Measurements and Visualization on a 60-Degree Delta Wing in Oscillation, Stepwise Motion and Gusts</b> by P.-A. Torlund	10
<b>Caractérisation de Phénomènes Aérodynamiques Instationnaires à Grande Incidence</b> par O. Renier	11
<b>Scale Model Measurements of Fin Buffet due to Vortex Bursting on F/A-18</b> by C.A. Martin and D.H. Thompson	12
<b>X-31, Discussion of Steady State and Rotary Derivatives</b> by W. Kraus	13
<b>Use of a Stepwise Regression Techniques and Kinematic Compatibility for the Analysis of EAP Flight Data</b> by A.R. Perkins	14

**SESSION V – STABILITY AND CONTROL**

Chairman: D. Multhopp

<b>Aerodynamic Control of Fighter Aircraft by Manipulation of Forebody Vortices</b> by G.N. Malcolm and T.T. Ng	15
<b>Forebody Vortex Control Aeromechanics</b> by R.W. Guyton, R.F. Osborn and S.P. LeMay	16
<b>Dynamic Wind Tunnel Tests on Control of Forebody Vortices with Suction</b> by A.J. Ross, E.B. Jefferies and G.F. Edwards	17
<b>Transformation of Flightmechanical Design Requirements for Modern Fighters into Aerodynamic Characteristics*</b> by P. Mangold	18
<b>Aeroservoelastic Stability of Aircraft at High Incidence**</b> by J. Becker	19
<b>Round Table Discussion</b>	RTD

\* Contribution from the Flight Mechanics Panel.

\*\* Contribution from the Structures and Materials Panel.

## TECHNICAL EVALUATION REPORT

Mr. G. N. Malcolm, Technical Evaluator  
Eidetics International, Inc.  
3415 Lomita Blvd.  
Torrance, CA 90505 USA

### 1.0 EXECUTIVE SUMMARY

The purpose of this symposium, as suggested by its title, "Maneuvering Aerodynamics," was to present a variety of technical papers with a focus on aerodynamics and related subjects that are important to improve the ability of fighter aircraft and missiles to maneuver effectively in combat. Implied in this theme is a particular emphasis on high-angle-of-attack aerodynamics.

#### 1.1 Introduction

The organizer and chairman of the symposium, Dr. K. J. Orlik-Rückemann, set the tone of the meeting with his opening background comments. He identified a number of technical elements that will require special attention in the future in order to meet the challenges of the 1990's and beyond with more advanced and highly agile aircraft and missiles.

A summary of his opening comments is appropriate here to set the tone for the following review and discussion. Dr. Orlik-Rückemann suggests the following topics to be considered in our future efforts to advance the state of the technology for maneuvering aircraft, which implies high angle of attack rapid maneuvers.

#### (A) Flying At High Angles of Attack and Non-Zero Sideslip

- Strongly separated flows
- Forebody and leading-edge vortices
- Vortex burst, flow interactions, and buffet
- Unsteady flow, time lags
- Asymmetric flows
- Aerodynamic cross-coupling
- Strong nonlinearities

#### (B) Performing Rapid Angular Motions

- High angular rates
- Large-amplitude motions
- Transient maneuvers
- Motion-induced aerodynamic effects
- Dynamic lift and stall
- Forebody vortex control
- Leading-edge flow control
- Advanced experimental and computational methods

#### (C) Expanded Aerodynamic Data Base

- Analytical and computational predictions generally not available
- Reliance on experimental methods
- Increasing role of dynamic data
- Both oscillatory and rotary experiments needed
- Interference effects
- Complex motions
- Linear vs nonlinear techniques
- Better understanding of flow physics (detailed flow measurements)
- Effects of Re, M, rotation rates, etc.
- Correlation with flight (sub-scale and full-scale)

#### (D) Enhanced Aerodynamic Controls

- Conventional controls ineffective
- Forebody blowing (jets, slots), suction
- Forebody strakes (conformal, flat, chines, etc.)
- Moving canard surfaces
- Leading-edge blowing
- Active controls

#### (D) Unorthodox Configurations

- Strong configuration dependence
- Canards (closely coupled)
- Three-surface configurations
- High-fineness ratio fuselage and forebodies
- Highly-swept wings
- Vertical tail(s) - tail buffet

#### (E) Mathematical Modelling

- Prediction of dynamic behavior
- Aircraft design and/or modifications
- Design of flight control systems
- Input to flight simulators
- Planning flight tests
- Estimation of aerodynamic parameters

While not all of these are addressed in this symposium, many of them are subjects of active research and will be discussed in the symposium review and commentary.

### 1.2 Conference Summary

The range of subjects presented in this symposium

suggests that there is a broad technology base that must be addressed in order to develop fighter aircraft and weapons that will have improved agility and maneuverability. Agility is often associated only with maneuvering in the post-stall flight regime. While the post-stall regime is an important part of an enhanced flight envelope and, perhaps, the regime we know the least about, it is not the only arena of interest. Improved combat tactics that rely on increased control power and, therefore, increased maneuverability or agility are not solely dependent upon the ability to operate in the post-stall regime. Current aircraft are generally limited to angles of attack below their maximum lift capability because of a lack of lateral/directional stability or controllability in yaw or pitch. There are exceptions, but all existing fighter aircraft lack controllability at high angles of attack because of the ineffectiveness of conventional controls. If this envelope can be expanded to angles of attack near maximum lift, and if there is also adequate control power for increased maneuverability, significant tactical advantage in combat will be realized.

The symposium covered a broad range of topics grouped into the following categories for discussion in the review of the individual papers: (1) Basic Experiments/Basic Research Configurations with High Amplitude Motions, (2) Forced-Oscillation and Rotary-Balance Test Techniques, (3) Experiments on Operational / Experimental Aircraft Configurations, (4) Aerodynamic Prediction and Parameter Estimation Methods, (5) Forebody Vortex Control Technology, (6) Flight Mechanics and Structures Considerations, and (7) Flight Tests of the X-31A. It is also convenient to use this grouping as a framework for the review comments on the meeting as a whole.

In the past, static and dynamic wind tunnel tests using small-amplitude oscillation techniques were sufficient to determine the aerodynamic characteristics of aircraft configurations under development. The primary purpose for forced-oscillation tests was to determine dynamic stability characteristics. This was in an era where the objective was to acquire a high sustained turn rate and a low sustained turn radius and to have dynamic stability sufficient to damp any perturbations to the steady motion. Modern combat tactics, however, place more emphasis on maneuverability and achieving attained or instantaneous turn rate and the ability to point and shoot, not necessarily to close on the target from a rear position, where sustained turn rate and small turn radius were the key factors. The potential for using modern weapons such as all-aspect IR missiles from nearly any position requires an aircraft that can change the maneuver plane at will and can acquire the target before his opponent. The maneuvers to accomplish this require a greatly expanded flight envelope and aerodynamic control capability.

#### 1.2.1 Basic Experiments/Research Configurations

In order to appreciate the aerodynamic phenomena that are fundamental to the successful development of highly agile aircraft, it is necessary to acquire a fundamental knowledge of the fluid mechanics associated with this flight regime. This can best be accomplished by

beginning with experiments and related computations using simple configurations. Until recently, there was a lack of complete understanding of the aerodynamics of even simple configurations undergoing the high rates of rotation associated with high-agility maneuvers.

As outlined by the symposium chairman, there are many areas that will require increased emphasis if we are to achieve the goal of increased agility for present and future fighter aircraft. Understanding high angle-of-attack flows, both steady and unsteady components, is essential. There are many organizations who are performing experimental and computational research programs to increase our understanding of the fundamental flow physics, and in particular, of the impact of high rate motions on the interaction of the configuration and the surrounding flowfield. There are several papers in this symposium on studying aerodynamic phenomena associated with simple delta-type wing planforms undergoing high-amplitude pitch and roll motions, using flow visualization and force and pressure measurements. Papers 3, 8, and 10 provide some very good insight into the complex time-dependent flowfields that must be appreciated. The effects of time lags associated with vortex breakdown are especially important. Delays in the flowfield response to airframe motions must be accounted for in modeling the aerodynamics for simulation and for prediction of flight characteristics.

Experiments with simple models must be continued for acquiring the basic understanding essential for the development of adequate prediction methods and for assessing the magnitude of the unsteady or time-lag effects. It is also important to expand these efforts to more realistic configurations, where there are more complex interactive flowfields with vortices from forebodies, wing leading-edge extensions or canards, and the wing.

#### 1.2.2 Forced-Oscillation and Rotary-Balance Test Techniques

One of the requirements for acquiring appropriate data to represent the dynamic as well as static aerodynamics is to be able to perform the proper wind tunnel experiments. The development of new test techniques and test facilities is essential in order to determine the appropriate parameters. This is reflected in the increased emphasis to perform dynamic experiments besides the standard small-amplitude forced-oscillation rotational motions around the pitch, roll, and yaw axes to acquire dynamic stability derivatives.

Many researchers have developed capabilities for high-amplitude ramp motions in pitch (Papers 3, 8, and 10 are examples) to simulate rapid pitch-up and pitch-down maneuvers. Others have developed large-amplitude roll oscillation rigs to determine the nonlinear roll response characteristics to high-amplitude and high-rate roll motions (Papers 3 and 7). There is also increasing interest in the effects of unsteady aerodynamic components associated with high rates of change of angle of attack and sideslip  $\dot{\alpha}$  and  $\dot{\beta}$  or the so-called translational or plunging effects (Paper No. 9 is an



example). For conventional maneuvers at low angles of attack, the rotational effects, i.e., pitch rate ( $q$ ) and yaw rate ( $r$ ) are considered to overshadow the unsteady  $\dot{\alpha}$  and  $\dot{\beta}$  effects and they can be ignored in simulation models. This does not appear to be the case for the more aggressive maneuvers associated with high-agility aircraft. Testing capability to acquire the unsteady effects directly are being developed.

With the importance of nonlinear terms (variation of the aerodynamic coefficients with angle of attack and sideslip and rotation rates), it is more important to develop testing techniques that are close to producing the motions of interest, where superposition of individual experiments assuming linearity can no longer be used. This also presents formidable problems in how to mathematically represent the aerodynamic reactions, both for data reduction purposes and for inclusion in aerodynamic models for simulation. One of the most difficult challenges is to model the time-lag responses of the aerodynamic coefficients to the airframe motion variables. These are dependent upon motion frequency and amplitude, and often contain hysteresis effects. Developing techniques for measuring dynamic hysteresis effects and modeling them properly are one of the toughest challenges of the future, but in the new era of highly nonlinear aerodynamics the challenge must be met if we are to reliably determine the aerodynamic response of future fighter configurations.

In addition to the unsteady aerodynamics, steady aerodynamics in the presence of a pure rotational motion about the velocity vector (loaded roll) or a rolling motion around the flight path are also of prime interest. In the past, a conventional maneuver to change the maneuver plane would be to pitch down to near zero angle of attack, where roll capability is maximum, roll to the desired roll position or bank angle and then pitch up to the appropriate angle of attack to either hold a target in view or to turn. In a high-agility aircraft, this maneuver would be accomplished by rolling directly around the velocity vector without decreasing angle of attack. This motion is essentially the same motion as a spin motion, except it is controlled rather than out-of-control. The rotational flowfield is the same, and can be reproduced in the wind tunnel by a rotary-balance apparatus.

Rotary-balance experiments were used primarily in the past to determine the aerodynamic coefficients of aircraft configurations in a spin motion in order to predict equilibrium spin conditions and spin recovery techniques. This apparatus is now a key experimental apparatus to ascertain the aerodynamics of a controlled loaded roll maneuver. The aerodynamic coefficients are typically very nonlinear with rotation rate in roll around the velocity vector and cannot be determined properly in a rotational motion around the airplane body axes. This test technique is in active use in many NATO countries. AGARD Advisory Report 265 documenting the work by AGARD Working Group 11 on Rotary-Balance Testing for Aircraft Dynamics describes in detail the apparatuses and test methods of all of the participating countries.

A discussion of new forced-oscillation test techniques is

presented in Paper No. 9, and recent experiments conducted with rotary-balance apparatuses are presented in Papers 6 and 11. The effects of component buildup and an attempt to simulate higher Reynolds number on a trainer configuration in a rotary motion are described in Paper No. 6. A unique rotary-balance apparatus which also measures oscillatory terms is discussed in Paper No. 11.

### 1.2.3 Experiments on Operational/Experimental Aircraft Configurations

Unsteady aerodynamics associated with high angle of attack flight conditions can have an impact on the structural integrity of an aircraft as well as its performance. Configurations with twin vertical tails suffer from rather severe buffeting driven by the unsteady flowfield produced by bursting vortices from the wing leading-edge extensions. The F/A-18 is the best known example of this problem. While a fix has been adopted for the F/A-18, it is important to understand the fluid mechanics of this phenomenon and how to avoid it in future aircraft. Research is ongoing, including flow visualization and unsteady force and pressure measurements to determine the important factors that influence the magnitude and frequency of the unsteady loads. Paper No. 12 reviews wind tunnel and water tunnel experiments on the F/A-18 providing some insight on the LEX burst phenomena and the relationship to tail buffeting.

The X-31A experimental aircraft developed by Rockwell International and MBB is now in the initial stages of flight testing. Paper No. 13 provides a thorough discussion of the design process and wind tunnel testing that has been conducted in order to support the development of this unique airplane. This aircraft was developed specifically to demonstrate the technical feasibility and tactical utility of high AOA maneuvering.

### 1.2.4 Aerodynamic Prediction and Parameter Estimation Methods

The prediction of the aerodynamic characteristics of fighter aircraft at high angles of attack is a difficult task. While some CFD methods have shown success in computing the steady flow characteristics around actual aircraft configurations such as the NASA study of the F/A-18, there are no reliable computational methods to calculate the highly separated flows associated with aircraft at high angles of attack, particularly unsteady or rate dependent flowfields. Many researchers are working to develop methods that can be used in preliminary design to estimate the aerodynamic forces and moments associated with high angles of attack. One of the challenges is to accommodate the complexity of separated and vortex flows, even for static cases. An even more complex problem is how to represent the dynamic effects, particularly since these effects are more prominent than ever before, because of the high rotation rates associated with increased agility-type motions. Papers No. 5 and 7 discuss some of the problems and proposed methods for dealing with them. Paper No. 14 describes an investigation of a method to extract nonlinear aerodynamic coefficients from flight

test data, which will be required if we are to be able to compare flight test derived aerodynamics to wind-tunnel test results or predictions.

### 1.2.5 Forebody Vortex Control

Controllability requirements at high angles of attack (high AOA) are difficult to meet with conventional control surfaces. Other techniques are being evaluated for increased control power at high AOA, such as thrust vectoring and forebody vortex control. One of the potential advantages of forebody vortex control is that the forebody vortices become stronger as angle of attack increases in contrast to the available control power from conventional control surfaces such as the rudder which is decreasing. One of the requirements for a highly agile aircraft at high angles of attack is robust yaw control, which translates into robust roll control around the velocity vector. Several methods of vortex control are described in this symposium in Papers 15, 16 and 17 including pneumatic techniques such as blowing and suction and rotatable miniaturized forebody tip strakes.

The state of the art of forebody vortex control is advancing rapidly. Forebody strakes and possibly blowing slots or jets are planned for flight evaluation in the future on the NASA F/A-18 HARV. Full-scale wind tunnel tests are in progress at NASA Ames on an F/A-18 aircraft in the Ames 80 x 120-ft wind tunnel to evaluate not only the baseline aerodynamic characteristics at full-scale Reynolds numbers, but to measure the aerodynamic forces and moments created by forebody strakes, forebody aft blowing jets and tangential slots. Sub-scale wind tunnel tests are continuing as well with several configurations including the F/A-18, F-16, X-29A and generic configurations to further advance the state of forebody vortex technology. This area of research has significant interest in many NATO countries because of its potential benefits for high angle of attack control.

Thrust vectoring is another means of producing pitch and yaw control power and this technique was discussed briefly in the context of its application to the X-31A experimental aircraft in Paper No. 2. Flight tests are also underway at present with the F/A-18 HARV at NASA Ames Dryden Flight Research Center to investigate the benefits of thrust vectoring. A modification to the flight test airplane provides for thrust vectoring both in pitch and yaw. It seems likely that some combination of forebody vortex control and thrust vectoring will be used in the future for the required levels of controllability.

### 1.2.6 Flight Mechanics and Structural Considerations

Papers were invited from the AGARD Flight Mechanics Panel and the Structures and Materials Panel to discuss the impact of increased maneuverability requirements on these two technology areas. Papers 18 and 19 discuss these subjects. One of the problems is to transform the flight mechanics design requirements into aerodynamic characteristics, particularly with the inclusion of dominant dynamic effects. In the past, many of the dynamic terms were sufficiently small compared to the static terms in the equations of motion that they could

be ignored. At high angles of attack with accompanying high rates of motion, the dynamic terms cannot be ignored. It is difficult to predict the flight mechanics behavior based solely on static aerodynamic coefficients when, in fact, the actual flight behavior is heavily dependent on dynamic contributions and automatic control system augmentations to the basic aerodynamics. It has become increasingly important for the aerodynamicist, the flight mechanicist and the developer of the automatic flight control system to work together in the preliminary design and development stages.

It has also become imperative to include aeroservoelastic effects in the evaluation of the stability of an airframe at high angles of attack. Methods employed for low angles of attack which depend on linear unsteady aerodynamic theory associated with level flight will not be adequate. Paper No. 19 discusses a possible methodology to predict nonlinear aeroservoelastic contributions.

### 1.2.7 Flight Tests of the X-31A

A review of the development of the X-31A flight simulation and an update of the flight test program was presented in Paper No. 2. Performance levels were discussed and the dependency of the combat benefits on high agility and accompanying high angle of attack flight are evaluated. This program will provide an opportunity to compare flight test and wind tunnel results in a flight regime that has never been compared before. Essential will be the ability to record and analyze flight test data that can be used to compare to predictions, where they exist, and wind tunnel data. It is not clear how well dynamic data can be extracted from X-31A flight tests. Nor is it clear whether the X-31A flight simulation model has incorporated the appropriate dynamic terms associated with the free-flight motions. Careful analysis of the flight test data for dynamic data, particularly time lags and hysteresis, should be done to shed some light on how important these terms really are in full-scale flight.

### 1.2.8 General Comments

There is widespread interest in "maneuvering aerodynamics" and all of the technology disciplines that relate to highly agile aircraft. This symposium focused primarily on the aerodynamic aspects of highly agile aircraft and was very timely and very valuable. The next generation of aircraft will likely include specifications for significantly increased agility, both for offensive and defensive combat tactics. It will be very important that the aircraft designer have as much information available to him as possible during the early stages of development. Continuing the process of sharing technology in this area through timely symposia or, perhaps, working group activities should result in the ability to design better aircraft in the future. AGARD symposia such as this should be continued, at least every three years, to support the process of developing improved prediction and

experimental methods pertinent to high-angle-of-attack, high-maneuverability flight.

## 2.0 REVIEW OF PRESENTED PAPERS

The conference program and presentations were generally organized around three general topics, (1) High Angle of Attack Aerodynamics, (2) Dynamic Experiments, and (3) Stability and Control. The primary purpose of this technical review is not to systematically critique each paper and pass judgement on its relative quality or importance. The real purpose is to point out the more relevant points made by each paper in the overall context of "maneuvering aerodynamics" including the relation of the papers to each other, and to offer some comments and discussion related to the open session following the formal presentation of the papers.

In this review, each of the papers will be discussed briefly but not in the same order as they were presented. The purpose is not to critique or judge them comparatively, but to provide a brief summary of the contents to make the technical evaluation reasonably self-contained. An attempt is made to group them more closely by subject and to provide a general view of the work that has been performed.

### 2.1 Basic Experiments/Research Configurations with High Amplitude Motions

Papers were presented by three authors with the basic objective of understanding the flow physics on simple delta or double-delta wing configurations undergoing high amplitude oscillatory motions either in pitch or roll.

**Paper No. 3**, by Nelson, Arena and Thompson (Notre Dame University, USA) examined the fundamental flow dynamics in wind tunnel tests of a simple 70° delta wing undergoing pitch oscillations from 0° to 60° and an 80° delta wing undergoing a limit cycle roll oscillation (wing rock). The experiments provided measurements of aerodynamic loads, surface pressures, and flow visualization with measurements of vortex position and vortex breakdown location as a function of the model motion. The primary purpose was to understand the relationship between the motion of the model and the characteristics of the flowfield in response to the motion. The pitch experiments were designed to investigate hysteresis in the positions of the leading edge vortex cores and vortex breakdown locations relative to static locations observed on configurations undergoing large-amplitude oscillatory motions. Previous work had concluded that for unsteady motions, where breakdown is not present, the aerodynamic characteristics behave in a quasi-static manner. However, for ranges of amplitudes where breakdown is present over the wing, hysteretic behavior is observed resulting in substantial overshoot in the aerodynamic forces for oscillatory or transient pitching maneuvers. The interest in this phenomenon is to possibly exploit the increased lift for increased agility.

The results of these experiments showed that pitch oscillations over a range of 0° to 30° produced virtually

no hysteresis and the forces and pressures fluctuated in phase with the pitching motion, the reason being that the leading edge vortex burst locations were aft of the wing trailing-edge. For the wing oscillations from 2° to 60° large overshoots compared to the steady state values of normal force and upper surface suction pressures were observed on the upstroke and large undershoots on the downstroke. The amount of overshoot increases with increased frequency of oscillation. The paper shows detailed pressure distributions in both chordwise and spanwise directions with oscillation amplitude, illustrating the movement of the vortex core position with model motion.

The experiments conducted on the 80° delta wing revealed important information about the causes of wing rock motions. Experiments show that the variation of the leading edge vortex core position above the wing with roll angle varies considerably comparing a static wing to one undergoing roll oscillations. The dynamic positions of the vortices exhibit a time lag phenomenon which account for hysteresis effects. The position of the vortex above the wing greatly affects the wing pressure distribution and, consequently, the rolling moment. The time lag in the normal position (above the wing) of the wing vortices with respect to the static position is the primary cause for wing rock. Since wing rock can occur when vortex breakdown is behind the wing, vortex breakdown is not the cause of wing rock. In fact, it is observed that vortex breakdown actually provides a damping moment, resulting in the required damping to limit the buildup in roll oscillation amplitude.

**Paper No. 10**, by Torlund (FFA, Sweden) also investigates the effects of pitch motions on a delta wing. He conducted wind tunnel experiments measuring forces and moments and using flow visualization on a 60° delta wing in oscillation and stepwise motions and in gusts. Time histories and aerodynamic derivatives of the normal force and pitching moment were measured for the oscillatory motions in pitch with 4° and 8° amplitudes at 0° to 35° angle of attack. Stepwise motions up to 90° angle of attack with both positive and negative steps of 20° starting at 10° angle of attack and the full 90° in one step were also investigated. Responses to the stepwise motions were compared to those predicted from the results of the oscillation tests. They correspond well for low angles of attack but differ significantly at moderate to high angles of attack. Long time delays (up to 30 to 40 chord passages of the flow) in the formation of the leading-edge vortices and in the accompanying normal force and pitching moment result when the dynamic motion passes the angle of attack where the vortex burst location reaches the model apex at a steady state condition. The amount of the delay is strongly dependent on the reduced frequency of the motion.

Results from gust experiments were compared to results from the stepwise motions and similar time delays were observed. The combination of these two experiments provide the potential for means to separate  $\dot{\alpha}$  and  $q$  effects. Results appear to be relatively independent of

Reynolds number differences. A more detailed understanding of the effects of the time delays, such as hysteresis, can be obtained by consulting the paper. The important message from these experiments is the appreciation of the long time delays that are encountered in high amplitude motions that cannot be predicted on the basis of small amplitude oscillatory data. The nonlinearities and hysteresis effects can only be assessed by testing the model in the angle of attack and rotation rate combinations that are of interest.

**Paper No. 8**, by Cunningham (General Dynamics, USA) and den Boer (NLR, Netherlands) is the latest paper in a series dealing with the results from an extensive and detailed set of experiments in the NLR 2.25m x 3.0m Low Speed Tunnel on a pitching straked-wing (double-delta with 76° and 40° sweep) model. The model was oscillated about mean angles of attack ranging from -4° to 48° with amplitudes varying from 2° to 18°, including some experiments at sideslip angles of -5° and +5°. Force, pressures and flow visualization data were obtained. A unique method of simultaneously displaying pressure and flow visualization data was used to enhance the understanding of the flow physics, particularly the relationship between the off-surface flowfield and the surface pressures, during the oscillatory motions. A large matrix of mean incidence, amplitude and frequencies were tested to provide for systematically separating the effects of each of these parameters. The regions of linear and nonlinear force and moment development and the reasons for the differences related to the vortex formation and breakdown are clearly shown.

In the mid-incidence range of angle of attack from 8° to 38°, lag in vortex bursting on pitch-up or the persistence of vortex burst on pitch-down was shown to significantly affect the pressure distributions and resulting forces and moments, including evidence of hysteresis with angle of attack variations. For the high incidence range from 22° to 50°, the persistence of vortex burst to angles of attack beyond static stall was shown to be responsible for dynamic lift overshoot with pitch up and persistence of stalled flow was responsible for dynamic lift undershoot for pitch down. Tests at non-zero sideslip revealed interesting nonlinear effects on rolling moment coefficient. This paper presents an extremely detailed explanation of the relationship of the flowfield to the surface pressures and forces for a wide matrix of pitching motion variables and should be read in detail to fully appreciate the complexity of the flowfields that we must deal with.

## 2.2 Forced-Oscillation and Rotary-Balance Test Techniques

Three papers were presented describing experiences with a new forced-oscillation apparatus at the RAE and the challenges of measuring aerodynamic data on rotary-balance rigs at AerMacchi and ONERA.

**Paper No. 9**, by O'Leary and Weir (RAE, UK), presents and discusses a new oscillatory rig developed at

the RAE for the measurement of derivatives due to acceleration in heave and sideslip, or  $\ddot{\alpha}$  and  $\ddot{\beta}$  derivatives. Wind tunnel tests were performed with the two RAE High Incidence Research Models (HIRM 1 and 2). The paper describes in some detail the rig, the models, and the initial tests and discusses the test results. The requirement for such a rig is based on the fact that with swept and delta wing configurations flying at high angles of attack, there is an increased importance of  $\ddot{\beta}$  in determining the directional stability characteristics. Rotational experiments, such as the traditional forced-oscillation experiments, where the model is oscillated in pitch or yaw motions cannot separate the effects of acceleration and rotation. A separate heaving or sideslip motion rig is required to measure  $\ddot{\alpha}$  and  $\ddot{\beta}$  effects.

The paper describes the operational features of the rig and demonstrates its capability with a presentation of aerodynamic data on HIRM 1 and HIRM 2. For these configurations,  $\ddot{\alpha}$  effects are small for angles of attack up to 16° regardless of the reduced frequency. At higher angles  $\ddot{\alpha}$  effects are significant but decrease in magnitude with increasing frequency. At angles of attack up to 25° the  $\ddot{\beta}$  effects are minor but at higher angles, similar to  $\ddot{\alpha}$ , the effects are larger but decrease with increased oscillation frequency. The paper discusses the effects of the foreplanes (canards) and the vertical tail (fin). Comparisons are made between (1) the results from typical "rotary" experiments which provide combined and inseparable acceleration and rate derivatives, and (2) the individual acceleration and rate derivatives determined from translational oscillation experiments and "whirling-arm" experiments, respectively. For these experiments, it was concluded that  $\ddot{\beta}$  effects are more important at high angles of attack than for low angles of attack. Serious consideration should be given to including these acceleration derivatives in aerodynamic mathematical models of combat aircraft for simulation and for flight.

**Paper No. 6**, by Visintini, Pertile, and Mentasti (AerMacchi, Italy) is a review of wind tunnel test data on an advanced trainer configuration with the purpose of defining and understanding the aerodynamics associated with high angles of attack (to 90°) including effects of model component buildup and forebody fineness ratio and cross section shape. Examples are also presented related to complexities of high angle of attack wind tunnel testing, including forebody symmetries and problems of simulating Reynolds number with artificial transition strips. Both static and rotary-balance test results are discussed.

Component buildup (or breakdown) tests showed the dependence of static stability in pitch on the LEX and body "shelves" and the importance of the forebody shape on directional stability. Rotary data showed two distinct ranges for the way aerodynamic coefficients vary

with angle of attack. In the 20° to 40° range the aerodynamic data show regular and fairly linear behavior with rotation rates, which means the aerodynamic wind-axis roll characteristics can be reasonably well represented by roll damping derivatives, at least at rotation rates near zero. Above 45° AOA, however, the wind-axis rolling moment is highly unstable and nonlinear, dominated by forebody vortex instability and couplings with natural forebody vortex asymmetry.

The primary effects of forebody shape on roll damping appear at angles of attack from approximately 50° to 70°. In general, the main contribution to high AOA behavior has been identified and for the class of shapes of this study the forebody shape is of utmost importance only above 40° AOA. Large couplings occur between sideslip, rotation, and longitudinal aerodynamic coefficients. For this class of airplane, it appears that a forebody of circular cross section leads to minimum pitching moment coupling with sideslip angle and roll rate.

Utilizing transition strips to simulate high Reynolds number flows on fighter-class aircraft models at high angles of attack has been investigated and variations in the wind tunnel data for common coefficients is substantial. A methodology needs to be developed to make use of this capability and to be able to rely on it. Most tests are done on the rotary balance without any type of transition strips.

However, most tests provide data obtained at Reynolds number that are much lower than flight and the experimenter needs to be cautious in the manner in which they are extrapolated to flight test. More work needs to be done, in general, to understand if and how transition strips can be used to simulate higher Reynolds number conditions, particularly at high angles of attack where the forebody plays a dominant role.

Paper No. 11, by Renier (ONERA, France) discusses two apparatuses used at ONERA in Lille to perform dynamic tests at high angles of attack. One is the unique rotary-balance system which can provide the usual rotary-balance data with constant angle of attack and sideslip, i.e., pure rotational motion about the wind axis and also oscillatory data by using the capability to incline the rotational axis of the apparatus with respect to the wind axis, thereby producing a sinusoidal oscillation in angle of attack and sideslip in conjunction with the rotational motion. This produces unsteady forces and moments in the presence of steady force and moment contributions resulting from the rotation around the velocity vector. This technique provides an alternative approach to the conventional forced-oscillation test rigs where the unsteady aerodynamics result from small-amplitude oscillations in a planar motion, similar to that discussed in the paper by O'Leary.

A second apparatus capable of producing large amplitude oscillations or ramp motions in pitch, yaw, or roll was also described. The application of this apparatus is to investigate dynamic aerodynamic effects of motions related to those expected from highly agile aircraft which will result in high angles of attack and sideslip

and high rates. The utilization of these results in aerodynamic modelling is also discussed.

### 2.3 Experiments on Operational/Experimental Aircraft Configurations

Two papers were presented describing experiments on the F/A-18 and the X-31A configurations over a large angle of attack range. The discussions include both water tunnel and wind tunnel results.

Paper No. 12, by Martin and Thompson (ARL, Australia) reviews wind tunnel tests to investigate the characteristics of tail buffet on the F/A-18 due to bursting of the leading-edge extension (LEX) vortices and water tunnel tests to visualize the LEX vortices bursting phenomena with and without a LEX fence, comparing burst location with measurements from wind tunnel and flights tests and to determine the effect of engine inlet flow rate on the LEX vortex burst location.

The wind tunnel tests used surface mounted pressure transducers on the wing below the LEX vortex burst location and on the fin (vertical tail) to measure the magnitude and frequency of the pressure fluctuations associated with burst phenomena. The burst vortex contains energy over a moderately narrow frequency range and the center frequency is linearly proportional to the free stream velocity. The vortex burst location moves forward and the burst pressure field frequency decreases with increasing angle of attack. The burst frequency also changes when the fin is removed, showing that the burst characteristics are sensitive to the downstream pressure field, i.e., whether the fin is there or not. Fin bending mode response is strongly coupled to the burst frequency with maximum fin response occurring when the burst frequency is close to the natural frequency in bending of the fin.

With the LEX fence in place, the amplitude of the unsteady pressures was reduced significantly, while the energy is spread over a wider frequency range, resulting in reduced fin response. Flow visualization showed there is little difference in the location of vortex burst but that there is a second vortex emanating from the leading edge of the LEX in the vicinity of the fence. These two vortices interact and burst simultaneously.

Water tunnel tests on a 1/48-scale F/A-18 model confirmed the location of LEX vortex burst with angle of attack and also showed that the amount of flow into the engine inlet can also have an effect on the vortex burst location, with the vortex burst location moving aft with increased inlet flow.

Paper No. 13, by Kraus (MBB, Germany) discusses some of the early configuration definition work for the X-31 aircraft, and experimental aircraft developed by Rockwell and MBB to explore the high-angle-of-attack arena pertinent to highly agile or supermaneuverable fighters of the future. The paper reviews results from static and dynamic wind tunnel tests where a large matrix of configuration components was systematically evaluated. This aircraft is designed to have natural aerodynamic stability throughout the angle of attack range (up to 70°) except for low angles of attack where

it is statically unstable in pitch for performance reasons. In some critical regions in which the natural stability cannot be achieved, artificial stability is provided by moving control surfaces with sufficient motion remaining to provide sufficient control power for maneuvers. Static wind tunnel tests were conducted on a wide variety of configurations with many different wings, tails, canards, vertical fins, ventral fins, forebodies, and nose and inlet strakes. The effects of all of these configuration variations are discussed.

Dynamic tests, consisting of rotary-balance and free-spinning tests at NASA Langley were also conducted to evaluate the stability characteristics in a rotational motion and comparisons were made between predictions of spin motions based on rotary balance data and those observed in the free-spin tests. In the normal flight regime the aircraft is well-damped in roll and yaw. Above stall, about 40° AOA, roll and yaw stability decrease and become undamped, resulting in the possibility of departure above 60° AOA with an unaugmented airplane. However, with roll input controls, the autorotative moments can be counteracted. The only known spin condition is at an AOA around 86°. Comparisons between predicted spin characteristics and those observed in the free-flight motion in the spin tunnel showed very similar behavior. Effects of wing trailing-edge flap deflection and canard settings on the spin characteristics are also noted.

#### 2.4 Aerodynamic Prediction and Parameter Estimation Methods

Two papers describing work on prediction of nonlinear aerodynamic characteristics, including unsteady effects at high angles of attack and one paper describing a new approach to parameter identification methodology applicable to the nonlinear regime of high-angle-of-attack flight are discussed.

**Paper No. 7**, by Jenkins (WL/FIGC, USA) and Hanff (IAR, Canada) addressed the problem of how to represent the highly nonlinear and unsteady airloads experienced by aircraft configurations undergoing large amplitude motions. In this particular study, roll oscillations are the focus. The study presents results from a theoretical investigation and experiments conducted on a 65° delta wing in high-amplitude roll oscillations. Non-linear aerodynamic response modelling for flight mechanics analyses requires that the oscillatory data be formulated for arbitrary (unknown a priori) motions. This study focuses on establishing the relationship between the nonlinear indicial response model (the time domain model developed by Tobak, Chapman and Schiff) and the reaction hypersurface model proposed by Hanff. Both methods can handle aerodynamic hysteresis effects. Both have certain advantages to the flight mechanist and the aerodynamicist interested in fundamental physical phenomena. The objective of this paper was to show that the hypersurface model is, in fact, a special case of the indicial response model.

The reaction hypersurface represents the aerodynamic response as a surface in a space defined by a set of orthogonal axes where the independent variables are the

primary motion variables and their time derivatives, and the dependent variable is one of the six force and moment coefficients. No assumptions are made regarding the linearity of the response to the motion variables. This study concentrates on body-axis rolling motions. The properties of the hypersurface model are studied using Hanff's dynamic force and moment data from a rolling delta wing model which contain strong nonlinear effects.

A preliminary analysis of static and oscillatory roll data from the 65° delta wing experiments at 30° angle of attack indicates that despite the absence of static hysteresis (in the variation of rolling moment with roll angle) the corresponding hypersurface model (in mathematical form) must acknowledge the presence of at least two critical points in the static rolling moment curve (at roll angles of  $\pm 7^\circ$ ) which corresponds to a rapid movement of the leeward wing vortex-breakdown position to the trailing edge. The results also indicate that a hypersurface in at least four dimensional space (roll angle and its two first derivatives and rolling moment) is required to fully represent the rolling response for the case studied. Additional tests will need to be studied to assess the impact of the critical points. An extensive set of forced-oscillation tests will be run by Hanff in the Wright Laboratory 7 x 10-ft Subsonic Aerodynamic Research Lab (SARL) tunnel in June of 1991.

**Paper No. 5**, by Ferretti, Bartoli, and Salvatore (Aeritalia, Italy) addresses the problem of prediction of some of the aerodynamic phenomena leading to degradation of aircraft performance in the high subsonic regime. The study focuses on two kinds of wings, those with moderate sweep angles and those with greater than 60° sweep (delta wings). The moderately swept wing represents the case with "attached flow" degrading to separated when shock-boundary layer interactions occur, and the delta wing represents "vortical flow" (separated flow at the leading edge) whose onset, development, and bursting is ruled by the surrounding flowfield. In both cases, however, the effects on aircraft aerodynamic characteristics are felt as buffeting, loss of control power, and uncommanded pitch, yaw, and roll motions up to the limit of the aircraft operational envelope.

This paper presents the approach to both of these problems by Alenia Aeronautica. For the conventional wing of moderate sweep, it is well known that trailing edge divergence (a change in the trailing edge pressure and an increase in the boundary-layer thickness) marks the onset of unsteady effects such as buffeting. Prediction of the occurrence of trailing edge divergence would enable a prediction of onset of buffet. Analysis of wind tunnel pressure data has led to a criteria that can be used to predict buffet. The basis of the prediction method is to utilize available computational codes that can predict the pressure distributions over the wing at reasonable cost and within a reasonable amount of time.

For delta wings, featuring realistic rounded leading edges, transition from attached flow to vortical flow at the leading edge has been shown to be the main cause

for early loss of linearity in the aerodynamic coefficients. From wind tunnel tests a relationship between the bound pressure level on the leading edge and the onset of vortical flow has been shown. With the provision that additional studies are needed to correlate wind tunnel with flight results, an engineering tool has been developed to allow prediction of vortical flow onset by the use of theoretical codes. Further analyses are being carried out to discover relations between vortex breakdown and pressure levels on the wing.

**Paper No. 14**, by Perkins (BAe, UK) describes an investigation into the capabilities and accuracy of an equation error method of aerodynamic parameter identification using stepwise regression techniques. Examples are shown from flight results from responses of the British Aerospace Experimental Aircraft Program (EAP). Derivatives extracted from flight data of EAP show good agreement with wind tunnel experiments. The disadvantages of an equation error method can be minimized by having accurately measured flight data, meaning having high quality flight instrumentation. An evaluation was performed using simulated responses and the method can extract non-linear aerodynamics. The effect of typical instrumentation errors and noise on the simulated responses gives a reduction in accuracy of extracted derivatives. The methods of extracting non-linear aerodynamics are described. One advantage of this method over the well-known Maximum Likelihood method is that the structure of the aerodynamic model does not need to be defined initially, nonlinear effects can be accommodated, and large quantities of data can be processed.

The equation error method using stepwise regression techniques has been shown to work successfully for analysis of flight data from the EAP aircraft. Given sufficient flight data with adequate information content, the full nonlinear aerodynamic characteristics can be extracted fairly accurately.

## 2.5 Forebody Vortex Control Technology

Three papers were presented reviewing recent work on the development of various methods of forebody vortex control for enhancing the controllability of fighter aircraft in the medium to high angle of attack range.

**Paper No. 15**, by Malcolm and Ng reviewed some work performed by Eidetics International, including wind tunnel tests on a generic fighter configuration and water tunnel tests on an F/A-18 model. The generic fighter configuration was tested with forebody strakes and forebody blowing jets. The review showed the effects of deploying small strakes near the tip of the model forebody, a tangent-ogive configuration with fineness ratio of 4.0. Large yawing moments could be generated in either direction in proportion to the strake height. Blowing jets (blowing aft or forward tangential to the forebody surface on the leeward side) can also produce large yawing moments (larger than that produced by a fully deflectable rudder) at modest blowing rates.

Water tunnel tests with F/A-18 models showed that the

forebody vortices can be manipulated and resulting yawing moments can be controlled with either leeward side blowing jets similar to the generic fighter or with longitudinal slots near the tip of the forebody on either side near the maximum half-breadth. Both techniques control the vortices by controlling local separation. Small tip-mounted strakes that rotate as a pair around the longitudinal axis of the model also showed the potential for precise control of the vortices with miniaturized strakes. The key to generating large controllable yawing moments is to locate the controlled devices for interfering with the natural forebody flow as close to the forebody apex as possible.

**Paper No. 16**, by Guyton, Osborn, and LeMay (WL/FIMM, USA) reviewed recent wind tunnel experiments on X-29A, F-16, and a generic chine forebody configuration with a cropped 55° delta wing using forebody blowing as the technique for controlling the forebody vortices. Experiments conducted on a 1/3-scale X-29A model with jets blowing aft from a leeward side location approximately 0.5 forebody diameters aft of the apex and about 135° radially from the windward side showed yawing moments in a direction coinciding with the side on which the jet was placed, similar to previous experiments on a generic fighter configuration and the F/A-18 discussed in Paper No. 15. The behavior of the yawing moment with sideslip in the presence of blowing was encouraging, demonstrating high levels of yaw moment control up to sideslip angles of 10°.

A 1/15-scale F-16 model was tested with blowing jets on the leeward sides and slots on the sides of the forebody to produce a slotted jet flow tangential to the model surface in the circumferential direction. Contrary to other data on the X-29A with blowing jets and with other data on the generic fighter and F/A-18, a right blowing jet produced a left yawing moment and vice versa. It is not clear why there is a difference on an F-16. This bears further investigation, with some flow visualization.

A generic fighter with a 55° cropped delta wing and a chine-shaped forebody more like the expected U. S. Advanced Tactical Fighter configuration was chosen to investigate the potential control power when the configuration does not have the circular or elliptical cross section typical of today's fighter configurations. Blowing on the forebody configuration was not successful in generating yaw control power alone. With this type of configuration there is much higher potential for influencing rolling moment and pitching moment than on conventional configurations.

**Paper No. 17**, by Ross, Jefferies, and Edwards (RAE, UK) describes experiments on a UK research aircraft configuration, High Incidence Research Model (HIRM), using forebody suction for controlling the position and strength of the forebody vortices. Similarly to forebody blowing, forebody suction controls the vortices by controlling boundary layer separation, delaying it on the side where suction is activated. The suction coefficients, while not defined the same as the blowing coefficients, are very small in terms of the required suction pressures and fluid mass

flow rates. The suction holes are mounted symmetrically on the leeward side of the forebody very close to the tip, a key to making the suction technique work so well.

Results show that very small suction coefficients can influence the vortices and the yawing moment significantly, and the direction of the yawing moment generated corresponds to the side on which suction occurs.

Experiments on a free-to-yaw rig in the wind tunnel are discussed with demonstrations showing that with alternating left and right suction, the yawing motion at moderate and high angles of attack can be fully controlled without the rudder.

## 2.6 Special Papers from the Flight Mechanics Panel, and Structures and Materials Panel

Two papers were presented from non-Fluid Dynamics Panel sponsored authors. One, sponsored by the Flight Mechanics Panel concerns the transformation of flight mechanics design requirements of modern fighters into aerodynamic characteristics. The other is a paper sponsored by the Structures and Materials Panel related to the aeroservoelastic stability of aircraft at high incidence.

Paper No. 18, by Mangold (Dornier, Germany) is a discussion of the requirements and difficulties in meeting those requirements to take the desired flight mechanics characteristics, including handling qualities, agility, maneuverability, controllability, etc. and relate these to definable aerodynamic characteristics that the preliminary designer can incorporate into his design. This is particularly difficult for an aircraft that will be heavily augmented by the flight control system for stability, especially at the preliminary design stage since the flight control system will not have yet been designed. To be successful in achieving optimum performance and superior handling qualities it is necessary to define a set of flight mechanics criteria which properly translate the most important flight mechanics requirements into aerodynamic requirements.

This paper reviews some of the ideas presented by the author in an AGARD FMP Symposium on Flying Qualities in Quebec, Canada in October 1990 and activities of AGARD FMP Working Group 17. One of the fundamental premises for development of new criteria is that static derivatives alone are not sufficient to characterize the behavior of an aircraft in a highly maneuverable state at high angles of attack, especially to maintain dynamic stability. It is necessary to consider dynamic derivatives or coefficients like roll and yaw damping. Agility around the velocity vector at high angles of attack is mainly a matter of yaw and roll control power, putting more emphasis on rudder control power and yaw damping.

Criteria such as  $C_{n\dot{\delta}}$  are no longer adequate as a criteria to define acceptable or unacceptable lateral/directional stability characteristics. At the operational angles of attack consistent with present-day and future

fighters, some of the important design features have changed, particularly maximum lift and usable angles of attack, which means that the static and dynamic lateral/directional derivatives are dominated by forebody vortices from the nose, strakes, or canard.

One of the conclusions is that because of the complex aerodynamic effects at high angles of attack it will be necessary to design the "basic configuration" by some optimization loops. During the design process specialists from the flight mechanics disciplines, aerodynamics, flight control law designers and overall design departments have to form a close team in order to end up with a well-balanced design. The communication lines between these groups must be established early and kept open in order to avoid costly and time-consuming difficulties in later design phases.

Paper No. 19, by Becker (MBB, Germany) discusses a possible methodology to predict aeroservoelastic stability of an aircraft at high angles of attack including nonlinear aerodynamic effects. Using linear unsteady aerodynamic theory associated with level flight conditions to predict aeroservoelastic and flutter calculations for medium to high angle of attack conditions could be in serious error since effects of separated flow and leading edge vortices are not accounted for. These effects may be introduced into the aeroservoelastic analysis using a correction method and measured unsteady pressure distributions from wind tunnel tests. The correction method is described. An example for illustration and from which wind tunnel data were used is a half model of tactical fighter type aircraft with a delta wing, a foreplane and half a fuselage installed at the wind tunnel wall. Experimental results are reviewed and an interpretation with application to the prediction method is discussed. Some of the conclusions include (1) effects of high incidence unsteady aerodynamics on the open loop characteristics of low frequency elastic modes are small and the increase in aerodynamic elastic mode damping with incidence effects may have reduced the increase in mode excitation, (2) effects of high incidence unsteady aerodynamics on higher frequency elastic modes are large, (3) prediction method for high incidence unsteady aerodynamics is validated by wind tunnel tests, and (4) high incidence aerodynamic effects have to be considered in aeroservoelastic stability predictions.

## 2.7 Flight Tests of the X-31A

Paper No. 2, by Ross (MBB, Germany), even though the first paper to be presented following the meeting chairman's opening remarks, is an appropriate paper to discuss last because it is the future flying laboratory to investigate many of the phenomena discussed in all the previous papers. The primary role of the X-31A is to demonstrate the technical feasibility and tactical utility of high AOA and post-stall maneuvering. Simulation results have shown the importance of (1) attained rather than sustained turn rate and (2) small attained radius of turn, which can only be achieved by approaching and exceeding the stall limit. In statistical analysis of manned and digital combat simulation studies, the sensitivity of the exchange ratio to the maximum allowable angle of attack during post-



stall maneuvering indicates that the increased benefit above 60° AOA becomes small, suggesting that a maximum trim capability in pitch to 70° AOA is sufficient. Pitch down capability is of critical importance to allow transition back to the higher speed envelope. It is also important to have pure aerodynamic recovery in case of failure of the thrust vectoring system. Yaw control power becomes dominant at high angles of attack and body-axis roll less important. The flight control system must take care of the proper blending of control in the yaw and roll axes with angle of attack, including the contribution from thrust vectoring.

The more important aerodynamic characteristics of the X-31A are summarized including the effectiveness of the canards in producing pitching moments, the benefits of thrust vectoring in yaw to assist the control inputs from the rudder at high angles of attack and the demonstration that sufficient roll power (body-axis) can be generated throughout the AOA range by differential trailing-edge wing flap deflections.

Performance levels are reviewed including velocity vector roll rates, turn rate, turn radius, minimum-time heading reversals, etc. and comparisons are made to conventional fighter aircraft. Flight test status was discussed. Aircraft 1 had performed 25 flights up to mid April. Thrust vectoring vanes have been installed and will be tested with deflections in May, 1991. Penetration into the post-stall regime is scheduled for the last half of 1991.

### 3.0 Review of Round Table Discussion

Following presentation of the papers, a Round Table Discussion was conducted with participants' contributions recorded and transcribed. The transcription of the RTD follows the papers. The discussion was initiated and prompted by several prepared statements or questions presented by the meeting technical evaluator and comments by the symposium chairman. The following topics were discussed:

#### 3.1 Reynolds Number Effects - How to simulate in the wind tunnel?

The question of how to evaluate Reynolds number effects is not new nor is it peculiar to maneuvering aerodynamics. However, methods have been used for wind tunnel tests, primarily for testing models with attached flow, to simulate boundary layer transition by careful placement of transition strips consisting of various sizes of grit on the surface of the wing, near the leading edge, and on various fuselage and empennage components. These techniques have proven to be very useful in artificially tripping a laminar boundary layer and causing it to transition to turbulent flow as if it were experiencing natural transition at higher Reynolds numbers consistent with full-scale flight. The question is how do we simulate higher Reynolds numbers with tests of fighter aircraft configurations at high angles of attack with separated flows and, particularly, how do we deal with simulating the proper flow on aircraft forebodies?

Paper No. 6 by Visintini showed some results from experiments conducted at AerMacchi where transition strips were employed to simulate transition on the forebody. Results showed poor repeatability and a high dependency on where the strips were placed. It is apparent that the guidelines for how and where to use transition strips for application to high angles of attack are not clear. Comments from the floor included observations that many wind tunnel tests are conducted at Reynolds numbers where the flow is transitional and, therefore, very sensitive to small differences in Reynolds numbers. Test results at low Reynolds numbers where the boundary layer is laminar, for example on forebodies, often have the same behavior as tests conducted at high Reynolds numbers where the boundary layer is turbulent. Artificial transition may force the aerodynamic results to be even less comparable to high Reynolds number results. In order to fix transition strips and know whether they are effective and correct, one needs to know the answer for the full-scale case, information that is often lacking. Vortex flows generated by sharp leading edges are shown to be relatively independent of Reynolds number. However, this may not always be the case. Caution was expressed using the example of a noseboom mounted chine whose separated flow vortex affects the vortex flow immediately aft on the forebody. The overall flowfields, even though they may be similar at the strake location, may not be independent of Reynolds number, in which case we may see something quite different in flight than on the ground in ground-based test facilities. Little is known about the dependency of dynamic effects on proper use of transition strips primarily because few, if any, experiments have been performed with transition strips. With the model in motion, the location of transition is continuously changing. It is not clear whether time-varying natural transition can be approximated by a fixed transition strip.

#### 3.2 Time Lag Effects - How to determine in wind tunnel and flight tests and how to incorporate into aerodynamic models for simulation?

A suggestion was made to account for time lags in a linear sense by treating the aerodynamic reaction as a transfer function which would require dynamic tests to define the transfer function. In the nonlinear sense, including the history effects, we are forced to look at indicial response or hypersurface type models. This makes the problem more difficult for the flight mechanics people, though, since they can no longer use small perturbations or derivatives in the equations of motion. It was also pointed out that the measured nonlinearities in wind tunnel tests occur at relatively high rates, and in some cases at rates which are higher than those encountered by full-scale aircraft. However, the higher rates are not inconsistent with those experienced by control surfaces. The flight mechanics people have a difficult time in incorporating time-lag information into the simulation model, particularly the time lags associated with ramp motions because of the dependency on the specific motion history.

### 3.3 Effects of $\dot{\alpha}$ and $\dot{\beta}$ ?

Generally, it was felt that these effects are increasingly important with higher angles of attack. Recent experiments have shown that the aerodynamic coefficients dependent on translational or heaving motions can be significant. Simulation aerodynamic math models often provide for these terms, but historically the aerodynamicist has not been able to provide the individual component values. Increased emphasis is being placed on developing testing apparatuses to acquire separately, the rate derivatives and the time-dependent derivatives, such as  $Cm_{\dot{q}}$  and  $Cm_{\dot{\alpha}}$  or  $Cn_{\dot{r}}$  and  $Cn_{\dot{\beta}}$ .

There is also a recognition that the development of criteria to predict departure from controlled flight must consider more than just static aerodynamic coefficients. Criteria developed in the past such as  $Cn_{\dot{\beta}dyn}$ , which, in fact, does not contain any dynamic terms, and others which assumed small angles of attack are no longer adequate. Dynamic terms must be included in order to predict the departure tendencies of modern fighter aircraft. An additional problem is how to include the effects of control system inputs in a highly augmented aircraft, particularly in the early design stages before the details of the flight control laws are known.

### 3.4 Effects of dynamic lift on moderately swept wings?

Extensive research has been done on dynamic lift of two-dimensional airfoils, and more recently on highly swept delta wings with substantial leading edge vortices to investigate three-dimensional effects of high amplitude high rate ramp motions. There does not seem to be much data on moderately swept wings, for example from  $30^\circ$  to  $50^\circ$ . Since most fighter aircraft have moderately swept wings, there would seem to be a need for more information on how to exploit dynamic lift for configurations more like actual full-scale aircraft. The data on highly swept wings is pertinent to wing leading-edge extensions and some experiments have been done with double delta wings which represent the case of moderately swept wing with a LEX.

### 3.5 What are the chances of getting feedback from flight test results related to time lag effects?

The X-31A may provide an opportunity to measure time-lag effects from full-scale flight tests, but it is not clear whether the flight tests that are planned will, in fact, be able to determine time lag effects. It would appear that the expected responses of the X-31A to control inputs or to unsteady aerodynamic inputs do not assume that time lags are likely to be significant. MBB suggest that we wait for flight test results to assess their existence and importance. Flight data obtained on the F-16 several years ago identified time lag effects, particularly lift overshoot, which prompted some of the current research at General Dynamics by Cunningham.

### 3.6 What is the role of CFD in computing the aerodynamics due to high-rate motions?

CFD calculations have experienced good success in recent years in computing the flow characteristics of forebodies and wing leading-edge extensions, and to some degree the entire aircraft at moderate angles of attack including separated flows. These have, for the most part, been steady flows. The time has come to begin the task of calculating unsteady flows and there appears to be some optimism that this can be done, particularly for the type of maneuvers that have been associated with highly maneuverable aircraft.

An AGARD meeting addressing unsteady aerodynamics will be held in October, 1991 in San Diego, with expectations that the role of CFD for unsteady aerodynamics computations will be addressed.

### 3.7 Does the aircraft designer and the aerodynamics test community understand each other's needs?

It is not clear that the communication link is well established. Perhaps just as important is the communication between the preliminary designer and the flight mechanistic. It is more important than ever before that these two groups work together in the early stages of aircraft definition. AGARD symposia such as this one can help to forge the link between the various technical disciplines.

### 3.8 How applicable are forebody vortex control methods to forebodies with chine-shaped cross sections?

Most experiments to date have dealt with forebodies with either circular or elliptic cross sections. Chine-shaped forebodies, representative of advanced fighter configurations, have a sharp side edge that will provide a more defined, and perhaps more stable location for separation. With the fixed location for flow separation, the question is which forebody vortex control methods will work, if any, successfully and which ones will not. Research with these types of configurations has just begun. It is expected that the forebody vortices will be more difficult to manipulate than for a smooth forebody surface.

### 3.9 Is it likely that forebody vortex control and thrust vectoring can be used in a complementary arrangement?

It is unlikely that forebody vortex control only will be used unless there is a need only for yaw control and there is no need for additional pitch control. There are significant advantages to each, but they are not direct competitors for all flight conditions. Forebody vortex control is not applicable to low angle of attack and to low  $q$  conditions. Depending on the specific technique used to control the vortices, it may or may not be dependent on the availability of engine bleed air. Thrust vectoring only works if the engine is running. Loss of

control power must be considered if thrust vectoring is lost due to an engine out. At this point in time, there is room for both techniques to be considered.

**3.10 What are Reynolds number and rate (dynamic) effects on forebody vortex control?**

Neither of these effects have been evaluated yet. Reynolds number effects will be explored with the full-scale F/A-18 tests now under way in the NASA-Ames 80 x 120-ft wind tunnel, where three forebody vortex control techniques will be tested: blowing jets, blowing slot and conformal strakes. Subscale experiments with a 6%-scale model of the F/A-18 will be conducted by

Eidetics International in the Ames 7 x 10-ft wind tunnel to measure effects of jet and slot blowing and miniaturized tip strakes. Tests will also be conducted with the 6%-scale model on a rotary-balance apparatus with forebody blowing.

**3.11 What is accessibility of flight test data?**

All too frequently, there is a tendency to develop elaborate flight test programs but once the airplane is in the air the program often runs short of funds to fully exploit the opportunities to get detailed flight test data that can be of significant benefit to the research community. There needs to be additional emphasis on making maximum use of our flight test vehicles.

**X-31 ENHANCEMENT of AERODYNAMICS  
for MANEUVERING beyond STALL**  
Hannes Ross  
Deutsche Aerospace/Military Division  
Messerschmitt-Bölkow-Blohm GmbH  
P.O.Box 80 11 60  
D-8000 München 80

## **1. Introduction**

Current fighter aircraft are generally limited to angles of attack (AOA) below their maximum lift capability ( $\alpha_{clmax}$ ). Pilot inputs and hence aircraft maneuvering become usually limited when approaching the stall limited (Fig. 1-1).

Primary reason for this situation are the degrading aerodynamic lateral/directional characteristics and reduced control power in the high AOA regime, often resulting in uncontrolled maneuvers/departures/spins. Some aircraft have for these reasons reduced roll control inputs as well as Aileron/Rudder-Interconnect (ARI) systems installed to avoid uncoordinated flight conditions at higher AOA. Others have limitations as to the number of consecutive rolls they are allowed to fly even in the conventional AOA regime to prevent uncontrollable pitch-up/Beta excursions due to inertia coupling and engine gyroscopic moments.

In the last ten years new efforts have started to improve control capability in this flight regime. F-14, F-15 and F-18 have demonstrated AOA excursions up to about 65 degrees and the Su-27 and MIG-29 have performed impressive pitch maneuvers even exceeding AOA's of 90 degrees. However, all of the above mentioned maneuvers are performed in the pitch plane with little or no capability left for roll control around the velocity vector.

A number of experimental aircraft programs have been initiated to explore the high AOA and the poststall regime to broaden the knowledge base. The flight test objectives range from basic understanding and investigation of aerodynamic flow phenomena (X-29, a/c no. 2 high AOA test vehicle, F-18 High Angle of Attack Research Vehicle/HARV) to the incorporation of thrust vectoring capability (HARV) and finally to the demonstration of technical feasibility and tactical utility of high AOA maneuvering (X-31 A).

## **2. Tactical POST-STALL (PST) Maneuvering**

### **2.1 Combat Simulation Results**

Numerous manned and computerized close in combat (CIC) simulations have been performed since the late 1970ies and - assuming all-aspect IR missiles and guns - have shown a dominance of head-on encounters with increasing importance of

- attained (rather than sustained) turn rate (ATR)
- small attained radius of turn (ART) Fig. 2-1.

CIC simulations performed with a/c with/without AOA limits showed a very impressive improvement of 2 to 3 in combat capability as defined by

- time to first shot
- time in firing position
- kill probability
- time in disadvantage position etc.

These results were achieved in one on one and multi bogey situations showing similar trends (Fig. 2-2).

The basic questions/trade-offs

- can CIC be avoided by beyond visual range attack and
- can aircraft maneuverability be offset/decreased or even be relaxed by improved missile off-boresight capability and improved missile maneuverability have of course been investigated and led to the well known answers that

- CIC can not be avoided, in particular in an outnumbered situation where multitarget (BVR) capability is a requirement
- high off boresight capability ( $> 60^\circ$ ) is difficult to achieve because of fire control and missile flight performance limitations and result in a significant reduction of single shot kill probability (SSKP)

High ATR's and ART's are therefore essential performance characteristics for a future fighter designed for BVR and CIC.

Looking at the well known Rate of Turn vs Mach Number plot (Fig. 2-3) it becomes immediately evident that ART's can only be improved by approaching and exceeding the stall limit.

## **2.2 PST Maneuver/Design Requirements**

Maneuver/Design Requirements have been derived by statistical analysis of manned and digital combat simulations. The Mach-Altitude envelope in which PST maneuvers were observed is identified in Figure 2-4. PST entry is limited by the maximum dynamic pressure which in combination with the CL max results in the maximum allowable load factor of the aircraft. PST maneuvers have been performed up to altitudes of 7 km and down to speeds below Mach 0.1.

Sensitivity of the exchange ratio to the maximum allowable angle of attack during PST maneuvering indicates that the increase in benefit above 60 degrees angle of attack becomes small. Thus a maximum trim capability up to 70 degrees has been suggested. Figure 2-5 shows an AOA frequency distribution during PST maneuvering which is in good agreement with the sensitivity analysis.

The control power requirements in terms of acceleration capability around the body axis in pitch, roll and yaw are shown in figure 2-6. For unstable configurations the pitch down capability is of critical importance to allow a quick recovery from PST attitudes to transition back into the higher speed envelope. Also a pure aerodynamic recovery must be possible in case the thrust vectoring system fails to operate.

Roll control power requirements around the body axis can be relaxed with higher angle of attack because large body axis roll angles would immediately result in excessive angles of sideslip which cannot be tolerated.

Yaw control power becomes more dominant with increasing angle of attack. At 90 degrees angle of attack the roll around the velocity vector is identical to a pure yawing maneuver. However, the available yaw capability at high angles of attack is determined by the (constant) side force from thrust vectoring.

The need for thrust vectoring support to achieve tactical relevant maneuvering capability in the high AOA regime requires that the propulsion system is working at all times. Therefore sufficient airflow as well as engine inlet compatibility throughout the angle of attack and sideslip regime must be insured. The engine should allow full throttle operations throughout the PST regime. The thrust to weight ratio of the aircraft should exceed a value of one (SLS) which is satisfied by most modern configurations.

Another important aspect is that the flight control system mechanization must allow to control the roll around the velocity vector by a stick command only. Therefore the flight control system must take care of proper mixing of body axis roll and yaw as a function of AOA.

Given a "normal" thrust/weight ratio of more than 1 at sealevel it was found that a thrust deflection of about 10 - 12 degrees should be sufficient to satisfy the maneuver requirements, provided that the basic aerodynamic design has reasonable longitudinal and lateral directional characteristics. Nozzle deflection characteristics in terms of deflection velocity and deflection rates must be compatible with those of aerodynamic surfaces.

## **3. The X-31A, a Demonstrator for the Technical Feasibility and Tactical utility of PST Maneuvering**

### **3.1 Configuration Description**

In May 1986 the Defense Advance Research Agency (DARPA) and the German Ministry of Defense signed an MOA to develop two aircraft and to demonstrate in flight the technical feasibility of poststall maneuvering. The

aircraft was designated X-31A and became the first vehicle in the famous series of "X"-planes to be developed internationally. Figure 3-1 identifies the major external and internal characteristics of the X-31A. The delta canard configuration is powered by a single G.E. F 404 engine. The aerodynamic configuration integrates the design requirements for excellent supersonic performance combined with unprecedented subsonic high angle of attack maneuvering capability. The belly inlet with a drooping lower lip is particularly suited for high angle of attack operation. The long coupled all movable canard reduces aircraft stability and thereby improves subsonic and supersonic performance. Together with the trailing edge flaps it also provides pitch moments for trim, stability and control. The canard deflection is scheduled such that it will not stall considering trim and control inputs. Leading edge flaps improve lateral/directional stability characteristics, in particular in the high angle of attack regime and also the maneuver performance at lower angles of attack.

The most dominant external feature which distinguishes this aircraft from other delta canard configurations are the three thrust vectoring vanes mounted to the aft fuselage of the aircraft which allow thrust vectoring in the pitch and yaw axis.

As might be expected for a low cost program the aircraft has been designed and built using a lot of existing structural and subsystem components (e.g. canopy and windshield, landing gear ECS, hydraulic, electric, propulsion system etc.).

To further improve the simplicity of the design and manufacturing process the aircraft has a dry wing.

### 3.2 Aerodynamic Characteristics

Figure 3-2 shows a smooth lift curve versus angle of attack distribution with a maximum lift coefficient of about 1.1 at 30 degrees angle of attack which is reduced to .6 at 70 degrees angle of attack.

Figure 3-3 shows the incremental pitching moment capability of the trailing edge flap vs. angle of attack. In particular the pitch down capability is markedly decreased. The pitching moments due to canard deflection are shown on Figure 3-4 and indicate that by deflecting the canard into the wind a significant pitch down moment can be achieved. Figure 3-5 shows the combined pitch control power of canard and trailing edge. It clearly indicates that the critical area is at high angle of attack where the pitch down capability is about 40% of the remaining pitch-up control power. The X-31 has been designed considering a requirement that the aircraft has to be recoverable from high angle of attack even without the assistance of the thrust vectoring system, i.e. considering failure or malfunction of the thrust vectoring system or an engine flame-out. This required a careful development and fine tuning of the aerodynamic characteristics as well as the proper CG location.

Sufficient roll control power can be generated throughout the angle of attack range by differential trailing edge flap deflection.

The incremental yawing moment due to rudder deflection (Figure 3-6) indicates that above 40 degrees angle of attack the remaining control power is insufficient to satisfy trim, stability and control power requirements.

A comparison of the control power requirements for tactical maneuvering as defined in Fig. 2-6 vs the available values shows that these can be achieved if aerodynamic and thrust vectoring capability in pitch and yaw are combined. Body axis roll requirements are satisfied without T.V. augmentation (Fig. 3-7).

### 3.3 Thrust Vectoring System

Fig. 3-8 shows the principal arrangement of the thrust vectoring system. It consists of three vanes which are mounted to the aft airframe structure and can be deflected around a fixed hingeline. Simultaneous deflection allows the adjustment of the vanes to the plume size resulting from a variation of power setting (Fig. 3-9) and Mach/altitudes. The combination of two vanes deflected into the jet, - the remaining vane deflected outward -, allows to vary the direction and magnitude of the sideforce component in pitch and yaw. Deflection characteristics are incorporated into the control laws. When the thrust vectoring system is engaged, control commands are distributed by the FCS between aerodynamic surfaces and T.V. vanes considering their effectiveness.

The structural design of the thrust vectoring system consists of a light weight/temperature resistant Carbon/Carbon vane mounted to a metal structure with lugs for the hingeline and the actuator attachment. The

vanes are covered by a metal roof which is designed to carry the aero loads when the vanes are deflected outward (up to 60 degrees) to improve the deceleration capability of the aircraft.

Consistent with the design requirements and aerodynamic characteristics the thrust vectoring system is used to improve stabilization and control power in the pitch axis at low  $q$ /high AOA. Due to the single engine aircraft configuration no augmentation is possible in the roll axis. Because of the insufficient rudder effectiveness in the AOA regime above 40 degrees trim, stabilization and control augmentation is provided by the thrust vectoring system in the yaw axis (Fig. 3-10).

It should be noted the total control power available from aerodynamic surfaces and/or thrust vectoring devices must consider the requirements to compensate inertia coupling effects as well as engine gyroscopic moments throughout the angle of attack range.

### 3.4 Performance

Figure 3-11 shows a typical example of the roll control capability around the velocity vector versus angle of attack. The rolling velocity is a function of Mach-number and altitude and as one can see there is a substantial capability available at high angles of attack.

Figure 3-12 shows the envelope expansion with respect to turn rate capability at low mach numbers if the stall limit can be exceeded. Obviously the amount of performance improvement is depending on the plane of maneuvering which in this particular case is horizontal. Two other extremes are identified in Figure 3-13 where the maneuvering is performed in a vertical plane. In this case the maximum performance is achieved in the upper point of a vertical loop and the minimum performance is achieved at the bottom of a vertical loop. The differences in performance are due to the impact of the earth gravity.

The hedged areas identify the optimum angle of attack to achieve a maximum turn rate at a given mach number altitude condition. The vertical topline represents maximum achievable instantaneous performance.

A typical clinical PST maneuver is shown in Fig. 3-14. This particular maneuver requires a 180 degree heading reversal in the minimum amount of time with the constraint to come back at the same altitude and approximately the same speed. Figure 3-15 shows a comparison of this very maneuver as flown in manned simulations with an aircraft with unlimited angle of attack capability (up to 70 degrees), and an aircraft limited to 30 degrees angle of attack. The starting mach numbers are about the same and so are the end mach numbers. The unlimited aircraft achieves a considerably smaller radius of turn and higher turn rates below  $M=2$  which in total results in a shorter time to perform this maneuver and, if performed properly in an aircombat situation potentially in a positional advantage. Fig. 3-16 shows time histories for a PST maneuver.

The envelope of the X-31 (Fig. 3-17) with respect to the conventional performance is limited by an angle of attack of 30 degrees on the left hand side, a max. altitude line of 40 Kft, a max. Mach number of 0.9 and a max. line of 800 lbs/sq.ft. Overlapping is the envelope in which PST maneuvers can be performed. There is a roll control limit to the left hand side which needs to be explored during flight testing, since the X-31 does not have a roll control augmentation. The engine limit is resulting from a time limit for fixed throttle positions and also needs further exploration as well. The maximum mach number for PST maneuvers is currently identified as 0.7. Again, this limit needs to be investigated by flight tests and could be varying to higher and/or lower mach numbers. Entry into PST from high  $q$ /Mach numbers is limited by a  $q$ -line at which the structural limit of 9 g is reached at  $CL_{max}$ .

### 4. Flight Test Status

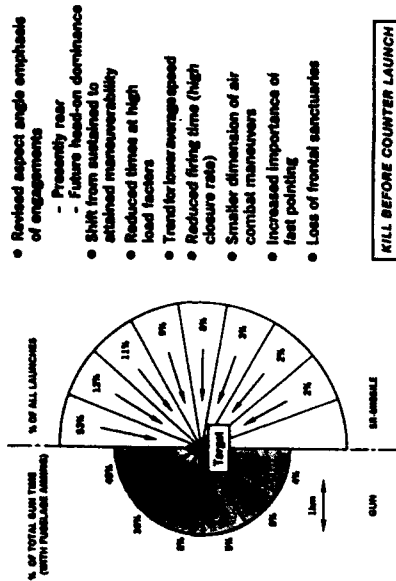
Up to mid-April 1991 25 flights with about the same number of flight-hours have been flown with the two aircraft (Fig. 4-1). Most of the flights have been performed with aircraft 1. After demonstrating the system operation flights were dedicated to investigate handling qualities throughout the conventional flight regime up to 0.9 mach number and 40,000 ft altitude. Testing of flight loads and flutter tests are in process.

The thrust vectoring vanes have been mounted on the aircraft and flown on aircraft no. 1 since flight no. 10 in a fixed position. Ground test of the vanes at various power settings and various deflections into the jet have verified the basic concept in terms of loads and temperatures. Initial flights with moving vanes to check the deflection laws as defined in the control law package will commence in May. Penetration into the PST regime is scheduled for the second half of 1991.

**5. Summary**

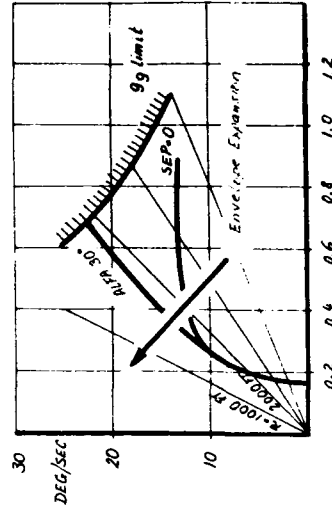
- X-31 has matured from a concept to 2 flying Demonstrator a/c
- predicted high AOA performance meets or exceeds design goals
- The integrated propulsion and multi-axis thrust vectoring control system are essential for high AOA maneuvering. Structural integrity of the T.V. system has been verified by ground tests.
- Exploration of the conventional envelope as a prerequisite to PST flights is in progress.
- Flight testing of the T.V. system will start by June followed by penetration into the PST flight regime in the second half of 1991.





Changes in Short Range Air Combat Characteristics

Fig. 2-1



Desired Envelope Expansion

Fig. 2-3

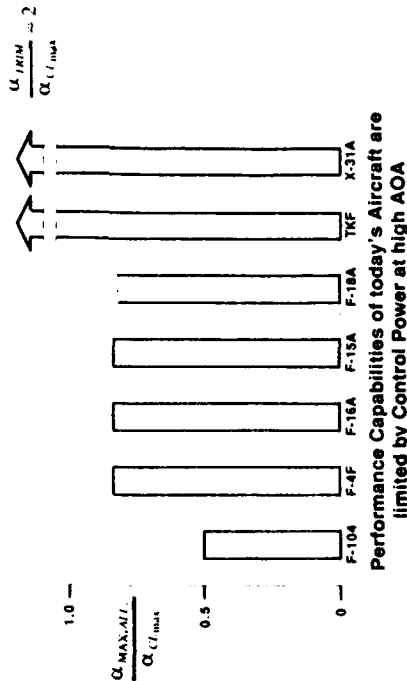


Fig. 1-1

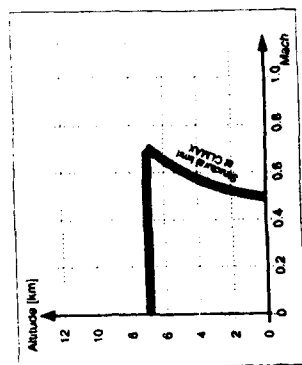


SUPERMANEUVERABILITY

No. of engagements: SMB + GUN: Gun only:	331 138		
1. Time to first firing possibility	SMB + GUN	2:1	2.8:1
2. Time to shooting position	SMB	2:1	
	GUN	6:1	18:1
3. Engagement value		3.4:1	4.2:1

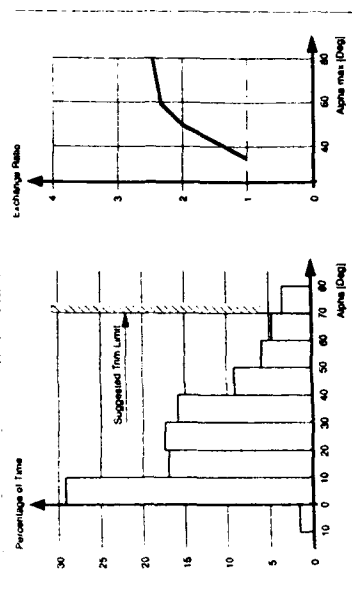
MIBB/IABG-COMBAT SIMULATION

Fig. 2-2



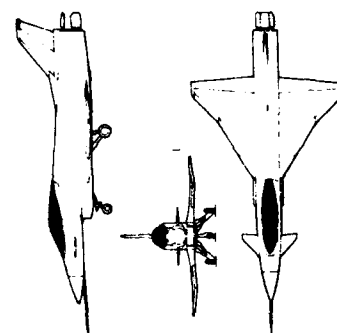
Post Stall Envelope  
for tactical maneuvering

Fig. 2-4



AOA Frequency Distribution

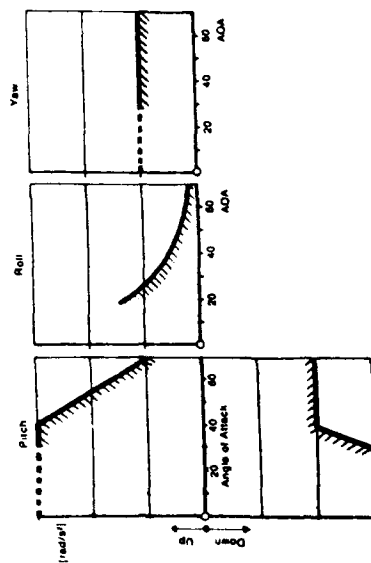
Fig. 2-5



TO Weight 7100 kp  
Internal Fuel 1850 kp  
Engine GE F-404  
Length 13.2 m  
Height 4.6 m  
Span 7.3 m

Three View

Fig. 3-1



Control Power at High Angles of Attack

Fig. 2-6

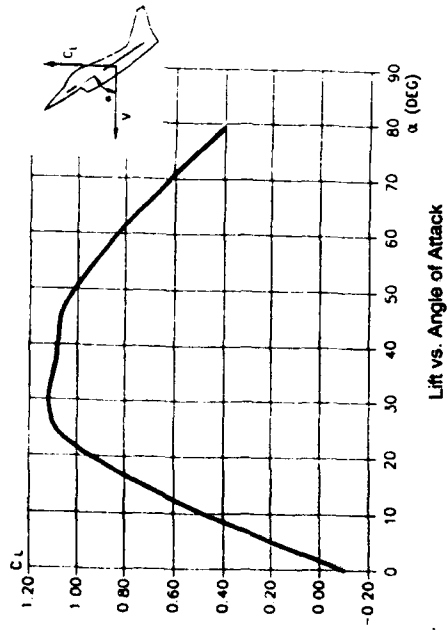


Fig. 3-2

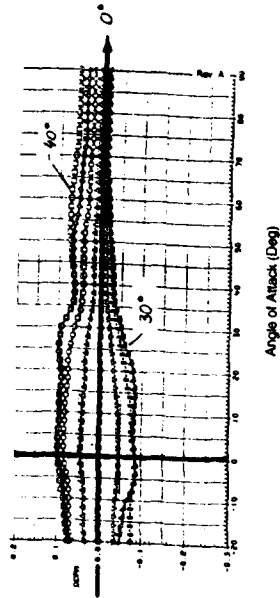


Fig. 3-3

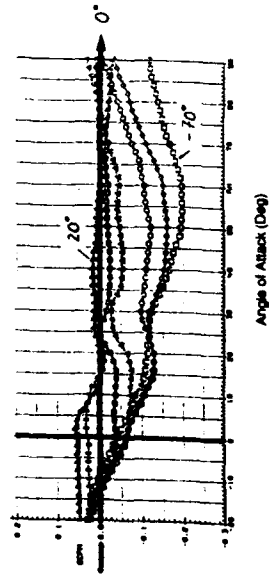


Fig. 3-4

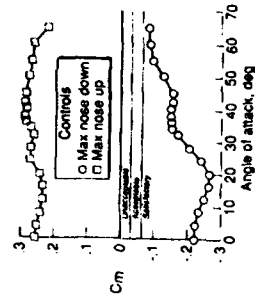
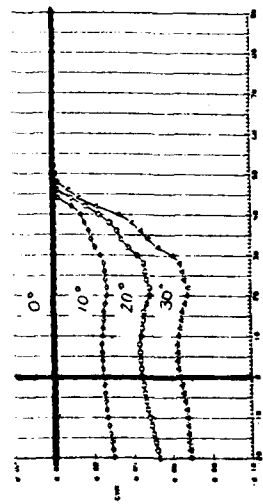
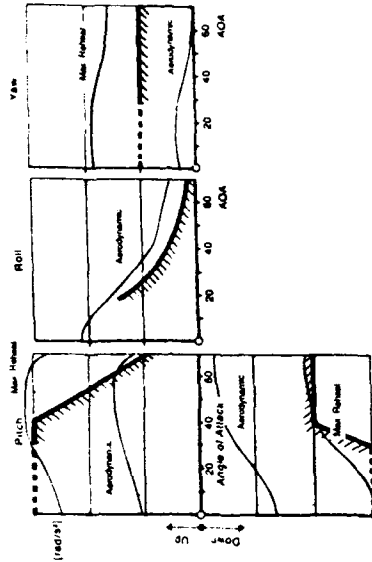


Fig. 3-5

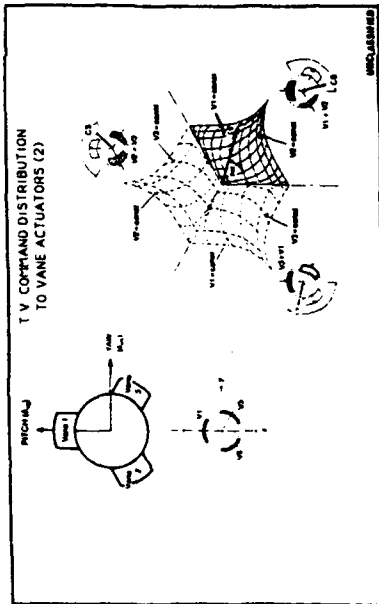


Incremental Yawing Moment  
Due to Rudder Deflection

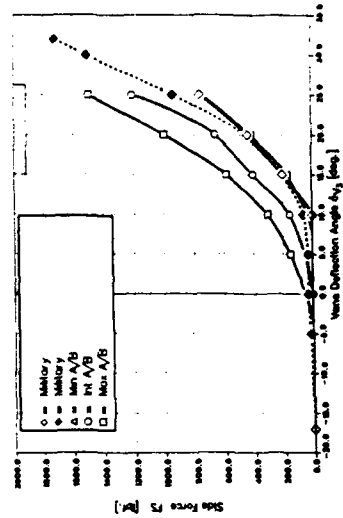
Fig. 3-6



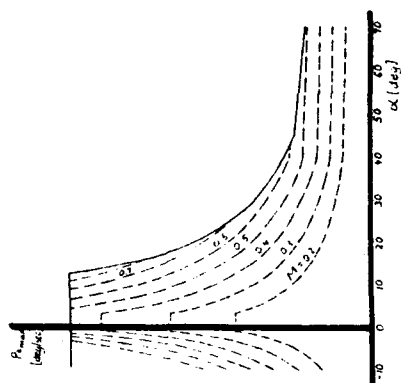
Control Power at High Angles of Attack  
Fig. 3-7



Thrust Vectoring Deflection Laws  
Fig. 3-8



Thrust Vectoring Ground Test  
Fig. 3-9

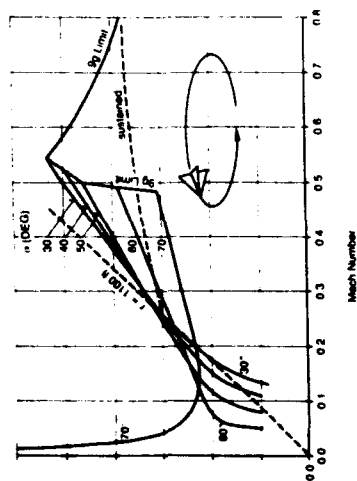


Roll Command Around The Velocity Vector  
Fig. 3-11

	Trim	Stabilization	Control	Inertia Coupling Engine Gyroscopic
Pitch	No	Yes	Yes	No
Roll	-	-	-	-
Yaw	Yes	Yes	Yes	Yes

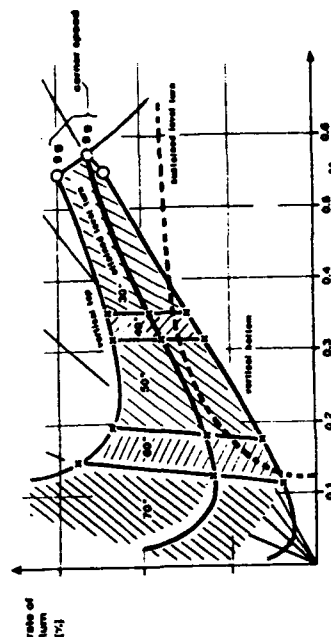
Thrust Vectoring Utilization  
AOA > 30°

Fig. 3-10

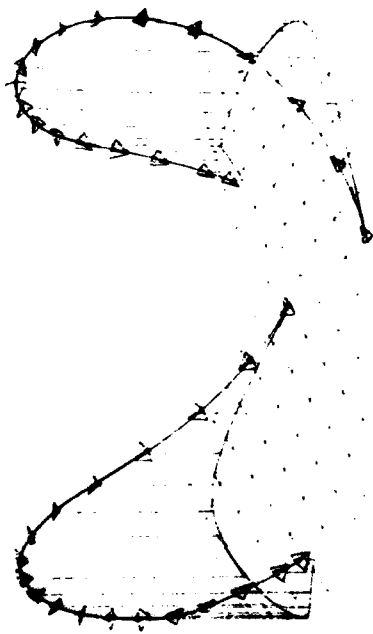


PST Maneuver Performance, Level Turn

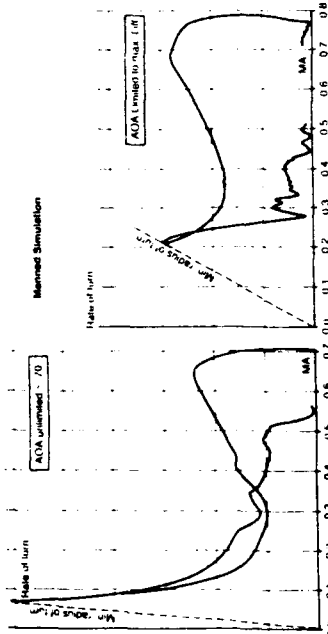
Fig. 3-12



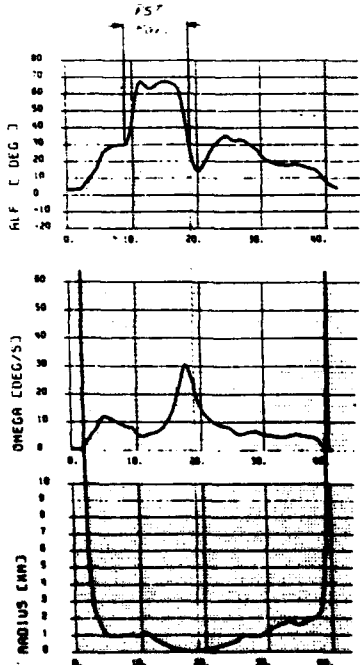
Max. Attained Turn Rate  
Fig. 3-13



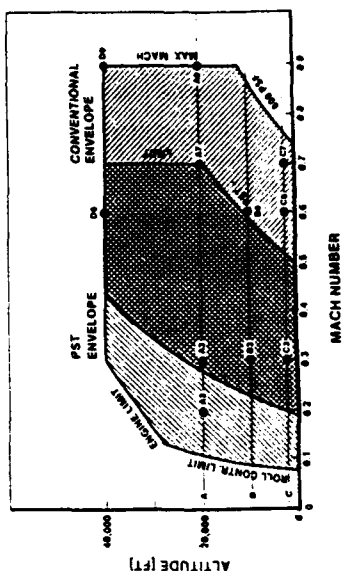
180 Deg. Heading Reversal with PST  
Fig. 3-14



180 Deg. Heading Reversal  
AOA limited vs unlimited AC  
Fig. 3-15



High Turn Rates and Low Turn Radius at High AOA  
Sample PST Maneuver Characteristics  
Fig. 3-16



Flight Envelope  
Fig. 3-17

	a/c 1	a/c 2	Total
Number of Flights	22	3	25
Flight Time (hrs)	22	2.7	24,7
Max. Mach/ Alt	0,9 / 40 kft		
Max. KIAS (knots)	367		
Max AOA(deg)	20		
Max.struct. loadf.(g)	5		

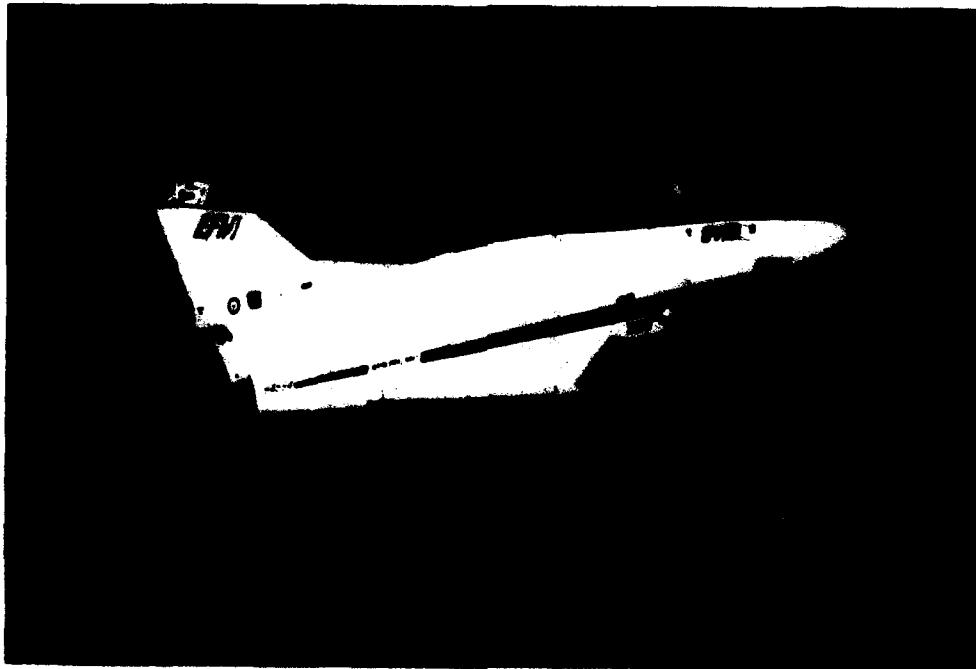
Flutter-, Loads- , and H.Q. Tests ongoing

First Government Pilot Evaluation Flights successfully completed

## X-31 Flight Test Status

22.April 1991

Fig. 4-1



# AERODYNAMIC AND FLOWFIELD HYSTERESIS OF SLENDER WING AIRCRAFT UNDERGOING LARGE-AMPLITUDE MOTIONS

by

Robert C. Nelson, Andrew S. Arena Jr. and Scott A. Thompson  
Department of Aerospace and Mechanical Engineering  
University of Notre Dame  
Notre Dame, Indiana 46556  
United States of America

## ABSTRACT

The implication of maneuvers through large-angles-of-incidence is discussed by examining the unsteady aerodynamic loads, surface pressures, vortical position and breakdown on slender, flat plate delta wings. Two examples of large amplitude unsteady motions are presented. First, the unsteady characteristics of a 70 degree swept delta wing undergoing pitch oscillation from 0 to 60 degrees is examined. Data is presented that shows the relationship between vortex breakdown and the overshoot and undershoot of the aerodynamic loads and surface pressure distribution. The second example examines the leading edge vortical flow over an 80 degree swept wing undergoing a limit cycle roll oscillation commonly called wing rock.

## NOMENCLATURE

### Symbols

b	Wing span, in (cm)
c	Root chord, in (cm)
f	Pitching frequency, Hz
I <sub>x</sub>	Rotational moment of inertia
k	Reduced frequency, $k = 2\pi fc/U_\infty$
L	Roll moment
L <sub>aero</sub>	Roll moment due to aerodynamic forces
L <sub>bearing</sub>	Roll moment due to bearing friction
P	Pressure, psi (Pa)
P <sub>∞</sub>	Freestream static pressure, psi (Pa)
Q <sub>∞</sub>	Freestream dynamic pressure, psi (Pa), $Q_\infty = \rho U_\infty^2/2$
s	Local semi-span length, in (cm)
S	Wing area, in <sup>2</sup> , (cm <sup>2</sup> )
t	Time (sec)
U <sub>∞</sub>	Freestream velocity, ft/s (m/s)
x	Chordwise position, measured from the wing apex, in (cm)
y	Spanwise position, measured from the wing centerline, in (cm)
y <sub>l</sub>	Left vortex spanwise location variable
y <sub>r</sub>	Right vortex spanwise location variable
z <sub>l</sub>	Left vortex normal location variable
z <sub>r</sub>	Right vortex normal location variable
α	Angle of attack, deg
φ	Roll angle, deg
μ	Freestream air dynamic viscosity, lbf s/ft <sup>2</sup> (kg/m s)
ρ	Freestream air density, slug/ft <sup>3</sup> (kg/m <sup>3</sup> )

### Abbreviations

C <sub>L</sub>	Lift coefficient
C <sub>l</sub>	Roll moment coefficient
C <sub>p</sub>	Pressure coefficient, $C_p = (P_{tap} - P_\infty)/Q_\infty$
Re	Reynolds number, based on root chord, $Re = \rho U_\infty c/\mu$

### Subscripts

∞	Infinity, refers to freestream condition
tap	Refers to condition at pressure tap

## INTRODUCTION

The flow field surrounding a slender aircraft at large-angles-of-incidence is dominated by the vortices generated on the forebody, leading edge extensions, wing and control surfaces. The leeward wake structure can be extremely complicated due to the interactions between the various vortices. The aerodynamic forces created by such complicated flow patterns are in general nonlinear. In order to understand and predict the motion of aircraft in this nonlinear region, new mathematical formulations for the aerodynamic models must be developed and an improved understanding of the relationship between the separated flow field and the aerodynamic loads needs to be established. Methods for modelling the nonlinear aerodynamics are just starting to be developed.<sup>1,2</sup> In addition, experiments are being conducted to provide information on the unsteady aerodynamic characteristics of slender aircraft maneuvering at large angles of attack.<sup>3-12</sup>

The unsteady motion of a delta wing results in a modification of the flow field in response to the maneuver. This can result in delays of flow separation and vortex formation at low-angles-of-attack, and changes in vortex location and the onset of breakdown at higher-angles-of-attack. During oscillatory or periodic motions, a hysteresis develops in the positions of the vortex core and the vortex breakdown relative to the static locations. Due to the hysteresis in the flow field, there is a corresponding modification of the aerodynamic loads on the delta wing. The results presented in the following section are used to show the importance of flow field hysteresis in either vortex position or breakdown on the unsteady loads and surface pressure distributions of simple delta wing planforms.

Ashley, Katz, Jarrah, and Vaneck<sup>12</sup> have recently published a paper summarizing the current state of unsteady swept wing aerodynamics research. Theoretical, computational, and experimental research involving both flow field behavior and aerodynamic forces and moments is described. Ashley, et al., concluded that for unsteady pitching maneuvers where vortex breakdown is not present, the aerodynamic characteristics behave in a quasi-static manner. However, for ranges of motion where breakdown is present over the wing, hysteretic behavior is observed.

At high-angles-of-attack the leading edge vortices can undergo a transition known as vortex breakdown, which can cause a loss of both lift and nose-down pitching moment. Unsteady swept wing aerodynamics at very high-angles-of-attack are characterized by hysteretic behavior; typically for ranges of incidence precluding vortex breakdown, hysteresis effects are not as pronounced. A substantial overshoot in the aerodynamic forces is typically seen for oscillatory or transient pitching maneuvers. For a dynamically pitching wing it may be possible to exploit this overshoot or delay the detrimental effects of breakdown.

Flying at high-angles-of-attack is intrinsically an unsteady flight regime, and as such an understanding of the unsteady aerodynamics of swept wings is of value. An understanding of these dynamic, high-angle-of-attack phenomenon is of particular concern during the landing and take-off stages of operation for a swept wing aircraft. During such phases these aircraft must operate at high incidence to obtain the necessary high lift coefficient. In addition, military applications stand to gain an expanded combat maneuvering envelope from such an understanding. Maneuvers such as nose pointing and velocity vector turning involve high-angles-of-attack and successful execution would necessitate the ability to anticipate the dynamic reaction of the flow field to the maneuver. Fundamental flow mechanisms need to be quantified before effective flight control systems can be developed.

This paper will review the current understanding of large-angle-of-attack unsteady motions on the aerodynamic and



vortical wake characteristics. The discussion will emphasize the fluid mechanic mechanisms governing the nonlinear aerodynamic loads. Emphasis will be given to showing the relationship between the force and moment coefficients, surface pressures and the flow field structure. The examples of unsteady motion include single-degree-of-freedom, large amplitude, pitching or rolling motions. A  $70^\circ$  wing was used for the pitch oscillation tests. This sweep angle was chosen as a value for which a great deal of information exists in the literature. As it was also desired to examine dynamic effects that could be associated with limit cycle wing rock, an  $80^\circ$  wing was used for the roll oscillation tests. Wing rock has been documented for wings with this sweep angle. Flow visualization tests were conducted on both wings to identify static and dynamic vortex characteristics. In addition, for the pitch oscillation tests, both static and dynamic surface pressures were obtained. For the roll oscillation tests angular velocity and roll moment were obtained during the buildup and steady state stages of wing rock. Static and dynamic surface pressures were also measured.

## EXPERIMENTAL RESULTS

### Pitching Delta Wing

Unsteady force measurement for large amplitude motions is a relatively new area of research, but the limited number of studies that are available have documented the hysteretic nature of the forces and moments. Bragg and Soltani<sup>3</sup> conducted an experiment using a  $70^\circ$  sweep wing oscillating in pitch. Hysteretic behavior was noted in the dynamic loads; the amount of which was a function of the pitch rate. This was also seen by both Brandon and Shah<sup>4,5</sup> and Jarrah.<sup>6,7</sup> Brandon and Shah examined the effects of both sinusoidal and ramp pitching motions. They reported a large overshoot of the forces relative to the steady state values. Brandon and Shah suggested that this may be due to a lag in the separation and reattachment of the leading edge vortices during the dynamic maneuver. Jarrah utilized delta wings with aspect ratios of 1, 1.5, and 2 and angle of attack ranges of  $0-30^\circ$  and  $0-60^\circ$ . He saw a large overshoot in the aerodynamic coefficients for the  $0-60^\circ$  motion, and noted that this overshoot was a function of the aspect ratio as well as the pitch rate. Figure 1 is an example of Jarrah's data that clearly shows the large aerodynamic hysteresis.

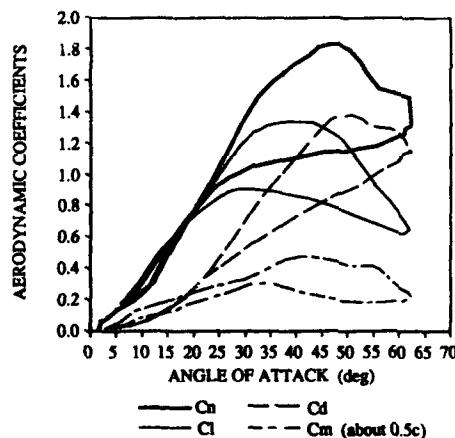


Figure 1. Unsteady Aerodynamic Coefficients for a Slender Delta Wing. Aspect Ratio = 1.0,  $k = 0.03$ ,  $Re = 635,000$ , Pitch Amplitude =  $0-60^\circ$ . (From Jarrah).

Unsteady delta wing research has shown the force and moment coefficients to overshoot or undershoot the static values depending on both the type of unsteady maneuver and the motion history. For example, if the model pitches from  $0-45^\circ$ , the peak overshoot in  $C_L$  will be higher than if the model pitches from  $25-45^\circ$ . An example of the dynamic normal force coefficient for a pitching delta wing is shown in Fig. 2 along

with the static curve. This data was obtained by Brandon and Shah<sup>4</sup> using a force and moment balance to measure the dynamic loads on a pitching delta wing. If the dynamic lift can be maintained, then it would be possible to increase the maneuvering performance of airplanes. However, to exploit dynamic lift a better understanding of unsteady slender wing aerodynamics will be required than is presently available.

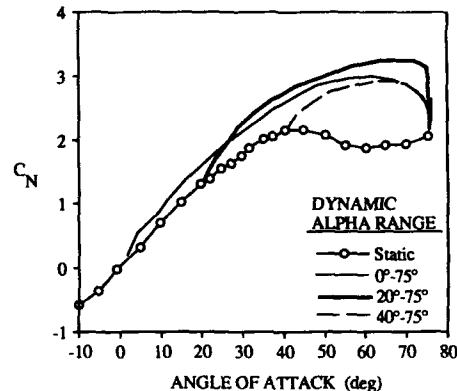


Figure 2. Dynamic Lift Overshoot of a Slender Delta Wing. Leading Edge Sweep Angle =  $70^\circ$  (From Brandon and Shah).

### Surface Pressure Distributions

The unsteady pressure data for pitching oscillations over an angle of attack range of  $0-30^\circ$  showed pressures fluctuating in phase with model motion, and little overshoot from the static values. This is consistent with force measurement made by Jarrah. On the other hand, the pressures for a  $2-60^\circ$  angle of attack range (a range of motion including the existence of vortex breakdown over the wing) showed large overshoots from the steady state values. In addition, during the high-angle-of-attack portion of the motion, the upstroke (angle of attack increasing) pressure coefficients were typically much lower than the downstroke values. Pitch rates of 0.90 and 0.45 Hz were examined; and for the lower rate there was little difference between upstroke and downstroke pressures at the low-angles-of-attack.

For the  $70^\circ$  wing, steady surface pressure measurements were made with the wing at a fixed angle of attack, over a range of  $2-60^\circ$  angle of attack. The Reynolds number was 420,000. Figure 3 is a sketch of the model geometry and pressure orifice locations. Pressure profiles were obtained along all three arrays of pressure taps on the wing surface.

The static data is presented in Figs. 4 and 5. Figure 4 shows data taken along a line of constant span location, at  $y/s = 0.60$ . Each pressure distribution consists of pressures measured from twelve chord locations from  $0.35c-0.90c$ . From Fig. 4 it can be seen that the pressure profiles up to  $10^\circ$  are effectively the same. Above this angle the pressures begin dropping, and at  $40^\circ$  the minimum  $C_p$  has been reached at most of the chord locations sampled. It is near this angle of attack that  $70^\circ$  sweep delta wings typically achieve a maximum lift coefficient.<sup>6,7,13,14,15</sup> The lowest pressure coefficient measured is a  $C_p$  of  $-3.75$ , at the 35% chord location.

Above  $40^\circ$  angle of attack the pressures begin rising. At  $50^\circ$  the pressure distribution has roughly the same shape and slope as that of the lower incidence curves, for example  $30^\circ$  incidence. However, from  $50^\circ$  to  $60^\circ$  the upper surface pressures become more uniform, indicating the onset of fully separated flow over the surface of the wing. At  $60^\circ$  the profile is very flat, at a  $C_p$  of  $-1.3$ .

Figure 5 shows the spanwise pressure distribution at a chord location of 75%. This figure is labeled in terms of negative span locations; this is used to differentiate the left (negative) side of the centerline from the right (positive) side, as viewed from the rear. As in the previous figure, angles of attack

from 2-60° are shown. It is important to note that the upper surface bevel extends from the leading edge to a span location of 76%  $y/s$  on either side. Hence, along the 75% chord line the outboard two pressure taps are located on the bevel, and the next tap is at the interface between the bevel and the flat upper surface.

From Fig. 5 it can be seen that the pressures at these three taps change with angle of attack even at the very low angles, from 2-10°. Note that the pressure at 60%  $y/s$  is effectively constant up to 10° as was seen in Fig. 4. Above 10° a suction peak is evident in the pressure profile, due to the presence of the leading edge vortex over the surface of the wing. Although the vortex core is located some distance above the wing, its presence can be detected at the surface by this minimum pressure peak. As the vortex moves inboard with increasing angle of attack (see Jarrah<sup>6,7</sup>, Roos and Kegelman<sup>14</sup>, and Parker<sup>15</sup>), so does the suction peak. At 15° it is located at approximately 76%, and by 40° it has moved to approximately 64%. The value of this peak pressure changes only slightly from 30-40°; the primary difference occurring over those angles of attack is a broadening of the peak and a decrease of the inboard pressures.

The suction peak reaches its minimum value of  $C_p = -2.0$  at 40° angle of attack. Above this angle the spanwise pressures begin increasing. As in Fig. 4, from 50-60° the pressures are leveling out and by 60° the pressure distribution has become nearly uniform. The suction peak is only slightly visible at 50°, and is completely gone by 60°.

As with the steady pressure data, the unsteady pressure distributions for the 70° wing were all obtained at a Reynolds number of 420,000. Dynamic angle of attack ranges of 0-30° and 2-60° were used. Two pitch rates were examined, corresponding to reduced frequencies of  $k = 0.0764$  and 0.1528. The tests conducted over the range of 0-30° revealed that the surface pressures oscillated in phase with the model motion. No consistent hysteresis effects were seen; this is consistent with the trends seen by other researchers who examined ranges of motion where vortex breakdown did not exist over the wing (see Ref. 12 for further information on this point). The data for this range of motion has been documented in Ref. 11 and will not be presented here.

Figures 6 and 7 contain data for the range of motion of 2-60°. The reduced frequency was 0.0764, corresponding to 0.45 Hz. Twelve chord locations from 0.35-0.90c were sampled, all at a constant span location. Figure 6 shows the data plotted as a function of angle of attack in order to illustrate the overshoot and hysteresis characteristics. The pressures from the

0.35c, 0.55c, and 0.75c chordwise locations at a fixed  $y/s = 60\%$  are displayed in the three parts of Fig. 6. Both the direction of motion and the corresponding static data are shown on each curve for reference. The vertical lines drawn through the 40, 50, and 55° angles will be used as a reference for Fig. 7. The upstroke pressures approximately follow the static pressures up to an angle of 40°. At this point the steady case pressures begin increasing while the unsteady case pressures continue to decrease. This can be seen at each of the three chord locations shown in Fig. 6. This effect, when integrated over the entire surface of the model, produces the overshoot in lift coefficient seen by other researchers.<sup>3,6,7</sup> For the 35% location this overshoot is as high as 60% above the static value. The downstroke pressures are higher than both the upstroke and the steady pressures. The downstroke pressures become equal to the upstroke pressures between 25-30° angle of attack. Below this angle the unsteady and steady curves are effectively the same for each chord location. This is true of each of the chord locations sampled in addition to the three shown in Fig. 6.

Figure 7 shows the instantaneous pressure profiles along the ray from 0.35c-0.90c, taken at each of the three angles of attack (40°, 50°, 55°) indicated in Fig. 6. Figure 6 shows the overshoot of individual taps throughout the motion. Fig. 7 shows the overshoot of all twelve taps at one-angle-of-attack during the motion. The lines superimposed on Fig. 7 correspond to those tap locations in Fig. 6. At 40° only the pressures from 0.35-0.55c have begun to overshoot the steady values; the other chord locations are still at or close to their steady values. By 50° the upstroke pressures are lower than the steady pressures at each chord location. At 55° the unsteady pressures have still not collapsed although they have decreased slightly from the 50° values. The downstroke pressures indicate a separated flow condition over the wing, and as such, they match the steady pressures which also reflect that condition. At

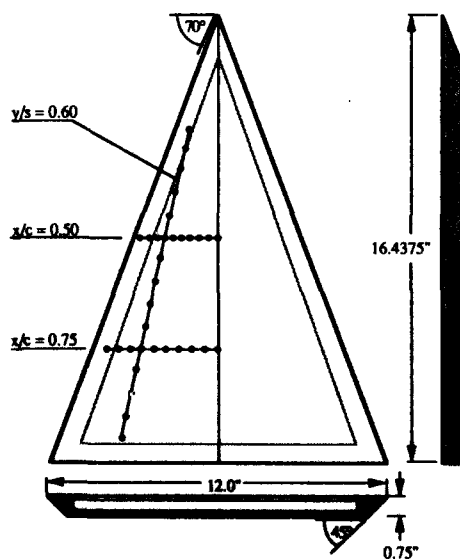


Figure 3. 70° Delta Wing Pressure Model.

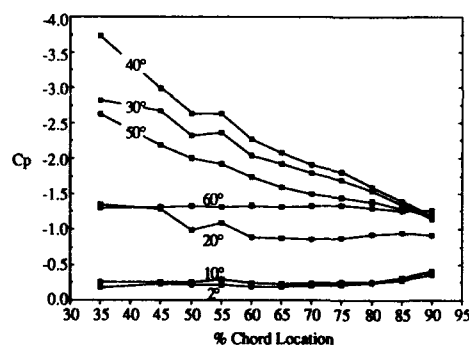


Figure 4. Chordwise Steady Pressure Data.  $y/s = 60\%$ . 2-60° Angle of Attack.  $Re = 420,000$ .

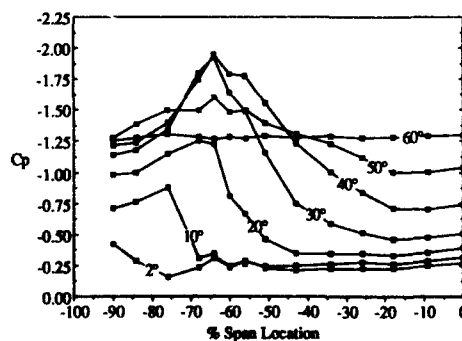


Figure 5. Spanwise Steady Pressure Data.  $x/c = 75\%$ . 2-60° Angle of Attack.  $Re = 420,000$ .

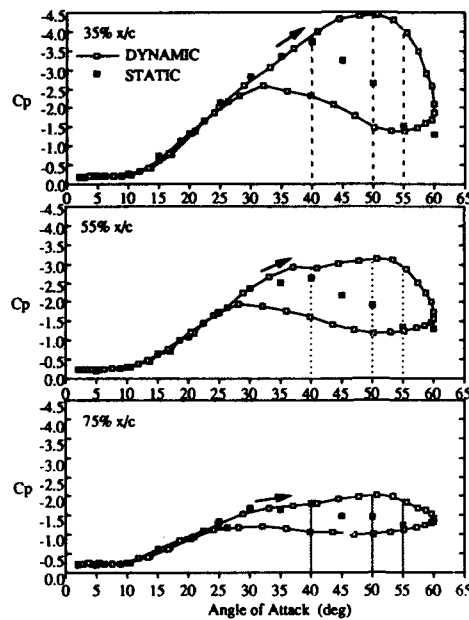


Figure 6. Unsteady Pressure Coefficient as a Function of Angle of Attack for Three Chord Locations;  $x/c = 35\%$ ,  $55\%$ ,  $75\%$ .  $k = 0.0764$ . Static Data also Shown.  $Re = 420,000$ . Highlighted Angles of Attack Refer to Fig. 4.

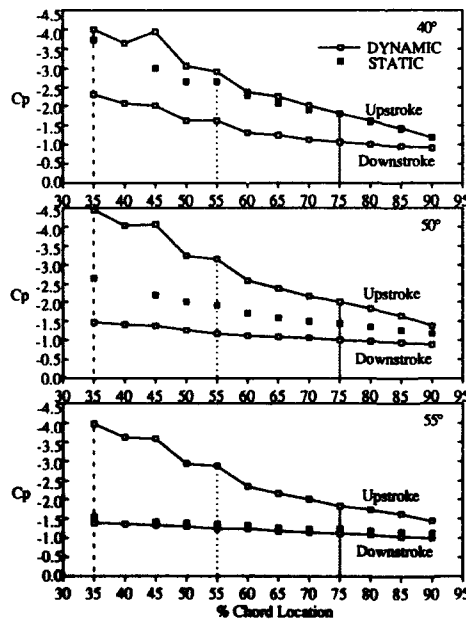


Figure 7. Instantaneous Chordwise Pressure Profiles for both Upstroke and Downstroke. Three Angles of Attack Shown;  $40^\circ$ ,  $50^\circ$ ,  $55^\circ$ .  $k = 0.0764$ .

$50^\circ$  the downstroke pressures also show fully separated flow, while the steady pressures are somewhat lower. As the model continues pitching down, the pressures at each chord location begin decreasing. By  $40^\circ$  the pressure distribution is no longer flat; this indicates that the leading edge vortices have reformed over the surface of the wing.

Figure 8 shows pressure data taken along a line of pressure taps located at a constant chord location of  $0.75c$ . This data shows instantaneous pressure profiles at a specific angle of attack and for the lower reduced frequency of  $k = 0.0764$ . The same three angles of attack are shown as in the previous plots;  $40^\circ$ ,  $50^\circ$ , and  $55^\circ$ . The  $60\%$   $y/s$  pressure tap has been singled out as a reference; it also exists in the constant span data, shown in Figs. 6 and 7.

At  $40^\circ$  angle of attack, the upstroke unsteady pressures are essentially the same as the steady pressures, at each of the spanwise locations sampled. Increasing to  $50^\circ$  the steady pressures begin to rise while the upstroke pressures remain low, until by  $55^\circ$  the upstroke pressure coefficients are almost twice the steady values. The steady data and the downstroke pressures are essentially the same.

#### WING ROCK FOR SLENDER WINGS

Slender, flat plate, delta wings having leading edge sweep angles greater than  $76$  degrees have been observed to exhibit a limit cycle roll oscillation at angle of attack. This limit cycle rolling oscillation is commonly called "wing rock." By definition, a limit cycle motion is one that reaches a steady state oscillation independent of the initial conditions. Figure 9 is an example of the limit cycle rolling motion of an  $80$  degree delta wing measured on a free-to-roll system incorporating an air bearing. The wing rock roll angle amplitude increases with increasing angle of attack as illustrated in Fig. 10. When vortex breakdown starts occurring over the wing above  $\alpha = 35^\circ$  the amplitude drops sharply.

The wing rock motion was analyzed by obtaining angular velocity and angular acceleration from the roll angle time histories. This information was very useful in studying the limit

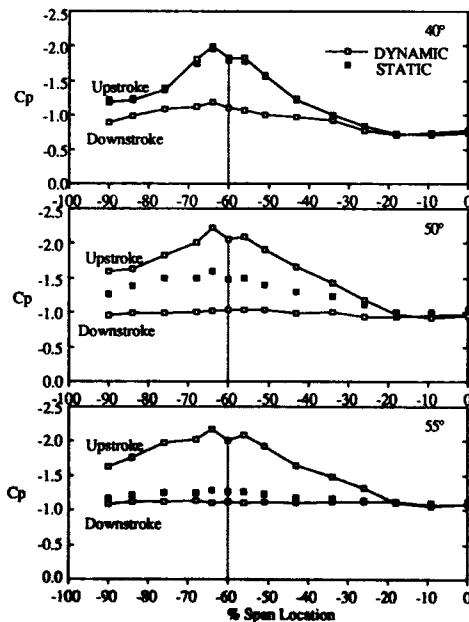
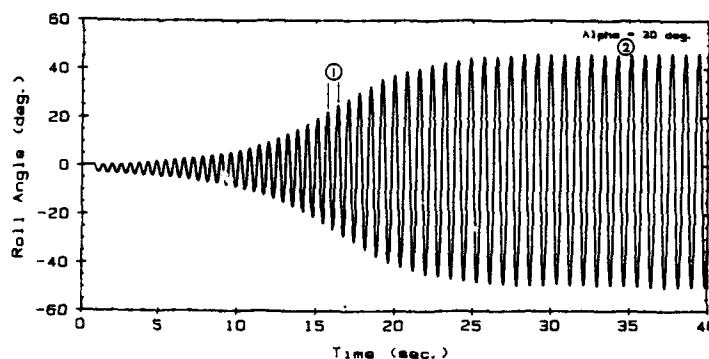
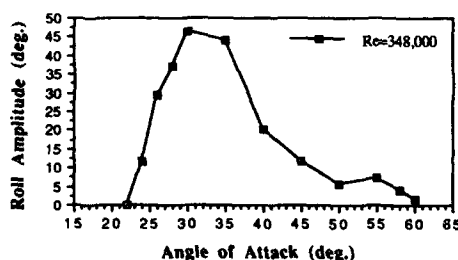


Figure 8. Instantaneous Spanwise Pressure Profiles for both Upstroke and Downstroke.  $x/c = 75\%$ . Three Angles of Attack Shown;  $40^\circ$ ,  $50^\circ$ ,  $55^\circ$ .  $k = 0.0764$ .

Figure 9. Time History of Wing Rock Buildup ( $\alpha = 30^\circ$ ).Figure 10. Wing Rock Roll Amplitude versus Angle of Attack.  $Re = 348,000$ .

cycle behavior of the motion. The determination of  $\dot{\phi}$  and  $\ddot{\phi}$  involved a two step data reduction process. First, the roll angle time history data was low pass filtered. This was necessary to remove the digital "steps" in the data which would manifest itself as high frequency noise when differentiated. Central differencing schemes were then used to determine  $\dot{\phi}$  and  $\ddot{\phi}$ . Validation of this method may be found in Ref. 16.

Roll moment coefficient could be obtained from the angular acceleration data. The calculation of  $C_l$  is made simple by the fact that the model is constrained to one-degree-of-freedom. The equation of motion for the system is:

$$I_x \ddot{\phi}(t) = \Sigma L(t) \quad (1)$$

where:  $\Sigma L = L_{\text{aero}} + L_{\text{bearing}}$

With the use of the air bearing apparatus  $L_{\text{bearing}}$  may be neglected, effectively isolating the aerodynamic effects on the wing. In coefficient form, the equation may be written:

$$C_l(t) = \frac{I_x \ddot{\phi}(t)}{qSb} \quad (2)$$

Using a torsional pendulum technique, the rotational moment of inertia  $I_x$  was determined experimentally. With this result, the aerodynamic rolling moment coefficient  $C_l$  could then be easily calculated.

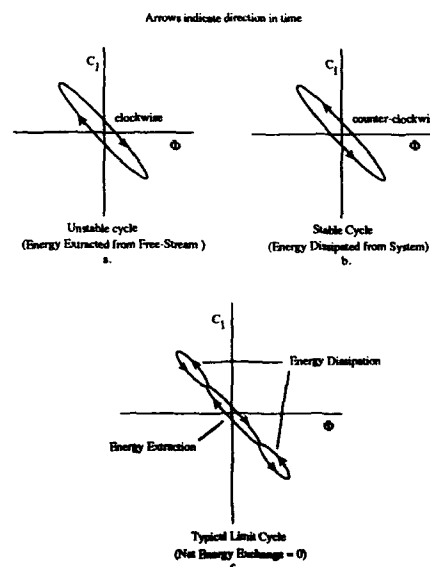
With  $C_l$  known, the energy exchange technique used by Nguyen, Yip, and Chambers<sup>17</sup> was helpful in analyzing the mechanisms driving the limit cycle oscillation. For the single-degree-of-freedom motion, the energy is equal to the applied torque times the angular velocity. The energy added to or extracted from the system during the motion for a specific time interval can be expressed as:

$$\Delta E = qSb \int_{t_1}^{t_2} C_l(t) \dot{\phi}(t) dt \quad (3)$$

This expression for the energy exchange may be written in a more convenient form by rewriting the equation in terms of the instantaneous roll angle  $\phi(t)$ :

$$\Delta E = qSb \oint C_l(\phi(t)) d\phi \quad (4)$$

where  $C_\phi$  is the curve obtained by plotting  $C_l$  as a function of the instantaneous roll angle  $\phi(t)$  for a given time interval. The physical interpretation of Eq. 4 is that the energy exchanged in a cycle of motion is directly related to the area enclosed by the rolling moment curve. When the loop encloses an area in a clockwise sense, energy is being added to the system, whereas counterclockwise loops indicate that energy is being dissipated from the system. Figure 11 is a graphical representation of the energy for several different rolling motions.

Figure 11. Typical  $C_l$  vs  $\phi$  Curves Showing Energy Exchange.

In Figure 9, two cycles of the motion are identified, one cycle in the build up portion of the motion and the other when the limit cycle is reached. The buildup cycle and steady state cycle were singled out for a more detailed analysis as cycle 1 and cycle 2. The dynamic roll moment characteristics of the buildup cycle (cycle 1) may be seen in Fig. 12. Note the clockwise loop in the plot which indicates a dynamic instability, and that the restoring moment is roughly linear with roll angle. Energy is being fed to the system, therefore the roll angle amplitude is increasing. The loop is very thin which accounts for the fact that the buildup happens very slowly. Figure 13 is the analogous plot of the roll moment coefficient after the system has reached steady state (cycle 2). The unstable region of the plot still exists between  $-22^\circ$  and  $20^\circ$ , but two stable damping "lobes" have formed for the larger roll angles. The area of these lobes equals the area of the unstable portion of the plot such that the net energy exchange is zero. This condition is necessary for the limit cycle oscillation to be sustained.

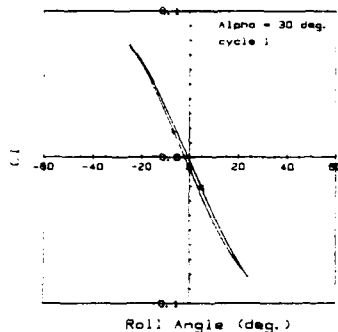


Figure 12.  $C_l$  versus  $\phi$  for Cycle 1 (Buildup).

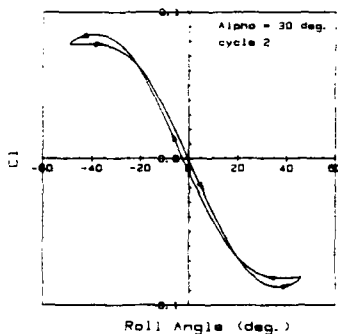


Figure 13.  $C_l$  versus  $\phi$  for Cycle 1 (Steady State).

#### Rolling Wing: Vortex Trajectory Results

It is known that vortex position above a delta wing is a function of roll angle (or sideslip). Jun and Nelson<sup>18</sup> have shown a dependence of vortex position vs. roll angle for an  $80^\circ$  sweep delta wing experimentally. The results indicate that the static and dynamic vortex trajectories differ greatly. The dynamic position of the vortices exhibits a time lag phenomenon which accounts for the appearance of hysteresis. Time lag in vortex position has also been seen in numerical simulations by Konstantinopoulos, Mook and Nayfeh<sup>19</sup> using an unsteady vortex lattice model coupled with a single-degree-of-freedom equation of motion, and has been suggested with analytical arguments by Ericsson.<sup>20</sup> The vortex position above a delta wing greatly affects the pressure distribution and it is thought that the movement of the leading edge vortices may be a driving mechanism in the wing rock motion.

The purpose of these experiments was to correlate the position of the leading edge vortices with the model motion during wing rock to determine the effect of dynamic vortex movement on the model motion. With the apparatus developed for this study, the vortex position during wing rock could be related to time, roll angle, angular velocity, and rolling moment.

The angle of attack chosen for these experiments was  $30^\circ$ . The reason for this choice is twofold. First, since wing rock is present even in the absence of vortex breakdown, the fundamental mechanisms causing the motion can be further isolated by operating at an angle of attack where breakdown is not seen. Secondly,  $\alpha=30^\circ$  yields the largest roll excursions, hence the motion of the vortices are large in amplitude which reduces the percentage of error when digitizing the video images of the vortices.

Steady vortex experiments were first conducted for a comparison with the unsteady results. Left and right vortex position refers to a view from the trailing edge of the wing. The static results show that as one side of the wing moves downward, its associated vortex moves inward both spanwise and normally, and vice versa on the upward wing. Note that use of the word normal refers to a coordinate system that rotates with the wing; hence normal distance is the distance perpendicular to the plane of the wing surface. When the vortex position is analyzed during wing rock, the results differ greatly from the static case. Figures 14a and 14b show the normal and spanwise static positions of the vortices and the position during two steady state cycles of wing rock. The normal dynamic position of the vortices exhibits a large hysteresis loop whereas none is discernable in the spanwise position of the vortices.

The results obtained from this analysis reveal some interesting phenomena which have not been reported previously. A time lag exists in the position of the vortices during the wing rock cycle, however this time lag manifests itself in only one aspect of the motion. The time lag in vortex position is only seen in the normal vortex position. No time lag is seen in the spanwise position of either vortex.

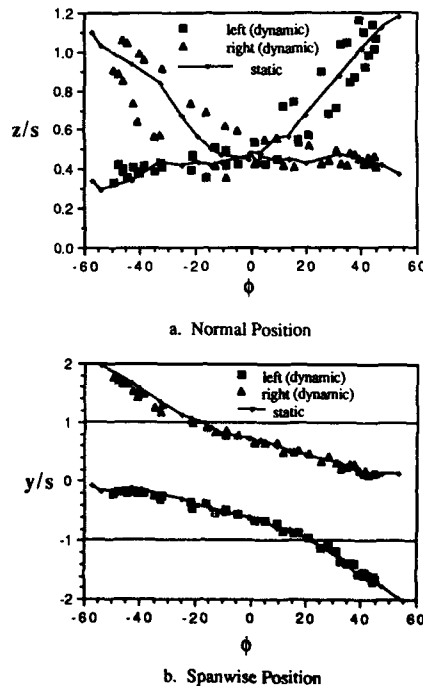


Figure 14. Static and Dynamic Vortex Position vs.  $\phi$  @ 95% Chord ( $\alpha = 30^\circ$ ).

In order to analyze the effect that vortex motion has on wing rock, all of the factors which contribute to rolling moment should be kept in mind. The contribution to the rolling moment due to the leading edge vortices is a function of their position, strength and state (i.e. whether breakdown has occurred). From the flow visualization data, the position and state of the vortex can be determined. However, vortex strength is unknown.

An argument may be made as to how vortex strength varies with roll angle. For a model constrained to roll around its longitudinal axis, the downward wing will experience an effective decrease in sweep whereas the upward wing will see an effective increase in sweep. For a given angle of attack, less sweep implies a stronger vortex. Therefore one can conclude that the variation in vortex strength due to roll angle will contribute to a static restoring moment. In addition, one might expect a lag in vortex strength due to the convective time lag associated with the transport of vorticity along the wing for a dynamic model. This would of course, create a lag in the restoring moment.

Since asymmetry in vortex position is one of the factors that will contribute to the rolling moment, a method was developed for interpreting the data which quantifies the normal and spanwise vortex asymmetries. Figure 15 is a sketch of asymmetric vortex position used to define asymmetry parameters  $\Delta z$  and  $\Delta y$ .  $\Delta z$  is a measure of the normal asymmetry between the two vortices and is defined such that a positive  $\Delta z$  will favor a positive rolling moment. Similarly,  $\Delta y$  is a measure of the spanwise asymmetry of the vortices and is defined such that a positive  $\Delta y$  will favor a positive roll moment (assuming  $y/s$  is not greater than 1). The asymmetry parameters are defined as follows:

$$\begin{aligned}\Delta z &= z_r - z_l \\ \Delta y &= |y_l| - |y_r|\end{aligned}\quad (5)$$

While  $\Delta z$  and  $\Delta y$  indicate the direction of the contribution to rolling moment due to vortex position asymmetry, the actual magnitude of their contributions is unknown.

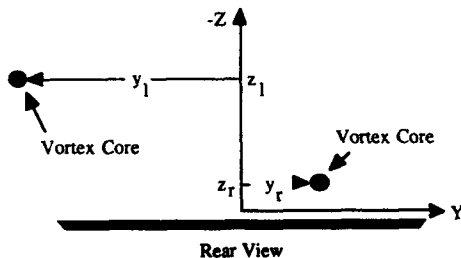


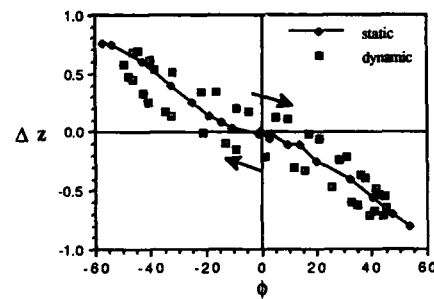
Figure 15. Sketch of Asymmetric Vortex Position.

Figures 16, a and b, are plots of  $\Delta z$  and  $\Delta y$  for the static case and for the two steady state cycles of wing rock. The static normal asymmetry is seen to contribute to a restoring moment since the downward wing vortex is closer to the wing surface than the upward wing vortex. The static spanwise asymmetry can be seen to contribute to a roll moment in the opposite sense since the downward wing vortex moves closer to the root chord, and the upward wing vortex moves away from the root chord. However, the contribution from spanwise asymmetry in vortex position to roll moment must be dominated by the contributions from normal asymmetry and vortex strength asymmetry for the static restoring moment to be produced. Also note that there is hysteresis in vortex position asymmetry confined to the direction normal to the wing, which is consistent with the fact that the time lag in vortex movement is confined to the normal direction.

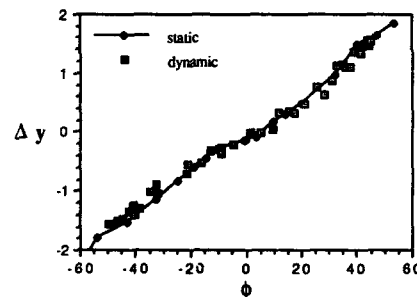
If restoring and positive damping moments alone were present, the wing would damp out in time if perturbed. Therefore there must be an aerodynamic phenomenon that generates a destabilizing moment during wing rock. Likely candidates for the mechanisms responsible for the destabilizing moment include the time lag in vortex position and/or a time lag

in vortex strength. In this study, only the contribution to roll moment from the lag in vortex position could be analyzed.

The hysteresis phenomena seen in Figs. 14 and 16a can alone provide the instability necessary to sustain the wing rock motion if a time lag in vortex strength is not present. With no significant time lag in vortex strength, vortex strength asymmetry will only contribute to a restoring moment and not the destabilizing moment necessary to sustain wing rock. In Fig. 14, the time lag in normal vortex position is seen. Figure 16a shows that due to the time lag, a switch to a restoring moment contribution from the normal vortex position asymmetry does not occur until approximately  $20^\circ$  for positive roll rates, and approximately  $-20^\circ$  for negative roll rates. Compare this result to the  $C_l$  vs.  $\phi$  result in Fig. 17 which corresponds to two steady state cycles of vortex motion. It can be seen that the unstable region of the plot lies between  $-20^\circ$  and  $20^\circ$ . The lag in asymmetry must be great enough to overcome the roll damping moment which increases for small roll angles due to higher



a. Normal Asymmetry



b. Spanwise Asymmetry

Figure 16. Steady and Unsteady Vortex Asymmetry at  $0.95c$  ( $\alpha = 30^\circ$ ).

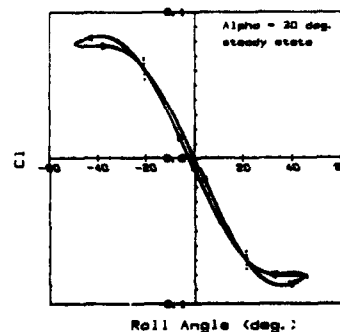


Figure 17.  $C_l$  versus  $\phi$  for Two Steady State Cycles of Motion

angular velocity. The leveling off of the  $C_l$  vs  $\phi$  curve is most likely due to the leveling off of the vortex position time histories seen in Fig. 14 when the vortex approaches the wing. These results suggest that the time lag in normal vortex asymmetry may be a mechanism responsible for wing rock. These results motivated a further study of the phenomenon which will yield the unsteady surface pressures on the model. The data may be correlated with the motion of the model and the vortices to gain a better understanding of the aerodynamic mechanisms at work.

#### Effect of Vortex Breakdown on Wing Rock

In Ref. 21, static and dynamic vortex breakdown characteristics during wing rock were presented. In the current study, the data is presented in a manner which reveals the effect of vortex breakdown on the wing rock motion. Data is available in the literature which has shown vortex breakdown to have a damping effect on the motion.<sup>22</sup>

As with vortex position, vortex breakdown contributes to a rolling moment on the wing through asymmetry. For this reason, a vortex breakdown asymmetry parameter  $\Delta x$  was defined. If the distance of the breakdown from the apex is greater on the left side of the wing than that on the right, the asymmetry will contribute to a positive rolling moment. Figure 18 is a sketch showing the asymmetry in vortex breakdown.  $\Delta x$  was defined such that if the asymmetry favors a positive rolling moment then  $\Delta x$  is positive:

$$\Delta x = x_l - x_r \quad (6)$$

where  $x_l$  and  $x_r$  are the chordwise vortex breakdown locations from the apex, of the left and right vortices respectively (as viewed from the trailing edge).  $\Delta x$  was plotted with roll angle to better show the effect of breakdown on the model motion.

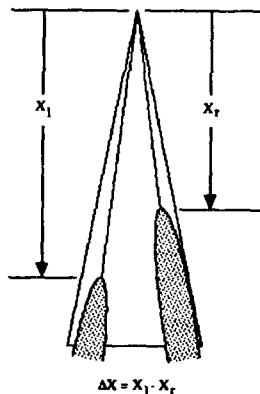


Figure 18. Sketch of Asymmetric Vortex Breakdown.

Figure 19 shows static and dynamic vortex breakdown parameter  $\Delta x$  vs. roll angle for  $\alpha=40^\circ$ . The effect of vortex breakdown on the model is very apparent in this plot. Since the slope of the  $\Delta x$  vs.  $\phi$  curve is positive for all roll angles for the static case, the static data suggests that the effect of vortex breakdown on wing rock is to create a roll divergence. However, the results from the dynamic experiments suggest a very different effect. Due to the large time lag, the effect of dynamic breakdown on the wing is to have a damping effect on the motion. This is due to the fact that the parameter  $\Delta x$  always favors a rolling moment in the opposite direction to the rotation. This analysis cannot give the magnitude of the contribution to the rolling moment of the wing, but it does provide the insight into qualitatively, how the dynamic motion of the breakdown affects the wing.

From these results it appears that the effect of vortex breakdown during wing rock is to provide a damping moment. Vortex breakdown does not seem to contribute to roll divergence for the experiments conducted. It is clear that extrapolating static

vortex breakdown results to the dynamic case may be very misleading.

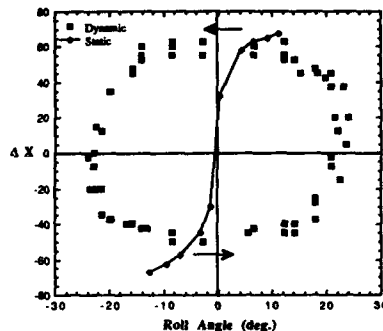


Figure 19. Static and Dynamic Vortex Breakdown Asymmetry ( $\alpha = 40^\circ$ ).

#### Surface Pressure Measurements

Static pressure data was taken at 3 chordwise stations (30%, 60% and 90%) for a range of roll angles from  $-45^\circ$  to  $45^\circ$ . Reynolds number for the tests was 400,000, and the angle of attack was  $30^\circ$ . The static data will serve as a baseline for comparison with dynamic pressure data taken on a wing undergoing wing rock.<sup>23</sup>

Figure 20 shows typical spanwise pressure profiles at the 60% chord location for some of the negative roll angles tested. Surface pressure coefficient is shown on the bottom and top surfaces of the wing. The suction peak on the left side of the wing is seen to increase up to a roll angle of  $-25^\circ$  where it then decreases. The peak is also seen to move toward the root chord. The suction peak on the right side of the wing is seen to decrease as roll angle becomes more negative.

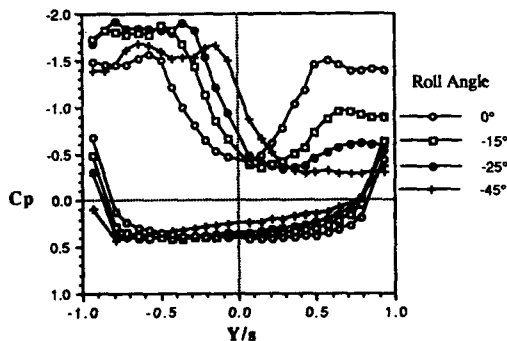


Figure 20. 60% Chord Pressure Profiles for Several Roll Angles.

The chordwise trend in spanwise pressure distribution may be seen in Fig. 21. The data shown is at the 30%, 60% and 90% stations for a roll angle of  $0^\circ$ . The upper surface pressure coefficient increases with chord location whereas the lower surface pressure coefficient changes little with chord station.

Results from static flow visualization of vortex core location was correlated with spanwise pressure coefficient. Typical results may be seen in Fig. 22 which is a view from the trailing edge of the wing. The data shown is at the 60% chord station for roll angles of  $0^\circ$ ,  $-25^\circ$  and  $-45^\circ$ . As the wing is rolled in a negative direction, the vortex on the left side of the wing moves inboard and towards the surface. The corresponding suction peak moves inboard with the vortex, however even though the vortex is closer to the wing at a roll angle of  $-45^\circ$  than  $-25^\circ$ , the suction peak is lower. On the right side of the wing the suction peak reduces as the vortex moves away from the wing, and also moves outboard. These pressure profiles reveal how

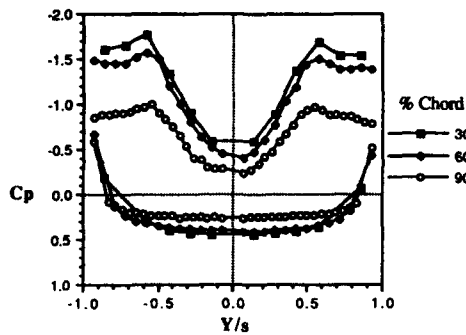


Figure 21.  $\phi = 0^\circ$  Pressure Profiles at 30%, 60%, and 90% Chord.

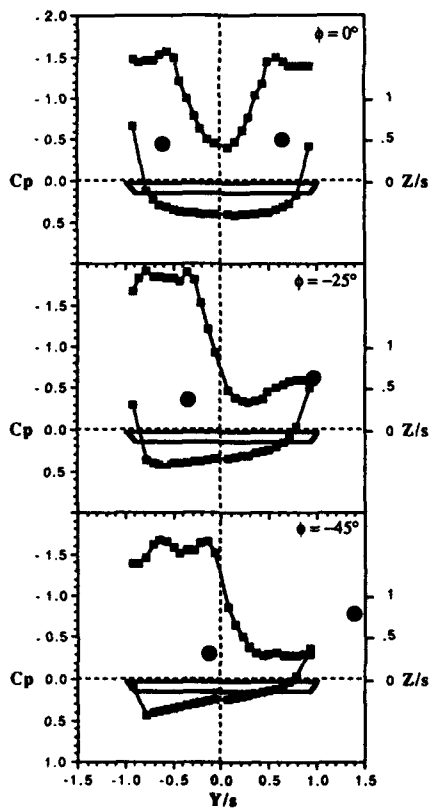


Figure 22. Typical Pressure Profiles and Vortex Core Locations at 60% Chord.

restoring moments are generated on the wing.

The roll moment vs.  $\phi$  curves reveal how the limit cycle is sustained during wing rock. However, this roll moment curve is an integrated effect of the surface pressure distributions on the wing. Flow visualization results also reveal a great deal about the behavior of the flowfield on the oscillating wing. However flow visualization alone can not quantify how the unsteady flowfield generates the wing rock motion. For these reasons, a study to measure the unsteady surface pressures on a wing undergoing wing rock has begun. These preliminary surface pressure experiments were conducted at a Reynolds number of 400,000 and at the 60% chord location to compare with the static results.

Figure 23 shows unsteady pressure data for 3 roll angles and both rotational directions. For  $\phi = 0^\circ$ , the pressure distributions corresponding to positive and negative roll rates differ measurably. The suction peaks are symmetric in a spanwise sense, but with respect to magnitude, the suction peaks on the upward travelling side of the wing is greater. This generates a roll moment in the direction of rotation, creating an instability. For  $\phi = -25^\circ$ , the difference between the profiles is much less discernable. Distributions for both roll directions favor a restoring moment as seen in the static pressure data. The small difference between the dynamic distributions is to be expected when the data is viewed in light of the roll moment curve. For  $\phi = -25^\circ$ , the roll moment hysteresis has just entered a region of damping and the difference in moment between positive and negative directions is small.

Maximum roll angle reached is  $-45^\circ$ . The suction peak in this pressure distribution is lower than that seen for  $\phi = -25^\circ$  which is consistent with that seen in the static data. The cause of the slope reduction in the roll moment data for large roll angles,

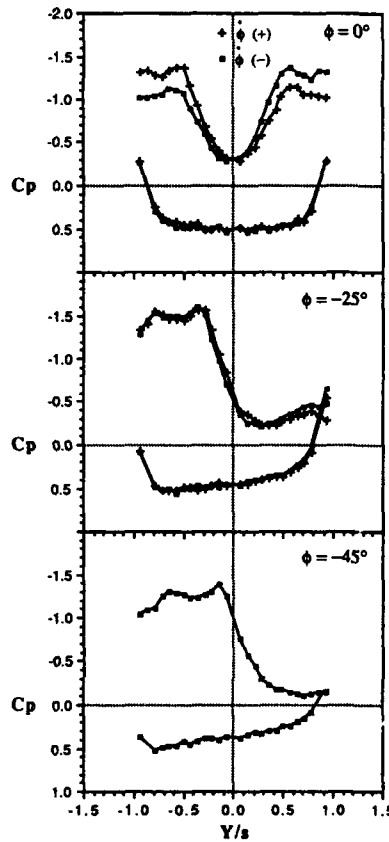


Figure 23. Spanwise Pressure Profiles @ 60% Chord (During Wing Rock).

may be explained with the pressure distributions. Above a roll angle of  $-25^\circ$ , the suction peaks begin to decrease with increasing roll angle. This is also seen in the static pressure distribution data.



## CONCLUSIONS

The pitching tests conducted over an angle of attack range of  $0-30^\circ$  showed very little hysteretic behavior. The surface pressures oscillated in phase with the model motion, and reached minimum values as the wing reached its maximum angle of attack. The pressures showed little deviation from the static values during the unsteady motion. These trends were apparent for both the reduced frequencies tested, and no apparent difference existed due to the change in pitch rate. The pressure data was seen to have similar general characteristics as normal force data obtained from the literature.

For the larger pitching range of  $2-60^\circ$ , large overshoots in the unsteady pressure coefficient were seen. The unsteady pressures follow the steady pressures on the upstroke, then continue to decrease as angle of attack increases for an additional  $10-15^\circ$ . On the downstroke, the upper surface continues to show full separation to an angle of attack where, for the steady case, coherent leading edge vortices exist. This results in an undershoot of the downstroke pressures relative to the steady pressures. When this is considered along with the large overshoot on the upstroke, a significant hysteresis is observed for the unsteady pressures, with upstroke pressure coefficients being as high as 2.5 times the downstroke values. This data was also seen to qualitatively compare with the normal force data for a wing of similar aspect ratio.

The constant chord data showed similar trends as the constant span data. Large hysteresis loops were seen at span locations at or near the suction peak. The static data showed this suction peak to exist from 60-70% of the local semi-span, depending on the angle of attack. This was also the case for the dynamic motion, where a hysteresis was seen in the suction peak; the location of the peak was seen to be a function of the direction of instantaneous model motion.

Dynamic roll moment results reveal hysteresis loops in buildup, steady state, and damping cycles of the wing rock motion. The dynamic roll moment data are very helpful in analyzing the wing rock motion. Flow visualization experiments were conducted to determine the contribution of vortex position to the roll moments generating wing rock in the absence of vortex breakdown. Static results indicate that the vortex on the downward wing moves closer to the wing and the root chord while the vortex on the upper wing moves away from the surface of the wing and the root chord. Dynamic results reveal a hysteresis in vortex position with roll angle. When the normal and spanwise positions are analyzed separately, the hysteresis was found to be entirely in the normal position to the wing. No hysteresis was found in spanwise position. The hysteresis in normal position favors a destabilizing contribution to the roll moment on the wing. When the motion of the vortices was analyzed further by plotting position vs. time, it was found that the hysteresis was generated by a time lag. There is no time lag associated with the spanwise position of the vortices.

When the model was held fixed at zero roll angle, no vortex position asymmetry was observed for any angle of attack investigated in this study. The vortex position was found to be a function of roll angle (sideslip). For each static roll angle there exists a unique vortex position. Vortex "lift-off" at zero-roll angle which is seen on forebodies, was not experienced by the  $80^\circ$  sweep delta wing.

From the results obtained in this study, a mechanism contributing to the destabilizing moment necessary to sustain the wing rock motion appears to be the time lag in the normal vortex position. The destabilizing moment must be great enough to overcome the stabilizing effect of roll damping, for the oscillation to grow in amplitude. The destabilizing roll moment hysteresis was found to correlate with the switch to a contribution to a restoring moment in the normal vortex position which supports the hypothesis. The destabilizing moments in the steady state are balanced by damping forces after the switch to a restoring moment has occurred, thus sustaining the steady state oscillation. It must be noted however that an investigation into the dynamic characteristics of vortex strength asymmetry was not conducted in this study. If a significant time lag exists in vortex strength asymmetry, this may also contribute to the destabilizing moments necessary to sustain wing rock.

This research was designed to study the components of an unsteady free flight maneuver by examining two of the three-degrees-of-freedom, pitch and roll, in isolated experiments. It was seen that hysteresis effects existed for both the pitching

wing and the rolling wing. However, for the pitching wing these unsteady effects appeared to be a vortex breakdown dominated phenomenon; that is, for ranges of motion where breakdown did not occur the hysteresis effects were considerably less pronounced. In contrast, hysteresis effects were clearly evident in the rolling wing results, even without the occurrence of breakdown.

## ACKNOWLEDGEMENTS

This research was sponsored by: the University of Notre Dame Department of Aerospace and Mechanical Engineering; NASA Langley Research Center, Hampton, VA, under grant NAG-1-727; NASA Ames Research Center, Moffett Field, CA, under grant NCA2-406; and the United States Air Force Office of Scientific Research under grant AFOSR-90-0321.

## REFERENCES

1. Hanff, E. S., "Non-linear Representation of Aerodynamics of Wing Rock of Slender Delta Wings," AIAA-85-1831, Aug. 1985.
2. Hanff, E. S. and Jenkins, S. B., "Large-Amplitude High-Rate Roll Experiments on a Delta and Double Delta Wing," AIAA-90-0224, Jan. 1990.
3. Bragg, M. B., and Soltani, M. R., "An Experimental Study of the Effect of Asymmetrical Vortex Bursting on a Pitching Delta Wing," AIAA-88-4334, August, 1988.
4. Brandon, J. M., and Shah, G. H., "Effect of Large Amplitude Pitching Motions on the Unsteady Aerodynamic Characteristics of Flat-Plate Wings," AIAA-88-4331, August, 1988.
5. Brandon, J. M., and Shah, G. H., "Unsteady Aerodynamic Characteristics of a Fighter Model Undergoing Large-Amplitude Pitching Motions at High Angles of Attack," AIAA-90-0309, January, 1990.
6. Jarrah, M. A. M., "Unsteady Aerodynamics of Delta Wings Performing Maneuvers to High Angle of Attack", Ph.D. Dissertation, Stanford University, December, 1988.
7. Jarrah, M. A. M., "Low-Speed Wind-Tunnel Investigation of Flow about Delta Wings, Oscillating in Pitch to Very High Angle of Attack", AIAA-89-0295, January, 1989.
8. Cunningham, A. M. Jr., den Boer, R. G., Dogger, C. S. G., Geurts, E. G. M., Persoon, A. J., Retel, A. P., and Zwaan, R. J., "Unsteady Low-Speed Wind Tunnel Test of a Straked Delta Wing, Oscillating in Pitch (Parts I through VI)", AFWAL-TR-87-3058, April, 1988.
9. Cunningham, A. M. Jr., "A Critique of the Experimental Aerodynamic Data Base for an Oscillating Straked Wing at High Angles", Fourth Symposium on Numerical and Physical Aspects of Aerodynamic Flows, California State University, January, 1989.
10. Thompson, S. A., Batill, S. M., and Nelson, R. C., "Unsteady Surface Pressure Distributions On A Delta Wing Undergoing Large Amplitude Pitching Motions", AIAA-90-0311, January, 1990.
11. Thompson, S. A., Batill, S. M., and Nelson, R. C., "Delta Wing Surface Pressures for High Angle of Attack Maneuvers", AIAA-90-2813, August, 1990.
12. Ashley, H., Katz, J., Jarrah, M. A. M., and Vaneck, T., "Unsteady Aerodynamic Loading of Delta Wings for Low and High Angles of Attack", Proceedings from International Symposium on Nonsteady Fluid Dynamics, June, 1990.
13. McKernan, John F., "An Investigation of the Breakdown of the Leading Edge Vortices On a Delta Wing at High Angles of Attacks", Master's Thesis, University of Notre Dame, January, 1983.
14. Roos, F. W., and Kegelmann, J. T., "An Experimental Investigation of Sweep-Angle Influence on Delta-Wing Flows", AIAA-90-0383, January, 1990.
15. Parker, A. G., "Aerodynamic Characteristics of Slender Wings with Sharp Leading Edges - A Review", Journal of Aircraft, Vol. 13, March, 1976, pp. 161-168.
16. Arena, A. S. Jr., "An Experimental Study of the Nonlinear Wing Rock Phenomenon", MS Thesis, University of Notre Dame, April 1990.
17. Nguyen, L. T., Yip, L. and Chambers, J. R., "Self-Induced Wing Rock of Slender Delta Wings", AIAA-81-1883, August 1981.

18. Jun, Y. W. and Nelson, R. C., "Leading Edge Vortex Dynamics on a Delta Wing Undergoing a Wing Rock Motion", AIAA-87-0352, January 1987.
19. Konstadinopoulos, P., Mook, D. T. and Nayfeh, A. H., "Subsonic Wing Rock of Slender Delta Wings", *Journal of Aircraft*, Vol. 22, No. 3, March 1985.
20. Ericsson, L. E., "The Fluid Mechanics of Slender Wing Rock", *Journal of Aircraft*, Vol. 21, No. 5, May 1984.
21. Arena, A. S. Jr., and Nelson R. C., "The Effect of Asymmetric Vortex Wake Characteristics on a Slender Delta Wing Undergoing Wing Rock Motion", AIAA-89-3348, August 1989.
22. Arena, A. S. Jr., and Nelson, R. C., and Schiff, L. B., "An Experimental Study of the Nonlinear Dynamic Phenomenon Known as Wing Rock", AIAA-90-2812, August, 1990.
23. Arena, A. S. Jr., and Nelson, R. C., "Unsteady Surface Pressure Measurements on a Slender Delta Wing Undergoing Limit Cycle Wing Rock", AIAA-91-0434, January, 1991.

# PREDICTION OF AERODYNAMIC PHENOMENA LIMITING AIRCRAFT MANOEUVRABILITY

by

A. Ferretti A. Bartoli A. Salvatore

Alenia Aeronautica  
Corso Marche 41  
10146 Torino  
Italy

## SUMMARY

The following paper presents the synthesis of recent experiences concerning the effects of shock induced separation on conventional airplanes flying at high subsonic speeds. Efforts have been concentrated in Alenia in synthesizing a prediction criterion for detecting onset of the wing aerodynamic phenomena leading to buffet and mishandling of such airplanes. Comparison of mishandling and buffet onset envelopes theoretically derived with those experimentally measured on an airplane is given evidencing the consistency of the methodology.

For non conventional, highly swept wings featuring leading edge vortical flow at high subsonic speed and moderate angle of attack, the analysis of wind tunnel results has allowed the definition of a prediction criterion for transition from attached to vortical flow.

This change in the wing flow structure is responsible for remarkable non linearities in the aerodynamic coefficients of the aircraft and could limit manoeuvrability in certain areas of the flight envelope. Efforts in implementing these concepts in the aerodynamic design process of such wing planforms are stressed as well as the need for further studies concerning a deeper understanding of the fluid dynamic conditions ruling the vortex break down.

## INTRODUCTION

This paper addresses the problem of predicting some of the aerodynamic phenomena leading to degradation of aircraft performance in the high subsonic regime.

Two kinds of wing planforms are considered: those with moderate leading edge sweep angle and those swept at angles greater than 60° (delta wings). Distinction between the two planforms is due to the different flow structure developing on the corresponding wings: the former being characterized by "attached flow" degrading in separated one when heavy shock boundary layer interaction occurs, the latter being characterized by "vortical flow" (separated flow at the leading edge) whose onset, development and bursting is ruled by the surrounding aircraft flow field.

In both cases, however, the effects on aircraft aero characteristics are felt as buffeting, loss of control power, uncommanded pitch, yaw, roll motions up to limit the aircraft operational envelope. Good transonic manoeuvrability is one of the most important requirements for modern defense aircraft, combat taking place at high speed and high load factor in order to achieve high sustained and attained turn rates; for modern transport aircraft cruising at high speed/high altitude, good performance are limited by the buffet boundary.

The accurate prediction of the onset of this boundary, as well as the intensity of the involved phenomena is therefore of paramount importance for both types of aircrafts. This paper presents the Alenia Aeronautica approach to the problem.

## CONVENTIONAL WING PLANFORMS

### Generalities

In fig.1 an outline of the effects that wing flow separation could lead on an airplane, both in terms of structure vibration and rigid body modes affecting stability and control is given as an example. Buffet and mishandling boundaries are assessed through extensive testing of instrumented prototypes collecting data of different nature. Accelerometers located in various position: wing tip, pilot's seat, aircraft centre of gravity, together to pilot's rating provide a base for assessment of buffet levels. Outputs of inertial platform give evidence of rigid body modes such as pitch, and roll dynamic oscillations. In fig.2 an example of flight registrations concerning topic parameters is presented. The analysis of these kind of results allows definition of the boundaries presented in fig.1.

A defense aircraft has to operate within these boundaries up to angle of attack for which maximum usable lift is reached. To this concern the presence of progressive deterioration of handling qualities, such as that presented in fig.1, is well judged by the pilots that can easily recognize, through the feeling of a vibrational level or mild pitch and roll oscillations, when the operational limits of their aircrafts are near to be reached. For transport type aircrafts the buffet boundary is as important a parameter as drag is since the maximum cruising lift coefficient is limited by the requirement to maintain a 1.3 margin to buffet onset. The cruise lift coefficient for maximum aerodynamic efficiency increases with wing aspect ratio; if the buffet boundary is not high enough to maintain this margin then the full potential of the wing aspect ratio can not be utilised. Furthermore for this kind of aircraft as well the characteristics at angle of attack beyond buffet-onset must be known at least to limit, by the use of avionics and flight control system, from reaching conditions were dangerous situation such as pitch-up may be encountered.

Although the onset of separation on three dimensional wing can be predicted today by transonic theoretical codes, leading to identification of buffet onset envelope early in the project, prediction of aerodynamic excitation after separation is still a very complicated task.

The assessment of separation intensity (buffet) is still based on model test in wind tunnel.

Particular test techniques such as unsteady pressure measurements and wing-root bending moment have been developed in the past; the analysis of this kind of data allows assessment on the severity of buffet even though the dependency from Reynolds number still represents a risk factor in their applicability to full scale airplane. Description of these techniques go beyond the scope of the present paper.

In the following, example of theoretical predictions of buffet/mishandling onset and comparison with experimental results will be given after having reviewed some of the transonic flow peculiarities useful in the understanding of the prediction techniques.

#### Critical fluid dynamic conditions for flow separation

It is well known that strong shock-turbulent boundary layer interaction (that is of practical interest on today's aircrafts) is the cause for onset of flow separation on airfoils and wing sections. Plenty of bibliography is available on the subject, however it is useful to recall the nature of shock-induced separation in order to explicit the conditions for which it occurs and those for which its effects are felt. In fig.3 (from ref.1) the classical transonic flow evolution over an airfoil and downstream, along its wake, are sketched at increasing  $\alpha$  values.

First occurrence of shock-induced separation occurs between stages I and II in form of a separation bubble at the foot of the shock. Increase of incidence causes the growing of the bubble and of the boundary layer thickness at the trailing edge (T.E.) that in turn effects the pressure distribution along the wake as shown in fig.3 at stage III. A change in T.E. pressure (divergence) takes place in order to self adapt to the far downstream pressure and this causes a response in the circulation with associated loss of linearity in the related forces and moments coefficient.

This is a well established understanding among aerodynamicists, however T.E. divergence not only marks the onset of separation effects on the wing section considered in terms of "kinks" in the sectional forces and moment coefficients, it will also mark the onset of unsteady effects such as buffeting. An explanation of this can be sought considering the fluctuations in the magnitude of the overall loading excited by the separated flow via the T.E. pressure.

Recent experiences gained in Alenia through flight testing of an instrumented airplane prove this concept. In fig.4 a layout of pressure transducers of dynamic type on a wing section of a defense aircraft is presented. Transducers were glued on the wing upper surface and faired with rubber discs in order to reduce the interference due to their protuberance (about 1 mm.) to a reasonably level.

Typical quasi steady maneuvers (roller coaster and wind up turns) allowed collection of pressure data throughout the flight envelope.

A time history of flight parameters (Mach,  $\alpha$ ,  $\delta$ ) and pressure response is given in fig.5 for a manoeuvre started at MACH close to 0.8.

Analysis of such responses allows to identify the following topics:

-Suction peak development in the leading edge area (pressure pick ups A,B,C) as soon as the incidence is increased: T=t1.

-Development of a shock wave for  $.45x/c5.5$  (pressure pick ups E,F) at moderate Alphas T:t2.

This is well represented by the recompression exhibited by transducer F and the corresponding expansion evidenced by transducer E denoting an increase in Mach number ahead of the shock (M1): as greater M1, as stronger the normal shock, as lower M2. It is important to note that despite a shock wave is acting on the dynamic transducers E and F, a "static" response is given up to a certain event as it will be described in the following.

-Constant level of T.E. pressure (transducer H located at  $x/c=0.98$ ) up to a certain Alpha value: T=t3. This value corresponds to the maximum strength of the shock wave acting across transducers E and F. A further increase in angle of attack causes divergence in T.E. pressure evidenced by recompression towards less positive pressure levels and finally onset of a dynamic response at T=t4.

As a matter of fact now, after the T.E. pressure has diverged, oscillations on the signals of transducers C,D,E,F and H itself are evident.

On the contrary in the leading edge area a progressive build-up of the suction peak takes place (transducers A and B) without evidence of dynamic oscillations up to the maximum  $\alpha$  reached during the wind-up turn manoeuvre. Note that when reaching a characterized by T=t4 the sustaining of the turn rate at constant velocity is not more possible, the amount of thrust available by the engine at a fixed setting balances the aerodynamic drag and a further increase in drag due to lift causes the airplane to start a deceleration as evidenced in the lowering of Mach number at almost constant altitude in fig. 5a.

Contemporaneously a mild mishandling of the aircraft is evidenced by the oscillations in the roll rate at an angle of attack immediately after the T.E. divergence and progressive degradation of flying qualities occurs at higher angle of attack, after the maximum usable load factor is reached, as depicted in the high roll rate presented in the bottom portion of fig. 5a.

In the same figure the time hystory of two accelerometers located in the wing tip and pilot's seat is presented, giving evidence of the correlation between T.E. divergence and buffet onset.

In fig.5b correlation of the onset of mishandling and buffet is given with the longitudinal characteristics of the airplane. Loss of linearity in the lift coefficient ( $C_l$ ) versus angle of attack is clearly visible for  $\alpha=\alpha(t4)$ . At the corresponding  $C_l$  a break in the pitching moment coefficient is evidenced as well implying a variation in loading distribution spanwise and chordwise on the wing.

Obviously the location of the instrumented wing section has a bit of importance in the correlation with phenomena felt by the aircraft as a whole: selection of a wing span location more outward would have implied for this wing an early occurrence of T.E. divergence (in terms of time and

therefore angle of attack) with respect to those characterizing the buffet onset envelope of the aircraft. Summarizing the T.E. divergence of a selected wing section marks precisely the onset of loss of linearity in the aerodynamic coefficients, felt as a mild mishandling, and the onset of dynamic response in the wing flow field, felt as a dynamic response of the airplane structure. Key factors in predicting onset of mishandling and buffet phenomena of an airplane are therefore the accurate prediction of these fluid dynamic characteristics and the identification of a wing span section representative of the spreading of the phenomenon to such an extent to be felt by the airplane.

#### Prediction of T.E. divergence

A massive amount of experimental data concerning either 2D and 3D experiments on swept wings in wind tunnel have been analyzed. Their applicability to full-scale aircraft has been assessed through comparisons with flight measured data. In fig.6 from Ref.2 a comparison between wind tunnel and flight pressure data relevant to a wing section is presented giving evidence of a good agreement. Results were collected in wind tunnel with the "transition free" technique. Transition strips (carborundum grits of a selected diameter) are usually located at a few % of the model wing sections providing boundary layer transition from laminar to turbulent at the same location that occurs on the airplane; however their presence can be detrimental if the correct interaction between shock wave and turbulent boundary layer has to be simulated in wind tunnel. For such case an "aft transition" (ref.3) such as that provided by the absence of transition strips assures the right shock wave strength and position on the wing section considered, as demonstrated in fig.6. Having assessed the level of confidence in the wind tunnel predictions a deep analysis of pressure data has been carried out aiming at developing a prediction criterion for T.E. divergence (rif.4). Following the valuable studies performed by Haines and Bateman in early investigations about shock induced separation, a locus identifying local Mach number ahead of shock wave (M1) and position along the chord at which this shock takes place when divergence (up to a certain amount) occurs, has been defined.

In fig.7 evidence of such locus is given for different geometries. The results presented here are either from 2D and 3D experiments; in the 3D case consistency in airfoil geometry with respect to the 2D case was assured.

The agreement between 2D and 3D correlation exhibited in fig.7 implies that in spite of wing sweep, twist, aspect and taper ratios the flow behaves as in the 2D case up to the conditions leading to T.E. divergence and provided that the fuselage effects be small (as in the wing outboard panel).

The correlation discloses its value in associating the physical phenomenon of T.E. divergence to the shock strength and position that determine it; the section geometry influencing these two last parameters that are suitable to be predicted by CFD codes at least before the critical value in T.E. divergence has occurred.

The availability of a suitable 2D/3D code able to predict transonic flow with boundary layer interaction at a reliable level is a key factor now.

Powerful 2D/3D Navier-Stokes and Euler solvers coupled to boundary layer routines have been developed recently. Their applicability to engineering problem is a matter of different nature: budget and time constraints. More often they are applied in the verification step, when a final geometry has to be assessed. Cheaper and simpler methods are widely applied in the aerodynamic design process when different geometries have to be evaluated at a reasonable cost and within a limited amount of time. In fig.8 an example of pressure distributions computed on a wing by a full potential code adopting a conservative scheme are presented.

In fig.9 the buffet/mishandling onset envelope obtained by utilizing the above mentioned code and the criterium of fig.7 is presented in comparison to flight test data evidencing the reliability of the methodology set up.

Definition of these boundaries is now feasible at a relatively low cost during the early phase of aircraft development, when different airfoil shapes have to be evaluated and wing geometrical characteristics as thickness, twist and camber distributions optimized. On the contrary, prediction of further flow degradation and consequent aircraft response has to rely today on testing of scaled models in wind tunnel.

#### NON CONVENTIONAL WING PLANFORMS: DELTA AND DOUBLE DELTA WINGS

##### Generalities

Very highly swept wings have the potential to achieve low drag at supersonic lifting conditions by virtue of keeping the leading edge at an angle of sweepback greater than the angle weak shock wave makes with the freestream at corresponding Mach numbers (subsonic leading edge).

This peculiarity, however, is coupled to the well known proneness of highly swept wings to develop leading edge (L.E.) vortex separation and increase in drag due to lift. At a given sweepback angle, as sharper the L.E. as lower the angle of attack at which the vortex will develop suddenly.

This characteristic is not typical of supersonic regime only; in fact L.E. separation and vortex formation characterizes low aspect ratio, highly swept wings in subsonic regime as well. Experimental studies have shown that even at low angle of attack the flow over such wings separates at the leading edge and rolls up into spiral vortex. A sketch of such complex flow structure is given in fig.10; flow attachment lines have been observed inboard of the vortex sheets and indicate that the air is drawn over the vortex and accelerated downward. The presence of the vortices induces strong local suction peaks which result in an increase in lift, usually referred to as vortex lift, relative to that predicted by linear theory. This effect in lift is desirable in some cases to increase the low lift coefficient typical of low aspect ratio wings, and it allows instantaneous manoeuvres at high angle of attack typical of military aircraft. The change in loading associated to vortex lift can significantly alter the pitching moment characteristics

depending on the wing geometry. Discussion in this paper is primarily concerned with the effect on longitudinal characteristics and rigid body modes in high subsonic regime, this affecting the manoeuvrability of modern defense aircraft to a great extent.

#### Critical fluid dynamic conditions for leading edge separation

In the analysis of separated flow around swept leading edge wings it has been found useful to correlate the data in terms of conditions normal to the leading edge by utilizing simple sweep theory, fig.11. The velocity components normal to the plane of a flat topped delta wing ( $\beta=0$ ) " $W_n$ " and normal to the leading edge of the wing " $U_n$ " are:

$$W_n = U_{\infty} \sin \alpha$$

$$U_n = U_{\infty} \cos \alpha / \lambda$$

The incidence angle normal to the leading edge  $\alpha_n$  and the normal Mach number  $M_n$  are:

$$\alpha_n = \arctg (W_n/U_n) = \arctg (\tan \alpha / \cos \alpha / \lambda)$$

$$M_n = M_{\infty} \cos \alpha / \lambda \sqrt{1 + \sin^2 \alpha} / \lambda$$

Experimental correlations by Stanbrook and Squire (ref.5) identified the boundary region that separates the conditions in terms of  $\alpha_n$  versus  $M_n$  for which attached flow or leading edge separation flow exist. Such boundary is presented in fig.12 for a flat topped delta wing with a sharp leading edge.

The leading edge vortex, in this case, develops on the entire L.E. of a sharp airfoil wing, while the effect of rounding it is to reduce the adverse pressure gradient especially in the inboard sections of the wing.

Separation, for these leading edges, starts from the wing tip and moves inboard when the angle of attack is increased. Rounded L.E. are of practical interest either in commercial supersonic or military aircraft, both of them having to fly efficiently at low speed as well. Additionally, these kind of wings are usually highly twisted and cambered from supersonic cruise drag minimization considerations.

How all these geometrical characteristics affect vortex onset? In general, the type of flow over a wing depends on the combination of the above mentioned geometrical characteristics, on flight conditions and on the effects of other airplane components. All of these contribute to the pressure distribution on the wing that, in turn, governs the nature of the flow on the wing itself.

Recent experience carried out in ALENIA on configurations featuring delta and double delta wings allowed a better understanding of the fluid dynamic conditions leading to vortex onset for highly swept wings with rounded L.E.

Extensive testing in wind tunnel of models designed and manufactured in ALENIA and instrumented with internal strain gauges balances and pressure ports on the aerodynamic surfaces allowed gathering of valuable data. In fig.13 is presented the diagram  $\alpha_n$  vs  $M_n$  obtained from the elaboration and analysis of wind tunnel data relating to a delta canard model.

The locus identified in fig.13 is applicable to the specific wing geometry under consideration.

The conditions  $\alpha, M$  for which the transition from a flow typology to another sets up can be correlated with local behaviour of global coefficient curves; by this point of view a study to find a correlation link between forces/moments coefficients and pressure coefficients on the wing has been carried out for different delta wing configurations.

It has been found that, at a fixed Mach number, a precise relation does exist between the onset of vortex flow on the wing section considered and the exceedement of a certain pressure level. In the example presented in fig.14, featuring a delta wing configuration characterized by generous leading edge radius, the transition from attached flow (fig.14a) to vortical flow from tip to apex (fig.14b/c) is presented at increasing  $\alpha$ . This movement is ruled by the achievement of the critical pressure level for vortex onset ( $C_{pmin}$  v.o.) on the section considered, as sketched in fig.15. At different Mach numbers different critical pressure coefficients for vortex onset have been identified. In fig.16 the  $C_{pmin}$  for vortex onset versus free stream Mach number is presented in comparison to  $C_{p}$  vacuum. At a fixed airfoil section and Mach number the curve gives the value for which the transition from "attached" to vortical flow sets up.

The transition curve is not dependant on the delta wing geometrical characteristics ( $\lambda, \alpha, etc...$ ) being it obtained on the basis of pure fluid dynamic considerations. In fact, studies carried out on different delta and double delta wings have produced similar results leading to the correctness of the overall prediction procedure.

Since it is well known that the transition from one flow typology to another one causes remarkable effects on global coefficients, the natural extension of the transition criteria is the prediction of the conditions  $\alpha, M$  for which longitudinal coefficients present areas of problems.

In fig.17 is presented the typical behaviour of the incidence of vortex onset ( $\alpha_v$  v.o. relating to the corresponding  $C_{pmin}$  v.o.) versus span for a fixed Mach number. The analysis of longitudinal coefficients on the double delta wing considered has shown a clear correlation between the onset/development of vortex flow on the wing and the loss of linearity in longitudinal coefficients. This kind of correlation (see fig.17) is well confirmed for the all delta wing configurations examined. The collection of data of other similar wings featuring vortical flow will permit a better definition of the numerical form of the curve  $C_{pmin}$  v.o. vs Mach number allowing a complete and definitive assessment of this prediction criterion.

Meanwhile engineering tools are being developed in order to implement the knowledge accomplished with the analysis of experimental results in the aerodynamic design process of delta wings. For example application of codes based upon linearized theory (panel methods) within the attached flow boundary became feasible for highly swept wings by monitoring of bound values for  $C_{pmin}$  v.o. On the other side the use of more costly Euler solvers could be limited at  $\alpha$ -Mach values belonging to the vortical region previously determined. Indeed the availability of flight test results will allow a better consolidation of the methodology set-up.

### CONCLUSIONS

A brief presentation of the flow structure characterizing conventional swept back wings and delta wings has been given focusing on the conditions leading to loss of linearity in the aerodynamic coefficients and onset of unsteadiness in the wing flow field. The high subsonic regime only has been considered. For conventional wings the shock induced boundary layer separation has been analyzed and consolidation of the valuableness of trailing edge criterion has been provided on the basis of time dependant flight test results. An engineering tool for predicting T.E. divergence, based upon Haines and Bateman studies, has been presented and its reliability demonstrated on the basis of comparison with experimental results. For delta type wings, featuring realistic rounded leading edges, transition from attached to vortical flow at L.E. has been demonstrated to be the main cause for early loss of linearity in the aerodynamic coefficients. Analysis and synthesis of experimental results in wind tunnel has evidenced the existence of a relation between the achievement of a bound pressure level on the L.E. and the onset of vortical flow. Provided that further studies are needed, especially in order to correlate wind tunnel results to full scale aircraft behaviour, an engineering tool is being developed allowing prediction of vortical onset by the use of theoretical codes. Further analysis are being carried out in order to evidence possible relations between vortex break-down and pressure levels on the wing aiming at synthetizing a correlation criterion.

### REFERENCES

- 1) H.H.Pearcey  
Shock-induced separation and its prevention by design and boundary layer control  
J.C.Lachmann 1961
- 2) B.Bellati  
Pressure Plotting - Prime esperienze ALN  
ALN Report N°AG/FTR-G-061/FTE
- 3) J.A.Blackwell  
Scale effects on supercritical airfoils  
11 th Congress of ICAS 1978
- 4) A.Ferretti A.Bartoli A.Tommasi  
Definizione di un criterio teorico-sperimentale per la determinazione dell'insorgenza del buffet tramite l'uso di programmi di calcolo teorici  
ALN Report N° 06/RT/TS27/88185
- 5) A.Stanbrook, L.C.Squire  
Possible type of flow at swept L.Es.  
Aeronautical Quarterly Vol.15 1964

TIME →

MACH

ALPHA

PITCH RATE

LOAD FACTOR

STICK

ONSET MILD

ONSET RISKY

ROLL RATE

ROLL-AXIS

Diagram illustrating a jet aircraft in a steep climb. A vertical line of points A through H is shown. A dashed line from the aircraft's nose points to point A. A curved line below the points is labeled  $X/C$ . A scale at the bottom shows distances from 0 to 100.0.

FIG. 4

LAYOUT OF PRESSURE TRANSDUCERS  
INSTALLED ON A WING SECTION  
OF A DEFENSE AIRCRAFT



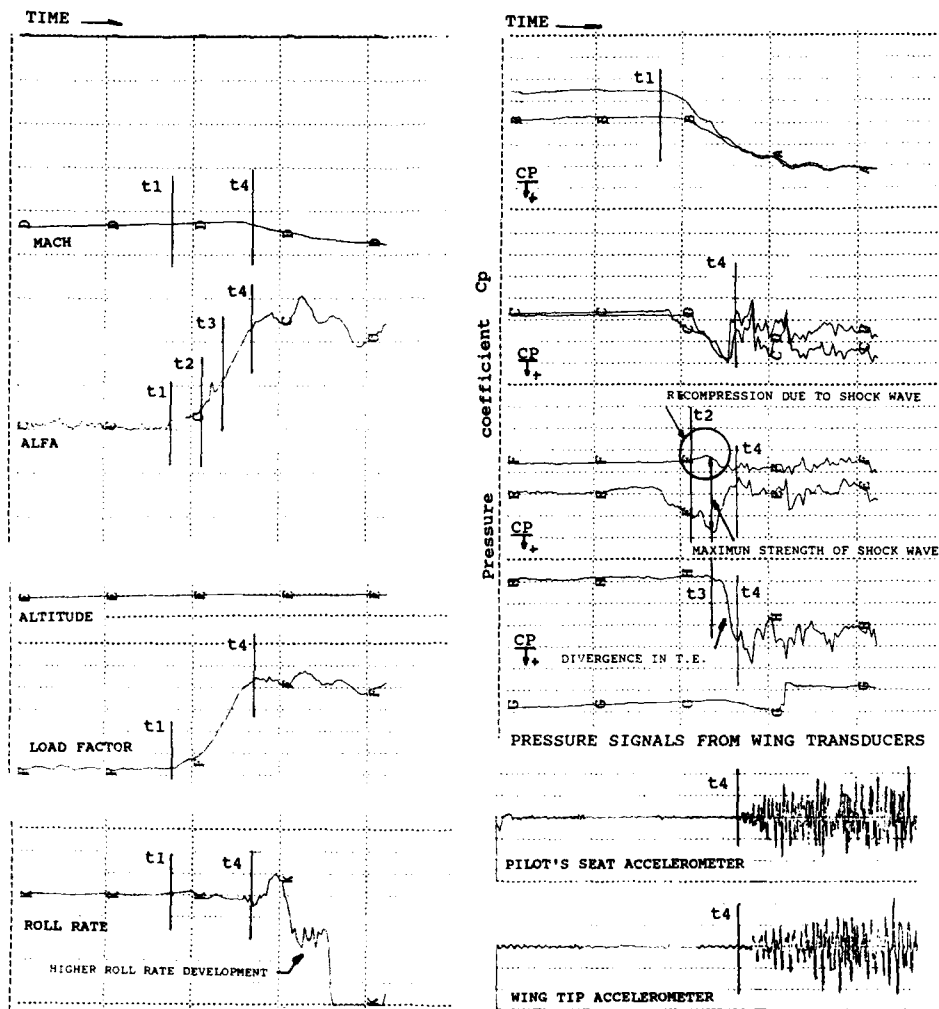


FIG. 5A  
FLIGHT RECORDING-WIND UP TURN MACH= 0.8

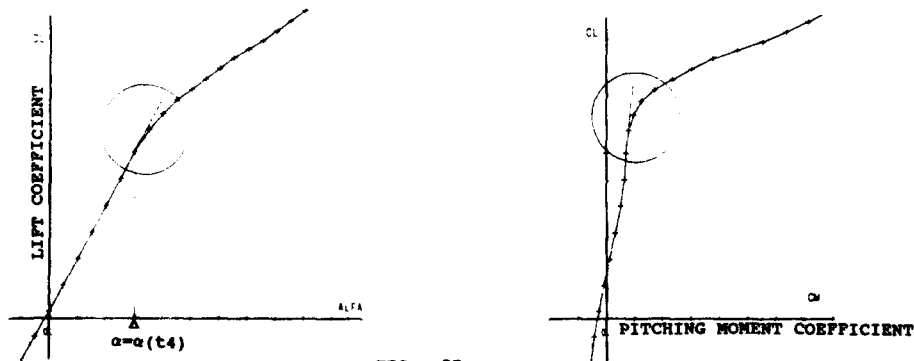


FIG. 5B  
LOSS OF LINEARITY DUE TO SHOCK INDUCED SEPARATION

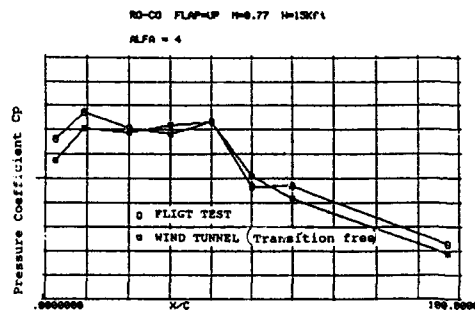


FIG. 6

WIND TUNNEL AND FLIGHT TEST  
 RESULTS COMPARISON

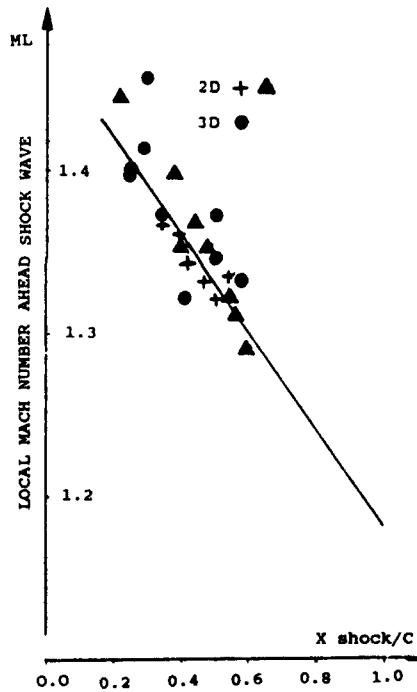


FIG. 7

2D AND 3D CORRELATION BASED  
 ON EXPERIMENTAL RESULTS.

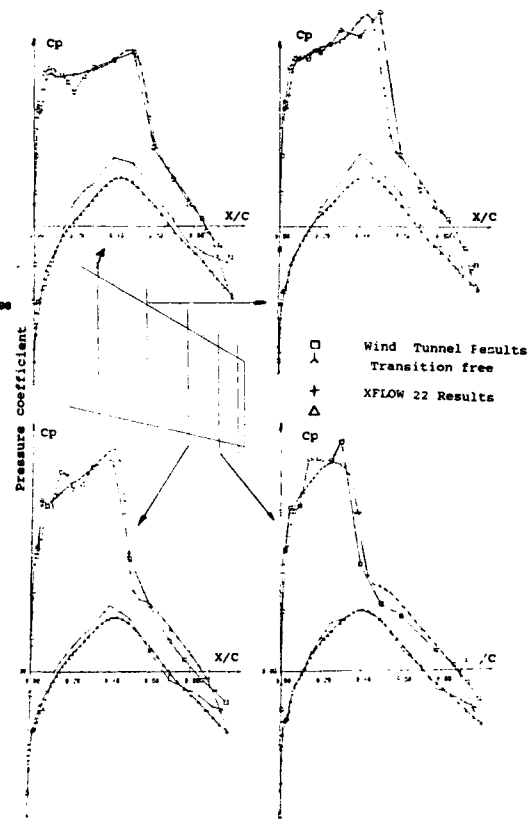


FIG. 8

PRESSURE DISTRIBUTIONS ALONG WING SPAN.  
 COMPARISON OF THEORETICAL AND  
 EXPERIMENTAL RESULTS

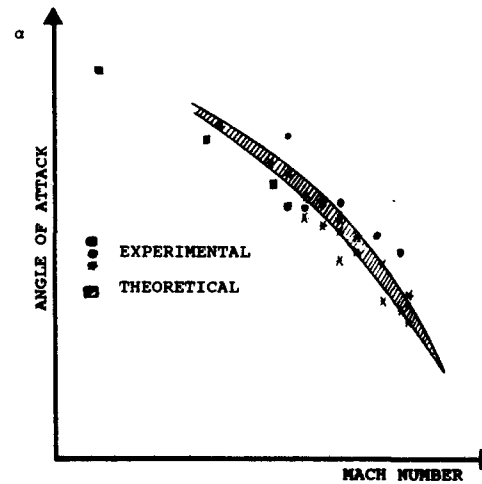


FIG. 9

COMPARISON OF BUFFET/MISHANDLING ONSET  
 ENVELOPE THEORETICALLY COMPUTED AND  
 MEASURED ON THE AIRCRAFT

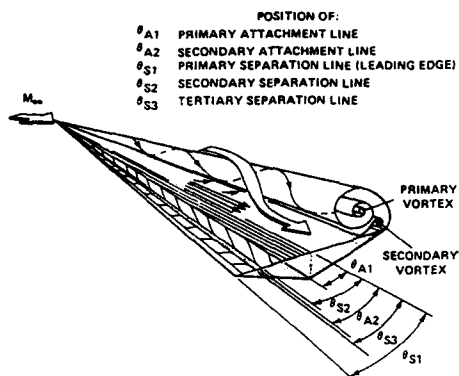


FIG. 10  
VORTICAL FLOW STRUCTURE

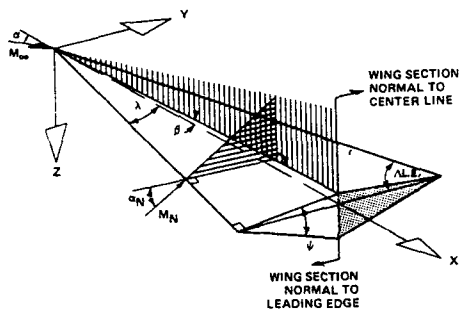


FIG. 11  
DELTA WING GEOMETRY AND FLOW COMPONENTS

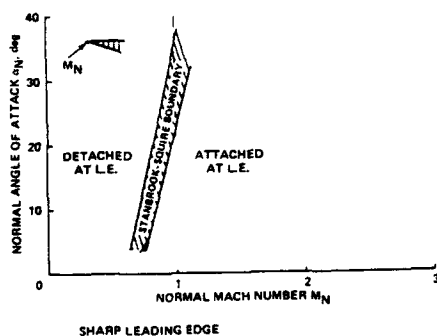


FIG. 12  
DETACHED AND ATTACHED LEADING EDGE FLOW

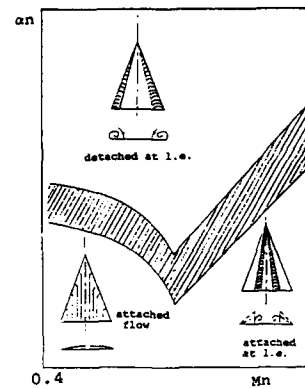
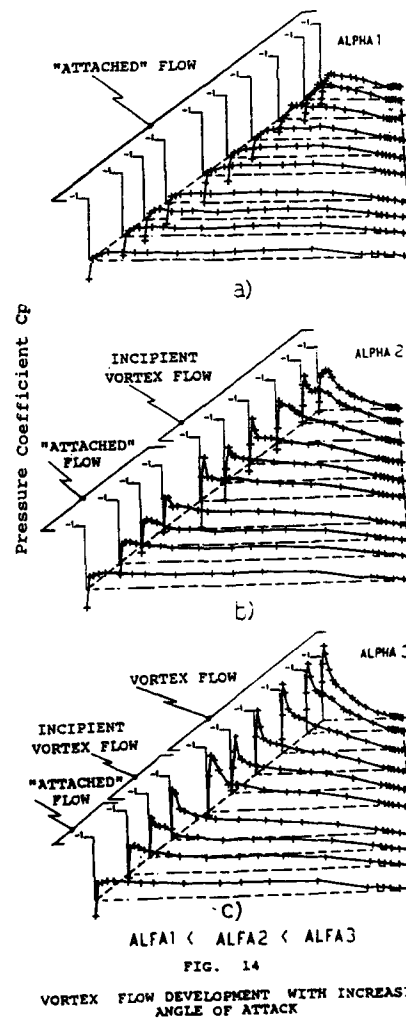
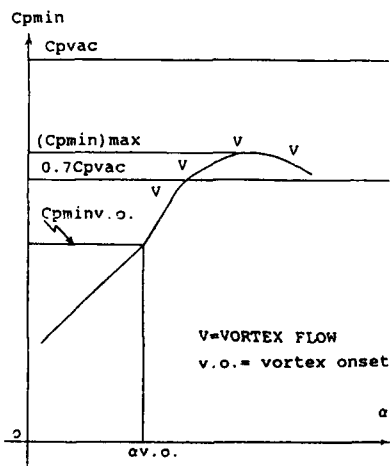
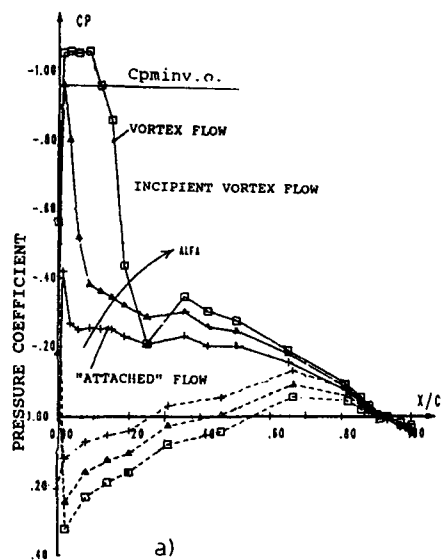


FIG. 13  
an - Mn DIAGRAM FOR A DELTA WING CONFIGURATION: ALENIA WIND TUNNEL MODEL RESULTS ANALYSIS





b)  $C_{pmin}$  VERSUS  $\alpha$

FIG. 15

CRITICAL PRESSURE LEVEL FOR VORTEX-ONSET  
( $C_{pmin}$ )

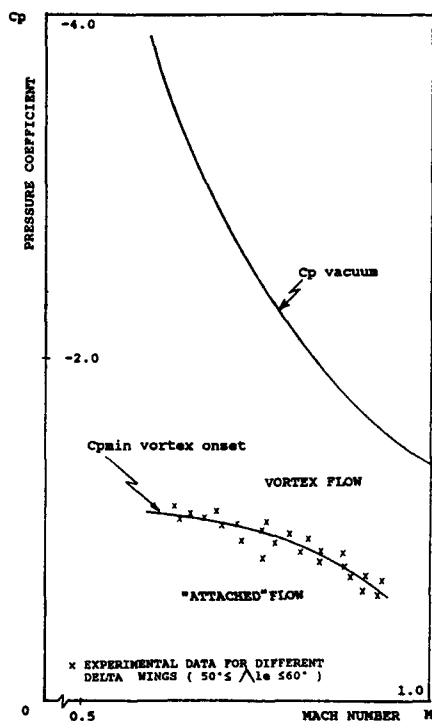


FIG. 16

CRITICAL PRESSURE COEFFICIENT ( $C_{pmin}$  v.o.)  
OF THE TRANSITION FROM ATTACHED TO VORTEX  
FLOW: PREDICTION CRITERION

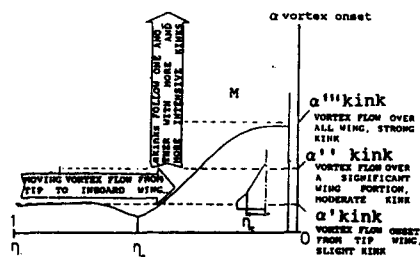


FIG. 17

CORRELATION BETWEEN VORTEX FLOW ONSET/DEVELOPMENT  
AND THE LOSS OF LINEARITY IN  
PITCHING MOMENT COEFFICIENT

## PARAMETRIC EFFECTS OF SOME AIRCRAFT COMPONENTS ON HIGH-ALPHA AERODYNAMIC CHARACTERISTICS

L. Visintini, R. Pertile, A. Mentasti  
Aermacchi S.p.A.  
Aerodynamics Dept.  
Via Sanvito, 80  
21100 - Varese  
(Italy)

### SUMMARY

A wind tunnel test activity was performed with the purpose of defining and understanding the high AOA aerodynamic characteristics of an advanced trainer aircraft configuration. The tests included static and rotary balance measurements in the full  $0^\circ$  to  $90^\circ$  AOA range. The presentation includes a discussion of effects of model breakdown and of forebody finess ratio and cross section. Examples are also given about special difficulties related to subscale high AOA wind tunnel testing.

### 1. INTRODUCTION

The time when the flight envelope of aircraft was defined by the development of flow separations on the wings and the term "High Angle of Attack" meant the angles of attack of wing stall is now more and more over.

Aerodynamic technology, pushed by fundamental research and increasing requirements of good flight qualities in a broader flight envelope now allows in principle to design aircraft without well defined boundaries in their angle of attack envelope. The demand is more and more towards some level of "carefree handling", mainly meant to relief the pilot from the need to closely monitor its flight condition in order to avoid uncontrolled departures. For combat aircraft, flight in an unlimited angle of attack range is even going to become an operational manoeuvre.

Such extension of the flight envelope is permitted on one side by the largely improved knowledge of the physics of vortex flows, which play a key role in this regime, and on the other by the technology of flight control by active fly-by-wire systems that permit to manage configurations having highly nonlinear aerodynamic characteristics, provided that enough control power is available.

All research on high angle of attack aerodynamics has necessarily to be done by empirical tools, i.e. by means of wind tunnel testing, possibly supported by water tunnel testing to get insight into the flow structures. Computational Fluid Dynamics cannot yet give any

significant contribution to the results. Also, the present knowledge of these flows does not lend itself to easy generalizations and a large often unexplained configuration dependence is normally present.

A few examples of more or less systematic studies of effects of aircraft configuration on high angle of attack aerodynamic characteristics have been published in the past<sup>1-4</sup>.

A large number of more fundamental papers on the fluid dynamics of vortex flows at high angle of attack is also available<sup>5-10</sup>, but our knowledge is still far from complete.

The present study has been started within the framework of the collection of design data for the definition of a new training aircraft for the year 2000. It is felt that the impact on the configuration design of the high angle of attack flight requirements should be investigated in an early phase so that limitations in the flight envelope or difficulties in the flight control system design are limited as much as possible, along the philosophy described in ref. 11.

The present research differentiates from others on the fact that primary emphasis is on flight qualities for safety and FCS design and that extensive dynamic (rotary) tests have been included.

Also, a realistic aircraft configuration is considered, and the variation of geometrical parameters (i.e. forebody parameters like finess ratio, etc.) is limited within the range which is considered applicable for this class of aircraft.

For the present study, a research low-speed wind tunnel model has been tested on both static and rotary balances in the full angle of attack range from  $0$  to  $90^\circ$ .

The investigation as reported here covers mainly the contribution of model components, and the effects of variations in forebody shape.

Further effects like LEX size and shape, wing planform, tail position and dihedral etc. have also been investigated or are planned for the near future but will not be presented here.

The analysis of results has been aimed to identify the main effects on the parameters which are considered to be of larger importance for high AOA flight. But since no simple criterium exists in order to establish a figure-of-merit of the different configurations, a planned next step of this research will include modelling of the aerodynamics of some of the tested configurations and making off-line simulations in order to compare final flight qualities.

## 2. TEST DESCRIPTION

### 2.1 Model datum configuration

The model used for the research is depicted in fig. 1. It is representative of an early preliminary study of the advanced trainer aircraft mentioned above in 1:9 scale. It is an F-16 type configuration featuring low wing with LEX's, ventral inlet of high aspect ratio, all moving horizontal tailplanes supported by fuselage "shelves", single central fin. The wing has movable leading edge droops which can be scheduled with AOA and full span flaperons in two sections. The model is somewhat simplified in geometry in order to allow high modularity and interchangeability of forebody (ahead of the cockpit), LEX's, wings, body shelves, tailplane and fin.

For the purpose of the test a reference configuration had to be defined. On the basis of the rationale described in the following section 4.1 the reference configuration features leading edge drooped  $30^\circ$  and tailplane at  $+30^\circ$  (full nose down control). This configuration is considered as representative of flight at angles above  $25^\circ$  to  $30^\circ$  when droop is deflected for optimum drag polar and flight qualities, and tailplane is deflected by FCS for recovery to lower angles of attack. Flaps are set at  $0^\circ$  because of the small contribution to pitching moment and adverse effects on flight qualities.

Preliminary tests have supported these assumptions.

The datum configuration also features a flattened ("shark") forebody shape, this being the choice initially made for the reference aircraft.

All data reported in the following analysis will refer to the above defined configuration if not explicitly stated.

### 2.2 Configuration variables

The investigation presented here covers the following configurations variables:

- a) model buildup, in order to identify the main contributors to each aerodynamic coefficient and to the main non linearities.  
In order to limit the number of configurations to be tested and the number of "interference" terms to be analyzed, the following build-up sequence has been chosen:
  - body + fin
  - wing-body + fin
  - wing-body + LEX + fin
  - wing body + LEX + body shelves + fin
  - complete

$\left. \begin{array}{l} \text{wing-body + fin} \\ \text{wing-body + LEX + fin} \\ \text{wing body + LEX + body shelves + fin} \end{array} \right\} \begin{array}{l} \text{wing contribution} \\ \text{LEX contribution} \\ \text{"shelves" contrib.} \end{array}$ 
 $\left. \begin{array}{l} \text{wing-body + LEX + fin} \\ \text{wing body + LEX + body shelves + fin} \end{array} \right\} \text{HT contribution}$
- b) forebody shape. A set of 6 different forebodies have been tested, featuring variations of cross section (circular, elliptic, flattened), slenderness ratio and apex angle (figs. 2-3). Of course the change in shape had to be limited to the fore part because of the need to blend the shape to the existing fuselage. Also the range of parameters tested is not very large and was limited to what considered realistically feasible on the actual aircraft. For this reason it was not expected to see any of the "extremes" that have been shown in the past by basic research on this topic.

### 2.3 Tests

The tests have been performed in Aermacchi low speed wind tunnel at a wind velocity of about 50 m/sec giving a chord Reynolds number of 1.1 Million.

Three different setups have been used:

- a static balance with ventral strut support, used for tests up to  $40^\circ$  AOA;
- a static balance with rear sting support, for tests between  $45^\circ$  to  $90^\circ$  AOA;
- the Aermacchi rotary balance<sup>12-13</sup>, used for tests in rotary conditions and using a rear sting for  $0^\circ < \alpha < 45^\circ$  and a dorsal sting for  $45^\circ < \alpha < 90^\circ$ .

The test matrix included normally:

- in static conditions,  $\alpha$  sweeps at  $0^\circ$  and  $10^\circ$  of sideslip and  $\beta$  sweep\* at  $20^\circ$  to  $90^\circ$  incidence with  $4^\circ$  to  $5^\circ$  alpha step, plus some effects of control deflection;
- in rotary conditions tests at the same angles of attack as above at zero sideslip. Effect of sideslip has been analyzed in a limited way on the datum configuration only.

### 3. EXPERIMENTAL DIFFICULTIES OF HIGH-AOA TESTING

#### 3.1 Reynolds number simulation

High angle of attack aerodynamics is dominated by vortex flows originating from separation lines which are often located on the smooth surfaces of forebodies, canopies, etc. Although vortex flows in themselves are very little sensitive to Reynolds number, the type and position of separation lines may be strongly affected, thus creating "indirect" scale effects according to the definition of ref. 14. When testing at subscale Reynolds number of about 1.1 Millions referred to chord or  $300 + 350000$  referred to forebody width, it is observed that most separation lines of the forebody originate from laminar separations (subcritical flow). At full scale it is expected that most separations will originate from turbulent separations.

For this reason it was decided to fix transition on the forebody sides by using two longitudinal rows of small cylinders (1.5 mm diam, .25 mm height).

The position of such rows is chosen on the basis of flow visualizations to be in front of the laminar separation line at any combination of angle of attack and sideslip to be tested. The effectiveness of such transition strips is dramatic. Fig. 5 shows as an example effects on roll damping from rotary balance tests of the datum configuration.

It is assumed that the presence of transition strips should force the correct flow "structure" and only "direct" Reynolds effect should remain.

In any case the presence of transition may be the source of other testing difficulties. Fig. 6 shows the story of four test repeats on the rotary balance after transition strip replacement or modification. It is evident that asymmetries, irregularities or wear of the strips are biased by the natural asymmetry of the flow with unpredictable even though understandable results.

#### 3.2 Coupling between natural asymmetries and asymmetric flow conditions

It is a well documented fact that all slender forebodies have an angle of attack range where natural asymmetries (i.e. asymmetric forces in a nominally symmetric flow condition) arise <sup>5,8</sup>. Such asymmetries create two kind of difficulties. First they are of random nature and can be triggered by small flow and model irregularities which are rarely repeatable.

Secondly when testing for effects of asymmetric flow (sideslip or rotation) a complex

coupling occurs which often makes interpretation of the results difficult, specially when trying to assess stability derivatives about zero.

In particular the two effects (flow asymmetry and natural asymmetry) are not additive. What normally occurs is that for large asymmetric flow conditions the flow effect dominates over natural asymmetry and anti-symmetric data are obtained as expected. For low sideslip or rotation the natural asymmetry dominates. Transition from one flow condition to the other may occur either progressively (fig. 7) or abruptly (fig. 8) at different positive or negative values of sideslip or rotation according to the sense of the natural asymmetry. Thus the effects of natural asymmetry cannot be represented by simple zero shifts and cannot be subtracted by simply averaging out data for positive and negative sideslip or rotation.

### 4. CRITERIA FOR ANALYSIS

#### 4.1 Aircraft design criteria

Criteria for analysis of wind tunnel results must be based on aircraft design requirements. The design requirement tentatively considered for the advanced training aircraft under consideration are relatively "modest" compared to some other fighter application but nevertheless represent a significant challenge compared to the past. Such criteria can be summarized in the following:

- the aircraft must be controllable and manoeuvrable up to maximum lift angle of attack of approx.  $30^\circ$ ;
- the aircraft must be safely recoverable from exceedances of this limit without loss of control;
- as a consequence, even if an angle of attack limiter will be required in the FCS such limit will not have to be mandatory, in order to avoid undue limitations in the aircraft agility at angles of attack lower than  $30^\circ$ .

#### 4.2 Static longitudinal coefficients

The main criterion for longitudinal characteristics is that the configuration will need to have available negative pitching moment at any angle of attack at full nose down controls in order to guarantee recovery from high AOA overshoots. In the worst condition the pitching moment should include contributions from sideslip and roll rate. The required margin shall take account of the inertia coupling and nose up contribution from intake mass flow and will guarantee a given value of pitch acceleration.

In the present report, the effect of sideslip has been quantified in terms of change of pitching moment for 20° of sideslip.

#### 4.3 Static latero-directional coefficients

The data have been analyzed for the following aspects:

- natural asymmetries, which should be limited;
- stability derivatives  $C_{n\beta}$  and  $C_{l\beta}$  at small sideslip angles ( $|\beta| < 5^\circ$ ), which are representative of departure tendencies;
- available control power in roll and yaw.

For this analysis roll and yaw coefficients are expressed in body axes.

#### 4.4 Rotary data

Aermacchi experience with many aircraft designs strongly supports the importance of roll damping for aircraft stability at high angle of attack, and this position is now widely accepted by many different investigators 11,13,15.

For the present quick look to results, rotary balance data have been analyzed in terms of roll damping around wind axis.

### 5. RESULTS

It is clearly impossible, within the space available, to give a systematic presentation of all the large amount of results. In the following, attention is drawn only to the most significant findings related to the parameters identified in section 4 and to rotary data whose availability in the literature is much limited.

#### 5.1 Model breakdown

##### 5.1.1 Static longitudinal coefficients

No unexpected findings. The minimum values of the pitching "recovery" moments (fig. 9) which are normally seen between 30 and 70° can be attributed in large part to the presence of the LEX. But its contribution is significantly offset by other configuration components like the so called body "shelves". An important contribution of sideslip to the pitching moment ( $\Delta C_{m(\beta)}$ ) is present. It is dominated by the body and marginally affected by the presence of the wing (fig. 10).

##### 5.1.2 Static latero-directional coefficients

Asymmetries at zero sideslip are concentrated in the 45° to 75° range and are only attributable to the body with some reductions due to wings and LEX's. (fig. 11)  
Directional stability (fig. 12) shows the typical

drop and minimum between 30 and 50° which is due to adverse yaw induced at the tail by the asymmetric position and bursting of the wing and LEX's wake and vortices. At higher AOA the body shows a rapid increase of directional stability which becomes very strong.

Presence of wings and LEX's greatly reduce this stability which still remains positive or neutral up to 90° AOA.

Lateral stability (fig. 12) shows in the 20 to 30° range a marked reduction due to the progressive bursting of wing and LEX vortices. In this range lateral stability was shown to be adversely affected by horizontal tail presence and deflection, possibly leading to reversal at 30 to 35°.

At higher AOA lateral stability is only produced by body fin and marginally modified by wing and remains fairly linear and constant.

##### 5.1.3 Rotary data

Rotary data of the configuration show two distinct ranges. In the 20 to 40° AOA range the data show a regular and fairly linear behaviour which can be represented by roll damping derivatives at least in a range of rotation rates around zero.

Above 45° AOA the behaviour is highly unstable and non linear and is dominated by the forebody instability and couplings with natural asymmetries.

In the lower AOA range it is fairly easy to define and interpret the contribution of each component (fig. 13).

The body+fin has a negligible contribution to roll damping up to 32° AOA, steadily increasing later up to about 40% of the total. The wing itself, which obviously gives most of the contribution up to 20° AOA, shows autorotation at 24°. This autorotation is postponed to 32° and virtually eliminated (zero damping) by the presence of the LEX's, this effect being clearly very similar to the beneficial effect of LEX's on maximum lift. The horizontal tail has an unexpected high damping contribution which is evident both at 20 to 28° and 36 to 42°, but is not able to offset the zero damping situation at 32° AOA.

The typical behaviour in the higher (50° to 80°) AOA range is represented in fig. 14 which shows the situation at 60°.

Here the main contribution comes from the body which shows a highly unstable behaviour which, similarly to the positive static directional stability, is mainly the effect of an abrupt switch in between two anti-symmetrical flow states.

In a crude way, since a positive rotation creates a positive local sideslip at the forebody, the positive side force created by sideslip, which explains the high directional stability, also explains the high positive



autorotation.

The other model components have also a significant contribution, mainly in reducing the maximum autorotative rolling moment, with the exception of the tail which acts in the opposite way. But in any case the final result is not qualitatively different from the body alone.

## 5.2 Forebody geometry effects

### 5.2.1 Static longitudinal coefficients

Forebody shape shows a significant effect on pitching moment at 40 to 90° AOA (fig. 15). Differences may be as large as  $\Delta C_m = .2$ . Shapes creating more lift and consequently more pitch up moment are the flattened ones ("shark" or elliptic) while the circular ones are creating the least lift and pitching moment.

Important cross coupling effects also occur due to forebody shape.

Large positive  $\Delta C_{m, \beta}$  effects occur in the range 24 to 70° AOA (fig. 16). Positive pitching moments as high as 0.3 may be created by the flattened or longer noses, the lowest being the shortest circular forebody. Similar couplings are created by rotation (fig. 17).

All these effects are very important to be taken into account for the design of safety margin for high AOA recovery, for simulation and spin prediction.

### 5.2.2 Static latero-directional coefficients

The onset of natural asymmetries (fig. 18) is in the range of 30 to 45° for all forebodies. It occurs earlier for the flattened noses, though not in fully systematic way. The extent of the asymmetries, which may be as large as .06 in  $C_n$ , does not show a definite correlation with forebody shape, this being explainable with their random nature which would require a statistical approach.

Asymmetries disappear above 70° AOA. Directional stability at small sideslip (fig. 19) is only influenced in a similar range of 40° to 90° AOA. All forebodies show a steep increase in stability at about 50° AOA with the circular noses coming a little earlier than the flattened ones. What is mainly evident from the results is that the high apparent stability in these conditions is mainly due to an abrupt switch between two asymmetric states of the flow which is induced by sideslip (fig. 20). When this state is reached further changes in sideslip have an unstable response and no stable state exist outside  $\beta = \pm 6^\circ$  approx.

Differently from directional stability lateral stability at small sideslip (fig. 19) is influenced only between 30 and 50°. This is probably explained by the fact that this influence is created by interaction of forebody

vortices with wing/LEX flow. At higher AOA forebody vortices are burst before reaching the wing. In any case the influence is not large, with some detrimental effect due to the longest flat nose.

At these moderate angles of attack (30 to 40°) all forebodies show a tendency to roll reversal at high sideslip. The onset of this reversal is strongly dependent on forebody shape and is delayed for the circular ones (fig. 21).

### 5.2.3 Rotary data

The effect on roll damping of forebody shape seems to be concentrated in the 50° to 70° AOA range, which coincides with the range of important natural asymmetries. Within this range large rolling moments are generated but also the interpretation of results is made more difficult by the high sensitivity to any disturbance leading to low test repeatability. Most forebodies show a large instability, with the exception of the bluff circular nose and, partially, of the elliptic and long circular ones (fig. 22). On this topic the testing was not conclusive and the problem will have to be addressed again in the future.

The most interesting and unexpected finding was the effect of roll rate on pitching moment already mentioned in section 5.2.1 (fig. 17).

As already noted above in sect. 5.1.3, this effect hints that, at these attitudes, forces created by the forebody depend, in a first approximation, only on the local flow direction and thus rotation can somewhat be traded with sideslip. This is also supported by some tests at sideslip which clearly show a horizontal shift of the curves: the change in the induced sideslip at the nose corresponding to the shift in rotation rate (4 to 7°) correlates well with the geometric sideslip (fig. 23).

## 6. CONCLUSIONS

The present research was very useful in highlighting the main features of the aerodynamic behaviour at high AOA of the configuration of concern, identifying its sources and some margins of change and correlating it with typical behaviours of this class of geometries.

In particular the following points can be summarized.

- a) High AOA testing has some inherent difficulties that require careful attention, with particular reference to Reynolds number simulation which appears to be vital in order to obtain results applicable to the full scale aircraft.
- b) The main contributions to high AOA behaviour have been identified. For this class of configuration forebody shape is of the utmost importance only above 40° AOA.

- c) Fairly large values of natural asymmetries have been found. The onset angle of such asymmetries seems to correlate well with published results (fig. 24)
- d) Large couplings between sideslip and rotation and longitudinal aerodynamic coefficients (pitching moment in particular) have been shown. These effects have to be taken into account for the design of safety margins for pitch recovery and for correct prediction of flight behaviour at these attitudes.
- e) For a configuration of this class a forebody of circular cross section seems to be largely preferable, leading to minimum pitching moment and  $Cm_{y, \delta}$  and  $Cm_{x, \delta}$  couplings, maintaining positive directional stability above  $50^\circ$  AOA, no roll reversal at high sideslip.  
The possibility to achieve positive roll damping could not be definitely demonstrated by the tests.  
Increasing forebody fineness ratio shows detrimental effects, as expected.

Further tests will be required to investigate the effects of forebody apex blunting and appendages like small strakes for further improvement of the behaviour.

#### REFERENCES

- 1) H.John, W.Krans - High Angle of Attack Characteristics of Different Fighter Configurations  
AGARD CP247
- 2) A.M.Skow, G.E.Erickson - Modern Fighter Aircraft Design for High Angle of Attack Manoeuvring  
AGARD LS121
- 3) G.Wedekind - Influence of Configuration Components of Statically Unstable Combat Aircraft on the Aerodynamic Design for High Angles of Attack  
AGARD LS121
- 4) A.M.Skow, A.Titiriga, W.A.Moore - Forebody-Wing Vortex Interactions and their influence on Departure and Spin Resistance  
AGARD CP247
- 5) E.R.Keener, G.T.Chapman - Onset of Aerodynamic Side Forces at Zero Sideslip on Symmetric Forebodies at high Angles of Attack  
AIAA Paper 74-770
- 6) G.E.Erickson, W.P.Gilbert - Experimental investigation of Forebody and Wing Leading Edge Vortex interactions at high Angles of Attack  
AGARD CP-342, 1983
- 7) D.J.Peake, M.Tobak - Three dimensional flows about Simple Components at Angle of Attack  
AGARD LS121
- 8) J.M.Brandon, D.G.Murri, L.T.Nguyen - Experimental Study of Forebody Geometry on High Angle of Attack Static and Dynamic Stability and Control  
ICAS-86 Paper 5.4.1
- 9) R.M.Hall - Influence of Reynolds Number on Forebody Side Forces for a 3.5 Diameter Tangent-ogive Bodies  
AIAA Paper 87-2274
- 10) R.C.Ward, J.Ketz - Boundary Layer Separation and the Vortex Structures Around an Inclined Body of Revolution  
AIAA Paper 87-2276
- 11) P.Mangold - Integration of Handling quality aspects into the Aerodynamic Design of Modern Unstable Fighters  
AGARD FMP Meeting on FLIGHT Qualities, Ottawa, 1990
- 12) R.Marazzi, D.Malara, M.Lucchesini, S.Comoreto, F.Pacori - Use of a Small Scale Wind Tunnel and Model Shop at Aeronautica Macchi as an Industrial Tool  
AGARD CP-348, Sept. 1983
- 13) Rotary Balance Testing for Aircraft Dynamics  
AGARD AR-265, Dec. 1990
- 14) Boundary Layer Simulation and Control in Wind Tunnels  
AGARD AR-224, 1988
- 15) J.R.Chody, J.Hodgkinson, A.M.Skow - Combat Aircraft Control Requirements for Agility  
AGARD CP-465, 1989

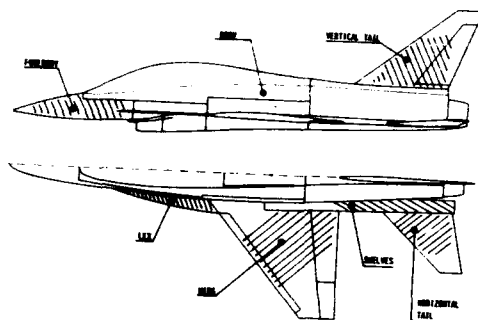


Fig. 1 - Sketch of the wind tunnel model used for the investigation

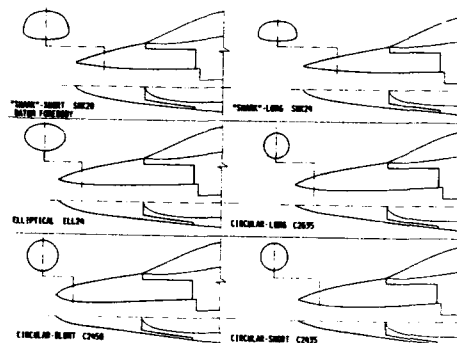


Fig. 2 - The set of forebodies investigated

FOREBODY	CROSS SECTION	SLENDERNESS $L_w/D_w$	$Q_{10}$ (DEG.)
"SHORT"-SHORT SHK20	"SHORT"	2.0	/
"SHORT"-LONG SHK20	"	2.4	/
CIRCUL.-SHORT C2435	CIRCULAR	2.4	35.0~
CIRCUL.-LONG C2435	"	2.6	35.0~
CIRCUL.-BLUNT C2450	"	2.4	50.0~
ELLIPTICAL ELL24	ELLIPTIC	2.4	/

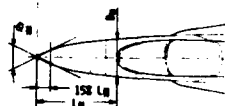


Fig. 3 - Main geometrical parameters of the forebodies



Fig. 4 - The model during high angle of attack static tests

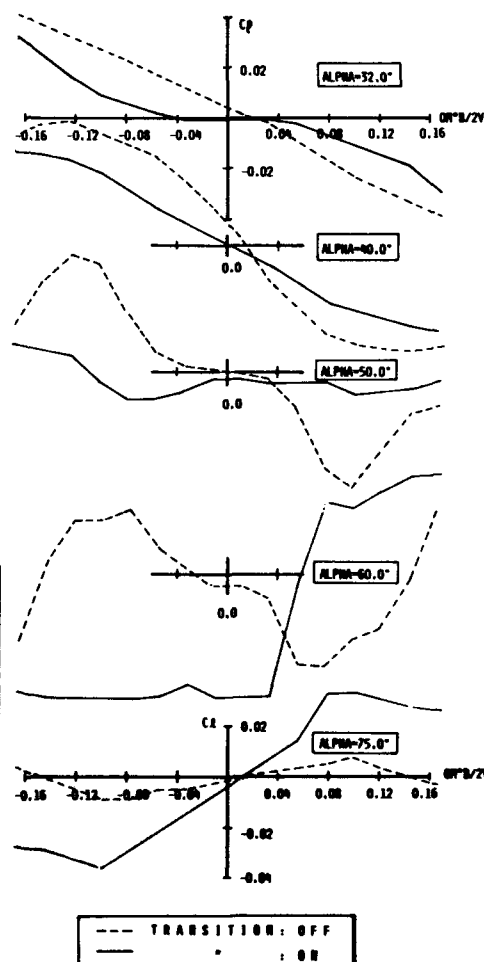


Fig. 5 - Effect of longitudinal transition trips on the forebody

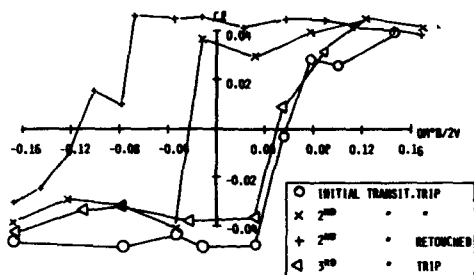


Fig. 6 - Repeatability of results at high angle of attack (60°, rotary test) after successive changes or modifications to the transition strips

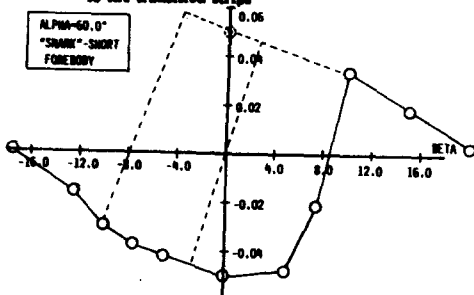


Fig. 8 - Coupling between natural asymmetry and flow asymmetry. Asymmetry abruptly switched between two states (dashed lines show the symmetrical, unstable state and other possible opposite state).

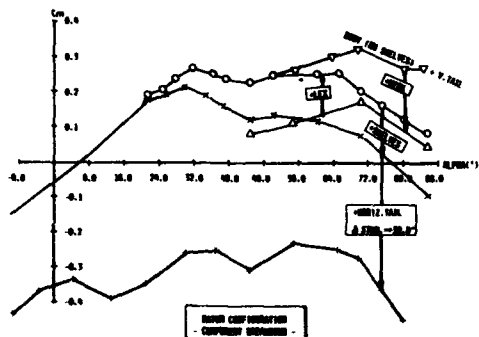


Fig. 9 - Contribution of model components to static pitching moment at zero sideslip



Fig. 10 - Contribution of model components to pitching moment change due to sideslip

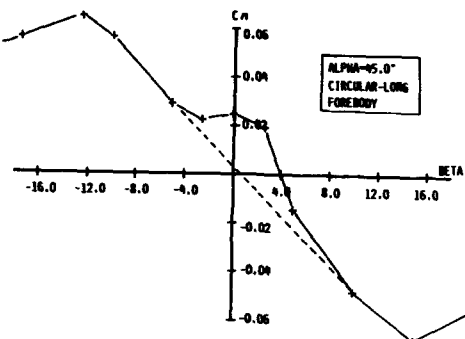


Fig. 7 - Coupling between natural asymmetry and flow asymmetry in a static test at sideslip: natural asymmetry gradually disappears

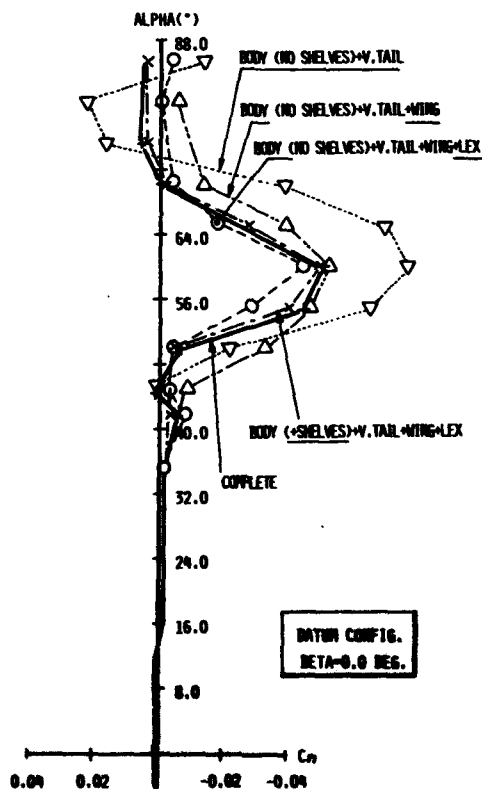


Fig. 11 - Natural asymmetries at zero sideslip: model breakdown

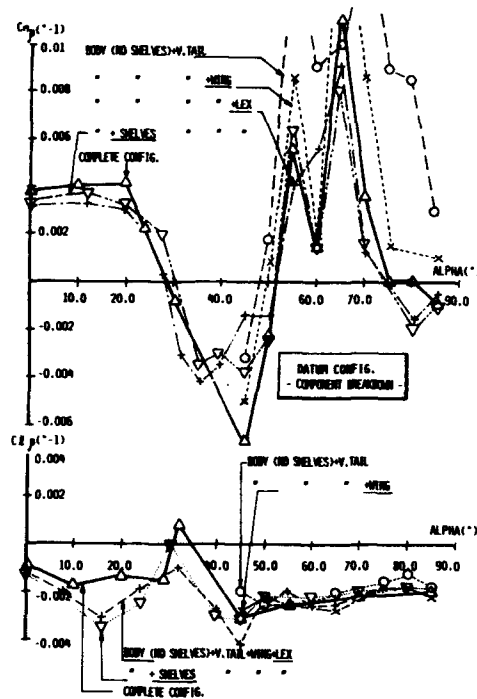


Fig. 12 - Directional and lateral stability

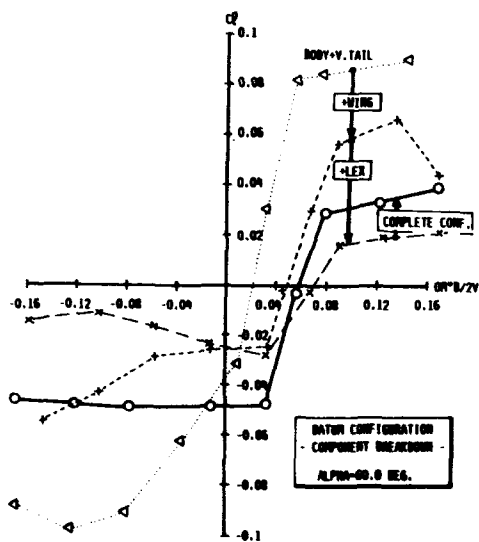


Fig. 14 - Typical model breakdown effects on roll damping at high AOA

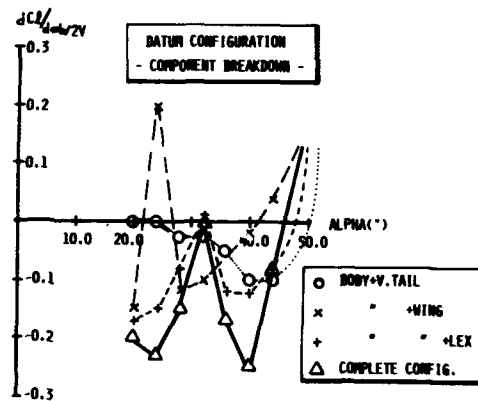


Fig. 13 - Contribution of model components to roll damping - Moderate angles of attack

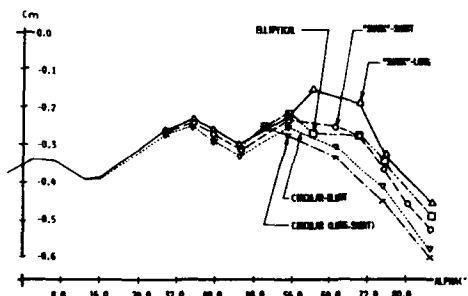


Fig. 15 - Forebody effect on static pitching moment at zero sideslip

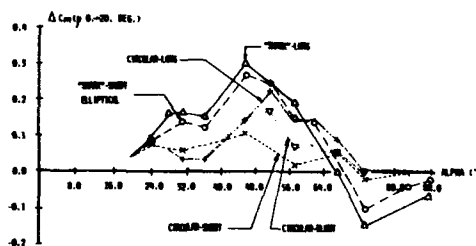


Fig. 16 - Forebody effects on pitching moment change due to sideslip

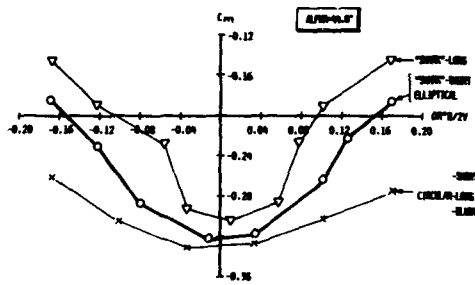


Fig. 17 - Forcbody effects on pitching moment change due to rotation

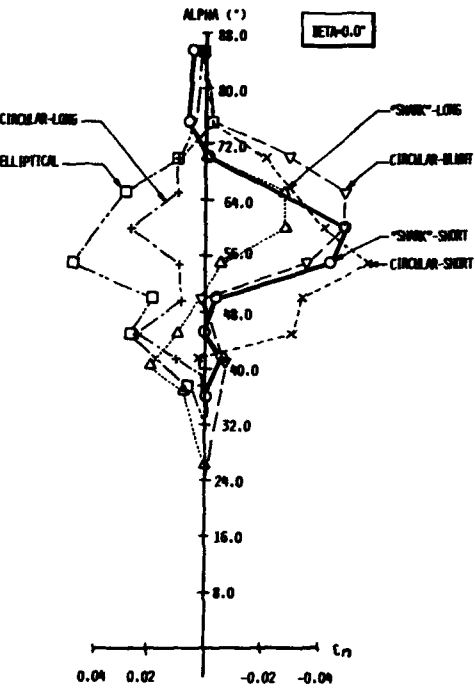
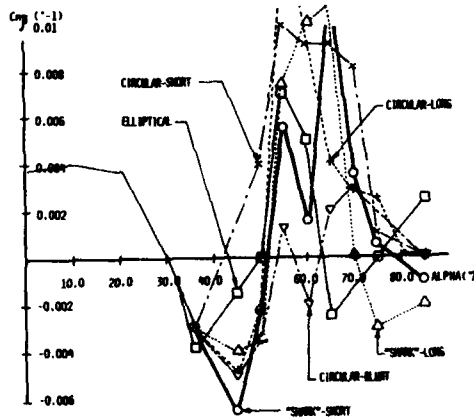


Fig. 19 - Directional and lateral stability effects of different forcobodies

Fig. 18 - Natural asymmetries at zero sideslip of different forcobodies

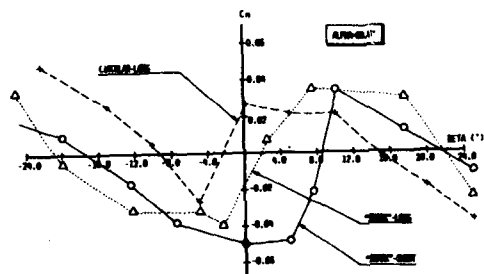


Fig. 20 - Typical yawing moments due to sideslip at high angle of attack

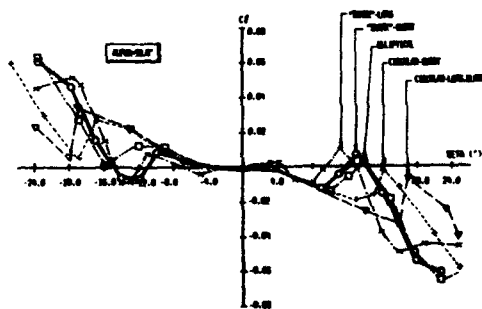


Fig. 21 - Variation with forcbody shape of roll reversal at high sideslip

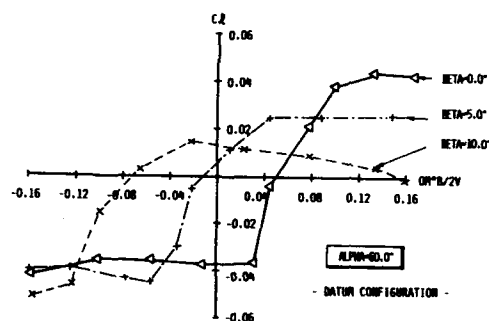
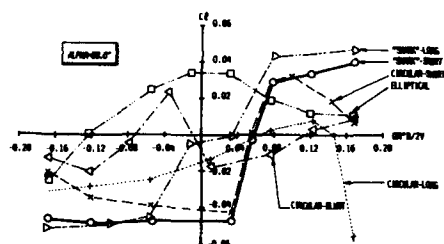


Fig. 22 - Roll damping at high AOA with different forebodies Fig. 23 - Effects of sideslip on roll damping at high AOA

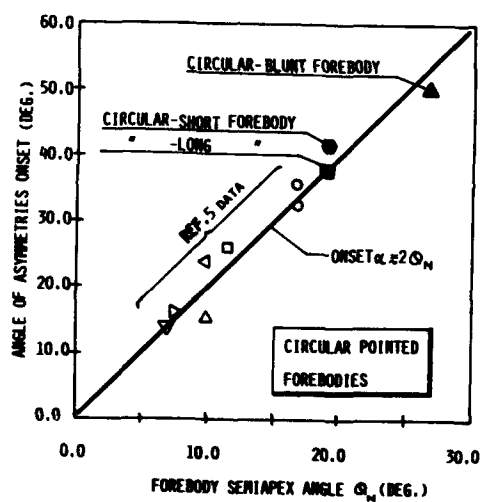


Fig. 24 - Correlation of asymmetry onset angle with data from ref. 5

# Non-linear Airloads Hypersurface Representation - A Time Domain Perspective

J. E. Jenkins  
Wright Laboratory  
WL / FIGC  
Wright-Patterson AFB, Ohio 45433-6553  
U. S.

and

E. S. Hanff  
Institute for Aerospace Research  
Ottawa, Ontario  
Canada

## Summary

Representation of nonlinear and unsteady airloads by the reaction hypersurface model is shown to be a special case of the nonlinear indicial response model. The principal requirement is that the motions are analytical (in the strict mathematical sense) to ensure uniqueness. Static and roll oscillation test data for a 65 degree delta wing at an angle of attack of 30 degrees were analyzed using the theoretical relationships between the two models. Analysis results indicate that the existence of singularities in the static rolling moment variation with roll angle invalidate the current model. Additional experiments are planned to resolve this issue.

## Nomenclature

A	Amplitude
b	Wingspan
$C_l$	Rolling Moment coefficient = $l / (q_\infty S b)$
$C_L$	Lift coefficient = $L / (q_\infty S)$
k	Reduced frequency = $(\omega b) / (2 U_\infty)$
p	Reduced roll rate
q	Reduced pitch rate
$q_\infty$	Dynamic Pressure
r	Reduced yaw rate
S	Model planform area
t	Non-dimensional time = $(2 U) / b$
$U_\infty$	Freestream velocity
$\alpha$	Angle of attack
$\beta$	Sideslip angle
$\sigma$	Pitch angle (of body-fixed model axis)
$\phi$	Roll angle (body axis)
$\phi_0$	Roll angle offset for harmonic test conditions (mean value)
$\tau$	Indicial response onset time (non-dimensional)

## Introduction

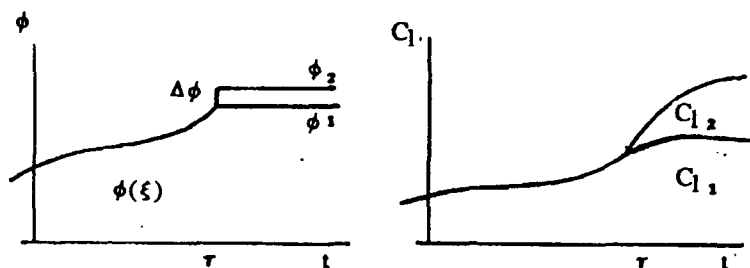
Large-amplitude dynamic force and moment data typically exhibit nonlinear dependencies on amplitude and frequency. Often these effects can be attributed to "simple" nonlinear variations in static force and moment data; sometimes aerodynamic hysteresis is the cause. However, conventional linear models (e.g. stability derivatives) are incapable of correctly accounting for the observed frequency

and/or amplitude effects when applied to harmonic motions. "Dynamic stall", wing rock, and nose slice are all dynamic high angle-of-attack phenomena for which linear models fail. Appropriate nonlinear models are not generally available.

Non-linear aerodynamic response modeling for flight mechanics analyses requires that the oscillatory data be put into a form which is applicable to arbitrary (not known a priori) motions. The current work focuses on establishing the relationships between the nonlinear indicial response model (the time domain model developed by Tobak, Chapman, Schiff<sup>1,2</sup> and others) and the reaction hypersurface model proposed by Hanff.<sup>3</sup> Both are of particular interest since they are conceptually capable of handling aerodynamic hysteresis effects. However, detailed studies (based on experimental data and designed to test the hypotheses underlying these developments) are lacking. The hypersurface representation offers advantages (to the flight mechanist) over time domain models. On the other hand, the nonlinear indicial response can, in principle, accommodate a wide variety of physical phenomena. The objective of this paper is to show that the hypersurface model is, in fact, a special case of the more general indicial model. In particular, the assumptions required to "recover" the hypersurface, and the restrictions thus imposed, are explored.

In the sections to follow, properties of the hypersurface model, derived from the nonlinear indicial response, are studied using Hanff's<sup>4</sup> dynamic force and moment data for a rolling delta wing. The use of these data is especially appropriate because strongly nonlinear behavior is exhibited, including the existence of multiple attractors and strong history effects. Shown in Figure 1 are results from free-to-roll experiments conducted in concert with the dynamic force tests. Phase-plane plots for two release points show two distinct trim points are observed, near 0 and 21 degrees roll angle (a third also exists at -21). Note also that at the intersection of the trajectories near zero roll angle and positive roll rate,  $\dot{\phi}$  is decreasing for the negative release angle (solid curve), while the reverse is true for the dashed curve. We must conclude that the rolling moments for the two cases are of opposite sign even though  $\phi$  and  $\dot{\phi}$  are matched. Since there are only differences in the motion history leading up to the





intersection, we must also conclude that there are significant history effects on the net moment, which includes both "stiffness" and damping terms.

### Nonlinear Indicial Responses

The nonlinear indicial response is defined in terms of two motions as shown in the sketch above. Note that both motions are generated by the "reference motion",  $\phi(\xi)$ , defined for  $-\infty < t$ ; however:

$\phi_1$  matches  $\phi(\xi)$  for  $-\infty < t \leq \tau$ , and is held constant at  $\phi(\tau)$  for  $t > \tau$ ;

while

$\phi_2$  also follows  $\phi(\xi)$  for  $t \leq \tau$ , but jumps instantaneously to  $\phi_1(\tau) + \Delta\phi$  for  $t > \tau$ .

As shown by Tobak and Chapman,<sup>1</sup> the dependence of nonlinear indicial responses on reference motion requires that they be expressed mathematically as a functional, i.e.,

$$C_{L\phi}[\phi(\xi); t, \tau] = \lim_{\Delta\phi \rightarrow 0} \frac{C_L[\phi_2(t)] - C_L[\phi_1(t)]}{\Delta\phi} \quad [1]$$

The functional dependency on prior motion,  $\phi(\xi)$ , distinguishes the nonlinear indicial response from its linear counterpart. The notation on the L.H.S. of Eq. [1] is that of Tobak and Chapman<sup>1</sup> and is intended to make explicit that  $\phi_1$  belongs to a family of motions, all generated by  $\phi(\xi)$ , but constrained to remain constant beyond the instant denoted by  $\tau$ .

Equation [1] defines the Frechet derivative of the functional  $C_L[\phi_1(t)]$ . Tobak, Chapman and Unal<sup>2</sup> suggest that bifurcations of physically realizable (asymptotically stable to small perturbations) steady-state "solutions" corresponding to  $\phi_1$  are signaled by loss of Frechet differentiability. They also note that changes in equilibrium flow topology can lead to a loss of analytic dependence on a parameter (e.g.  $\phi$ ) and thus invalidate the Frechet derivative. Both cases are of considerable interest to the study of hysteresis effects.

As shown by Tobak and Chapman,<sup>1</sup> aerodynamic responses to arbitrary motion inputs can be calculated through the use of a generalized superposition integral. If a bifurcation in the steady-state response occurs (or the Frechet derivative becomes singular for any reason) at a "critical time"  $\tau_c$ , the integral has the form:

$$C_L(t) = C_L(t, \phi(0)) + \lim_{\epsilon \rightarrow 0} \left[ \int_0^{\tau_c - \epsilon} C_{L\phi}[\phi(\xi); t, \tau] \frac{d\phi}{d\tau} d\tau + \int_{\tau_c + \epsilon}^t C_{L\phi}[\phi(\xi); t, \tau] \frac{d\phi}{d\tau} d\tau + \Delta C_L(t, \phi_c) \right] \quad [2]$$

where:

$$\Delta C_L(t, \phi_c) = C_L[\phi(\xi); t, \tau_c + \epsilon] - C_L[\phi(\xi); t, \tau_c - \epsilon]$$

Thus, the superposition integral is split to allow the solution to change discretely to a new equilibrium state (and to avoid the singularity in the Frechet derivative). Although  $\Delta C_L$  allows for a (potentially discontinuous) change in equilibrium state, it is a function of time that in the limit approaches the new value.

### Reaction Hypersurface

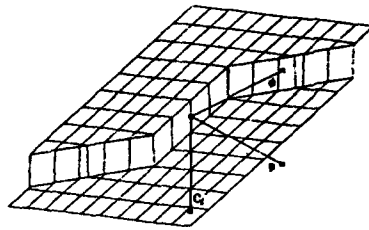
The reaction hypersurface represents the aerodynamic response as a surface in a space defined by a set of orthogonal axes where the independent variables are the primary motion variables (and their time derivatives), and the dependent variable is one of the six force and moment coefficients. In theory, there is no limit on the number of independent variables. Using lift coefficient expressed in stability axes as the example:

$$C_L = f(\alpha, \dot{\alpha}, \ddot{\alpha}, \dots, \beta, \dot{\beta}, \ddot{\beta}, \dots, p, \dot{p}, \ddot{p}, \dots, q, \dot{q}, \ddot{q}, \dots, r, \dot{r}, \ddot{r}, \dots)$$

No assumptions regarding the linearity of the response, with respect to the motion variables, are made. In fact, hysteresis effects can be represented. An idealized rate-dependent hysteresis case is shown below in a 3-space.

Herein attention is restricted to body-axis rolling motions (corresponding to Hanff's experiments). Therefore only one primary motion variable,  $\phi$ , and its derivatives are considered. However, the techniques discussed below are not limited in this way and may be applied to the more general case.

In the following sections, issues concerning uniqueness of the hypersurface and its derivation, starting from the nonlinear indicial response model



and the generalized superposition integral, are examined. This is followed by a description of the procedures used to derive analytical expressions for the rolling delta-wing data in hypersurface form. Hanff and S. B. Jenkins<sup>4</sup> have previously presented a three dimensional reaction surface for the same data in tabular form.

#### Reaction Hypersurface Uniqueness

Consider the space of independent (motion) variables, in this case the body-axis roll angle  $\phi$ , and its derivatives.  $\phi(t)$  is assumed to be an analytic function and therefore has derivatives of all orders. Is there a unique aerodynamic response corresponding to each point in this "phase-space"?

First,  $\phi(t)$  can be mapped into a curve in phase-space, i.e., trajectories in this space are parametric representations for the motion, with  $t$  the parameter. Now, suppose that two such curves,  $\phi_1(t)$  and  $\phi_2(t)$ , intersect at  $t=a$  as shown in the sketch below. There is a distinct possibility that the particular responses (e.g.  $C_l$ ) associated with the two trajectories will disagree at  $t=a$ , because of different histories (recall the discussion regarding Figure 1).

Expressing  $\phi_1$  in terms of a Taylor series (recall that analytic motion has been assumed):

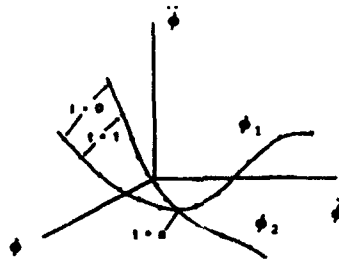
$$\phi_1(t) = \phi_{1a} + \dot{\phi}_{1a}(t-t_a) + \frac{1}{2!} \ddot{\phi}_{1a}(t-t_a)^2 + \dots$$

$$+ \frac{1}{3!} \ddot{\phi}_{1a}(t-t_a)^3 + \dots \quad [3]$$

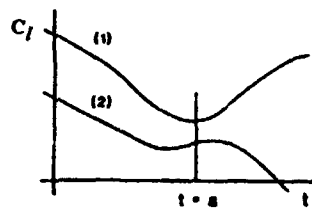
where the subscript "a" indicates that the quantity is evaluated at  $t=t_a$ , (corresponding to the point of intersection). In phase space, the coordinates of the point of intersection are:  $\phi_{1a}, \dot{\phi}_{1a}, \ddot{\phi}_{1a}, \dots$ . Thus, if  $\phi_2$  is represented by its Taylor series (expanded about  $t=t_a$ ), clearly  $\phi_1(t) \equiv \phi_2(t)$ . That is, only one analytic curve may pass through a given point in this space and the situation shown in the sketch cannot occur, given the condition of analytic motion and the luxury of an infinite-dimensional space.

This result guarantees that one may discriminate between different analytic motions given a large enough space. On the other hand, there is no need to differentiate between motions that yield identical aerodynamic responses. The extent to which the flow-field "remembers" prior events is the factor that determines the required number of dimensions.

History effects arise from two sources when interpreted in terms of the indicial response model. First as shown by Eq. [1], the response to a small step input in the nonlinear case depends on the motion,  $\phi(\xi)$ , leading up to the step change. Second, the response at time "t" due to an arbitrary motion input depends on the aggregate effect of all previous step changes as given by Eq. [2]. The purpose of the following section is to show how these effects impact the hypersurface representation.



Motion



Rolling Moment Responses

### Derivation from Indicial Response Model

Possible simplifications to the functional representation for indicial responses have been suggested by Tobak and Schiff.<sup>2</sup> For an analytic motion, the functional form of the indicial response can be replaced by a function of the motion parameters evaluated at the step onset condition. That is Eq. [1] can be put into the form:

$$C_{1\phi}(\phi(\xi); t_0, \tau) = C_{1\phi}(t_0, \tau; \phi(\tau), \dot{\phi}(\tau), \ddot{\phi}(\tau), \dots) \quad [4a]$$

where:

$\phi(\xi)$  has been replaced by its Taylor series (expanded about the onset time  $\tau$ ) and thus can be expressed as a function of  $\phi$  and its derivatives all evaluated at  $t = \tau$ .

and

$t = t_0$  designates the particular time at which the indicial response is being observed.

On physical grounds, the "distant" past can be expected to be less important to the step response than the motion characteristics just prior to onset, suggesting, perhaps, that only a few Taylor series coefficients need to be retained. In subsequent discussions, the motion variables which are retained as arguments of the function on the RHS of Eq. [4a] will be referred to as "onset parameters" (or sometimes as "active onset parameters").

The hypersurface model requires that the aerodynamic reaction,  $C_l$  in this case, be expressed in terms of the motion state at the observation time,  $t_0$ , not onset time  $\tau$  as done in Eq. [4a]. However, recall that  $\phi(\xi)$  is defined up to and including  $t = t_0$ . Thus with this understanding,  $\phi(\xi)$  can be expanded in a Taylor series about any point, say  $t_0$ , and Eq. [4a] can just as easily be written:

$$C_{1\phi}(\phi(\xi); t_0, \tau) = C_{1\phi}(t_0, \tau; \phi(t_0), \dot{\phi}(t_0), \ddot{\phi}(t_0), \dots) \quad [4b]$$

where:

$$\tau \leq t_0 \leq t_0$$

Note again however, that the notation serves as a reminder that the defining motion for the indicial response is constrained to be held constant for  $t > \tau$ . That is the response due to the step input at  $t = \tau$  cannot be influenced by subsequent events, even though the function  $\phi(\xi)$  has been represented by its behavior beyond  $t = \tau$ .

Thus, for an analytic motion, Eq. [2] can be put into the form:

$$\begin{aligned} C_l(t) &= C_l(t, \phi(0)) + C_{1l}(t, \tau_c; \phi(\tau_c), \dot{\phi}(\tau_c), \ddot{\phi}(\tau_c), \dots) \\ &+ C_{1l}(t, \tau_c; \phi(t), \dot{\phi}(t), \ddot{\phi}(t), \dots) \\ &+ \Delta C_l(t, \phi(\tau_c)) \end{aligned} \quad [5]$$

where:

$\phi(\xi)$  has been expanded about  $t_0 = \tau_c$  in the first integral ( $C_{1l}$ ) and in  $\Delta C_l$

$\phi(\xi)$  has been expanded about  $t_0 = t_0$  in the second integral

and

the subscript on  $t_0$  has been dropped since there is no longer ambiguity between the observation time and the running time variable in the functionals.

Note that Eq. [5] gives the instantaneous rolling moment coefficient in terms of instantaneous motion variables ( $\phi(t)$  and its derivatives), the locus of critical points expressed in phase-space coordinates ( $\phi(\tau_c), \dot{\phi}(\tau_c), \ddot{\phi}(\tau_c), \dots$ ) and an explicit dependence on time.

The importance of the time dependence depends on the relative sizes of characteristic times for the motion, indicial responses and  $\Delta C_l$ . For "slow" motions it will be important only near  $t=0$  and, in the case of bifurcation, for  $t$  close to  $\tau_c$ . When needed, a mapping of the time variables into phase-space coordinates will complete the transformation. It is informative to accomplish this by finding the inverse of Eq. [3]. That is with  $t_0=0$ , define:

$$G(\phi, t) = 0 = \phi - \phi_a - \dot{\phi}_a t - \frac{1}{2!} \ddot{\phi}_a t^2 - \frac{1}{3!} \ddot{\phi}_a t^3 - \dots$$

Now look for a Taylor series for  $t$  in terms of  $\phi - \phi_a$

$$\frac{dt}{d\phi} = \frac{G_\phi}{G_t}$$

where the subscripts denote partial derivatives.

Higher order derivatives are obtained by successive application of the chain rule. Upon evaluating the derivatives at  $\phi_a$ , which corresponds to  $t=0$ , we have:

$$t \approx A_1(\phi - \phi_a) + A_2(\phi - \phi_a)^2 + \dots + A_n(\phi - \phi_a)^n + \dots \quad [6]$$

where the  $A_i$ ,  $i=1, 2, \dots, n, \dots$ , depend only on time derivatives of  $\phi$  evaluated at  $t=0$ ; e. g.,

$$A_1 = \frac{1}{-\dot{\phi}_a}, \quad A_2 = \frac{\ddot{\phi}_a}{(-\dot{\phi}_a)^2}, \quad \dots$$

Note that  $G_t = 0$  is a singular point of the transformation. Note also, that the implicit function for  $t$ , which was derived based on the function  $\phi(t)$ , can be replaced by one based on  $\phi$ -dot (or any other derivative) near singular points.

Thus, the explicit time dependence can be eliminated if the reference points for the time variation ( $\phi$  and its derivatives evaluated at  $t=0$ ) are known. That is, the time mapping is a property of the space and is unique once the locus of reference points is specified. For many flight mechanics problems a convenient choice would be along bifurcation (Frechet derivative singularity) boundaries since the starting transients often die out quickly and can be

neglected.

Motion history effects therefore impact a truncated hypersurface in the following ways. A dependence of the indicial response on a particular set of onset motion parameters dictates the *minimum* dimensions of the phase space. Note however, that a  $\phi$  and  $\dot{\phi}$  dependency always exists because of the quasi-steady contributions and  $\dot{\phi}$  appears explicitly in the superposition integral. Secondly, sufficient dimensions must be retained to track time in regions where the time variations are important. Each additional term retained in Eq. [6] requires higher derivatives of  $\phi$  and thus more dimensions.

One further observation needs to be made. In a truncated space, the uniqueness of the time mapping is lost. That is, we must be able to identify the particular trajectory being traversed in phase space to reconstruct its time history. Recall that the implicit function for  $t$  is based on the motion given by Eq. [3]. Therefore, truncation restricts the range of analytic motions that can be uniquely specified. We must retain enough terms to adequately approximate the actual motion over the interval where an explicit time variation in the aerodynamic response is important.

A significant advantage to the hypersurface representation is the replacement of  $\tau_c$  by a function of motion parameters, since bifurcation points are more naturally expressed in these terms. In fact, to apply the indicial response model one would have to carry auxiliary equations along to determine  $\tau_c$ .

#### Model Identification Procedure

Based upon the theory presented above, a hypersurface model for the rolling moment "output" for the 65-degree delta wing in response to a body axis rolling motion was investigated. The procedure used is outlined below.

The fundamental assumptions are:

- (1) Indicial responses are assumed to approach a steady-state (time-invariant) condition as elapsed time since onset becomes large. In these cases, it is convenient to introduce the "deficiency function"  $F$ :

$$F(\phi(\tau), \dot{\phi}(\tau), \dots, t-\tau) = C_{1\phi}(\phi(\tau), \infty) - C_{1\phi}(\phi(\tau), \dot{\phi}(\tau), \dots, t-\tau) \quad [7]$$

where the first term on the RHS is the steady-state rolling moment slope with respect to  $\phi$ .

$$C_{1\phi}(\phi(\tau), \infty) = \lim_{t-\tau \rightarrow \infty} C_{1\phi}(\phi(\tau), \dot{\phi}(\tau), \dots, t-\tau)$$

Note that if the equilibrium state is time-invariant, it depends only on the onset level.

- (2) The deficiency function is assumed to be analytic and therefore can be expanded in a Taylor series in terms of its onset parameters.

$$F(\phi(\tau), \dot{\phi}(\tau), \dots, t-\tau) = F_0(0, t-\tau) \quad [8]$$

$$+ F_{\phi}(0, t-\tau) \phi(\tau) + 0.5 F_{\phi\phi}(0, t-\tau) \phi^2(\tau) + \dots \\ + F_{\dot{\phi}}(0, t-\tau) \dot{\phi}(\tau) + 0.5 F_{\dot{\phi}\dot{\phi}}(0, t-\tau) \dot{\phi}^2(\tau) + \dots \\ + \dots$$

Note that mixed partial derivatives will also appear and that the form of the deficiency function now known. In the following discussion, the term "onset function" is used to describe the onset parameters and products of onset parameters which appear on the RHS of Eq. 8; i.e.,  $\phi$ ,  $\phi^2$ ,  $\dot{\phi}^2$ , etc.

- (3) No static hysteresis effects are present. The carefully conducted experiments revealed no evidence to suggest hysteretical behavior.

- (4) An asymptotic expansion approximation to the superposition integral, as derived in Reference 6, can be used to identify relevant onset parameters. This assumption is not essential, however, it allows a linear regression analysis to be used in the identification. Requirements are that the test frequencies be less than the reciprocal of the indicial response time constants. In the nonlinear problem, it also requires that harmonic frequencies (of the motion) observed in the rolling moment response also be less than the reciprocal of the time constants. The essentials of the analysis are outlined below.

Given a harmonic motion about a fixed offset angle, i.e.,

$$\phi(t) = \phi_0 + A \cos(k t)$$

Using Eqs. [7] and [8] to describe the indicial response and expanding the superposition integral in an asymptotic expansion, the steady-state part of response can be shown<sup>6</sup> to have the form:

$$C_1 = G_0 + G_1 \cos(k t) + G_2 \cos(2 k t) + G_3 \cos(3 k t) \\ + \dots \\ + H_1 \sin(k t) + H_2 \sin(2 k t) + H_3 \sin(3 k t) \\ + \dots \quad [9]$$

where:

in-phase ( $G_i$ ) and out-of-phase ( $H_i$ ) coefficients are sums of contributions from the relevant onset functions. The  $G_i$  also contain the quasi-steady part of the response. For example, if an onset function,  $\phi^2$ , is important (among other possibilities),

$$G_1 = A \{ C_{1\phi} - I_2 k^2 + I_4 k^4 - \dots \} \\ + \frac{(A^3 + 4A\phi_0^2)}{8} \{ C_{1\phi\phi} - J_2 k^2 + J_4 k^4 - \dots \} \\ + \dots \quad [10a]$$

$$H_2 = - \frac{A^2 \phi_0 k}{2} (J_1 - 4J_2 k^2 + \dots) + \dots \quad [10b]$$

and

$I_2$  is the second integral of  $F_0$  evaluated at  $\tau=t$ ,  $J_1$  is the first integral of  $F_2$  evaluated at  $\tau=t$ , etc..

The variation with amplitude and offset for selected onset functions is shown in Table I.

Thus, contributions from each onset function can be related to multiple integrals of the corresponding deficiency function terms,  $F_0$  etc. Given amplitude, offset and frequency from the test conditions, a regression analysis can be set up to identify the active onset functions (the undetermined constants in the regression equation being the integrals in of the deficiency functions). Finally, knowledge of successive integrals of the deficiency functions allows an estimate of the indicial response time constants associated with each onset parameter to be made.

Recall that the quadrature component is free from quasi-steady effects, thus identification of the active onset parameters is best accomplished using these data. In addition, it turns out that for the pertinent onset parameters, the dynamic response in quadrature with the motion are lower order in frequency than the corresponding in-phase dynamic response terms (see Eqs. [10]). Thus for both reasons it is inherently more accurate to perform the identification on the quadrature component. The known relationship between the two components can then be exploited to give an independent check on the results.

## Results

An analysis of the in-phase and quadrature components (the first and second lines of Eq. [9] respectively) for the rolling 65 degree delta-wing data at an angle of attack of 30 degrees was performed using a step-wise multiple regression technique. The corrected sample coefficient of determination,  $r_c^2$ , is about 0.97 for each component. Active onset functions, as identified by this analysis, are shown in Table II below. Figures 2 and 3 show comparisons between the mathematical model and experiment.

In Figure 2, measured Fourier coefficients for the out-of-phase components (the imaginary parts of experimental FFT coefficients for the rolling moment), including coefficients for the first four harmonics are correlated against corresponding model coefficients ( $H_1$  through  $H_4$  in Eq. [9]). All test conditions at 4 Hertz,  $k = 0.08$ , and 7 Hertz,  $k = 0.14$ , are represented. Note that each test condition provides 4 points on this plot.

In-phase component results are shown in Figure 3. Here, in-phase rolling moment vs. roll angle is presented at offset angles of 0 and 42 degrees

for all amplitudes tested at  $k = 0.14$ . However, in order to obtain these results, only the mean value of the quasi-steady contributions ( $G_0$ ) as determined from the static experiments) could be retained in Eq. [9]. This contradicts what the theory says we must do (all the  $G_i$  contain quasi-steady terms). There were also discrepancies in the magnitudes of the contributions due to the identified onset functions between the in-phase and quadrature components. That is the  $I_i$ 's (or  $J_i$ 's) belonging to each component are related by the appropriate time constants. Even though there is relatively good agreement in the time constants the magnitudes did not check. However, there was agreement in the identification of the most significant onset functions in each case as shown in Table II.

The source of these discrepancies is believed to be a loss of analytic dependence of the static rolling moment on roll angle (near  $\pm 7$  degrees). Evidence supporting this conclusion is shown in Figures 4, 5, and 6. Note the steep gradients in the static data near the origin as shown in Figure 4. Large changes in equilibrium states over small a small variation in roll angle is a warning signal that should not be ignored. Hanff and Ericsson's<sup>7</sup> analysis of the flow physics in the static case offers an explanation. The mechanism appears to be a rapid aft movement in the leeward wing vortex-breakdown position to the trailing edge at roll angles around 7 degrees (at lower roll angles, the movement of the break-down point is rather small). Substantially longer times to reach equilibrium states can be expected when changes in flow topology occur.<sup>2</sup>

Finally, the contrast in the measured rolling moment time histories shown in Figures 5 and 6 is dramatic. The rolling moment response for a 5 degree amplitude harmonic oscillation about a 14 degree offset is essentially quasi-steady, as shown in Figure 5. However as the amplitude is increased to 12 degrees (Figure 6), substantial dynamic effects are apparent as the roll angle approaches 7 degrees from above. The dynamic effects then decay after the roll angle goes through 7 degrees again in the second half of the cycle.

All of this suggests that, despite the absence of static hysteresis, there are at least two singularities present (at about  $\pm 7$  degrees) which were not taken into account. Further analysis, primarily to identify the increment(s) in equilibrium state,  $\Delta C_l(t, \phi(\tau_c))$ , as required at singular points, and to better identify the indicial response characteristics between the singular points awaits additional data.

Another roll oscillation test program will be conducted shortly at the 7 x 10 ft. SARL wind tunnel at WPAFB. Its principle objectives are to establish the impact of support and wall interference on this type of testing, to obtain supplementary data as suggested by the analysis of the previous tests and finally, to establish the effect of Reynolds number. Table III summarizes the tests to be conducted at the same Reynolds number as used in the early tests, which are more relevant to the subject at hand. Conditions to be repeated in order to establish interference effects are shown in plain characters,

whereas supplementary ones are indicated in bold print. As can be observed, the latter reflect the need to obtain data at lower reduced frequencies to fill the gap between the static data and those for  $k = 0.08$ . These data will be especially useful for separating indicial response characteristics from the purely time dependent  $\Delta C_l$  effects. Note also that additional surface oil flow visualization tests are planned to obtain a better understanding of the static behavior at roll angles between 0 and 7 degrees.

### Conclusions

Hanff's reaction hypersurface has been shown to be a special case of the nonlinear indicial response model. It is a mapping of the time-domain response onto an infinite-dimensional space consisting of the primary motion variables and their derivatives. Motions are required to be analytic (in the strict mathematical sense) to ensure uniqueness. Given a locus of time-reference points in the space, time variations can be tracked. In a finite-space approximation, the minimum dimension to avoid ambiguities (in the surface representing the aerodynamic reaction) can be related directly to active indicial response onset parameters. Additional dimensions may be required if transients near critical points cannot be neglected.

A preliminary analysis of static and oscillatory roll data for a 65 degree delta wing at 30 degrees angle of attack indicates that the corresponding hypersurface model (in mathematical form) must acknowledge the presence of at least two critical points in the static rolling moment curve. These points correspond to large movements in the vortex break-down point on the leeward wing for a small change in roll angle. Time-histories of measured rolling moment responses at  $k = 0.08$  suggest (when compared to static characteristics) that significant dynamic effects are present when the critical points are encountered. At the same reduced frequency, the response is quasi-steady for motions which avoid these points. Additional tests are planned to fully examine this behavior.

Finally, the results indicate that a hypersurface in at least a four dimensional space (roll angle and its first two derivatives as independent variables) is required to fully represent the rolling moment

response for the case studied.

### Acknowledgements

The authors wish to thank Mr S. Jenkins of the IAR and Mr. J. Tromp of Wright Laboratory for their technical counsel and support in the preparation of the manuscript. This work was conducted under a Joint Research Program of the U.S. Air Force Office for Scientific Research and Wright Laboratory, Institute for Aerospace Research and Canadian Dept. of National Defence. The support of these organizations is also gratefully acknowledged.

### References

1. Tobak, M. and Chapman, G. T., "Nonlinear Problems in Flight Mechanics Involving Aerodynamic Bifurcations", AGARD CP-386, Paper 25, May 1985
2. Tobak, M. and Schiff, L. B., "Aerodynamic Mathematical Modeling - Basic Concepts", AGARD Lecture Series No. 114, Paper 1, March 1981
3. Hanff, E. S., "Dynamic Nonlinear Airloads Representation and Measurement", AGARD CP-386, Paper 27, May 1985
4. Hanff, E.S., and Jenkins, S.B., "Large-Amplitude High-Rate Roll Experiments on a Delta and Double Delta Wing", AIAA paper 90-0224, January 1990.
5. Tobak, M. and Chapman, G. T., and Unal, A., "Modeling Aerodynamic Discontinuities and Onset of Chaos in Flight Dynamical Systems", Annales des Telecommunications, May-June 1987
6. Jenkins, J. E., "Simplification of Nonlinear Indicial Response Models - Assessment for the 2-D Airfoil Case", AIAA Journal of Aircraft, To be published.
7. Hanff, E. S. and Ericsson, L. E., "Multiple Roll Attactors of a Delta Wing at High Incidence", presented at the AGARD Symposium on Vortex Flow Aerodynamics, Netherlands, October 1990.

Table I - Influence of Nonlinear Onset Functions

Coefficient	$\phi^2$	$\dot{\phi}$	$\phi \dot{\phi}$
$C_{l_0}$	0	$A^2$	$A^2 \phi_0$
$G_1, H_1$	$A^3 + 4A\phi_0^2$	0	$A^3$
$G_2, H_2$	$A^2 \phi_0$	$A^2$	$A^2 \phi_0$
$G_3, H_3$	$A^3$	0	$A^3$

Table II - Active Onset Functions

In-phase	linear, $\phi$ , $\phi^2$ , $\phi^4$ , $\phi \dot{\phi}$
Quadrature	linear, $\phi$ , $\phi^2$ , $\phi^4$ , -

**Table III - SARL Roll Experiments Test Matrix (1991)**  
(65° Delta wing,  $Re = 2.4$  million)

TEST	$\sigma$ (deg.)	$\phi_0$	A	k
Static force	30, 35	$\pm (70, 56, 42, 28, 14, 7, 6, 5, 4, 3, 2, 1, 0)$	N/A	0
Dynamic force	30, 35	42, 28, 14, 7, 3, 0	5, 12, 19, 26, 33, 40	0.02, 0.04, 0.08, 0.14
Free-to-roll	30, 35	-65 to 65	N/A	0
Static surface pressure	30, 35	$\pm(42, 28, 14, 7, 6, 5, 4, 3, 2, 1, 0)$	N/A	0
Dynamic surface pressure	30, 35	$\pm 28$ 0 0, 7, 42	26, 40 5, 12, 19, 26, 33, 40 5, 26, 40	0.02, 0.04 0.02, 0.04 0.14
Laser sheet flow visualization	30, 35	0 42, 28, 14, 0	5, 12, 19, 26, 33, 40 5, 12, 19, 26, 33, 40	0.02, 0.04 0.14
Surface oil-flow visualization	30, 35	42, 28, 14, 7, 5, 3, 1, 0	N/A	0

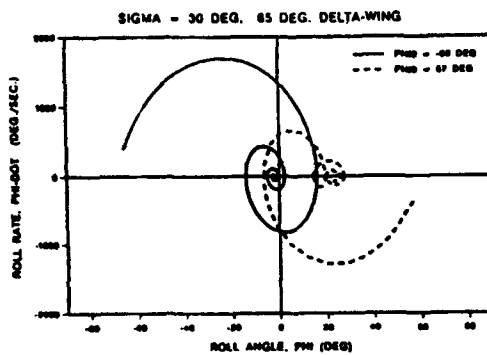


Figure 1 - Free-to-Roll Tests

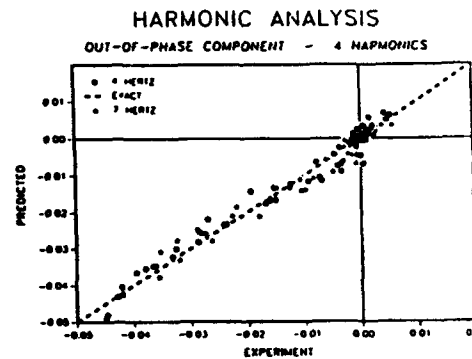


Figure 2 - Quadrature Correlation

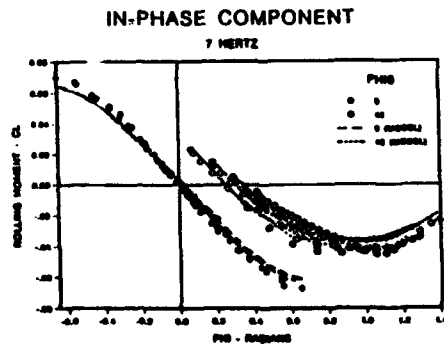


Figure 3 - In-phase Correlation

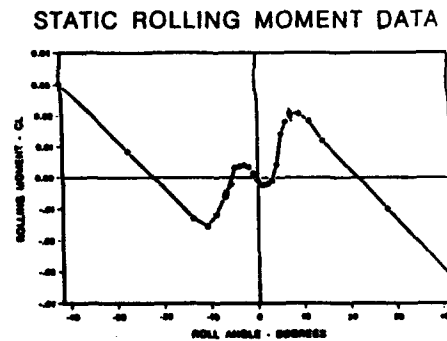
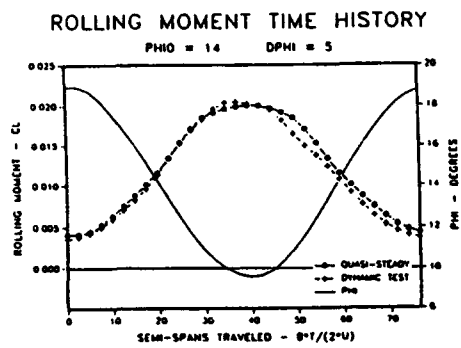
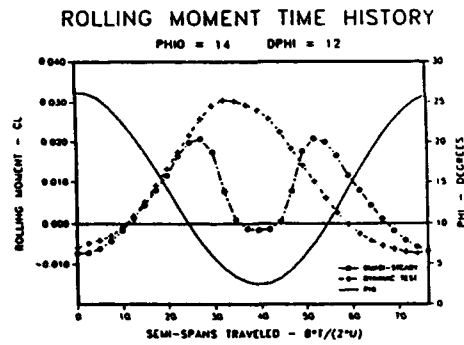


Figure 4 - Static C

Figure 5 -  $C_1$  Time HistoryFigure 6 -  $C_1$  Time History



# ANALYSIS OF UNSTEADY FORCE, PRESSURE AND FLOW-VISUALIZATION DATA FOR A PITCHING STRAKED WING MODEL AT HIGH ANGLES OF ATTACK

by

A.M. Cunningham, Jr.  
General Dynamics  
Fort Worth  
Texas

R.G. den Boer  
National Aerospace Laboratory (NLR)  
Anthony Fokkerweg 2  
1059 CM Amsterdam  
The Netherlands

## SUMMARY

Results are presented and discussed for the low speed test of a straked wing model oscillating in pitch that was conducted during 1986 at the National Aerospace Laboratory of The Netherlands in cooperation with General Dynamics. The model was oscillated about mean angles of attack ranging from -4 deg to 48 deg with amplitudes varying from 2 deg to 18 deg for a maximum incidence range of -8 deg to 50 deg. It was also oscillated in pitch at side slip angles of +5 deg and -5 deg. Force, pressure and flow-visualization data were recorded, processed and documented in a final report and stored on digital and analog magnetic tapes. This paper presents a brief description of the model and test program, in addition to the steady and unsteady aerodynamic characteristics. Steady and unsteady pressure and flow-visualization data are used to provide a better understanding of the phenomena observed in the aerodynamic characteristics. Particular emphasis is placed on the nature of dynamic vortex structure interplay with the forces and moments for symmetric flows. These concepts are then used to gain insight to the developments of asymmetric forces and moments for the model pitching at side-slip.

## 1.0 INTRODUCTION

Post stall maneuvering capability requirements for fighter aircraft are becoming a distinct possibility as emphasized in recent research programs being conducted by NASA, U.S. Air Force, U.S. Navy and DARPA. Two basic classes of hi- $\alpha$  maneuvers have evolved: (1) a low-speed rapid turn with high decelerations going into the turn and high accelerations coming out of the turn; and (2) a rapid pitch-point fire maneuver at higher speeds.<sup>1,2</sup> The first type of maneuver is akin to a "hammerhead" stall where as the second is a pitch-pulse similar to that demonstrated by Pougachev in a Russian Su-27 at the Paris Air Show in 1989, nicknamed the "Cobra" maneuver.

Although aerodynamic loads encountered in low speed rapid turns would be small, those produced during rapid pointing maneuvers at higher speeds would be significant and highly dynamic. Moreover, the dynamic aerodynamic loads in the latter case would be quite different from sustained maneuver loads in both magnitude and character. Hysteresis effects in forces and moments as well as dynamic overshoots of steady maximum forces are typical of the differences. Many of the current fighter aircraft which have the potential to perform such maneuvers are straked wing configurations as exemplified by the F-16, F-18, MiG-29, and Su-27. Thus, the unsteady aerodynamic loads on these aircraft would be produced by vortex flows

peculiar to straked wing plan-forms, subject to bursting and stalled conditions at high incidences and high pitch rates.

In order to better understand the development of unsteady air loads for these fighters maneuvering beyond stall, a low speed wind tunnel test of an oscillating straked wing model was performed during 1986 in a cooperative program between General Dynamics and the National Aerospace Laboratory (NLR) of The Netherlands.<sup>4</sup> The testing was funded by the Air Force Wright Research and Development Center using the model that was designed and built at NLR with funds provided by General Dynamics and NLR.

Several papers have been written describing both the 1986 test and subsequent analyses of the results of that test.<sup>5,6,7,8</sup> This paper is a follow-on to Reference 8 with the purpose of providing a better understanding of the non-linear aerodynamic phenomena described in that reference. Particular emphasis will be placed on the nature of dynamic vortex structure interplay with aerodynamic forces experienced by the straked wing model. Unsteady pressure data will be used to provide the link between flow-visualization and force data for symmetric pitching motions. These concepts will then be used to gain insight to the developments of asymmetric forces and moments for the model pitching at side-slip. Emphasis will be placed on the flow regimes that are dominated by vortex, burst vortex and/or stalled flows on either the windward or leeward wings or both.

## 2.0 MODEL AND TEST PROGRAM

The full-span model shown in Figure 1 was instrumented with a six-component balance, 42 in-situ pressure transducers, nine vertical accelerometers and an angle-of-attack sensor. Boundary layer transition was not fixed on the model. The model was mounted on the dynamic support system also shown in Figure 1 with the capability of maximum amplitudes of  $\pm 18$  deg (36 deg peak-to-peak) and maximum frequencies of 16 hz (limited to  $\pm 2$  deg amplitude). The total incidence range was from -8 deg to 50 deg with the capability of statically yawing the model and support system as indicated in Figure 1. Flow-visualization of the vortex structure was accomplished with smoke injection from the model nose with laser light sheet illumination. For unsteady flows, the laser sheet was pulsed in phase with model motion to provide illumination at a fixed model incidence during the cycle. The laser light sheet was positioned at each of the spanwise pressure sections so as to provide a spatial correlation between pressure and flow-visualization data.

Force, pressure and flow-visualization data were obtained for a wide variety of static and dynamic conditions at incidences up to 50 deg and are fully documented in References 4 and 5. The tests were conducted

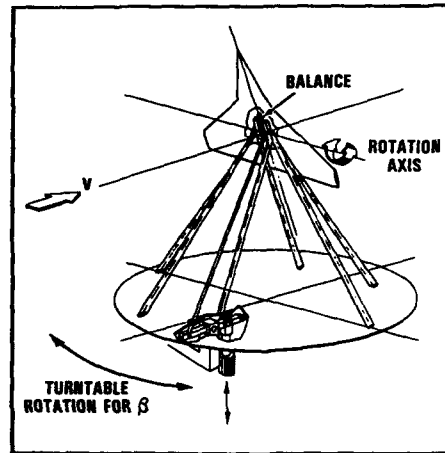
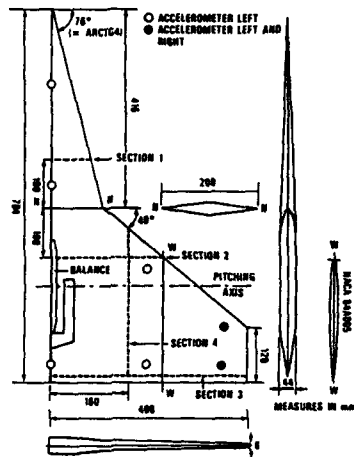


Figure 1 Straked Wing Model, Instrumentation, and Dynamic Support System

ed in the NLR 2.25 x 3.00m<sup>2</sup> Low Speed Tunnel using a matrix of mean incidence, amplitude and frequency so that the effects of pitch rate, amplitude and incidence range could be systematically separated. Time histories as well as harmonic component results were recorded for forces, moments and pressures. Results were also obtained for the model pitching at fixed yaw angles of  $\pm 5$  deg. Sign conventions for the forces, moments, and angles are shown in Figure 2.

### 3.0 SYMMETRIC FLOW

The key to understanding the unsteady aerodynamics is to first understand the steady aerodynamics. The combination of force, pressure and flow-visualization data available from this test makes it possible to break down the angle of attack range of -8 deg to 50 deg into definable flow regimes separated by smaller transition regimes.

#### 3.1 Symmetric Steady Aerodynamic Characteristics

The variations of steady normal force,  $C_N$  and pitching moment,  $C_m$  with angle of attack,  $\alpha$ , are shown in Figure 3 for zero side-slip. Important flow field characteristics and transitions are also denoted where the "sections" referred to in those notations are the pressure transducer rows

shown in Figure 1. Corresponding steady pressure data for all four sections are shown in Figure 4 for  $\alpha = 10$  deg, 22.4 deg, 36 deg and 42.3 deg. The pressure data were chosen to highlight various flow regimes and transitions.

The "Linear" range of aerodynamic force development is clearly evident in Figure 3 in both the  $C_N$  and  $C_m$  data from  $\alpha = -8$  deg to 8 deg. Beyond 8 deg, the  $C_N$  and  $C_m$  curves show an upward change in slope that is indicative of the development of vortex flows over both the wing and strake. This is illustrated by the pressure data and sketch of vortex structure in Figure 4 at  $\alpha = 10$  deg for pressure Section 2. The small peak at  $2y/b = 0.45$  is produced by the strake vortex and the stronger peak at  $2y/b = 0.8$  by the wing vortex.

The vortex flow range continues to develop until  $\alpha = 18$  deg to 19 deg where a distinct break occurs in the  $C_N$  and  $C_m$  data. This break signals the onset of vortex burst which represents the limit of vortex strength that can be maintained by the flow fields. Bursting tends to occur simultaneously for the wing and strake vortices when the two merge.<sup>8,9</sup> The pressure data and sketch of burst vortex structure for  $\alpha = 19$  deg in Figure 4 show well developed vortices at both the forward pressure sections (1 and

$$\begin{aligned}
 C_N &= \frac{N}{SQ} & c_r &= \text{ROOT CHORD} \\
 C_m &= \frac{m}{SQc_r} & b &= \text{SPAN} \\
 C_T &= \frac{T}{SQ} & Q &= \text{DYNAMIC PRESSURE} \\
 C_l &= \frac{l}{SQb} & S &= \text{SURFACE AREA} \\
 f &= \text{FREQ, Hz} \\
 k &= \frac{2\pi f c_r}{2V} \\
 V &= \text{FREE STREAM VELOCITY}
 \end{aligned}$$

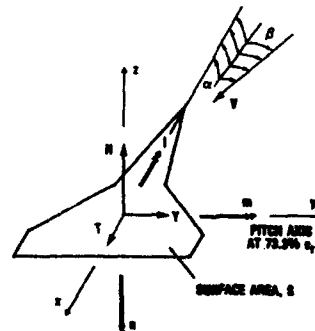


Figure 2 Coordinate System and Term Definitions

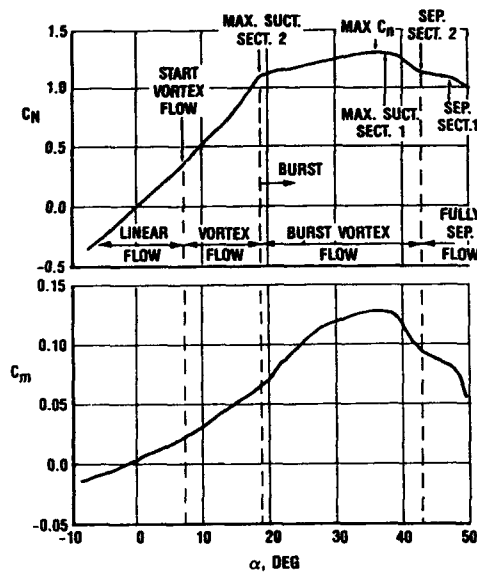


Figure 3 Steady Force and Moment Results for Symmetric Flow

2) but a deterioration of pressure recovery on the out-board half of the trailing edge section (3).

For increasing  $\alpha$  in the burst vortex regime, the strake vortex strength increases but the burst point continues to move forward. These opposing trends result in a much lower slope in the  $C_N$  curve as shown in Figure 3, however, the slope is almost constant from  $\alpha = 19$  deg to about 34 deg. The gain in lift forward, due to strake vortex strength increase, and the loss in lift aft, due to vortex burst forward movement, produces a pitch-up in the  $C_m$  curve as shown in Figure 3. The pressure data and

sketches of burst vortex development in Figure 4 for  $\alpha = 19$  deg, 22.4 deg, and 36 deg show the deterioration of the wing vortex strength at Section 2 and the continued increase of the strake vortex strength up to 36 deg at Section 1.

Beyond the maximum value of  $C_N$  at  $\alpha = 36$  deg the flow over the entire wing and strake rapidly collapses to completely separated or flat plate flow. Under these conditions for increasing  $\alpha$  the normal force is falling off and the center of pressure is moving toward the geometric centroid of the planform as indicated by a rapid decrease in pitching moment. The pressure data at  $\alpha = 42.3$  deg in Figure 4 show that the pressure distributions are nearly flat at about the same level for all sections except Section 1 on the strake. At this angle, the strake vortex burst has progressed forward of Section 1 as shown in the sketch for  $\alpha = 42.3$  deg.

### 3.2 Symmetric Unsteady Aerodynamic Characteristics

The symmetric unsteady aerodynamic characteristics for the pitching straked wing model at zero side-slip have been discussed extensively in References 6, 7, and 8. Since then, a new format has been developed which combines the pressure and flow-visualization data presented in Reference 4 into a side-by-side surface presentation at every 1/8 of the oscillation cycle. This form also highlights the changes at each point of the cycle by comparing current characteristics with those at the previous point in the cycle. Pressures, vortex paths, vortex core locations, and estimated vortex burst points are all treated in this manner. The side-by-side presentation of the spatial relationships of pressures and vortex structure further clarifies the relationship between off-surface flow-fields and surface pressures.

Discussions of symmetric unsteady flows in this section will be restricted to two incidence ranges at an intermediate reduced

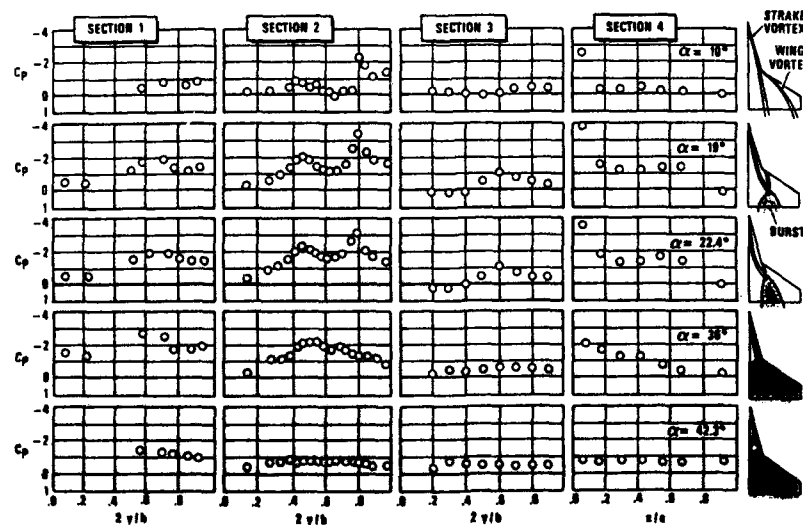


Figure 4 Variation of Steady Pressure Distributions with Alpha

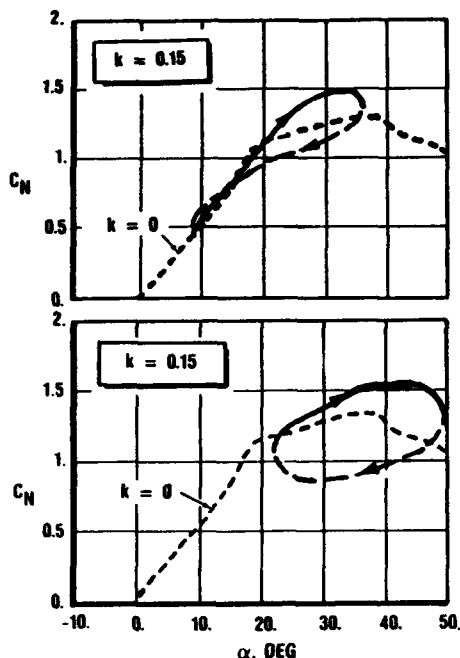


Figure 5 Unsteady Normal Force Results in Symmetric Flow

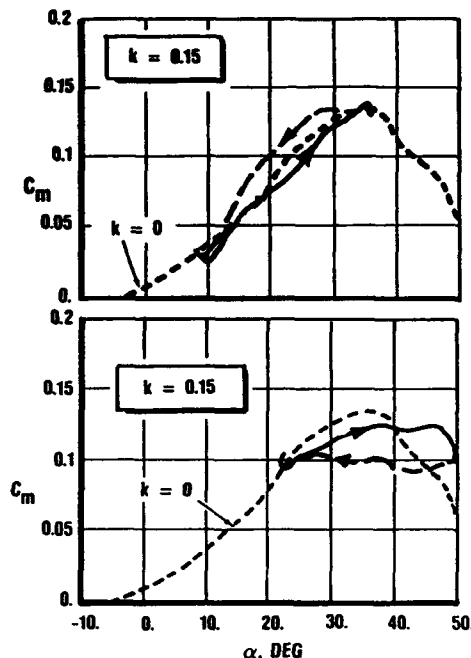


Figure 6 Unsteady Pitching Moment Results in Symmetric Flow

frequency,  $k = 0.15$ . The mid-incidence range of  $\alpha = 8$  deg to 36 deg for pitch oscillation will cover vortex flow and burst. The higher range of  $\alpha = 22$  deg to 50 deg begins in vortex burst and ends in stalled flow. For ease of reference in the following discussions, the normal force,  $C_N$ , and pitching moment,  $C_m$ , results from earlier references are repeated in Figures 5 and 6 respectively, for model pitch oscillations at the two incidence ranges and  $k = 0.15$ .

The first set of pressure and flow-visualization data to be discussed is presented in Figure 7 for the mid-incidence range of 8 deg to 36 deg. The arrangement consists of surface instantaneous pressure plots on the left and instantaneous smoke pattern outlines on the right with time increasing shown by the large arrows. The instantaneous value of  $\alpha$  and direction of pitch rate ( $\dot{\alpha}$ ) are both denoted at each point in time. In all cases, lowest  $\alpha$  conditions are at the bottom of the figures and highest  $\alpha$  conditions at the top of the figures.

Notations are presented in Figure 7(a) at  $\alpha = 8.4$  deg for symbol definitions. Current pressure distributions and projected vortex paths are denoted as solid lines and previous results as dashed lines. As an example, for  $\alpha = 8.4$  deg, the dashed data are the same as current data for the previous condition at  $\alpha = 12.5$  deg,  $\dot{\alpha} < 0$ , Figure 7(h). The smoke pattern outlines as traced from the instantaneous flow-visualization photographs, are always shown for the current angle. Also noted are the strake vortex vertical and lateral core position loci with a symbol denoting the current core position. These loci are shown twice scale

size for clarity and are not shown if the strake vortex has burst at the corresponding point in time and light sheet location.

Beginning at  $\alpha = 8.4$  in Figure 7(a) the flow fields are dominated by the strake and wing vortices where neither are burst and the latter is producing the highest suction peak as seen in the pressures. Progressing  $1/8$  of a cycle to the next angle,  $\alpha = 12.5$  deg, Figure 7(b), the same flow conditions exist except that suction has increased more for the strake vortex than for the wing vortex. The wing vortex is moving inboard and the strake vortex is moving away from the wing. Since surface suction is growing under the strake vortex, then its strength is increasing at a rate sufficient to more than offset the loss in suction that occurs due to displacement of that vortex away from the wing.

At  $\alpha = 22.3$  deg, in Figure 7(c), the wing and strake vortex have combined into a burst. This bursting has occurred just prior to the current angle as is indicated by the shape of the smoke pattern at the trailing edge. The "tail" pattern denoted in the figure is characteristic of post bursting, within 1 deg, as has been seen in other photographs for smaller amplitudes which highlight the burst process. This point corresponds to the break in the dynamic  $C_N$  loop ( $\dot{\alpha} > 0$ , Figure 5) and a pitch-up break in the  $C_m$  loop ( $\dot{\alpha} > 0$ , Figure 6) both at 22 deg. Suction under the wing vortex at Section 2 has changed very little but has increased significantly under the strake vortex, even though the latter has moved further away from the wing surface. A large increase in suction at both the trailing edge (Section 3) and chordwise (Section 4)

positions is a result of bending the strake vortex in the span-wise direction and bursting of both vortices.

Beyond burst at  $\alpha = 32.1$  deg, in Figure 7(d) the burst point moves forward and the strake vortex moves further away from the wing. An outboard movement of the strake vortex is also seen at Section 1 which is greater than that seen at Section 2. Suction under the wing vortex at Section 2 has dropped significantly as a result of lifting that vortex by the strake vortex and the downstream burst point moving forward. Suction under the strake vortex at Section 2 is still increasing, thus, indicating continued growth of its strength to offset its displacement away from the wing. This region corresponds to points in the  $C_N$  and  $C_m$  dynamic loops ( $\dot{\alpha} > 0$ , Figures 5 and 6) where dynamic lift is at a maximum and  $C_m$  pitch-up is still increasing.

At the maximum incidence,  $\alpha = 36.1$  deg, in Figure 7(e), burst of the strake vortex has moved forward of Section 2 as indicated by the smoke pattern at that section. Suction has also fallen off under the strake vortex as a result of the bursting; however, not much change has occurred for the wing vortex. Since pitch rate is zero, the aerodynamic lag effect is disappearing and the unsteady flow fields are "catching up" with the steady characteristics at the peak angle as is also indicated in the  $C_N$  and  $C_m$  loops.

At the beginning of pitch-down,  $\alpha = 32.1$  deg, in Figure 7(f), very little change is noted from the peak incidence of  $36.1$  deg. Suction is generally falling and flow re-establishment has progressed very little as a result of reverse aerodynamic lag (tendency of the flow-fields to remain at a more separated condition). This reverse lag as contrasted with positive lag on pitch-up is very apparent in the comparison of results in Figures 7(d) and 7(f) at  $\alpha = 32.1$  deg. This comparison also highlights the differences in the  $C_N$  and  $C_m$  dynamic loops in Figures 5 and 6 for pitch-up and pitch-down.

At the mean incidence,  $\alpha = 22.3$  deg, in Figure 7(g), where vortex bursting occurred on pitch-up, the strake burst point has moved aft of Section 2. The suction levels have fallen from the previous angle and are slightly lower overall under the strake vortex than those shown for pitch-up at  $\alpha = 22.3$  deg, Figure 7(c). The weaker suction peak under the wing vortex for  $\dot{\alpha} < 0$  as compared with that for  $\dot{\alpha} > 0$  is probably indicative of the source for much lower  $C_N$  values on pitch-down in Figure 5.

Just prior to the lowest angle at  $\alpha = 12.5$  deg, in Figure 7(h), the flow fields have been fully re-established. The burst has moved off of the trailing edge and the wing vortex suction peak is again reformed. The strake vortex has moved closer to the wing but has diminished significantly in strength as indicated by the large drop in suction under that vortex. In agreement with the  $C_N$  and  $C_m$  results in Figures 5 and 6, very few differences are noted between the  $\dot{\alpha} > 0$  and  $\dot{\alpha} < 0$  distributions at  $\alpha = 12.5$  deg in Figures 7(b) and 7(h).

Finally, completing the cycle by progressing from  $\alpha = 12.5$  deg, to  $\alpha = 8.4$  in

Figure 7, very few changes take place with exception of dropping of suction levels and movement of the strake vortex toward the wing. This is essentially the reverse of pitch-up from  $8.4$  deg to  $12.5$  deg and reflects the nearly linear behavior of the aerodynamics in this incidence range as noted in the  $C_N$  and  $C_m$  results in Figures 5 and 6.

The second set of pressure and flow-visualization data is presented in Figure 8 for the high incidence range of  $22$  deg to  $50$  deg. The format is identical to that used in Figure 7 with the exception that the wing vortex vertical/lateral position locus is shown at Section 2 rather than the strake vortex loci at Sections 1, 2 and 3. Since this incidence range begins in burst vortex flow at  $22$  deg and ends in stalled flow at  $50$  deg, the strake vortex is burst most of the time as is evident in the smoke pattern sketches.

Beginning at  $\alpha = 22.1$  deg, in Figure 8(a) the pressure distributions are very similar to those shown in Figure 7(c) for pitch-up at  $\alpha = 22.3$  deg. The smoke patterns indicate a similar but more deteriorated flow-field in Figure 8(a) which is attributed to  $\dot{\alpha} = 0$ . Likewise comparisons of  $\alpha = 22.1$  deg in Figure 8(a) with results in Figure 7(g) at  $\alpha = 22.3$  deg, on pitch-down, shows the suction levels to be about the same. Less flow-field deterioration is noted in Figure 8(a) which is attributed to negative pitch rate in Figure 7(g).

Similar characteristics are seen at the next angle,  $\alpha = 25.2$  deg, in Figure 8(b). Vortex structures are similar with both moving inboard at Section 2 and burst moving forward. Suction levels are increasing, thereby increasing lift as shown by the dynamic  $C_N$  loop in Figure 5. More lift is being generated on the aft portion of the wing as indicated by less dynamic  $C_m$  pitch-up trends when compared with the steady characteristics.

At the mean angle,  $\alpha = 36.0$  deg, in Figure 8(c), the strake vortex burst suddenly moves forward of Section 2 and the wing vortex has moved away from the wing. Strake vortex bursting has reduced the increase in suction levels while wing vortex motion away from the wing has produced a net loss in suction. Divergence of the pressures along Sections 3 (trailing edge) and 4 (chordwise) are indicative of massive vortex bursting. This condition is close to the maximum dynamic levels of  $C_N$  and  $C_m$  as shown in Figures 5 and 6.

Further deterioration is evident at  $\alpha = 45.8$  deg, in Figure 8(d) where bursting has moved forward of Section 2 for the wing vortex and forward of Section 1 for the strake vortex. Suction levels have either stayed about the same or fallen significantly from the previous position. A separation that now appears between the bottom of the smoke pattern outline at the trailing edge and the wing surface is attributed to stalled flow. The falling suction levels agree with falling values of dynamic  $C_N$  and  $C_m$  in Figures 5 and 6.

At the peak angle,  $\alpha = 49.8$  deg, in Figure 8(e), the flow fields are completely stalled with exception of small regions of vortex flows on the strake. Suction levels

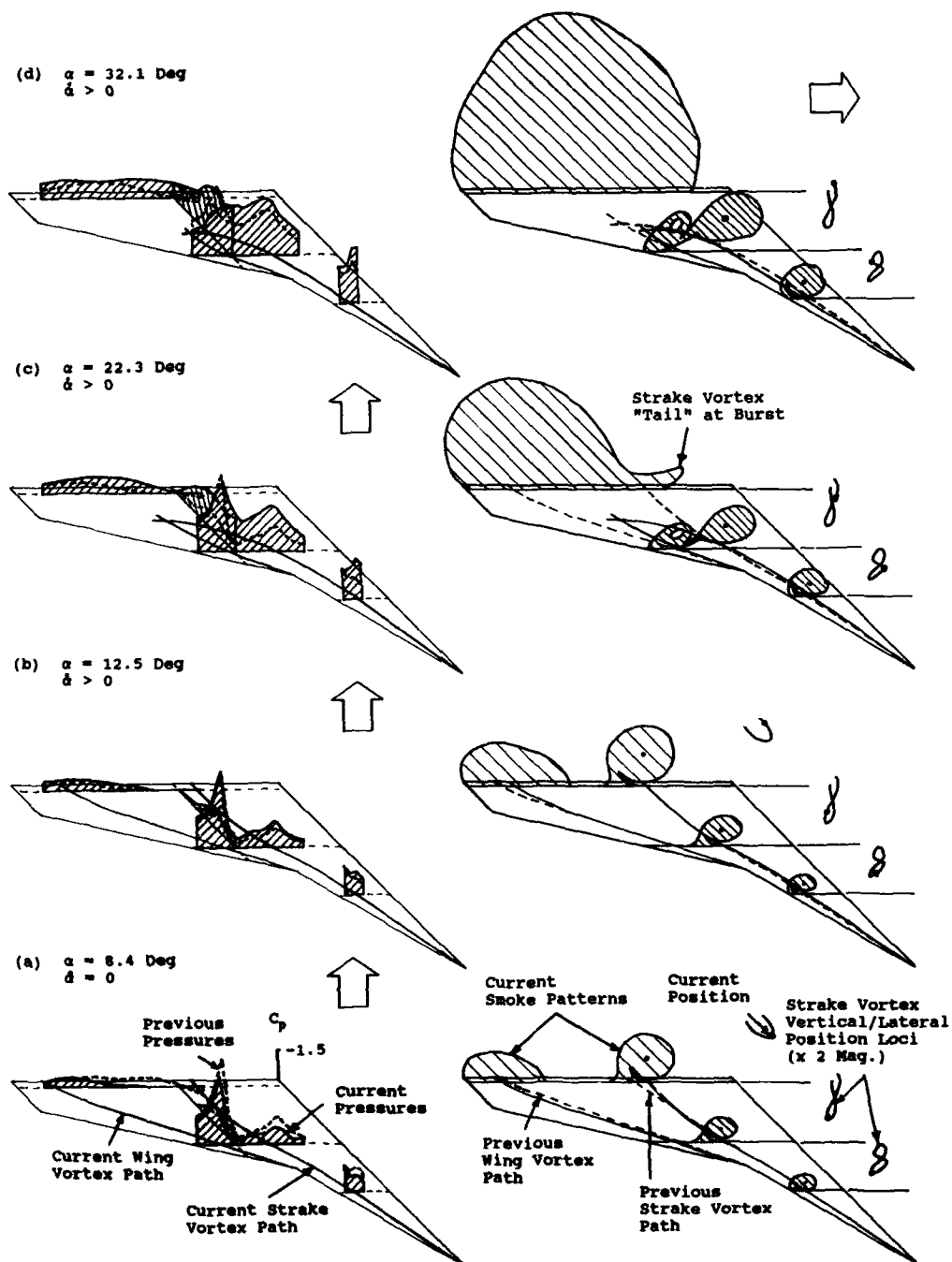
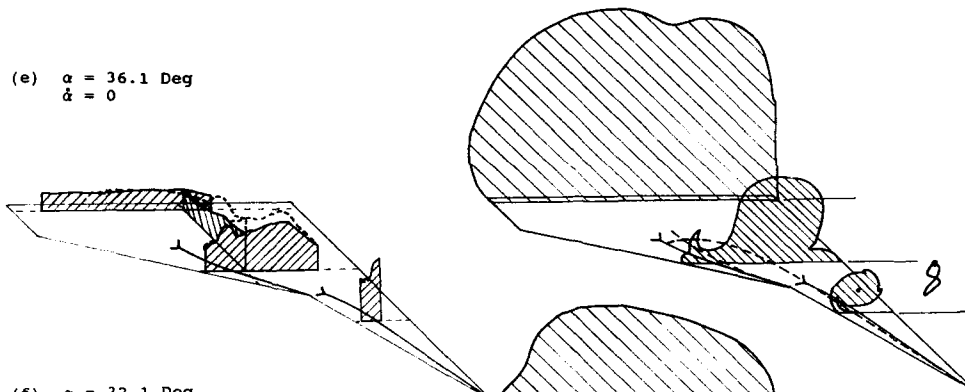
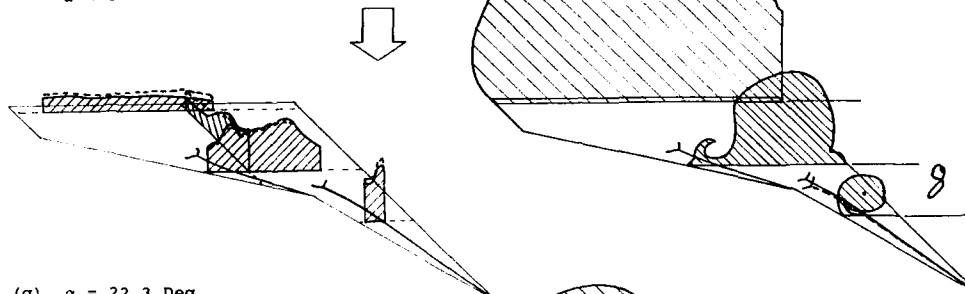


Figure 7 Time History Presentation of Pressure and Flow-Visualization Data at  $k = 0.15$  and Mid-Incidence,  $\alpha = 8$  Deg to 36 Deg

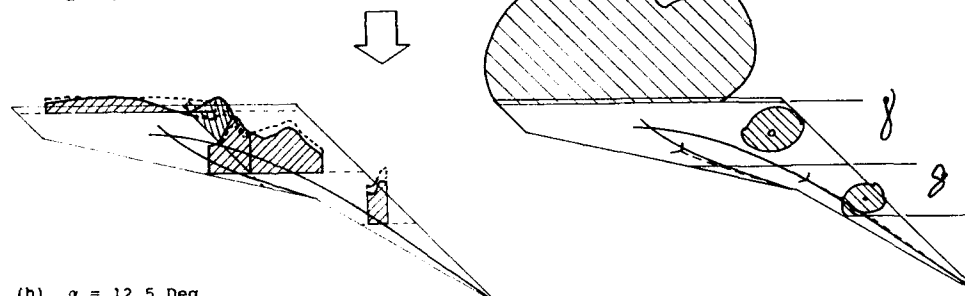
(e)  $\alpha = 36.1 \text{ Deg}$   
 $\delta = 0$



(f)  $\alpha = 32.1 \text{ Deg}$   
 $\delta < 0$



(g)  $\alpha = 22.3 \text{ Deg}$   
 $\delta < 0$



(h)  $\alpha = 12.5 \text{ Deg}$   
 $\delta < 0$

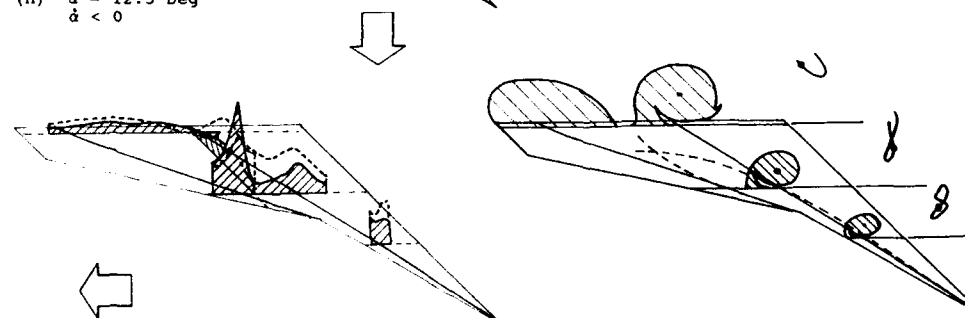


Figure 7 (Concluded)

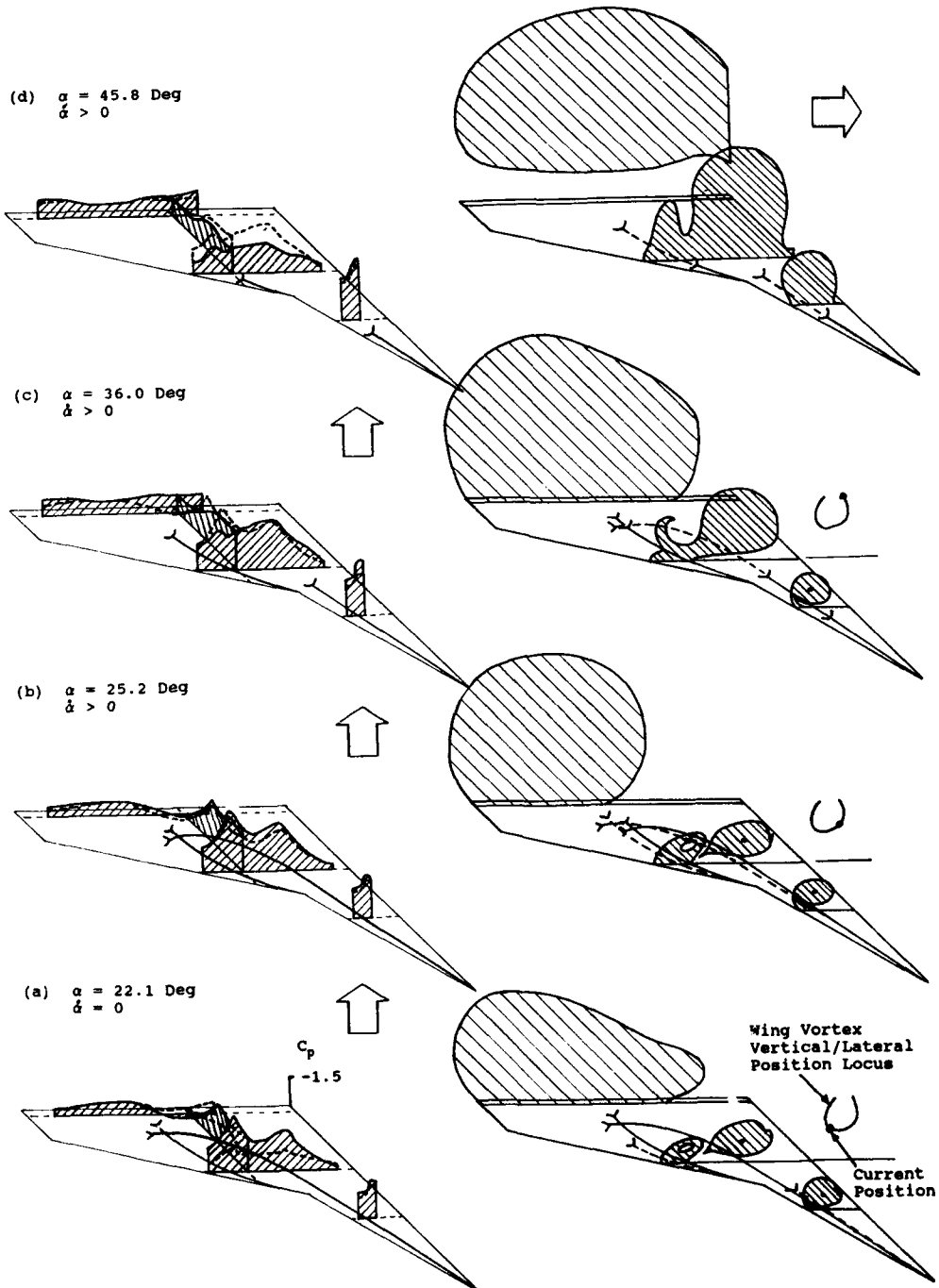
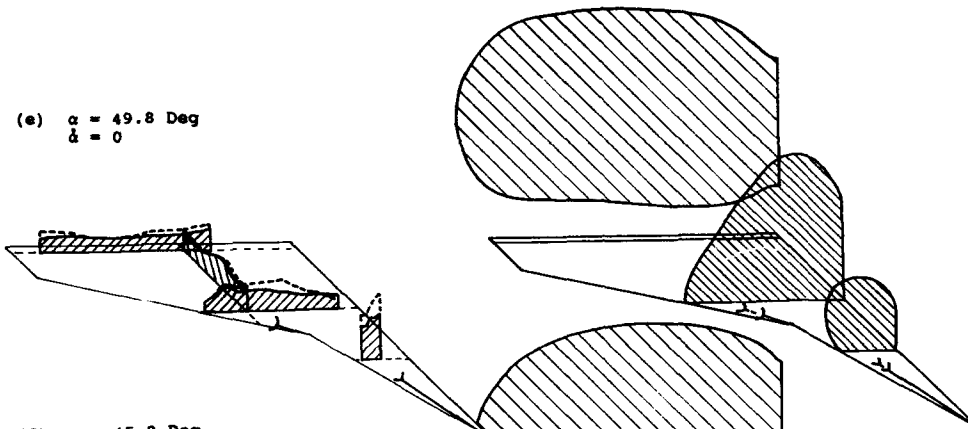


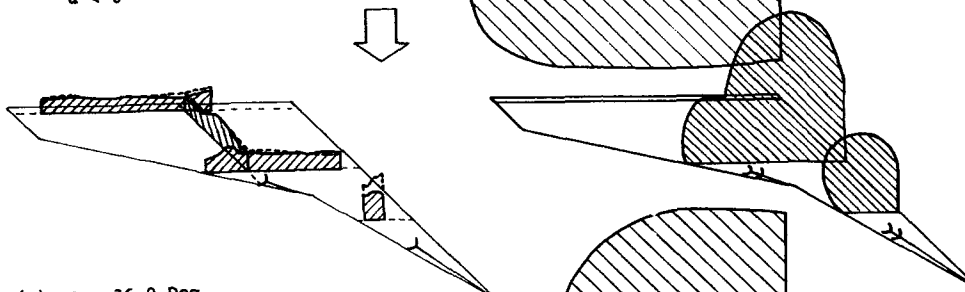
Figure 8 Time History Presentation of Pressure and Flow-Visualization Data at  $k = 0.15$  and High-Incidence,  $\alpha = 22$  Deg to 50 Deg



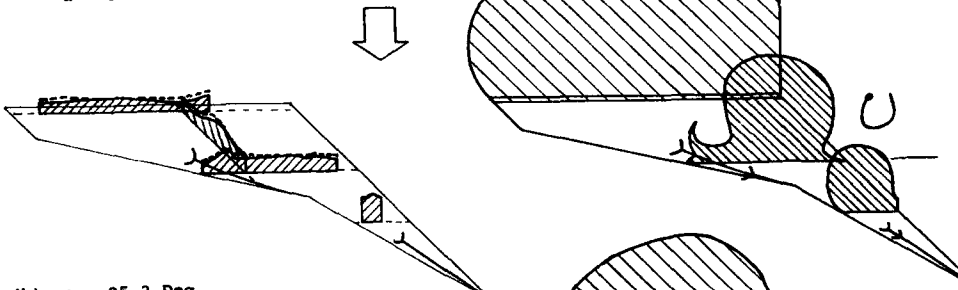
(e)  $\alpha = 49.8 \text{ Deg}$   
 $\dot{\alpha} = 0$



(f)  $\alpha = 45.8 \text{ Deg}$   
 $\dot{\alpha} < 0$



(g)  $\alpha = 36.0 \text{ Deg}$   
 $\dot{\alpha} < 0$



(h)  $\alpha = 25.2 \text{ Deg}$   
 $\dot{\alpha} < 0$

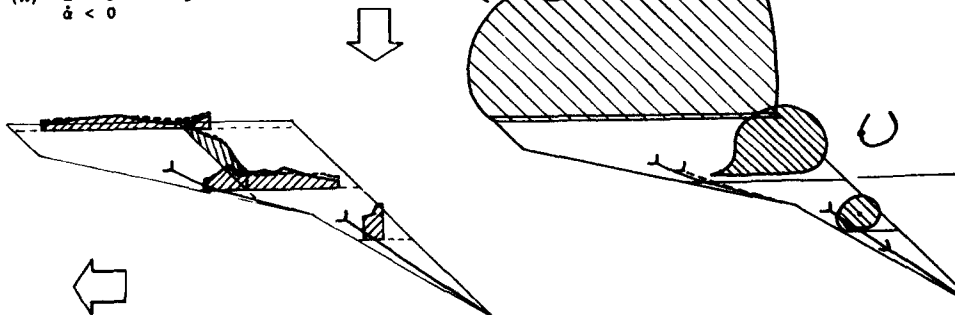


Figure 8 (Concluded)

have still fallen further and massive separation is evident in the smoke pattern outlines. The further reduction of  $C_N$  and  $C_m$  in Figures 5 and 6 reflect these characteristics.

On pitch-down at  $\alpha = 45.8$  deg, in Figure 8(f), the flow field characteristics and pressures show little change from the previous conditions at  $\alpha = 49.8$  deg, with exception of reduction of suction levels at Section 1. This reduction is a result of continued deterioration of the strake vortex with negative pitch rate and results in a slight  $C_m$  pitch-down. Comparisons between  $\dot{\alpha} < 0$  and  $\dot{\alpha} > 0$  for  $\alpha = 45.8$  deg show that a positive pitch rate results in much higher suction levels over the entire wing, especially on the strake, which lead to the higher dynamic  $C_N$  and  $C_m$  values seen in Figure 5 and 6 for pitch-up vs pitch-down.

At the mean angle,  $\alpha = 36.0$  deg, in Figure 8(g), again the flow-field characteristics and pressures are similar to those at the previous angle of  $45.8$  deg. A slight overall lowering of suction levels agrees with dynamic  $C_N$  and  $C_m$  trends in Figures 5 and 6. It appears, however, that the wing vortex burst point has moved aft of Section 2 but has not had much effect on pressures. Comparisons between  $\dot{\alpha} > 0$  and  $\dot{\alpha} < 0$  for  $36.0$  deg show an even more pronounced effect of positive and negative pitch rates. This is evident in the pressures, smoke pattern outlines and strake vortex positions.

At  $\alpha = 25.2$  deg in Figure 8(h), not much change has occurred since the previous angle of  $36.0$  deg which represents a stark example of the persistence of stalled flows. These characteristics are seen to be more similar to those at the peak angle of  $49.8$  deg than those at  $\alpha = 25.2$  deg in Figure 8(b). This condition also corresponds to the point of minimum dynamic  $C_N$  in Figure 5.

Continuing to the minimum angle  $\alpha = 22.1$  deg, the change is very pronounced from the previous condition at  $\alpha = 25.2$  deg. The strake vortex burst moved quickly aft of Section 2 and the wing vortex moved closer to the wing and increased strength. All suction levels increased and trailing edge divergence was reduced thus leading to the return of dynamic  $C_N$  and  $C_m$  values to near their static values. The reduction of negative pitch-rate to zero allowed the flow-fields to "catch-up" and re-establish the burst vortex flow characteristics at  $22.1$  deg.

In summary, with a new format for presenting unsteady pressure and flow-visualization data, it has been possible to more clearly relate the development of dynamic flow-field characteristics with force and moment data trends for the oscillating straked wing model. In the mid-incidence range of  $\alpha = 8$  deg to  $38$  deg, lag in vortex bursting on pitch-up or the persistence of vortex burst on pitch-down was shown to significantly affect the pressure distributions and hence, dynamic force and moment results. Vortex strength and position were also seen to have counteracting effects on pressures. In the high-incidence range of  $\alpha = 22$  deg to  $50$  deg, the persistence of burst vortex flows to angles beyond static stall was shown to be responsible for significant dynamic lift overshoot with pitch-up. Likewise, the even greater persistence of

stalled flows was shown to be responsible for significant dynamic lift undershoot with pitch-down. Burst vortex flow re-establishment from stalled flow took at least  $3/8$  of a cycle on pitch-down; but only a little more than  $1/8$  of a cycle was required for stall on pitch-up.

#### 4.0 ASYMMETRIC FLOW WITH SIDE-SLIP

The important flow transitions discussed above for symmetric flows are equally important for asymmetric flows with side-slip. The principle difference is that side-slip affects where and how these transitions occur and it causes them to occur differently on the windward and leeward wings. This is best understood by first examining the steady aerodynamics as was done above for symmetric flows. The unsteady aerodynamics are then developed by considering the effects of dynamic lag on the steady aerodynamics.

##### 4.1 Steady Aerodynamic Characteristics with Side-Slip

Measurements were made with the model placed at  $15$  deg side-slip by rotating the turn table as shown in Figure 1. Steady normal force,  $C_N$ , pitching moment,  $C_m$ , and rolling moment,  $C_l$ , variations with  $\alpha$  are shown in Figure 9 for side-slip of  $\beta = -5$  deg. These curves were constructed from mean values of forces and moments taken from low amplitude and/or low frequency unsteady data since no steady side-slip data were recording during the test. For reference, corresponding results for symmetric flow,  $\beta = 0$  deg, are also shown in Figure 9 as dashed lines.

Similar to the symmetric data, the "linear" range in Figure 9 is evident in the  $C_N$  and  $C_m$  data from  $-8$  deg to  $8$  deg. Beyond  $8$  deg the development of vortex flow is also seen in Figure 9 but the effect of side-slip is indicated by an earlier (1 deg) pitch-up in the  $C_m$  curve at about  $17$  deg. This is a result of earlier vortex bursting on the windward wing. Above vortex burst, the developments of  $C_N$  and  $C_m$  follow trends similar to those shown for symmetric flow in Figure 3. The lower levels for either quantity are due to earlier development of vortex bursting on the windward wing. It is also clear in the  $C_m$  curve that fully separated flow occurs earlier with side-slip.

The more important result shown in Figure 9 is rolling moment,  $C_l$ , variation with  $\alpha$ . For the sign conventions shown in Figure 2,  $\beta = -5$  deg places the nose right and positive  $C_l$  is for windward wing to roll up. Positive  $C_l$  is therefore stabilizing for negative  $\beta$  since it tends to reduce  $\beta$ . Thus, in the linear range up to  $\alpha = 8$  deg, the development of  $C_l$  with  $\beta$  is stabilizing as a result of the windward wing with lower sweep experiencing higher lift than the leeward wings as is normally expected in linear flow.

The development of vortex flows, beginning at about  $8$  deg to  $10$  deg, signals the onset of a destabilizing trend in  $C_l$ . Under these flow conditions the windward wing rolling moment increase with  $\alpha$  is less than that of the leeward wing. This is attributed to (1) a more rapid growth of the strake vortex induced lift inboard on the windward

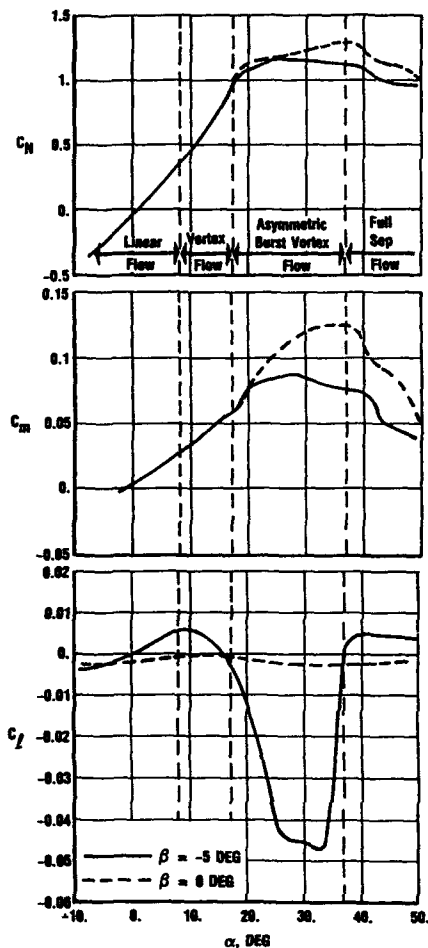


Figure 9 Steady Force and Moment Results for Asymmetric Flow

wing and (2) slower growth of the wing vortex induced lift outboard on the windward wing. The strake flow fields act like a simple delta wing in that lift on the windward strake increases with incidence over that on the leeward strake. The slower growth of wing vortex induced lift on the outboard windward wing is believed to be caused by displacement of that vortex through influence of a stronger strake vortex as indicated by pressure data in Reference 4.

The destabilizing trend in  $C_l$  that began with onset of vortex flows is greatly intensified with vortex bursting. This trend is consistent with highly swept delta wings where burst is initiated on the windward wing because of the lower sweep. Burst development on the windward wing precedes that on the leeward wing and, thus, maintains a destabilizing tendency to roll the leeward wing up. This downward slope continues until about 25 deg where it abruptly changes to a nearly flat "bottom" or "bucket". The occurrence of this "bucket" also

coincides with static  $C_{Nmax}$  and  $C_{mmax}$  as noted in the other curves shown in Figure 9. The pressure data in Reference 4 indicate that the windward wing is fully separated at about 25 deg.

Within the "bucket", the windward wing remains essentially unchanged from its fully separated condition and contributes very little to the development of  $C_N$ ,  $C_m$ , and  $C_l$  with  $\alpha$ . Since  $C_N$ ,  $C_m$ , and  $C_l$  are nearly constant over the  $\alpha$  range of the "bucket", about 25 deg to 33 deg, the development of vortex burst over the leeward wing apparently has little effect on lift. The destabilizing "bucket" is abruptly terminated starting at about 33 deg where the  $C_l$  curve becomes stabilizing at 37 deg. This is attributed to stalling of the leeward wing. The stabilizing level of  $C_l$  remains nearly constant from about 40 deg up to 90 deg as has been shown in other tests of the subject straked wing planform.

#### 4.2 Unsteady Aerodynamic Characteristics with Side-slip

The asymmetric unsteady pressures associated with the pitching straked wing model with side-slip and how they relate to dynamic rolling moments are presented in this section. These results were obtained with the model dynamically pitching at turntable positions of 5 deg and -5 deg relative to the freestream direction. Since the pressure instrumentation was located on the right wing, a side-slip of 5 deg (nose left) provided windward wing pressures and likewise leeward wing pressures were obtained for a side-slip of -5 deg (nose right). The unsteady pressure data documented in Reference 4 for side-slip did not include time-histories but only the first harmonic and, hence, do not reveal all of the non-linearities present in the asymmetric flow-fields in the manner shown in Figures 7 and 8. Much can be learned from these data, however, as will be shown in the following discussions. For sake of completeness and ease of reference, the unsteady non-linear curves for rolling moment,  $C_l$ , from Reference 8 are repeated here in Figure 10 for the two incidence ranges to be discussed in this section.

Rolling moment data are shown in Figure 10 for the mid-incidence range,  $\alpha = 8$  deg to 36 deg, which encloses both vortex burst and stalled flows on the windward and leeward wings. Results for the two frequencies,  $k = 0.09$  and  $0.15$ , exhibit very different dynamic  $C_l$  hysteresis loops as can be seen in the figure. In steady flow, burst occurs at 17 deg and stall at about 25 deg to 27 deg on the windward wing, where as these transitions occur at about 25 deg and 37 deg respectively on the leeward wing. The aerodynamic lag associated with asymmetric unsteady flows, shifts the angles at which these points occur in the same manner as occurs in symmetric flows. Thus, the "Figure 8" characteristics at  $k = 0.09$  in Figure 10 is an almost quasi-steady distortion with simple lag of the "bucket". Delay of burst development on the windward wing is indicated by the slower development of the destabilizing trend on pitch-up. It is also evident that the windward wing stalls at about  $\alpha_{max}$  as indicated by the depth of the dynamic "bucket". On pitch-down, the leeward wing rapidly stalls as indicated by the return to

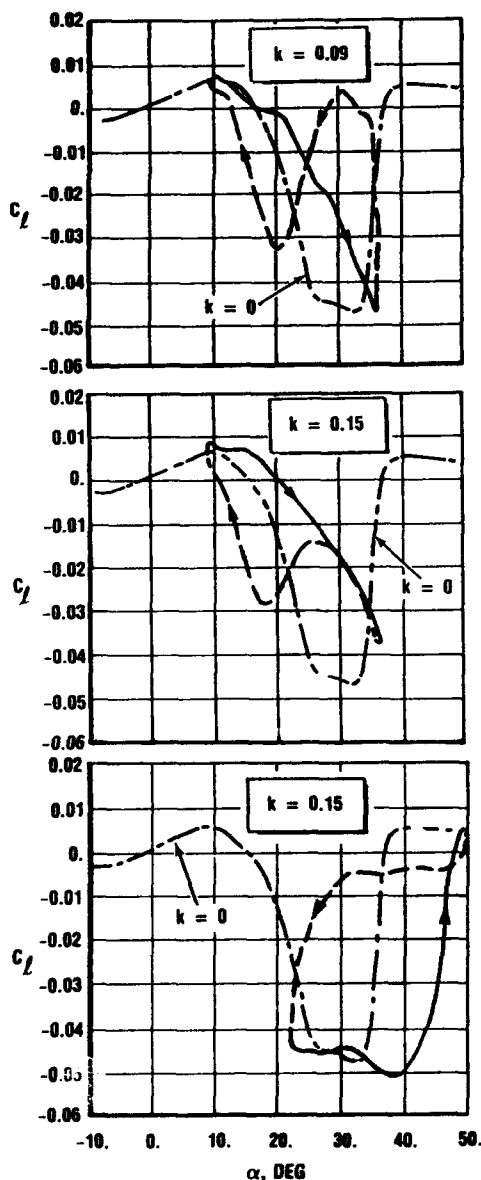


Figure 10 Unsteady Rolling Moment Results

stable values of  $C_l$  and remains so down to about 30 deg where it appears that burst vortex flow is being re-established on the leeward wing which drives  $C_l$  unstable. Another "bucket" is formed by burst vortex flow being re-established on the windward wing. This "bucket" is shallower and extends to lower angles, both as a result of aerodynamic lag. The dynamic mechanism of unbalance between windward and leeward wings on pitch-down is the same as in steady flow but is simply modified by the lag.

The dynamic  $C_l$  hysteresis loop in Figure 10 for  $k = 0.15$  is quite different from that for  $k = 0.09$ . This difference is attributed simply to the leeward wing not stalling at  $\alpha_{max}$  as a result of higher aerodynamic lag at the higher frequency. Justification for this hypothesis is based on the fact that  $C_l$  does not return to the stabilizing values at  $\alpha_{max}$  which is indicative of stall on both wings. Also, the dynamic  $C_l$  curve retraces the pitch-up curve on pitch-down to about 30 deg where it begins to depart and develops a dynamic "bucket" similar to that seen for  $k = 0.09$ . This case will be examined further with pressure data after first discussing the case for  $k = 0.09$  in Figure 10.

Unsteady first harmonic pressure data for oscillation from 8 deg to 36 deg with  $\beta = 5$  deg at  $k = 0.09$  are shown in Figure 11. Pressures are shown at all four sections and consist of the mean values,  $C_p$ , the in-phase pressures (or real part) divided by oscillation amplitude,  $C_p'$ , and the out-of-phase pressures (or imaginary part) divided by oscillation amplitude,  $C_p''$ . The unsteady first harmonic pressure,  $C_p(t)$ , is expressed as

$$\frac{C_p(t)}{\Delta\alpha} = (C_p' + iC_p'')e^{i2\pi ft}$$

where  $t$  is time in seconds and  $\Delta\alpha$  is the oscillation amplitude (1/2 peak-to-peak) in radians. The sign convention is  $C_p'$  positive at peak angle and  $C_p''$  positive at maximum positive pitch rate. Distributions are shown for the leeward and windward wings at  $\beta = 5$  deg as well as for  $\beta = 0$  deg. Symbol definitions are also shown but are kept consistent throughout the following discussions.

In Figure 11, it is clear that the rolling moments will be higher on the leeward wing as compared with the windward wing and the symmetric wing for  $\beta = 0$  deg. This is shown by the higher suction levels on the outboard part of the leeward wing which is attributed to delayed breakdown of the wing/stroke vortex system. This delay is a result of weakened coupling between the two vortex systems on the leeward wing caused by (1) a weaker stroke vortex as shown by stroke pressures at Section 1 and (2) a stronger but more outboard wing vortex as shown by higher suction at Section 2 ( $y/2b \approx 0.8$ ) and a more outboard "hump" at Section 3 ( $y/2b \approx 0.7$ ) corresponding to the wing vortex. The weaker stroke vortex is a result of higher sweep of the leeward stroke, 81 deg vs 76 deg, as is typical of simple delta wings. The stronger wing vortex is a result of a more stable vortex flow over a 45 deg swept leading edge as opposed to a 40 deg sweep. The higher swept outboard panel also maintains a greater separation between the wing and stroke vortices which was shown in the previous discussions of Figures 7 and 8 to be critical in the breakdown of this vortex system. Thus, the leeward wing sees a delayed breakdown, weaker stroke vortex induced suction and stronger and more outboard wing vortex induced suction all of which produce a higher rolling moment as compared with the windward wing and the symmetric wing for  $\beta = 0$  deg.

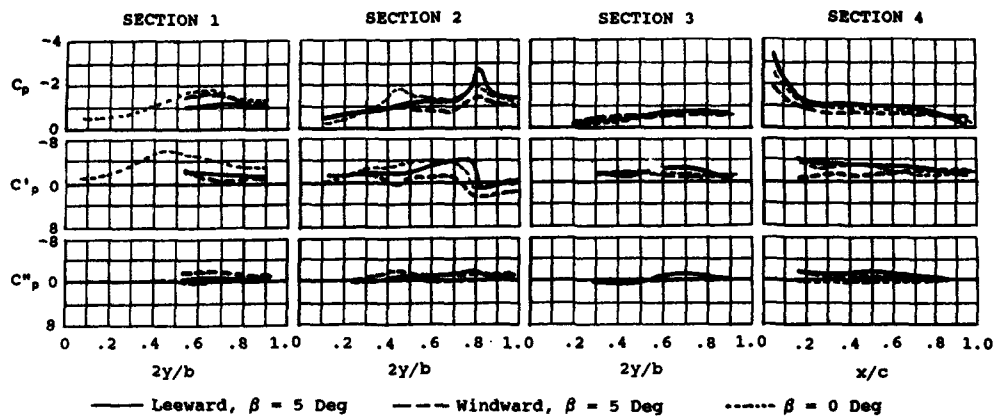


Figure 11 Asymmetric Unsteady First Harmonic Pressures for Incidence Range of 8 Deg to 36 Deg,  $k = 0.09$

The windward wing pressures in Figure 11 show the opposite characteristics. The strake vortex is stronger at Section 1 as it would be for a simple delta, but at Section 2 there is strong evidence of earlier flow deterioration through breakdown of the wing/strake vortex system. Flatter and lower pressure distributions at Sections 3 and 4 are indicative of nearly stalled flows characteristic of higher incidence ranges. With few exceptions, all suction level distributions on the windward wing are lower than those for  $\beta = 0$  deg. The wing vortex formed on the 35 deg swept leading edge is not as stable as that on the 45 deg sweep. This leads to an earlier breakdown of the entire windward wing vortex system and an earlier occurrence of stall as though the wing were placed at a higher incidence. This concept will be discussed further at a later point on this section.

At the higher frequency,  $k = 0.15$ , pressures for oscillation from 8 deg to 36 deg with  $\beta = 5$  deg are shown in Figure 12. This corresponds to the higher frequency case of  $C_l$  vs  $\alpha$  in Figure 10. On pitch-up, it was speculated in Reference 8 that vortex burst did not occur on the leeward wing.

However, the pressure data in Figure 12 are more indicative of vortex bursting on the leeward wing. It is now postulated that (1) the leeward and windward wings' vortex systems burst on pitch-up, (2) the windward wing stalled on pitch-down starting at about 30 deg, and (3) the leeward wing did not encounter stall as was pointed out in earlier discussions. The differences between leeward wing pressures in Figures 11 and 12 are very subtle and clouded by the integrating effect of the first harmonic, however, they do point in the direction of less deteriorated flows for the higher frequency.

The windward wing pressures in Figure 12 at  $k = 0.15$  as compared with Figure 11 at  $k = 0.09$  show slightly higher suction levels as indicative of encountering less stalled flow during the oscillations. Almost all levels are higher at the higher frequency on both the wing and strake but again details of time history effects are obscured by the first harmonic integration.

Next, the higher incidence case is considered for which pressure data are shown in Figure 13 for oscillation from 22 deg to 50 deg with  $\beta = 5$  deg and  $k = 0.15$ . The

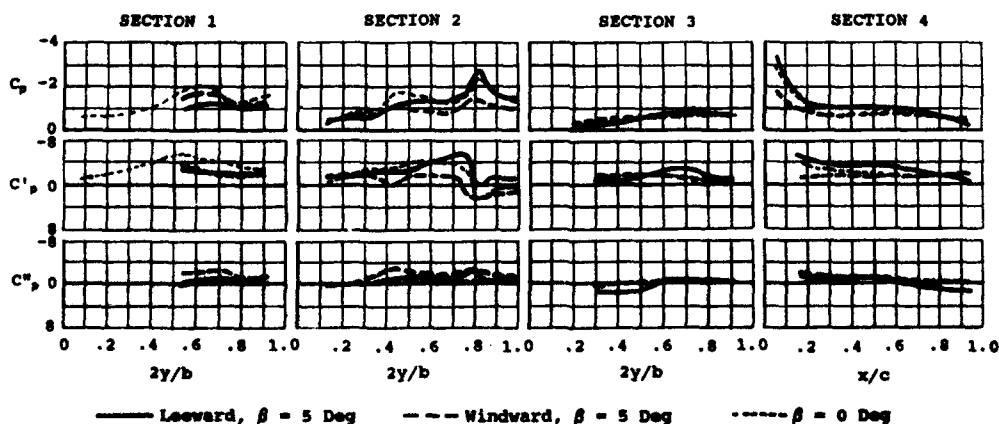


Figure 12 Asymmetric Unsteady First Harmonic Pressures for Incidence Range of 8 Deg to 36 Deg,  $k = 0.15$

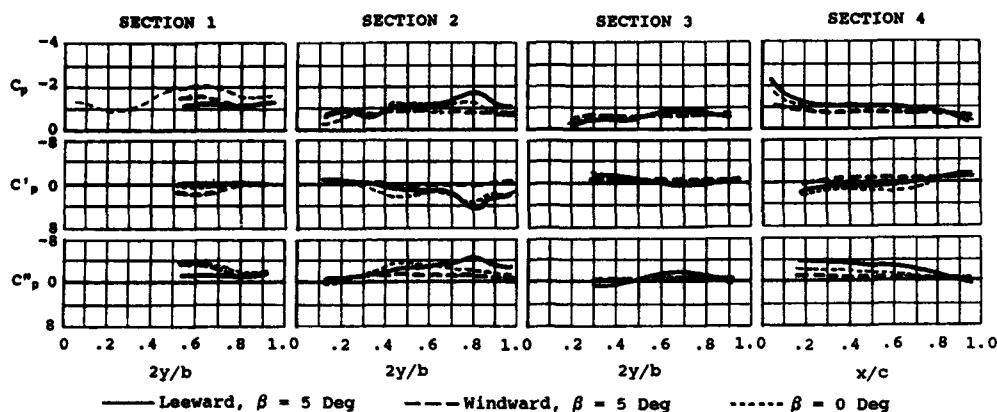


Figure 13 Asymmetric Unsteady First Harmonic Pressures for Incidence Range of 22 Deg to 50 Deg,  $k = 0.15$

same format is used as in Figures 11 and 12. This case also corresponds to the  $C_p$  vs  $\alpha$  results shown in Figure 10 at the higher incidence range. In this case, the rolling moments flip-flop between the maximum unstable condition in the "bucket" on pitch-up and slightly unstable condition on pitch-down. It is postulated for this case that the windward wing is stalled during the entire cycle and that the leeward wing (1) stalls at maximum incidence and remains so until minimum incidence where (2) it returns to burst vortex flow which is maintained up to maximum incidence. The windward wing pressures in Figure 13 are flat and very nearly the same level over the entire wing with exception of Section 1 on the strake. This characteristic is indicative of stalled flow during the cycle. The leeward wing pressures are more like those for  $\alpha = 0$  deg and are indicative of a combination of burst vortex and stalled flows during the cycle. This was shown in the discussions concerning Figure 8 in symmetric flow.

In all of the above discussions, references have been made to characteristics on the windward or leeward wings appearing more like characteristics at higher or lower incidence ranges respectively. These com-

parisons can be made directly with the pressure data and parallels drawn between symmetric and asymmetric flow-field characteristics. An example of such comparisons, Case 1, is shown in Figure 14 where leeward wing pressures from Figure 12 are compared with pressures from a symmetric case for oscillation at a lower incidence range from 7 deg to 31 deg. The idea that the leeward wing acts like it is at a lower incidence range is clearly supported by the comparison in Figure 14. With exception of the strake vortex pressures at Section 1 and inboard of Section 2, the two data sets agree quite well, especially for  $C_p$  and  $C'_p$ .

A second comparison in Figure 15, Case 2, shows the windward wing pressures from Figure 13 and those for  $\beta = 0$  deg and oscillation from 40 deg to 48 deg. The  $\beta = 0$  deg data are in fully separated flow during the entire cycle. The agreement of these pressures with windward wing pressures from Figure 13 verifies the postulation that for oscillation from 22 deg to 50 deg at  $\beta = 5$  deg, the windward wing is fully stalled.

A third comparison in Figure 16, Case 3, shows windward wing data from Figure 12 which covers vortex, burst vortex, and

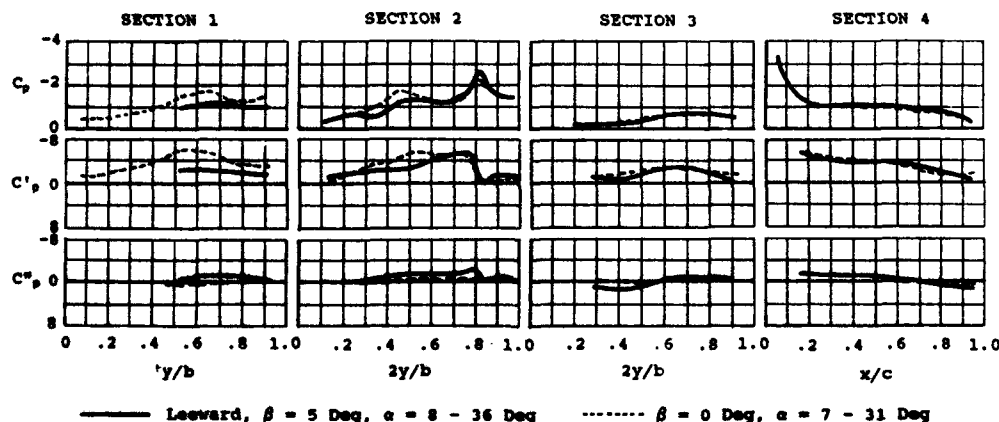


Figure 14 Correlation Between Asymmetric Pressures and "Equivalent" Symmetric Pressures,  $k = 0.15$ , Case 1

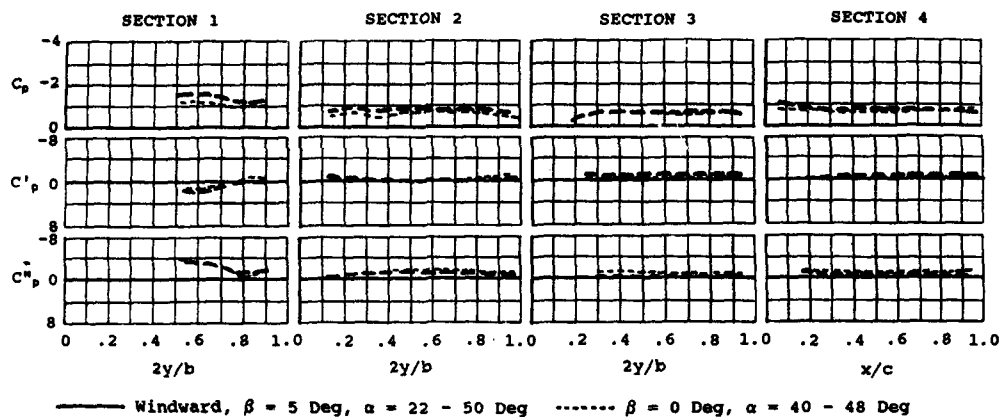


Figure 15 Correlation Between Asymmetric Pressures and "Equivalent" Symmetric Pressures,  $k = 0.15$ , Case 2

stalled flows during the oscillation from 8 deg to 36 deg. Since two flow transitions are covered in this case, no near match is possible in the existing symmetric data set of Reference 4. Bounding the problem, however, is possible as shown in Figure 16. An upper bound is posed by the pressures in Figure 12 for  $\beta = 0$  deg since vortex burst occurs later than for the windward wing and stall is not encountered. A lower bound is posed by the  $\beta = 0$  data from Figure 13 where the flow is either burst vortex or stalled. As can be seen, the windward wing data from Figure 12 generally fall near to or in-between the bounding data sets. Thus, even though the non-linear effects are integrated into the first harmonic, the pressure data resulting from traversing two flow transitions can be bounded by two pressure data sets that traverse each of the flow transitions separately.

In summary, unsteady first harmonic pressure data were used to establish flow-field conditions on the leeward and windward wings for the straked wing model pitching at a side-slip angle of 5 deg. In the low incidence range for pitching from 8 deg to 36 deg at  $k = 0.09$ , it was shown that the leeward wing experienced vortex, burst vortex, and stalled flows similar to those that would exist on the wing pitching over a lower incidence range in zero side-slip. At  $k = 0.15$ , the leeward wing did not experience stall which significantly altered the dynamic rolling moment characteristics. The windward wing was shown to encounter vortex, burst vortex and stalled flows at both frequencies and therefore did not contribute significantly to the rolling moment anomalies. In the high incidence range for pitching from 22 deg to 50 deg at  $k = 0.15$ , it was shown that the leeward wing flip-flopped between burst vortex and stalled flows which produced the flip-flop characteristics in rolling moment. The windward wing was stalled during the entire cycle.

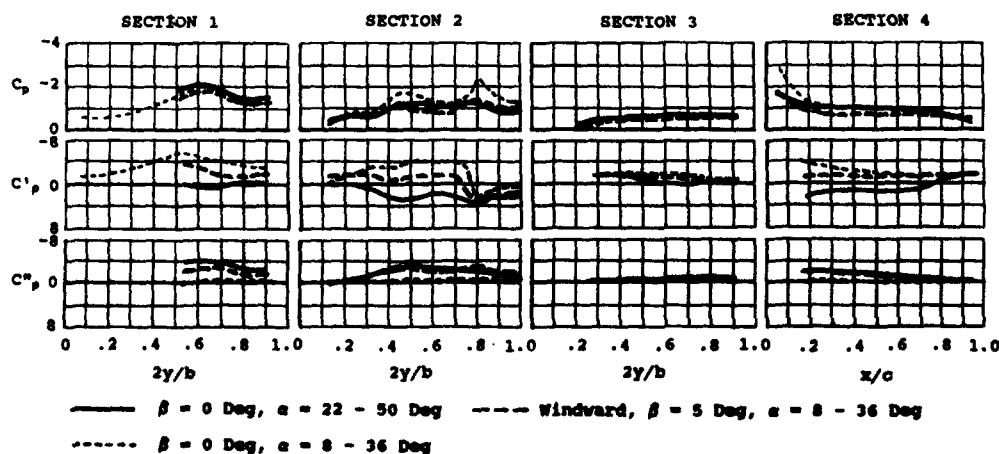


Figure 16 Correlation Between Asymmetric Pressures and "Equivalent" Symmetric Pressures,  $k = 0.15$ , Case 3

## 5.0 CONCLUSIONS

This paper has presented a discussion of unsteady pressure and flow-visualization results from the low speed wind tunnel test of an oscillating straked wing model. The model was oscillated in pitch in symmetric flow and in a yawed plane in asymmetric flow. The pressure and flow-visualization data were used to provide a better understanding of the phenomena observed in the aerodynamic characteristics. Particular emphasis was placed on the nature of dynamic vortex structure interplay with the forces and moments for both symmetric and asymmetric flows.

Discussions were based on four basic flow regimes identified in earlier references as (1) linear, (2) vortex, (3) burst vortex, and (4) fully separated or stalled flows. How these various regimes shifted as a result of dynamic and/or asymmetric effects was used to explain the observed trends in force and moment data.

By simultaneously presenting unsteady pressure and flow-visualization data, it was possible to relate the development of dynamic flow-field characteristics with force and moment data trends for the oscillating straked wing model. In the mid-incidence range of  $\alpha = 8$  deg to 36 deg, lag in vortex bursting on pitch-up or the persistence of vortex burst on pitch-down was shown to significantly affect the pressure distributions and hence, dynamic force and moment results. Vortex strength and position were also seen to have counteracting effects on pressures.

In the high-incidence range of  $\alpha = 22$  deg to 50 deg, the persistence of burst vortex flows to angles beyond static stall was shown to be responsible for significant dynamic lift overshoot with pitch-up. Likewise, the even greater persistence of stalled flows was shown to be responsible for significant dynamic lift undershoot with pitch-down. Burst vortex flow re-establishment from stalled flow took at least  $3/8$  of a cycle on pitch-down; but only a little more than  $1/8$  of a cycle was required for stall on pitch-up.

Unsteady first harmonic pressure data were used to establish flow-field conditions on the leeward and windward wings for the straked wing model pitching at a side-slip angle of 5 deg. In the low incidence range for pitching from 8 deg to 36 deg at  $k = 0.09$ , it was shown that the leeward wing experienced vortex, burst vortex, and stalled flows similar to those that would exist on the wing pitching over a lower incidence range in zero side-slip. At  $k = 0.15$ , the leeward wing did not experience stall which significantly altered the dynamic rolling moment characteristics. The windward wing was shown to encounter vortex, burst vortex and stalled flows at both frequencies and therefore contributed little to the rolling moment anomalies.

In the high incidence range for pitching from 22 deg to 50 deg at  $k = 0.15$ , it was shown that the leeward wing flip-flopped between burst vortex and stalled flows which produced the flip-flop characteristics in rolling moment. The windward wing was stalled during the entire cycle.

Equivalence was demonstrated between asymmetric and symmetric flow-fields. Leeward and windward wing characteristics were shown to be similar to symmetric characteristics at lower and higher incidence ranges, respectively. This similarity was valid as long as the respective wing in asymmetric flow encountered the same flow-transitions as did the symmetric wing case.

## REFERENCES

- Herbst, W. B.: "Future Fighter Technologies", *Journal of Aircraft*, Vol. 17, August 1980, pp. 561-566.
- Cunningham, A. M., Jr.: Invited Presentation, U.S. Government sponsored "Workshop on Supermaneuverability", Air Force Wright Research and Development Center, 5-7 June 1984.
- Lang, J. and Francis, M. S.: Unsteady Aerodynamics and Dynamic Aircraft Maneuverability", AGARD-CP-386, May 1985.
- Cunningham, A. M., Jr., den Boer, R. G., et al: Unsteady Low-Speed Wind Tunnel Test of a Straked Delta Wing, Oscillating in Pitch, AFWAL-TR-87-3098 (Parts I through VI), April 1988.
- den Boer, R. G. and Cunningham, A. M., Jr.: "Low Speed Unsteady Aerodynamics of a Pitching Straked Wing at High Incidence - Part I: Test Program", *Journal of Aircraft*, Vol. 27, January 1990, pp. 23-30.
- Cunningham, A. M., Jr. and den Boer, R. G.: "Low Speed Unsteady Aerodynamics of a Pitching Straked Wing at High Incidence - Part II: Harmonic Analysis", *Journal of Aircraft*, Vol. 27, January 1990, pp. 31-41.
- Cunningham, A. M., Jr.: "A Critique of the Experimental Aerodynamic Data Base for an Oscillating Straked Wing at High Angles", Proceedings Fourth Symposium on Numerical and Physical Aspects of Aerodynamic Flows, California State University, Long Beach, California, 16-19 January 1989.
- Cunningham, A. M. Jr., and den Boer, R. G.: "Steady and Unsteady Aerodynamics of a Pitching Straked Wing Model at High Angles of Attack", presented at the AGARD FDP Symposium "Vortex Flow Aerodynamics", Scheveningen, The Netherlands, 1-4 October 1990.
- Cunningham, A. M., Jr. and Bushlow, T.: "Steady and Unsteady Force Testing of Fighter Aircraft Models in a Water Tunnel", AIAA Paper No. 90-2815, (1990).



## MEASUREMENT OF DERIVATIVES DUE TO ACCELERATION IN HEAVE AND SIDESLIP

by  
C.O. O'Leary, B. Weir and J.M. Walker  
Aerodynamics Department  
Royal Aerospace Establishment  
Bedford MK41 6AE, UK

## SUMMARY

Derivatives due to acceleration in heave and sideslip, the  $\dot{\alpha}$  and  $\dot{\beta}$  derivatives, have been measured for the two RAE High Incidence Research Models, HIRM 1 and HIRM 2. Dynamic measurements were also made of the 'static' derivatives due to  $\alpha$  and  $\beta$ .

The paper describes the design of a new oscillatory rig, lightweight models and tests in a low speed wind tunnel. Tests were made over a range of frequencies and model configurations.

Results showed that, at high angle-of-attack, derivatives due to acceleration in sideslip, in particular, could be large and varied significantly with frequency of oscillation. Effects of model configuration are also presented. There was good correlation between  $C_{m\dot{\alpha}}$  and measurements of  $(C_{mq} + C_{m\dot{\alpha}})$  and  $C_{mq}$  from other rigs. Dynamic effects on derivatives due to sideslip angle,  $C_{n\dot{\beta}}$  and  $C_{l\dot{\beta}}$  were significant.

## LIST OF SYMBOLS

b	wing span, m
$\bar{c}$	aerodynamic mean chord, m
$C_l$	rolling moment coefficient rolling moment/ $qSb$
$C_m$	pitching moment coefficient pitching moment/ $qS\bar{c}$
$C_n$	yawing moment coefficient yawing moment/ $qSb$
$C_N$	normal force coefficient normal force/ $qS$
q	dynamic pressure, $N/m^2$
q	rate of pitch, rad/s
r	rate of yaw, rad/s
V	wind speed, m/s
$\alpha$	angle-of-attack, rad or deg
$\beta$	angle-of-sideslip, rad or deg
$\delta_f$	flap angle, deg
$\eta_c$	foreplane angle, deg

$\eta_c$	tailplane angle, deg
$\omega$	circular frequency, rad/s
$\Omega_c$	frequency parameter for heave tests, $\omega\bar{c}/2V$
$\Omega_b$	frequency parameter for sideslip tests, $\omega b/2V$

## Derivatives:

$C_{l\beta}$	$\partial C_l / \partial \beta$
$C_{m\alpha}$	$\partial C_m / \partial \alpha$
$C_{n\beta}$	$\partial C_n / \partial \beta$
$C_{N\alpha}$	$\partial C_N / \partial \alpha$
$C_{l\dot{\beta}}$	$\partial C_l / \partial (\dot{\beta}b/2V)$
$C_{m\dot{\alpha}}$	$\partial C_m / \partial (\dot{\alpha}\bar{c}/2V)$
$C_{n\dot{\beta}}$	$\partial C_n / \partial (\dot{\beta}b/2V)$
$C_{N\dot{\alpha}}$	$\partial C_N / \partial (\dot{\alpha}\bar{c}/2V)$
$C_{Nq}$	$\partial C_N / \partial (q\bar{c}/2V)$
$C_{mq}$	$\partial C_m / \partial (q\bar{c}/2V)$
$C_{nr}$	$\partial C_n / \partial (rb/2V)$
$C_{lr}$	$\partial C_l / \partial (rb/2V)$

## Abbreviations:

ADR	Acceleration Derivative Rig
FSR	Flexible Sting Rig
WA	Whirling Arm

## 1 INTRODUCTION

Up to the early 1950's it had generally been considered that derivatives due to acceleration in heave and sideslip, ie rate of change of angle-of-attack ( $\dot{\alpha}$ ) and rate-of-change of sideslip ( $\dot{\beta}$ ), were not of great significance in determining motion characteristics as compared with the corresponding derivatives due to pitch and yaw rates (q and r), an exception being the downwash lag effect on pitching moment ( $C_{m\dot{\alpha}}$ ) on tailed aircraft. With the advent

of swept and delta wings it became apparent that the  $\dot{\beta}$  derivatives in particular were significant in the prediction of lateral-directional stability characteristics at high angle-of-attack. Attempts were made to measure  $\dot{\beta}$  derivatives in wind tunnels with some success<sup>1,2,3</sup>, but these early innovative tests in the 1950's were not continued because of the belief that future combat aircraft would be stand-off missile launchers with no requirement for manoeuvring at high angle-of-attack. In later years there was renewed interest in  $\dot{\beta}$  derivatives<sup>4,5</sup> and it was concluded<sup>6</sup> that for swept and delta wing aircraft at high angle-of-attack the  $\dot{\beta}$  derivatives were large and significant. Since it is not possible to separate the effects of yaw rate and sideslip rate ( $r$  and  $\beta$ ) in conventional rotary forced-oscillation tests, some mathematical models use the combined derivatives such as  $(C_{nr} - C_{n\dot{\beta}} \cos \alpha)$  and these usually give reasonable agreement between actual and predicted flight characteristics<sup>6</sup>. However, this approximation may not be appropriate in all cases. In Ref 5 it is stated that the "use of rotary forced oscillation data to represent derivatives due to pure angular rates is erroneous at high angles-of-attack". While this may be a rather sweeping statement, since  $\dot{\beta}$  effects would also be dependent on manoeuvre and configuration, there is an obvious need to determine  $\dot{\alpha}$  and  $\dot{\beta}$  derivatives to improve the prediction of aircraft flight characteristics. It may be possible to calculate approximate values using flow-field-lag theory<sup>7</sup> but reliability is questionable. A small-amplitude oscillatory rig is an obvious experimental method.

At RAE Bedford a multi-degree-of-freedom oscillatory rig or Flexible Sting Rig<sup>7</sup> (FSR) has been developed and operated over many years. Rotary derivatives are routinely measured and although models are oscillated in heave and sideslip, derivatives due to  $\dot{\alpha}$  and  $\dot{\beta}$  are not accurately determined due to masking by inertial effects from the conventional, rather heavy, wind-tunnel models tested on the rig. However, with the development of new model construction techniques using strong, lightweight materials, it became possible to make combat aircraft models of span 1-1.5 m, weighing less than 6 kg but able to sustain a normal force of 1000 N. Since the oscillation frequency could not be varied on the existing oscillatory rig, (which was anyway unsuitable for testing lightweight models), a new inexorable rig was designed for the measurement of derivatives due to acceleration in heave and sideslip.

This paper describes the design of the rig, balance and models, and the initial tests made on two representative combat aircraft models. Results are

presented on the effects of frequency and configuration and are correlated with data from other sources.

## 2 DESIGN CONSIDERATIONS

In designing the rig there were two main objectives:

1. For optimum accuracy of measurement it was necessary to maximise the ratio of aerodynamic to inertial forces acting on the balance.
2. To allow tests over a range of frequency parameter, the rig required a support structure of high rigidity. The active components of the rig also needed to be of high stiffness/weight ratio so that the lowest natural frequency of the rig was significantly higher than the maximum oscillation frequency.

The first objective could only be attained by use of purpose-built light models. Conventional wind-tunnel models were unsuitable. Fortunately, light models of the HIRM 1 and HIRM 2, had been built for tests on a Whirling Arm (WA) facility. These models have wing spans of approximately 1.2 m and a mass of only 6 kg, compared with 60 kg for the same size conventional models. Naturally, strength of the model was limited by the construction method and materials used, but for low speed tests the normal force limit of 1000 N was sufficient. The model was designed for sting mounting with accommodation for a strain gauge balance, which suited the present application.

A rigid support structure in the form of twin quadrants (Fig 1) is a feature of the 13ft x 9ft Low Speed Wind Tunnel at RAE Bedford and suited the requirements of the present rig. Design of the sting and balance, the oscillating mechanism and the choice of power source required most consideration.

Existing strain gauge balances were not sufficiently sensitive for measurement of model loads at the relatively low wind speeds envisaged ( $\approx 30$  m/s). The application called for a light, sensitive five-component balance (axial force excluded). The requirement for the sting was for low mass and high stiffness to minimise deflection under inertial and aerodynamic loading.

To obtain the required amplitudes of angle-of-attack and sideslip ( $\pm 2^\circ$ ) the specification for amplitude and frequency of motion was  $\pm 50$  mm at 4 Hz and  $\pm 30$  mm at 6 Hz. The test angle-of-attack range was specified as  $0^\circ$  to  $40^\circ$ . It became apparent that the most practicable method of satisfying these requirements was to mount a rotary power source on the sting carriage and mechanically convert the rotary motion into linear oscillatory motion. The most appropriate, and available, power source was a hydraulic motor, since it was relatively compact and the pump could be accommodated outside the wind-tunnel working section.

A description of the Acceleration Derivative Rig (ADR), resulting from the above requirements, is given in the following section.

### 3 DESCRIPTION OF RIG AND DATA ACQUISITION SYSTEM

The main component of the rig, shown in Figs 1 and 2, is a model support sting which can be oscillated in heave or sideslip. Forces acting on the model are measured by a strain gauge balance which is integral to the sting. The flared downstream end of the sting is mounted on a swinging arm assembly which converts a rotational shaft drive to translational harmonic motion using a 'scotch yoke' slider-in-a-slot mechanism shown in Fig 2. Amplitude of the motion is varied by adjusting the throw of the slider within a limit of  $\pm 50$  mm. The slot is aligned in the horizontal plane for heave motion and in the vertical plane for sideslipping motion. Change of alignment is accomplished by rotating the whole swinging arm assembly through  $90^\circ$ . The sleeve mounting for the swinging arm fits over the shaft housing and is bolted to the housing in either of the two positions. The shaft is driven by a hydraulic motor whose speed is controlled by a servo valve. Maximum oscillation frequencies are 4 Hz at an amplitude of 50 mm and 6 Hz at 30 mm amplitude. A hydraulic power pack, situated outside the working section of the tunnel, supplies the motor with fluid at 1500 psi pressure via a rigid pipe and swivel joint linkage as shown in Fig 1. The whole assembly is mounted on a carriage which is traversed along the twin support quadrants to vary model angle-of-attack. For the current tests angle-of-attack was limited to  $42^\circ$ .

Model motion is measured with an accelerometer in the model, the sensitive axis being aligned in the appropriate direction for the test. The signal is also used to cancel outputs of the strain gauge balance due to inertial loading.

The data acquisition system is similar to that used for FSR tests<sup>7</sup>. Strain gauge balance and accelerometer signals are amplified and filtered using matched 20 Hz filters. In addition, phase lags are introduced in the strain gauge signals so as to match the accelerometer to better than  $0.2^\circ$  over the frequency range of the tests. Interactions are eliminated within a signal mixing unit. After conversion to digital form the in-phase and in-quadrature components of the signals are determined using a discrete Fourier transform and the components are normalised with respect to the reference accelerometer signal.

### 4 DESCRIPTION OF MODELS

General arrangements of HIRM 1 and HIRM 2 are shown in Figs 3 and 4 respectively. HIRM 1 is a three-surface configuration with a wing of supercritical section. The wing leading edge is swept at  $42^\circ$  and drooped at  $20^\circ$  for these high angle-of-attack tests. HIRM 2 is typical of a delta-canard agile fighter with a wing

leading edge sweep of  $58^\circ$ . Flaperons shown were set at zero for these tests. Both models have a rectangular section fuselage with rounded corners which blends into a circular section nose forward of the foreplanes. Principal dimensions and moment reference centres are given in Figs 3 and 4.

The models were manufactured from lightweight materials, principally a close-cell foam with an external skin consisting of a fibre-glass 'scrim' of thickness varying between 0.2 mm and 0.4 mm. The balance housing is a thin-walled aluminium tube. Control surface settings are discretely adjustable. Each model weighs less than 6 kg.

### 5 METHOD OF TEST

Before testing in the wind tunnel, the accelerometer was calibrated dynamically against a master instrument on a platform driven by an electro-magnetic vibrator. The calibration factor was checked over a range of frequencies and amplitudes. The strain gauge balance was calibrated by static loading in the usual way and first order balance interactions were removed.

With the model fitted to the balance, signals due to inertial loading were cancelled, wind off, at the required test frequencies and amplitudes using the accelerometer tare controls on the mixing unit. For the actual tests, wind-on data was further corrected by subtracting residual wind-off signals at the same frequency and amplitude. Maximum angular deflection of the model due to sting bending was  $0.2^\circ$  at 4 Hz,  $\pm 50$  mm amplitude.

Amplitude of oscillation was set manually by adjusting the throw on the slider, and frequency was set by adjusting the speed of the hydraulic motor to the required value.

HIRM 1 and HIRM 2 were both tested in the heaving and sideslipping modes for a range of frequencies, amplitudes and model configurations. However, most of the results presented in this paper are limited to three frequencies at maximum amplitude. The lowest heave and sideslip frequency parameters were similar to those of the short period and dutch roll oscillations of a typical combat aircraft. Wind speeds, determined by strength limitations of the rig and models, were 25 m/s for the heave tests and 30 m/s for sideslipping tests. Reynolds number, based on aerodynamic mean chord, was approximately one million. Transition trips were not used on either model. The normalised in-phase and in-quadrature components of the signals were converted to derivatives, in body axes, using the appropriate calibration factors and frequencies as shown in the Appendix. Although all five balance signals were recorded for both heaving and sideslipping tests, results are presented only for normal force and pitching moment in the heaving mode, and yawing moment and rolling moment in the sideslipping mode. Data for cross coupling derivatives have not, as yet, been analysed.

Since the results were to be correlated with results from tests with the FSR no attempt was made to include the still air damping, or 'virtual inertia', in the measurements by shrouding the model for wind-off tests. This may be included in future tests.

## 6 RESULTS AND DISCUSSION

### 6.1 Effects of frequency

Effects of frequency on the normal force and pitching moment derivatives due to  $\dot{\alpha}$ ,  $C_{N\dot{\alpha}}$  and  $C_{M\dot{\alpha}}$  are shown in Fig 5 for HIRM 1.

Results are presented for frequencies of 2 Hz, 3 Hz and 4 Hz giving frequency parameters,  $\Omega_c (= \omega/2V)$  of 0.097, 0.145 and 0.194. Amplitude of oscillation was  $\pm 50$  mm. In terms of perturbation in angle-of-attack, the amplitudes were  $\pm 1.5^\circ$ ,  $\pm 2.2^\circ$  and  $\pm 2.9^\circ$  respectively.

At angles-of-attack up to  $16^\circ$  both the  $\dot{\alpha}$  derivatives are small for all frequencies but at higher angles-of-attack the effect of frequency is significant. For  $\Omega_c = 0.097$  there are significant excursions from zero which are progressively diminished as frequency increases to  $\Omega_c = 0.145$  and  $0.194$ . Previous tests<sup>2</sup> have shown that flow separates on part of the wing surface at  $\alpha \approx 17^\circ$  and the effect of the transition phase to fully stalled flow is evident on both derivatives for  $17^\circ < \alpha < 25^\circ$ . There are also increases in magnitude at the highest angles-of-attack tested. The magnitude of these derivatives depends on the lag in the development of lift on the foreplane, wing and tailplane as angle-of-attack varies and  $C_{M\dot{\alpha}}$ , in particular, will also be influenced by the lag in downwash at the tail. As shown in Fig 5, these effects are reduced as frequency is increased.

Effects on the longitudinal 'static' derivatives,  $C_{N\alpha}$  and  $C_{M\alpha}$ , are also shown in Fig 5. Increasing frequency causes some reduction in  $C_{N\alpha}$  and a positive shift in  $C_{M\alpha}$ . Again, sharp changes in magnitude for  $16^\circ < \alpha < 20^\circ$  diminish as frequency increases.

Effects of frequency on the lateral derivatives  $C_{N\dot{\beta}}$ ,  $C_{Y\dot{\beta}}$ ,  $C_{N\beta}$  and  $C_{Y\beta}$  for the canard-configured HIRM 2 are shown in Fig 6. As for the heave tests, oscillation amplitude was 50 mm and results are presented for frequency parameters  $\Omega_b (= \omega/2V)$  of 0.233, 0.349 and 0.465. Corresponding angle-of-sideslip amplitudes were  $\pm 1.5^\circ$ ,  $\pm 2.2^\circ$  and  $\pm 2.9^\circ$ .

Up to  $\alpha = 25^\circ$  the  $\dot{\beta}$  derivatives are relatively small with little frequency effect. For  $\Omega_b = 0.233$  there are then rapid increases in both derivatives but increases are progressively less at the higher frequencies. It is probable that there are two main contributions to these derivatives: firstly, there is a lag in the

vortex flow over the wings due to  $\dot{\beta}$  and secondly, there is a lag of sidewash at the fin. It is probable that the former is the major contributor to  $C_{N\dot{\beta}}$  while the latter has most effect on  $C_{Y\dot{\beta}}$ . The effects of configuration will be addressed more fully in a later section. It is again apparent that, as for the  $\dot{\alpha}$  derivatives, increase in frequency diminishes the effects of  $\dot{\beta}$ , as found in previous work<sup>2</sup> at similar frequency parameters.

Effects of frequency on the directional and lateral 'static' derivatives  $C_{N\beta}$  and  $C_{Y\beta}$  for HIRM 2 are also significant (Fig 6). Up to  $\alpha \approx 30^\circ$  directional stability  $C_{N\beta}$  is reduced by increasing frequency, approximately 40% reduction between values for highest and lowest frequencies at  $\alpha = 0^\circ$ . For  $32^\circ < \alpha < 38^\circ$  the negative excursion in  $C_{N\beta}$  is greater at low frequency. When the model was tested with the fin off (not presented) there was negligible frequency effect on  $C_{N\beta}$  at low  $\alpha$ , indicating that increasing frequency reduces fin effectiveness. Early NASA tests<sup>2</sup> on a  $60^\circ$  sweep delta model showed that  $C_{N\beta}$  was at a maximum for  $\Omega_b = 0.12$ . The lateral stability derivative  $C_{Y\beta}$  is not affected by frequency at low angle-of-attack but for  $\alpha > 28^\circ$  there is a much greater loss in stability (more positive) at lower frequency. Similar effects were noted in the work of Ref 2.

The effect of amplitude at a common frequency is shown in Fig 7, for the derivatives  $C_{M\dot{\alpha}}$  (HIRM 1),  $C_{N\dot{\alpha}}$  and  $C_{Y\dot{\beta}}$  (HIRM 2). Results are shown for amplitudes of 30 mm ( $\delta\alpha = \pm 1.7^\circ$ ) and 50 mm ( $\delta\alpha = \pm 2.9^\circ$ ) at  $\Omega_c = 0.194$  for  $C_{M\dot{\alpha}}$  and  $\Omega_b = 0.465$  for the lateral derivatives. In each case the effect of amplitude is small. For amplitudes less than 30 mm measurement accuracy was degraded. Except for Fig 7, all results presented in the paper relate to 50 mm amplitude.

### 6.2 Effects of configuration

#### 6.2.1 Effects of foreplanes on $\dot{\alpha}$ derivatives for HIRM 2

The effect of the presence of foreplanes on  $C_{N\dot{\alpha}}$  and  $C_{M\dot{\alpha}}$  is shown in Fig 8 for  $\Omega_c = 0.14$ . For angles-of-attack up to  $\alpha = 28^\circ$ ,  $C_{N\dot{\alpha}}$  is small and negative with and without foreplanes, but for  $28^\circ < \alpha < 42^\circ$  the derivative is relatively large and positive, with some reduction due to the presence of foreplanes. With foreplanes on,  $C_{M\dot{\alpha}}$  is positive at low  $\alpha$  (as for HIRM 1, Fig 5) but for  $\alpha > 28^\circ$ , when  $C_{N\dot{\alpha}}$  becomes large, there is a significant shift to negative values which is increased by the removal of foreplanes. Also noticeable is a positive excursion in

$C_{m\dot{\alpha}}$  at  $\alpha = 19^\circ$  which is only present with foreplanes on. Overall, foreplanes tend to reduce  $\dot{\alpha}$  effects on HIRM 2.

#### 6.2.2 Effect of foreplanes on $\dot{\beta}$ derivatives for HIRM 2

The effect of foreplanes on  $C_{n\dot{\beta}}$  and  $C_{l\dot{\beta}}$  is shown in Fig 9 for  $\Omega_b = 0.233$ . Up to  $\alpha = 25^\circ$   $C_{n\dot{\beta}}$  is constant at about 0.1 for both configurations but increases rapidly with  $\alpha$  to reach a peak of 0.8, foreplanes on,  $\alpha = 36^\circ$ . With foreplanes off there is a substantial increase in  $C_{n\dot{\beta}}$  for  $\alpha > 16^\circ$ . Trends in the variation of  $C_{l\dot{\beta}}$  are similar with a rapid increase in magnitude as  $\alpha$  increases beyond  $25^\circ$ . Here again foreplanes have the effect of reducing the magnitude of the derivative at high angle-of-attack. A possible explanation for these effects is that the foreplane wakes reduce the lateral flow lag through interaction with the wing vortices.

#### 6.2.3 Effect of fin on $\dot{\beta}$ derivatives for HIRM 2

As shown in Fig 10, the fin makes a major contribution to  $C_{n\dot{\beta}}$ . There is a small positive increment due to the fin at low  $\alpha$ , but for  $\alpha > 25^\circ$   $C_{n\dot{\beta}}$  is markedly increased when the fin is on. In contrast there is little fin effect on  $C_{l\dot{\beta}}$ , where the magnitude of both fin-on and fin-off measurements are small at low  $\alpha$  but increase rapidly for  $\alpha > 28^\circ$ . These results suggest that lag of sidewash over the fin is the major source of  $C_{n\dot{\beta}}$  but translational flow lag effects on the wings, unaffected by the presence of the fin, cause large increases in  $-C_{l\dot{\beta}}$  at high  $\alpha$ .

#### 6.3 Comparison with static and other oscillatory data

##### 6.3.1 Derivatives due to $\alpha$ and $\beta$

Acceleration Derivative Rig (ADR) measurements of  $C_{m\dot{\alpha}}$  and  $C_{m\dot{\beta}}$  for HIRM 1 are compared with results from static and oscillatory tests in Fig 11. The latter were obtained with the FSR which is routinely used to measure derivatives at RAE7. With this rig the derivatives were determined from a pitching oscillation, as opposed to a heaving oscillation in ADR tests. In the case of the ADR and FSR results, comparisons are made for similar values of  $\Omega_c$ . 'Static'  $C_{m\dot{\alpha}}$  and  $C_{m\dot{\beta}}$  were determined from the slopes of  $C_m$  and  $C_m$  against angle-of-attack. All tests were made at a similar Reynolds number. There is reasonable agreement between the three sets of results for  $\alpha < 20^\circ$  but at high  $\alpha$  the ADR measurement of  $C_{m\dot{\alpha}}$  is greater. In pitching

tests with the FSR,  $C_{m\dot{\alpha}}$  and  $C_{m\dot{\beta}}$  are measured as in-phase terms whereas in tests with the ADR they are measured as in-quadrature terms during heaving motion. Thus the measurements are made in different kinematic states. At high angle-of-attack, the presence of large areas of separated flow may have dynamic effects which could cause the apparent discrepancies between the different sets of data.

Corresponding comparisons are made for the lateral derivatives  $C_{n\dot{\beta}}$  and  $C_{l\dot{\beta}}$  of HIRM 2 in Fig 12. There is reasonable agreement between the three sets of results for  $C_{n\dot{\beta}}$  except that ADR results indicate greater directional instability (more negative) for  $28^\circ < \alpha < 35^\circ$ . Differences in measurements of  $C_{l\dot{\beta}}$  are more dramatic. Sideslip frequency has a major effect on the magnitude of this derivative at high  $\alpha$ , as discussed in section 6.1 and shown again in Fig 12. However, the loss in lateral stability, ie a positive shift in  $C_{l\dot{\beta}}$ , is much less according to FSR results at a similar value of  $\Omega$ . Results from static tests agree fairly closely with ADR results for the lowest frequency,  $\Omega_b = 0.233$  but are less negative than FSR data, a feature which was noticed in previous tests on a swept wing model<sup>9</sup>. The kinematics of FSR and ADR lateral tests is similar to longitudinal tests so that  $C_{n\dot{\beta}}$  and  $C_{l\dot{\beta}}$  are measured as in-phase terms during yawing oscillations with the FSR and as in-quadrature terms in a sideslipping oscillation with the ADR. The results in Fig 12 indicate that there is a strong dynamic effect on  $C_{l\dot{\beta}}$  at high angle-of-attack and also that measurement technique is significant.

##### 6.3.2 Derivatives due to $\dot{\alpha}$ and $\dot{\beta}$

$C_{m\dot{\alpha}}$  for HIRM 1 is compared with ( $C_{m\dot{\alpha}} + C_{m\dot{\beta}}$ ) from FSR tests and  $C_{m\dot{\alpha}}$  from WA tests<sup>10</sup> in Fig 13. In a WA test the model is fixed to the end of a beam and whirled about a horizontal axis. The model travels in a static annular test channel, wings in the vertical plane. Such a test allows measurement of forces due to rate of pitch only as opposed to a rotary pitching test in a wind tunnel (FSR) where forces due to  $q$  and  $\dot{\alpha}$  cannot be separated. The measurements show that  $C_{m\dot{\alpha}}$  is fairly constant at approximately -6 up to the highest test angle-of-attack of  $28^\circ$  and the fluctuations in ( $C_{m\dot{\alpha}} + C_{m\dot{\beta}}$ ) for  $\alpha > 16^\circ$  are due to variation in  $C_{m\dot{\beta}}$ .

For HIRM 2, the damping-in-yaw derivative ( $C_{nr} - C_{n\dot{\beta}} \cos \alpha$ ) and the cross damping ( $C_{lr} - C_{l\dot{\beta}} \cos \alpha$ ) from FSR tests<sup>11</sup> are compared, in Fig 14, with  $C_{n\dot{\beta}} \cos \alpha$  and  $C_{l\dot{\beta}} \cos \alpha$  respectively from ADR

tests. These comparisons suggest that at low and moderate  $\alpha$  the  $\beta$  terms constitute up to one third of the combined derivatives but at high  $\alpha$ , say  $\alpha > 30^\circ$ , the  $\beta$  term is perhaps 90% of the total.  $C_{nr}$  and  $C_{lr}$  can also be measured on the WA but results for HIRM 2 are not yet available.

In making these comparisons it must be recognised that, as for  $\alpha$  and  $\beta$  derivatives, the combined derivatives were obtained from pitching and yawing oscillation tests whereas  $\alpha$  and  $\beta$  terms were measured during heaving and sideslipping oscillations. Also, a WA test is roughly equivalent to a static wind-tunnel test. How these differences in kinematics may influence the derivatives is open to conjecture. The magnitude of the  $\alpha$  and  $\beta$  derivatives at high angle-of-attack has implications for the mathematical models used for prediction of flight characteristics and for identification of derivatives from flight responses. A systematic investigation of these effects showed that there were large differences in the lateral stability characteristics when  $\beta$  terms were ignored and "...derivative extraction at high angle-of-attack produced erroneous values for the lateral-directional stability derivatives at conditions where the  $\beta$  derivatives are large."

## 7 CONCLUSIONS

1. Tests have been made to measure the acceleration derivatives of two combat aircraft configurations at angles-of-attack up to  $42^\circ$ .
2. At high angles-of-attack, generally  $\alpha > 30^\circ$ , these derivatives could be large. Frequency parameter had a strong effect.
3. The fin made a major contribution to the derivative  $C_{n\dot{\beta}}$ .
4. Derivatives due to  $\alpha$  and  $\beta$ , measured with the ADR, were compared with results from static tests and tests with the FSR. The comparisons indicated that there were significant dynamic effects on these 'static' derivatives, especially on  $C_{l\dot{\beta}}$ .
5. There was good correlation between  $C_{m\dot{\alpha}}$ , ( $C_{mq} + C_{m\dot{\alpha}}$ ), and  $C_{mq}$  as measured by the ADR, FSR and WA respectively. Comparison of  $C_{n\dot{\beta}} \cos \alpha$  and  $C_{l\dot{\beta}} \cos \alpha$  with ( $C_{nr} - C_{n\dot{\beta}} \cos \alpha$ ) and ( $C_{lr} - C_{l\dot{\beta}} \cos \alpha$ ) respectively, indicated that

at high angle-of-attack the  $\beta$  terms were dominant.

6. The magnitudes of acceleration derivatives at high angle-of-attack is such that serious consideration should be given to their inclusion in mathematical models of combat aircraft.

## APPENDIX

### Determination of derivatives from test data

Signals in volts are:

- M = pitching moment
- Z = normal force
- N = yawing moment
- L = rolling moment
- A = accelerometer

Subscripts 'ph' and 'qd' refer to in-phase and in-quadrature components respectively.

Other parameters needed for reduction to aerodynamic derivatives are:

k(with suffix) = calibration constant

$\omega$  = circular frequency of oscillation (rad/sec)

V = wind speed, m/s

q = dynamic pressure, N/m<sup>2</sup>

S = wing area, m<sup>2</sup>

$\bar{c}$  = aerodynamic mean chord, m

b = wing span, m

Derivatives are calculated in body axes as follows:

$$C_{m\dot{\alpha}} = [M_{qd}/A \cdot k_M/k_A \cdot \omega \cdot V/qS\bar{c}]/\cos \alpha$$

$$C_{m\dot{\alpha}} = [M_{ph}/A \cdot k_M/k_A \cdot 2V^2/qS\bar{c}^2]/\cos \alpha$$

$$C_{n\dot{\alpha}} = [-Z_{qd}/A \cdot k_Z/k_A \cdot \omega \cdot V/qS]/\cos \alpha$$

$$C_{n\dot{\alpha}} = [-Z_{ph}/A \cdot k_Z/k_A \cdot 2V^2/qS\bar{c}^2]/\cos \alpha$$

$$C_{n\dot{\beta}} = N_{qd}/A \cdot k_N/k_A \cdot \omega \cdot V/qSb$$

$$C_{n\dot{\beta}} = N_{ph}/A \cdot k_N/k_A \cdot 2V^2/qSb^2$$

$$C_{l\dot{\beta}} = L_{qd}/A \cdot k_L/k_A \cdot \omega \cdot V/qSb$$

$$C_{l\dot{\beta}} = L_{ph}/A \cdot k_L/k_A \cdot 2V^2/qSb^2$$

## REFERENCES

- 1 D. R. Riley, J. D. Bird, L. R. Fisher. "Experimental determination of the aerodynamic derivatives arising from acceleration in sideslip for a triangular, a swept and an unswept wing". NACA RM L55A07, March 1955.
- 2 J. H. Lichtenstein, J. L. Williams. "Effect of frequency of sideslipping motion on the lateral stability derivatives of a typical delta-wing airplane". NACA RM L57F07, September 1957.
- 3 J. H. Lichtenstein, J. L. Williams. "Low-speed investigation of the effects of frequency and amplitude of oscillation in sideslip on the lateral stability derivatives of a 60° delta wing, a 45° sweptback wing and an unswept wing". NASA TN D-896, May 1961.
- 4 L. T. Nguyen. "Evaluation of importance of lateral acceleration derivatives in the extraction of lateral-directional derivatives at high angles of attack". NASA TN D-7739, October 1974.
- 5 P. L. Coe, A. B. Graham, J. R. Chambers. "Summary of information on low-speed lateral-directional derivatives due to rate-of-change of sideslip  $\dot{\beta}$ ". NASA TN D-7972, September 1975.
- 6 A. J. Ross, G. F. Edwards. "Correlation of predicted and free-flight responses near departure conditions of a high incidence research model". AGARD-CP-386, November 1985.
- 7 C. O. O'Leary. "Wind-tunnel measurement of aerodynamic derivatives using flexible-sting rigs". AGARD-LS-114, May 1981.
- 8 C. O. O'Leary. "Dynamic tests on a High Incidence Research Model (HIRM) in a low speed wind tunnel". RAE TR 84111, November 1984.
- 9 C. O. O'Leary. "Wind-tunnel measurement of lateral aerodynamic derivatives using a new oscillatory rig, with results and comparisons for the Gnat aircraft". ARC R&M No 3847, October 1977.
- 10 M. J. Mulken, A. O. Omerod. "Steady-state experiments for measurements of aerodynamic stability derivatives of a high incidence research model using the College of Aeronautics Whirling Arm". CoA Report No 9014, August 1990.
- 11 C. O. O'Leary, B. Weir. "The effects of foreplanes on the static and dynamic characteristics of a combat aircraft model". AGARD-CP-465, April 1990.

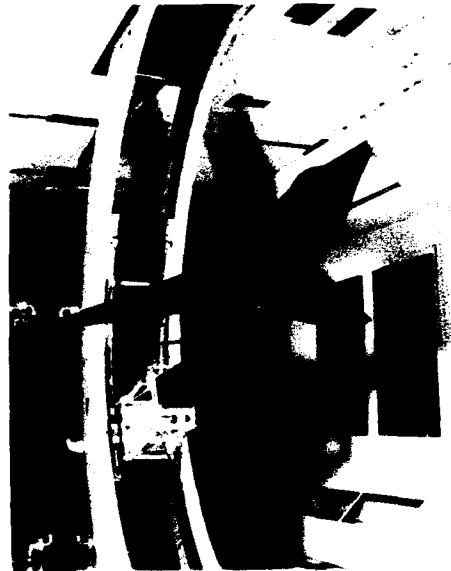


Fig 1 HIRM 1 on acceleration derivative rig configured for heave tests in 4m x 2.7m wind tunnel

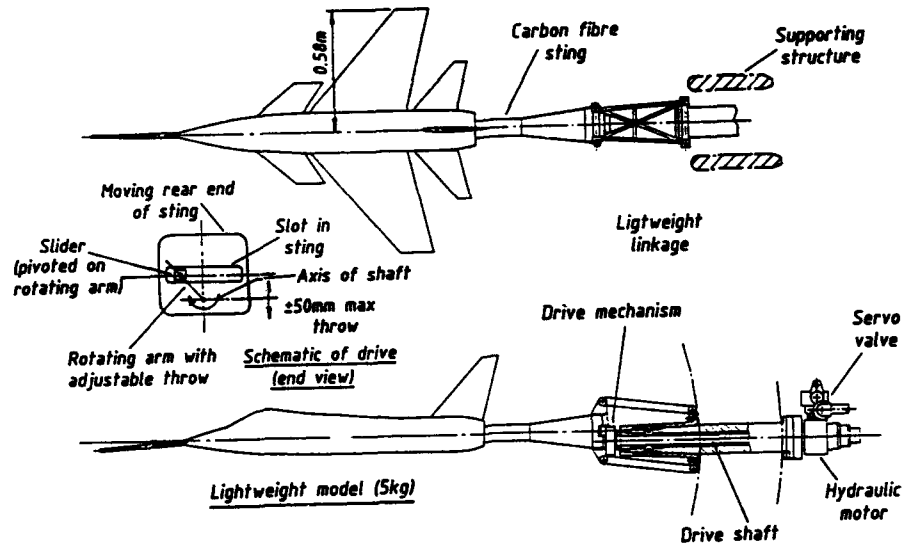


Fig 2 GA of acceleration derivative rig

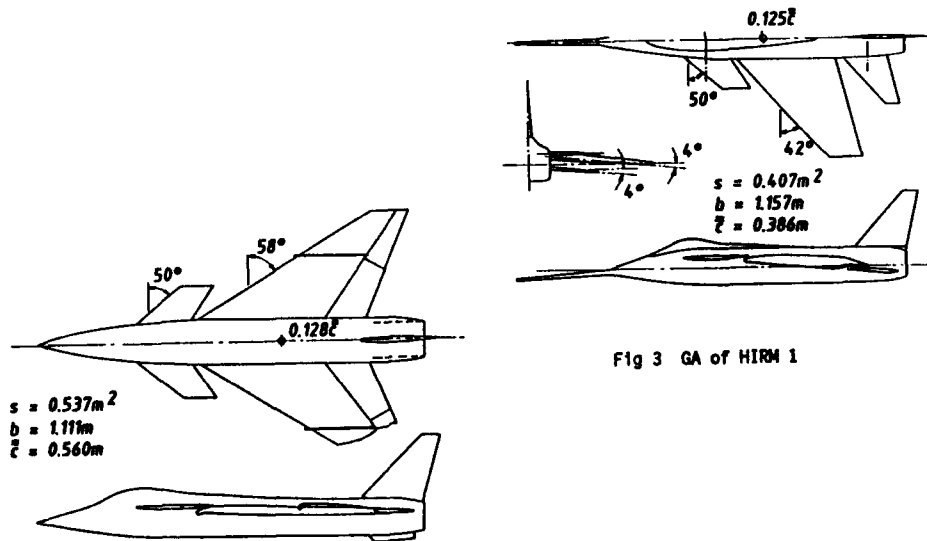


Fig 3 GA of HIRM 1

Fig 4 GA of HIRM 2



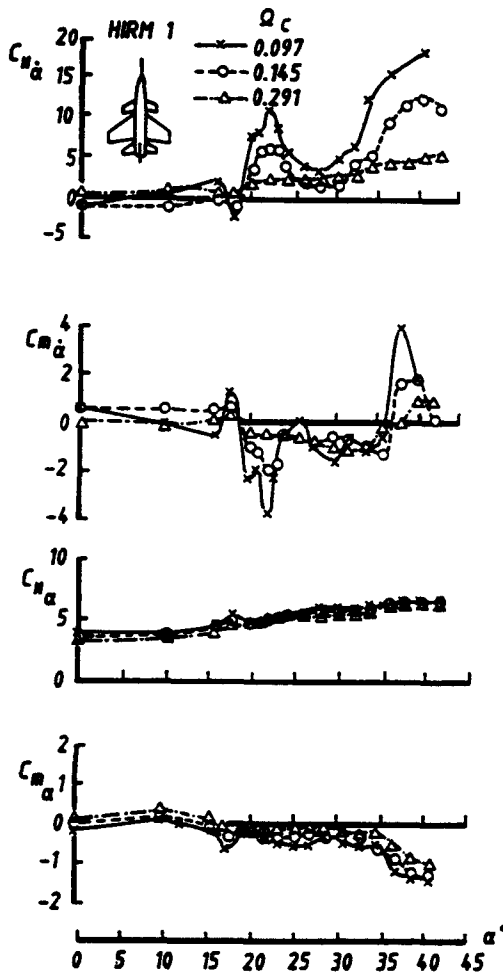


Fig 5 Effect of frequency on longitudinal derivatives. HIRM 1,  $\eta_c = 0^\circ$ ,  $\eta_T = 0^\circ$

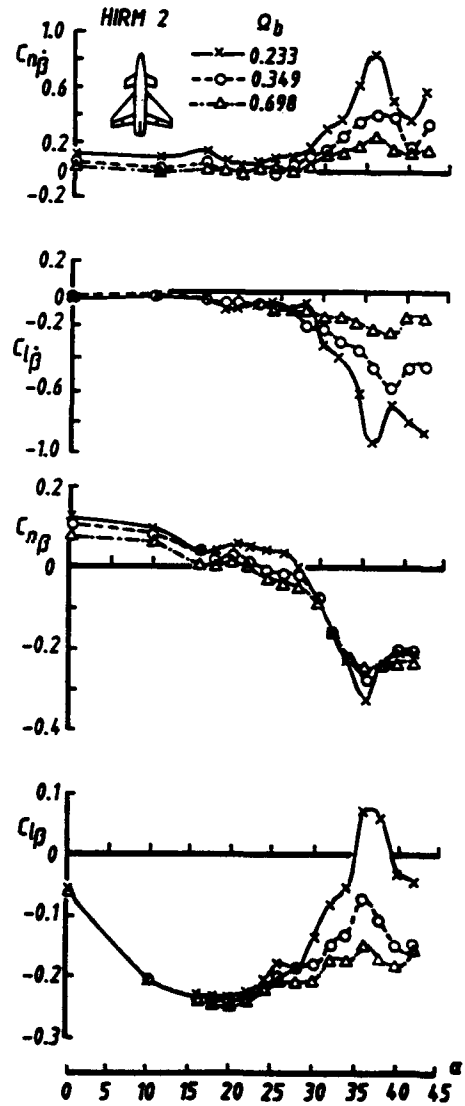


Fig 6 Effect of frequency on lateral derivatives. HIRM 2,  $\eta_c = 0^\circ$ ,  $\delta_T = 0^\circ$

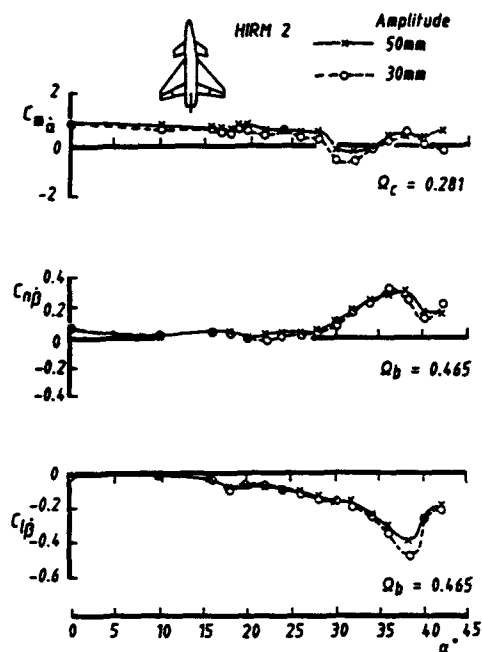


Fig 7 Effect of oscillation amplitude on acceleration derivatives. HIRM 2,  $\eta_c = 0^\circ$ ,  $\delta_f = 0^\circ$

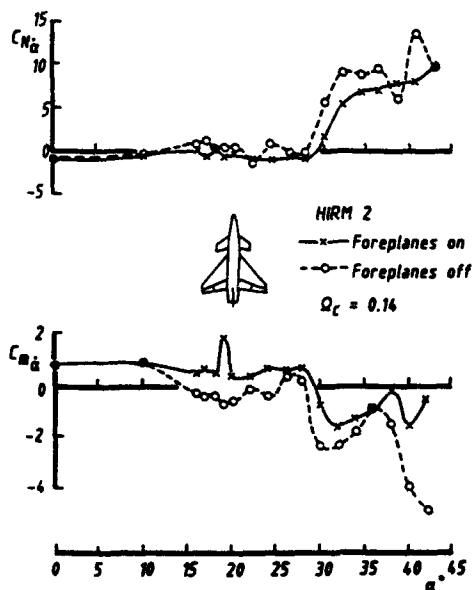


Fig 8 Effect of foreplanes on  $\dot{\alpha}$  derivatives. HIRM 2,  $\delta_f = 0^\circ$

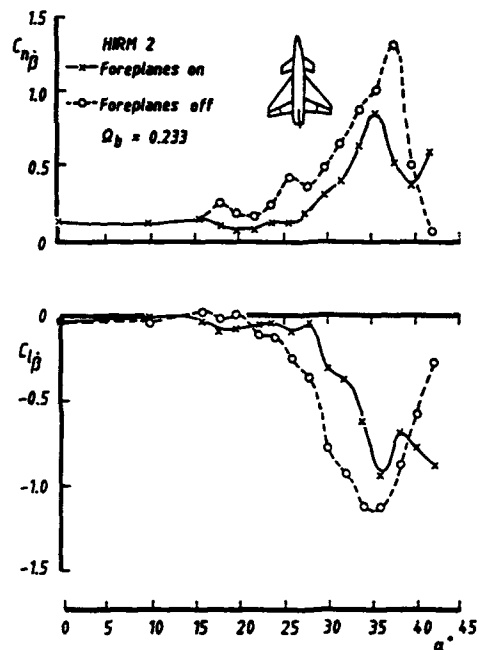


Fig 9 Effect of foreplanes on  $\dot{\beta}$  derivatives. HIRM 2,  $\delta_f = 0^\circ$

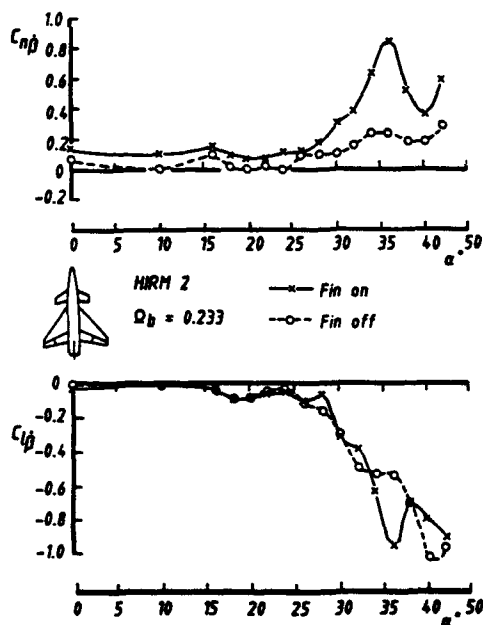


Fig 10 Effect of fin on lateral derivatives. HIRM 2,  $\eta_c = 0^\circ$ ,  $\delta_f = 0^\circ$

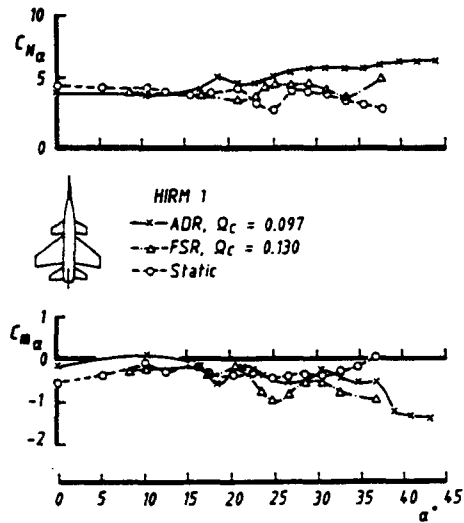


Fig 11 Comparison with static and other oscillatory data,  $\alpha$  derivatives. HIRM 1,  $\eta_c = 0^\circ$ ,  $\eta_T = 0^\circ$

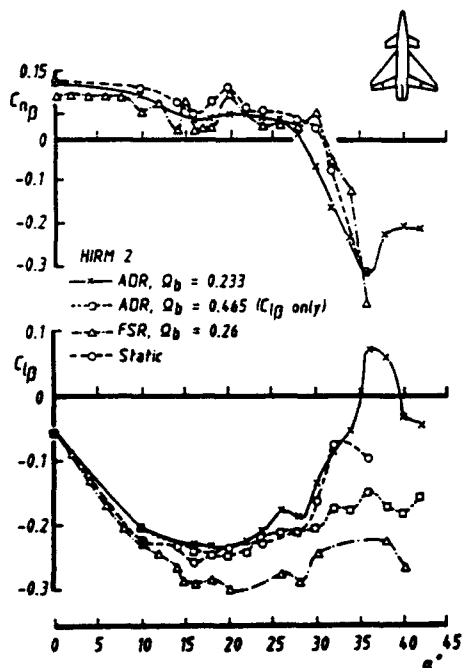


Fig 12 Comparison with static and other oscillatory data,  $\beta$  derivatives. HIRM 2,  $\eta_c = 0^\circ$ ,  $\delta_T = 0^\circ$

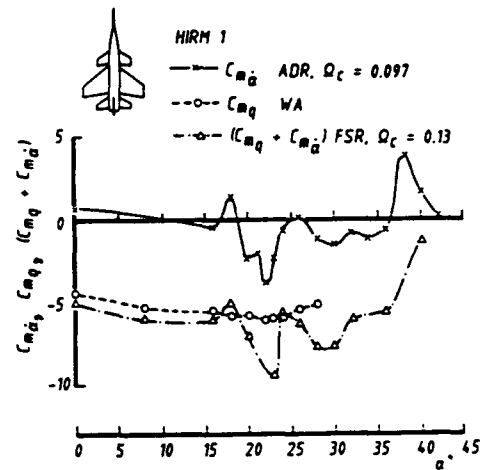


Fig 13 Correlation of  $C_{m\alpha}$  with  $C_{mq}$  and  $(C_{mq} + C_{m\alpha})$ . HIRM 1,  $\eta_c = 0^\circ$ ,  $\eta_T = 0^\circ$

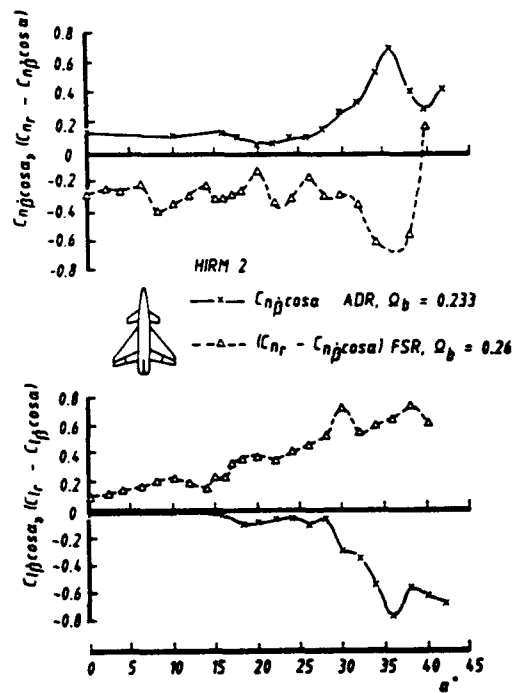


Fig 14 Correlation of lateral derivatives. HIRM 2,  $\eta_c = 0^\circ$ ,  $\delta_T = 0^\circ$

# WIND TUNNEL FORCE MEASUREMENTS AND VISUALIZATION ON A 60-DEGREE DELTA WING IN OSCILLATION, STEPWISE MOTION AND GUSTS

Per-Åke Torlund

FFA, The Aeronautical Research Institute of Sweden  
P.O.Box 11021, S-16111 Bromma, Sweden

## Abstract

A 60-degree delta wing has been tested in pitching motion in FFA's low-speed wind tunnel L2 at the Royal Institute of Technology. Harmonic oscillation tests with 4° and 8° amplitude at 0 to 35° angle of attack were carried out. The reduced frequency was between .003 and .195. Both dynamic aerodynamic derivatives and time histories of the normal force and pitching moment were recorded. The same model was also tested in a stepwise motion up to 90° angle of attack. The steps were positive and negative with 20° amplitude starting every 10°, also steps over the full 90° were made. The angle of attack rates were chosen to correspond to the oscillation tests, the maximum being 360°/s and the acceleration 13500 °/s<sup>2</sup>. The tunnel speed was 57 m/s in most cases and the centerline chord was .5 m. The response to the step motion was compared to the response predicted from the results of the oscillation tests. These coincide fairly well at low angle of attack whereas large discrepancies are evident at moderate angle of attack. Long time delays are seen when the dynamic motion passes the angle of attack where the vortex burst reaches the apex at steady state conditions. Some visualization of vortex burst position in the oscillation and stepwise motion tests were made with smoke and Schlieren optics and correlated to the force measurements. The 60 degree delta wing has also been tested in a recently completed gust generator. Force measurements for gusts compared to step motion in pitch show the same long time delays. Comparing gust and step response during the motion gives the possibility to separate  $\dot{\alpha}$  and  $q$  effects.

## Nomenclature

$a$  constant see  $\alpha_g$   
 $C_M$  pitching moment coefficient  
 $C_N$  normal force coefficient  
 $mac$  mean aerodynamic chord (m)

$c_r$  root chord (m)  
 $f$  frequency (Hz)  
 $k$  reduced frequency =  $\pi f c_r / U_\infty$   
 $Re$  Reynolds number  
 $U_\infty$  free stream velocity (m/s)  
 $q_\infty$  free stream dynamic pressure (Pa)  
 $\alpha$  angle of attack (°)  
 $\alpha_g$  equivalent angle of attack  
 $\alpha_g = \alpha + a^* \Gamma$  (°)  
 $\Gamma$  angle of gust generator wings (°)

## Subscripts

$s$  static conditions  
 $q$  rotation derivative  
 $\dot{\alpha}$  angle of attack rate derivative

## I. Introduction

The requirements for maneuverability in fighter aircraft is, like always, increasing. Recent trends include post-stall maneuvering to high angles of attack and relaxed static stability. This leads to high pitch rates in a part of the envelope where traditional dynamic derivatives may not be sufficient to model the response of the aircraft. In order to get a better physical understanding of these high angle of attack, dynamic flow phenomena a series of low speed wind tunnel tests have been conducted at FFA. A large part of these tests were carried out with a schematic delta wing model with 60 degree sweep. Some of the reasons for this choice of model is; a relatively simple interpretation of visualizations and an aspect ratio comparable to modern fighters. Several types of tests were carried out including harmonic pitching motion, stepwise pitching motion and gusts in pitch.

## II. Experimental Technique and Setup

### Wind Tunnel

The tests were carried out in FFA's low speed wind tunnel L2 at the Royal Institute of Technology in Stockholm. The wind tunnel has a closed circuit with a 2x2 m<sup>2</sup> test section with cut corners giving a 3.6 m<sup>2</sup> cross section. The maximum speed is approximately 65

m/s. The turbulence intensity is .1 - .2 % depending on tunnel speed.

#### Model

The model used for these tests was a flat plate 60 degree delta wing with .577 m span and .5 m root chord. To achieve a good path for the Schlieren optics the leading edge was beveled on the pressure side only. The trailing edge was cut off at a right angle to fix the pressure side separation as well as possible. The wing was originally made from 4 mm aluminium plate. This was later changed to a 3 mm plywood core with .5 mm carbon fibre pressure laminated to each side. This increased the natural frequency considerably. A boat shaped fairing under the wing covered the balance and linkages. The model is shown in Fig. 1.

#### Motion System

The model was installed on a braced strut from the tunnel floor as shown in Figure 2. When the angle of attack range was increased from 0°-43° to -2°-92° the top of the strut was swept back 45°.

The oscillatory test was driven by a flywheel through a long pushrod giving an almost sinusoidal motion. The maximum frequency was 5 Hz which translates to a reduced frequency ( $k$ ) of .195 at 40 m/s.

The step motion was driven by a 2 kW stepper motor for most of the tests presented here. This was recently exchanged for an AC servo which should be able to produce any motion, including harmonic, within the speed and acceleration limits of 400 °/s and 18000 °/s<sup>2</sup>. The torque is then geared up through a 6:1 cog belt drive. On the output shaft of this there is a drive arm that is connected with a carbon fibre pushrod to a lever on the model strut. From there the torque is transmitted by two pretensioned steel push-pull rods to a frame around the balance in the model.

The model was rotated around its 55 % root chord and 29 mm (5.8 %  $c_r$ ) below the upper surface of the wing. The angle of attack was measured by a potentiometer on this axle.

#### Gust Generation

The gust generator consists of eight short wings on the side walls at the beginning of the test section as shown in Figure 2. The wings are synchronised to the same angle by a linkage driven by a 2 kW stepper motor. All wings have flaps which are

mechanically geared to their setting angle. Several means were used to achieve a uniform downsweep across as much of the width of the test section as possible:

- The four wings on top and bottom have a larger span.
- A winglet connects the tips of the central wings.
- The flaps on the central wings have a different gear ratio compared to the top and bottom ones.

At present the largest possible angle of attack change at the reference point is 13.6° and 12° at the wingtips of the model.

#### Force Measurements

The forces and moments were measured with a custom built lightweight five component balance.

#### Data Acquisition and Reduction

Data were recorded at 700 Hz in most cases. After an anti aliasing filter the signals were A/D converted ( 16 bits ) and stored.

Dynamic derivatives were calculated as the out of phase components of the forces and moments.

For the time histories for the harmonic motion several loops were averaged. Mass forces were measured once and approximated with a simple function. This was scaled with the frequency squared and subtracted from the time histories. The individual loops were also simply plotted on top of each other to get a feel of the spread in the data.

The stepwise pitching motion gave a low signal to noise ratio, in the order of 10%, due to the high pitch acceleration. For each motion several time histories of the mass forces were recorded wind off and averaged. The total forces were then recorded wind on in the same way. The mass forces were subtracted and the resulting response was digitally filtered. If the variance between the averaged cycles was too high the result was rejected. This was sometimes an indication of mechanical problems. For the gust tests the model remained stationary except for elastic effects so the signal analysis was less critical.

The model was set to the angle for the test and a zero included the tare effects. One digitally filtered time history normally gave a sufficient signal quality.

#### Visualization

A smoke generator producing evaporated

kerosene could be mounted in the streamline fairing on the model. The smoke was ejected through a 1.5 mm tube under the starboard leading edge 10 mm aft of the wing apex. A large flash unit aft and outboard of the model was used when taking photographs of the smoke. It was found that a relatively long flash duration (.0015 s) helped average the structure in the smoke and make it appear fairly smooth.

In order to get a comparison to the smoke visualization a Schlieren optics system was used. It was possible to see the vortices at 40 m/s. Very small vortices could be studied. Since an optical axis parallel to the mechanical axle for the motion was chosen the port and starboard vortices could not be separated. The system was useful, but suffered from low productivity compared to the smoke visualization because the edge in the Schlieren aperture had to be set for each picture. Also the available optics had a diameter of only 180 mm so it had to be moved and realigned often. The light for the Schlieren optics comes from a spark discharge of  $2 \times 10^{-6}$  s duration.

### III. Results and Discussion

#### Static : Force Measurement : Reynolds Number Effects

The sharp leading edge was used to reduce the sensitivity to Reynolds number as much as possible. The static measurements of pitching moment and normal force for Reynolds number  $0.71 \times 10^6$  and  $2.26 \times 10^6$  are presented in Figure 3. The main difference is that the sharp break occurs at less than one degree lower angle of attack for the higher Reynolds number.

#### Static : Visualization

Figure 4 shows the vortex burst position as a function of angle of attack. Smoke and Schlieren results from these tests agree fairly well. Between the apex and  $10\% c_x$  it is possible, with some practice, to detect the existence of a vortex but not the burst position. With Schlieren optics, however, a 5 mm ( $1\% c_x$ ) vortex can be seen. For comparison some Schlieren results by Wentz (1) are included. The models used had a two-sided  $7.5^\circ$  bevel and a square leading edge respectively. The vortex burst is located further aft for the same angle of attack with an increasing bluntness of the leading edge.

#### Oscillation : Force Measurement

When this configuration was tested for ordinary dynamic derivatives it was found that both  $C_{M_0} + C_{M_{\dot{\alpha}}}$  and  $C_{N_0} + C_{N_{\dot{\alpha}}}$  reached very high levels at  $25^\circ$  angle of attack and beyond, as seen in Figure 5. To investigate the reason for this time histories were recorded for oscillation with  $\pm 8^\circ$  amplitude at  $20^\circ$ ,  $25^\circ$ ,  $30^\circ$  and  $34.6^\circ$  mean angle of attack. These are presented as loops in pitching moment and normal force over angle of attack in Figure 5 - 8. For the lowest angle of attack,  $20^\circ$ , the dynamic response is a typical damping; a loop centered on the static curve. For  $25^\circ$  angle of attack the response is different. The motion now reaches the sharp break in the static curves at  $32^\circ$  angle of attack. Here a hysteresis loop forms in the pitching moment at low reduced frequencies, but decreases for higher frequencies. At the lower end of the  $\pm 8^\circ$  motion there is, however, a damping loop which increases in magnitude with frequency. The same phenomena are less evident in normal force since both loops have the same sign there. At the higher angles of attack presented here ( $30^\circ$  and  $34.6^\circ$ ) the hysteresis loop and the damping loop seem to coincide and simply grow with frequency.

#### Oscillation : Visualization

Schlieren optics visualisation of vortex burst position on the oscillating model was carried out for two of the angles of attack where force measurements had been made. The result is shown as loops over angle of attack in Figures 10 and 11. Twelve photos, one every 30 degrees of phase angle, were taken for each reduced frequency. The motion had to be stopped before each photo to change the flash synchronisation. Thus the points on the curves come from not only different cycles but also have a separate start of the motion. The fact that the measured points still fall on reasonably smooth curves is taken as a sign of fairly good repeatability. At  $25 \pm 8$  degrees angle of attack there is a vortex on the wing for the complete cycle for the two higher reduced frequencies ( $k = .045$  and  $.195$ ). At the lowest reduced frequency ( $k = .012$ ) the vortex breaks down before the motion reaches its peak angle of attack at  $33$  degrees and does not appear until below  $30$  degrees. This correlates with the pitching moment in Figure 7. The lowest reduced frequency at which the pitching moment goes down to the static post stall level is  $.012$ . Also

the pitching moment stays at this level over roughly the same angle of attack range as the vortex is gone. At  $30 \pm 8$  degrees the vortex breakdown reaches the apex for all reduced frequencies. When comparing with the pitching moment in Figure 8 the angles of attack for the quick changes up or down coincide fairly well with the vortex going on or off.

#### Stepwise Motion : Force Measurement

The model was pitched stepwise with different angle of attack rates. Only the pitch rate corresponding to a reduced frequency of .195 is presented here, at 57 m/s this means  $360^\circ/\text{s}$ . The pitch acceleration was always  $13500^\circ/\text{s}^2$ .

Figure 12 presents a sample time history of angle of attack, normal force and pitching moment. The most obvious feature is the long time delay from the stop of the motion until the static values for the new angle of attack is reached. In this case the delay is about 0.4 seconds or in other words 32 root chord passages for the flow. The figure also contains the value of the static pitching moment and normal force for the same angle of attack. To this the dynamic derivatives presented in Figure 5 have been added. The normal force predicted is not far from the measured response during the motion, but of course this simple model can not predict anything after the motion stops. In pitching moment the predicted response is further from the measurement during the motion. The same comparison gives better agreement at low angles of attack.

There is a relatively low sensitivity to Reynolds number for the case shown in Figure 13. It should be noted that the signals for all cases have gone through the same filters. Since the highest Reynolds number case also has the fastest motion some of the difference in normal force is probably caused by the filter.

Time histories for  $20^\circ$  steps up and down starting every  $14^\circ$  angle of attack are presented in Figures 14 and 15. Long time delays are apparent on all ramps passing  $32^\circ$  angle of attack where the sharp break in the static curves is located.

Figure 16 shows the response to a step from  $20^\circ$  to  $40^\circ$  angle of attack as a function of angle of attack. The response to the down going step over the same range has been added. The same steps as in Figure 14 and 15 are presented as a function of angle of attack in Figure 17. The steps from  $0^\circ$  to  $90^\circ$  angle of attack and down

over the same range have been included. If a linear model could describe these step responses the  $90^\circ$  steps would follow the envelope of the  $20^\circ$  steps. It does not. The "history" of the flow must be taken into account to model the response of these steps, especially when passing the angle of attack for the vortex breakdown reaching the wing apex and disappearing.

#### Stepwise Motion : Visualization

The time history for the vortex burst position for the step from  $20^\circ$  to  $40^\circ$  angle of attack is shown in figure 18 compared to the static burst position. The vortex burst reaches the wing apex approximately when the motion stops with a small delay compared to the static values. The normal force and pitching moment show delays, after the vortex disappears, in the order of 20 chord passages before they reach their static values.

Figure 18 also shows the visualization result for the step down over the  $40^\circ$  to  $20^\circ$  range. Here the vortex restart is delayed until after the motion has stopped. The vortex burst position is then further delayed before it reaches steady state. The normal force and pitching moment reach their static values at the same time as the vortex, if not before. It should be noted that the photos indicated by the dots come from different steps which probably explains why the burst position is not a monotonous function of time.

Figure 19 shows the dynamic vortex burst position visualized with smoke for the  $90^\circ$  steps up and down compared to the static case. The vortex burst reaches the apex at roughly the angle of attack for maximum normal force.

#### Gusts : Force Measurement

A gust that changes the angle of attack 13 degrees in .05 seconds can be induced. The gust is well defined in time but varies in space as shown in Figure 20. The gust flow field is basically vertically convergent and horizontally divergent. An equivalent angle of attack is defined as

$$\alpha_g = \alpha + a^*\Gamma$$

where  $\Gamma$  is the angle of the gust generator wings and  $a^*$  a constant that is adjusted so that a slow gust produces a response close to that of static angle of attack change. Three "slow gusts" are compared to the static case in figure 21. The normal force for the gusts is linear and

close to the static values. The pitching moment coincides with the static curve for zero gust generator angle, but falls below it at both ends.

Figure 22 presents the time histories for three positive gusts compared to steps over the same  $\alpha$  ranges and with the same speed. The  $15.5^\circ$  to  $28.5^\circ$  case only shows significant difference during the motion. This should be mainly the difference between  $\dot{\alpha}$  and  $q$  response. If the difference in  $\alpha$  between the front and aft end of the model is disregarded the gust produces an  $\dot{\alpha}$  only. For the  $21.5^\circ$  to  $34.5^\circ$  and  $28.5^\circ$  to  $41.5^\circ$  cases there are some differences during the motion that may be due to the lack of rotation for the gust. The time delays after the motion are roughly the same for the gusts and the steps.

The same observations hold for the negative gusts in figure 23.

The comparison between gust and step motion during the actual motion is highlighted in figures 24 and 25 where the same cases are plotted over angle of attack.

#### IV. Conclusions

A 60 degree schematic delta wing has been tested in oscillation, stepwise motion and gusts.

Both the static results and the response to stepwise pitching are relatively insensitive to Reynolds number in the .7 to 2.3 million range. This configuration has a sharp break in both pitching moment and normal force at 32 degrees angle of attack. By visualization with smoke and Schlieren optics this has been correlated to the vortex reaching the wing apex and disappearing.

When passing this angle of attack up or down dynamically, time delays in the forces, sometimes as long as 30 to 40 chord passages of the flow, are measured especially when the motion stops a few degrees after the critical angle.

Time delays are seen for gusts as well as for oscillation in pitch and stepwise pitching motion.

These time delays have correlated with delays in vortex breakdown in all cases where good visualization have been achieved. The delays in the forces can, however, be much longer. Comparing stepwise pitching motion with gusts can separate  $\dot{\alpha}$  and  $q$  derivatives. The limited angle of attack range of the gust generator ( $13^\circ$ ) limits the study of time history effects though.

#### References

- 1 Wentz, W.H., "Wind Tunnel Investigations of Vortex Breakdown on Slender Sharp-Edged Wings", NASA CR-98737.
- 2 Wolffelt, K.W., "Investigation of the Movement of Vortex Burst Position with Dynamically Changing Angle of Attack for a Schematic Delta Wing in a Water Tunnel With Correlation to Similar Studies in a Wind Tunnel", AGARD-CP-413, 1986, pp.27-1-27-8.
- 3 Bragg, M.B., and Soltani, M.R., "Measured Forces and Moments on a Delta Wing During Pitch-Up", Journal of Aircraft, Vol.27, No.3, 1990 pp. 262-267.



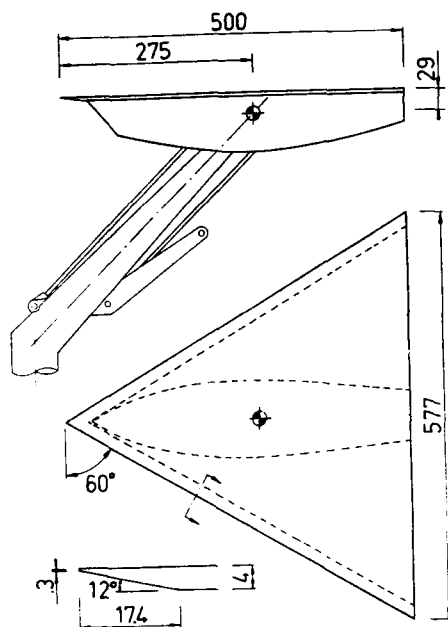


Figure 1 Wind Tunnel Model.  
Dimensions in mm.

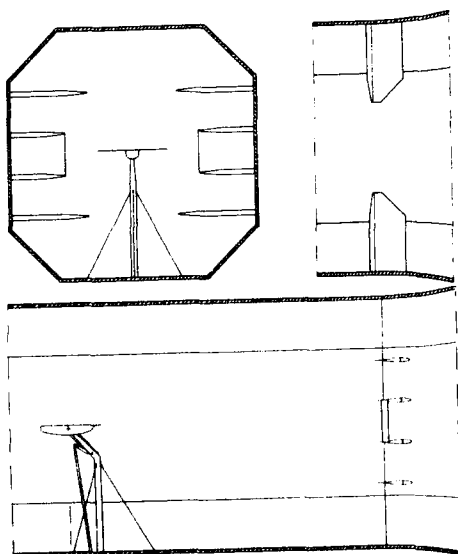


Figure 2 Model Installation  
and Gust Generator.

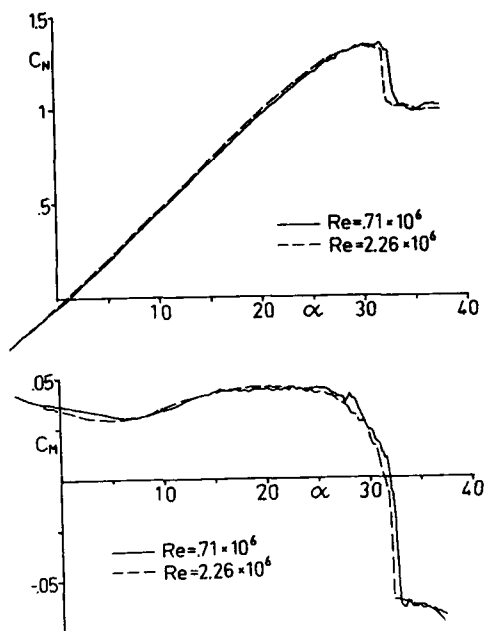


Figure 3 Static Reynolds Number Check.

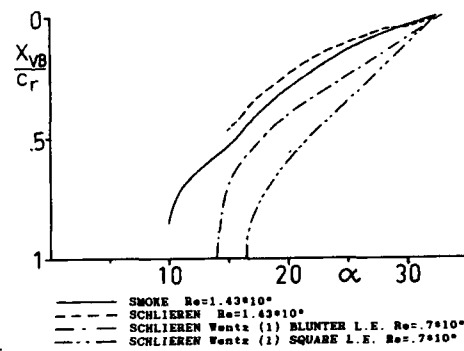


Figure 4 Vortex Burst Position; Static  
Visualisation.

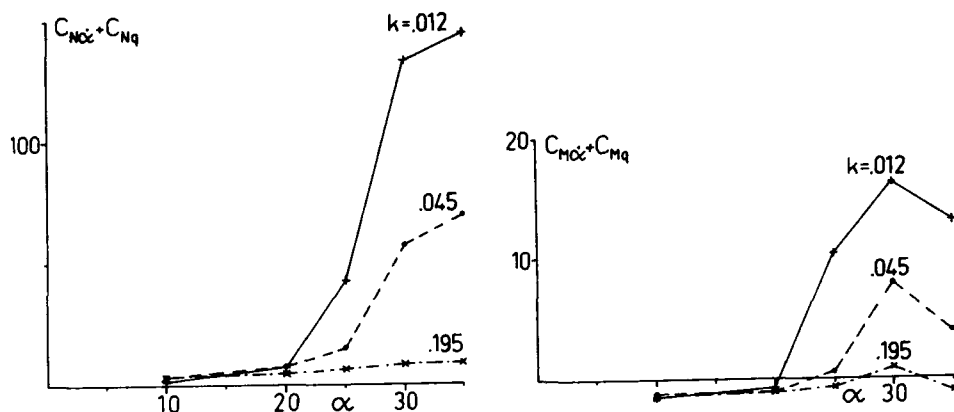


Figure 5 Dynamic Derivatives in Pitch  
Derived from Harmonic Oscillations.  
Amplitude  $\pm 8^\circ$ .

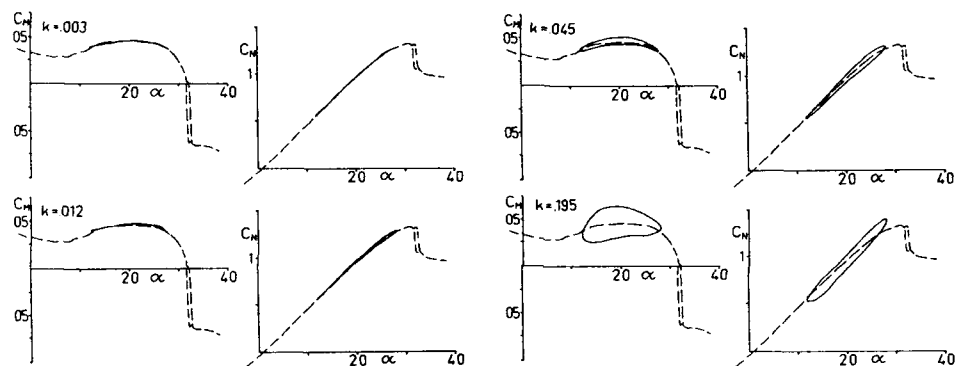


Figure 6 Pitching Moment and Normal  
Force during Oscillation as a Function of  
Angle of Attack.  $\alpha = 20^\circ \pm 8^\circ$   $Re = 1.43 \times 10^6$

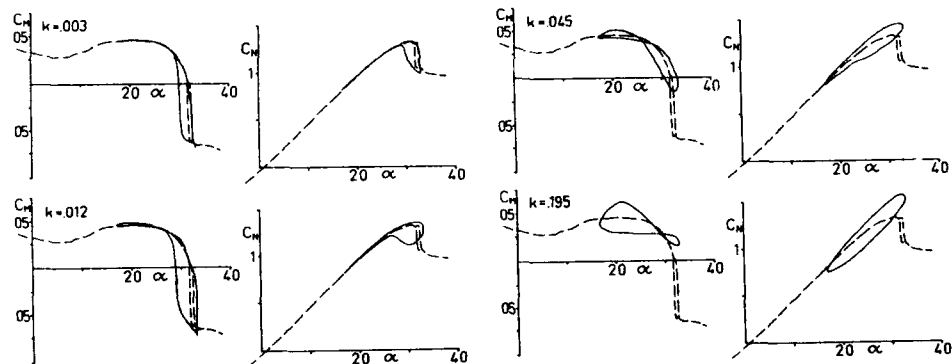


Figure 7 Pitching Moment and Normal  
Force during Oscillation as a Function of  
Angle of Attack.  $\alpha = 25^\circ \pm 8^\circ$   $Re = 1.43 \times 10^6$

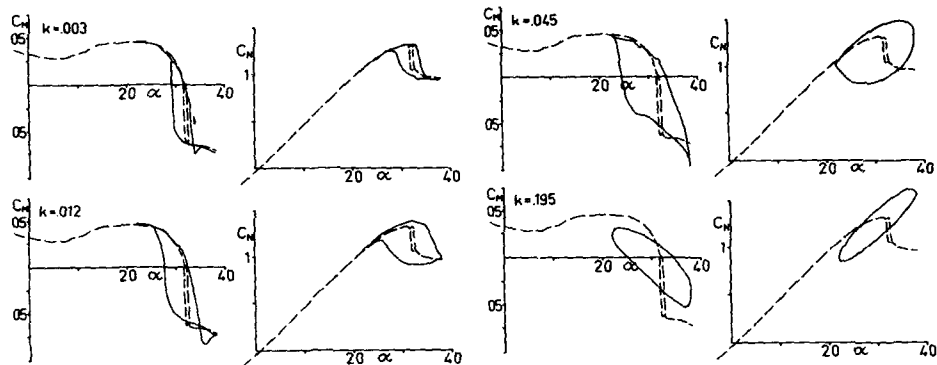


Figure 8 Pitching Moment and Normal Force during Oscillation as a Function of Angle of Attack.  $\alpha=30^\circ \pm 8^\circ$   $Re=1.43 \times 10^6$

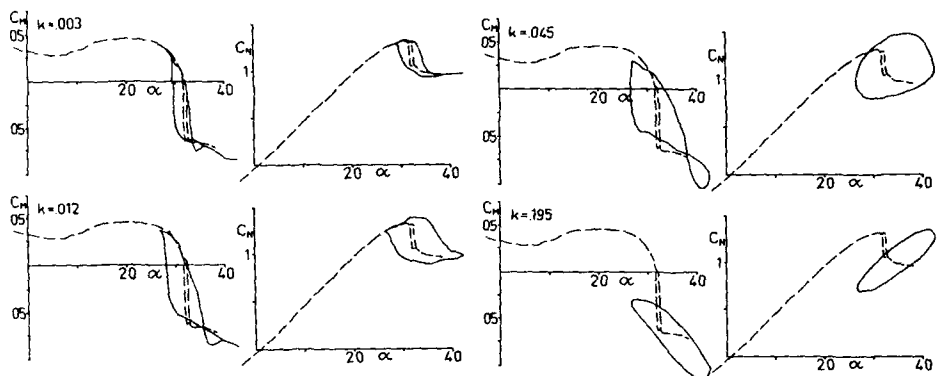


Figure 9 Pitching Moment and Normal Force during Oscillation as a Function of Angle of Attack.  $\alpha=34.6^\circ \pm 8^\circ$   $Re=1.43 \times 10^6$

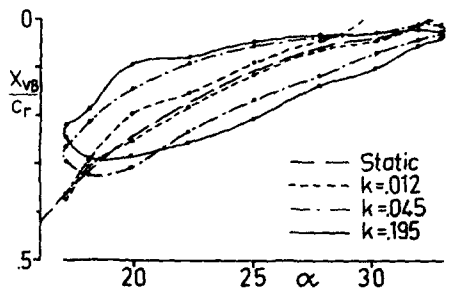


Figure 10 Vortex Burst Position during Oscillation, Visualization with Schlieren Optics. Dots Indicate Photos.  $\alpha=25^\circ \pm 8^\circ$   $Re=1.43 \times 10^6$

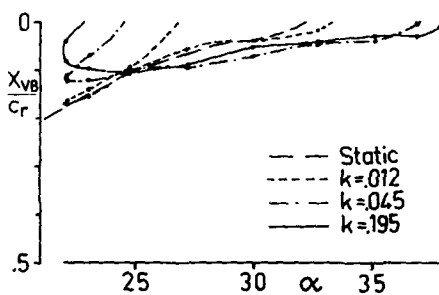


Figure 11 Vortex Burst Position during Oscillation, Visualization with Schlieren Optics. Dots Indicate Photos.  $\alpha=30^\circ \pm 8^\circ$   $Re=1.43 \times 10^6$

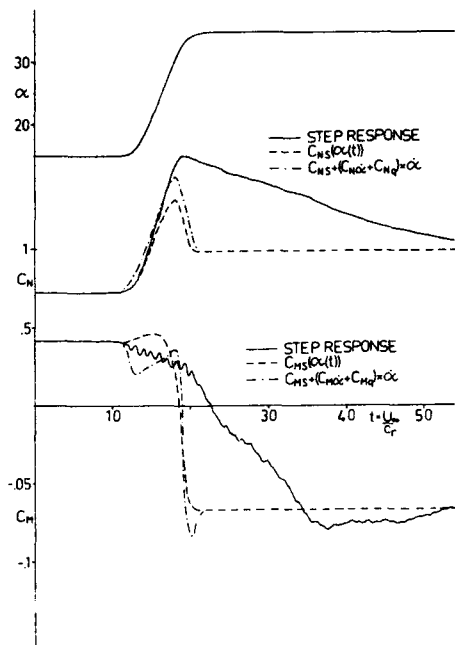


Figure 12 Time History for Stepwise Pitching Motion and Response Predicted from Static and Oscillatory Tests.  $\alpha=15^\circ-35^\circ$ ,  $\dot{\alpha}=\pm 252^\circ/\text{s}$   $Re=1.43 \times 10^6$

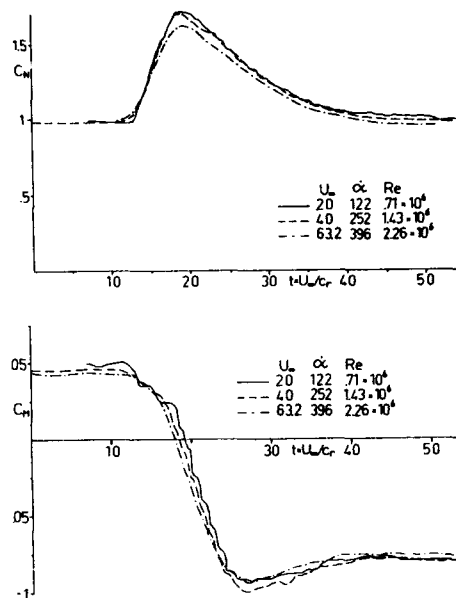


Figure 13 Reynolds Number Check for Stepwise Pitching Motion.  $\alpha=20^\circ-40^\circ$

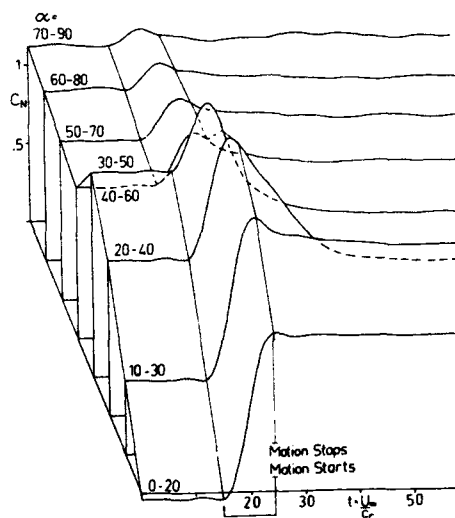
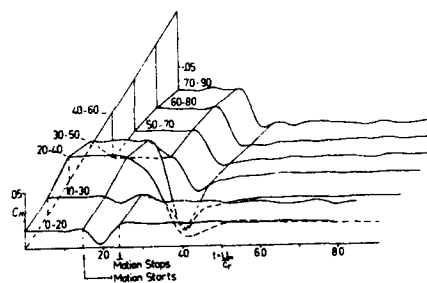


Figure 14 Time Histories for Stepwise Pitching Motion.  $20^\circ$  Increments Up.  $Re=2.02 \times 10^6$



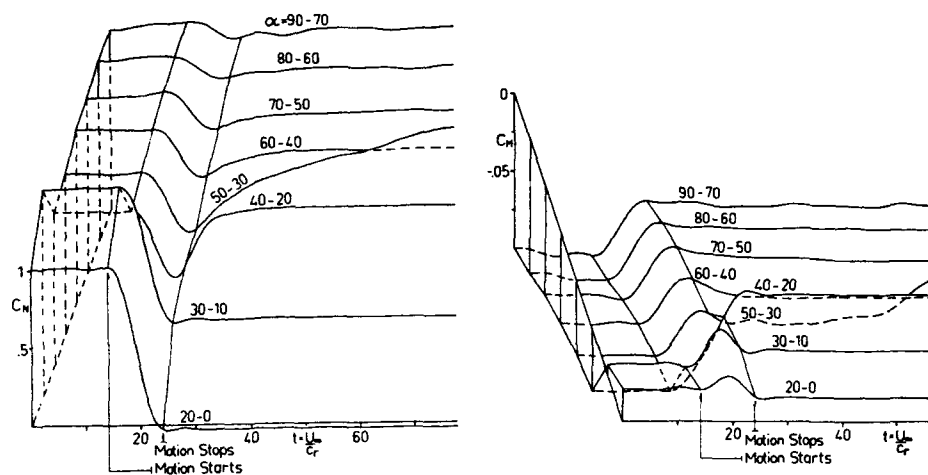


Figure 15 Time Histories for Stepwise Pitching Motion.  $20^\circ$  Increments Down.  $Re=2.02 \times 10^6$

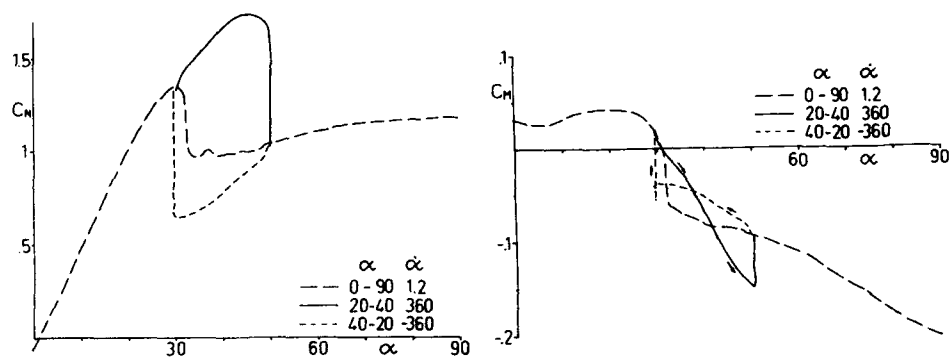


Figure 16 Response to Stepwise Pitching Motion.  $Re=2.02 \times 10^6$

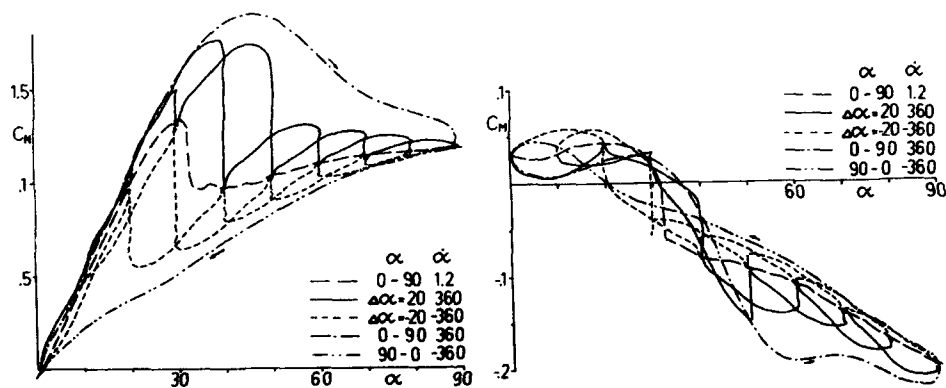


Figure 17 Response to Stepwise Pitching Motion. Comparison of  $90^\circ$  Steps to Envelope of  $20^\circ$  Steps.  $Re=2.02 \times 10^6$

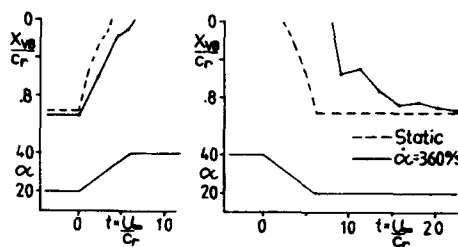


Figure 18 Vortex Burst Position during  $\alpha=20^\circ-40^\circ$  and  $40^\circ-20^\circ$  steps, Visualization with Schlieren optics.  $Re=2.02 \times 10^6$

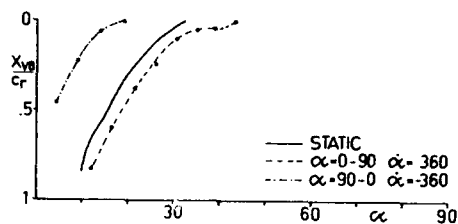


Figure 19 Vortex Burst Position during  $90^\circ$  steps up and down, Visualization with Smoke.  $Re=0.71 \times 10^6$

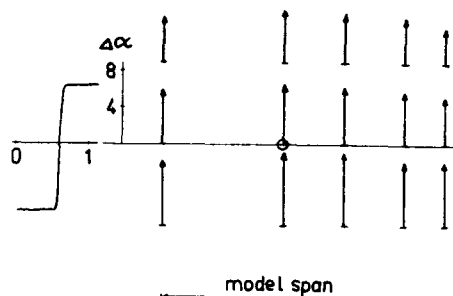


Figure 20 Angle of Attack Induced by Gust Generator at Model Position. Time history at left.

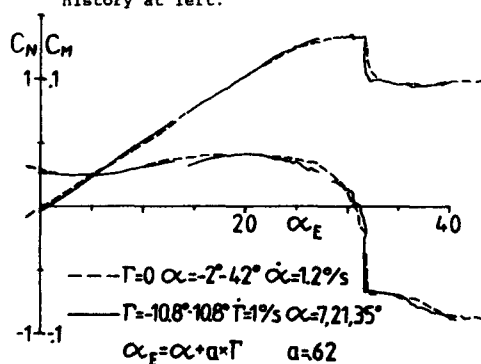


Figure 21 "Static Gusts", at three Model Settings  $\alpha=7^\circ, 21^\circ, 35^\circ$ , Compared to Angle of Attack change at same Rate.  $Re=2.02 \times 10^6$

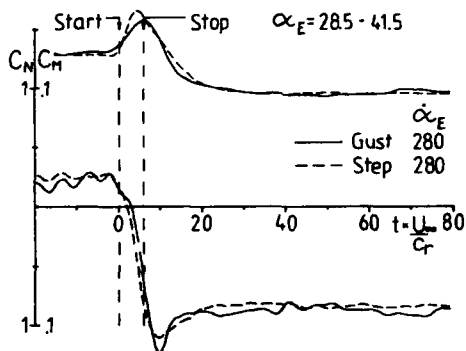
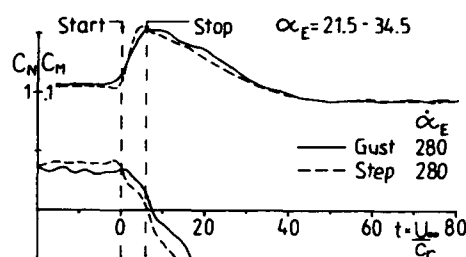
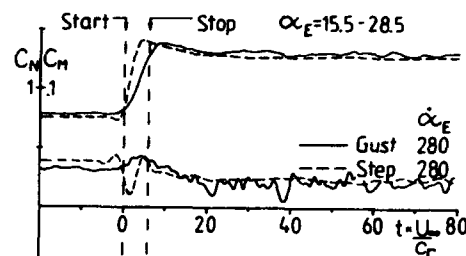


Figure 22 Time Histories for Positive Gust Response. The Start and Stop Times indicated are compensated for the Flow Time from the Gust Generator to the Model.  $Re=2.02 \times 10^6$

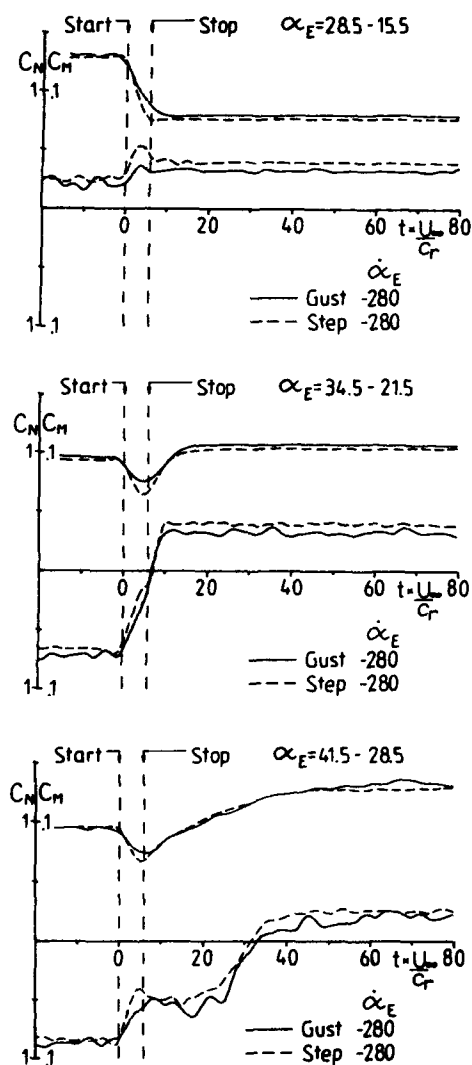


Figure 23 Time Histories for Negative Gust Response. The Start and Stop Times indicated are compensated for the Flow Time from the Gust Generator to the Model.  $Re=2.02 \times 10^6$

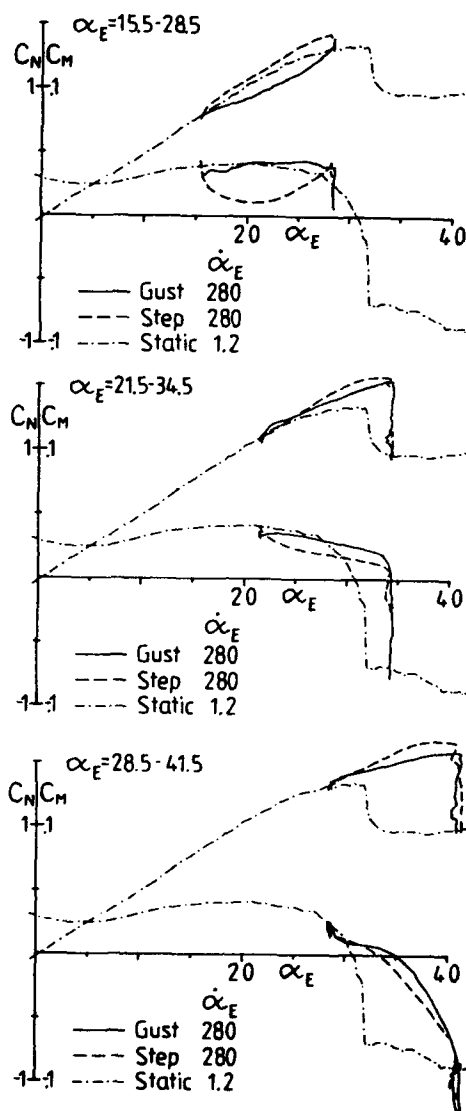


Figure 24 Response to Positive Gusts Plotted over Angle of Attack.

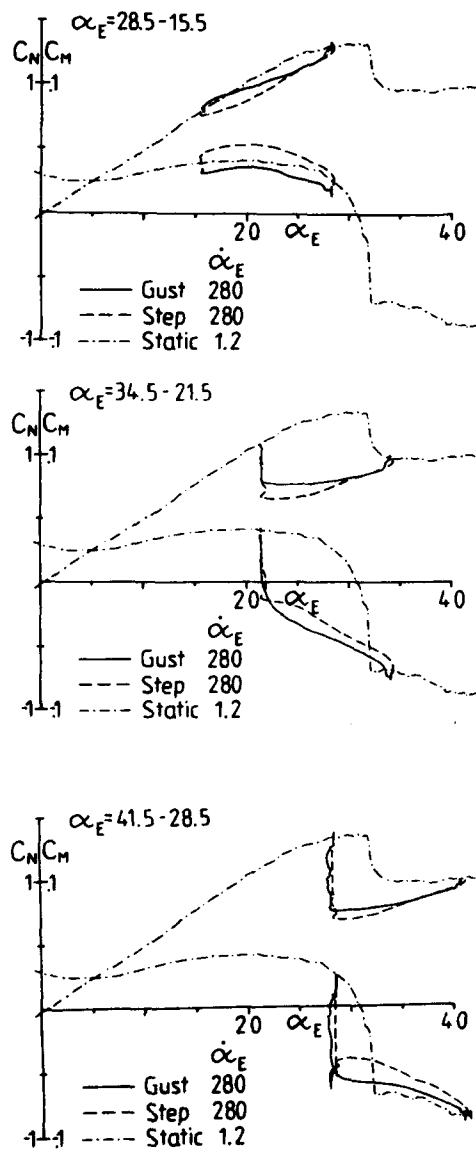


Figure 25 Response to Negative Gusts  
Plotted over Angle of Attack.



**Caractérisation de phénomènes aérodynamiques instationnaires  
à grande incidence**

by

O. Renier

ONERA-IMFL

5, Boulevard Paul Painlevé

59000 Lille

France

**Résumé**

Il est établi que les manoeuvres dynamiques d'un avion d'armes à grande incidence sont le siège de phénomènes aérodynamiques instationnaires de grande amplitude. Ceux-ci ne peuvent être négligés dès que l'on veut maintenir et optimiser le contrôle du mouvement et des attitudes de l'aéronef.

Certaines installations de soufflerie permettent de caractériser ces effets instationnaires. La balance rotative de l'IMFL, en soumettant une maquette d'avion à un mouvement conique oscillatoire a déjà permis de mesurer l'effet de larges variations d'incidence et de dérapage sur différentes géométries d'avions. Un modèle mathématique à base de fonctions de transfert permet de rendre compte de façon satisfaisante de ces phénomènes.

L'IMFL est doté depuis peu d'un moyen d'essai original dans une soufflerie basse vitesse. Celui-ci permet de réaliser des mouvements angulaires dynamiques divers et variés en tangage et/ou en lacet d'un aéronef autour de son centre de gravité, notamment des mouvements périodiques sinusoïdaux, des rampes de vitesse. Il permet encore de simuler l'évolution réelle de l'assiette longitudinale de l'avion de combat lors d'une manoeuvre de pointage. Les performances de cette installation (discretion aérodynamique, vitesse angulaire 600 deg/sec) en font un moyen d'essai privilégié pour l'étude et la caractérisation des phénomènes aérodynamiques de petite ou grande amplitude à grande incidence, en complémentarité avec la balance rotative.

L'exposé comportera donc une présentation de ces moyens d'essais; des résultats illustreront le potentiel de ces outils de simulation dynamique et les techniques de modélisation seront abordées.

**Abstract**

Dynamic manoeuvres of an aircraft at high angles of attack are known to be the origin of unsteady, large amplitude aerodynamic phenomena. These phenomena cannot be neglected if the control of aircraft attitudes and movements has to be optimized.

Such unsteady effects can be characterized on specific wind-tunnel test facilities. Already effects of large incidence and sideslip variations of various aircraft geometries have been measured on the IMFL rotary balance during oscillatory coning motions. They have been globally taken into account in mathematical models using transfer functions.

An original test apparatus has been set up in the IMFL low speed wind-tunnel. Various dynamic pitch and/or yaw motions can be carried out on an aircraft model: sinusoidal or constant angular rate motions or typical pointing manoeuvre attitude evolution. The large performance of this apparatus (low level of airstream perturbation, high angular speed -600°/s) allows to characterize and analyze small and large amplitude, high angles of attack aerodynamic phenomena.

In the proposed paper those test facilities will be described, their dynamic simulation potentialities will be illustrated by some results and modelisation techniques used will be

approached.

#### Notations

$\alpha, \beta$	incidence, dérapage
$\varphi, \theta, \Phi$	angles d'Euler
$C_l, C_m, C_n$	coefficients aérodynamiques de moment de roulis, tangage, lacet
$C_x, C_y, C_z$	coefficients aérodynamiques de force axiale, latérale, normale
$\alpha', \beta'$	vitesse de variation d'incidence $d\alpha/dt$ et de dérapage $d\beta/dt$
$\dot{\theta}', \ddot{\theta}'$	vitesse et accélération angulaires $d\theta/dt, d^2\theta/dt^2$
$\lambda$	angle entre les vecteurs rotation $\Omega$ et vitesse aérodynamique $V$

#### Introduction

L'extension du domaine de vol des avions d'armes, souci permanent des avionneurs, a longtemps été freinée par les frontières naturelles de l'aérodynamique : existence de non linéarités, pertes de stabilité sur certains axes, décollement des écoulements sur les surfaces de contrôle ou sur la voilure complète.

Les systèmes de contrôle de l'avion (commandes de vol électriques) permettent de surmonter certains de ces obstacles : atténuer les effets non linéaires, contrôler les instabilités, etc...

Ce contrôle n'est possible que si le comportement aérodynamique dans le domaine de vol a pu être caractérisé de façon suffisamment fine, selon les différentes sollicitations susceptibles d'être rencontrées en vol. Des moyens d'essais différents sont alors nécessaires pour traduire les effets de mouvements angulaires, de la variation d'incidence, du Mach, de la turbulence...

Aujourd'hui l'ambition affichée des avionneurs est d'étendre au delà du décrochage le domaine du vol contrôlé.

Le principal avantage attendu est l'obtention d'un vecteur force normale

aérodynamique important en module et dont l'orientation, pouvant être choisie dans un domaine plus grand, permet des modifications importantes de la trajectoire, diminue le rayon de virage, ce qui constitue un avantage certain en combat aérien.

En contrepartie, l'incursion aux grandes incidences présente deux inconvénients majeurs : une augmentation significative de la traînée qui induit une forte diminution de la vitesse donc de l'énergie totale de l'aéronef ; l'apparition d'instabilités aérodynamiques coïncidant avec la perte partielle ou totale d'efficacité de certaines gouvernes conventionnelles.

L'émergence de gouvernes moins conventionnelles (canards, strakes,...) associée à des commandes de vol élaborées permet le maintien d'un contrôle relatif des attitudes de l'aéronef à grande incidence. Néanmoins, pour que la perte d'énergie totale ne constitue pas une entrave rédhibitoire, les excursions au delà du décrochage doivent rester brèves ce qui signifie que la dynamique de telles manoeuvres est très importante.

Toute étude préliminaire pour préparer l'avion super manoeuvrant passera donc par la caractérisation du comportement aérodynamique selon des sollicitations nouvelles dans un domaine plutôt subsonique, aux grandes et très grandes incidences, et notamment à des variations rapides de l'incidence et du dérapage, et à des vitesses de roulis et de tangage élevées.

L'objet de cet exposé est de présenter les apports sur ce sujet développés autour de deux moyens d'essais spécifiques en soufflerie de l'IMPL : la balance rotative et le nouveau montage dynamique dénommé "pqr". La cinématique de ces moyens d'essais permet la réalisation de sollicitations dynamiques en particulier sur les variables incidence, dérapage et vitesse de tangage avec des amplitudes et des fréquences qui peuvent être très

importantes.

Après un rappel du contexte dans lequel sont menées les études grandes incidences à l'IMFL, et une description rapide de chaque montage et de sa cinématique, des résultats obtenus sont présentés et analysés. Différentes approches de modélisation des résultats sont proposées et discutées et des confrontations avec des essais en vol illustrées.

#### Les grandes incidences à l'IMFL

Les études en mécanique du vol décroché sont historiquement liées à la mise en oeuvre de la soufflerie verticale à l'IMFL en 1966 (fig. 1). Cette soufflerie est dite de "vrille" car elle permet l'observation de tels mouvements sur des maquettes d'avions de dimension typique 1 mètre, lancées manuellement dans la veine et dont le poids est équilibré par les forces aérodynamiques générées par le courant d'air ascendant piloté en vitesse par un opérateur. Le diamètre de la veine -ouverte- étant de 4 mètres, il est possible d'analyser certains mouvements transitoires : changement d'équilibre, sortie de vrille induite par des instabilités ou par un braquage radio piloté des gouvernes, influences des conditions initiales.

Ce sont plus de 200 configurations de maquettes d'avions qui ont été testées en soufflerie pour des besoins de certification, de recherche de consignes pour récupérer le vol contrôlé, pour déterminer des dispositifs de secours ou encore pour proposer des modifications géométriques. Des études paramétriques ont également été menées sur des maquettes modulables pour cerner l'influence du centrage, des surfaces des gouvernes, du décentrage latéral ou encore l'impact des virures d'avant-corps, de quille sous fuselage, etc. C'est par la variété des études et des configurations étudiées que se sont forgés le savoir faire et la réputation de l'établissement.

L'ensemble des résultats acquis décrivent essentiellement des

comportements et l'influence des divers paramètres sur ceux-ci. Les comportements sont quantifiés par un nombre limité de variables globales comme l'attitude moyenne, la durée d'un tour de vrille stabilisée, le nombre de tours de vrille avant récupération, etc. Des variables plus qualitatives précisent la nature des agitations perturbant le mouvement ou encore le type de sortie de vrille.

Il y a une quinzaine d'années s'est fait sentir le besoin d'analyser de façon plus précise et plus quantitative le phénomène de la vrille. C'est donc en ce sens qu'a été développé un dispositif tournant de mesures d'efforts globaux sur maquette en soufflerie, appelé balance rotative. Celle-ci est équipée d'un certain nombre de degrés de liberté associés aux critères servant à caractériser un mouvement de vrille: l'attitude moyenne, l'angle d'assiette latérale, le taux de rotation, le cap relatif (calage angulaire de la maquette dans le repère tournant), le rayon de vrille, le taux d'agitations, figuré par un angle entre les vecteurs vent et rotation générant lors du mouvement des variations périodiques de l'incidence et du dérapage, d'amplitude variable (fig.2).

Cette approche cinématique devait permettre de retrouver, en simulant un mouvement de vrille stabilisée légèrement oscillatoire, l'équilibre entre les moments d'inertie et les moments aérodynamiques mesurés par la balance. Ce montage justifiait alors pleinement l'appellation de montage de "simulation dynamique". La figure 3.a illustre à ce titre la nature des évolutions de l'incidence et du dérapage au cours d'une vrille échelle 1 et celles reproduites par le montage.

De fait cette installation trouva un créneau d'utilisation beaucoup plus large que celui circonscrit à la vrille. En effet la cinématique permet une exploration assez exhaustive des effets aérodynamiques induits par la rotation dans un large domaine d'incidence et de dérapage. Dès lors

ce montage est utilisé pour générer des bases de données de coefficients aérodynamiques globaux. Ces bases ont été dans le cadre d'études générales exploitées de façon à construire un modèle mathématique de représentation des efforts aérodynamiques. A partir de là il est possible de réaliser des simulations numériques du vol de l'avion et d'étudier la sensibilité des résultats à divers paramètres.

Le souci de confronter les résultats trouvés ainsi par la simulation à la réalité a conduit l'IMFL à développer des moyens expérimentaux permettant de réaliser des essais en vol de maquettes et de restituer quantitativement l'état et les coefficients aérodynamiques de l'avion au cours du vol. L'instrumentation des maquettes en capteurs accélérométriques et gyrométriques, et de la station en moyens optiques fixes a permis d'étudier le mouvement de vrille d'une maquette dans la soufflerie verticale ainsi que des trajectoires à forte dynamique de tangage d'une maquette non motorisée catapultée dans le laboratoire d'étude de perte de contrôle et des grandes incidences (fig.4).

Parallèlement d'autres moyens de caractérisation aérodynamique ont été développés. L'étude des mouvements d'échappée en roulis ("wing-rock") est aujourd'hui faisable par l'adaptation d'un dispositif sur la balance rotative. Enfin, l'étude des mouvements à forte dynamique de tangage est aujourd'hui réalisable à l'aide d'un moyen d'essais nouveau appelé "pqr" et installé dans soufflerie horizontale basse vitesse de l'IMFL.

#### La balance rotative de l'IMFL

Nous avons eu l'occasion d'évoquer ce moyen d'essais dynamique et sa contribution dans l'identification des paramètres de stabilité dynamique à faible incidence. Rappelons en quelques lignes les principales caractéristiques de ce dispositif. Celui-ci est installé dans la soufflerie verticale de l'IMFL, à

retour à veine ouverte, circulaire de 4 mètres de diamètre. La vitesse de vent est limitée à 40m/s. La cinématique permet de positionner une maquette dans un large domaine d'incidence dérapage (fig.5). La rotation de la balance peut s'effectuer à une fréquence voisine de 2 Hz. L'originalité de cette installation tient en ce que l'ensemble des parties tournantes peut être incliné d'un angle  $\lambda$ , limité à 20 degrés par rapport à la direction du vent infini amont. Il en résulte que le mouvement conique classique (les paramètres incidence, dérapage, taux de rotation sont constants dans le temps) devient conique oscillatoire dès que le paramètre  $\lambda$  est non nul (incidence et dérapage varient cycliquement et en quadrature au cours d'un tour avec une amplitude  $\lambda$  ; les taux de rotation demeurent constants (fig.6)).

C'est cette particularité qui, utilisée à faible incidence, nous permet d'identifier sur cette seule installation et à l'aide d'essais appropriés les paramètres de stabilité d'un modèle linéaire:  $C_{mq}$ ,  $C_{m\dot{\alpha}}$ ,  $C_{lp} + C_{l\dot{\beta}} \sin \alpha$  etc... (fig.7)

Aux incidences supérieures, les essais coniques oscillatoires mettent en évidence l'invalidité de l'hypothèse de linéarité et l'apparition des phénomènes d'hystérésis liés aux instabilités des écoulements, ou au retard à leur établissement, et dont le décrochage dynamique est une illustration (fig.8).

Ces phénomènes sont maintenant bien connus. Et bien que l'écoulement soit de nature différente entre les cas bi- et tri-dimensionnels, les courbes caractéristiques de l'évolution des coefficients de force normale  $C_z$  et de moment de tangage  $C_m$ , mesurés sur une aile en flèche lors de tels essais sont tout à fait similaires à celles obtenues depuis la caractérisation d'un profil bi-dimensionnel en oscillation de tangage (fig.9).

La balance rotative de l'IMFL a donc

été conçue pour simuler notamment des mouvements de type vrille. Le paramètre  $\lambda$ , angle entre les vecteurs rotation et vitesse correspond, pour un mouvement de maquette à centre de gravité immobile à l'amplitude des agitations couplées ( $\alpha$  ;  $\beta$ ) se superposant au mouvement moyen stationnaire de la vrille.

Mais ce paramètre est aussi par définition une variable aérodynamique. Il peut donc être calculé à tout instant au cours d'un essai en vol de vrille de l'avion. La figure 10 présente l'évolution du couple ( $\alpha, \lambda$ ) au cours d'une vrille qui se stabilise après agitations à une incidence moyenne de  $40^\circ$  environ ; le paramètre  $\lambda$  est alors voisin de  $2^\circ$  ce qui traduit un régime très légèrement oscillatoire. Mais il faut noter que dans toute la phase d'entrée en vrille  $\lambda$  tend vers  $90^\circ$  ce qui correspond à un mouvement de tangage pur à cabrer, que le pilote donne à l'avion pour aller chercher l'incidence de décrochage. Puis par l'action du gauchissement et de la direction le mouvement de rotation en roulis et en lacet devient prépondérant ; le paramètre  $\lambda$  diminue. Mais dans toute la phase transitoire, les amplitudes des variations d'incidence et de  $\lambda$  sont très importantes et la valeur limite  $\lambda = 20^\circ$  de la balance rotative est très largement dépassée.

Il y a quelques dizaines d'années l'entrée en vrille de l'avion constituait la première incursion -involontaire- dans le domaine des grandes incidences. Si aujourd'hui elle n'est provoquée volontairement que pour des besoins de certification ou pour l'acrobatie aérienne, elle n'en demeure pas moins intéressante à étudier car il y a une bonne similitude entre la dynamique de l'entrée en vrille et celle d'une manoeuvre de type pointage de l'axe avion ou d'un demi-tour tri-dimensionnel. La figure 11 présente l'évolution temporelle de  $\lambda$  au cours d'une telle manoeuvre (simulée). L'incidence a été limitée à  $35^\circ$ . La valeur de  $\lambda$  reste élevée et proche de  $90^\circ$  le long de la

trajectoire.

Si la balance rotative constitue un moyen privilégié de caractérisation aérodynamique à grande incidence, il présente une certaine limite d'utilisation. Par définition, le mouvement conique privilégie en premier lieu la rotation autour d'un axe proche du vent:  $\Omega = p_a$ , taux de roulis aérodynamique. En fonction de l'incidence, il se projettera selon  $p$  ou  $r$ , taux de roulis et de lacet, exprimés en axes avion et qu'il privilégie donc par rapport à la vitesse de tangage dont l'obtention n'est possible que si on met la maquette en dérapage.

Par ailleurs, les variations couplées d'incidence dérapage, obtenues en mouvement conique oscillatoire induisent des effets aérodynamiques qui ne sont généralement séparables qu'aux faibles incidences.

Enfin les effets de montage, interaction maquette- dispositif peuvent en particulier être source à grande incidence du décrochage prématuré des surfaces portantes, surtout dans le domaine des faibles vitesses ( $V < 40 \text{ m/s}$ ).

L'étude il y a une dizaine d'années d'un dispositif de soufflerie sollicitant une maquette selon les 3 axes  $p, q$  et  $r$  a montré la difficulté d'interprétation des résultats de mesures du fait d'une discrétion aérodynamique insuffisante du montage.

#### Le montage dynamique "pqr"

C'est pour ces raisons que l'IMFL a doté sa soufflerie horizontale basse vitesse d'un outil de simulation dynamique orienté vers la caractérisation aérodynamique d'une maquette lors de mouvements à forte dynamique de tangage ( $q_{\text{max}} = 600^\circ/\text{s}$ ) et dessiné de façon à minimiser les interactions avec la maquette (fig.12).

Ce montage reproduit cinématiquement les degrés de libertés associés aux angles d'Euler couramment utilisés en

mécanique du vol. Les angles  $\Psi$  (cap) et  $\Phi$  (assiette latérale) sont ajustables mais constants au cours d'un essai. Le degré  $\theta$  (assiette longitudinale) est motorisé. L'ensemble est installé dans la soufflerie horizontale de l'IMFL, de diamètre 2.4 mètres, en configuration veine ouverte. La maquette est montée par un dard arrière, son centre de gravité est immobile. L'ensemble a été dessiné de façon à rejeter hors veine les éléments "lourds" du dispositif. L'utilisation de matériaux composites, à la fois légers et rigides pour les parties mobiles (bras et dard) a permis d'obtenir des performances tout à fait intéressantes. Ses caractéristiques sont les suivantes:

$$\begin{aligned} -25^\circ < \Psi < +25^\circ \\ -15^\circ < \Phi < 105^\circ \\ -90^\circ < \theta < 100^\circ \\ |\dot{\theta}| < 500^\circ/\text{s} \\ |\dot{\theta}| < 5000^\circ/\text{s} \\ V < 50\text{m/s} \end{aligned}$$

fréquence 1er mode structural: 13.5 Hz  
(masse typique maquette: 3.5 Kg)

La motorisation de l'axe en  $\theta$  est assurée par un vérin rotatif hydraulique capable d'accélération et de vitesses élevées.

Les possibilités cinématiques de ce dispositif peuvent être illustrées par la figure 13, donnant les relations entre les angles d'Euler  $\Psi$ ,  $\theta$  et  $\Phi$  et les angles  $\alpha$  et  $\beta$ .

Il apparaît que:

- toute variation de  $\theta$  induit une variation d'incidence et/ou du dérapage quels que soient  $\Psi$  et  $\Phi$ ;

- à  $\Phi$  nul, le domaine  $-90^\circ < \alpha < 100^\circ$ ,  $-25^\circ < \beta < 25^\circ$  peut être exploré en variations d'incidence à iso dérapage. Dans ce cas, on a la relation  $q = \alpha'$ ;

- à  $\Phi$  égal à  $90^\circ$ , incidence et dérapage sont échangés ainsi que les taux de lacet et de tangage.  $r$  et  $\beta'$  sont liés par la relation  $r = -\beta'$  et les effets de ces paramètres peuvent être caractérisés jusqu'à  $25^\circ$  d'incidence.

Le champ d'étude offert par ce montage

est donc multiple:

- En statique, la caractérisation dans un très large domaine d'incidence ( $-100^\circ < \alpha < 100^\circ$ ), pour des dérapages inférieurs à  $25^\circ$  peut être réalisée dans d'excellentes conditions aérodynamiques. En particulier au delà de  $40^\circ$  le bras en fibre de carbone sort totalement du champ de la veine d'expérience de la soufflerie.

- L'identification de certains paramètres de stabilité à faible incidence ( $\alpha < 25^\circ$ ) est possible. Des termes comme  $(C_{m\alpha} + C_{m\alpha'})$ ,  $(C_{nr} - C_{n\beta} \cos \alpha)$  peuvent être calculés pour différentes valeurs de l'incidence, par des sollicitations de type harmonique d'amplitude modérée en  $q$  ( $\alpha'$ ) ou en  $r$  ( $-\beta'$ ).

Il faut noter que le centre de gravité de la maquette demeurant fixe dans la veine, l'écriture d'une accélération nulle en ce point  $\Gamma(g) = 0$  conduit à des relations intrinsèques entre les variables aérodynamiques et en particulier entre  $\beta'$ ,  $\alpha$ ,  $p$  et  $r$ :

$$\beta' + r \cos \alpha - p \sin \alpha = 0$$

Comme pour les essais sur balance rotative, soumis à la même contrainte, ce montage n'apporte pas la possibilité de découpler les effets de  $p$ ,  $r$  et  $\beta'$ . Par contre, il réalise une sollicitation différente à l'intérieur de cette relation et à ce titre est tout à fait complémentaire du montage tournant puisqu'il permet par combinaison des types d'essais, d'augmenter les précisions sur deux des paramètres identifiables  $C_{lp} + C_{l\beta} \sin \alpha$ ,  $C_{lr} - C_{l\beta} \cos \alpha$  ainsi que l'illustre la figure 14.

- Les effets stationnaires des variations d'incidence peuvent être caractérisés.

Le dispositif de pilotage du mouvement a été déterminé de façon à imposer une loi  $\theta(t)$  quelconque dans la limite de la bande passante de l'ensemble actionneur + partie mobile + maquette. En particulier peuvent être réalisées (fig.15):

- des lois sinusoïdales

$$\theta(t) = \theta_0 + \theta_M \sin 2\pi f t.$$

Les valeurs de  $\theta_M$  et de  $f$ , amplitude et fréquence de la sollicitation sont soumises aux seules contraintes:  
 $|\dot{\theta}'_{\max}| = 2\pi f \theta_M < 500^\circ/\text{s}$  et  $|\ddot{\theta}''_{\max}| = 4\pi^2 f^2 \theta_M < 5000^\circ/\text{s}$  et dans la limite du débattement disponible:  $-100^\circ < \theta < 100^\circ$ .  
 Le choix d'une amplitude faible (1 à  $2^\circ$ ) et d'une fréquence de l'ordre de 5 Hz correspond à une sollicitation typique de dispositif en oscillations forcées. En limitant la fréquence à 1 Hz des oscillations de tangage de très grande amplitude ( $100^\circ$ ) peuvent être obtenues.

- des lois de type rampe  $\theta = \theta_0 + \theta' t$ ,  
 $\theta' = \text{constante}$ .

Ces essais sont plus sévères que les précédents au sens où, pour obtenir une vitesse de tangage  $\theta'$  constante sur l'intervalle  $[\theta_1, \theta_2]$  le plus large possible, il faut utiliser l'accélération maximale  $\theta''$  lors des phases de mise en vitesse et de décélération avant arrêt.

- des lois quelconques  $\theta(t)$ .

Celles-ci peuvent être choisies de façon à reproduire l'historique de l'incidence d'une manoeuvre de type pointage de l'axe avion à grande incidence et retour au vol normal. Des essais en vol d'une maquette d'avions d'armes, réalisés dans les laboratoires de l'IMFL ont permis de produire des excursions à grande dynamique de tangage, par braquage à cabrer, puis à piquer des élevons et des canards, dont l'évolution typique de l'incidence est tout à fait reproductible sur le montage "pqr" (fig. 3b).

#### Traitement des essais

Le traitement des essais provenant de montages de simulation dynamique nécessite une attention particulière. Qu'elles soient produites par une balance rotative ou un montage "pqr", les mesures sont généralement entachées de bruits parasites, correspondants à des modes structuraux des montages, fortement sollicités

lors de tels essais.

Sur la balance rotative, la rotation en cap des parties tournantes est continue et régulière, les efforts pulsés de la gravité étant compensés par une régulation de la vitesse autour d'une valeur nominale. Les fréquences propres de l'ensemble, identifiées au préalable à chaque campagne d'essai, sont généralement supérieures à 15 Hz et donc aux fréquences des phénomènes instationnaires qui nous intéressent. La sollicitation étant périodique, l'élimination des fréquences structurales est aisément réalisée par un traitement FFT.

Sur le montage "pqr", le mouvement est contrôlé par un système de pilotage de l'actionneur hydraulique, prenant en compte des informations de pression, de vitesse et de position angulaire. La commande d'un mouvement donné est obtenue en appliquant à l'entrée de ce système la consigne  $\theta_c(t)$  à suivre. Le mouvement effectivement réalisé prend en compte la fonction de transfert de l'ensemble.

Il s'ensuit qu'à une loi demandée  $\theta_c$  sinusoïdale correspond une loi effective sensiblement de même type, mais pouvant comporter de légères distorsions sous forme d'harmoniques, faibles en amplitude mais non nulles, et qui sont mesurées par la balance. Traduites sous forme d'ondulations résiduelles, elles diminuent légèrement la précision de la mesure car il est délicat de supprimer par traitement ces fréquences qui peuvent être faibles et traduire une réalité aérodynamique.

Le traitement des essais de type rampe, ou plus généralement de ceux pour lesquels une loi quelconque est programmée, s'apparente à celui qu'on applique à des essais en vol. Un filtrage passe bas, à une fréquence qu'il faut déterminer en fonction des raies structurales du montage et des réponses à des sollicitations harmoniques préalables, constitue l'approche souhaitable.

Lors d'essais sur des montages dynamiques en soufflerie, la procédure classique de traitement par différence entre un essai "avec vent" et un essai cinématiquement similaire "sans vent" n'est pas rigoureuse. En effet, des efforts aérodynamiques faibles peuvent résulter d'un mouvement rapide de la maquette dans l'air au repos. Ceci n'est particulièrement sensible que sur les mesures de moments, dans le cas où le c.g. de la maquette est maintenu immobile.

On substitue à cette procédure celle qui consiste à calculer les efforts induits par les forces de gravité et d'inertie qui, retranchés aux efforts mesurés lors d'un essai avec vent, font apparaître la seule contribution aérodynamique.

Cette démarche, tout à fait rigoureuse, nécessite au préalable une identification précise des parties pesées par la balance : centre de pesée, moments d'inertie. Cette identification est possible à l'aide du moyen d'essais lui-même, par des essais sans vent appropriés.

Cette démarche est indispensable pour le traitement des essais sur le montage "pqr". En effet, la reproductibilité rigoureuse de l'historique  $\theta(t)$ , au cours d'un essai, n'est pas assurée comme pour la balance rotative, par des liaisons cinématiques intrinsèques. Le système de pilotage du mouvement est influencé par la charge aérodynamique lors de l'essai avec vent, et on relève lors de mouvements de type "rampe" de légers écarts de vitesse  $\dot{\theta}$  pour la même position  $\theta$ .

Le montage "pqr" offre une bonne discrétion aérodynamique du fait d'un montage de la maquette par dard arrière notamment. En contre partie, le bras semi elliptique, reprenant en son milieu l'embase du dard, objet de mouvements amples et rapides, est sujet à des déformations d'autant que le couple moteur est appliqué à une extrémité du bras, l'autre étant libre en rotation. La recopie de position angulaire, placée à proximité de

l'actionneur, fournit une information d'attitude  $\theta$ , qui a été comparée à des informations gyrométriques et accélérométriques en provenance de la maquette. Les capteurs embarqués (deux accéléromètres en "Z", situés à l'avant et à l'arrière, et un gyromètre en tangage) présentent des signaux corrélés, mais légèrement déphasés par rapport à l'information de position. Ce décalage met en évidence la déformation élastique de l'ensemble bras+dard. Il traduit un écart pouvant atteindre environ 2 degrés entre l'attitude indiquée et celle réelle de la maquette lors d'un essai sinusoïdal d'amplitude  $15^\circ$  et de fréquence 1 Hz.

La souplesse du montage est donc à intégrer dans le traitement de la mesure. Deux démarches sont possibles :

- 1- instrumenter la maquette (à l'aide d'une instrumentation légère de façon à limiter l'ajout de masse et donc la diminution de la fréquence du premier mode structural) ;
- 2- déterminer par le calcul, pour chaque maquette, la déformation dynamique de l'ensemble des parties mobiles en fonction du mouvement et des efforts mesurées par la balance.

#### Analyse des essais

Une fois effectuée la phase de traitement de mesures, la reconnaissance des phénomènes instationnaires est réalisée par l'analyse des coefficients aérodynamiques globaux et la recherche des paramètres influents. Comme déjà évoqué plus haut, les phénomènes dynamiques observés sur des maquettes de l'avion complet relèvent de la même nature que ceux aujourd'hui bien reconnus sur des profils bi-dimensionnels. Rappelons ici les caractéristiques les plus marquées depuis les figures 8,16 et 17, relatives à des essais sur balance rotative.

La variation rapide d'incidence sur



une maquette d'avion induit des variations de force de portance et de moment de tangage, très importantes en module et dont l'amplitude dépend: du sens de variation de l'incidence, de l'amplitude et de la fréquence de la sollicitation et de l'incidence moyenne autour de laquelle sont effectués les essais. La figure 8 présente l'influence de l'amplitude et de l'incidence moyenne sur une géométrie d'avion à aile en flèche, la figure 16 celle de l'incidence moyenne sur une maquette d'avion à voilure delta et la figure 17 celle de la fréquence sur une plaque delta. On constate que:

- 1- l'influence des variations d'incidence est significative dès que l'incidence franchit la limite de décrochage statique ;
- 2- l'amplitude du phénomène croît avec l'amplitude des oscillations et avec leur fréquence ;
- 3- la montée rapide en incidence a pour effet de prolonger la caractéristique statique bien au delà de l'incidence de décrochage statique.

Comme pour un profil, le phénomène apparaît directement piloté par la vitesse de variation d'incidence. Cette similitude semble indiquer une faible dépendance des coefficients longitudinaux vis-à-vis du dérapage et des taux de rotations  $p$  et  $r$  nécessairement non nuls lors des essais coniques oscillatoires et donc à la nature hélicoïdale de l'écoulement moyen autour de la maquette.

Les figures 18 à 20 présentent les tracés d'essais issus du montage dynamique "pqr", réalisés sur une maquette d'avion à voilure delta. Elles illustrent respectivement:

- 1- l'effet d'incidence moyenne lors d'essais sinusoïdaux, d'amplitude  $10^\circ$ . Ces courbes peuvent être comparées à celles de la figure 18 relative à des

essais coniques oscillatoires de même amplitude. Bien que les mouvements soient de nature cinématiquement différente, l'apparition de phénomènes instationnaires de grande amplitude se produit dès l'incidence de décrochage statique. On notera également l'inversion de la stabilité en tangage (donnée par le sens de parcours des essais) ;

- 2- l'effet de très grande amplitude ( $A=30^\circ$ ) lors d'un essai à 1 Hz (fig.19) ;

- 3- l'effet de deux sollicitations de type "rampe", réalisant l'une, le parcours  $[0^\circ, 60^\circ]$  en incidence, l'autre le parcours inverse (fig.20). La vitesse de tangage est comparable à celle de l'essai précédent à environ  $30^\circ$  d'incidence. Il est intéressant de noter que les effets instationnaires dans ce cas sont encore plus importants. En particulier la rampe en incidence décroissante ne rejoint pas la caractéristique statique avant la fin de l'essai. Ceci souligne une fois de plus l'importance de l'historique  $\alpha(t)$  dans le comportement de l'écoulement sur les surfaces portantes de la maquette.

Les caractéristiques latérales, au travers des coefficients globaux  $C_y$ ,  $C_l$  et  $C_n$  présentent une plus grande "résistance" à l'analyse. Issus d'essais sur la balance rotative, les effets conjugués de l'incidence et du dérapage viennent se superposer à ceux supposés de  $p$ ,  $r$  et  $\beta$  et compliquent ainsi l'interprétation des courbes comme celles de la figure 21.

#### Modélisation

L'analyse des effets instationnaires sur les coefficients aérodynamiques globaux mesurés sur la balance rotative comme sur le montage "pqr" a donc montré le rôle prépondérant, en

ce qui concerne les caractéristiques longitudinales, de la vitesse de variation d'incidence  $\alpha'$ . La difficulté d'analyse des caractéristiques latérales nous amène à faire quelques hypothèses afin d'élaborer une donnée moins "hermétique" à la compréhension.

On fait donc l'hypothèse que les effets purement instationnaires (induits par la variation rapide de  $\alpha$  ou  $\beta$ ) viennent s'ajouter à ceux mesurés lors de sollicitations stationnaires. Cette hypothèse d'additivité des effets nous permet d'écrire que la contribution instationnaire  $\Delta C_i$  peut être calculée par :

$$\Delta C_i = C_i \text{ global} - C_i \text{ modèle stationnaire}$$

La partie stationnaire doit donc avoir été caractérisée et modélisée par ailleurs de façon à traduire les effets statiques (incidence, dérapage, gouvernes) ainsi que les effets de la rotation stationnaire (termes induits par la vitesse de roulis en repère aérodynamique).

Le traitement des essais coniques oscillatoires s'appuie donc sur d'autres essais, statiques, et coniques non oscillatoires, fournis par le même moyen d'essai. Par contre le traitement des essais oscillatoires du montage "pqr" fait nécessairement appel à des essais stationnaires qui ne peuvent être fournis par la même installation.

L'élaboration d'une donnée traduisant l'effet purement instationnaire a été réalisée pour les coefficients longitudinaux et latéraux. La figure 22 présente les tracés des contributions instationnaires  $\Delta C_z$  et  $\Delta C_m$  pour différents essais coniques oscillatoires en fonction de l'incidence.

L'hypothèse d'additivité ne semble pas être remise en cause sur ces caractéristiques longitudinales. Chaque essai présente la forme d'une courbe fermée sensiblement elliptique dont la dimension et l'inclinaison

dépend de l'incidence et de l'amplitude. Il apparaît donc que l'approche de la modélisation de ces effets par fonction de transfert est envisageable.

Les courbes de la figure 23.a sont relatives aux contributions instationnaires en moment de roulis  $\Delta C_l$ , tracées pour différents essais en fonction du dérapage. Le parallélisme que l'on est naturellement enclin à établir entre les coefficients transversaux et la variable  $\beta'$  ne permet pas de mettre ici en évidence de façon aussi claire l'influence des différents paramètres sur les contributions latérales. A cela plusieurs raisons sont possibles: non validité de l'hypothèse d'additivité des effets aérodynamiques; influence simultanée de plusieurs variables aérodynamiques  $\alpha$ ,  $\beta$ ,  $\beta'$ ,  $p$ ,  $r$ ,...

Le tracé d'essais, nécessairement en nombre limité, dans un plan ( $\Delta C_i, \beta$ ) ne donne qu'une vue trop parcellaire de l'information contenue dans l'ensemble des essais. Une autre approche consiste à projeter la base de données dans un espace à plusieurs dimensions ( $\Delta C_i, \alpha, \beta', \lambda$ ) et à visualiser différents plans ( $\Delta C_i, \beta'$ ) en paramétrant les autres variables. La figure 23.b présente la contribution instationnaire  $\Delta C_l$  en fonction de  $\beta'$ , pour tous les essais de faible amplitude  $\lambda = 2^\circ$  et pour différentes valeurs de l'incidence moyenne  $\alpha_m$ . Cet éclairage particulier souligne la dépendance "attendue" à la vitesse de variation de dérapage  $\beta'$ , tout en faisant apparaître l'influence de la valeur moyenne de l'incidence.

Cette approche, telle qu'elle a été ici réalisée, enlève toute notion temporelle à l'analyse. Celle-ci peut cependant être introduite par l'adjonction parmi les variables de la dérivée temporelle des quantités  $\Delta C_i$ .

#### Modélisation par interpolation

Comme nous l'avons dit plus haut, la modélisation des effets instationnaires peut être approchée par des fonctions de transfert. Avant

de développer ce point, citons une autre possibilité originale, qui peut être envisagée dès l'instant où une base de données "instationnaires" importantes peut être obtenue. Elle consiste à approximer les effets instationnaires qui apparaissent le long d'une trajectoire de l'avion, caractérisée par son état aérodynamique  $x = (\alpha, \beta, p, q, r, \delta_j, \dots)$  et de sa dérivée, par ceux qui sont générés au cours d'essais coniques oscillatoires "tangents" (incidence et dérapage moyens, amplitude, vitesse de rotation) et qui sont calculés au point de tangence par interpolation depuis des essais coniques oscillatoires voisins disponibles dans la base de données (figure 24)

Cette approche ne fait pas apparaître explicitement la notion de temps, autrement que par la prise en compte des dérivées  $\alpha'$  et  $\beta'$ .

Elle présente naturellement une certaine restriction puisqu'elle consiste à projeter l'état de l'avion, défini dans un espace à  $n$  dimensions sur une hypersurface dont les équations sont celles des liaisons cinématiques de la balance rotative.

De même, en s'appuyant sur la similitude d'un mouvement de l'aéronef avec une rotation conique oscillatoire elle privilégie les mouvements de nature hélicoïdale (vrilles, tonneaux) au détriment de ceux où la vitesse de tangage devient importante (ressource, dépointage axe avion).

Cette approche a par contre l'avantage de ne pas faire appel à une structure de modèle particulière et de calculer les efforts aérodynamiques directement depuis les mesures. Actuellement à l'étude, l'intégration dans la base de données d'essais issus du montage dynamique "pqr" devrait permettre d'élargir le domaine de validité de ce type de modélisation.

#### Modélisation par fonction de transfert

L'analyse des contributions instationnaires et l'influence des

différentes variables permet d'envisager pour les caractéristiques longitudinales la modélisation de ces contributions par une fonction de transfert  $H$  dont l'entrée sera la vitesse de variation d'incidence  $\alpha'$ , et dont les différents paramètres peuvent dépendre des variables aérodynamiques reconnues comme sensibilisantes (incidence,  $\lambda, \dots$ ) ainsi que des gouvernes.

Considérons une fonction de transfert simple du premier ordre. Lorsque l'incidence est faible, cette fonction se réduit à un terme de gain qui n'est autre que le paramètre de stabilité  $C_{L\alpha}$ , d'un modèle linéaire. Aux incidences plus élevées la constante de temps de la fonction  $H$  est non nulle et permet de traduire le décalage temporel entre la variation d'incidence et l'effet instationnaire.

Un raisonnement identique peut être conduit sur les caractéristiques instationnaires latérales en substituant à  $\alpha'$  le terme  $\beta'$ . Mais la complexité du phénomène en latéral limite les possibilités d'identification d'une fonction  $H$  élaborée.

La figure 25 qui présente la restitution d'un essai conique oscillatoire par un tel modèle, comparée à la mesure des coefficients globaux  $C_z$  et  $C_m$  illustre le fondement de la structure de la fonction  $H$  choisie.

#### Corrélation avec les phénomènes instationnaires à échelle avion

Le problème de la validation des mesures effectuées sur une maquette à échelle réduite, et de leur transposition au phénomène à grandeur réelle a trouvé une illustration par l'exploitation d'essais en vol de vrilles de l'avion considéré suffisamment instrumenté pour que soit possible la restitution de l'ensemble des variables et des coefficients aérodynamiques au cours du vol. La figure 26 présente l'évolution de l'incidence au cours d'un mouvement de vrille stabilisée qui comporte des

agitations importantes dont l'amplitude peut atteindre 20°. Par ailleurs ont été tracées au cours du temps les évolutions du coefficient de force normale  $C_z$  issu du vol et de celui calculé par le modèle. Dans un cas il s'agit d'un modèle aérodynamique stationnaire de l'avion, dans l'autre cas d'un modèle aérodynamique instationnaire, modèles identifiés depuis les essais sur la balance rotative.

Il apparaît d'une part que les effets instationnaires en vol sont importants en module et d'autre part que la prise en compte de ces contributions instationnaires mesurées en soufflerie permettent de réduire singulièrement les écarts avec le vol.

#### Conclusion et perspectives

L'extension du domaine de vol des avions d'armes et la recherche d'une manoeuvrabilité et d'un contrôle plus large conduit nécessairement les mécaniciens du vol à s'intéresser aux évolutions de l'aéronef à grande incidence, évolutions pouvant présenter une grande dynamique sur les différentes variables caractérisant l'état de l'avion.

Dans ce contexte, les montages de simulation dynamique de soufflerie présentent un grand intérêt pour la caractérisation des phénomènes aérodynamiques, indispensables pour prédire le comportement de l'avion "planeur" et l'élaboration des commandes de vol exploitant tout le potentiel aérodynamique de l'aéronef.

Avec les moyens d'essais que sont la balance rotative et depuis peu le montage dynamique "pqr", l'IMFL offre cette possibilité, en privilégiant pour l'un, les sollicitations en écoulement moyen hélicoïdal (taux de roulis aérodynamique important) et pour l'autre la simulation des mouvements à forte dynamique de tangage.

L'analyse des essais instationnaires, réalisés sur des maquettes d'avions montre la similitude des phénomènes

avec ceux bien connus relevés sur des profils bi-dimensionnels et dont le décrochage dynamique constitue une illustration.

L'importance des effets instationnaires confirme la nécessité de leur prise en compte dans un modèle d'évolution du vol de l'avion. La modélisation aérodynamique globale des phénomènes peut être réalisée sur les caractéristiques longitudinales et l'approche par fonction de transfert à coefficients non constants constitue une démarche satisfaisante. Leur prise en compte a permis de réduire de façon significative les écarts modèle-mesure aux cours d'essais à l'échelle avion de vrille, confirmant par ailleurs la réalité des phénomènes instationnaires sur l'avion.

Les caractéristiques instationnaires latérales mesurées sur balance rotative sont plus difficiles à analyser en raison de l'influence de plusieurs variables évoluant simultanément. Les sollicitations plus pures (en dérapage, en incidence) faciliteraient leurs compréhension.

Les développements expérimentaux actuellement envisagés concernent le nouveau montage dynamique "pqr". L'utilisation d'un dard coudé permettra de solliciter une maquette en dérapage à grande incidence. La motorisation du degré de liberté  $\Phi$  (axe de roulis) donnera la possibilité de réaliser des évolutions plus complexes en dérapage. Le montage justifiera pleinement son nom ("pqr") par la réalisation de sollicitations selon ces trois axes (au lieu de deux actuellement).

Outre l'amélioration des procédures d'essais (notamment par la prise en compte par le calcul des déformées du montage sous charges), cette installation pourrait être utilisée en contrôle "actif" pour une simulation de la trajectoire, c'est à dire en imposant les variations d'attitude qui respectent l'équation de moment de tangage ( $B_q = M$ ).

L'utilisation d'une maquette dont les

gouvernes sont motorisées devra permettre de valider une loi de commande pour la réalisation d'une trajectoire (évolution  $\alpha(t)$ ) donnée.

Enfin le développement des essais en vol de maquettes sera poursuivi, afin de permettre, à l'échelle de la maquette la validation d'un modèle aérodynamique élaboré. Cette validation s'appuie sur la corrélation entre le comportement observé en vol et celui prévu par la simulation.

#### Bibliographie

"The phenomenon of dynamic stall"  
Mac Croskey W.J.  
VKI LS 1981-4

"Etude de synthèse grandes incidences"  
D. Tristrant  
Rapport ONERA/IMFL n° 88/23

"Manoeuvrabilité des avions d'armes à grande incidence"  
F. Descatoire - O. Renier  
Rapport ONERA/IMFL n° 88/16

"Récents développements des techniques de simulation dynamique appliquées à l'identification des paramètres de stabilité"  
D. Tristrant - O. Renier  
Agard CP 386 Göttingen 1985

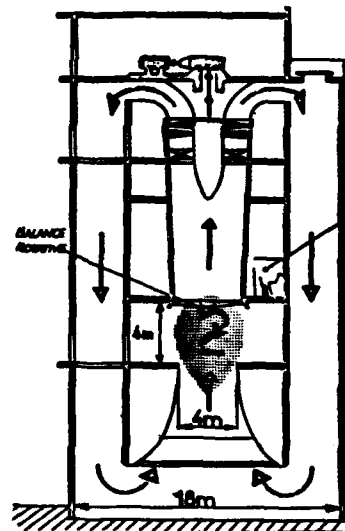


Fig1 Vue de la soufflerie verticale de l'IMFL

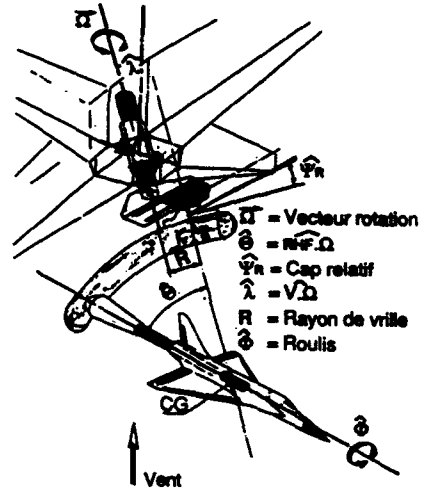


Fig2 Cinématique de la balance rotative

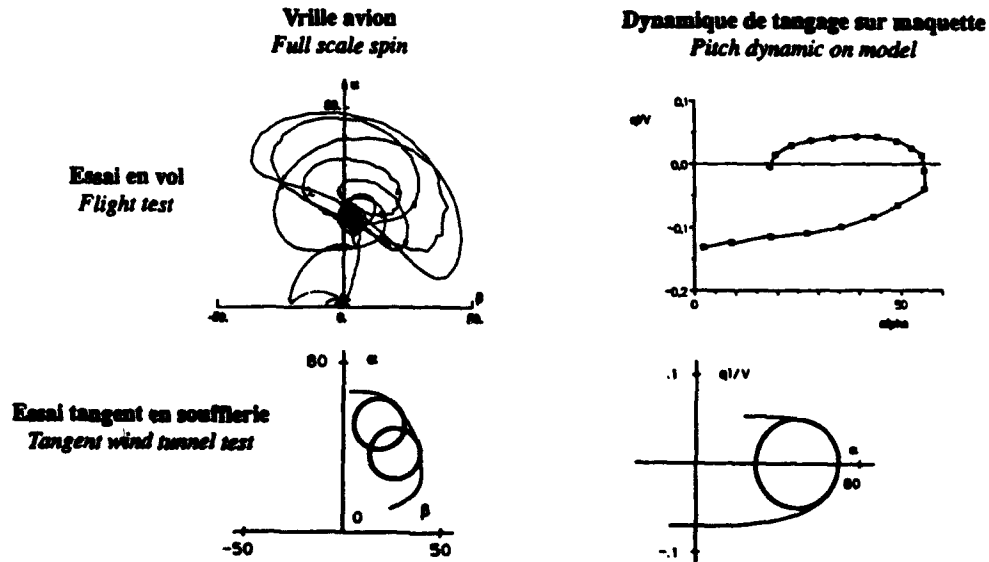


Fig3 Trajectoire: a- dans le plan  $(\alpha, \beta)$  d'une trajectoire de vrille et d'un essai conique oscillatoire; b- dans le plan  $(\alpha, q)$  d'un essai en vol dynamique de tangage et d'un essai oscillatoire sur le "pq"



Fig4 Laboratoire d'essais en vol "BS" de l'IMFL

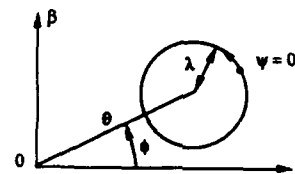
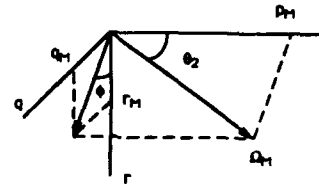
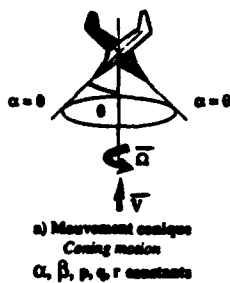
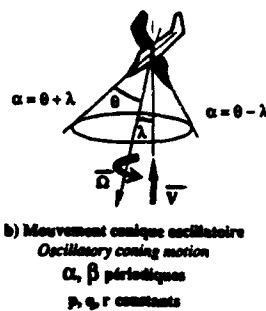
Balance rotative  
Rotary balanceFig5 Balance rotative; couverture des plans  
(α, β) et (p, q, r)a) Mouvement conique  
Cone motion  
 $\alpha, \beta, p, q, r$  constantsb) Mouvement conique oscillatoire  
Oscillatory cone motion  
 $\alpha, \beta$  périodiques  
 $p, q, r$  constants

Fig6 balance rotative: mouvements caractéristiques

	Relations cinématiques Kinematics relations	Paramètres identifiables Identifiable parameters
Mouvement conique Cone motion	$r = p \tan \alpha$ $q = p \tan \beta / \sin \alpha$ $\alpha = \theta$ $\beta = 0$	$C_{\theta}$ $C_{\theta} \sin \alpha + C_{\theta} \sin \alpha$
Mouvement conique oscillatoire Oscillatory cone motion	$\alpha = q \cdot \tan \beta (r \sin \alpha + p \cos \alpha)$ $\beta = p \sin \alpha - r \cos \alpha$	$C_{\theta} + C_{\theta} \sin \alpha$ $C_{\theta} - C_{\theta} \sin \alpha$

Fig7 Balance rotative: paramètres identifiables

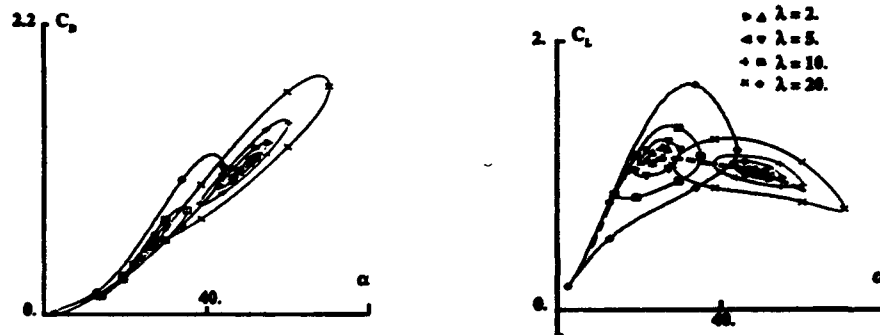
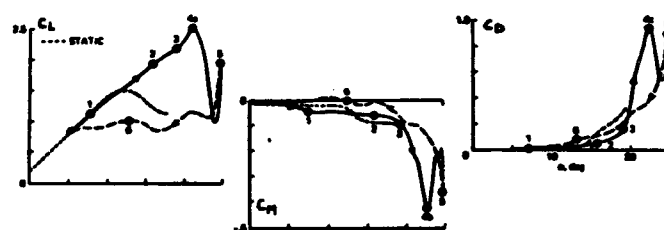
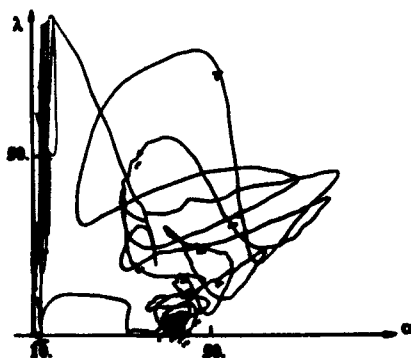
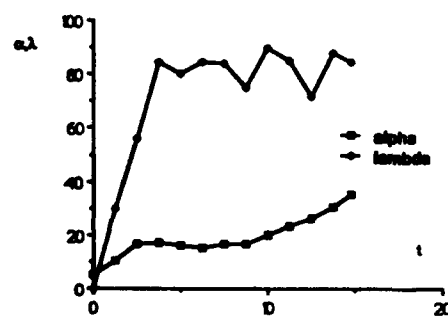


Fig8 Balance rotative; aérodynamique instationnaire



Oscillation d'incidence Incidence oscillation  
 $\alpha = 15^\circ + 10^\circ \sin \omega t$

Fig9 Décrochage dynamique sur un profil Naca en oscillation d'incidence (Mac Croskey)

Fig10 Evolutions dans  $(\alpha, \lambda)$  au cours d'une viréeFig11 Evolution de  $\lambda$  lors d'une manoeuvre de pointage (simulation)



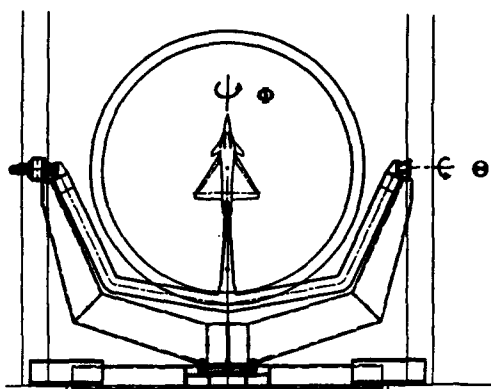


Fig12 Vue du montage "pqr"

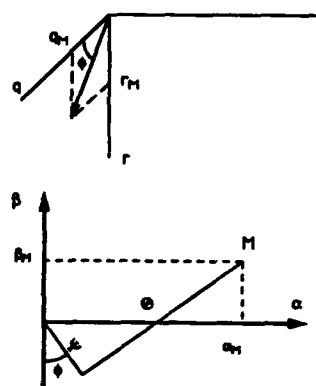


Fig13 Montage "pqr": couverture des plans (α,β) et (p,q,r)

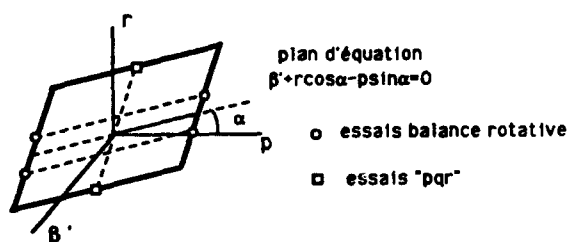


Fig14 Répartition comparée des essais dans le plans (β',p,r)

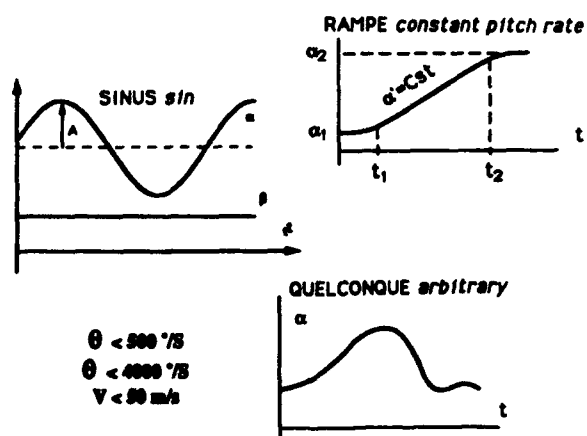


Fig15 Montage "pqr": Mouvements caractéristiques

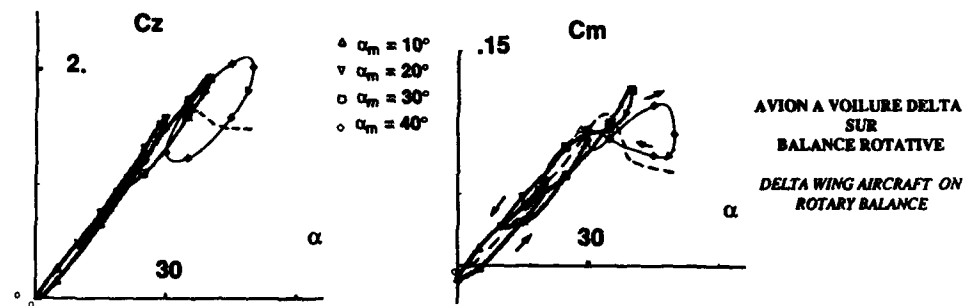


Fig16 Balance rotative: effet de l'incidence moyenne sur les phénomènes instationnaires

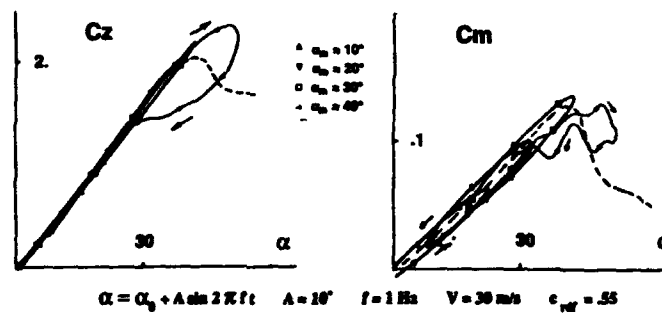
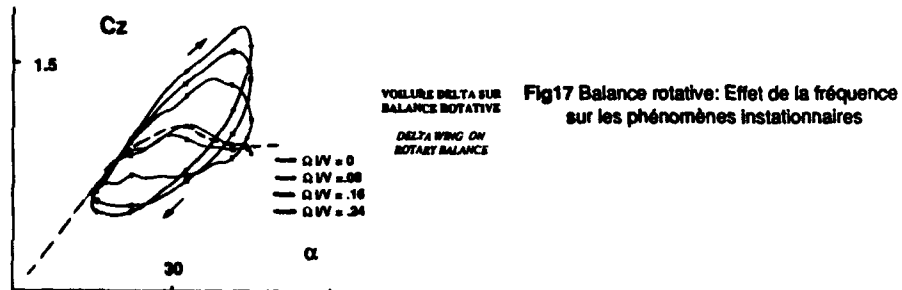
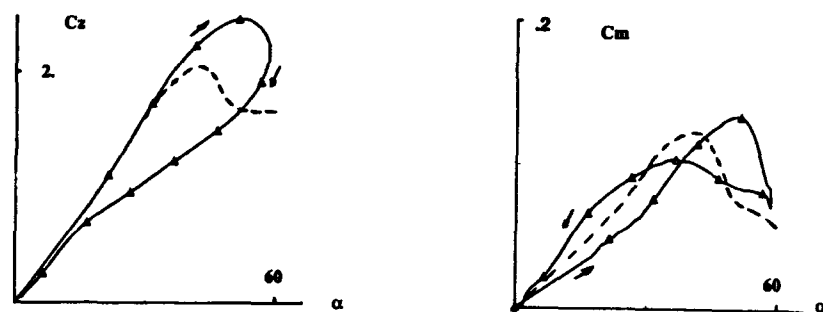


Fig18 Montage dynamique "pqr": effet de l'incidence moyenne



$$\alpha = \alpha_0 + A \sin 2\pi f t \quad A = 30^\circ \quad f = 1 \text{ Hz} \quad \alpha_0 = 30^\circ \quad V = 30 \text{ m/s} \quad c_{ref} = .55$$

Fig19 Montage dynamique "pqr": essai sinusoïdal de grande amplitude

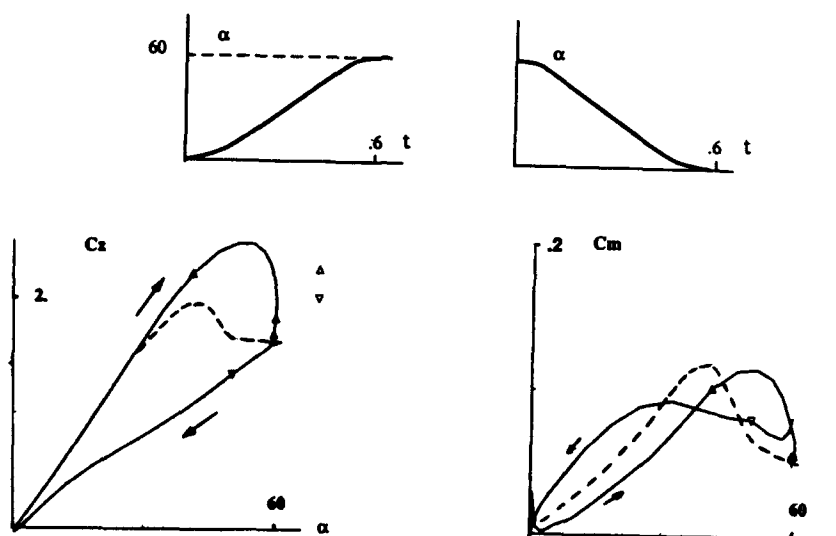
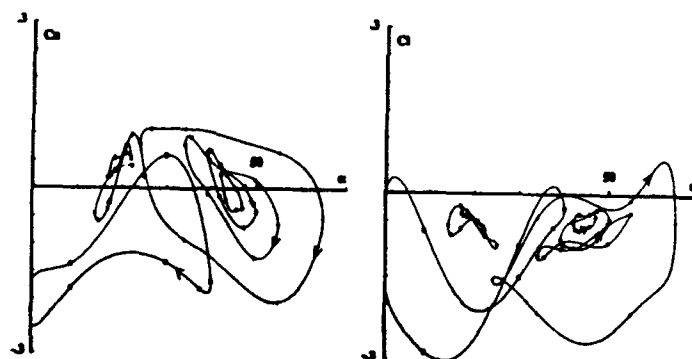


Fig20 Montage dynamique "pqr": essais de type "rampe"

Fig21 Balance rotative:  
effets instationnaires latéraux

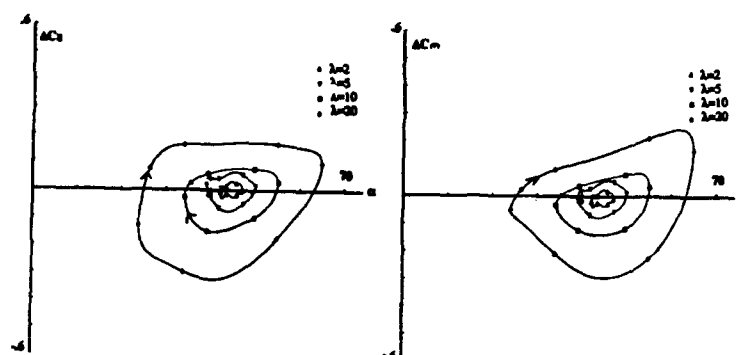
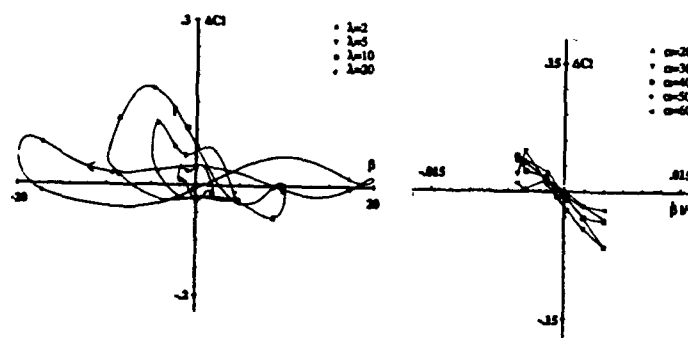
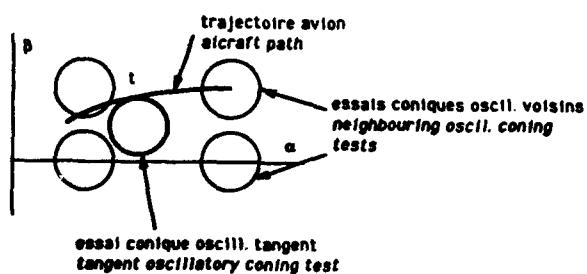
Fig22 Contributions instantanées  $\Delta C_z$  et  $\Delta C_m$ Fig23 Contributions instantanées  $\Delta C_1$ : a- tracé d'essais; b- projection dans  $(\Delta C_1, \beta)$  d'essais d'amplitude  $2^\circ$ 

Fig24 Illustration du principe de la modélisation par interpolation

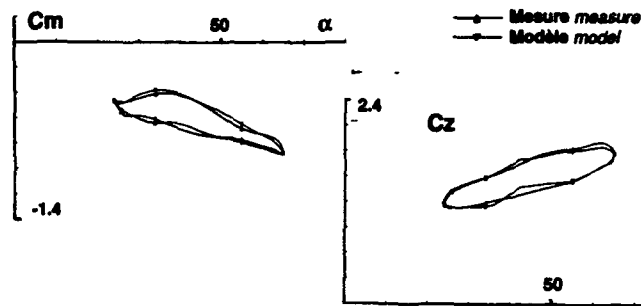


Fig25 Modélisation par fonction de transfert: comparaison modèle-essai

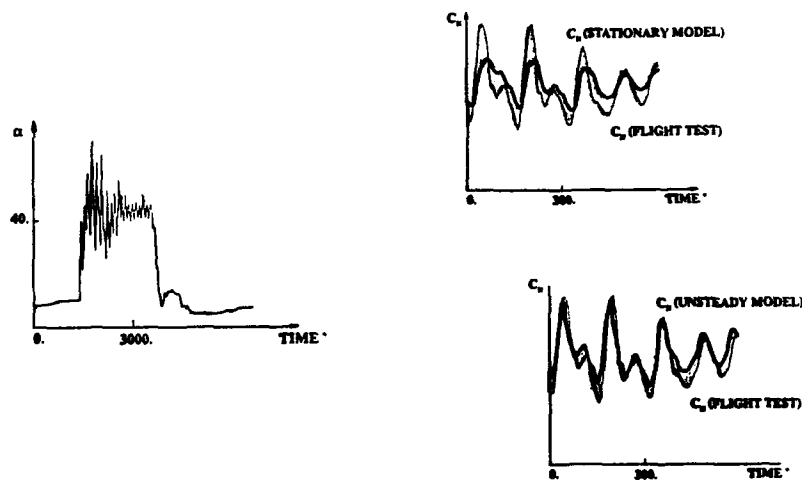


Fig26 Validation du modèle instationnaire sur des essais de vrille

# SCALE MODEL MEASUREMENTS OF FIN BUFFET DUE TO VORTEX BURSTING ON F/A-18

by

C. A. Martin and D. H. Thompson

AERONAUTICAL RESEARCH LABORATORY  
DEFENCE SCIENCE AND TECHNOLOGY ORGANISATION  
MELBOURNE, AUSTRALIA

## Summary

Tests have been carried out on scale models of the F/A-18 in a wind-tunnel and in a water tunnel to investigate the characteristics of tail buffet due to bursting of the wing leading edge extension (LEX) vortices. The wind-tunnel programme covered the measurement of unsteady surface pressures and accelerations at the tail of a 1/9th scale model, for cases with and without the LEX fences fitted. Flow visualisation of the vortex behaviour was carried out using smoke and a laser light sheet. Extensive flow visualisation tests were also carried out on a 1/48th scale model in a water tunnel to investigate the effects of engine intake flow and of the LEX fence on burst characteristics. Various aspects of these test programmes are covered in this paper.

## 1 Introduction

The severe buffet experienced at the tail of the F/A-18 due to vortex bursting is an example of a generic problem that can occur on aircraft which employ vortical flows to generate lift at high angles of attack. A substantial reduction in buffet on the F/A-18 was achieved by installing fences on the upper surface of the wing leading edge extensions (LEXes) to modify the vortical flow field. Considerable research is being carried out to understand the nature of vortex breakdown and also to characterise, for the F/A-18, the resulting pressure field and its influence on structural response.

At the Aeronautical Research Laboratory the physical mechanisms underlying vortex breakdown are being investigated using a number of approaches, including computational methods and wind and water tunnel facilities. Research has been reported in Reference [1] on a computational investigation of vortex breakdown in a flow situation with simple boundary conditions. In this paper results from investigations of vortex breakdown on wind-tunnel and water-tunnel models of the F/A-18 are discussed. The wind-tunnel programme covered the measurement of unsteady pressures and fin vibrations for cases with and without the LEX fence fitted. Flow visualisation of the vortex behaviour was carried out using smoke and laser light sheet. The water tunnel investigation used both dye and hydrogen bubble techniques to identify the axial position of the vortex breakdown of the LEX vortices and to investigate the effects of engine inlet flow and the effect of the LEX fences on flow field behaviour. Details of the changes in the vortex flow field are presented. Further details of the model tests are given in References [2] and [3].

## 2 Wind Tunnel Tests

### 2.1 Model, Test Equipment and Test Procedures

A 1/9th scale model of the F/A-18 aircraft was constructed at the Aeronautical Research Laboratory for testing in the Laboratory's low-speed wind tunnel. Carbon fibre was used extensively for fabrication of the fuselage and flying surfaces. All flying surfaces were reinforced with high tensile aluminium spars, which also formed the structural sub-frame and load attachment points of the model.

For the present investigation, a wing with fixed-leading edge (L.E.) flap deflection of 34° was designed. This L.E. flap angle corresponds to the flap setting for flight at angles of attack greater than 25.6° and Mach numbers less than 0.6.

For the purposes of this investigation, the port vertical stabilizer was provided with three pairs of pressure tapings. Each pair consisted of tapings located at the same spanwise and chordwise stations but on opposing sides of the fin. This arrangement allowed for the measurement of differential pressure across the fin. A single pressure tapping on the outboard side of the fin was located alongside a fin tip accelerometer. Two surface mounted pressure transducers were positioned on the port wing upper surface just below the position of the vortex burst. The pressure tapings and transducer locations are given in Figure 1.

The model was mounted on a pitch/roll rig via a six component strain gauge balance. All output signals from the transducers were recorded and analysed on a Wavetek 804a Fast Fourier Transform (FFT) Analyser. Prior to the tests, all transducers were calibrated against a Digiquartz pressure reference of known accuracy and checked for thermal drift. All transducers were found to be within 1% of calibration certificate values. Manufacturers' calibration certificate values were used for all data reduction during the test.

The tests were conducted in the ARL 2.7m by 2.1m low speed wind tunnel at velocities of 30 to 60 m/sec, corresponding to a dynamic pressure range of 250 to 2200 Pa and Reynolds numbers from  $0.54 \times 10^6$  to  $1.6 \times 10^6$  based on the mean aerodynamic chord of the model.

## 2.2 Frequency Characteristics of the Unsteady Pressure Field in the Vortex Burst

Unsteady pressure measurements from two transducers mounted on the port wing surface, and from a pressure transducer and an accelerometer mounted on the port fin, see Figure 1, were analysed to determine the frequency characteristics of the vortex burst.

Typical Power Spectral Density (PSD) results are presented in Figures 2 to 5 for an angle of attack of  $26.5^\circ$  and for a range of tunnel speeds. The PSD plots are the average of 30 ensembles. The results show that the pressure field due to the vortex burst contains energy over a moderately narrow frequency band. The band width and centre frequency differ slightly between the wing surface and fin locations. However, the overall frequency content is seen to be a strong function of tunnel speed. The centre of the energy band for the rear surface pressure transducer was located visually using the analyser cursor and the results are presented as a function of tunnel speed for a range of angles of attack in Figure 6. The centre frequency increases linearly with increasing tunnel speed, and the gradient increases with decreasing angle of attack.

Flow visualisation tests and wing surface unsteady pressure measurements were carried out on the model with the fins removed as well as with the fins in place. The position of the vortex burst was defined for a range of angles of attack by the introduction of a smoke filament just below the junction of the forward tip of the LEX and the fuselage. Results of the flow visualisation studies were recorded on video tape. Figure 7 shows that, with fins removed, the vortex burst point moves further aft for the same angle of attack, while the frequency analysis shows that the centre frequency of the burst increases (Figure 8). These changes, due to removal of the fins, shows that the vortex burst characteristics are sensitive to the downstream pressure field.

From this data, which covers only a few angles of attack, the vortex burst position and the burst frequency show significant correlation. However, both parameters are also functions of angle of attack. At this stage, the underlying dependencies are not yet understood. Further work is being carried out on simple delta wings to provide a better understanding of the relationships between the angle of attack and the burst characteristics, such as burst position and burst frequency.

Time correlation calculations were carried out on the signals from the two wing surface pressure transducers which were located 100 mm apart in a streamwise direction. The correlation was calculated by applying an inverse Fourier transform to the cross power spectrum, which had previously been obtained from averaging Fourier transforms of thirty ensembles. The resulting correlation plot provides an estimate of the dominant frequency in the pressure field and also an estimate of the pressure field convection velocity. The frequency estimates agree closely with those obtained from the power spectrum measurements. The pressure field convection velocity is shown in Figure 9 to be 0.4 times the free stream velocity for the case at  $23.5^\circ$  angle of attack and 0.29 free stream velocity for  $28.5^\circ$  angle of attack.

In summary, analysis of the surface pressure measurements shows that with increasing angle of attack, the vortex burst location moves forward and the burst pressure field frequency and convection velocity decrease.

When the fins are removed, the burst location moves aft, for a given angle of attack, and the burst frequency increases.

## 2.3 Fin Response to Buffet Excitation

Using a single accelerometer mounted as shown in Figure 1, measurements were made of the port fin acceleration response to identify the conditions for maximum excitation. Surface pressure measurements were also made at a pressure port located close to the accelerometer. The pressure was transmitted through a 0.6 mm I.D. plastic tube to a transducer located on the fuselage inboard of the fin.

Prior to the wind-tunnel programme, vibration tests were carried out on the model fin to establish its structural characteristics. Only the primary bending mode was investigated. The results of these tests are presented in Figure 10. It should be noted that the model fin structure was not specifically designed to match full scale stiffness or structural dynamic characteristics. However, since the frequency of the primary bending mode of 68 Hz lies within the range of frequencies that occur in the vortex burst of the 1/9th scale model at normal tunnel speeds, excitation of the fin would be expected.

In general, the magnitude of the fin response will depend upon the temporal and the spatial distribution of energy in the pressure field relative to the fin structural modes, and also on the free stream dynamic pressures. The temporal distribution of energy in the pressure field was discussed in Section 2.2 where it was shown that the centre frequency of the energy associated with the vortex burst is a linear function of tunnel free stream velocity and also varies with angle of attack as well as with vortex burst position. The instrumentation was not sufficiently extensive to allow simultaneous pressure measurements to be made across the fin surface. Consequently the influence of the spatial distribution of the pressure field has not yet been determined.

To account for the effects of free stream dynamic pressure the measurements of pressure and acceleration at the fin tip have been normalised with respect to dynamic pressure. In Figures 11 and 12 the value of the normalised pressure, measured from the PSD curves at the fin natural frequency, and the peak normalised acceleration response show a similar variation with speed. From these figures, the peak fin responses occur between 35 and 40 m/sec for the  $26.5^\circ$  angle of attack case, and at around 40 m/sec for the  $31.5^\circ$  angle of attack case. Note that these data are measured at 5 m/sec intervals and so the peak locations cannot be established accurately. Based on the frequency scaling results given in Figure 6, the tunnel free stream velocities at which the peak pressure frequency matches the fin natural frequency of 68 Hz are, 35 m/sec for  $26.5^\circ$  angle of attack, and 40 m/sec for  $31.5^\circ$  angle of attack. These results indicate that when the effect of dynamic pressure is taken into account, the maximum normalised fin response occurs when the frequency of the peak pressure field and the fin natural frequency are approximately matched. Peak accelerations at the tip of the fin, obtained from time histories, were of the order of 120 'g' in the conditions of maximum excitation. This corresponds to a fin tip amplitude of 6.44 mm at the fin bending frequency of 68 Hz. The spatial distribution of pressures will also influence the fin response. However, further measurements of differential pressure loading would be required to determine the magnitude of this influence.

## 2.4 Measurements with Wing LEX Fence Fitted

With the LEX fence fitted the pressure measurements indicated a marked change in the vortex burst unsteady pressure field. The magnitudes of the unsteady pressures, are reduced significantly, Figure 13, while the energy is distributed over a wider frequency band. The modified pressure field produces significantly reduced fin response, as shown by the results in Figure 14 for an angle of attack of  $26.5^\circ$  and varying sideslip angle.

Flow visualisation measurements showed little change in the longitudinal location of the vortex burst with the fence in place, although the vertical location and general shape of the burst region was altered slightly. Feeding smoke into the flow beneath the LEX and using a cross-flow laser light sheet confirmed the existence of a second vortical structure emanating from the leading edge extension alongside the fence, Figure 15. The second structure interacts with the primary vortex and also exhibits bursting. Further investigations are needed to provide a complete explanation for these flow interactions, and for the significant reduction in the resulting pressure field. Complementary flow visualisation results obtained in a water tunnel are described in Section 3.

## 3 Water Tunnel Tests

### 3.1 Model, Test Equipment, and Test Procedures

A 1/48 scale model of the F/A-18 was used for the water tunnel tests. A standard plastic hobby kit was provided with surface dye ports and the engine inlets were connected to a suction pump through individual flow meters and valves. The wing leading-edge and trailing-edge flaps could be fixed at various deflection settings and the horizontal tail surfaces could be locked at any desired deflection angle. LEX fences could also be attached to the model.

The tests were carried out in the ARL Flight Mechanics Branch horizontal-flow water tunnel, which has a test section 380 mm wide, 510 mm deep, and 1.52 m long. The model was mounted inverted on a sting and C-strut, and positioned in pitch and yaw by remotely-controlled DC motors.

For flow visualisation, liquid food dyes from a pressurised supply could be injected through ports positioned at locations around the model nose, on the fuselage sides ahead of the engine inlets, just beneath each LEX apex, and on the LEX upper and lower surfaces. Flow patterns were also visualised using the electrolytic generation of small hydrogen gas bubbles from a cathode strip beneath each LEX leading edge to act as flow tracers.

General illumination of the model and dye patterns was provided by lamps mounted beneath and in front of the test section. A light sheet generated by a laser beneath the test section was used in conjunction with the hydrogen bubbles to illuminate flow patterns in a cross-flow plane.

Video cameras provided side, plan, and cross-flow plane views of the model. A PC-based image processing system acquired and stored video images from which model angle of attack and the position of flow features such as vortex

breakdown were measured directly. In addition, most flow patterns were recorded on videotape. Conventional film photography was used to provide higher quality images in some cases.

### 3.2 Effect of Engine Inlet Flows

On the F/A-18, the engine inlets are located beneath the LEX/wing leading-edge junction, and so the possibility exists that flow into the inlets might influence the behaviour of the vortex above the LEX in this region. Tests were carried out in the water tunnel to explore this possibility. Vortex breakdown positions were measured for various inlet flow rates, and the results are shown in Figure 16. The inlet flow rate is scaled using the ratio  $V_i/V_0$ , where  $V_i$  is the mean velocity through the inlet and  $V_0$  is the freestream velocity. Examination of F/A-18 flight records showed that during a typical period of air combat manoeuvring, lasting for some 100 seconds at full throttle, the aircraft operated at angles of attack greater than  $15^\circ$ , and at estimated inlet velocity ratios greater than 3.0 for more than 50% of the manoeuvring period. For nearly 20% of the period, the estimated velocity ratio exceeded 4.0, and the peak value was about 5.5. Figure 16 shows that the inlet flow does have an effect on the axial position of vortex breakdown, tending to shift it downstream. The downstream shift increases with inlet velocity ratio until, at a velocity ratio of 8.1, the shift is about 20% of the model length.

The effect of engine inlet flow on the overall flow structure in the LEX region was investigated in more detail by injecting dye through ports in the starboard fuselage side beneath the LEX and ahead of the inlets. Dye was also injected through a port beneath the LEX leading edge, outboard of the engine inlet. Figure 17 shows dye patterns obtained for various inlet flow rates, at an angle of attack of  $30.5^\circ$ . With no flow into the inlet, there is a region of complex flow beneath the LEX. Dye from the fuselage ports moves forward along the fuselage side to the LEX apex, up around the apex and into the LEX vortex core. Dye from the port beneath the LEX leading-edge moves outboard beneath the LEX, around the leading-edge and into the vortex system.

For a velocity ratio of 2.48, the separated region beneath the LEX has disappeared. Dye from all the fuselage side ports moves downstream and into the splitter slot or into the inlet itself. The vortex breakdown has shifted downstream, and the vortex core, upstream of the breakdown, has been deflected downwards to lie roughly parallel to the LEX upper surface.

For a velocity ratio of 8.1, dye from the port beneath the LEX leading edge is sucked into the inlet. At high inlet flow rates, observation of hydrogen bubbles generated along the LEX leading-edge indicates that, just ahead of this dye port, the normal upward flow around the LEX leading-edge does not occur. In fact, fluid passes down around the LEX leading-edge from the upper to the lower surface.



The effect of inlet flow at an inlet velocity ratio of 8.1 at other angles of attack is shown in Figures 18 to 21. At an angle of attack of  $19.5^\circ$ , Figures 18 and 19, the vortex core is deflected inboard and the vortex breakdown has shifted from a position just ahead of and outboard of the fin leading-edge at  $V_f/V_0 = 0$ , to a position behind and inboard of the leading-edge. At an angle of attack of  $25.4^\circ$ , Figure 20 and 21, the corresponding shift in vortex breakdown position is from just aft of the wing leading-edge / LEX junction to just ahead of the fin leading-edge.

Flow into the engine inlet, by modifying the flow patterns beneath the LEX, may be causing local changes to the effective spanwise camber of the LEX. It has been shown in wind tunnel Reference[5] and water tunnel Reference[6] tests that increasing the spanwise camber of a delta wing shifts the vortex breakdown position downstream. It is possible that a similar mechanism is producing the results observed for the LEX vortex in the present tests.

The effect of inlet flow on the position of vortex breakdown may be significant in relation to wind tunnel testing. Most wind tunnel tests of the F/A-18 have been performed using flow-through inlets. The water tunnel tests described here have shown that it may be necessary to simulate inlet flows to model accurately the behaviour of LEX vortex breakdown in the wind tunnel. At ARL, appropriate comparative wind tunnel tests with inlet flow simulation are planned to check on this point.

### 3.3 Effect of LEX Fences

As shown in Figure 22, the fitting of the LEX fences has little effect on the vortex breakdown axial position, confirming the wind tunnel test results described above. However, the fences do modify the vortex system structure to some extent, particularly at angles of attack in the range  $15^\circ - 30^\circ$ . Figures 23 to 26 show comparative fence-off and fence-on side and plan views for two angles of attack. At an angle of attack of  $19.5^\circ$ , Figures 23 and 24, the fence causes the development of a slight spiral in the vortex core, which is deflected initially upward and inboard, then downward and outboard. The breakdown itself is shifted outboard slightly. At an angle of attack of  $25.4^\circ$ , Figures 25 and 26, the vortex core kink caused by the fence is still present but is less apparent than at the lower angle of attack.

For angles of attack up to about  $27^\circ$ , with breakdown occurring close to or downstream of the fence position, the physical appearance of the breakdown is altered by the addition of the fences. With the fences off, the breakdown is clearly defined as a sudden deformation and expansion of the core dye filament. With the fences fitted, the breakdown appears less distinct, with a more gradual thickening of the core dye filament upstream of the breakdown proper (Figures 23 and 25.)

Thus it appears that the favourable effect on fin dynamic loading produced by the fences is not the result of any major axial shift in vortex breakdown position, but rather is due to a change in the nature of the flow downstream of the breakdown, combined with a slight lateral shift in the position of the breakdown, at least at the lower angles of attack.

To investigate further the behaviour of the flow in the vicinity of the fence, the hydrogen bubble technique was used, in conjunction with laser sheet illumination. In a typical case, Figure 27 shows successive sections through the hydrogen bubble sheets as the light sheet is moved downstream past the fence location. Near the forward end of the fence, the vortex cross section is typical of that above a delta wing. The sheet of fluid separating from the leading edge rolls up smoothly into a spiral vortex above the LEX and inboard of the leading edge. Further downstream, in the vicinity of the fence mid-chord, a kink develops in the separated sheet. This kink develops into a second vortex, of the same sense as the main LEX vortex. The second vortex moves inboard and upwards over the main vortex, then downwards on the inboard side of the main vortex. Ultimately, the two vortices merge. These results parallel the observations made using smoke in the wind tunnel tests described above. The interaction between the two vortices accounts for the kinks that develop in the LEX vortex core upstream of the breakdown when the fences are fitted, and also for the slight outboard displacement of the LEX vortex core. The interaction of the two vortices may affect the frequency of any unsteady flow component downstream of the breakdown, and may thus contribute to the effectiveness of the fences in reducing fin vibration. The techniques used in the flow visualisation tests described here did not allow the detection of any such frequency changes.

When attempting to measure the vortex breakdown position with fences on, it was found that, for a small angle of attack range, the breakdown was not clearly defined by dye injected at the LEX apex. The dye filament in the vortex core appeared to deflect and spread out into a curved sheet, without displaying the usual clearly defined stagnation point at breakdown.

To study this flow in more detail, dye was injected through a hole on the LEX underside at about the same chordwise position as the fence. This dye passed outboard beneath the LEX, upwards around the LEX leading-edge and into the second vortex. Dye was also injected through a hole on the LEX upper surface upstream of the fence. Dye from this hole passed downstream over the LEX upper surface and into the second vortex. Some examples of the flow patterns observed are shown in Figure 28. It was found that the principal breakdown was in fact occurring in the second vortex, and that the deflection and spreading of the main vortex core dye was due to the core deflecting and 'smearing' around the breakdown in the second vortex. This flow pattern was observed clearly at relatively low flow velocities (about 30 mm/s), and for an angle of attack range of about  $17^\circ - 22^\circ$ . At higher velocities, diffusion and mixing of the dye filaments made it impossible to distinguish which vortex broke down first. However, breakdown of the second vortex may account for the change in appearance of the LEX vortex breakdown caused by the fitting of the fence.

#### 4 Conclusions

Exploratory measurements carried out using a small number of high frequency pressure transducers and a small accelerometer on a 1/9th scale wind-tunnel model have provided valuable insight into the character of the vortex burst and subsequent fin vibration on the F/A-18. Pressure measurements made on the wing surface below the vortex burst and on the fin show that the burst pressure field contains energy over a moderately narrow frequency band. The centre frequency of the energy is a linear function of free stream velocity. Fin tip acceleration measurements show that the fin bending mode response is strongly coupled with the burst characteristic frequency and hence with free stream velocity. The burst characteristic frequency is also modified when angle of attack is changed or when the fin is removed. Tests carried out with the leading edge extension fences fitted showed that the magnitude of the unsteady pressures was reduced significantly while the energy extended over a wider frequency band. The associated fin tip acceleration, was significantly reduced. Flow visualisation measurements indicated little change in the location of the vortex burst, but confirmed the existence of a second vortical structure with the fence in place. The second structure interacts with the primary vortex and also exhibits bursting. Complementary flow visualisation tests in a water tunnel generally confirm the wind tunnel measurements of vortex breakdown burst position. The effect of the LEX fence in producing a second vortex which interacts with the main LEX vortex and which also undergoes bursting was also confirmed. Water tunnel tests also indicated that engine inlet flow could have some effect on the position of vortex burst. This will require further investigation on larger scale wind-tunnel models.

#### References

- [1] Lopes, J.M. 'Axisymmetric Vortex Breakdown Part 1. Confined Swirling Flow.' *Journal of Fluid Mechanics*, 221:533-522, Dec 1990.
- [2] Martin, C.A. Glaister, M.K. MacLaren, L.D. Meyn, L.A. and Ross, J. 'F/A-18 1/9th Scale Model Tail Buffet Measurements', *Flight Mechanics Report 188 Aeronautical Research Laboratory, Melbourne Australia*
- [3] Thompson, D.H. 'Water Tunnel Flow Visualisation of Vortex Breakdown over the F/A-18', *Flight Mechanics Report 179 Aeronautical Research Laboratory, Melbourne Australia, October 1990.*
- [4] Zimmerman, N. H. and Ferman, M. A., 'Prediction of Tail Buffet Loads for Design Applications. Vols I and II', *Naval Air Development Center Report, NADC 88043-60, July 1987.*
- [5] Earnshaw, P.B. Lawford, J.A. 'Low-Speed Wind-Tunnel Experiments on a series of Sharp-Edged Delta Wings' *ARC R and M 3424 (1966)*
- [6] Thompson, D.H. 'A Water Tunnel Study of Vortex Breakdown Over Wings with Highly Swept Leading Edges' *ARL AERO Note 356 Aeronautical Research Laboratory, Melbourne Australia. (1975)*

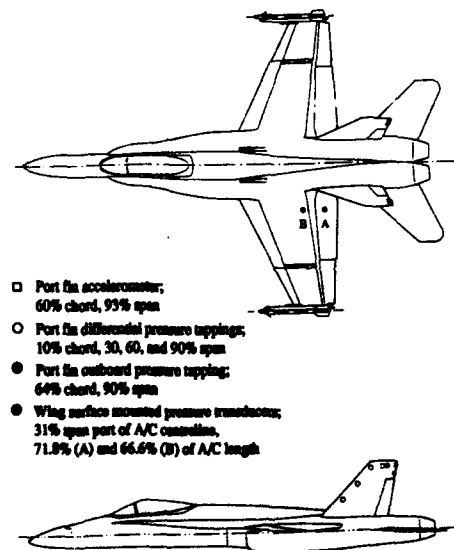


Figure 1: Location of pressure tapings and transducers

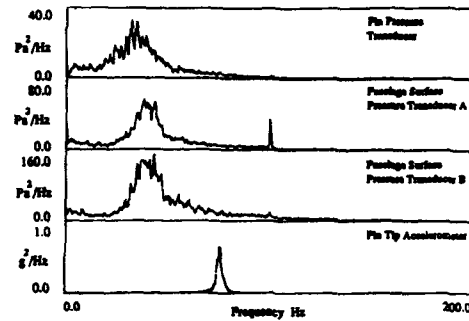


Figure 2: Power Spectral Density results for 26.5° angle of attack and tunnel speed 20 m/sec

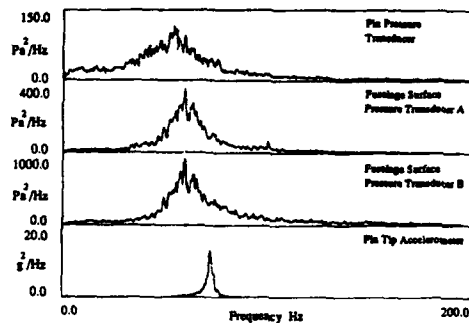


Figure 3: Power Spectral Density results for 26.5° angle of attack and tunnel speed 30 m/sec

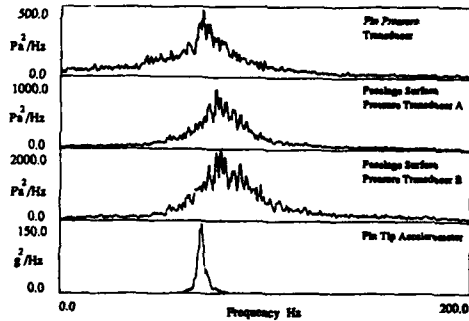


Figure 4: Power Spectral Density results for 26.5° angle of attack and tunnel speed 40 m/sec

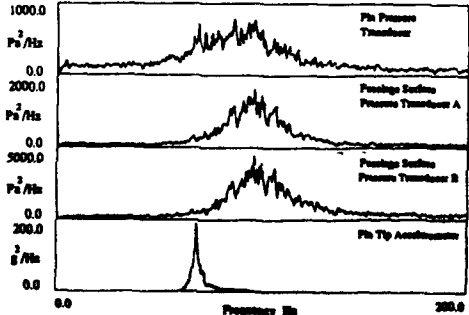


Figure 5: Power Spectral Density results for 26.5° angle of attack and tunnel speed 60 m/sec

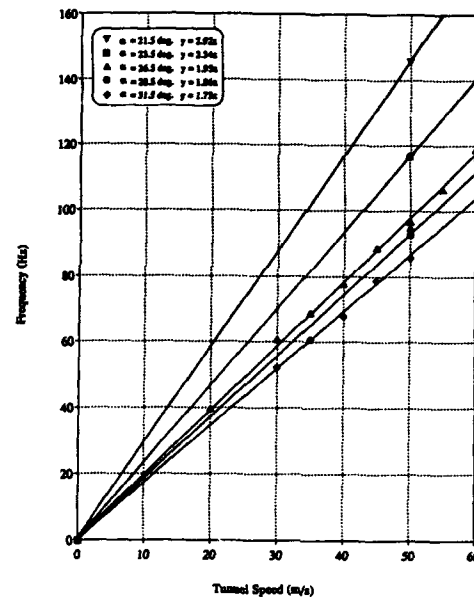


Figure 6: Variation of vortex burst frequency with tunnel speed - fins on

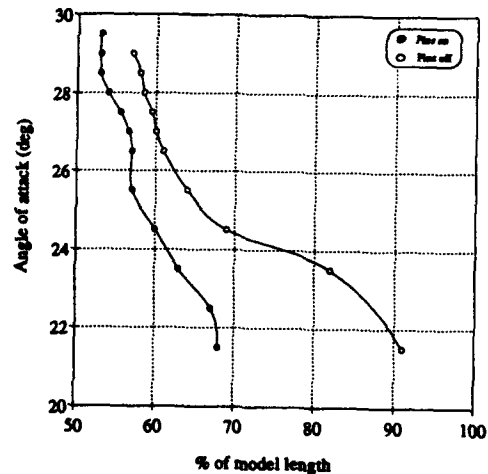


Figure 7: Location of Vortex Burst Position

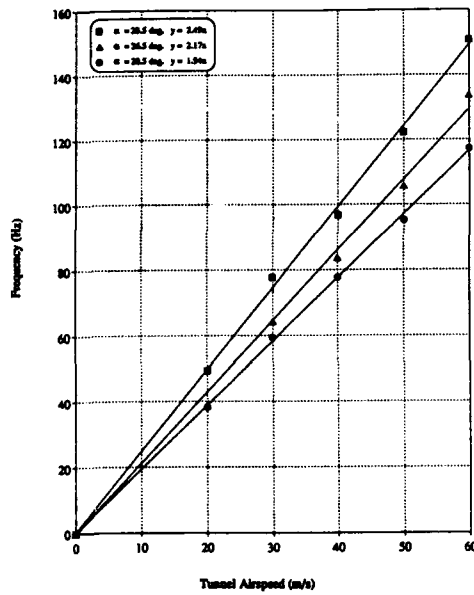


Figure 8: Variation of vortex burst frequency with tunnel speed - fins off

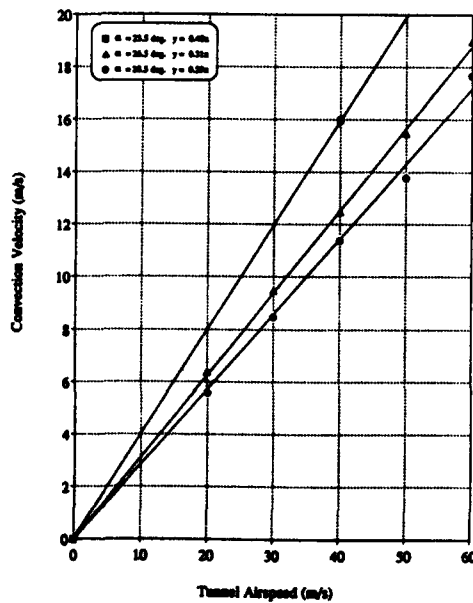


Figure 9: Variation of pressure field convection velocity with tunnel speed - fins off

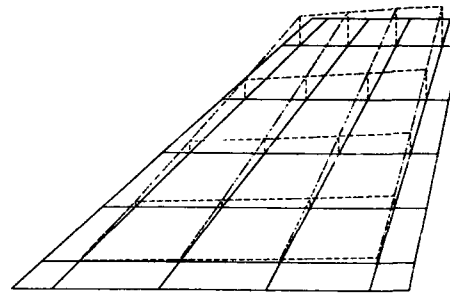


Figure 10: 1/9th scale F/A-18 wind tunnel model fin mode shape from vibration tests

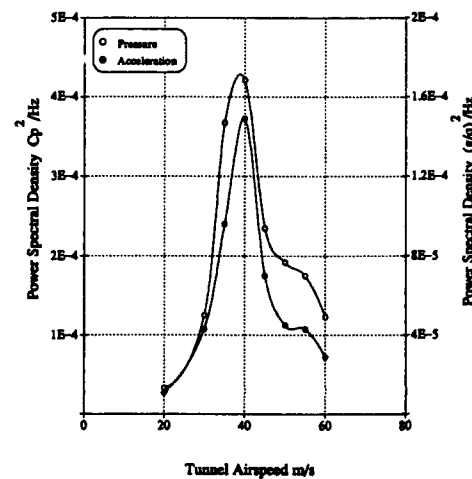


Figure 11: Port fin-tip surface pressure and acceleration measurements angle of attack 26.5° - variation with tunnel speed

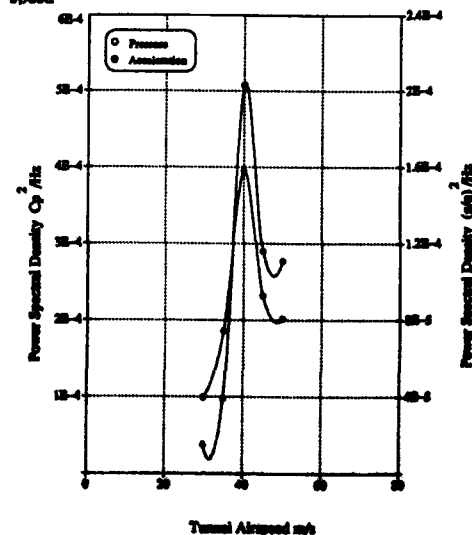


Figure 12: Port fin-tip surface pressure and acceleration measurements angle of attack 31.5° - variation with tunnel speed

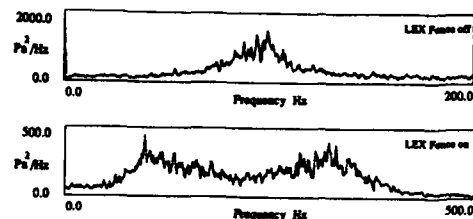


Figure 13: Power Spectral Density results for 26.5° angle of attack and tunnel speed 40 m/sec fence on

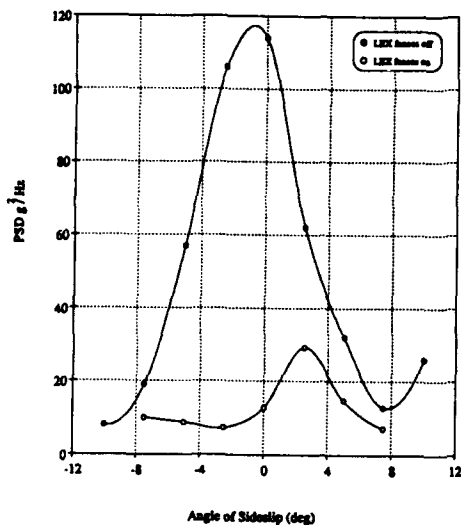


Figure 14: Power Spectral Density of port fin-tip acceleration measurement at 26.5° angle of attack and 50 m/sec tunnel speed - variation with sideslip angle



Figure 15: Flow visualization of vortex flow with LEX fence fitted

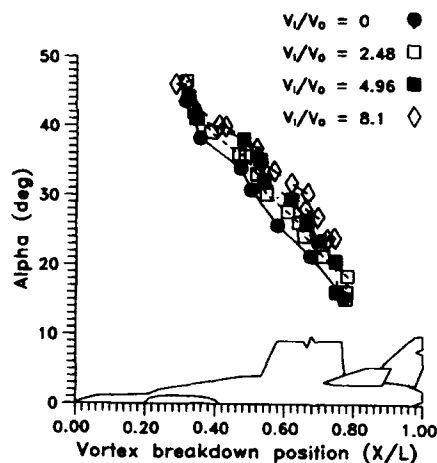


Figure 16: Vortex breakdown position over F/A-18 - Effect of engine inlet flow (LEF/TEF = 35°/0°;  $V_0 = 80$  mm/s)



Figure 17: Vortex flow patterns over F/A-18 - Effect of engine inlet flow ( $V_i/V_0 = 0.0, 2.48, 8.1$ ; Angle of Attack = 26.5 deg, LEF/TEF = 35°/0°;  $V_0 = 80$  mm/s)

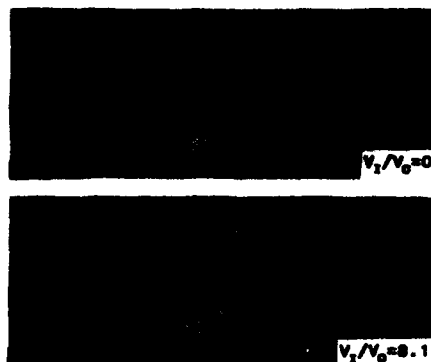


Figure 18: Effect of engine inlet flow (Angle of Attack=19.5 deg (side view)  $V_1/V_0=8.1$ ; LEF/TEF=35°/0°;  $V_0=80$  mm/s)

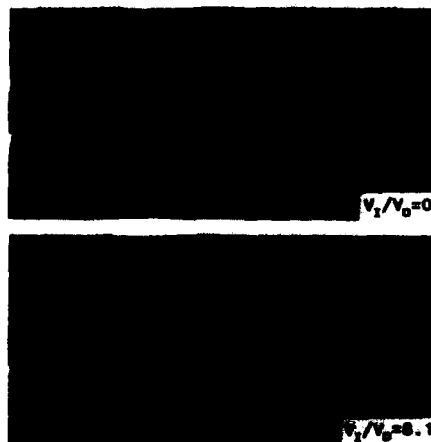


Figure 19: Effect of engine inlet flow (Angle of Attack=19.5 deg (plan view)  $V_1/V_0=8.1$ ; LEF/TEF=35°/0°;  $V_0=80$  mm/s)

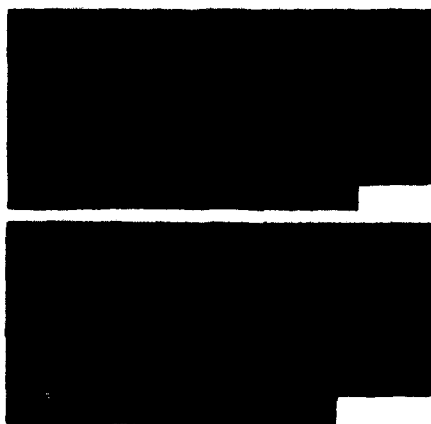


Figure 20: Effect of engine inlet flow (Angle of Attack=25.4 deg (side view)  $V_1/V_0=8.1$ ; LEF/TEF=35°/0°;  $V_0=80$  mm/s)

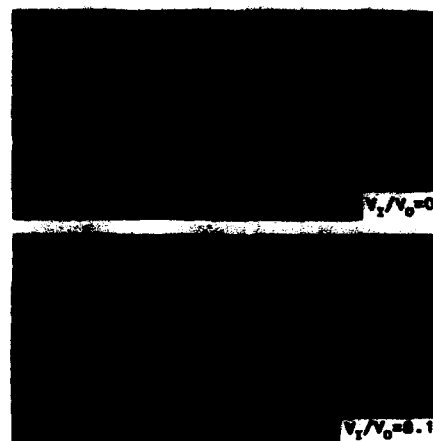


Figure 21: Effect of engine inlet flow (Angle of Attack=25.4 deg (plan view)  $V_1/V_0=8.1$ ; LEF/TEF=35°/0°;  $V_0=80$  mm/s)

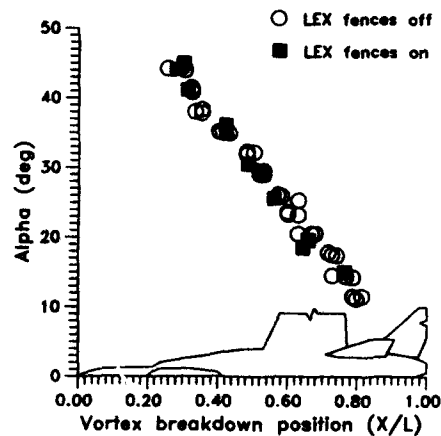


Figure 22: Vortex breakdown position over F/A-18 - Effect of LEX fences ( $V_1/V_0 = 6.0$ ; LEF/TEF = 35°/0°;  $V_0 = 80$  mm/s)

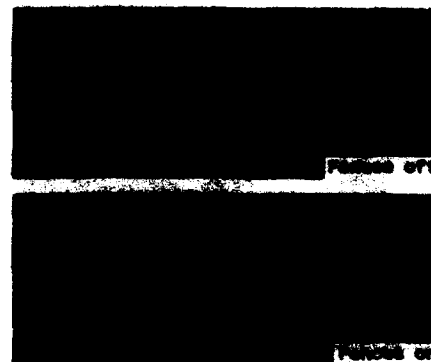


Figure 23: Effect of LEX fences on vortex flows over F/A-18 (Angle of Attack = 19.5 deg (side view) LEF/TEF = 35°/0°;  $V_0 = 80$  mm/s;  $V_1/V_0 = 0$ )

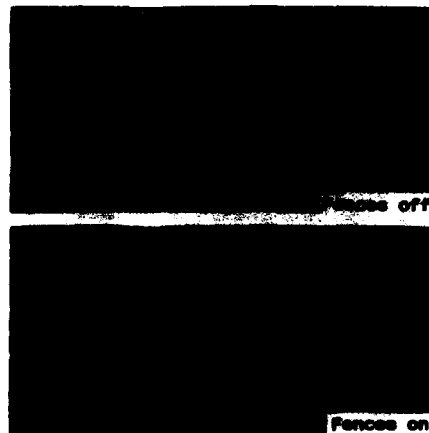


Figure 24: Effect of LEX fence on vortex flows over F/A-18 (Angle of Attack = 19.5 deg (plan view) LEF/TEF = 35°/0°;  $V_0 = 80 \text{ mm/s}$ ;  $V_I/V_0 = 0$ )

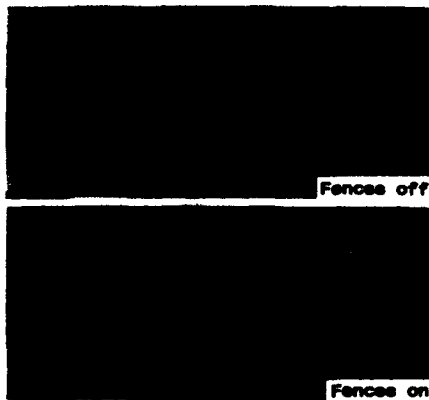


Figure 25: Effect of LEX fence on vortex flows over F/A-18 (Angle of Attack = 25.4 deg (side view) LEF/TEF = 35°/0°;  $V_0 = 80 \text{ mm/s}$ ;  $V_I/V_0 = 0$ )

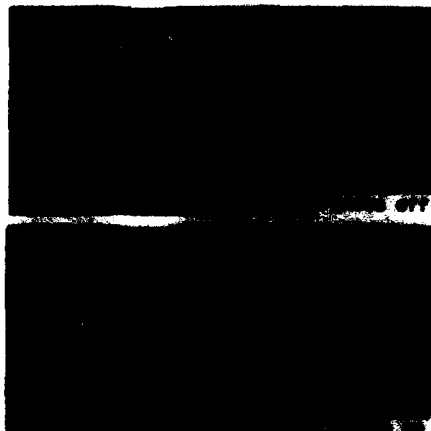


Figure 26: Effect of LEX fence on vortex flows over F/A-18 (Angle of Attack = 25.4 deg (plan view) LEF/TEF = 35°/0°;  $V_0 = 80 \text{ mm/s}$ ;  $V_I/V_0 = 0$ )

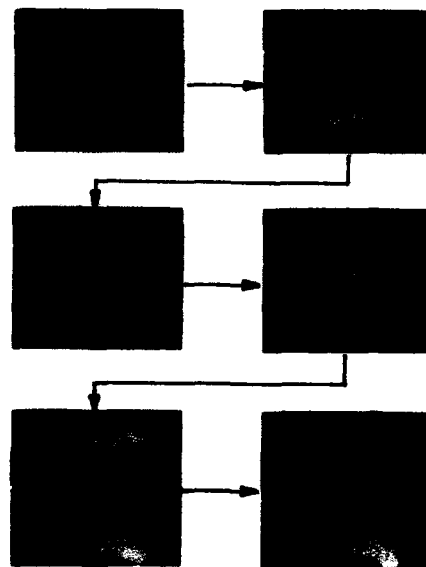


Figure 27: Cross-sections of LEX vortex system passing over and downstream of fence

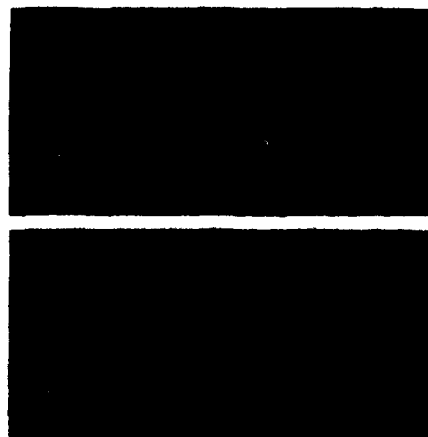


Figure 28: Breakdown in second vortex with fences on (Angle of Attack = 19.5 deg (side view) LEF/TEF = 35°/0°;  $V_0 = 30 \text{ mm/s}$ ;  $V_I/V_0 = 0$ )

## **X-31, DISCUSSION OF STEADY STATE AND ROTARY DERIVATIVES**

by

W. Kraus  
MBB Flugzeuge, Postfach 801160,  
8000 München 80, Germany

### **1. INTRODUCTION**

The X-31A high agility airplane has been designed to operate with excellent aerodynamic qualities not only in the normal flight regime, but also at high angles of attack. The aircraft has been designed to have natural aerodynamic stability about all three axis in the entire angle of attack range - except at small angle of attack, where the aircraft is unstable in pitch for performance reasons. In some critical regions in which the natural stability cannot be attained, the control power required to achieve stability is provided to the appropriate axis by artificial control, still leaving sufficient control power for maneuvers.

In a basic wind tunnel development program, a configuration has been tailored which fulfills most of the demanded requirements by aerodynamic means. Both the results and the way how these results were obtained will be presented in this paper.

Besides this static behavior, each aircraft has dynamic characteristics, which decide whether or not the airplane will diverge. Additional wind tunnel tests has been conducted in a spin tunnel to evaluate these characteristics. An analysis of the data is presented including steady state spin modes.

### **2. BASIC CONFIGURATION DEVELOPMENT PROGRAM IN THE WIND TUNNEL**

At the very beginning of the post stall adventure stands a basic paper reporting on studies to identify proper high angle of attack configurations [1]. This basic research started with a modular model in a low speed wind tunnel (see Fig. 1). Several types of wings, tails, strakes and control surfaces were analysed and finally yielded the delta canard configuration as an optimum balance between modern fighter design in the supersonic region and post stall capability at low subsonic speed, as shown in [1]. The configuration was developed for the EFA / J90 fighter program including the post stall features, which later on in the program were cancelled for cost reasons. Basic problems during this time were thought to be mainly directional and lateral stability and sufficient control power at high angles of attack. Problems in directional stability arise from the vertical tail being in separated flow behind the fuselage above  $\alpha = 40^\circ$ . Lateral stability of delta wing configurations is lost in the region of maximum lift when the leading edge vortices are bursting asymmetrically at sideslip angles (see Fig. 2 and 3), causing instable behavior until the airflow on both wings has separated. The loss of control power is a general problem due to flow separation on the whole configuration - separated flow on the controls will reduce their effectiveness down to the effect of removing their impingement area (impact area) out of the flow.



This post stall development work is summarized in a paper presented by myself in 1980 [2]. Based on this early work, the X-31 program was started in 1985 by Rockwell and MBB in a joint venture which led to a wind tunnel development program to fine tune the existing delta canard configuration. This fine tuning will be described in the following. Since appropriate theoretical tools were not available, the aerodynamic configuration development for the high angle of attack region was entirely based on wind tunnel work. Fig. 4 gives a survey of models and wind tunnels used. For the basic development the low speed force model (1/5 scale) was tested mainly in the low speed wind tunnel in Emmen, Switzerland, which has a test section of 5 \* 7 meters. A photo of this model in the tunnel can be seen in Fig. 5, showing the model in an inverted position at high angle of attack during evaluation of the influence of the sting support system.

To improve some of the configuration's unfavorable characteristics the use of strakes as flow controllers was contemplated. This was based on results found in a research work by Hummel [4], who examined the influence of strakes (as flow controller for vortex flow) on basic delta wing configurations. These strakes were now not only used at the wing apex region but also at the fuselage nose, body side and shoulder region. To check out all possibilities to influence the flow about the configuration, a set of nose, body, fuselage and intake strakes was defined. In addition, different wings and tails (different in size as well as position and shape), including ventral fins and winglets, were considered to improve the configuration. A survey of these devices is presented in Fig. 6.

A detailed description of all devices is shown in Figs. 7 - 10.

Fig. 7 : different vertical fins, including ventrals

Fig. 8 : different wing configurations, including wing strakes and winglets

Fig. 9, 10 : different body, nose and inlet strakes

All the different means to improve the configuration could not be tested for all possible control variations. So a critical control configuration was determined as a baseline on which improvement was carried out. From earlier testing on the EFA / J90 configuration [2] it was known that the critical case for lateral and directional stability occurs at angles of attack between  $30^\circ < \alpha < 50^\circ$ . The canard should then be in an unloaded position to minimize vortex interaction with the wing, which is then maximally loaded ( $\alpha = 30^\circ$ ) or even separated ( $\alpha = 50^\circ$ ) in this region (a rough schedule for a canard control law was found to be  $-\alpha \approx \delta_{can}$ ; this means the canard should be rotated into the freestream flow direction). Also it was known that the leading edge flaps should be at maximum down deflection to shift flow separation on the wing to higher angles of attack.

This gives the following control settings for the configuration selection process :

$\alpha$	=	$40^\circ$	angle of attack
$\delta_{can}$	=	$-40^\circ$	canard deflection (l.e. down)
$\delta_{le}$	=	$-40^\circ$	leading edge flap deflection (down)
$\delta_{te}$	=	$0^\circ$	trailing edge flap deflection

$\delta_{le} = -40^\circ$  (streamwise) was found to be the most effective deflection angle and  $\delta_{te} = 0^\circ$  was chosen because the trailing edge flap deflection doesn't influence lateral and directional stability greatly. Also, judging from earlier test experience, a yaw angle of  $\beta = 5^\circ$  proved to be acceptable to establish the lateral and directional stability derivatives.

**Note :**

Not the sideslip derivatives  $C_{n\beta}$  and  $C_{l\beta}$  are given in all following figures, but the the sideslip coefficients  $C_{n\beta=5}$  and  $C_{l\beta=5}$  at sideslip angle  $\beta = 5^\circ$  together with the zero values  $C_{n\beta=0}$  and  $C_{l\beta=0}$ , which is for comparison purposes just as good as the derivatives and gives the advantage to show the behavior of the coefficients at  $\beta = 0^\circ$  as well.

In the following the influence of nose and body strakes, vertical tails and ventrals is discussed step by step.

**Nose strakes :**

Four different nose strakes were used : forward and backward position and for both positions an upper and lower location (see Fig. 9, strakes RS9, RS10, RS11 AND RS12).

Nose strakes are well known to improve directional stability at angles of attack higher than  $40^\circ$ , but their benefit is very sensitive to location. They are acting in two ways :

1. improving deviation of the yawing moment for the  $\beta = 0^\circ$  case which is caused by an asymmetric shedding of the nose vortices (the nose strakes fix these vortices symmetrically to the fuselage)
2. for sideslip cases the nose vortices can be fixed by the strakes, generating a stabilizing moment at the nose. This may be dangerous in some cases, because this moment gives an autorotative contribution to the dynamic characteristics and therefore, has to be validated later on in the spin tunnel.

Both reactions can be achieved (see Fig. 11 and 12). The deviation from zero for the  $\beta = 0^\circ$  case is removed for all four positions. The most beneficial strake location for the sideslip case  $\beta \neq 0^\circ$ , however, is the backward downward position RS12. Here directional stability is attained for all  $\alpha > 40^\circ$ . For lateral stability the forward position gives best results, though the influence is not very strong. The impact on pitching moment is too small to be shown here.

The best solution RS12 is kept for all further tests.

**Body strakes :**

As proposed by Hummel [4], a body strake was mounted behind the canopy at the fuselage shoulder (see Fig. 9), and will be referred to as RS14. Fig. 13 shows a small improvement of the directional stability in respect of the instability jump at  $\alpha = 40^\circ$  and a small decrease in roll stability at the same angle of attack. However, pitch characteristics are smoothed out at stall conditions above maximum lift (see Fig. 14).

There is another position for such a strake to correct the unfavorable lateral stability, namely in the diverter region, as will be shown later after optimizing vertical tails.

#### Increased vertical tail and ventrals :

Fig. 9 shows the baseline vertical tail S27, a tail increased in span by 30% (S28) and the increased tail in most backward position (S34). As can be expected, with increasing span and backward position, directional stability improves and lateral stability is not affected. This gives in combination with the optimum nose strake configuration RS12 a remarkable improvement in directional stability and good lateral characteristics (see Fig. 15). A further improvement occurs with the addition of ventral fins to the S34 fin, named now S35 (see Fig. 9 for geometry and Fig. 16 for aerodynamic coefficients).

Up to now the best configuration has the following equipment, which from now on is called **New Baseline** :

- RS12 : nose strake
- S35 : vertical tail with increased span in aft position and ventral fin
- no body strake

The task now was to find an optimum position for the body strake.

#### Optimization of body strake location :

The body strake should retain the good pitch characteristics shown before and additionally provide good lateral and directional stability, as shown by Hummel [4]. Therefore the location was optimized with possible locations in the fuselage region between canard and wing in longitudinal direction and intake and canopy in vertical direction. The idea was to fix separation of the cross flow in this region at the fuselage side wall in the same manner as with the nose strakes in the nose region.

The results of the variation are shown in Figs. 17 to 20. From all locations in the region described above the position just below the diverter (at the upper edge of the intake side wall, see Fig. 6), named intake strake RS16, was the best one with respect to lateral and directional stability (Fig. 17). Pitch characteristics, Fig. 18, are still to be improved.

Further search finally led to a combination of the intake strake RS16 with the forward part of the original body strake RS13, now called RS18 and an additionally mounted mini wing strake WS. (This mini wing strake is not a wing strake as usual (producing a strong vortex interaction with the wing leading edge vortex); it is more a sharp edge (flow controller) to fix the separation of the flow. Large strake areas will also fix the separation, but will give unfavorable strong pitch up characteristics due to the interference with the wing vortex).

The combination of strakes described above gave the best compromise for lateral, directional and longitudinal stability (see Fig. 19 and 20).

So the finally selected strake configuration RS20 consists of:

- RS12     nose strake, (back, down)
- RS16     intake strake
- RS18     forward part of body strake
- WS       mini wing strake

The different strakes are mainly acting as follows:

- nose strake        : improves directional stability for  $\alpha > 40^\circ$
- intake strake      : cures lateral stability for  $30^\circ < \alpha < 40^\circ$
- body strake        : smoothes jump in  $C_{m\alpha}$  characteristics  
                              for  $30^\circ < \alpha < 40^\circ$
- mini wing strake : fine tuning for all problems

#### Selected configuration :

The improvements found for the critical control settings should now of course be also beneficial for other control settings and for different yaw angles. Figs. 21 and 22 show these different yaw angles and it is obvious that the principle behavior is not changed. Even if we look at  $\beta$  - polars ranging from  $-20^\circ$  to  $+20^\circ$  for several critical values, totally stable behavior can be found in lateral motion, and for directional stability stable behavior is given at least between  $-5^\circ < \beta < +5^\circ$ , as is shown in the detailed analysis in [3].

Fig. 23 shows that even for a leading flap edge setting of  $\delta_{le} = 0^\circ$  stable behavior is achieved in lateral and directional stability for relevant canard settings with respect to angle of attack, e.g.:

$\delta_{can}$ (canard setting)	stable behavior $\alpha$ - regime	
	$C_n$ (yaw )	$C_l$ (roll)
$-20^\circ$	$0^\circ < \alpha < 22^\circ$	$5^\circ < \alpha < 22^\circ$
$-30^\circ$	$0^\circ < \alpha < 70^\circ$	$5^\circ < \alpha < 70^\circ$
$-35^\circ$	$0^\circ < \alpha < 70^\circ$	$5^\circ < \alpha < 70^\circ$
$-40^\circ$	$0^\circ < \alpha < 70^\circ$	$5^\circ < \alpha < 70^\circ$
$-50^\circ$	$37^\circ < \alpha < 70^\circ$	$35^\circ < \alpha < 70^\circ$

This shows that a possible trim schedule in respect of good lateral and directional stability (here for the case  $\delta_{te} = 0^\circ$ ,  $\delta_{le} = 0^\circ$ ) is roughly between  $\delta_{can} = -\alpha$  and  $-\alpha/2$ , as stated already above. Even canard settings different from this control schedule (for maneuver cases) do not lead to a loss of stability.

Trim schedules :

Trim schedules are dictated by the pitch instability margin and the pitch characteristics of the configuration and strongly influence the following items

- control power about all axis  
(especially about pitch, with the vital question for enough recovery moment from high angles of attack )
- directional and lateral stability
- maximum trimmed lift coefficient
- trim drag

The necessary aerodynamic recovery moment in pitch from high angles of attack limits the maximum possible pitch instability margin as well as the maximum possible deflection rate of canard and flaps. A limit for the maximum instability margin is also given by the flight control system. On the other side the pitch instability should be high enough to meet the requested performance demands in the subsonic region - higher instability gives lower trim drag.

Besides choosing the pitch instability level, the designer can influence the pitch characteristics over angle of attack by means of adding strakes or changing wing shape, fuselage contour, stabilizers etc.

All this has to be balanced very carefully now to find the overall best configuration for the post stall and conventional performance requirements. This is of course a complicated and lengthy process and beyond the scope of this paper. So only the final optimum control law and the appropriate behavior of stability and control about all axis will be presented. A detailed discussion of the optimization process can be found in the analysis paper [3].

The final optimum trim schedule or control law for canard, leading and trailing edge flaps is plotted in Fig. 24. The leading edge flap is continuously deflected down with increasing angle of attack until the maximum deflection of  $40^\circ$  is reached at maximum lift. The canard is held at zero position until  $20^\circ$  angle of attack to allow the trailing edge flaps to be used to improve trim drag and maximum trimmed lift. From  $\alpha = 20^\circ$  on, the trailing edge flaps are brought back to zero position and the canard is continuously deflected downwards in direction of the free flow to reduce load both on canard and wing for optimum conditions for lateral and directional stability at high angles of attack.

Figs. 25 now depicts the result for the trimmed  $C_{m\alpha}$  curve and Fig. 26 for the directional and lateral stability - which is stable in the whole angle of attack region! The trimming was done with the canard, keeping leading and trailing edge flap in zero position. Fig. 27 illustrates the improvement in leading edge flap deflection and Fig. 28 shows the penalties incurred by using the trailing edge flaps which are deflected in the angle of attack region  $0^\circ < \alpha < 30^\circ$ .

In Figs. 29 and 30 the roll control power available for trimmed conditions is presented. The yaw control power is shown in Figs. 31 and 32. Both controls are fulfilling the desired maneuver

requirements for a fighter aircraft, see [5], when using some additional control power in yaw from a vector nozzle.

Finally it is shown in Fig. 33 in the so called "Weissman Plot" (where the lateral control departure parameter LCDP is plotted versus the directional dynamic stability  $C_{n\dot{\beta}dn}$ ) that up to 65° angle of attack no spin susceptibility should be expected. The Weissman Plot gives the design engineer a first idea how a configuration will behave regardless of the configuration being prone to spin or not. However clear statements with respect to departure behavior can only be drawn by including the influence of dynamic characteristics.

### 3. DYNAMIC BEHAVIOR AND SPIN MODES

To evaluate dynamic characteristics, wind tunnel tests on the base of a rotary balance measurement were conducted in the Langley Research Center's 20 foot Spin Tunnel. They helped to establish the developmental aircraft's steady state high angle of attack static and rotational aerodynamic characteristics. Data were obtained for a 1 / 7.5 scale model through an angle of attack range of  $0^\circ < \alpha < 90^\circ$  to define the aircraft's steady-state aerodynamic characteristics, both static and rotational, including the influence of sideslip, control deflections, speed brakes and thrust vanes. A photograph of the rotary balance apparatus installed in the Langley Spin Tunnel is shown in Fig. 34. An analysis of the data is presented in [7] and [8], including steady-state spin modes, predicted using the method described in [6]. A summary of these investigations is given in the following.

#### Discussion of dynamic characteristics :

As shown above, the X-31A is behaving extremely well in terms of static lateral and directional stability; for both the airplane is stable or at least neutral in the whole angle of attack regime for trimmed flight. Also control power about roll and yaw axes is available up to 90° angle of attack. Serious statements with respect to departure behavior, however, can only be made when the the influence of dynamic characteristics is included.

#### Lateral characteristics

The influence of rotation on the rolling moment characteristics of the basic airplane shows that in normal flight regime the airplane is highly damped in roll (see Figs. 35 and 36). As stall is approached, the level of damping decreases. After stall the configuration becomes autorotative in roll, remaining so through 60°. Above 60° the rolling moment is neutral to slightly propelling, as is the case for most airplanes. These characteristics indicate that departures from controlled flight are possible for the un-augmented airframe. In conjunction with a flight control system, this, however, will be no problem as long as sufficient roll control power is available - and the X-31A provides good roll power by means of ailerons (differential trailing edge flaps) throughout the whole angle of attack regime. As can be expected, control effectiveness decreases at higher angles of attack, but some control power is still maintained up to 90°.

For a critical case, say  $\alpha = 40^\circ$ , the test results of the lateral rotational derivatives are given with and without roll control

input (see Fig. 39). As can be seen, the existing roll power is large enough to stop a possible motion about the roll axis.

#### Directional characteristics

The basic airplane is damped in yaw through 40° angle of attack. At 45°, it becomes neutral and at 50° slightly propelling and remains autorotative up to 70°. Above 70° it is damped again, see [8]. The presence of the canard, however, has a major influence on the damping produced above 50° angle of attack. Especially for trim deflections, the autorotative regions are significantly reduced. The values for the complete configuration are shown in Figs. 37 and 38.

Figs. 35 and 37 are showing - besides the rotary derivative  $C_1 / (\Omega b / 2V)$  measured in the spin tunnel - theoretically estimated derivatives, indicated as "SNAKE Dataset", which fit quite well with the experimental data. In the conventional angle of attack region  $0^\circ < \alpha < 20^\circ$  a linear panel method was used, as is shown in [9]. Above maximum lift, a semi empirical method was used.

#### Predicted spin modes :

Rotary balance aerodynamic data can be used to predict steady-state spin modes at any specific attitude for a given set of masses and inertias. An outline of the method and the historical background are presented in [6]. For steady state spins to occur, the aerodynamic pitching, rolling and yawing moments must balance their respective inertial moments. A propelling aerodynamic moment must exist in order to maintain the airplane's rotation, the rolling moment being the primary driving term at low angles of attack, with the yawing moment becoming the dominant propelling component as angle of attack increases to the flat spin modes.

Since an erect rotating airplane always produces a nose up inertial moment, nose down aerodynamic pitching moments must exist to balance it and hence permit a spin. For airplanes with unstable or relaxed pitch stability (unstable at low  $\alpha$  and becoming more and more stable at high  $\alpha$ ), such as the X-31A, this condition may not be satisfied over a large portion of the angle of attack range for certain control deflections, thereby limiting possible spin modes. Fig. 40 presents the spin modes calculated for the X-31A ([7], [8]) at the weights and inertias corresponding to a basic mission loading with 60% internal fuel. No spin modes are predicted without lateral or directional control inputs for any normal canard or symmetrical trailing edge flap deflection. However, an extended canard setting of  $\delta_{can} = -70^\circ$ , which is not used by the flight control system, exhibits a moderately fast flat spin at 84° angle of attack of 2.7 seconds per turn. This is due to the propelling yawing moments this canard setting generates above 75° angle of attack.

Asymmetric trailing edge flap deflections are very effective at the spin attitude because of the adverse yaw they are capable of generating. Surface deflections against the spin produce a flat spin mode (at 85° to 87° angle of attack and 1.7 to 2.8 seconds per turn) for all canard deflections between 0° and -70°, exhibiting the fastest turn rates. The roll control surfaces, again due to their yawing moment effectiveness, when deflected with the spin, result in a no spin condition.

Generally it is not possible to predict actual recovery characteristics from these results since it is not known how readily the airplane will move from equilibrium spin condition for one control setting to a no spin condition for another. The actual sufficiency of recoveries can only be determined through dynamic testing and large six degree of freedom analytical calculations.

#### Comparison with experimentally determined spin modes :

Spin modes that were experimentally determined from free spinning tests of a dynamically scaled model of the X-31A in the Langley Spin Tunnel are compared with the predicted spin modes in Fig. 41. Experience has shown that the full scale airplane will either have a steady spin as predicted, or it will have an oscillatory spin mode whose average values of angle of attack and turn rate will equal the predicted steady values. Also, in some extreme cases, the oscillatory motions will be so severe that the airplane cannot stabilize in the spin. As shown in Fig. 41, there is excellent agreement between the experimental and predicted spins. For the X-31A, the experimental spin with pro spin rudder and ailerons for -60° canard setting is oscillatory, with the average angle of attack nearly equal to the angle of attack of the calculated spin.

The free spinning model tests showed that neutralizing the canard, again with ailerons deflected against the spin and pro spin rudder, produces a steady, flat spin mode (88° angle of attack at 2.0 seconds per turn) that agrees well with the predicted steady spin (87° at 2.4 seconds per turn). Deflecting the ailerons with the spin produces no spin mode, as is predicted.

#### 4. CONCLUSION

The configuration exhibits positive pitching moments over almost the entire tested angle of attack range with neutral controls, which commensurates with the intended relaxed pitch stability. Below stall, the X-31A exhibits good lateral directional static stability and is well damped in roll and yaw. As stall is approached, lateral stability is reduced and the aircraft becomes propelling in roll. If the aircraft is rolling about its body axis, difficulties can be encountered in terminating the roll rate in the 30° to 50° angle of attack region until large sideslip angles are attained. This situation is not approached if the aircraft rolls about the wind axis, which at high angle of attack is the only possible and significant maneuver. Fortunately, the existing control laws will ensure that the aircraft does roll only about the velocity vector.

The vehicle is highly damped in yaw through 40° angle of attack. However in the region of 50° angle of attack the damping is slightly reduced and a small zero sideslip yawing moment offset can be observed as well. Negative canard deflections generally result in an increase in yaw damping up to stall, but the same deflections have an adverse effect as angle of attack is further increased.

As is normally the case, the effectiveness of the aerodynamic controls is reduced between  $0^\circ < \alpha < 90^\circ$ . Nevertheless, a good level of longitudinal and lateral control power is available throughout the whole angle of attack range. The directional control provided by the rudder, however, is relatively ineffective



beyond 45° angle of attack - the reason for the configuration having a vector nozzle.

Movement of the trailing edge flap has large influence on the roll characteristics. Deflecting the trailing edge flap negatively, to produce a nose up pitching moment, significantly decreases the propelling moments, whereas the opposite is the case when the flap is deflected in a positive direction. Unfortunately, because of the relaxed pitch stability, a positive deflection is likely to be commanded at high angle of attack.

The aircraft probably has only one spin mode which is flat ( $\alpha = 86^\circ$ , 2.3 sec/turn). The yawing moment associated with the lateral control above 60° angle of attack is the parameter most responsible for this spin mode and for recovery. Spinning does not appear to be a problem with this configuration due to the lateral control effectiveness as well as the presently envisaged control laws that attempt to keep the aircraft from attaining spin angle of attack, and that may limit the available lateral control at such attitudes by giving priority to pitch control.

#### References

- [1] John H., Kraus W.  
High Angle of Attack Characteristics of Different Fighter Configurations  
Symposium on High A.O.A. Aerodynamics, AGARD  
4-6 Oct. 1978, Sandefjord, Norway
- [2] Kraus W.  
Delta Canard Configuration at High Angle of Attack  
12th ICAS Congress  
12-17 Oct. 1980, München
- [3] Kraus W.  
Analysis of Test Phase 13, P20-SNAKE (X-31) Low Speed Wind Tunnel Tests in Emmen  
MBB TN SNAKE/R/10  
12 Dec. 1985
- [4] Hummel D.  
Untersuchungen zur Rollstabilität von Tragflügeln bei großen Anstellwinkeln  
Teil 1 - 4  
TU Braunschweig, Berichtsnr. 79/4, 80/3, 81/2, 83/3  
1979 - 1983
- [5] Kraus W., Przibilla H., Haux U.  
Stability and Control for High Angle of Attack Maneuvering  
AGARD FMP-Symposium : Criteria for Handling Qualities of (CP 333) Military Aircraft  
Fort Worth, Texas USA  
19. - 22. Apr. 1982
- [6] Bihle W., Barnhart B.  
Spin Prediction Techniques  
Journal of Aircraft, Vol. 20, No. 2  
Feb. 1983

- [7] Dickes E., Barnhart B.  
An Aerodynamic Math Model of the SNAKE (X31) Airplane for  
Simulation of Flight Motions  
BAR 86-10  
Sep. 1986
  
- [8] Dickes E.  
Analysis of Static and Rotational Aerodynamics at High Angle  
of Attack for the X-31A Aircraft  
BAR 88-1  
June 1988
  
- [9] Sacher P., Kraus W., Kunz R.  
Computational Aerodynamic Design Tools and Techniques Used  
at Fighter Development  
AGARD Symposium : The Use of Computers as a Design Tool  
(CP 280)  
Neubiberg, Germany  
3. - 6. Sept. 1979

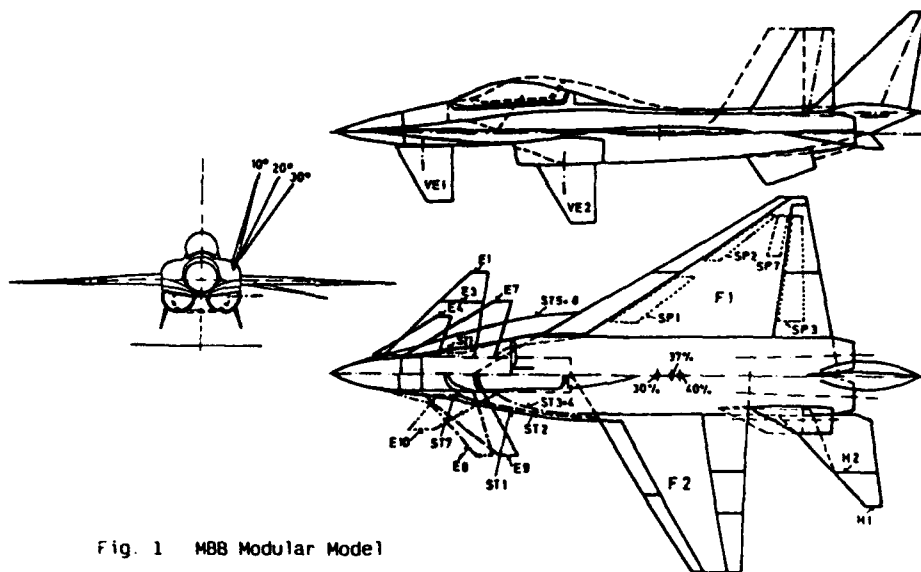


Fig. 1 MBB Modular Model



Fig. 2 Flow Visualization of Leading Edge Vortices on a Delta Canard Configuration

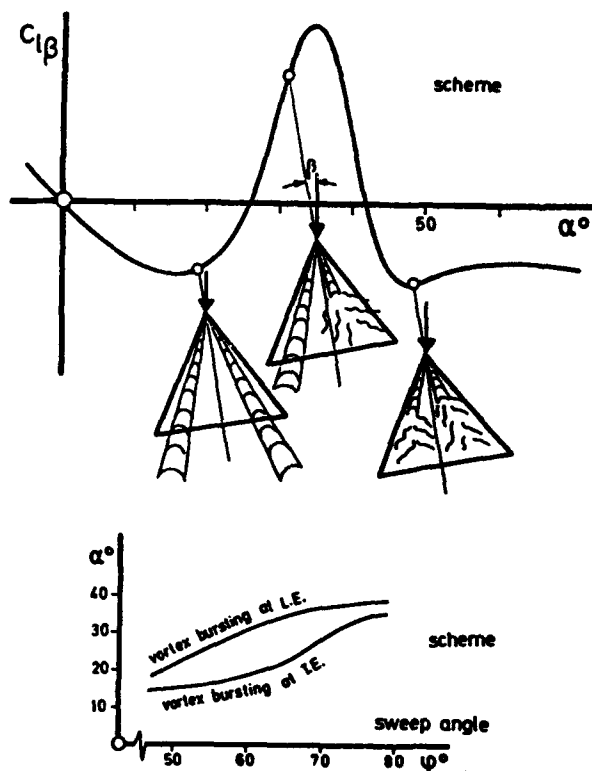


Fig. 3 Roll Stability Versus Angle of Attack for a Pure Delta Wing

Wind Tunnel Models Used		Wind Tunnels Used	
Low Speed Force	1/5	Low Speed LRC	4 * 7 m, VSTOL
Rotary Balance	1/7.5	TWT Rockwell	4 * 4 ft
High Speed Force	1/10	Low Speed Emmen	5 * 7 m
Forced Oscillation	1/5	(Switzerland)	
Free Spin Model	1/30	Spin Tunnel LRC	20 ft Ø

Fig. 4 Wind Tunnel Models and Wind Tunnels Used



Fig. 5 Wind Tunnel Model

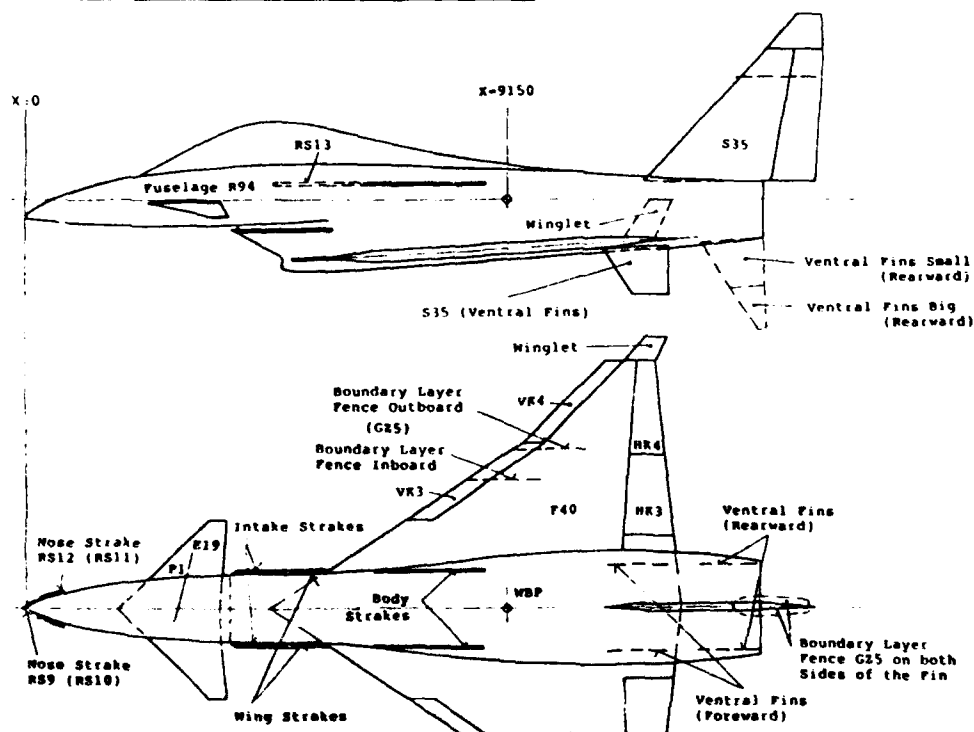


Fig. 6 Survey of Devices Used on the X-31 to Improve High Angle of Attack Characteristics


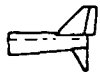









S25	Single Fin (TKF/J90) With Double Wedge Profile		S30	= S27 • Double Ventral Fins High Span, Rearward Position	
S26	Single Fin (S25) • Single Ventral Fin		S31	= S27 • Double Ventral Fins Low Span, Forward Position	
S27	Single Fin: P20 SNAKE With Double Wedge Profile		S32	= S27 • Double Ventral Fins Low Span, Rearward Position	
S28	= S27 • 30% Span Increase		S33	= S28 • Double Ventral Fins Low Span, Forward Position	
S29	= S27 • Double Ventral Fins High Span, Forward Position		S34	= S28 in Rearward Position (+70 mm)	
			S35	= S34 • Double Ventral Fins Low Span, Forward Position	

Fig. 7 Devices to Improve High AOA Characteristics.  
Different Vertical Fins (incl. Ventral Fins)

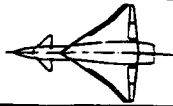
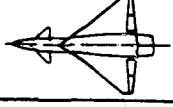
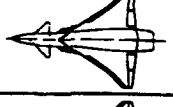
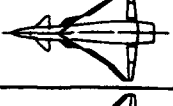
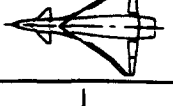
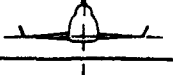

F40	SNAKE-Configuration P20 (Basic) Plain Wing with Double Wedge Profile	
F41	Plain Wing (F40) With Straight Leading Edge	
F42	Plain Wing (F40) with 36 Strake (3% of Wing Area) Pitch = 30°/75°	
F43	Plain Wing (F40) with 36 Strake Pitch = 40°/80°	
F44	Plain Wing (F40) with 16 Strake Pitch = 75°	
F45	Plain Wing (F40) with winglets up	
F46	Plain Wing (F40) with winglets down	

Fig. 8 Devices to Improve High AOA Characteristics.  
Different Wing Configuration

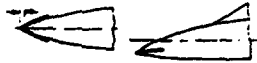

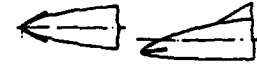
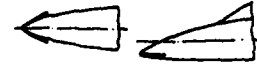





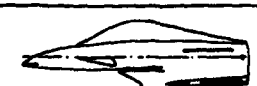
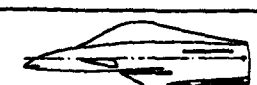
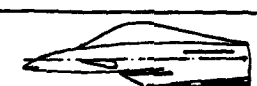


RS09	Body Nose Strake Foreward Upward	
RS10	Body Nose Strake Foreward Downward	
RS11	Body Nose Strake Backward Upward	
RS12	Body Nose Strake Backward Downward	
RS13	Body Strake Wing Apex + Canopy Fuselage Shoulder Region	
RS14	Body Strake RS12 + RS13	
RS15	Body Strake Short Version of RS13 in Foreward Position + RS12	
RS16	Intake Strake + RS12	
RS17	Diverter Strake (between Intake Strake RS16 and Body Strake RS13) + RS12	
RS18	Short Version of RS13 in Rearward Position + RS12	
RS19	= RS18 + RS16 + RS12	
RS20	= RS18 + RS16 + Wing Strake vs + RS12	
RS21	= RS19 without RS18	
RS22	= RS21 + RS15	

Fig. 9/10 Devices to Improve High AOA Characteristics.  
Body and Nose Strake Variation

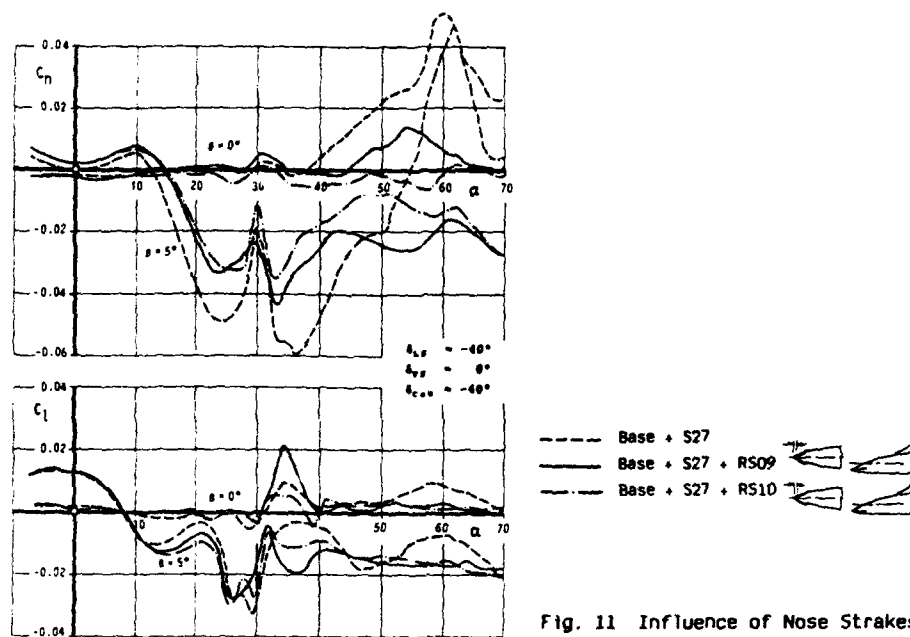


Fig. 11 Influence of Nose Strakes

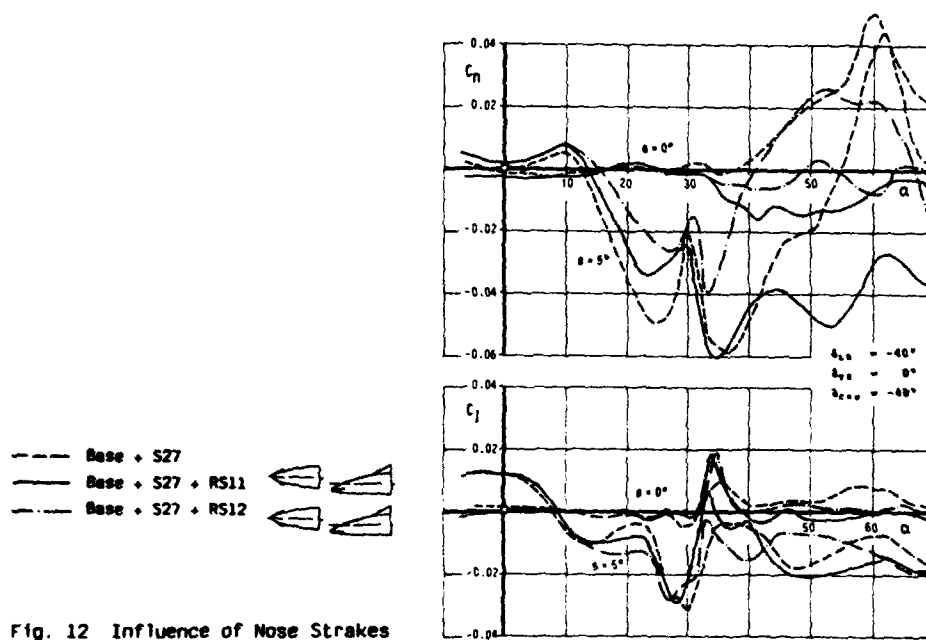


Fig. 12 Influence of Nose Strakes



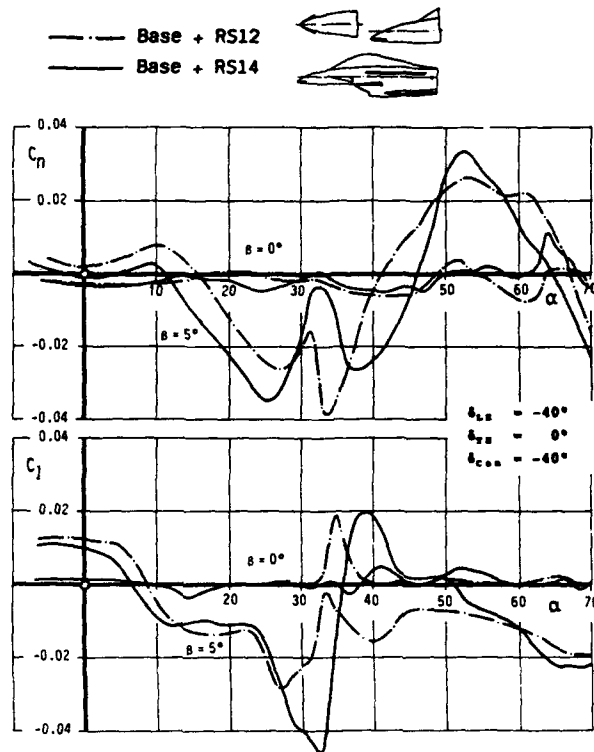


Fig. 13 Influence of Body Strakes

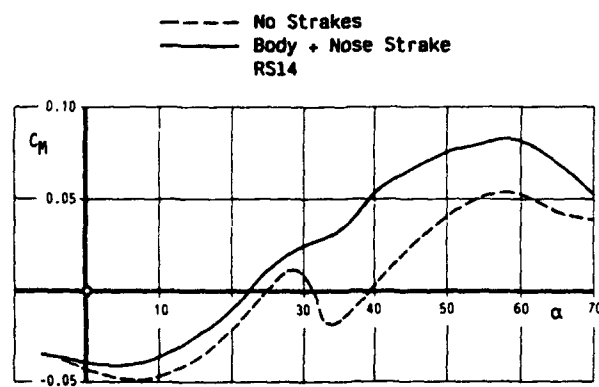


Fig. 14 Influence of Body Strake on Longitudinals

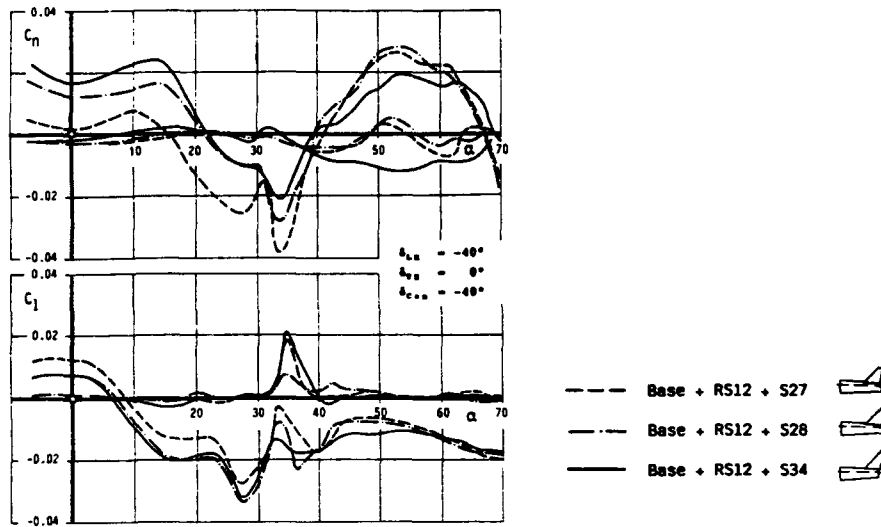


Fig. 15 Influence of Increased Span of Vertical Tail and Aft Position

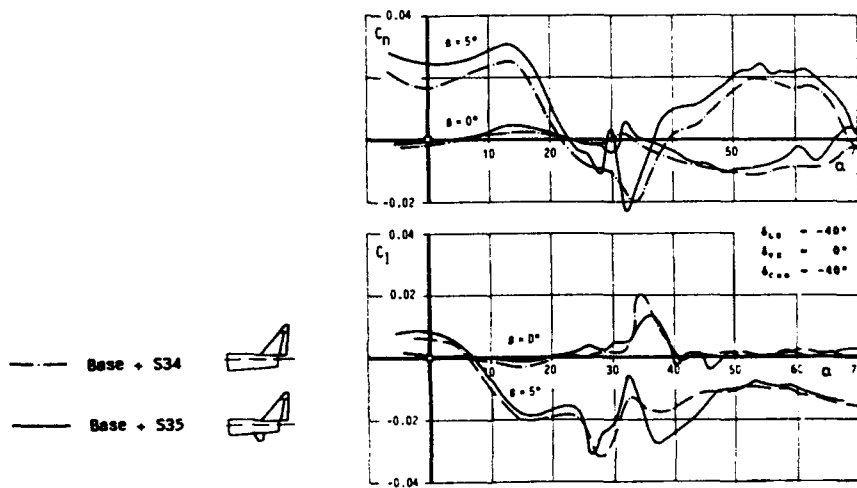


Fig. 16 Influence of Ventral Fins

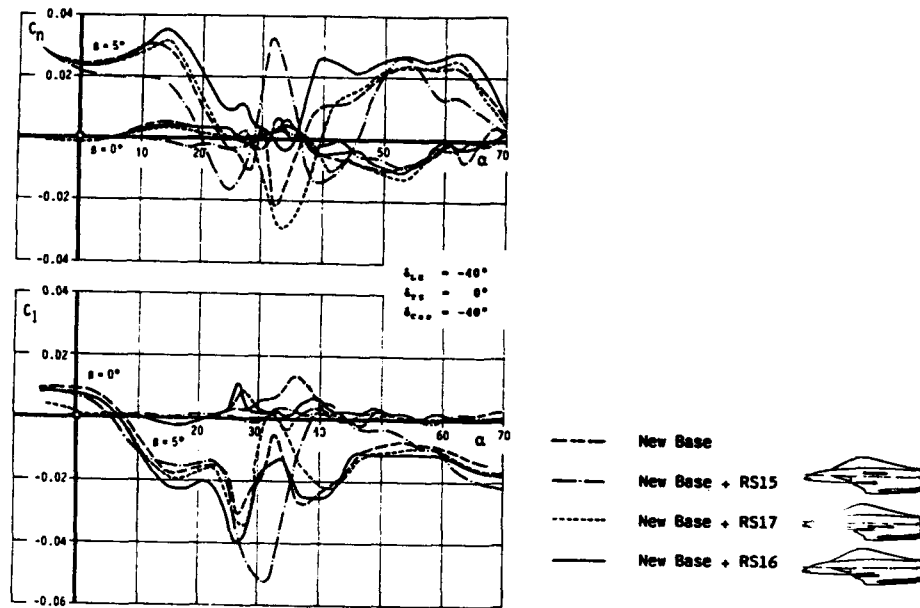


Fig. 17 Influence of Body Strake Variation

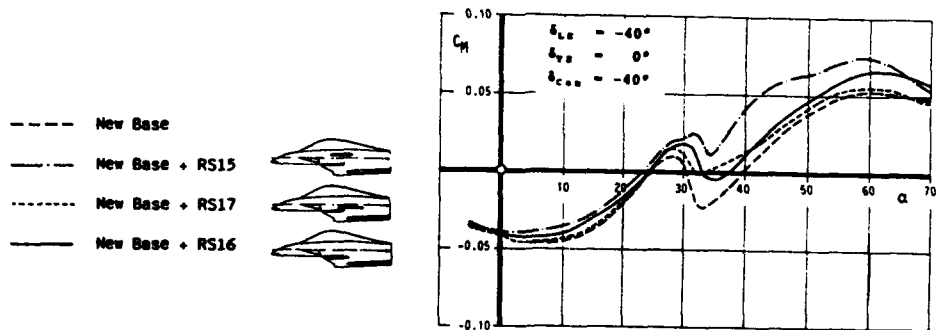


Fig. 18 Influence of Body Strake Variation on Longitudinals

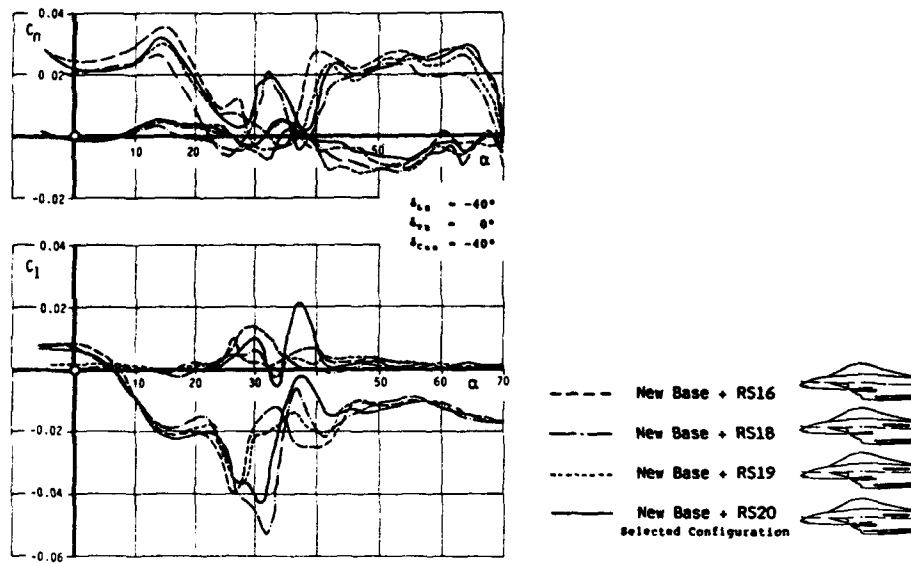
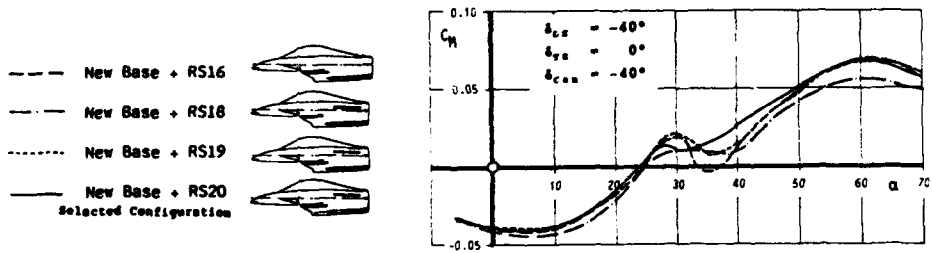
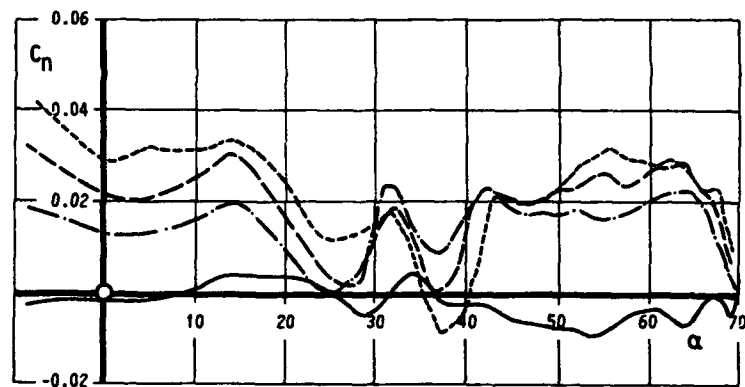


Fig. 19 Influence of Body Strake Variation

Fig. 20 Influence of Body Strake Variation  
on Longitudinals



—	$\beta = 0^\circ$	$\delta_{L2} = -40^\circ$
- - -	$\beta = 3^\circ$	$\delta_{L2} = 0^\circ$
- · - · -	$\beta = 5^\circ$	$\delta_{C22} = -40^\circ$
· · · · ·	$\beta = 7^\circ$	

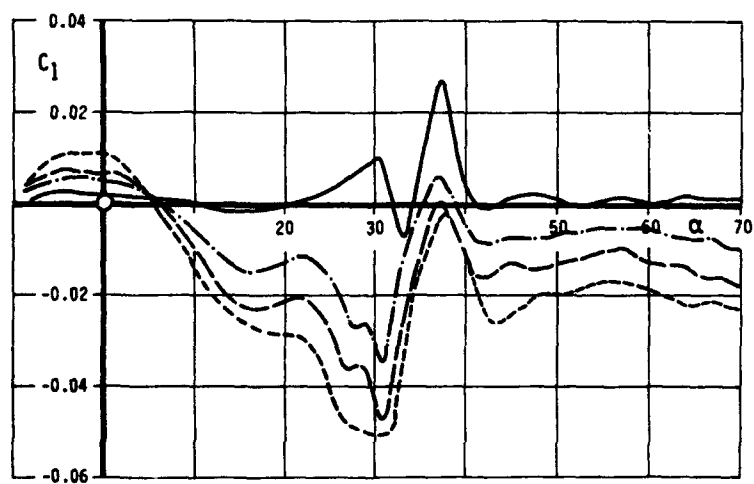


Fig. 21 / 22 Selected Configuration

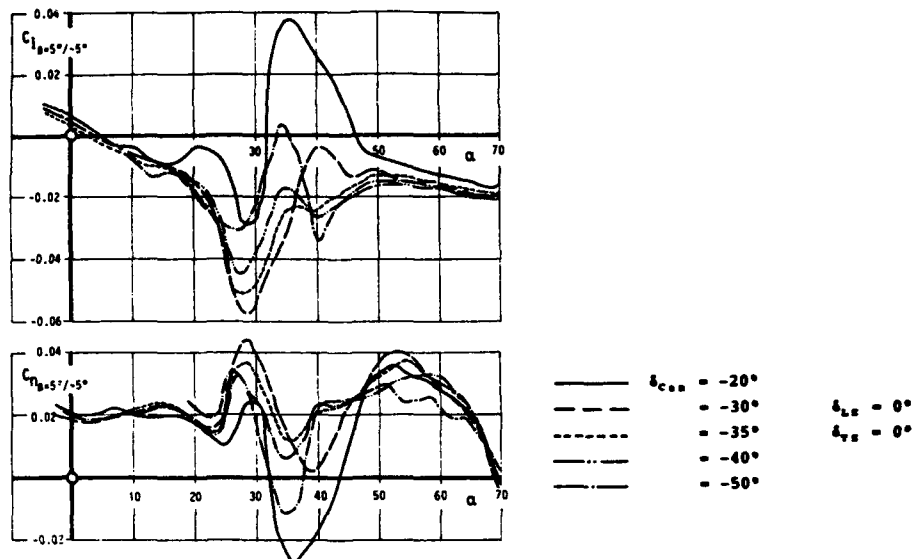


Fig. 23 Influence of Canard Deflection on the Selected Configuration

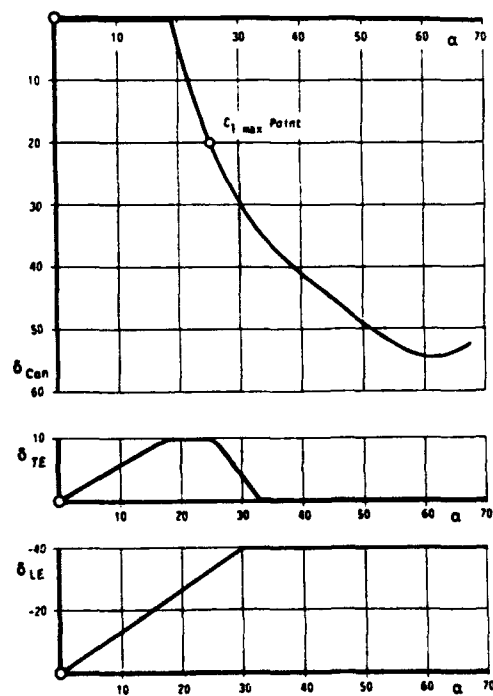


Fig. 24 Proposal for Control Law: Canard, Trailing and Leading Edge Flap

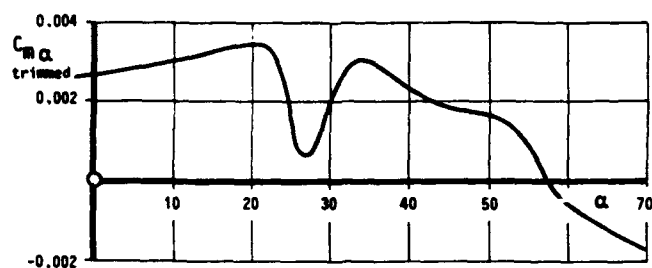


Fig. 25 Trimmed Pitch Characteristics

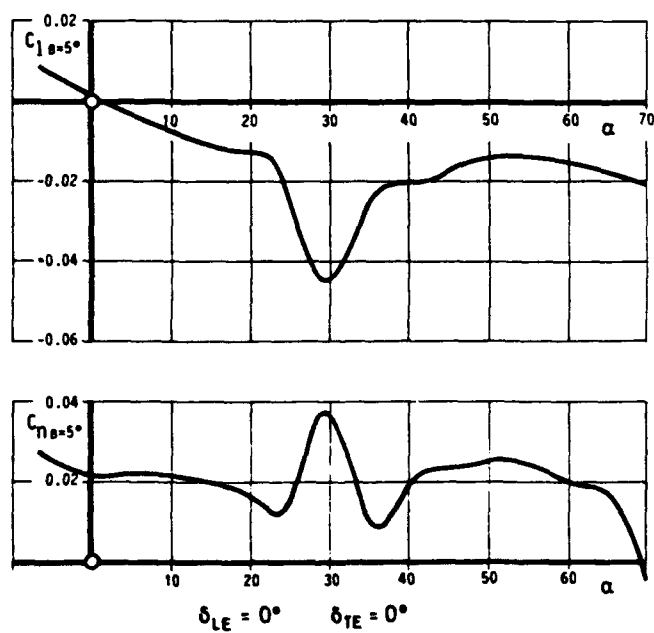


Fig. 26 Trimmed Lateral and Directional Stability

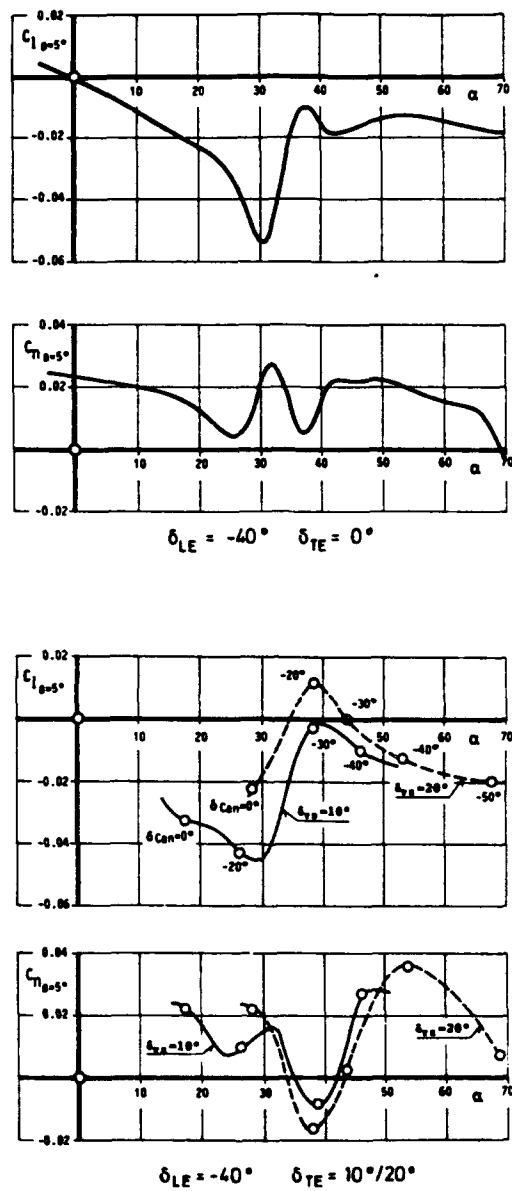


Fig. 27/28 Trimmed Lateral and Directional Stability by Use of Trailing Edge Flaps



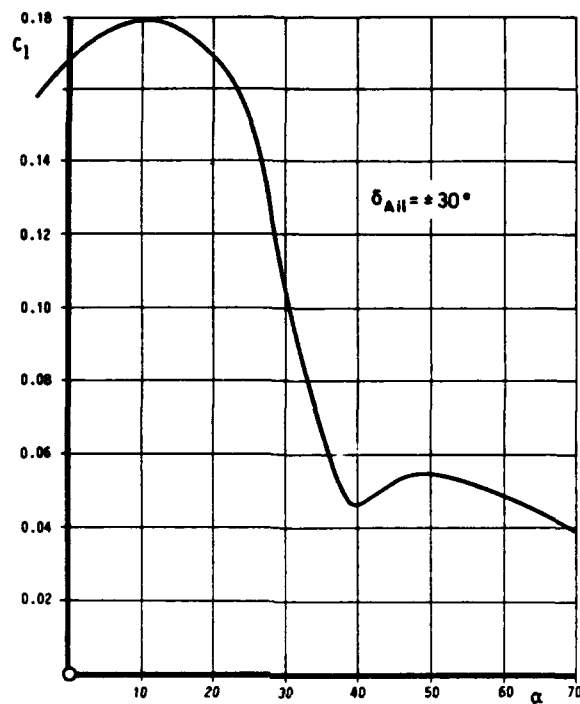


Fig. 29 Roll Control for Trimmed Conditions

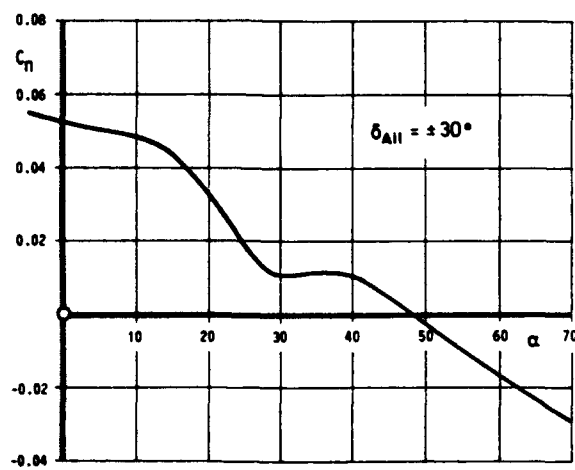


Fig. 30 Roll Control (Yawing due to Roll Control) for Trimmed Conditions

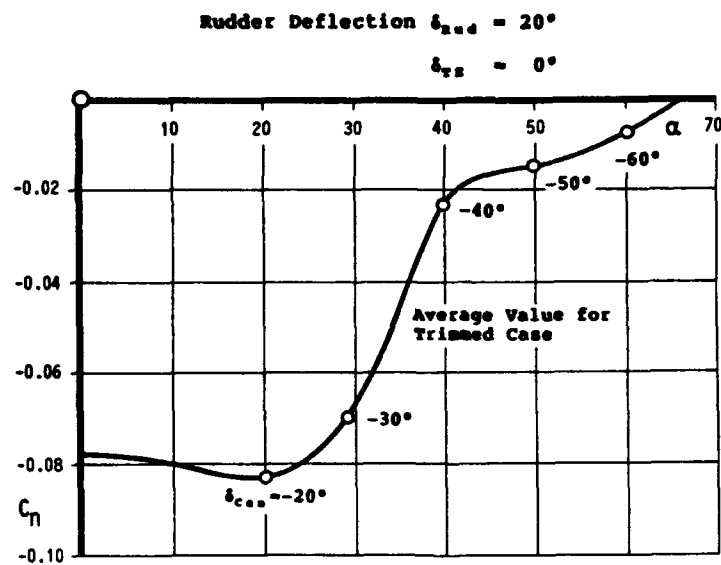


Fig. 31 Yaw Control for Trimmed Conditions

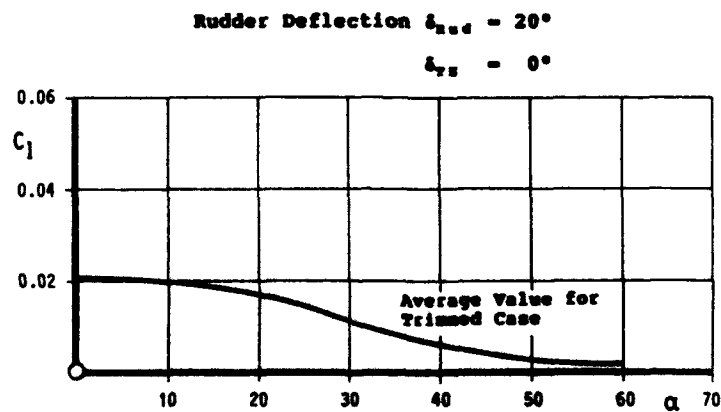
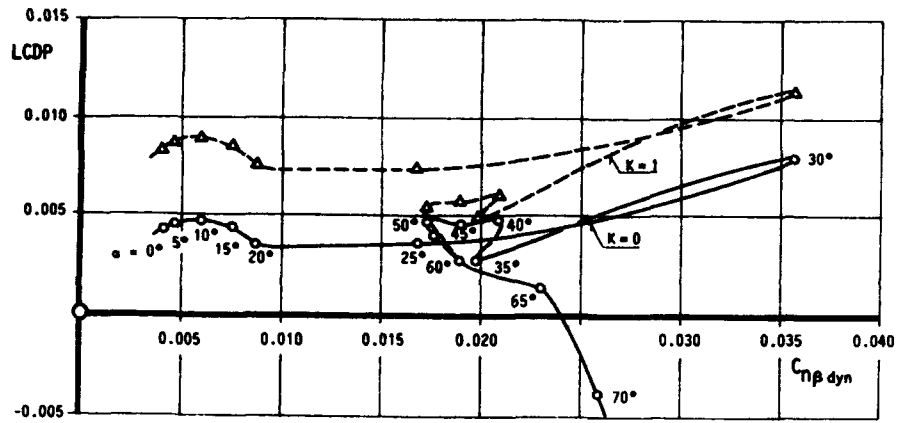


Fig. 32 Yaw Control (Rolling due to Yaw Control) for Trimmed Conditions



$$LCDP = C_{n\beta} - C_{l\beta} \frac{C_{n\delta A11}}{C_{l\delta A11}} + K \left( \frac{C_{n\delta A11}}{C_{l\delta A11}} C_{l\delta \text{rud}} - C_{n\delta \text{rud}} \right)$$

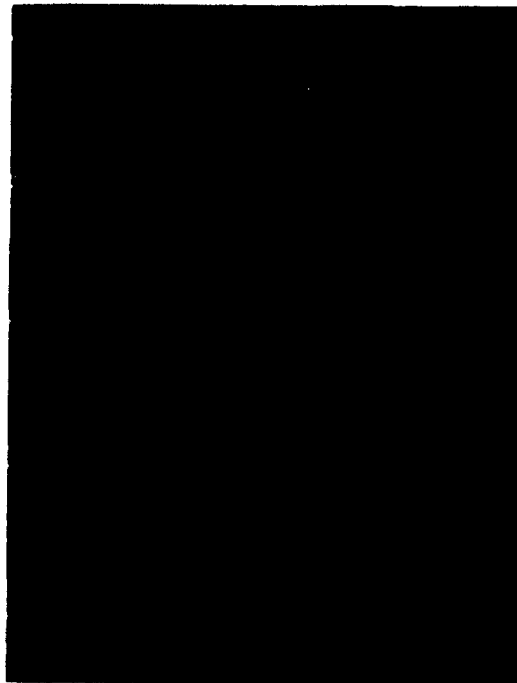
Fig. 33 LCDP versus C<sub>nβdyn</sub>

Fig. 34 Rotary Balance Model in the Langley Spin Tunnel

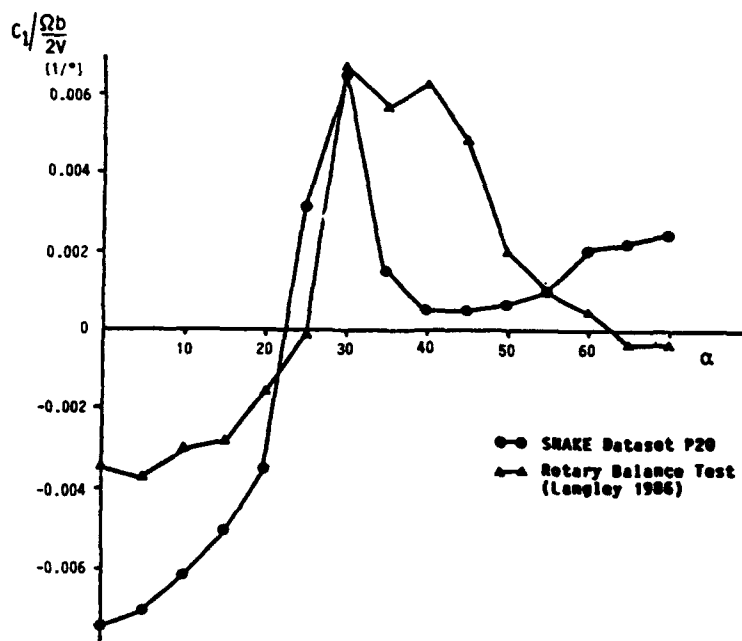


Fig. 35 Body Axis Roll Moment due to Wind Axis Rollrate

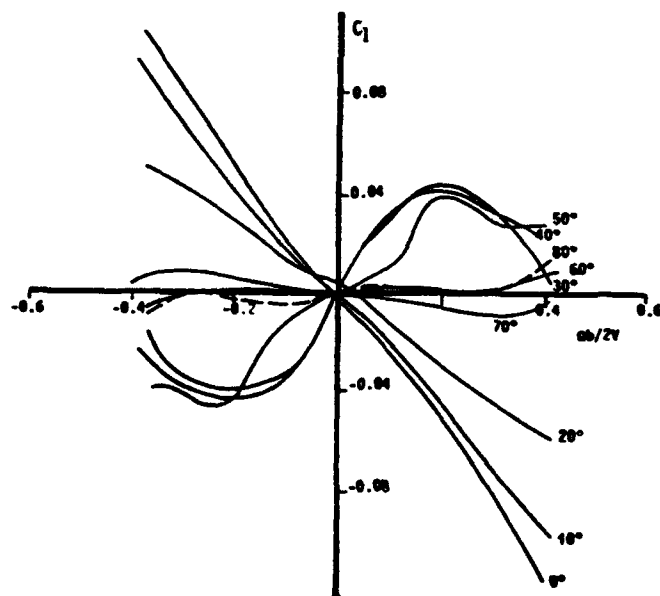


Fig. 36 Body Axis Roll Moment Versus Angular Velocity

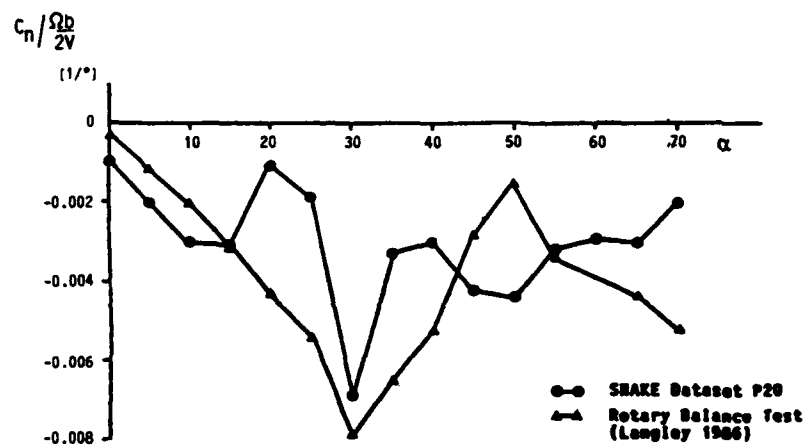


Fig. 37 Body Axis Yaw Moment due to Wind Axis Rollrate

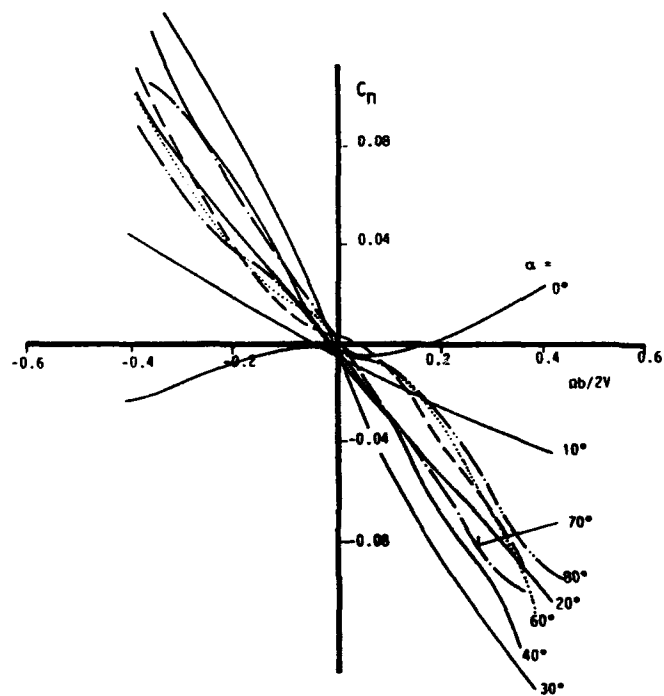


Fig. 38 Body Axis Yaw Moment Versus Angular Velocity

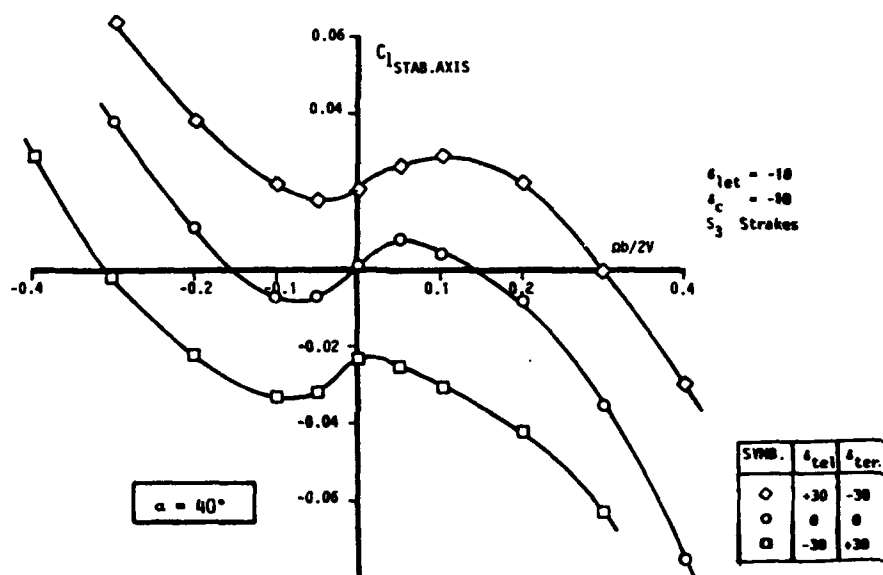


Fig. 39 Aileron Efficiency Versus Angular Velocity

CONTROL DEFLECTIONS					PREDICTED SPIN MODE				
$\delta_{tet}$ inbd/outbd deg	$\delta_c$ deg	$\delta_r$ deg	$\delta_{ter}$ deg	$\delta_{ter}$ deg	$\alpha$ deg	section	db/2V	$\beta$ deg	$V_D$ ft/sec
-40/-32	+20	0	0	0	No Spin (High- $\alpha$ pitch trim possible)				
0	-40				84	2.7	.11	4.2	253
-40	-60				No Spin (High- $\alpha$ pitch trim possible)				
-70	-40				No Spin				
-40	+20	-30	-30	+30	No Spin (High- $\alpha$ pitch trim possible)				
-60	-40				84	5.2	.03	4.2	420
-40	-60				86	2.5	.11	-4.4	256
-60	-40				86	2.3	.12	-1.8	254
-70	-40				84	2.8	.15	-0.8	250
0	-60				86	1.8	.15	-0.9	256
-40	-70				86	1.7	.16	-0.9	255
-60	0				87	2.3	.12	-1.8	255
-70	+20	-40	+30	+40	86	2.3	.12	-1.8	254
-40	-40				87	2.1	.13	-2.7	256
-60	-70				87	1.7	.17	-2.0	255
-40	0	-30	-30	-40	85	2.8	.10	-1.8	258
					75	6.4	.04	0.2	259
					No Spin				

All spins calculated on pilot's right at an altitude of 25,000 ft for the following weight and inertial conditions

Weight = 12,610 lbs  
 $cg = 23.9\%c$   
 $I_{xx} = 3231 \text{ slug ft}^2$   
 $I_{yy} = 28462 \text{ slug ft}^2$   
 $I_{zz} = 29669 \text{ slug ft}^2$

Fig. 40 Predicted Erect Spin Modes for the X-31A Airplane

SOURCE	AIRCRAFT	CONTROL DEFLECTION					PREDICTED SPIN MODE			
		$\delta_{lef}$ deg	$\delta_c$ deg	$\delta_r$ deg	$\delta_{ail}$ deg	$\delta_{str}$ deg	$\alpha$ deg	$\frac{\text{sec}}{\text{turn}}$	$\frac{\Omega b}{2V}$	$\frac{V}{D}$ ft/sec
SPIN TUNNEL CALCULATED	X-31A X-31A	-40/-32 ↓	0 ↓	-30 ↓	-30 ↓	+40 ↓	88	2.0	.15	243
							87	2.4	.13	230
SPIN TUNNEL CALCULATED	X-31A X-31A	↓	-60 ↓	↓	↓	↓	82 (88)*	2.0	.14	250
							94 86	1.9	.16	232
SPIN TUNNEL CALCULATED	X-31A X-31A	↓	+20 ↓	↓	+40 ↓	-30 ↓	NO SPIN NO SPIN			

Unless noted otherwise, all spins calculated to pilot's right at an altitude of 20,000 ft for the following weight and inertial conditions:

Weight = 12,850 lbs.  
 cg = 23.8%  
 $I_{xx}$  = 3329 slug ft<sup>2</sup>  
 $I_{yy}$  = 29887 slug ft<sup>2</sup>  
 $I_{zz}$  = 30882 slug ft<sup>2</sup>

Actual NASA Spin Tunnel Model Loading #1

\*Oscillatory spin, average value in parenthesis

Fig. 41 Comparison of Experimentally Determined and Analytically Predicted X-31A Erect Spin Modes

# USE OF STEPWISE REGRESSION TECHNIQUES AND KINEMATIC COMPATIBILITY FOR THE ANALYSIS OF EAP FLIGHT DATA

by  
A R Perkins  
Senior Aerodynamicist  
British Aerospace (Military Aircraft) Ltd  
Warton Aerodrome  
Preston  
Lancashire  
PR4 1AX  
England

## Summary

This paper describes an investigation into the capabilities and accuracy of an equation error method of aerodynamic parameter identification using stepwise regression techniques. The results of the method are presented for flight responses of the British Aerospace EAP aircraft which has multiple control surfaces and high levels of longitudinal instability together with significant non-linearities in the aerodynamic data. The benefit of kinematic compatibility processing of the flight data is also presented. The EAP flight responses are analysed up to an incidence of 30° using a technique for joining together several manoeuvres to form larger databases for analysis. The derivatives extracted by these techniques agree in general with the results of the wind tunnel measurements.

S	Reference area
b	Reference span
c	Mean aerodynamic chord
Cl	Coefficient of rolling moment
Cm	Coefficient of pitching moment
Cn	Coefficient of yawing moment
Cx	Coefficient of axial force
Cy	Coefficient of side force
Cz	Coefficient of normal force
EAP	Experimental Aircraft Programme
g	acceleration due to gravity
Ixx	Moment of inertia about x axis
Iyy	Moment of inertia about y axis
Izz	Moment of inertia about z axis
Ixz	Cross product of inertia
M	Mass (kg)
nx	axial acceleration
ny	lateral acceleration
nz	normal acceleration
p	roll rate
q	pitch rate
r	yaw rate
p	roll acceleration
q	pitch acceleration
r	yaw acceleration
u	Flight path velocity y axis
v	Flight path velocity y axis
w	Flight path velocity z axis
α	angle of incidence
β	angle of sideslip
ξ	differential flap
δ	symmetric flap
η	foreplane angle
ζ	rudder angle
θ	pitch attitude
φ	roll attitude
ψ	yaw attitude
ρ	air density

Derivatives of coefficients with respect to state and control surface variables are denoted by the convention,

Coefficient<sub>independent variable</sub>

for example,

$$C_{n\beta} = \frac{\partial C_n}{\partial \beta}$$

## 1. INTRODUCTION

This paper describes an investigation into the capabilities and accuracy of an equation error method of aerodynamic parameter identification using stepwise regression techniques. The results of the method are presented for both simulated and flight responses of the British Aerospace EAP aircraft. The flight data analysed includes highly dynamic manoeuvres up to the incidence limit on the aircraft of 30°.

The importance of processing the flight data to ensure kinematic compatibility is described which is an essential first step prior to parameter identification.

## 2. FEATURES OF THE EAP AIRCRAFT

The Experimental Aircraft Programme was conceived in 1983 to design and build a demonstrator aircraft for a wide range of new technologies.

The EAP aircraft configuration was chosen primarily for an air to air role with a secondary ground attack capability. These requirements dictate a design having high levels of subsonic and supersonic performance. The resulting configuration has a large cranked delta wing with a close coupled foreplane, Figure 1.

The aircraft has a high level of longitudinal instability and highly non-linear aerodynamic characteristics. The pitch control surfaces are four flaps and the all moving foreplane. The lateral controls are the use of differential flap and rudder.

The EAP aircraft was designed to feature carefree manoeuvring at 3 g protection when flying in the full control laws mode. This gives a wide range of possible manoeuvres with the unrestricted use of full roll, pitch and yaw controls.

During the flight testing of the EAP aircraft the cleared flight envelope was rapidly expanded using conventional flight test data gathering manoeuvres which are essentially small perturbation inputs designed to excite a particular mode in the aircraft response.

In order to clear the aircraft to its maximum incidence limits a high incidence flight test programme was flown. An anti spin parachute and gantry was fitted to the aircraft in order to be able to recover the aircraft in the event of a departure and spin.

These high incidence flight trials were highly successful with the aircraft remaining in control and within its incidence limits despite some very severe pilot inputs.



### 3. ANALYSIS METHODS USED ON EAP

The method of extracting aerodynamic information from aircraft flight responses that has been in use at BAe Warton for many years is a flight matching program. This method matches a calculated response to a flight measured response by varying selected aerodynamic derivatives, Figure 2. This method is an output error method with a maximum likelihood optimisation routine. It is suitable for linear systems and can cope with measurement noise.

The method has been used successfully to analyse some small amplitude manoeuvres and some rapid rolls on EAP but the method requires a large degree of engineering judgement in its use and in interpreting the results. Each flight manoeuvre must be analysed separately and the results from several manoeuvres may not be consistent. Most importantly the output error method cannot easily deal with non-linear systems and the aerodynamic characteristics of EAP at high incidence in common with many other aircraft are highly non-linear.

As a result of the known difficulties and deficiencies of the output error/maximum likelihood technique it was decided to look for an alternative method of aerodynamic parameter identification.

### 4. STEPWISE REGRESSION

The alternative to an output error method is to use an equation error method. This matches the measured aircraft response in terms of the six component force and moment time histories derived from the response via the kinematic equations of motion. The unknown aerodynamic parameters are estimated by minimising the sum of squared differences between the measured and calculated aerodynamic forces and moments, References 1 to 3, Figure 3. The usual problem with this technique is that the terms in the aerodynamic equation are not known. There will be some non-linear terms but it is not known which terms should be included.

There are several methods of dealing with this problem. The method which was adopted to analyse EAP data is the stepwise regression method. (See Appendix).

Stepwise regression can be described as a model building algorithm. A list of possible terms is defined and each term is examined individually for its usefulness in reducing the equation error and added into the model in a stepwise manner. At each step the terms not included are examined and the next term chosen for entry will be the one with the largest correlation with the component time history after adjusting for the terms already set.

At each step the parameter values are estimated using a least squares fitting routine. Terms incorporated at earlier steps are re-evaluated and those with low significance are rejected. The process continues until no more terms can pass a test of statistical significance. This method offers some major advantages over the maximum likelihood method, Figure 4.

The matching is performed at the level of the component equation rather than the time domain response. Therefore it is possible to extract individual component terms without the cross coupling effects in a time response.

The structure of the mathematical description of the aerodynamic equation does not need to be pre defined and can be extracted from the flight data.

Non-linear characteristics can be modelled via the candidate terms.

Large amounts of flight data can be processed simultaneously. The data does not need to be time continuous.

The only significant disadvantages, Figure 5, are that.

The answers are biased due to measurement errors and noise.

The terms are only found if they are statistically significant. This means that if the information content to extract a particular term is poor then the true system model is not found and errors are introduced.

### 5. PARAMETER IDENTIFICATION

An overview of the parameter identification process is shown in Figure 6. This overview emphasises the importance of the quality of the test data supplied to the parameter estimation algorithm. A worthwhile quote here is that 'The most sophisticated analysis techniques are worthless if you cannot believe the data'.

In order to minimise the disadvantages of the equation error/stepwise regression technique great importance is placed on the information content of the test data and on its measurement accuracy.

The information content can be maximised by ensuring that the aircraft response excites all of the response terms that are required to be extracted throughout the ranges required. The power of the input signal should be distributed uniformly over a wide frequency range.

The measurement accuracy can be maximised firstly by ensuring that the aircraft instrumentation is of the highest quality and secondly inconsistencies in the measured data can be removed by a state reconstruction or kinematic compatibility check on the data.

### 6. KINEMATIC COMPATIBILITY

There are several methods for data compatibility checking. The method used at British Aerospace is a method developed at RAe, Reference 4. This kinematic compatibility process uses the measured linear accelerations and angular rates as forcing functions for the kinematic equations. Values of velocity, incidence, sideslip, euler angles and spatial co-ordinates are calculated and compared to the measured values, Figure 7. The differences between calculated and measured are used to define a cost function which is then minimised using a weighted least squares method. This gives estimates of the instrumentation errors and allows all of the response terms to be recalculated based on the values of the kinematic states, linear velocities and euler angles. The angular accelerations are calculated by differentiation of spline fits to the angular rates.

### 7. EAP INSTRUMENTATION

The level of instrumentation available on EAP is of a high quality due to the use of a full authority quadruplex flight control system which requires high quality flight information. The incidence and sideslip information is obtained from four probes mounted on the front fuselage. A voter monitor

system ensures that any incorrect information is discarded. The linear accelerations and angular rates are obtained from high quality Aircraft Motion Sensor Units.

A number of EAP test manoeuvres were analysed using the kinematic compatibility program. This analysis indicated the levels of instrumentation errors. The noise levels on the instrumentation were estimated by subtracting the smoothed compatible response from the raw flight data plus instrumentation error. The noise levels were then analysed to determine the standard deviations and auto correlation factors which are shown in Figure 8. In general the noise levels are low on all terms except the lateral accelerometer. The linear acceleration data is basically raw instrumentation whereas the other signals all have structural coupling attenuation filters. The linear accelerations, yaw and pitch rates are close to white noise whereas the roll rate, incidence and sideslip have a large degree of colouring in the noise levels.

## 8. VALIDATION STEPWISE REGRESSION

In order to assess the capability of stepwise regression the method was applied to a simulated response where the aerodynamics are known and the level of non linearity of the aerodynamic structure can be varied. This validation process provided essential information on the use of stepwise regression and it was possible to demonstrate:

The method can extract non-linear aerodynamics from EAP simulated responses. Figure 9 shows a simulated pitch response analysed.

The effect of typical instrumentation errors and noise on the simulated responses gives a reduction in accuracy of the extracted derivatives.

The effect of kinematically processing the simulated responses with offset errors and noise is to improve the accuracy of the extracted derivatives, Figure 10.

## 9. NON LINEAR SYSTEMS

In order to extract the non-linear aerodynamics using stepwise regression there are two basic techniques. The first technique analyses the non-linear behaviour as a series of spline basis functions. These spline functions are piecewise polynomials and can be set as piecewise constants, linear or quadratic functions, Figure 11. The spline functions are defined at discrete values of the non-linear variable.

The second technique analyses the non-linear behaviour in one variable by partitioning the data with respect to that variable and only analysing the data within that data partition, Figure 12. This has the advantage of being simple and allows non-linearity in a second variable to be determined using a spline analysis within the partitioned data. The disadvantage of partitioning is that the number of data points analysed is reduced.

## 10. EAP FLIGHT DATA LATERAL

Two different types of lateral data gathering manoeuvre were used on EAP. A dutch roll manoeuvre generated by yaw control principally excites sideslip and a small perturbation lateral stick input with a timing relationship of 3-2-1-1 which principally excites the aircraft in roll. Since these manoeuvres are small perturbation over a small incidence range they can be analysed assuming a

linear aerodynamic model. This enables a comparison to be made with the results of the flight matching program using maximum likelihood, Figure 13.

The flight matching result analyses the manoeuvres separately whereas the stepwise regression analysis is done using the data from both manoeuvres. The results show a good agreement between stepwise regression and maximum likelihood methods.

## 11. EAP FLIGHT DATA LONGITUDINAL

In order to extract the longitudinal aerodynamic characteristics of EAP at high incidence the aircraft dynamic response data during the high incidence test flying of EAP was analysed. These manoeuvres were not specifically designed for parameter identification and consist of combinations of full pitch and lateral stick. The flight data from 10 different manoeuvres was added together looking at data over 20 ° of incidence. The resulting dataset consisted of 1000 data points covering 63 seconds of flight. This dataset was analysed using stepwise regression.

The pitching moment characteristics of EAP measured in the wind tunnel vary with incidence, flap angle and foreplane angle. Pitching moment derivative values with incidence are principally a function of incidence and flap angle, similarly for the flap power. This large block of flight data was analysed in several different ways in order to obtain consistent results.

Figure 14 shows the results of a spline analysis using constants over 1 ° incidence intervals. Also shown are the results from a partitioned data analysis using 1 ° data partitions over the same range. The two different methods are giving very similar results.

In order to extract the non-linearity of the pitching moment derivatives with flap angle a uniform excitation of the aircraft using the flaps is required throughout the incidence range. The data content in the flight data analysed, Figure 15, shows that there is only a limited range of control surface deflections at any given incidence with the majority of data points close to the trimmed values.

The analysis was repeated using data partitioning with flap angle and spline fitting with incidence, Figure 16. The control surface range analysed is 0° to 15° flap angle from 21° to 25° incidence and 0° to 20° flap angle from 24° to 28° incidence. A comparison is made with the EAP aerodynamic dataset which is shown as a single derivative value at the trimmed value of control angles. The derivatives extracted for longitudinal stability and control power agree in general with the results of the wind tunnel based aerodynamic dataset.

## 12. CONCLUSIONS

The application of an equation error method of parameter identification using stepwise regression techniques has been used to successfully analyse flight data from the EAP aircraft.

Given sufficient flight data with an adequate information content full non-linear aerodynamic characteristics can be extracted.

## REFERENCES

1. Klein V., Batterson J.G., Murphy P.C.  
Determination of Airplane Model Structure from Flight Data by using Modified Stepwise Regression.  
NASA TP 1916  
Oct 1981
2. Klein V., Batterson J.G.  
Determination of Airplane Model Structure from Flight Data using Splines and Stepwise Regression.  
NASA TP 2126  
March 1983
3. Klein V., Mayo M.H.  
Estimation of Aerodynamic Parameters from Flight Data of a High Incidence Research Model.  
ICAS Paper  
1986
4. Reid G.E.A.  
Validation of Kinematic Compatibility of Flight Data using Parameter Estimation Methodology.  
RAE TR 81020  
March 1981

## 13. APPENDIX STEPWISE REGRESSION

The aircraft response data is converted into the six component force and moment time histories about the defined reference position using the following equations:-

$$C_x = \frac{Mg}{0.5\rho V^2 S} n_x$$

$$C_y = \frac{Mg}{0.5\rho V^2 S} n_y$$

$$C_z = \frac{Mg}{0.5\rho V^2 S} n_z$$

$$C_l = \frac{4l_{xx}}{\rho V^2 b S} \left[ \dot{p} - \frac{(l_{yy} - l_{zz})}{l_{xx}} q r - \frac{l_{xz}}{l_{xx}} (pq + r^2) \right]$$

$$C_m = \frac{2l_{yy}}{\rho V^2 c S} \left[ \dot{q} - \frac{(l_{xx} - l_{zz})}{l_{yy}} p r - \frac{l_{xz}}{l_{yy}} (r^2 - p^2) \right]$$

$$C_n = \frac{4l_{zz}}{\rho V^2 b S} \left[ \dot{r} - \frac{(l_{xx} - l_{yy})}{l_{zz}} p q - \frac{l_{xz}}{l_{zz}} (p^2 - q r) \right]$$

The aircraft system is considered to be adequately represented by the linear system,

$$y(t) = \theta_0 + \theta_1 x_1(t) + \dots + \theta_{n-1} x_{n-1}(t)$$

In this equation,  $y(t)$  represents the resultant coefficient of aerodynamic force or moment (the dependent variable),  $\theta_i$  to  $\theta_{n-1}$  are the stability and control derivatives,  $\theta_0$  is the value of this particular coefficient corresponding to the initial flight conditions and  $x_i$  to  $x_{n-1}$  are the aircraft state and control variables ( $\alpha, \beta, \delta, \eta, \dots$  etc)

If a sequence of  $N$  observations on both independent and dependent variables are made at times  $t_1, t_2, \dots, t_N$  and if the measured data are denoted by  $y(t)$  and  $x_1(t), x_2(t), \dots, x_{n-1}(t)$  when  $i = 1, 2, \dots, N$  then these data can be related by the set of  $N$  linear equations,

$$y(i) = \theta_0 + \theta_1 x_1(i) + \dots + \theta_{n-1} x_{n-1}(i) + \varepsilon(i)$$

this equation includes the additional term  $\varepsilon(i)$  which is referred to as the equation error.

Stepwise regression is a procedure which inserts independent variables into a regression model, one at a time, until the regression equation is satisfactory. the order of insertion is determined by using the 'partial correlation coefficient' as a measure of the importance of variables not yet in the regression equation. The first independent variable from the postulated model is chosen as the one which is most closely correlated with  $y$ .

The correlation coefficient is a measure of the usefulness of the variable selected in reducing the residual variance. It is given for the variable  $x_j$  by the expression:-

$$r_{jy} = \frac{S_{jy}}{\sqrt{S_{jj} S_{yy}}}$$

where,

$$S_{jy} = \sum_N (x_j(i) - \bar{x}_j)(y(i) - \bar{y})$$

$$S_{jj} = \sum_N (x_j(i) - \bar{x}_j)^2$$

$$S_{yy} = \sum_N (y(i) - \bar{y})^2$$

where

$$\bar{x}_j = \frac{1}{N} \sum_N x_j(i)$$

and

$$\bar{y} = \frac{1}{N} \sum_N y(i)$$

If  $x_j$  is selected as  $x_1$  say, then the model

$$y = \theta_0 + \theta_1 x_1 + \varepsilon \quad (\text{equation a})$$

is used to fit the data.

The parameters are estimated by minimising the cost function

$$J = \sum_N [y(i) - \theta_0 - \theta_1 x_1(i)]^2$$

After this regression step the new parameter estimates are denoted  $\hat{\theta}_0$  and  $\hat{\theta}_1$ .

A new independent variable  $z_1$  is constructed by finding the residuals of  $x_1$  after regressing it on  $x_1$ , that is the residuals from fitting the model,

$$x_1 = \theta_0 + \theta_1 x_1 + \varepsilon$$

variable  $z_1$  is therefore given as,

$$z_1 = x_1 - \hat{\theta}_0 - \hat{\theta}_1 x_1$$

where  $\hat{\theta}_0$  and  $\hat{\theta}_1$  are the estimated parameter values after the regression of  $x_1$  on  $x_1$ .

Similarly the variables  $z_2, z_3, \dots, z_{n-1}$  are formed by regressing the variable  $x_2$  on  $x_1, x_3$  on  $x_1$  and so on.

A new dependent variable  $y'$  is represented by the residuals of  $y$  regressed on  $x_1$  using the model given by (equation a), that is,

$$y' = y - \hat{\theta}_0 - \hat{\theta}_1 x_1$$

In the next step, a new set of correlations which involve the variables  $y', z_1, z_2, \dots, z_{n-1}$  is formulated.

These partial correlations can be written as  $r_{jy'}$  meaning the correlation of  $z_j$  and  $y'$  are related to the model containing the variable  $x_1$ .

The expression for the partial correlation coefficients  $r_{jy'}$  is given by replacing  $y$  and  $x_j$  by  $y'$  and  $z_j$ .

The next variable added to the regression model is the variable  $x_j$  whose partial correlation coefficient was the greatest.

If the second independent variable selected in this way is  $x_j$  then the third stage of the selection procedure involves partial correlations of the form  $r_{jy \cdot x_1}$  ie. the correlations between the residuals of  $x_j$  regressed on  $x_1$  and  $x_j$  and residuals of  $y$  regressed on  $x_1$  and  $x_j$ .

At every step of the regression, the variables incorporated into the model in previous stages and the new variable entering the model are reexamined using the partial correlation coefficient.

A measure of the adequacy of the equation model at each regression step is given by the total F value which is the ratio of regression mean square to residual mean square defined as :-

$$F = \frac{N - n}{n - 1} \left[ \frac{\sum_N (\hat{y}(i) - \bar{y})^2}{\sum_N (y(i) - \hat{y}(i))^2} \right]$$

where

$$\hat{y}(i) = \theta_0 + \sum_n \theta_n x_n(i)$$

The model with the maximum F value is recommended as the best for a given set of data.

#### 14. APPENDIX ANALYSIS OF NOISE

For a sample of N data points with values  $x_i$  at each point i then

Mean

$$\bar{x} = \frac{1}{N} \sum_N x_i$$

Standard deviation

$$SD = \sqrt{\frac{1}{N-1} \sum_N (x_i - \bar{x})^2}$$

Autocorrelation

$$Autocorrelation = \frac{\sum_N x_i x_{i-1}}{\sum_N x_i^2}$$

(C) British Crown Copyright 1991/MD0

Published with the permission of the Controller of Her Britannic Majesty's Stationary Office

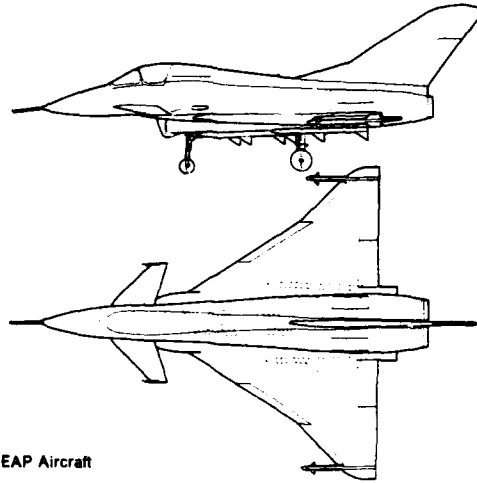


Figure 1. EAP Aircraft

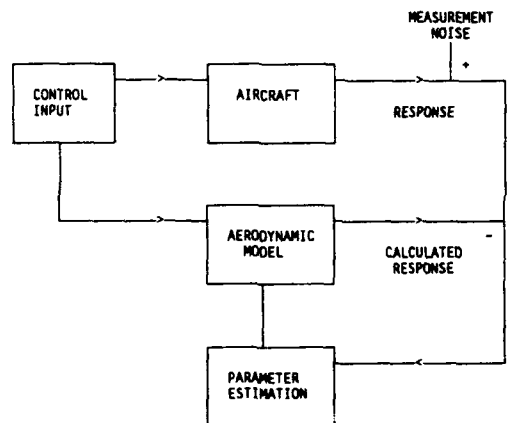


Figure 2 Flight matching process

$$y(i) = \theta_0 + \theta_1 x_1(i) + \dots + \theta_{n-1} x_{n-1}(i) + \varepsilon(i)$$

$y(i)$  represents the coefficient of aerodynamic force or moment.

$\theta_1$  to  $\theta_{n-1}$  are the stability and control derivatives.

$x_1$  to  $x_{n-1}$  are the aircraft state and control variables ( $\alpha, \beta, \delta, \eta, \dots$  etc)

$\varepsilon(i)$  is the equation error.

The parameters are estimated by minimising the cost function

$$J = \sum_N \left[ y(i) - \theta_0 - \sum_n \theta_n x_n(i) \right]^2$$

Figure 3. Equation error method

- *Matching performed at the level of the component equation*
- *Structure of aero model does not need to be pre defined*
- *Non linear characteristics can be modelled*
- *Large amounts of flight data can be processed*

Figure 4. Advantages of stepwise regression

- *Results are biased due to measurement errors and noise*
- *Only statistically significant terms found*

Figure 5. Disadvantages of stepwise regression

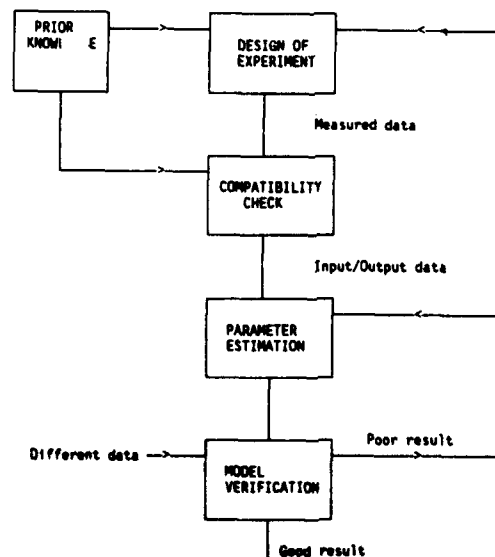


Figure 6 Parameter Identification process

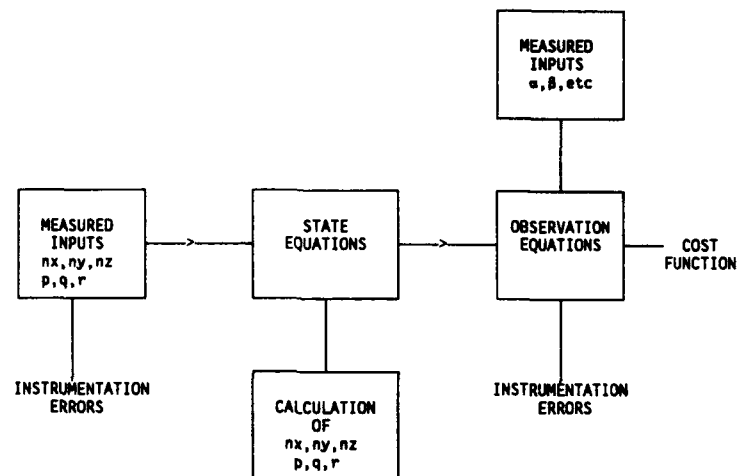


Figure 7 Kinematic Compatibility

TERM	Standard deviation	Autocorrelation
$n_y$ (g)	0.029	0.48
$n_z$ (g)	0.010	0.36
$p$ (deg/s)	0.097	0.83
$q$ (deg/s)	0.036	0.21
$r$ (deg/s)	0.020	0.52
$\alpha$ (deg)	0.040	0.83
$\beta$ (deg)	0.037	0.86

Figure 8. Noise levels on flight data

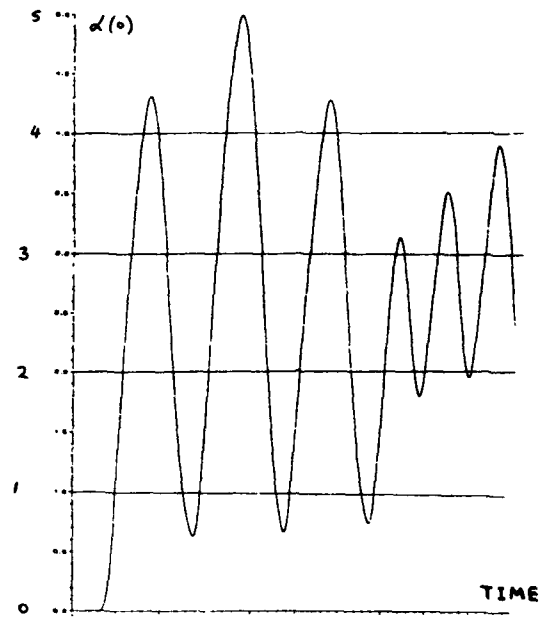


Figure 9. Simulated response

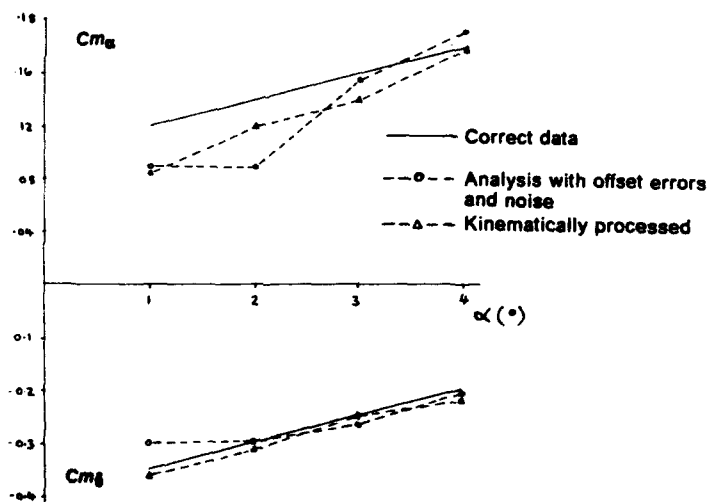


Figure 10. Simulated response



$$S_m(x) = \sum_n C_n x^n + \sum_k D_k (x - x_k)^m$$

Where

$$(x - x_k)^m = [(x - x_k)^m]_{x \geq x_k}$$

$$(x - x_k)^m = 0_{x < x_k}$$

$x_1$  to  $x_k$  are the knot values of  $x$  and  $C_n$  and  $D_k$  are constants.

For example.

$m = 1$  (piecewise linear)

$$S(x) = C_0 + C_1(x) + D_1(x - x_1) + D_2(x - x_2) + \dots + D_k(x - x_k)$$

$m = 2$  (piecewise quadratic)

$$S(x) = C_0 + C_1(x) + C_2x^2 + D_1(x - x_1)^2 + D_2(x - x_2)^2 + \dots + D_k(x - x_k)^2$$

Figure 11. Spline function

Partitioning is the analysis of the data in separate groupings.

$$C_n = C_n(\alpha, \beta, \rho, r)$$

can be analysed as

$$C_n(\alpha = 21^\circ) = C_n(\beta, \rho, r)_{20^\circ \leq \alpha \leq 22^\circ}$$

The dependence of the model on  $\alpha$  is eliminated.

Figure 12. Partitioning

TERM	Stepwise regression	Matching Dutch roll	Matching L3211	Dataset
$Cl_\beta$	-0.123	-0.103	-0.113	-0.094
$Cl_\xi$	-0.368		-0.369	-0.368
$Cl_\eta$	0.038	0.033		0.018
$Cl_p$	-0.580		-0.559	-0.550
$Cl_r$	0.200			0.160
$Cn_\beta$	0.099	0.094	0.084	0.096
$Cn_\xi$	-0.105		-0.095	-0.072
$Cn_\eta$	-0.095	-0.087	-0.097	-0.090
$Cn_p$	-0.061		-0.056	-0.110
$Cn_r$	-0.076			-0.360

Figure 13. EAP lateral flight analysis

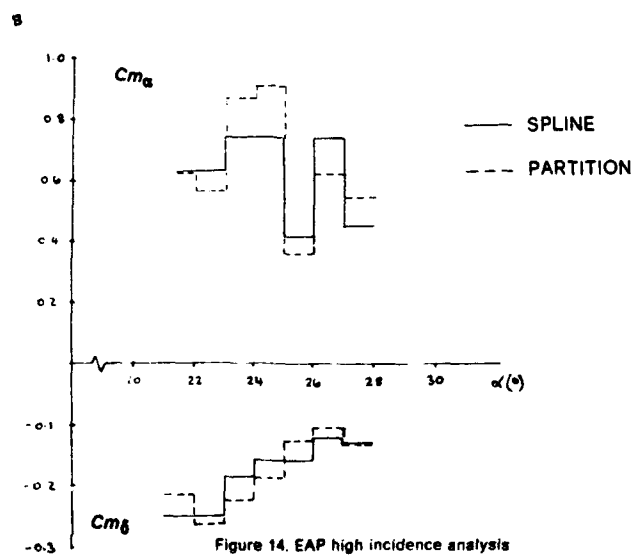


Figure 14. EAP high incidence analysis

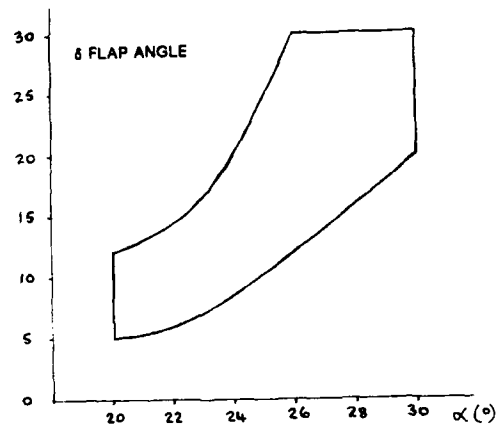


Figure 15. EAP high incidence data

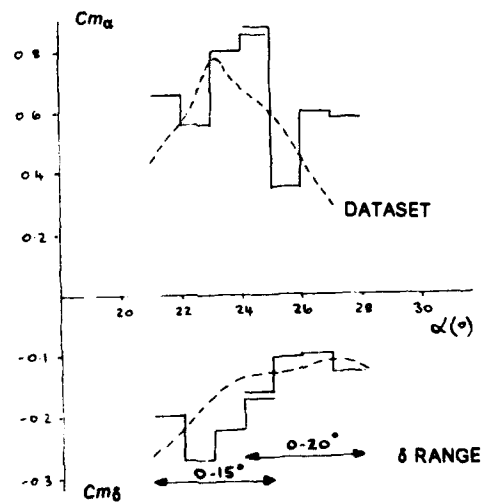


Figure 16. EAP high incidence analysis

# AERODYNAMIC CONTROL OF FIGHTER AIRCRAFT BY MANIPULATION OF FOREBODY VORTICES

Gerald N. Malcolm and T. Terry Ng  
Eidetics International, Inc.  
3415 Lomita Blvd.  
Torrance, CA 90505  
U.S.A.

## SUMMARY

Methods of enhancing aircraft controllability and maneuverability at high angles of attack by manipulating the forebody vortices are discussed. Pneumatic control methods including jet blowing, slot blowing, and suction, and mechanical control methods using forebody and nose-tip strakes are reviewed. The potential of various control devices in controlling the forebody flow and, thus, providing controlled yawing moments at high angles of attack are illustrated using wind tunnel results from a generic fighter and water tunnel results from an F/A-18.

## NOMENCLATURE

$A_{ref}$	reference wing area
$C_\mu$	momentum coefficient of blowing $= \dot{m} V_j / q_\infty A_{ref}$
$C_n$	yawing moment coefficient
$d$	forebody base diameter
$h_{ST}$	strake height
$l_{ST}$	strake length
$\dot{m}$	mass flow rate of the blowing jet or slot
$q_\infty$	free-stream dynamic pressure
$V_j$	average exit velocity of the blowing jet or slot
$\alpha$	angle of attack
$\beta$	angle of sideslip
$\phi$	angle from the windward meridian

## 1.0 INTRODUCTION

The flight envelope of current aircraft has been limited at least in part by controllability problems at high angles of attack, typically represented by sudden departures in roll and yaw and, in some cases, by pitchup or deep-stall. Reduced controllability places undesirable limits on the maneuverability and controllability of the aircraft and, in some cases, leads to uncontrolled flight modes such as spin. The typical flowfield around a modern fighter aircraft at moderate-to-high angles of attack is dominated by vortices. The presence of highly energetic vortices can and has been utilized to greatly enhance the performance of aircraft. These complex vortex flows can, however, become erratic as the angle of attack is increased and eventually contribute to degraded control capability. If there are means to locally control these vortex flows on the aircraft, one should be able to utilize this powerful force input to enhance the overall aircraft controllability.

Recent research efforts on fighter-type aircraft have indicated that some of the most promising methods for vortex control are movable forebody strakes and blowing and suction on the forebody surface. The strakes are either fixed to the forebody to enhance the stability characteristics, or deployed actively to provide additional control. The use of a fixed pair of forebody strakes attached symmetrically to the forebody (e.g., Refs. 1 through 4) has been shown to be effective in forcing naturally occurring asymmetric vortices at zero sideslip at high angles of attack to be symmetric. The large forebody sideforces and resulting yawing

moments are, therefore, either reduced significantly or eliminated. Stahl<sup>5</sup> demonstrates that, instead of a pair of strakes, a single large strake deployed along the leeward meridian of the entire forebody can also maintain vortex symmetry. Ng<sup>6</sup> shows that, possibly due to the dominating effect of the flow at the nose tip on the vortex flow, similar effects can be achieved by a small strake which extends over only a small portion of the tip region.

Actively deployed forebody strakes have been investigated as a potential means for enhancing high angle of attack controllability. Some examples of the investigations are shown in Refs. 7 and 8. Murri and Rao<sup>7</sup> studied the effectiveness of hinged deflectable strakes on a conical forebody in providing controlled yawing moments for a generic fighter configuration at high angles of attack. Malcolm et al<sup>8</sup> used a different form of deployable strakes which pivoted out of a tangent-ogive forebody about a hinge point with the strakes staying normal to the local surfaces. Several different strake lengths were tested. It was found that strakes extending over only a portion of the forebody were sufficient to provide similar control as longer strakes.

Large, asymmetrically deployed strakes create, in effect, a significantly asymmetrical forebody geometry and would naturally be expected to produce yawing moments, even at zero sideslip. In practice, however, the size of the control devices is a key issue. Many numerical and experimental studies (e.g., Refs. 9 - 13) have demonstrated that, under suitable conditions, a small perturbation at the tip region can lead to large asymmetries in the forebody flow and, therefore, large yawing moments. For instance, the control devices used in two recent studies<sup>13,14</sup> were substantially smaller in size than the strakes used by Murri and Rao<sup>7</sup> and Malcolm et al<sup>8</sup>. Zilliac et al<sup>13</sup> studied the effect of tip geometry on the vortex flow over a slender body of revolution. Variable nose-tip asymmetries in the form of a small deployable cylinder and rotatable machined flats were found to be highly effective in producing controlled sideforces, although the emphasis of the study was more on the effect of perturbations than control. The study by Moskovitz et al<sup>14</sup>, on the other hand, directly

addresses the use of a rotatable nose-tip perturbation in the form of an elliptic tip as a control device. Predictable and repeatable sideforce with nose-tip roll was obtained even at relatively moderate angles of attack and sideslip angles as large as 15°.

One of the main practical concerns on using movable strakes on the forebody is that, depending on the physical size and mechanical complexity, they may present unacceptable interference on the radar operation. Thus, pneumatic forebody vortex control has also been studied extensively as an alternative method of providing yaw control at high angles of attack. Investigations of forebody blowing techniques to control the forebody vortex orientation have been conducted in both water and wind tunnel experiments<sup>8, 17-19</sup> where asymmetric forebody vortices were switched in orientation by blowing under the high vortex. Two main forms of blowing have been studied: (1) blowing from a localized jet and (2) blowing from a tangential slot.

The study by Malcolm et al<sup>8</sup> on a generic fighter configuration shows that controlled yawing moments of various magnitudes can be produced by blowing either forward or aft from a localized jet. They also found an extremely effective synergistic effect of simultaneously blowing tangentially forward on one side and aft on the other, which cannot be achieved with either individual blowing scheme alone. Rosen and Davis<sup>18</sup> studied the effect of jet blowing on the forebody of the X-29 configuration numerically, again demonstrating the effectiveness of forward and aft blowing in controlling the forebody flow. Tavelle et al<sup>19</sup> show that similar control can be obtained on an F-18 configuration by blowing from a tangential slot along the fuselage.

One question of interest is how the various forms of vortex control actually function. While there is no doubt more than one means by which the vortex flow can be controlled and that a sufficiently strong perturbation can significantly alter the forebody flow, there may be certain fundamental mechanisms that are common to various control concepts such as jet blowing, slot blowing, suction, and strakes. The understanding of these mechanisms will likely lead to the development of more effective means of vortex control.

Several recent studies (Refs. 8, 17, and 20-22) on forebody vortex control performed at Eidetics and listed in Table I may provide information that is helpful in answering the above question. The present paper will review results from these studies which are relevant for the following objectives:

- (1) to investigate various aspects of forebody vortex asymmetry,
- (2) to provide insight into the fluid mechanisms that control the forebody vortex flow, and
- (3) to explore the potential of various control devices in controlling the forebody flow and thus providing controlled yawing moments at high angles of attack.

Due to length and time limitations, only brief discussions on various control methods can be presented in this paper. More complete results can be found in various references as listed.

## 2.0 EXPERIMENTAL SETUP

Detailed descriptions of the experiments listed in Table I are available in Refs. 8, 17, and 20 thru 22. For the generic fighter experiments, water tunnel tests were conducted in the NASA-Ames Dryden Flight Research Facility Flow Visualization Water Tunnel<sup>17</sup> at a flow speed of 3 in/sec, corresponding to a Reynolds number of about  $2 \times 10^4$  per ft. The wind tunnel tests were conducted in the NASA Langley Research Center 12-Foot Low Speed Wind Tunnel.<sup>8</sup> The tests were conducted at a dynamic pressure of approximately 5 psf and a Reynolds number of  $0.75 \times 10^6$  based on a wing mean aerodynamic chord of 1.85 ft. Water tunnel tests for the F-16<sup>20</sup> and F/A-18<sup>21,22</sup> experiments were conducted in the Eidetics 2436 Water Tunnel. Most of the tests were conducted at flow speeds of 3 to 5 in/sec.

Configuration	Control methods tested	Measurements	References
Generic fighter	<ul style="list-style-type: none"> <li>• jet blowing aft</li> <li>• jet blowing forward</li> <li>• deployable strakes</li> </ul>	<ul style="list-style-type: none"> <li>• water tunnel flow vis.</li> <li>• wind tunnel force and moment</li> </ul>	8 and 17
F-16	<ul style="list-style-type: none"> <li>• jet blowing aft</li> <li>• jet blowing forward</li> <li>• pulsed jet blowing aft</li> <li>• rotatable nose-boom strakes</li> </ul>	<ul style="list-style-type: none"> <li>• water tunnel flow vis.</li> </ul>	20
F/A-18	<ul style="list-style-type: none"> <li>• jet blowing aft</li> <li>• jet blowing forward</li> <li>• slot blowing</li> <li>• slot suction</li> <li>• rotatable nose strakes</li> </ul>	<ul style="list-style-type: none"> <li>• water tunnel flow vis.</li> <li>• water tunnel yawing moment</li> </ul>	21 and 22

Table I List of High Angle-of-Attack Forebody Vortex Control Experiment Conducted at Eidetics International

For the F/A-18 experiment, in addition to flow visualization, yawing moment measurements were performed with a strain gage sting.

The wind tunnel model of the generic fighter is shown in Fig. 1. The water tunnel model is basically similar except being smaller in size. Two models were used for the F-16 experiment: (1) a 1/20th-scale full model and (2) a 1/10th-scale forebody section model shown in Fig. 2. For the F/A-18 experiments, two models were used: (1) a 1/32nd-scale full model and (2) a 6%-scale forebody section model. The 1/32nd-scale model was constructed to accommodate only the nozzle blowing. The 6%-scale model had several different nose pieces which accommodate different methods of control including nozzle blowing, slot blowing, slot suction, and a rotatable nose-tip strake system as shown in Fig. 3.

### 3.0 FOREBODY VORTEX CONTROL USING PNEUMATIC METHODS

Results of pneumatic forebody vortex control--jet blowing, slot blowing, and suction--will be discussed.

#### 3.1 Visualization of the Effect of Pneumatic Forebody Flow Control on the Vortex Flow

##### 3.1.1 Jet Blowing Aft

The general effects of blowing aft underneath a forebody vortex are to delay the separation and move the vortex closer to the surface. Correspondingly, the separation on the opposite side is advanced and the vortex is moved farther off the surface. The induced asymmetry results in a higher suction on the blowing side and, thus, a yawing moment towards the same side. The effectiveness and nature of the control depends strongly on the angles of attack and sideslip which dictate the nature of the baseline flow. Results of the F/A-18 study will be used for illustration.

For  $\alpha = 35^\circ$  to  $55^\circ$ , the baseline F/A-18 forebody flow is symmetric. As demonstrated in Fig. 4a, by blowing under the right vortex at  $50^\circ$  angle of attack, it can be deduced that blowing under either vortex perturbs the vortical flow from a symmetric configuration into various degrees of asymmetry. Altering the vortex position by blowing also alters the

separation location, with a high vortex always associated with an early separation and vice versa. The results demonstrate that the magnitude of available control, as revealed by the maximum controllable vortex asymmetry, increases with the angle of attack due to the fact that the strength of the forebody vortices and their potential for large asymmetry also increases with  $\alpha$ .

For  $\alpha = 55^\circ$  to  $60^\circ$ , the forebody flow is naturally asymmetric. For the 6% F/A-18 model, without blowing the natural disturbances favor a left-vortex-high flow configuration which is associated with an earlier flow separation on the left side. Blowing underneath the right vortex delays the separation on the right side and moves the right vortex even closer to the surface while the opposite happens on the left. The non-blowing asymmetry is, therefore, enhanced and the right-pointing moment increased. On the other hand, blowing underneath the left vortex moves the left vortex closer to the surface. The non-blowing asymmetry and the right-yawing moment are, therefore, reduced and eventually reversed.

For  $\alpha = 60^\circ$  to  $65^\circ$ , the baseline flow is characterized by a "bi-stable" condition. Figure 4b shows the response of the flow to blowing at  $\alpha = 60^\circ$ . The photos were taken in time sequence to demonstrate the "bi-stable" nature of the flow. Starting from the upper left photo (Photo i), which shows a high left forebody vortex without blowing, the results show that the vortex orientation is not altered by blowing underneath the left vortex at  $C_{\mu} = 0.11 \times 10^{-3}$  (Photo ii). When  $C_{\mu}$  is increased to  $0.41 \times 10^{-3}$ , as in Photo iii, the vortex pattern is switched from an originally left-vortex-high orientation in Photo i to a right-vortex-high orientation. The observation is that, depending on which side blowing is administered, the forebody vortex flow can be switched between two stable, asymmetric states which are essentially the mirror image of each other. The vortex pattern, once switched from one configuration to the other, will stay essentially in the new pattern with the blowing off as in Photo iv with the exception being that the degree of asymmetry is slightly higher if the blowing is left on. While it is difficult to maintain a symmetric vortex pattern by blowing on one side only, an almost-symmetric flow

can be maintained by blowing simultaneously and approximately evenly on both sides. Even very minute changes in the blowing rates, however, will result in a large flow asymmetry. This demonstrates that a slight asymmetry can indeed cause the flow to assume one of the stable but asymmetric states. As demonstrated by results of simultaneous blowing on both sides, the role of a small unavoidable model geometric asymmetry seems mainly to bias the flow pattern towards one of the asymmetric states, even when the blowing is symmetrically applied to both sides. A sufficiently large transient perturbation such as a large sideslip change or blowing can switch the flow from one state to another.

The overall results on jet blowing demonstrate that sizable vortex asymmetry can be generated by aft blowing with relatively low blowing rates, typically less than  $1 \times 10^{-3}$ , even at large sideslip angles. Tests performed with the aft set of nozzles show that the control is significantly less effective when compared with the blowing nozzles closer to the tip of the nose. The blowing needed to produce a given vortex asymmetry could be ten times higher.

A strong coupling between the forebody and the LEX vortices can be observed. A high forebody vortex on one side is associated with a delayed LEX vortex breakdown on the same side. Thus, at zero sideslip, a positive (right wing down) rolling moment would be induced whenever a positive (nose right) yawing moment is generated and vice versa. That is, the yaw and roll moments would be such that a coordinated turn is produced with blowing.

### 3.1.2 Pulsed Jet Blowing Aft

Due to the time-lag effect, pulsing the blowing jet can potentially reduce the blowing required to produce a given yawing moment. That is, it may not be necessary to maintain steady blowing in order to produce a desired vortex pattern because one may be able to space the pulses by a period which is shorter than the time it takes for the vortices to reposition themselves after the blowing is stopped.

The effect of pulsed blowing on the forebody flow was demonstrated in the F-16 study.<sup>20</sup> Below a certain pulse frequency, the vortex pattern shows a periodic fluctuation,

which is directly related to the pulsing frequency. For high enough reduced frequencies, however, the vortex pattern becomes essentially steady as a result of the time-lag effects associated with the vortices and the separation. The results show that the primary function of blowing is the controlling of flow separation. At the initiation of blowing, the separated boundary layer reattaches due to the entrainment from the blowing jet along the surface. The blowing-side vortex responds to the change in the separation location and readjusts to a position closer to the surface and farther toward the leeward side. The interaction between the two vortices causes the primary separation on the other side to advance to the windward side and the vortex to move farther from the surface.

When the blowing is pulsed at a sufficiently high rate, the vortices will be "locked" into a fixed position due to the time-lag of the vortex response. From the flow visualization results, it is evident that the time-lag associated with flow separation is decidedly shorter than that associated with vortex position. Even when pulsed at a relatively high rate, the separation on the blowing side will respond essentially immediately to changes in the blowing condition. The separation on the non-blowing side, on the other hand, remains essentially steady. This is because the change in separation location on the non-blowing side is controlled by the changing vortex rather than the vortex being controlled by altering the separation location as on the blowing side. Thus the net result of pulsed blowing (at sufficiently high frequencies) is that the vortex pair and the separation at the non-blowing side become steady due to the time-lag effect, even though the separation on the blowing side is oscillating at the blowing frequency.

Whether pulsed blowing offers any advantages over steady blowing is not clear at this point. While a similar vortex pattern can be maintained with a lower average blowing rate with pulsed blowing than steady blowing, part of the benefit in the form of controlled yawing moment may be lost due to the periodic reversion of the separation on the blowing side to the non-blowing condition. A certain fractional loss in the maximum yawing moment, however, may be an acceptable trade-off in certain applications due to the potential reduction in blowing requirement.



### 3.1.3 Jet Blowing Forward

Based on results of the generic fighter, F-16, and F/A-18 studies (Refs. 8, 17, 20-22), the effect of forward blowing is strongly dependent on the model attitude, blowing rate, and position of the blowing nozzle. The fluid mechanics of forward blowing is not entirely understood at this point. There seems to be two primary effects of forward blowing. Near the nozzle exit where the jet velocity is high, entrainment effect dominates. Farther away from the exit, the jet is slowed down by the streamwise flow and a stagnation zone develops. The effect of blowing depends strongly on the blowing rate and the angle of attack.

At low-to-moderate blowing rates and when the natural separation location is far leeward such as at low angles of attack, the accelerated flow around this zone creates a suction region and a yawing moment towards the blowing side may be expected. At high angles of attack where the natural separation is far windward, forward blowing basically promotes early separation at low-to-moderate blowing rates and a yawing moment away from the blowing side is expected. One point of interest at all angles of attack is that while the local separation location is significantly altered at any blowing rate, the vortex position does not change significantly until at higher blowing rates where the blowing jet can reach the region close to the apex. Under this condition, the vortex on the blowing side is lifted from the surface and a yawing moment away from the blowing side may result.

At high blowing rates, entrainment effect of the blowing jet dominates and separation is delayed on the blowing side. In this case the effect of forward blowing is similar to that of aft blowing. That is, a yawing moment increment toward the blowing side is generated.

### 3.1.4 Slot Blowing

The effect of blowing tangentially from a slot along the side of the forebody will be illustrated using the F/A-18 water tunnel results.

#### 3.1.4.1 Aft Slot

Blowing from the aft slot has only minor effects on the primary vortex trajectory throughout the angle of attack range tested. Off-surface visualization reveals that from this blowing position, most of the blowing jet is being entrained after separation into the LEX vortex. Since the vorticity generated at the leading edge of the LEX predominates in most situations, the effect of the blowing jet on the LEX vortex (most noticeably the breakdown location) is relatively small. At higher angles of attack ( $> 50^\circ$ ), the blowing slot was located after the normal flow separation location and the blowing becomes less effective.

Surface dye flow visualization shows that the primary effect of slot blowing is to delay the flow separation on the blowing side. The effect increases progressively with the blowing rate. Thus even though the vortex trajectory is not altered, at zero sideslip conditions a yawing moment towards the blowing side is expected. This is in basic agreement with previous numerical and experimental studies reported in Ref. 19. The results in Ref. 19, however, show that the separation on the blowing side can be delayed much farther than was possible in the present experiment. In addition, a much stronger effect on the vortex trajectory than the present experiment was observed. This may be partly a result of the rather large difference in Reynolds numbers between the two studies. The computation in Ref. 19 was done at a Reynolds number of  $11.52 \times 10^6$  (turbulent) and the water tunnel results were obtained at Reynolds number of less than  $1 \times 10^5$  (laminar). Another potentially significant difference is that the computation in Ref. 19 always starts with a naturally symmetric vortex pattern, while in the present case the vortices can be highly asymmetric even in the absence of blowing.

#### 3.1.4.2 Forward Slot

Unlike blowing from the aft slot, blowing from the forward slot has a strong effect on the vortex trajectory. At sufficiently high blowing rates, the vortex on the blowing side moves close to the surface while the opposite happens on the non-blowing side. The control becomes effective at a lower angle

of attack ( $\sim 30^\circ$ ) compared with jet blowing ( $\sim 35^\circ$ ), although the location of the blowing nozzle is probably a major factor. The effect of blowing is strongly dependent on the axial location due to significant variations in local flow conditions along the blowing slot compared with the case of the aft slot.

An example of the flow visualization results is shown in Fig. 5 for  $\alpha = 50^\circ$ . Blowing does not have a strong effect on the vortices at  $C_{\mu} = 0.83 \times 10^{-3}$ . Surface flow visualization, however, reveals that flow separation is significantly delayed. At  $C_{\mu} = 1.32 \times 10^{-3}$ , blowing essentially eliminates the separation on the blowing side very near the tip region and the flow separates at the leeward meridian. The planform view reveals that the portion of the vortex at the apex region is eliminated and a new vortex reforms at a slightly aft region. Appreciable changes in the vortex trajectory were observed with the blowing-side vortex being at the low position. The separated shear layer can be seen to become unstable and roll up into individual vortices which interact with the forebody vortices farther downstream.

### 3.1.5 Surface Suction

For the F/A-18 experiment, suction was in the form of a slot along the  $135^\circ$  windward meridian. While no attempt was made to optimize the geometry of the slot, several slot lengths were tested and the control was found to be effective even with a relatively short slot (approximately 0.25" in length) if the slot is located close to the tip. At  $\alpha = 30^\circ$  and  $50^\circ$  and no sideslip, a very low suction rate ( $C_{\mu} < 0.3 \times 10^{-3}$ , based on the average velocity at the slot) was needed to effect the maximum asymmetry in the vortex flow pattern for the respective angles of attack. The results show that the control is effective even at relative large sideslip angles ( $> 20^\circ$ ), though higher suction rates are needed to effect similar changes in the vortex pattern compared with the no sideslip conditions.

## 3.2 Forces and Moments Generated by Pneumatic Control

The experimental results described in the following sections are intended to

demonstrate the effectiveness of various pneumatic methods in producing controlled forces and moments. The main emphasis was on the concepts of blowing in the forms of a jet and a slot.

### 3.2.1 Transient and Temporal Behaviors

Due to the slow testing speed of the water tunnel, certain transient and temporal behaviors are readily revealed by the yawing moment measurements. Figure 6 shows an example of the yawing moment history at  $\alpha = 50^\circ$  for the F/A-18 when blowing on the right side. The results reveal that the yawing moment can be highly unsteady, and that a large transient over-shoot in the yawing moment can occur when a perturbation (in the form of a jet in this case) is imposed or removed.

Above  $\alpha$  of about  $60^\circ$ , flow visualization reveals that the flow becomes "bi-stable". The yawing moment at  $\alpha = 60^\circ$  becomes more steady. The yawing moment can be switched between two essentially steady values by blowing, and keeping the blowing on after switching only changes the yawing moment by a relatively small amount.

### 3.2.2 Time-Average Behaviors

The steady-state, time-average yawing moment for the F/A-18 at  $\alpha = 50^\circ$  is plotted in Fig. 7 as a function of the blowing coefficient for slot blowing, jet blowing in the aft direction, and jet blowing in the forward direction. Positive  $C_{\mu}$  represents blowing on the right side, while  $-C_{\mu}$  represents blowing on the left side. The results show that without blowing the flow over the jet-blowing model is mostly symmetric, while the slot-blowing model shows a moderate negative yawing moment. This is in agreement with the flow visualization results in which the slot-blowing model shows a right-vortex-high configuration without blowing. This is probably due to a small geometric asymmetry in the slot locations on left and right sides of the forebody.

Figure 7 shows that for both the slot blowing and jet blowing in the aft direction, a

yawing moment towards the blowing side is produced while the opposite is true for jet blowing in the forward direction. This is again in agreement with the flow visualization results which show that the slot blowing and jet aft-blowing delay separation and move the vortex on the blowing side towards the surface, while forward blowing enhances separation on the blowing side. The results also show that slot blowing is the most effective in producing controlled yawing moments at steady-state conditions. Of the three blowing schemes, it produces the highest magnitude of yawing moment at a given blowing coefficient and the highest attainable yawing moment. The jet forward-blowing is the least effective in these regards.

Examples of the wind tunnel results of blowing aft on the generic fighter are shown in Figs. 8 - 11 (from Ref. 8). Figure 8 shows the case for the generic fighter (Fig. 1) with a clean forebody. Blowing is implemented on the right and left sides individually at different rates. The natural asymmetry for the non-blowing case is oriented to produce a positive yawing moment, which coincides with a vortex pattern where the right side vortex is closest to the forebody, thereby providing a higher suction force in the nose-right direction. By blowing on the right side, the already asymmetric condition is enhanced and the asymmetry persists to even higher angles of attack than for the non-blowing case. Blowing on the left side of the forebody is effective in changing the yawing moment in the opposite direction, but is not effective in completely overcoming the natural asymmetry for all angles of attack. Note also that the blowing coefficient needed is high compared with that of the F/A-18. This is due primarily to the more aft location of the nozzles on the generic fighter.

It would appear that the most effective technique for utilizing blowing to provide effective and controllable variation of the yawing moment would be to start with a baseline configuration which has a yawing moment inherently near zero through the angle of attack range and to perturb the moment away from zero. Figure 9 shows a case where the forebody was modified with symmetrically mounted nose strakes 1.0d in length, 0.05d in height at  $\phi = 105^\circ$ , which was found in earlier test results to be an effective strake geometry and placement to minimize the asymmetry of

the vortices. The effect of varying the blowing rate on either side is demonstrated. Increasing blowing produces increased yawing moment in the direction of the side on which blowing occurs. While the effects of blowing left and right are not exactly mirror images, the effects are very similar. The yawing moment produced by a  $30^\circ$  rudder deflection is plotted in the same figure for comparison. It can be seen that blowing starts to generate sizeable yawing moments when the rudder begins to lose its effectiveness at about  $30^\circ$  angle of attack. The  $C_{\mu}$  required to generate a maximum yawing moment similar to the  $30^\circ$  rudder at  $\alpha = 0^\circ$  is about  $7.5 \times 10^{-3}$ , and is about  $30 \times 10^{-3}$  in order to generate a yawing moment twice that of the rudder. While these blowing coefficients are rather high, the water tunnel results of the F/A-18 demonstrate that a substantial reduction in the blowing requirement can be achieved (as much as an order of magnitude) by moving the blowing nozzle closer to the tip and by optimizing the nozzle locations and geometry.

An indication of the effectiveness of blowing with different sideslip angles is shown in Fig. 10. The case shown is for an angle of attack of  $60^\circ$ . The progression of increased yawing moment with blowing rate in the direction of blowing seems to hold reasonably well with sideslip angles to at least  $20^\circ$ . The significance of the results shown in this figure is that with blowing on the appropriate side, a yawing moment can be generated that will overcome the negative directional stability which is evident without blowing, i.e.,  $C_n$  is negative for positive  $\beta$ . With blowing it is possible, for example to generate positive  $C_n$  for positive  $\beta$ .

Figure 11 shows the case for blowing forward on the left and blowing aft on the right at  $C_{\mu} = 0.03$ . Forward blowing can be seen to be generating yawing moments even at much lower angles of attack than aft blowing. There appears to be some significant influence at angles of attack as low as  $10^\circ$ . Blowing forward on the left side alone produces a moment to the left. At lower blowing rates, blowing forward produced a moment in a direction opposite to the blowing side, as was seen for the F-18 configuration in Fig. 7. It

appears that from this nozzle location a low blowing rate causes premature separation and, therefore, a force away from the blowing side and higher blowing rates delay separation and create a suction force on the direction of the blowing side. Blowing aft on the right side alone produces a moment to the right. The most interesting result is the result of combining these two blowing schemes to blow simultaneously. The initial presumption would be that the resulting moment would be a value that would be between the values for each of the two individual results. Figure 11, however, shows that the moment generated by forward blowing on the left is enhanced significantly in the same direction by blowing aft on the right instead of being modified in the direction of aft blowing alone. In fact, it appears that the magnitude of the additional moment created by the aft blowing is nearly equal to the magnitude of the aft blowing alone, but the direction is reversed. There is an extremely effective synergistic effect of the simultaneous blowing which cannot be achieved with either individual blowing scheme alone.

#### 4.0 FOREBODY FLOW CONTROL USING FOREBODY STRAKES

An asymmetric pair of strakes can produce asymmetries so that yawing moments can be produced to enhance aircraft controllability. The effectiveness of the control depends on the size, geometry, and position of the strakes. Figure 12 shows the effect of varying the height of the strake. The baseline configuration (no strakes) is plotted for reference. Results for three different strake heights are shown: 0.02d, 0.04d, and 0.08d for both left and right sides. The yawing moment data show near mirror images for left or right strakes of the same heights. The most significant information is the behavior of the yawing moment with the various strake heights. For example, at  $\alpha = 45^\circ$  the direction of the yawing moment for the smallest strake height (0.02d) on the left is to the left. When the strake height is increased to 0.04d, the moment is still to the left but decreased. When

extended to full height, the moment is reversed. It appears that between a strake height of 0.04d and 0.08d, the behavior of the forebody vortices are changed and the vortex pattern is reversed.

Hence, the effect of a strake on the forebody flow is strongly dependent on the height. It can be conjectured that at very small heights, the strake delays separation on the side where it is deployed by tripping the boundary layer and causing transition. This allows the flow to maintain a higher suction on the same side of the body, with the vortex positioned closer to the body than the vortex on the opposite side. At large heights, separation occurs essentially at the edge of the strake, thereby causing the separation to be closer to the windward side than the separation on the opposite side. This results in the vortex on the side with the strake being farther off the body than the one on the clean side, thereby producing a forebody sideforce and yawing moment contribution in a direction opposite to the side with the strake. The height of the strake where this "crossover" occurs is, undoubtedly, fairly sensitive to the Reynolds number. The flow on the forebody for these tests is undoubtedly laminar near the tip and transitional over the rest of the body and, thus, a small strake can be very effective in causing transition of the boundary layer from laminar to turbulent. Disturbances to the boundary layer flow and the immediate flowfield by strakes for a full-scale configuration, where the boundary layer is fully turbulent for all but the tip region, may have a significantly different result. The effect of a strake should also be dependent on the local boundary layer thickness and the location of the strake relative to the natural separation location which is strongly dependent on the angles of attack and sideslip.

Overall, the wind tunnel results show that yawing moments of different magnitudes and directions can be generated by extending the strake to different heights. The primary function of the strake is controlling the separation location. In practice, the required size of the strake is an important consideration. The following section will discuss the results of another control device based on rotatable, miniature nose-tip strakes.

## 5.0 FOREBODY FLOW CONTROL USING ROTATABLE, MINIATURE NOSE-TIP STRAKES

5.1 The rotatable nose-tip stake shapes were shown in Fig. 3. Tests were conducted with a single-stake and with a pair of strakes. The dual strakes are fixed at  $\pm 75^\circ$  from the windward side of the model (as shown in Fig. 3) and are rotated as a pair maintaining the  $150^\circ$  separation angle. The single-stake is rotated with the zero reference coinciding with the stake on the windward side of the model.

### 5.2 Visualization of the Effect of the Strakes on the Vortex Flow

The flow visualization results show that the rotatable nose-tip/boom strakes on the F-16 and F/A-18 start having a noticeable effect on the forebody vortices at  $\alpha$ 's above  $30^\circ$ . The effect is dependent on the angle of attack and the nature of the baseline flow. Results from the F/A-18 experiments will be used as examples.

From  $\alpha = 30^\circ$  to  $60^\circ$ , rotating the strakes on the F/A-18 to different positions can change the vortical flow from a symmetric configuration into various degrees of asymmetry. At any angle of attack, there appears to be a maximum attainable vortex asymmetry. The magnitude of available control, as revealed by the maximum attainable vortex asymmetry, is the same for the left and right sides and increases with the angle of attack. Figure 13 shows examples of the results at  $\alpha = 50^\circ$  for the dual strakes with no sideslip which demonstrate the various degrees of vortex asymmetry that can be achieved. As shown in Fig. 13, a symmetric deployment of the strakes in general results in a symmetric pair of forebody vortices. When the strakes are rotated to an asymmetric configuration, the side with a stake closer to the windward meridian is associated with a vortex closer to the forebody which implies a yawing moment pointing towards the same side. The control is effective even at a sideslip angle of  $20^\circ$ .

For  $\alpha$ 's above about  $60^\circ$ , the baseline vortex flow becomes bi-stable. The strakes do have an effect on the degree of vortex

asymmetry of the baseline flow. The natural asymmetry can be reduced or increased by a small amount by moving the strakes to different positions. The effect of the strakes, however, is apparently not sufficiently strong to overcome the natural asymmetry and forced the flow into a symmetric state even when the strakes are deployed symmetrically. While a symmetric vortex pattern cannot be induced by placing the strakes statically at any position, due to the time lag effect, a quasi-steady symmetric pattern can be maintained by oscillating the strakes rapidly about a symmetric position.

Overall, flow visualization demonstrated that the nose-tip strakes provide similar kinds of control on the forebody vortices as many other control methods such as large deployable strakes and blowing. The control is effective over wide ranges of sideslip ( $0^\circ$  to  $>20^\circ$ ) and angles of attack ( $\sim 30^\circ$  to  $65^\circ$  or higher). The vortices can be manipulated into different patterns by rotating the strakes to different angular positions.

### 5.3 Yawing Moments Generated by the Nose-Tip Strakes

The main purpose of the yawing moment results is to quantify the controlling effect of the nose-tip strakes. In addition to the dual-stake, a single-stake was tested to aid in the understanding of the control mechanism. For the single-stake, the zero roll angle was defined as when the stake is at the windward meridian ( $\phi = 0^\circ$ ). For the dual-stake, the zero position was when the strakes were symmetrically located at  $\phi = \pm 75^\circ$ .

The single-stake results are shown in Fig. 14. At  $\alpha = 50^\circ$  the yawing moment essentially switches between two extreme values. The moment direction switching occurs over very narrow angular ranges centered approximately about four roll angles:  $0^\circ$ ,  $60^\circ$ ,  $180^\circ$ , and  $300^\circ$ . When the stake is located at  $\phi$ 's from  $0^\circ$  to  $\pm 60^\circ$ , the yawing moment generated is toward the side with the stake. For the other angles, the yawing moment generated is away from the side with the stake. Flow visualization reveals that at  $\alpha = 50^\circ$  with the single-stake in place the

vortex flow tends to assume one of two asymmetric states, although symmetric flow can be maintained by carefully placing the strake at the four roll angles where the moment switches signs. Apparently, the single-strake creates rather sizable asymmetric disturbances at most rotational angles and thus the flow is "locked" into highly asymmetric states. The yawing moment at  $\alpha = 40^\circ$  varies more gradually with nose-tip roll angle and with smaller amplitude, providing an easier task to hold yawing moment at zero.

As shown in Fig. 15, the yawing moment generated by the dual-strake behaves vastly different from that of the single-strake. While the maximum yawing moments that can be generated are similar in magnitude to that of the single-strake, the dual-strake moment varies much more gradually with the nose-tip roll angle. That is, the second strake has a significant modulating effect on the first strake. Above  $\alpha$  of about  $60^\circ$ , flow visualization reveals that the flow becomes "bi-stable". Results at  $\alpha = 60^\circ$  show that the yawing moment can be controlled by the nose-tip roll angle but to a much lesser degree. A symmetric flow cannot be maintained with the strakes deployed symmetrically. The behaviors of the single- and dual-strake yawing moments at different nose-tip roll angle are explained in detail in Ref. 21.

## 6.0 DISCUSSIONS

Implications of the observed results on the flow asymmetries and various aspects of the control methods will be discussed in this section. Advantages and limitations of the control methods will be described and compared.

### 6.1 Mechanisms of Vortex Control

The various methods of vortex control all work on the principle of producing a forced asymmetry or a biased natural asymmetry. Common to all the methods tested is that very effective control on the vortex asymmetry can be obtained by controlling the separation near the tip region. In essence, the flow pattern is modified so that the effective geometry of the

tip is altered. The specific working mechanisms of the methods are described below.

#### 6.1.1 Jet Blowing

The primary function of jet blowing is the controlling of flow separation by entrainment. As sketched in Fig. 16a, at the initiation of blowing, the separated boundary layer reattaches due to the entrainment from the blowing jet along the surface. The blowing-side vortex responds to the change in the separation location and readjusts to a position closer to the surface and farther toward the leeward side. The interaction in the form of mutual entrainment near the apex region between the two vortices causes the primary separation on the other side to advance to the windward side and the vortex to move farther from the surface. Unfortunately, with a fixed blowing nozzle it is impossible to maintain the absolute optimal relationship between the blowing jet and the separated flow throughout the entire range of operation since the separation location changes with angles of attack and sideslip and the blowing rate. Thus, the position and the direction of the fixed nozzle would necessarily have to be compromised for the operating conditions of interest. Furthermore, the maximum attainable vortex asymmetry is limited by the angular location of the blowing nozzle which places a limit on how far the separation can be delayed.

#### 6.1.2 Slot Blowing

Slot blowing operates on the principle of circulation control. As depicted in Fig. 16b, blowing energizes the flow near the surface so that it is more capable of overcoming the adverse pressure gradient. The separation on the blowing side is therefore delayed. The resultant changes in vortex strength and trajectory then determine the eventual flow asymmetry.

Blowing from the aft slot location, while effective in controlling the local flow separation, does not affect the vortices at the region where their interaction is the strongest. The changes imposed in the aft location also do not result in changes upstream of the region. Blowing from the forward slot, on the other

hand, effects changes in the region where vortex interaction is the strongest and where the flow has a predominating effect on the vortex trajectory. The disturbance created in this region also propagates along the entire vortex. Thus the forward slot position is more effective from a pure aerodynamic standpoint.

Blowing from a fixed slot has the same limitation as jet blowing, i.e., an absolute optimal relationship between the blowing slot and the separation location cannot be maintained throughout the angle of attack and sideslip ranges. Care must also be taken in shaping the slot to prevent the onset of shear flow instability which results in the degeneration of the jet sheet into individual vortex filaments.

#### 6.1.3 Suction

As depicted in Fig. 16c, suction works on the principle of circulation control which means a high-energy boundary layer flow is maintained by pulling the high-speed flow toward the surface. Thus it functions in many ways similar to slot blowing. With the present slot arrangement, the suction required to effect a large vortex asymmetry is very low and the control is effective even at relatively large sideslip ( $>20^\circ$ ).

While suction from a slot was tested in this study and was shown to be very promising, other forms of suction may be potentially more effective. Continuous suction through a porous surface had been shown to provide a similar degree of control at a much lower suction rate (Ref. 23). Optimizing the location of the porous surface can further reduce the suction requirement. A distributed suction is also likely to be effective over a wide range of angles of attack and sideslip. More importantly, the suction requirement decreases rapidly with increasing Reynolds number (Ref. 23). Thus, at actual flight conditions, the suction level may be extremely low.

#### 6.1.4 Forebody/Nose-Tip Strakes

The rotatable nose-tip strakes are intended to influence directly only a small region near the tip of the forebody where the flow plays a predominating role in controlling the vortex position, while large strakes directly affect a much larger region aft of the tip. Large

strakes essentially dictate that a large portion of the forebody flow separates at the leading edges of the strakes. The small nose-tip strakes, on the other hand, can behave much like the vortex generators on many existing aircraft wings. As depicted in Fig. 16d, one of the perceived functions of the strakes is to generate small vortices which energize the boundary layer farther aft to delay flow separation. While the deflectable strake has a fixed hinge-line, the nose-tip strakes are free to rotate to any angular position. This allows the nose-tip strakes to be positioned more optimally relative to the forebody vortices and separation locations for a wider range of angles of attack and sideslip, especially if the left and right strakes can be made to rotate independently.

One important question is how small the strakes can be and still be effective as a control device. Small nose-tip devices such as those in Refs. 13 and 14 produce very little vorticity of their own. They seem to function mainly by providing a bias to the flow asymmetry near the tip region and, thus, would function most effectively when the forebody flow is at or near the naturally asymmetric regime. Large forebody devices such as the strakes used in Refs. 7 and 8 do produce sizable vorticity locally. Thus, one would expect these devices to be effective in controlling the forebody flow over a wider range of flow conditions when compared with the miniature devices. One of the determining factors on the size of the strakes is operational requirements such as anticipated angles of attack and sideslip.

### 6.2 Comparison of the Different Methods of Forebody Vortex Control

The advantages and limitations of each of the control methods will be discussed in this section. One important point to bear in mind is, especially in the cases of the suction and rotatable strakes, none of the methods tested has been optimized. The discussions are therefore based only on presently available results.

#### 6.2.1 Overall Effectiveness

One of the main differences among the control methods tested is their overall

effectiveness over an extreme wide range of angles of attack and sideslip. In this regard, the rotatable nose-tip strake seems to offer a potential advantage. Among the pneumatic control methods tested, suction is perhaps more effective due to the relatively non-localized effect of suction on the boundary layer. The slot and jet blowing are somewhat more restrictive since the fixed locations of the slots and the blowing nozzles cannot maintain an optimal relationship with the flow separation location throughout a wide range of operating conditions. Nevertheless, all the methods tested were shown to be capable of functioning effectively over a fairly wide range of angles of attack and sideslip.

#### 6.2.2 Blowing/Suction Requirements for Pneumatic Control

While there may be many other potential sources of blowing and suction, engine-bleed is assumed to be the source-of-choice for the present discussion. The present results show that the  $C_{\mu}$  requirements for the slot and the jet blowing are well within the limits of practicality. For the surface suction method, assuming that the suction is available from an ejector pump arrangement with the engine-bleed as the power source and that the available suction is about half the magnitude of the corresponding engine-bleed, the suction requirement is also low enough to be practical. It remains to be verified in future studies whether the values of the blowing and suction coefficients obtained in sub-scale water and wind tunnel tests are directly applicable to flight conditions.

#### 6.2.3 System Complexity and Intrusiveness on Other Operations

The blowing and suction systems should consist of very few moving parts. The physical sizes, both internal and external of the forebody, are the main considerations. The nozzle blowing is likely to have the simplest internal plumbing system and small external dimensions. The need to maintain desired forms of blowing and suction distributions would likely result in certain complexities in the plumbing systems for slot blowing and

suction. Slot blowing and especially suction will probably result in very small modifications to the external surface of the forebody. In comparison to the pneumatic methods, the forebody strakes will consist of more moving parts both external and internal of the forebody which may present more interference on other aircraft operations. Miniaturization of the system is thus a key priority. In this regard, the rotatable nose-tip strakes concept would seem promising.

#### 6.3 Comparison of Various Yaw Control Methods

To put the requirements for forebody blowing and the resulting yaw control moment into perspective compared to other means of yaw control including 1) conventional rudder control, 2) thrust vectoring, and 3) reaction jets on the forebody, a typical flight case will be used for illustration. We will assume an aircraft in the F/A-18 class with regard to size, thrust, wing area etc. We will evaluate the magnitude of the yawing moment that can be generated at an altitude of 15,000 ft at  $M=0.3$ . The example of forebody control by blowing will be based on an aft blowing jet near the tip of the forebody, as discussed in Section 3.1. Based on the results discussed in this paper and others, we will assume that a yawing moment coefficient that is equal in magnitude to that of a fully-deflected rudder at  $\alpha=0$  ( $C_n = 0.03$  in Fig. 9 for a generic fighter) can be generated by blowing with an aft-facing jet with a blowing coefficient of  $C_{\mu} = 0.001$ .

Also, for comparison to thrust vectoring, we will assume that the maximum thrust available from the two engines at 15,000 ft is 1/2 of the thrust available at sea level (32,000 lbs), i.e.,  $T=16,000$  lbs. The four options to be considered for yaw control are the following:

- 1) Rudder
- 2) Thrust vectoring
- 3) Forebody thrust reaction jets (normal to forebody surface)
- 4) Forebody pneumatic vortex control (with jets tangential to forebody surface blowing in the aft direction)



Referring to Fig. 17 the contributions to the yawing moments (YM) for the various control schemes are illustrated. Note that the yawing moment for vortex control in Fig. 17d is expressed as a linear variation with the blowing coefficient,  $C_{\mu}$ , which can be rewritten as shown to express the yawing moment as a multiplying factor or augmentation ratio times the yawing moment generated by the same mass flow from a reaction jet perpendicular to the forebody surface shown in Fig. 17c. The size of this factor,  $K_A$ , is dependent upon the effectiveness of the blowing scheme, i.e. its effectiveness in generating an asymmetric flow resulting in a yawing moment. We will now show a numerical comparison between these four examples at a typical flight condition where the following parameter values are appropriate:

$h = 15,000$  ft (altitude)  
 $M = 0.3$  (Mach number)  
 $V = 330$  ft/sec (flight velocity)  
 $q_{\infty} = 75$  lbs/ft<sup>2</sup> (based on  $h$  and  $V$ )  
 $A = 400$  ft<sup>2</sup> (wing area)  
 $b = 40$  ft (wing span)  
 $T = 16,000$  lbs (thrust)  
 $X_N = 33$  ft (nose distance from cg)  
 $X_T = 27$  ft (tail distance from cg)

With the assumed blowing coefficient of  $C_{\mu} = 0.001$ , the corresponding mass flow rate  $\dot{m}$  is calculated from

$$C_{\mu} = \frac{\dot{m} V_j}{q_{\infty} A}$$

( $V_j$  = jet velocity (sonic), 1100 ft/sec)

$$\dot{m} = \frac{C_{\mu} q_{\infty} A}{V_j} = \frac{(0.001)(75)(400)}{1100} = 0.0272 \text{ slugs/sec or } 0.88 \text{ lbm/sec}$$

If we now substitute the numerical data into the equations shown in Fig. 17, we can evaluate the respective contributions of each of the schemes:

1) Rudder (Fig. 17a)

$$(YM)_R = C_{n_{RUD}} q_{\infty} A b = (0.03)(75)(400)(40) = 36,000 \text{ ft-lbs}$$

2) Thrust Vectoring to match the rudder (deflection angle of 4.78°) (Fig. 17b)

$$(YM)_{TV} = (T \sin \theta) X_T = (16,000)(\sin 4.78^\circ)(27) = 36,000 \text{ ft-lbs}$$

3) Reaction Jets (Fig. 17c)

$$(YM)_{RJ} = \dot{m} V_j X_N = (0.88/32.2)(1100)(33) = 986 \text{ ft-lbs}$$

4) Vortex Manipulation for Control (Fig. 17d)

$$(YM)_{VMC} = C_{n_{VMC}} q_{\infty} A b = (0.03)(75)(400)(40) = 36,000 \text{ ft-lbs}$$

In comparison to the level of the yawing moment available from the rudder deflection of 36,000 ft-lbs, thrust vectoring at full thrust would require approximately a 4.78° deflection. The yawing moment generated by vortex control compared to that from the reaction control jet is a factor of 36,000/986 or 36.5 times larger. That is,

$$K_A = \frac{(YM)_{VMC}}{(YM)_{RJ}} = 36,000/986 = 36.5$$

Therefore, for the same blowing coefficient, jet blowing to manipulate the forebody vortices can be 36.5 times more effective than simply using the jets as a reaction jet thruster.

To put the blowing requirement of 0.88 lbs/sec into perspective, the engine bleed rates that are available for the F-18's F404 engine at an altitude of 15,000 feet at 80% throttle is approximately 4 lbs/sec per engine. Not all would be available for a forebody blowing system, but some percentage could possibly be used. As seen above, the maximum mass flow rate that might be required for a yaw control moment at least as large as the rudder's maximum contribution, is a total of 0.88 lbs/sec or 0.44 lbs/sec per engine. In other words, a blowing rate on the order of 10% of the available bleed air would be adequate to produce a yawing moment of 36,000 ft-lbs at the flight conditions used in this example. The most demanding case for a real combat situation might be as much as Mach 0.6 at the same altitude or higher. Since the mass flow

requirements for a given blowing coefficient,  $C_{\mu}$ , increase with  $q_{\infty}$ , increasing the Mach number to  $M=0.6$  from 0.3 would increase the mass flow requirements by a factor of 4 or approximately 40% of the available bleed air, an amount which may still be an achievable mass flow rate.

This comparison shows the viability of the forebody vortex control compared to other methods. It is also possible that the blowing requirements could be met by an independent onboard pressure system, at least for short duty cycles, and engine bleed would not necessarily be the only choice for a blowing source.

## 7.0 SUMMARY AND CONCLUSIONS

Several methods of controlling the forebody flow at moderate-to-high angles of attack were studied in water and wind tunnel experiments. The results can be summarized as follows:

1. The methods were shown to be effective over a wide range of angles of attack and sideslip. The characteristics of the control depend strongly on the baseline vortical flow which can take on several different forms as dictated by the aircraft attitudes and the presence of external perturbations.

2. The experiments demonstrated that all the methods tested work basically on the principle of separation control. The mechanisms: blowing, suction, and vortex generators, have been well-proven for applications on conventional aircraft wings for separation control. Applications of the control methods on the forebody flow, at least from a pure aerodynamic standpoint, enable many of the control methods that are impractical on the wings to become potentially practical on the forebody. Compared with the wings, control on the forebody is required over a much smaller area and, thus, physical requirements such as blowing and suction rates, and size and weight should be much smaller. The presence of two closely spaced vortices around the forebody enhances the effectiveness since controlling the separation also controls the vortices which can significantly increase the available control forces. The lengthy forebody

of a modern fighter further enhances the control effectiveness by providing a long moment arm.

3. In terms of blowing and suction requirements and/or mechanical complexity, most of the methods tested would seem at least potentially practical. Each method, however, offers its own advantages and disadvantages, and there is probably no single method which is the best for all situations. The optimal method for a given application is, perhaps obviously, dependent on the mission requirements, physical limitations, and the particular configuration.

4. Regardless of which particular form, the control is most effective when applied at the region close to the tip of the forebody. In essence, the flow pattern at the tip region is modified so that the effective geometry of the tip is altered.

## 8.0 ACKNOWLEDGEMENTS

Support for the F/A-18 study is provided by NASA-Ames Research Center under Contract NAS2-13155. The technical monitor is Dr. Lewis Schiff. Support for the generic fighter and F-16 studies was provided by the US Air Force Wright Research and Development Center, WPAFB, Ohio under Contract F33615-86-C-3623. The technical monitors are Mr. Stan Lash and Mr. Dieter Multhopp of the Flight Controls Branch, and Mr. Russell Osborne and Mr. Robert Guyton of the Aeromechanics Branch.

## 9.0 REFERENCES

1. Chapman, G.T., Keener, E.R., and Malcolm, G.N., "Asymmetric Aerodynamic Forces on Aircraft Forebodies at High Angles of Attack - Some Design Guides," AGARD CP-199, Conference on Stall/Spin Problems of Military Aircraft, Rhode Saint Genese, Belgium, Nov. 1975.
2. Skow, A.M. and Titiriga, A., "A Survey of Analytical and Experimental Techniques to Predict Aircraft Dynamic Characteristics at High Angles of Attack," AGARD CP-235, Conference on Dynamic Stability Parameters, Athens, Greece, May 1978.

3. Headley, J.W., "Analysis of Wind Tunnel Data Pertaining to High Angle of Attack Aerodynamics," AFFDL-TR-78-94, Vol. I, July 1978.
4. Hall, R. M., Erickson, G.E., Straka, W.A., Peters, S.E., Maines, B.H., Fox, M.C., Hames, J.E., and LeMay, S.P., "Impact of Nose-Probe Chines on the Vortex Flows about the F-16C," AIAA-90-0386, Jan. 1990.
5. Stahl, W., "Suppression of Asymmetry of the Vortex Flow Behind a Circular Cone at High Incidence," AIAA Paper 89-3372-CP, Aug. 1989.
6. Ng, T. T., "The Effect of a Single-strake on the Forebody Vortex Asymmetry," J. of Aircraft, Vol. 27, No. 9, Sept. 1990, pp. 844-846.
7. Murri, D.G. and Rao, D.M., "Exploratory Studies of Actuated Forebody Strakes for Yaw Control at High Angles of Attack," AIAA Paper No. 87-2557-CP, August 1987.
8. Malcolm, G.N., Ng, T.T., Lewis, L.C., and Murri, D.G., "Development of Non-Conventional Control Methods for High Angle of Attack Flight Using Vortex Manipulation," AIAA Paper 89-2192, July - Aug. 1989.
9. Moskovitz, C., Hall, R., and DeJarnette, F., "Effects of Surface Perturbations on the Asymmetric Vortex Flow Over a Slender Body," AIAA Paper 88-0483, Jan. 1988.
10. Degani, D. and Schiff, L.B., "Numerical Simulation of the Effect of Spatial Disturbances on Vortex Asymmetry," AIAA Paper 89-0340, Jan. 1989.
11. Degani, D., "Numerical Investigation of the Origin of Vortex Asymmetry," AIAA Paper No. 90-0593, Jan. 1990.
12. Hartwich, P., Hall, R., and Hemsch, M., "Navier-Stokes Computations of Vortex Asymmetries Controlled by Small Surface Imperfections," AIAA Paper 90-0385, Jan. 1990.
13. Zilliac, G., Degani, D., and M. Tobak, "Asymmetric Vortices on a Slender Body of Revolution," AIAA-90-0388, Jan. 1990.
14. Moskovitz, C., Hall, R., and DeJarnette, F., "Experimental Investigation of a New Device to Control the Asymmetric Flowfield on Forebodies at Large Angles of Attack," AIAA-90-0068, Jan. 1990.
15. Skow, A.M., Moore, W.A., and Lorincz, D.J., "Forebody Vortex Blowing - A Novel Concept to Enhance the Departure/Spin Recovery Characteristics of Fighter Aircraft," AGARD CP-262, Conference on Aerodynamics of Controls, Naples, Italy, May 1979.
16. Moore, W.A., Skow, A.M., and Lorincz, D.J., "Control of the Forebody Vortex Orientation by Asymmetric Air Injection - Application to Enhance Departure/Spin Recovery," AIAA Paper No. 80-0173, Jan. 1980.
17. Malcolm, G.N. and Skow, A.M., "Enhanced Controllability Through Vortex Manipulation on Fighter Aircraft at High Angles of Attack," AIAA Paper No. 86-2277-CP, Aug. 1986.
18. Rosen, B. and Davis, W., "Numerical Study of Asymmetric Air Injection to Control High Angle-of-Attack Forebody Vortices on the X-29 Aircraft," AIAA Paper 90-3004, Aug. 1990.
19. Tavella, D.A., Schiff, L.B., and Cummings, R.M., "Pneumatic Vortical Flow Control at High Angles of Attack," AIAA Paper No. 90-0098, Jan. 1990.
20. Ng, T.T., "Application of Forebody Blowing for Vortex Manipulation on the F-16," Eidetics Technical Report, 1989. Prepared for the U.S. Air Force under Contract No. F33615-86-3623.
21. Ng, T. T. and Malcolm, G. N., "Aerodynamic Control Using Forebody Strakes," AIAA Paper No. 91-0618, Jan. 1991.
22. Ng, T.T. and Malcolm, G.N., "Aerodynamic Control Using Forebody Blowing and Suction," AIAA Paper No. 91-0619, Jan. 1991.
23. Schlichting, H., Boundary Layer Theory, McGraw-Hill Book Company.

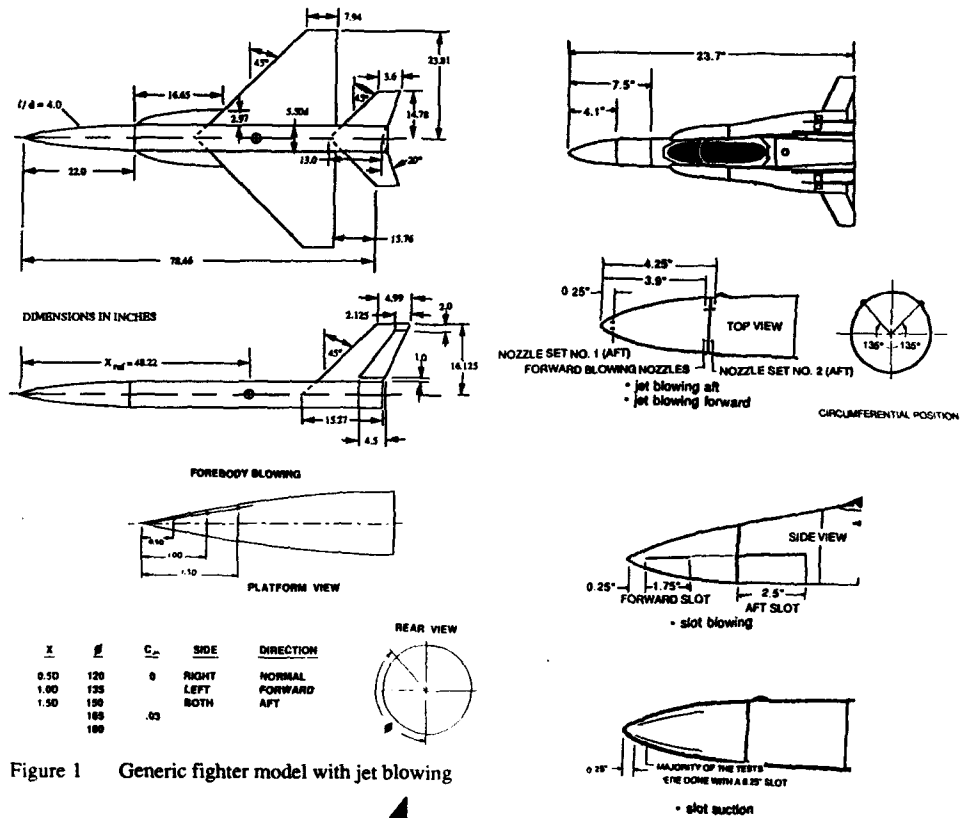


Figure 1 Generic fighter model with jet blowing

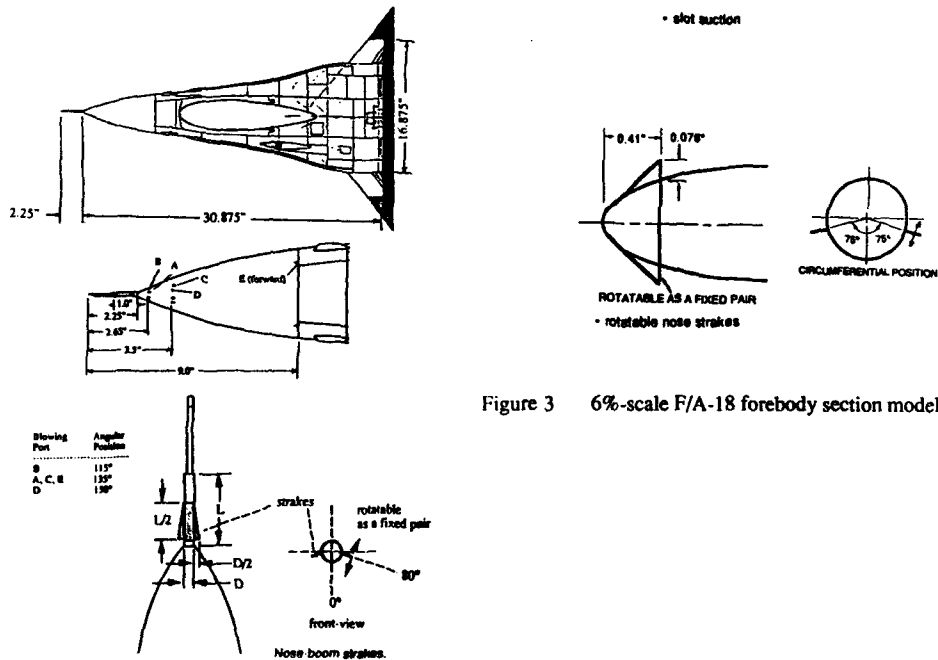
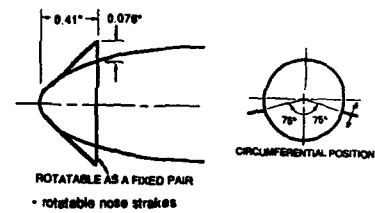


Figure 2 F-16 forebody section model

Figure 3 6%-scale F/A-18 forebody section model



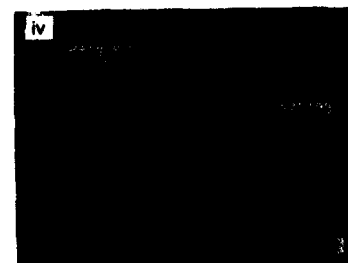
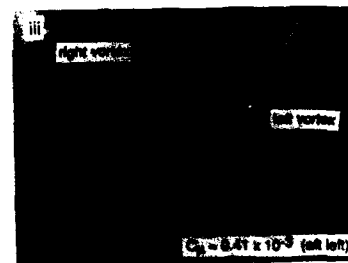
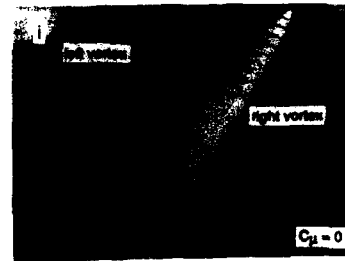
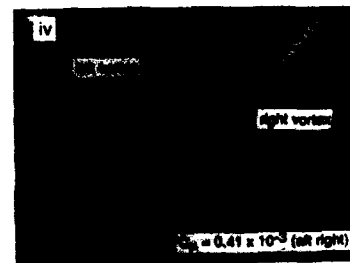
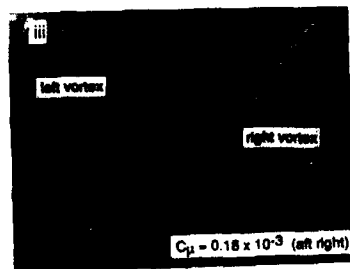
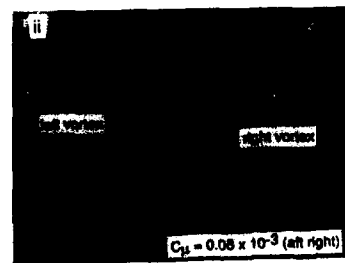
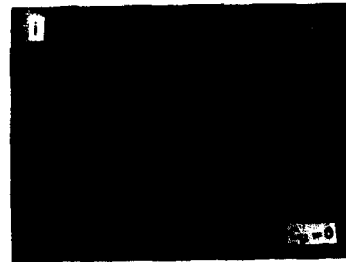


Figure 4a Forebody flow at 50° angle of attack with and without jet blowing aft; F/A-18

Figure 4b Forebody flow at 60° angle of attack with and without jet blowing aft; F/A-18

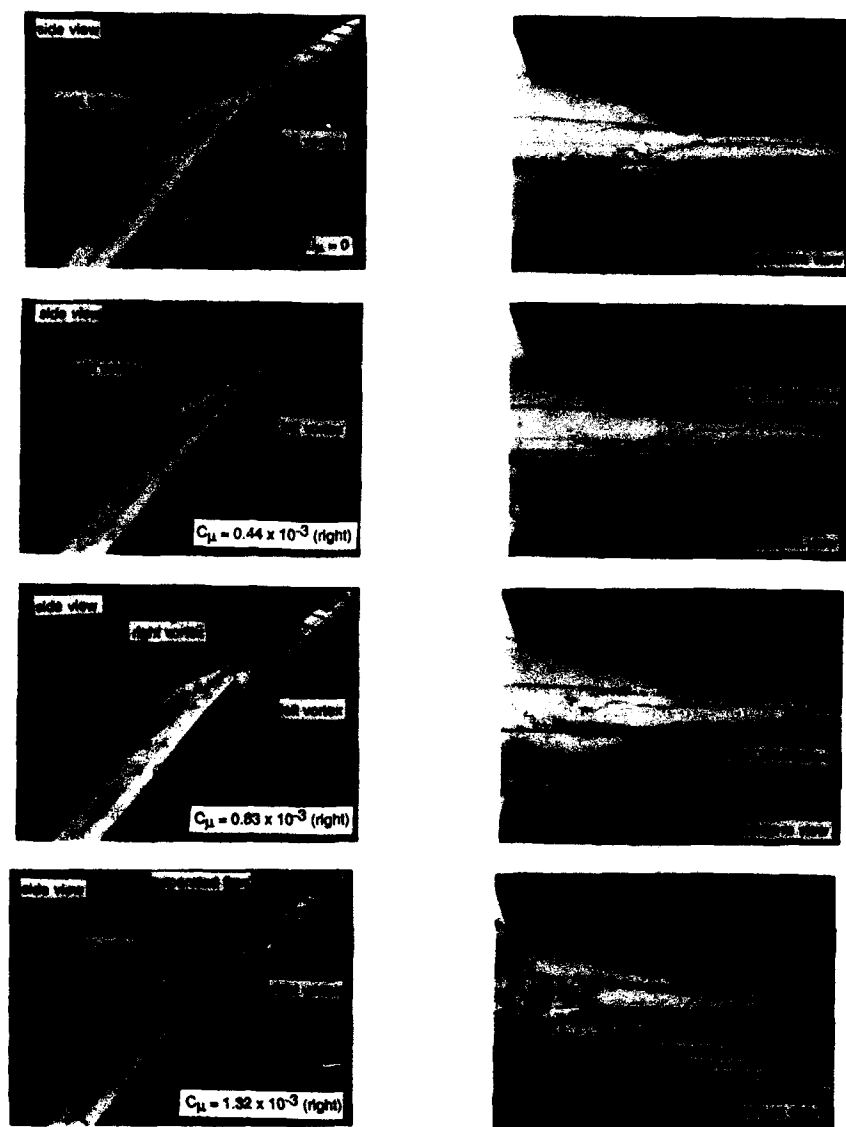


Figure 5 Flow around the 6%-scale F/A-18 model  
at  $\alpha = 50^\circ$  with blowing from the forward  
slot

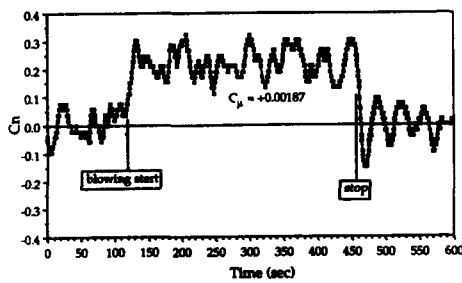


Figure 6 Yawing moment history of the 6% F/A-18 with jet blowing aft at  $\alpha = 50^\circ$

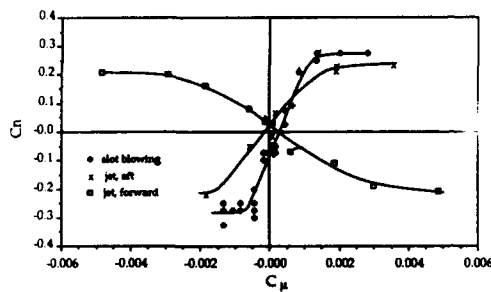


Figure 7 Steady-state mean yawing moment as a function of blowing rate for blowing from the forward slot, jet aft-blowing, and jet forward-blowing on the 6% F/A-18 at  $\alpha = 50^\circ$

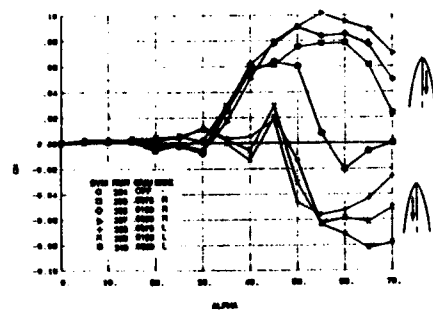


Figure 8 Yawing moment coefficient for baseline configuration, clean forebody, blowing aft at various rates from right or left ports at  $x/d = 0.5$  and  $\phi = 135^\circ$ ; generic fighter

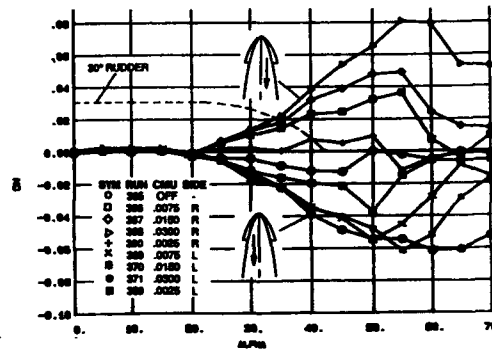


Figure 9 Yawing moment coefficient variation for several blowing rates for configuration with symmetric strakes,  $\phi = 105^\circ$ ,  $l_{ST} = 1.0d$ ,  $h_{ST} = 0.05d$ . Blowing aft on left or right side at  $x/d = 0.5$  and  $\phi = 135^\circ$ ; generic fighter

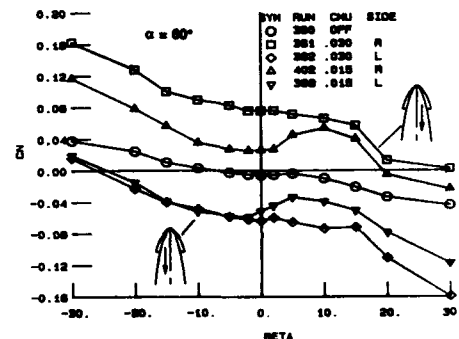


Figure 10 Effect of sideslip angle at  $\alpha = 60^\circ$  on yawing moment coefficient for configuration with symmetric strakes,  $\phi = 105^\circ$ ,  $l_{ST} = 1.0d$ ,  $h_{ST} = 0.05d$ . Blowing aft on left or right side at  $x/d = 0.5$  and  $\phi = 135^\circ$ ; generic fighter

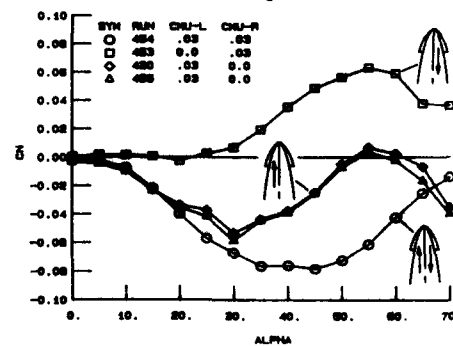


Figure 11 Yawing moment coefficient for configuration with symmetric strakes,  $\phi = 105^\circ$ ,  $l_{ST} = 1.0d$ ,  $h_{ST} = 0.05d$ . Blowing forward left at  $x/d = 1.0$  and  $\phi = 135^\circ$  and blowing aft right at  $x/d = 0.5$  and  $\phi = 135^\circ$ ; generic fighter

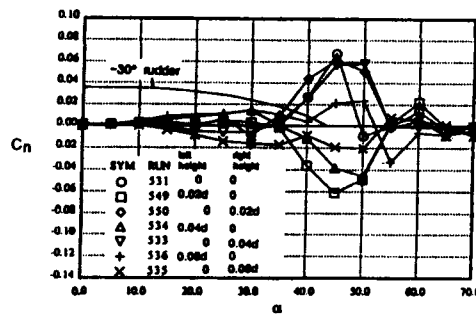


Figure 12 Effect of forebody strake height with individual strakes on either the left or right side (length = 1.0d,  $\phi = 105^\circ$ ): generic fighter

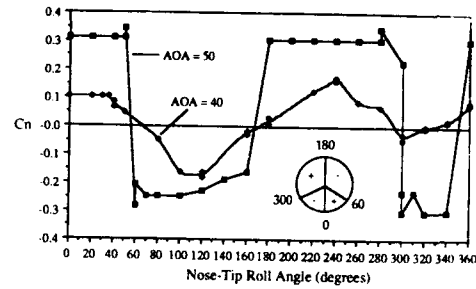


Figure 14 Steady-state mean yawing moment as a function of nose-tip roll angles for a single strake at  $40^\circ$  and  $50^\circ$  angle of attack; 6% F/A-18.

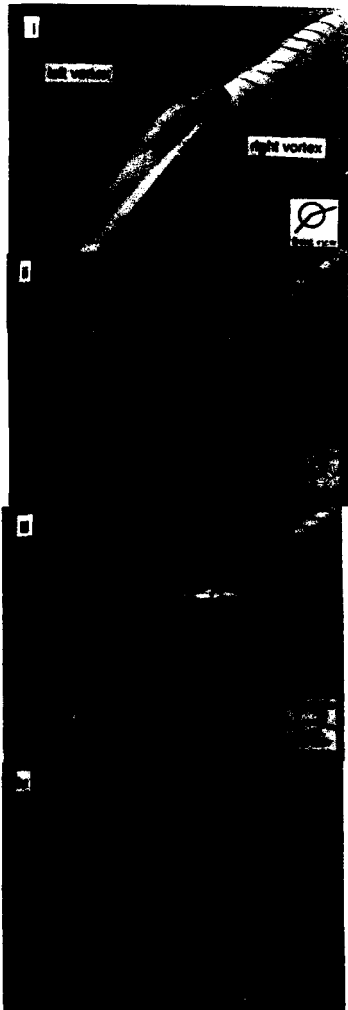


Figure 13 Effect of the rotatable dual-strake on the forebody flow at 50 degree angle of attack

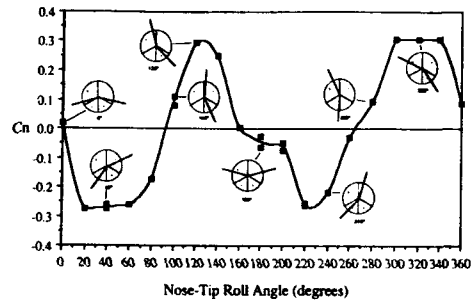


Figure 15 Steady-state mean yawing moment as a function of nose-tip roll angles for the dual-strake at 50 degree angle of attack; 6% F/A-18



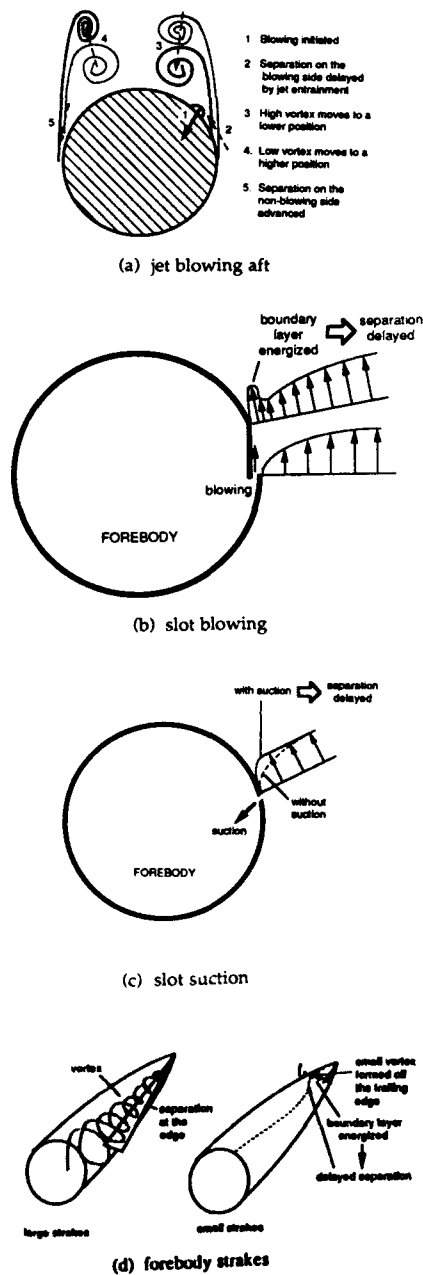


Figure 16 Fluid mechanical effects of various flow control

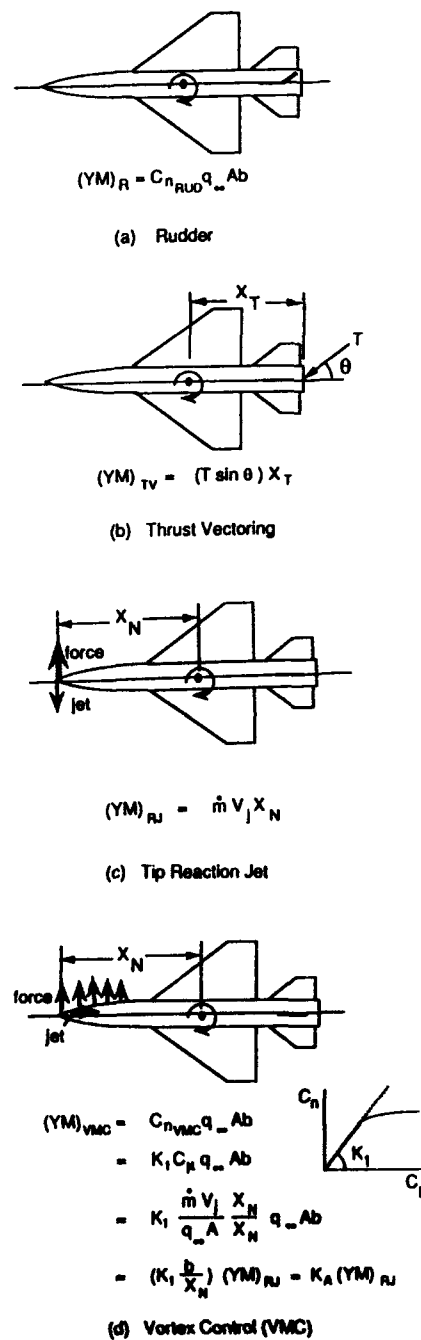


Figure 17 Comparison of various yaw control methods

## FOREBODY VORTEX CONTROL AEROMECHANICS

Robert W. Guyton  
 Russell F. Osborn  
 Scott P. LeMay

United States Air Force  
 Wright Laboratory  
 WL/FIMM  
 Wright-Patterson Air Force Base, Ohio 45433

Summary

Forebody vortex flow characteristics are discussed in terms of the forebody flowfield aerodynamics and the impact of this flow on the resulting forces and moments that limit combat maneuverability. Test results are presented for several pneumatic forebody vortex control designs applied to a 1/8 scale X-29 model, 1/15 scale F-18 model, and a 55 degree cropped delta/chined forebody model representative of future fighter configurations.

Introduction

Forebody generated vortices on the leeward side of an air combat aircraft can produce forces that dominate air vehicle trajectory control and adversely impact flight stability in the region beyond wing stall. For the purposes of analysis and discussion, forebody geometries can be separated into two categories; those that have cylindrical or elliptical cross sections typical of the F-5 and F-18 aircraft, and chined shapes which are appearing on modern fighter aircraft such as the YF-22 and YF-23.

The aerodynamics generated by the two types of forebody architectures are quite different. The elliptical/cylindrical shapes generate a bi-stable pair of vortices at high incidence (Figure 1) that produce asymmetric forebody forces and moments that change sign and magnitude with angle-of-attack. References 1 through 7 describe in detail the basic aerodynamics of rounded forebodies having different cross-sections, fineness ratios, planform and profile shapes. The forebody contribution to the overall aircraft aerodynamics at high angles-of-attack depends heavily on these shape parameters. Figure 2 from reference 1 graphically illustrates the swing in yawing moment coefficient experienced by the F-5F aircraft as it traverses through the high angle-of-attack flight region. The behaviour of zero sideslip yawing moments is determined by factors such as forebody length, cross sectional shape, nose apex angle, small surface imperfections at the nose apex, and downstream surfaces.

Precise control of forebody vortex asymmetries on elliptical/cylindrical shapes at high incidence can produce aircraft yawing moments equal to or greater in magnitude than those produced by the rudder operating at low angles-of-attack. Exploiting this phenomena for the purpose of increased air combat maneuverability is

a continuing program within the USAF Flight Dynamics Directorate. References 8 through 15 represent the highlights of documents generated on forebody vortex control in past years.

Chined forebodies are beginning to appear on modern combat aircraft, particularly those designed for use by the United States Air Force, because of the desire to keep aircraft mission survivability high by keeping the airframe radar signature low. The drawing in Figure 3 depicts a typical chined forebody shape that has been the subject of several recent experimental aerodynamic investigations. The flowfield generated by this forebody geometry consists of a pair of strong symmetrical vortices shed along each chine line that persist to very high angles-of-attack. At intermediate angles-of-attack the forebody and wing vortices commingle (Figure 4), resulting in limited available maximum lift and lift-to-drag performance, in addition to producing zero sideslip rolling and yawing moments of considerable magnitude. At very high incidences the lifting chined forebody produces a large destabilizing nose-up pitching moment which must be counteracted by large tail surfaces.

Chined forebody vortex flow control research is just currently getting a good start. The information available in this area is limited in scope and covers only basic concepts and ideas supported by experiments with models having features similar to next generation fighter aircraft. Basic research has shown that forebody controls can produce large rolling moments as well as effectively control wing and forebody chine vortex interactions that limit maneuverability potential. Research is beginning on pneumatic and mechanical concepts that either alter the chine vortex trajectory or prematurely burst the forebody chine vortex.

Wind Tunnel Tests

Following is a discussion of pneumatic forebody vortex control aeromechanics based on developmental research programs sponsored by the Wright Laboratories. The majority of the material presented addresses cylindrical/elliptical forebody vortex control techniques, since this area of research has received the most emphasis in the past two years. A limited amount of material for chined forebodies is presented for configurations having features similar to next generation fighter aircraft.

### X-29 Configuration

The objective of these wind tunnel tests was to apply the Malcolm forebody vortex control designs (Reference 10) to the X-29 configuration in order to bridge the gap from generic configurations to an optimized high performance fighter configuration. The ground rules for the design followed guidelines for a system that would be practical to implement at minimum cost. Therefore the designs reflect simplicity and should not be considered optimal.

Wind tunnel tests were conducted using the USAF 1/8 scale X-29 model shown in Figure 5. Tests on the full model were conducted in the Grumman Aerospace 7'x10' Low Speed Wind Tunnel at Mach=0.5 and at atmospheric pressure. Angle-of-attack and sideslip were varied from 0.0 to 44.0 and -10.0 to 5.0 degrees respectively. Aerodynamic force and moment data were obtained in these tests. Tests on the forebody model shown in Figure 6 were conducted in the Aeromechanics Divisions' 2'x2' Trisonic Wind Tunnel at Mach=0.3 at 0.5 atmospheres pressure. Angle-of-attack and sideslip were varied from 0.0 to 45.0 and from 0.0 to +10.0 degrees, respectively. Laser light sheet flow visualizations were obtained to add a more thorough understanding of the full model results. Both of these models were modified for forebody jet blowing and all forebody controllers/effectors were interchangeable between the models.

Results are presented for tangential forebody jet blowing with the nozzles located axially at 0.5 diameters from the nose apex and radially at the 135 degree location. The pertinent features from three variations on this nozzle placement are discussed. Force and moment data are presented in conjunction with flow visualizations to explain how the changes in the forebody vortex flowfield relate to forces generated by forebody blowing. The sense of direction for the flow visualization discussion is from an upstream view looking down the nose of the model. Annotations on the data plots refer to a cockpit perspective.

#### Single Jet Blowing Aft

Figure 7 shows the body axis yawing moment versus angle-of-attack for various blowing rates of either the left or right jet pointed tangentially aft. The magnitude of yawing moment generated became adequate for directional control above 40 degrees AOA for CMU=0.0105. Data for the various blowing rates show that the yawing moment response was largely proportional to the blowing rate. Figure 8 shows a representation of the changes in vortex positions observed in the forebody visualizations at 45 degrees angle of attack. The visualizations showed that without blowing the forebody vortices were in a nearly symmetric pattern. With the left jet turned on to CMU=0.010 the forebody vortices were in a highly asymmetric pattern with the left side vortex pulled down close to the surface. The lower pressures induced on the blowing side of the forebody result in a yawing moment towards the blowing side.

Peculiar characteristics for this blowing arrangement were observed at sideslip conditions. Figure 9 shows the body axis yawing moment versus sideslip angle at 44 degrees AOA. At low values of

beta (+ or - 3.0 degrees) the blowing jet provided a constant yawing moment increment. Beyond this sideslip range, the increment decayed and eventually reversed sign. Figure 10 shows the differences in the vortex positions between left jet and right jet blowing observed at  $\alpha=45.0$  degrees and  $\beta=8.0$  degrees. With the right jet blowing the right forebody vortex was pulled down closer to the surface as before in the zero beta case. However, with the left jet blowing an unexpected result was obtained. The left forebody vortex position was unchanged while the right forebody vortex was pulled closer to the surface as if the right jet were blowing. This can be explained in terms of the well documented sideslip behaviour of primary vortex separation lines (Reference 5) on horizontal ellipse forebodies and the importance of the jet location to these separation lines. When the left (leeward) vortex separation advances to a position low on the forebody due to increased sideslip, it moves beyond the influence of the left jet. At the same time, the right (windward) separation line is delayed to a point high on the forebody by the sideslip condition and moves into the region influenced by the left jet. In other words, the windward vortex can be manipulated with either jet because the primary separation line is close to both jets.

#### Jet Blowing at Strake Corner

Figure 11 shows the body axis yawing moment versus angle-of-attack with jets pointed at the strake trailing edge for blowing either the right or the left jet at CMU=0.010. The small increments below 5.0 degrees angle-of-attack are attributed to the jet exit momentum being pointed at nearly right angles to the fuselage axis. As the angle-of-attack was increased, adequate directional control was generated in the 15 to 35 degree AOA range. Above 40 degrees the increments decayed to zero and trends indicate a sign reversal at even higher angles-of-attack. Visualizations (not shown) revealed that the baseline case had strong symmetric nose strake vortices positioned close to the body surface. With the left jet blowing at CMU=0.010 the left nose strake vortex was displaced up and away from the surface. The deficit in vortex suction pressure on the blowing side results in a yawing moment away from the blowing side.

#### Dual Jets Blowing Aft

Figure 12 shows the body axis yawing moment versus sideslip obtained at 44.0 degrees angle-of-attack with dual jets pointed tangentially aft. The jets-off data indicate zero or slightly wandering directional stability at this angle-of-attack. With both jets blowing simultaneously at CMU=0.007, the directional stability was improved beyond the stability level observed at 0.0 degrees angle-of-attack. Figure 13 presents the flow visualizations obtained at 45 degrees AOA and zero sideslip. These visualizations show that both vortices were strengthened and pulled down close to the surface. This augments the natural stability which exists for this forebody at intermediate angles-of-attack. The stability increment is also effected by the decay of the leeward jet effectiveness with sideslip as observed in Figures 9 and 10 above.

### F-16 Configuration

A low-speed wind tunnel test was conducted to examine the prospects of using blowing to influence the forebody flowfield on a 1/15 scale F-16C model. The goal in applying blowing was to improve the lateral-directional stability and control characteristics of the F-16 at angles of attack greater than 30°, and it was hoped that blowing might provide a means with which to alleviate the "deep-stall" phenomenon the aircraft experiences in the 55° to 70° angle of attack range caused by an inadequate amount of nose-down pitch power. Figure 14 shows the model installation in the NASA Langley 7'x10' HST Wind Tunnel.

A 1/15 scale F-16C blowing forebody was fabricated and mated to an existing model modified to incorporate both jet nozzle and tangential slot blowing. Two pairs of symmetric jet blowing nozzles were located along the forebody as shown in Figure 15, with one pair being close to the tip of the aircraft's nosecone and the other farther aft near the radar bulkhead, and a pair of blowing slots was placed symmetrically on the radome. The blowing slots were designed so that a sheet of fluid was produced tangential to the forebody in order to control the forebody boundary layer.

The wind tunnel test was conducted at a freestream Mach number of 0.4 and the angle of attack was varied between 0° and 55°. At angles of attack of 30°, 35° and 40° beta polars were acquired for sideslip angles of -20° to 20°. The data consisted of 8-component force and moment data and some limited laser light sheet flow visualization data acquired using natural flow condensation. The test was performed at the NASA Langley 7ft x 10ft High Speed Tunnel. Figure 15 shows a photograph of the tunnel installation.

#### Jet Nozzle Blowing

The most successful jet nozzle blowing occurred with the nosetip nozzles located at FS 0.333. At the maximum angle of attack of 52°, symmetric blowing (blowing equally on both sides) at a  $C_\mu$  of 0.00825 produces an increase in the nose down pitching moment coefficient of 0.05.

Asymmetric blowing (blowing on one side only) with the nosetip nozzles produces large yawing moments at 0° sideslip as shown in Figure 16. Blowing at a  $C_\mu$  of 0.0082 from the starboard side nozzle produces a negative yawing moment coefficient of more than 0.06 at 52° angle of attack. At lower blowing rates, less yawing moment is generated. It is interesting to note that by blowing on the right-hand side of the forebody a nose left moment is generated. The right side blowing jet displaces the forebody vortex on the right-hand side to a position farther away from the fuselage. The blowing jet also causes the flow on the left hand side to stay attached to a point farther around the forebody due to the entrainment effect of the blowing jet on the right. This combination of effects produces a substantial side force to the left.

At FS 3.000, several jet nozzle blowing directions were investigated. The optimal direction was a 90° nozzle pointed directly aft into the LEX vortex core. Asymmetric blowing produces yawing moment coefficients of 0.02 and 0.03 for  $C_\mu$ 's of 0.00825 and

0.0115 respectively. In general, asymmetric blowing at this location is approximately 1/3 as effective as the asymmetric nosetip nozzle blowing.

#### Slot Blowing

Symmetric slot blowing is very effective in producing a nose-down pitching moment at high angles-of-attack. As shown in Figure 17, blowing at a  $C_\mu$  of 0.00125 per side increases the nose-down pitching moment coefficient by 0.12 at an angle of attack of 52°. The increase in nose-down pitching moment remains relatively constant up to 30° angle of attack, and then increases with increasing angle of attack. At this blowing rate the aircraft's lateral stability characteristics are not affected. Higher blowing rates reduce the nose-down pitch authority and undesirable yawing moments are generated. The blowing rate of 0.00125 per side was the lowest that could be accurately metered, and therefore the minimum blowing rate required to produce this nose-down effect is not known. Lower blowing rates may be capable of producing the same or even larger nose down pitching moments.

The low rate symmetric tangential slot blowing produces a nose-down pitching moment due to a reduction in the lift generated on the forebody. Tangential blowing causes the boundary layer to remain attached farther around the leeward side of the forebody resulting in delayed flow separation. This delay in separation inhibits the development of the forebody vortices, causing the observed reduction in forebody lift.

Asymmetric slot blowing is also very effective in altering the vortex flowfield patterns, producing a combination of effects. Blowing at the minimum  $C_\mu$  of approximately 0.0007 on the starboard side results in a positive yawing moment coefficient of 0.04 at angles of attack greater than 25° as shown in Figure 18. The amount of yawing moment generated decreases as the blowing rate is increased, as in the symmetric blowing case. Again, the minimum blowing rate required to produce the effect was not determined due to test equipment restrictions.

It is interesting to note that the two mechanisms which control the forebody flowfield produce similar fluid dynamic effects, but there means of achieving them are different. Asymmetric tangential slot blowing produces a yawing moment opposite that of asymmetric jet nozzle blowing for blowing on the same side. Slot blowing causes the flow to remain attached (on the blowing side) farther around the forebody due to the Coanda effect, and jet nozzle blowing causes the flow to remain attached (on the non-blowing side) due jet entrainment effects produced by the blowing nozzle. Each mechanism also displaces the forebody vortex opposite the side on which the flow stays attached.

#### Chined Forebody Jet Nozzle Blowing

A water tunnel study was conducted to determine the effects of blowing on the forebody chine/wing vortex interaction on a 0.04 scale generic fighter configuration having a 55° cropped delta wing and slender fuselage forebody with chine-like strakes. Tests were performed in the Aeromechanics Divisions' 2ft x 2ft Hydrodynamic Facility.

The freestream Reynolds number was 11,500 based upon the mean aerodynamic chord. The angle of attack was varied between 9° and 36° for angles of sideslip of 0° and 5°. Jet blowing coefficient based upon wing reference area was varied between 0.01 and 0.03. The wing and chine vortices were visualized using colored dyes, and still photography and video tape were used to record the data.

A 0.04 scale water tunnel model was used in this experiment and is shown in Figure 19. The model had a flat plate, untwisted, and uncambered 55° cropped delta wing with sharp leading edges beveled at 45° from the bottom surface. The wing had an aspect ratio of 1.8 and a wing taper area of 0.2. Sharp chine-like strakes were attached to the sides of the fuselage forebody in the wing plane, and were beveled in the same manner as the main wing. Jet blowing nozzles were positioned at several longitudinal locations along the chined forebody as shown in Figure 20. Four blowing ports were located on each side of the fuselage at  $x/l = 0.03, 0.26, 0.44,$  and  $0.64$ . All the blowing ports, except for the one at  $x/l = 0.03$ , could accept any one of a series of blowing jet nozzles which could be oriented in any direction.

#### Baseline Flow

The strakes produced a strong forebody vortex system which interacted with the wing vortex. This simulated rather well the vortex interaction of a more complex, blended chine forebody/wing configuration like those exhibited on the ATF prototypes YF-22 and YF-23. At the lowest angle of attack,  $\alpha = 9^\circ$ , the wing and chine vortices are fully developed and no vortex interaction or vortex breakdown occurs as shown in Figure 21. As the angle of attack increases, the wing and chine vortices begin to interact with each other and vortex breakdown, which first develops in the wake of the model, moves forward toward the trailing edge of the wing. The relative velocities induced by one vortex system on the other cause the chine vortices to be pulled down and underneath the wing vortices. At first this vortex interaction is favorable, in that vortex breakdown moves aft, but then leads to instabilities which promote vortex breakdown as illustrated in Figure 22.

An exhaustive matrix of locations and positions were investigated in order to determine the optimal blowing configuration. Only data from the optimal blowing configuration is presented in this paper. This configuration consists of a jet nozzle positioned at the second blowing port located slightly above the approximate mid-point of the strake ( $x/l = 0.26$ ). The jet nozzle was angled 30° aft from the fuselage normal, and 20° upward with respect to the wing plane.

#### Symmetric Blowing

Blowing symmetrically at a  $C_\mu$  of 0.03 per nozzle successfully decoupled the wing and chine vortices and delayed vortex breakdown up to an angle of attack of 30°. In Figure 23, a symmetric blowing case is compared with the baseline case at an angle of attack of 24°. The vortex interaction and breakdown locations for the wing and chine vortices move significantly aft. Applying blowing at a lower  $C_\mu$  of 0.01 per nozzle is also effective, but to a lesser degree. At this reduced blowing rate vortex breakdown and interaction can be

moved aft.

The entraining effect of the blowing jet causes the chine vortex to be pulled upward and away from the wing vortex, thereby delaying vortex interaction and in turn vortex breakdown. In Figure 24, the position of the blowing jet plume with respect to the wing and chine vortices is shown for  $C_\mu = 0.03$  and 15 degrees angle-of-attack case.

#### Asymmetric Blowing

Asymmetric blowing (blowing on one side only) was more effective in altering the vortex flowfield than symmetric blowing. Blowing asymmetrically at a  $C_\mu$  of 0.03 successfully decoupled the vortex interaction and delayed vortex breakdown on the blowing side up to an angle of attack of 36°, the limit of the investigation. In Figure 25, asymmetric blowing at a  $C_\mu$  of 0.03 is compared to the baseline case at an angle-of-attack of 30°. On the side with blowing, vortex breakdown does not occur above the wing surface and the location of vortex interaction moves aft to the wing trailing. In addition, on the side with no blowing the position of vortex breakdown is farther forward than the baseline case. This forward movement of the breakdown location was more prominent at the lower angles-of-attack. Also, cross-flow on the lower part of the fuselage was observed from the non-blowing to the blowing side as a result of jet entrainment. Blowing on one side alters the potential flowfield which produces an effective sideslip condition. This condition contributes to the large asymmetries observed with asymmetric blowing. A more detailed discussion of this test can be found in Reference 17.

#### Chined Forebody Slot Blowing

The testing was done at low subsonic speed, and the effectiveness of slot blowing at the chine line was deduced from upper surface pressure measurements on the wing panels. Figure 26 shows the details of the model and the locations of the surface pressure instrumentation. Model pressures at thirty degrees angle-of-attack, with and without symmetric slot blowing are presented in Figure 27. As can be seen in Figure 27, slot blowing eliminates the asymmetry in the upper surface baseline pressure distribution on the right wing panel caused by a forward wing vortex breakdown position. The full extent of symmetric slot blowing effects at high incidence can be seen in Figure 28 in terms of the local normal force coefficient. The wing apex load is uniformly reduced, and the normal force at the mid and aft wing stations develops symmetrically with angle-of-attack in marked contrast to the non-blowing case. Increasing the blowing momentum coefficient effectively increases the chine vortex strength as would be expected. However, the development of an effective chined forebody pneumatic flow control system is predicated on the fact that blowing coefficient magnitudes are less than  $CMU = 0.01$ . Blowing rates significantly higher than this level would be difficult to implement on an actual aircraft because of engine bleed constraints. Keep in mind that the chined forebody flow control results are for exploratory concepts, and that the slot size and location have not

been optimized. The elevated blowing rates required to produce these results can be reduced to acceptable levels through a concentrated system design optimization effort.

The effect of chined forebody blowing on aircraft rolling moment at high angle-of-attack is generated by blowing a single slot on either side of the forebody. A comparison of pressure distributions at  $\alpha=30^\circ$  with alternate left and right chine blowing is presented in Figure 29. The resulting non-symmetrical wing pressure distribution at both the center and aft model stations will generate a tolling moment in the direction of the unblown slot. The sectional rolling moment characteristics, Figure 30, indicate the effective lateral control potential of one-side slot blowing in the post-stall angle-of-attack flight region. Low speed visualizations with the left slot blowing are shown in Figure 31 for 40 degrees angle-of-attack. Unstructured separated flow exists on the unblown side, while strong wing and forebody vortices persist on the blown side as a result increased vortex strength and delayed vortex interaction. Further details of these results are presented in Reference 18.

#### Conclusions

Pneumatic forebody vortex flow control is an effective means of providing aerodynamic stability and control and improved maneuverability at intermediate through high angles-of-attack. The lack of moving surfaces makes pneumatic forebody control concepts attractive for application on the new generation of survivable fighter aircraft. Through concentrated system design optimization, required blowing rates are reduced to a fraction of available engine compressor bleed typically used for environmental controls and auxiliary subsystem power. Concentrated design optimization efforts at Wright-Patterson Air Force Base are indicating three-fold improvement in aerodynamic effectiveness at even lower blowing rates.

The status of pneumatic forebody vortex control technology is progressing from basic research investigations to developmental programs on specific system fighter aircraft with flight demonstration potential. Expanded parametrics in these developmental investigations are broadening the application beyond that of high angle-of-attack rudder power augmentation. Large influences in static stability, roll control, and pitch control are evident from these results. Future investigations will undoubtedly trade focus between basic and developmental programs, with increased emphasis on scale effects and angular rate aeromechanics.

#### Acknowledgements

The authors would like to gratefully acknowledge the Aeromechanics Division's Mechanical Instrumentation Group for the design and fabrication of the models used in these tests. Support by the Aeromechanics Division's Aero Optics Group in obtaining flow visualization data is also greatly appreciated. The flow visualization tests were conducted by Mr. William Gillard and Capt. Frank Luria of the Aeromechanics Division. The quantity and quality of these results were obtained through the dedicated efforts of the wind tunnel test crews from the Wright Laboratory's Trisonic Facility and Hydrodynamic Facility, the Grumman Aerospace Low Speed Wind Tunnel, the NASA Langley High Speed Tunnel, and the General Dynamics Fort Worth Division.

#### List of References

1. Osborn, R. F. and Headly J. W., "Analysis of Wind Tunnel Data Pertaining to High Angle-of-Attack Aerodynamics", AFFDL-TR-78-94, July 1978.
2. Rogers, L. W. and Erickson G. E., "Vortex Flow Correlation", AFWAL-TR-80-3143, January 1981.
3. Coe, P. L. and Chambers, J. R., "Asymmetric Lateral-Directional Characteristics of Pointed Bodies of Revolution at High Angles-of-Attack", NASA TND-7095, November 1972.
4. Carr, P. C. and Gilbert, W. P., "Effects of Fuselage Forebody Geometry on Low-Speed Lateral-Directional Characteristics of Twin-Tail Fighter Model at High Angles of Attack", NASA TP-1592, 1979.
5. Brandon, J. M. and Nguyen, L. T., "Experimental Study of Effects of Forebody Geometry on High Angle-of-Attack Stability", AIAA 86-0331, January 1986.
6. Keener, E. R. and Chapman, G. T., "Onset of Aerodynamic Side Forces at Zero Sideslip on Symmetric Forebodies at High Angles of Attack", AIAA 74-770, August 1974.
7. Turelli, R. R., "An Experimental Investigation of Steady Asymmetric Vortex Shedding From a Slender Body of Revolution at High Angles-of-Attack", USAF/APIT/GAE/AA/77D-15 Air Force Institute of Technology, December 1977.
8. Skow, A. M. and Peake, D. J., "Control of the Forebody Vortex Orientation by Asymmetric Air Injection", AGARD-CP-262-24, May 1979.
9. Malcolm, G. N. and Skow, A. M., "Enhanced Controllability Through Vortex Manipulation on Fighter Aircraft at High Angles of Attack", AIAA 86-2277-CP, August 1986.
10. Malcolm, G. N., Ng, T. T., Lewis, L. C. and Murri, D. G., "Development of Non-Conventional Control Methods For High Angle of Attack Flight Using Vortex Manipulation", AIAA 89-2192-CP, 1989.

11. Ross, A. J., Jeffries, E. B. and Edwards, G. P., "Control of Forebody Vortices Suction at the Nose of RAE High Incidence Research Model", RAE TM Aero 2172, 1990.

12. White, R. E., "Effects of Suction on High Angle-of-Attack Directional Control Characteristics of Isolated Forebodies", ViGYAN, Inc., unpublished, 1990.

13. Murri, D. G. and Rao, D. M., "Exploratory Studies of Actuated Forebody Strakes For Yaw Control at High Angles of Attack", AIAA-87-2557, August 1987.

14. Ng, T., "Aerodynamic Control of NASP-Type Vehicles Through Vortex Manipulation", AIAA-90-0594, January 1990.

15. Moskovitz, C., Hall, R. and Dejarnette, F., "Experimental Investigation of a New Device to Control the Asymmetric Flowfield on Forebodies at Large Angles of Attack", AIAA-90-0069, January 1990.

16. Rao, D. M., "Control of Vortex Interactions on a Chine Forebody/Delta Wing Configuration - A Feasibility Study", NAS2-12780, August 1988.

17. LeMay, S. P. and Rogers, L. W., "Pneumatic Vortex Flow Control on a 55 Degree Cropped Delta Wing with Chined Forebody", AIAA-90-1430, January 1990.

18. Rao, D. M. and Puram, C. K., "Low Speed Wind Tunnel Investigations of Mechanically and Pneumatically Controlled Forebody Chine Concepts", AFWAL-CN-F33615-89-C-3007, May 1990.

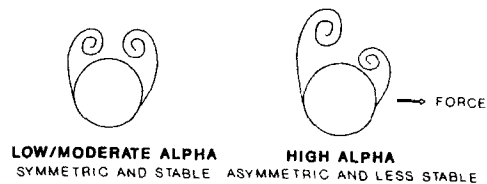


Figure 1. Elliptical/Cylindrical Forebody Characteristics

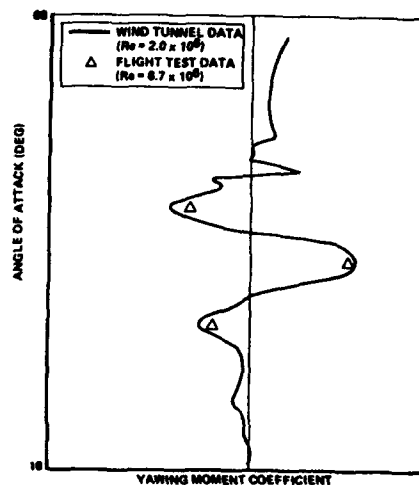


Figure 2. F-5F Zero Sideslip Yawing Moment Variation with Angle-of-attack

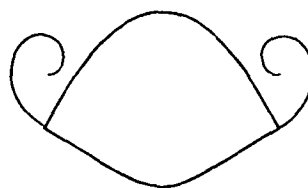


Figure 3. Chined Forebody Flow Pattern



Figure 4. Chined Forebody/Wing Vortex Interaction

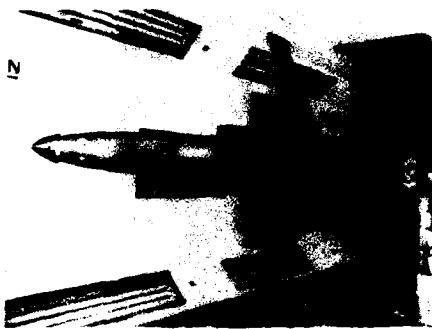


Figure 5. 1/8 Scale X-29 Installation

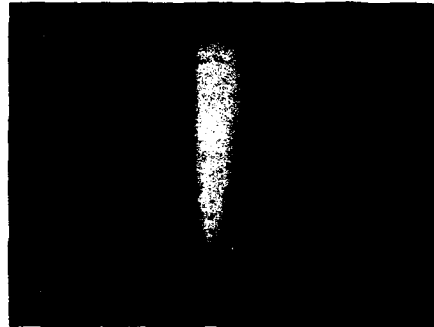


Figure 6. 1/8 Scale X-29 Forebody Model

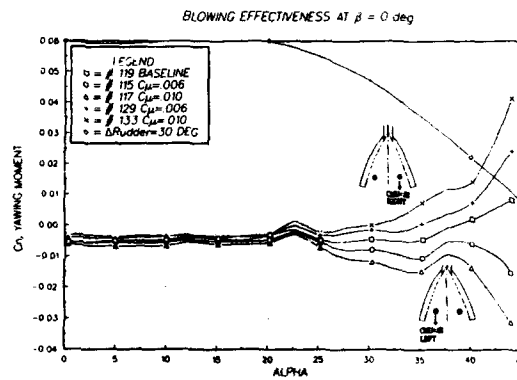
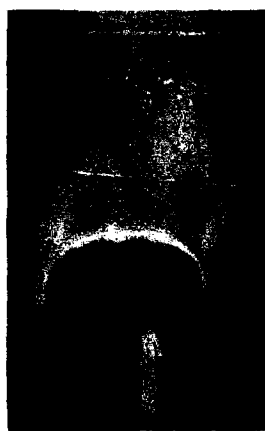


Figure 7. Yawing Moment Generated by a Single Jet Blowing Aft



RIGHT CMU = .018



BASELINE NO BLOWING



LEFT CMU = .018

Figure 8. Forebody Flow Visualisations for Single Jet Blowing Aft



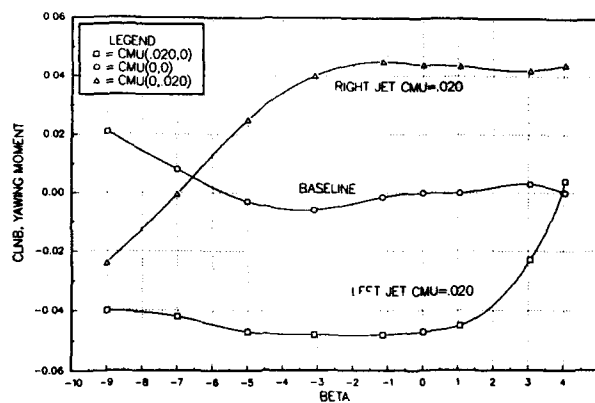
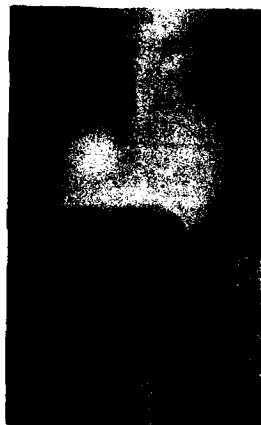


Figure 9. Sideslip Behaviour at  $\alpha=44^\circ$  for Single Jet Blowing Aft



RIGHT CMU = .018



LEFT CMU = .018

Figure 10. Forebody Flow Visualisations at Sideslip for a Single Jet Blowing Aft

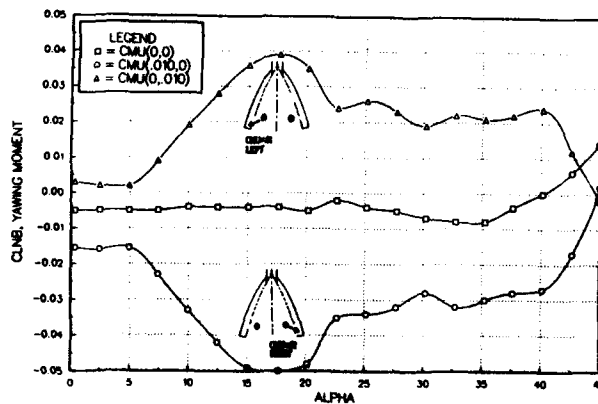


Figure 11. Yawing Moment Generated by a Single Jet Blowing at Strake Corner

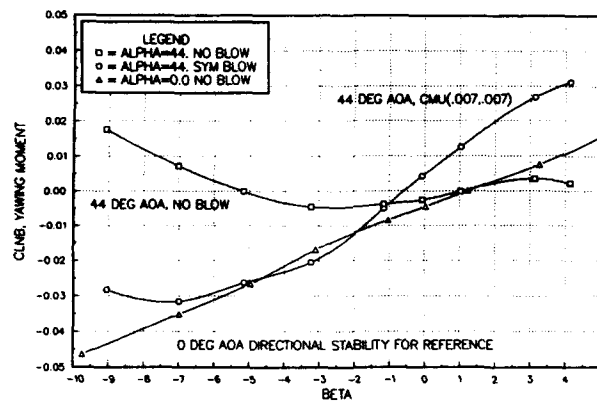


Figure 12. Sideslip Behaviour at  $\alpha=44^\circ$  for Dual Jets Blowing Aft

#### DIRECTIONAL STABILITY INCREMENT WITH BOTH JETS ACTIVE

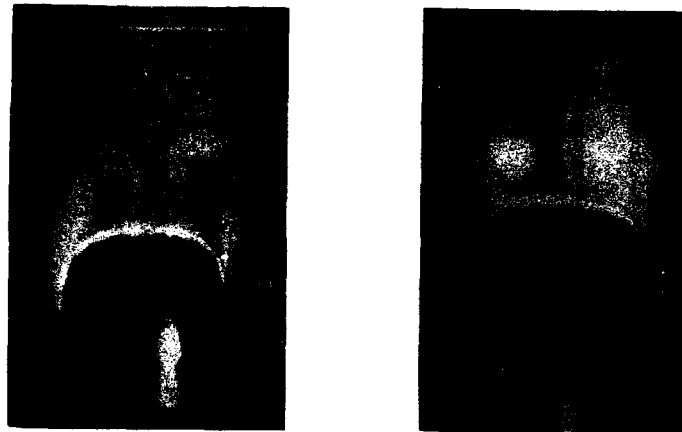


Figure 13. Forebody Flow Visualisations for Dual Jets Blowing Aft



Figure 14. 1/16 Scale F-16C Installation



Figure 15. 1/15 Scale F-16C Forebody Blowing Designs

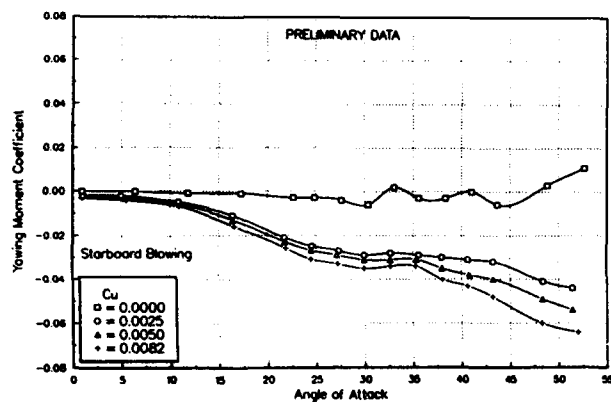


Figure 16. Yawing Moment Generated by a Single Jet Blowing Aft

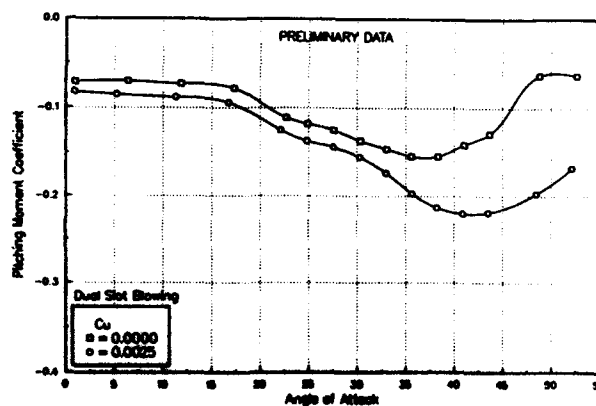


Figure 17. Pitching Moment Generated by Dual Slot Blowing

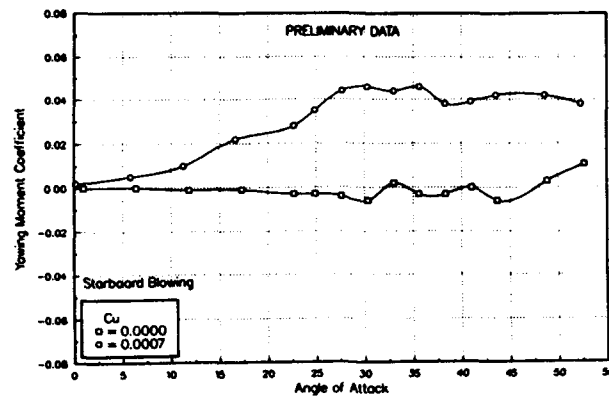


Figure 18. Yawing Moment Generated by a Single Slot Blowing



Figure 19. 55 Degree Chined Forebody Water Tunnel Model

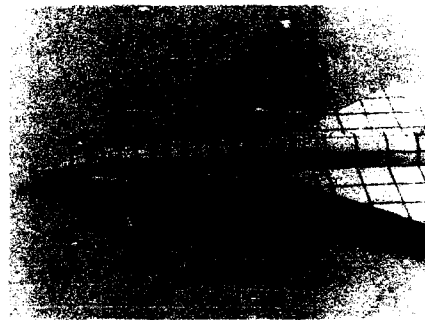


Figure 20. Blowing Port Locations on the 55 Degree Chined Forebody Water Tunnel Model

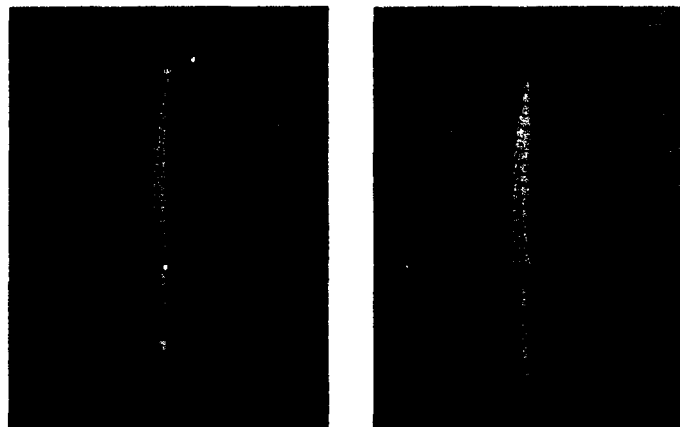


Figure 21. Forebody and Wing Vortices at 9 and 15 degrees for Baseline 55 Degree Chined Forebody Model



Figure 22. Forebody and Wing Vortices at 18 and 24 degrees for Baseline 55 Degree Chined Forebody Model

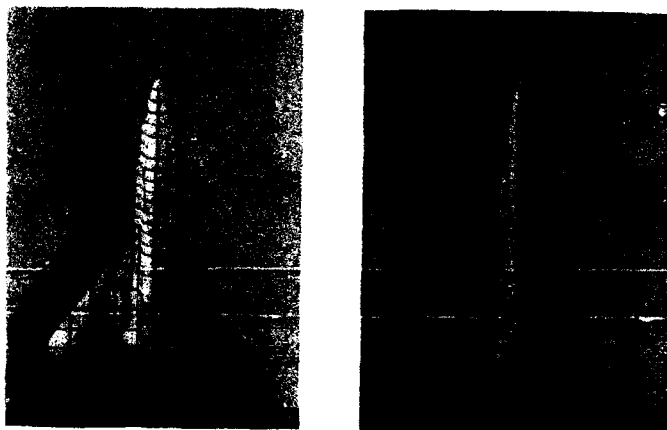


Figure 23. Effect of Symmetric Jet Nozzle Blowing at 24 degrees Alpha

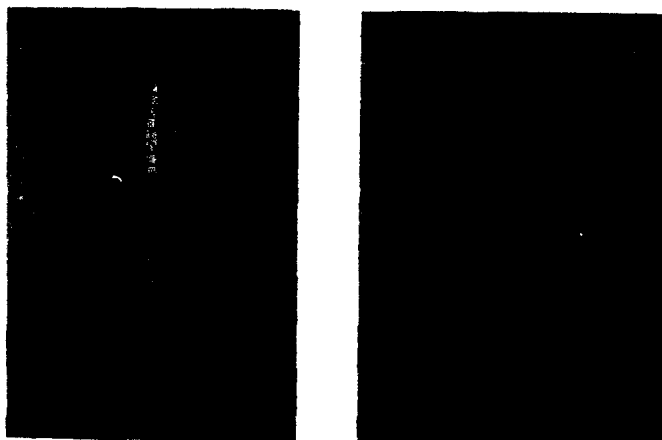


Figure 24. Optimum jet Nozzle Plume Trajectory at 18 degrees Alpha



Figure 25. Effect of Single Jet Nozzle  
Blowing at 30 degrees Alpha

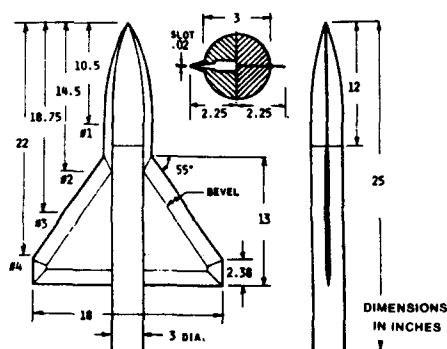


Figure 26. 55 Degree Chined Forebody  
Slot Blowing Wind Tunnel  
Model

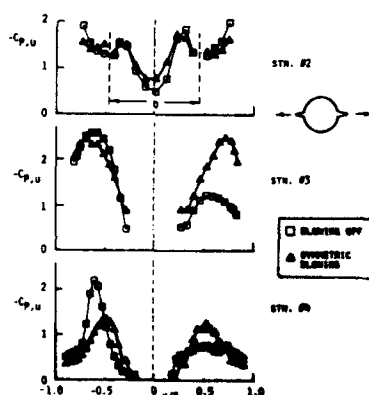


Figure 27. Effect of Symmetric Slot  
Blowing at 30 Degrees Alpha

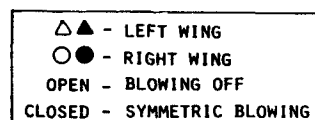


Figure 28. Effect of Symmetric Slot  
Blowing on Normal Force  
Coefficient

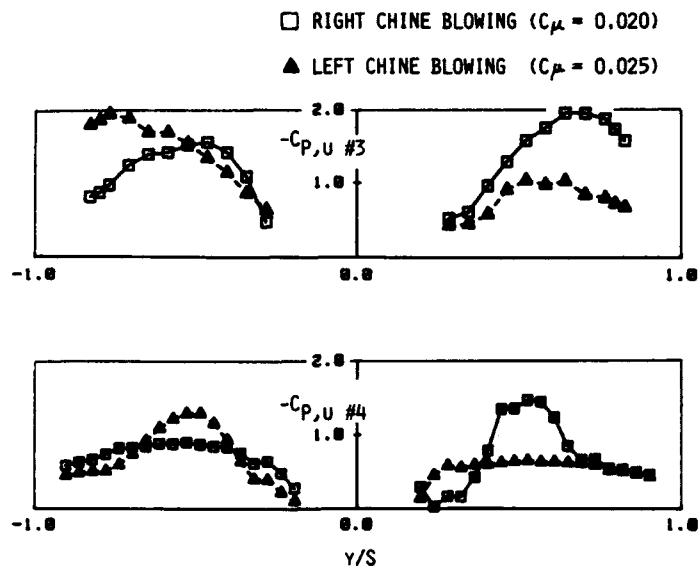


Figure 29. Effect of Single Slot Blowing on Wing Pressures at 30 degrees Alpha

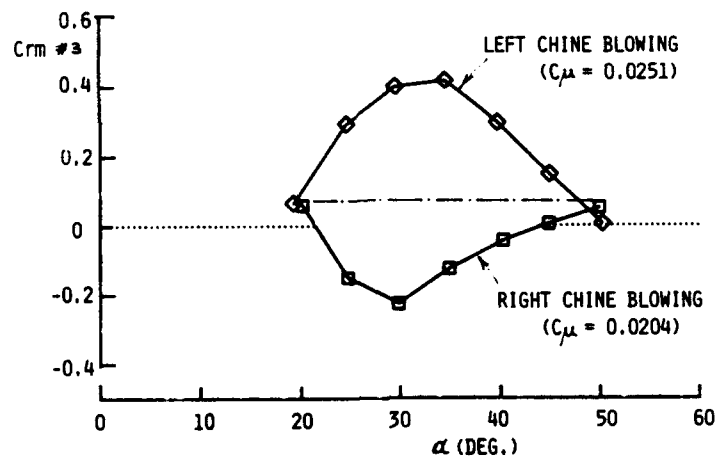


Figure 30. Effect of Single Slot Blowing on Rolling Moment Coefficient



Figure 31. Visualization of the Effect of Left Slot Blowing on the Vortical Flowfield Structure at 40 Degrees Alpha.

## DYNAMIC WIND TUNNEL TESTS ON CONTROL OF FOREBODY VORTICES WITH SUCTION

by

A. Jean Ross  
E. B. Jefferies  
Geraldine F. Edwards

Aerodynamics Department  
Royal Aerospace Establishment  
Farnborough, Hampshire GU14 6TD, United Kingdom

### SUMMARY

Extensive static and dynamic experiments have been made in low speed wind tunnels to investigate the possibility of using the yawing moment due to asymmetric forebody vortices for control at high angles of attack. The relative positions of the two vortices arising near the nose apex can be changed by applying differential suction through two small holes very near the tip. The resulting forces and moments measured in static tests have been analysed for the effects of forebody diameter and slenderness ratio. The RAE High Incidence Research Model has been controlled successfully on a free-to-yaw rig, indicating that the system could be used in flight. However, it could be expected that there are significant lags in the generation of the aerodynamic forces and moments. Experiments have been conducted on a simple missile model mounted on a sting rig, to measure the responses in yawing moment and sideforce due to sinusoidal variation over a range of frequencies of flow rates through the suction holes. The implications of these results for the proposed free-flight model tests are also discussed.

### 1 INTRODUCTION

The concept of using suction through small holes near the nose apex to control the vortices on a forebody at high angle of attack is being explored in a research programme using the High Incidence Research Model, HIRM1, static and dynamic wind-tunnel tests on a missile-type model<sup>1</sup> having given promising results. The lightweight model of HIRM1 has been tested<sup>2</sup>, with a series of undrooped forebodies designed to replace the original forebody, and results from static wind-tunnel tests in the RAE Bedford 13ft x 9ft Tunnel are described first. It has also been possible to obtain some data on a model the same size as the free-flight model, i.e. 9/4 times the size of the lightweight model, in the RAE Farnborough 5m Tunnel.

These results show that large sideforces and yawing moments are present for angles of attack above 30°, and these can be changed progressively by increasing flow rates through either the port or starboard hole at the nose. The maximum values of sideforce and yawing moment are limited by the condition that one of the asymmetric vortices is on the forebody surface, so increasing flow rate further cannot change the asymmetry. The results for several forebodies are discussed in Section 3, and scaling factors for the effect of forebody diameter and slenderness ratio are derived for comparison with results from the free-flight model. It was also found that the area scaling factor for flow rates needs to be related to nose geometry, rather than wing area, in order to obtain the correct range of effectiveness of control.

The lightweight model with the short forebody has been successfully controlled on a free-to-yaw rig, using angle of sideslip as feedback to a control law for minimising the error between actual and demanded sideslip. Flow rates to the port and starboard holes are controlled differentially by needle valves with servo actuators, which move according to the output of the control law. The experiment is described in Section 4, and responses for several levels of control authority are compared.

Investigation of the aerodynamic lags between change in flow rates to change in sideforce and yawing moment has been made on a simple missile configuration, using the large forebody mounted on a cylindrical afterbody. The actuators controlling the flow rates were moved sinusoidally, so that the phase shift of the yawing moment, measured by strain-gauge balance, could be analysed. A second-order response characteristic has been derived in Section 5, which gives an equivalent lag of less than 0.1 s, model scale.

The results are being used to design an active control system for the free-flight model of HIRM1, aiming to maintain roll about the velocity axis at angles of attack near 30° by minimising rate of yaw about the velocity axis. This control system will be added to the existing Departure Prevention System<sup>3</sup>, which has been flown successfully. The same nose cone, needle valves and actuators used in the wind-tunnel models will be fitted in the free-flight model, and suction applied via a small electric pump. It may also be possible to mount a free-flight model on a free-to-yaw rig in the 24ft Tunnel at RAE Farnborough, to make further checks on scaling effects.

### 2 DESCRIPTION OF MODELS AND TESTS

The 4/9-scale lightweight model (M2206) of the free-flight version of HIRM1 has been used for the static and dynamic tests in the RAE 13ft x 9ft Wind Tunnel. The GA (Fig 1) shows the drooped forebody and the largest of the undrooped forebodies. The original probe has been replaced by a sharp conical nose, which has two small holes of approximately 0.75 mm diameter, 7 mm back from the tip situated 30° down from the top plane of symmetry, as sketched in Fig 2. Flow rates are applied via suction through these holes, there being two separate chambers inside the forebody connected independently to the suction pump.

The same nose cone was used on all the forebodies tested on M2206, and also on M2149 (free-flight model scale) tested in the 5m Tunnel. Four undrooped forebodies have been tested on M2206, but the size of the forebody for M2149 is between these for both length and diameter, as shown in Fig 3a. The parameters defining the geometries



are given in Table 1, the large and short forebodies being tangent ogives with nose apex angle of  $27^\circ$  for the main section, and faired in to the fuselage near the front of the cockpit. The short forebody can also be lengthened by inserting cylindrical sections (see Fig 3b), so an intermediate and a long forebody have also been tested. The geometry of the original drooped forebody is also included in Fig 3 and Table 1. The forebody length is defined here as the distance between the apex and the junction of the fuselage and forebody for the free-flight model. However, all dimensions are for M2206, in mm.

Transition strips were placed along the  $80^\circ$  generator (measured from the bottom) of each of the forebodies, to cause turbulent separation behind the nose cone. Previous tests<sup>2,4</sup> had shown that the longitudinal station of the change from laminar to turbulent separation (which depends on Reynolds number) affects the magnitude of the maximum control powers in sideforce and yawing moment.

For most of the tests, canard was set at  $0^\circ$ , and tailplane at  $-15^\circ$ , giving a trim angle of attack near  $30^\circ$ . Some checks were made with canard setting of  $-10^\circ$ , and with tailplane at  $-20^\circ$ . However, the tests in the 5m Tunnel were made with canard at  $0^\circ$  and tailplane at  $-20^\circ$ .

Tunnel speed was 33 m/s for all the static results discussed here, giving a Reynolds number of  $0.9 \times 10^6$ . (The light-weight model is restricted to 33 m/s by strength considerations.) The data are referred to the centre of moments position at  $0.125\bar{c}$  as in all previous wind-tunnel tests on HIRM1.

The rig for the free yaw tests was a stronger version of that used in Ref 2. The model is mounted on a spindle with ball race which is supported by a vertical strut and allows angle of attack to be varied. The model is free to yaw about an axis normal to the fuselage datum, but freedom was restricted by wires attached between the rear fuselage and supports at the sides of the tunnel. The flow rates are actively controlled via the two needle valves, using angle of yaw as feedback to a proportional/integral/differential controller.

Static and dynamic tests have also been made in the RAE Farnborough 11 1/2 ft Tunnel using a simple body plus fins, made from the large forebody used on M2206 and a cylinder of circular cross-section. The model is shown in Fig 3c, with the position of the long transition strips used for these tests to ensure turbulent separation. The model was mounted on the cranked sting, so the angle of attack range was  $20^\circ$  to  $40^\circ$ . The static tests were conventional<sup>4</sup>, but for the dynamic tests the sideforce and yawing moment signals were recorded as the needle valves controlling flow rates were moved sinusoidally over a range of frequency. The data were measured at tunnel speeds of 20 m/s and 33 m/s. It should be noted that the aerodynamic coefficients are referred to the area, mean chord and span of M2206 wing, so that direct comparisons could be made with the data from the tests in the 13ft x 9ft Tunnel.

### 3 ANALYSIS OF STATIC RESULTS FOR ALL FOREBODIES

#### 3.1 Sideforce and yawing moments due to flow rates

A typical example of the variation of yawing moment with flow rate is shown in Fig 4a, as measured on the 'free-flight' model in the 5m Tunnel. Moments due to suction through the starboard hole are plotted on the right hand side, but those due to suction through the port hole are plotted with flow rate increasing in the negative direction. The flow rate (denoted by  $Q$ ) is here expressed in dimensional units,  $m^3/s$ . At this angle of attack of  $31.4^\circ$ , the asymmetry in the flow at zero suction is appreciable for this test, and the maximum moment is equivalent to about  $20^\circ$  of rudder deflection. The corresponding sideforce is plotted in Fig 4b.

The results for control powers for the forebodies listed in Table 1 have been analysed<sup>5</sup>, using the empirical fit to the form of equation derived in Ref 2. The comparison with experimental data is also shown in Fig 4. For example, the form of the equation for  $C_n$  is assumed to be

$$C_n = C_{nL} \gamma (3 - 2|\gamma|^{1/2}) \quad (1)$$

where  $\gamma = (Q - Q_0)/Q_L$ ,  $Q = Q_S - Q_P$  with  $Q_S > 0$  and  $Q_P > 0$ . The axis for  $Q$  is shown at the bottom of Fig 4a. The parameters  $C_{nL}$ ,  $Q_0$  and  $Q_L$  are obtained from the experimental data, where  $Q_0$  is the flow rate at which yawing moment is zero, and may vary from test to test because of the random asymmetry at zero suction. For flow rates greater than  $Q_0 \pm Q_L$ ,  $C_n$  remains at the constant values of  $\pm C_{nL}$ . The parameters  $Q_0$  and  $C_{nL}$  do not vary with the degree of asymmetry present at zero suction. The form of equation for  $C_y$  is analogous, although the values of  $Q_0$  and  $Q_L$  may be different at the same angle of attack, so an extra suffix, n or y, is added when necessary, but have been omitted on Fig 4 for clarity.

The previous reports<sup>2,4</sup> presented the results in terms of a non-dimensional flow rate coefficient,  $C_Q = Q/VS$ , where  $Q$  is expressed in  $m^3/s$  and  $S$  was taken to be wing area. The tests with the free-flight model in the 5m Tunnel showed that the range of effective flow rates is unchanged by model size (M2206 is 4/9-scale of M2149), so that  $S$  should relate to nose geometry in some way. For convenience, a nominal area of  $1 \text{ mm}^2$  has been used in this report, and the notation has been changed to  $C_q$  to avoid confusion.

The scaling of the experimental results for different forebody lengths and diameters has been done in stages, first for maximum control powers for sideforce and yawing moment,  $C_{yL}$  and  $C_{nL}$ , then for variation of these with flow rates. The results for the five forebodies tested in the 13ft x 9ft Tunnel were used to derive scaling factors, and the results from the 5m tests are used for validation.

All data were measured with the long transition strips on the forebodies. Most of the results for the large forebody are for canard  $-10^\circ$  (where the sample results for canard  $0^\circ$  showed only small effects), and those for the short, intermediate and long forebodies are for canard  $0^\circ$  (where again some results for canard  $-10^\circ$  showed insignificant changes). Tailplane is set at  $-15^\circ$ .

### 3.1.1 Maximum sideforce and yawing moment

The experimental results show that flow rates of  $3.3 \times 10^{-5} \text{ m}^3/\text{s}$  ( $C_q = 1.0$  for  $V = 33 \text{ m/s}$ ) through either port or starboard hole give the maximum effects, so that the values of  $C_{Y_L}$  and  $C_{n_L}$  are determined. Previous experiments on the asymmetries present for bodies alone (eg Ref 6), indicate that the maximum sideforce and yawing moment coefficients, when referred to body cross-sectional area, are dependent on nose apex angle (unchanged), and on slenderness ratio ( $= \ell/d$  where 'length' has to be defined for an aircraft configuration). The equivalent length has been suggested as that ahead of any lifting surface, so  $\ell/d$  is approximately the same for the large and short forebodies. The results for these were used first to check the dependence on cross-sectional area, the ratio being 0.415 for these two forebodies.

The sideforces for M2206 are referred to wing area, so the data for  $C_{Y_L}$  of the large forebody have been scaled by the ratio of cross-sectional areas, 0.415, and compared with data for the short forebody. The two sets of data scale very well over the angle of attack range  $22.7^\circ < \alpha < 35^\circ$ , as shown in Fig 5a, so the ratio of  $d^2$  may be used, ie a factor of 1.33 on the data for the short forebody to compare with data for the free flight model M2149. The unflagged symbols refer to results obtained from variation of flow rate at constant angle of attack, and the flagged symbols refer to results from maximum flow rates as angle of attack varied.

The yawing moments are referred to (wing area)  $\times$  (wing span), but the corresponding results (Fig 5b) for maximum yawing moment indicate that the scaling factor is  $d^2$  rather than  $d^3$ , although there is a consistent small change in the difference with angle of attack for  $22.7^\circ < \alpha < 33^\circ$ . The moment arm for the maximum sideforce is shown in Fig 5c, and the force is seen to act near a constant position for  $\alpha = 26.8^\circ, 28.9^\circ, 30.9^\circ$ , ie the range of interest for the free-flight experiments, with  $C_{n_L}/C_{Y_L} = 0.47$ . This moment arm from the centre of gravity (at Station 850), is 548 mm, and is close to the front of the cockpit, as shown by the sketch of the forebodies on the vertical scale.

The results for the short, intermediate and long forebodies were used to obtain a factor to account for forebody length/diameter ratio. It was found that the 'length' definition required to give the same  $\ell/d$  for the large and short forebodies was the length ahead of the mean centre of pressure for the maximum control powers. The variations of maximum sideforce and yawing moment with  $\ell/d$  for  $\alpha = 26.8^\circ, 30.9^\circ$  and  $35^\circ$  are shown in Fig 6, together with the factored results for the large forebody (flagged symbols). It is possible to derive approximate linear variations for the two lower angles of attack, in order to be able to interpolate for the free-flight model. A mean factor of 1.12 is indicated to account for the slightly larger value of  $\ell/d = 4.5$  relative to that of 4.3 for the short forebody.

Thus the results for the maximum sideforce and yawing moments due to the short forebody should be factored by  $1.33 \times 1.12 = 1.5$  to obtain results for comparison with those for the free-flight forebody. The inverse of this factor has been used with the results from the 5m Tunnel to obtain the comparison shown in Fig 5. (The flagged symbols refer to data measured during sideslip tests.) It appears that the magnitudes of sideforce and yawing moment are greater

than predicted. Alternatively, the same levels are obtained at angles of attack approximately  $1^\circ$  lower.

### 3.1.2 Variation of sideforce and yawing moment with flow rate

As stated above, a representative area of  $1 \text{ mm}^2$  has been used instead of wing area to derive flow rate coefficient, denoted by  $C_q$  instead of  $C_Q$  used in Refs 2 and 4. The factor between the two is given by

$$C_q = 0.407 C_Q \times 10^6 \quad (2)$$

The maximum slopes of  $C_Y$  and  $C_n$  with  $C_q$  are important parameters, and are proportional to  $C_{Y_L}/C_{qL,Y}$  and  $C_{n_L}/C_{qL,n}$  respectively (see equation (1)). Values were evaluated as functions of angle of attack from the results for the large and short forebodies. The two sets of data in Fig 7a indicate that a factor dependent on  $d^3$  is appropriate to obtain the scaling, of which  $d^2$  applies to  $C_Y$ , so  $C_{qL,Y}$  is assumed to be scaled by  $d^{-1}$ . However, the corresponding results for  $C_n$  collapse with the factor  $d^2$ , as shown in Fig 7b ie no scaling factor is required on  $C_{qL,n}$  for yawing moment.

The variation of the slopes with forebody length, shown for  $\alpha = 30.9^\circ$  in Fig 7c, gives a similar value of 1.12 for the factor between forebody length ratios of 4.3 and 4.5 as derived in Fig 6, so no further correction is required.

The corresponding factored results from the tests on the free-flight model in the 5m Tunnel are also shown in Figs 7a&b, and a similar difference to that shown in Fig 5 is apparent, except for the result at  $\alpha = 31.4^\circ$  measured while varying flow rates, where the value of  $C_{qL}$  is significantly lower than that derived during sideslip runs.

The approximate results derived for the free-flight model, on the basis of scaled values of  $C_{n_L}$  used with the approximate formula from equation (1), are compared with experimental data in Fig 8 for the range  $27.4^\circ \leq \alpha \leq 33.5^\circ$ . The values of  $C_Q$  were taken from the 5 m results. The under-estimate of maximum moment, and thus of the slope, is again obvious, but the trends with flow rate and with angle of attack are adequately represented. Note in particular that the flow rates at which the maximum effects are reached are independent of model size, ie the results collapse with  $C_q$  based on nose or hole size, but would not collapse with  $C_Q$  based on wing area (which would introduce a factor of 5.06 on the slope of the empirical results at zero  $C_n$ ).

### 3.2 Rolling and pitching moments

Application of flow rates causes changes to rolling and pitching moments, and results are discussed in Ref 5, with examples in Ref 2. Rolling moment is rather erratic, the type of variation with flow rates depending on both angle of attack and forebody length. It has not been possible to find an approximate formula to represent rolling moment, but the magnitudes appear to be small enough to be controlled by a roll-demand system.

For pitching moment, there is a local minimum at the flow rate corresponding to near-zero sideforce and yawing moment (ie for symmetric flow). As asymmetry develops on either side, the induced pressure distribution causes a pitch-up, which reaches a maximum before maximum sideforce or yawing moment occurs. The pitch-up moment is then reduced as the extreme asymmetry (one vortex on the

surface of the forebody) is approached. Thus it is apparent that pitching moments for configurations which develop asymmetric flows are likely to be random in magnitude, according to the degree of asymmetry present during the test.

### 3.3 Effects of sideslip

All the forebodies have been tested in sideslip, between  $\pm 4^\circ$ , and significant nonlinearities were measured on the large forebody. Small levels of flow rate caused significant changes to sideforce and yawing moment due to sideslip, and results are discussed in Ref 4. The results for the short and free-flight forebodies<sup>5</sup> are less sensitive to flow rate, and it is possible to derive linear mathematical models, with the derivatives  $C_{Y\beta}$  and  $C_{N\beta}$  approximately independent of flow rate.

## 4 DYNAMIC TESTS ON A FREE-TO-YAW RIG

A new vertical strut has been made to support the model on the free-to-yaw rig, to give a more rigid rig than that described in Ref 2. The model is mounted on a spindle with bearings, the spindle being normal to the fuselage axis, and the angle of attack can be adjusted to various constant settings. Restraint wires between the rear of the fuselage and the tunnel walls prevent the model yawing through large angles, and initial experiments were made with  $\pm 4^\circ$  freedom, later increased to  $\pm 6^\circ$ . The short forebody was used on the model for the results described here, and a ventral fin was added to give near-neutral static stability in yaw, as described in Ref 2.

The needle valves and actuators were mounted inside the model, the port and starboard servos being controlled by computer. The proportional/integral/differential controller was implemented on an analogue computer, which was situated outside the tunnel so that the gains  $K_C$ ,  $K_I$ ,  $K_D$  could be adjusted easily. A block diagram of the system is shown in Fig 9. Angle of sideslip was used as the feedback signal, and the error between actual and demanded angle of sideslip was minimised by changing the flow rates through the port and starboard holes differentially. It was also possible to change the values of the gains on the proportional, differential and integral components by adjusting the maximum flow rate available, although the relative ratios remained unchanged.

Some responses obtained at  $\alpha = 30^\circ$ ,  $V = 20$  m/s, are shown in Fig 10, where the maximum flow rate is being reduced in steps, Fig 10a-d. The time scales shown refer to arbitrarily chosen initial times, for ease of reference. The response of the model is given by the angle of sideslip, and the output of the controller should be zero for steady conditions. The positions of the port and starboard servos were monitored, and it should be noted that the 'closed' to 'open' directions on the vertical axis are opposite. The same is also true for the differential pressures measured in the port and starboard nose chambers, so the responses appear to be similar rather than mirror images.

The first set of responses on the left hand side (Fig 10a) are for a maximum flow rate coefficient of about 0.3 through either port or starboard hole. Initially, the model is being controlled to zero angle of sideslip, with higher flow rate through the port hole than starboard in order to maintain zero yawing moment. At  $t = 4$  s, a large demand in angle of sideslip is applied to the system, significantly larger than the  $6^\circ$  available with the restraint wires. This demand is held on until the model has settled, then is changed by a step to zero at about  $t = 10$  s. The model responds very quickly,

but overshoots to  $-2^\circ$  before settling to an oscillatory response about zero, with an amplitude less than  $1^\circ$ . The port needle valve is almost fully open, and the starboard nearly closed, but the model may be held at near-zero sideslip indefinitely, as shown by the remaining 25 s of record. The pressure transducers do not show the small amplitude oscillations, possibly due to lags caused by the tubing between the chambers and the transducers.

The second set of responses are for maximum flow rate coefficient of 0.22, so the gains have all been reduced to about 70% of their original values. The initial demand is not shown, and the demand for zero sideslip occurs at 6.5 s. Again the model returns to near-zero sideslip very quickly, within 0.5 s, but the overshoot is reduced. The residual oscillation is still present, of lower frequency but similar amplitude. The final needle valve positions are unchanged, but the differential pressures are smaller, consistent with the lower flow rates.

When the maximum available flow rate is reduced further, to a coefficient of 0.08, the controller does not have sufficient power to hold the model at near zero sideslip after the demand for zero, but a steady position of about  $5^\circ$  is reached, with port needle valve open, and starboard needle valve shut. If the flow rate is reduced to zero, the model diverges to the maximum  $6^\circ$  because of the asymmetric yawing moment, and is restrained by the starboard wire becoming taut.

Some experiments were also made with different values of gains, but no significant improvement was found. Intermediate values of demanded sideslip angle could also be held, but it was difficult to achieve large negative angles.

These responses indicate that the flow rates can be controlled actively, and that the control powers generated by differential flow rates are sufficient to overcome the asymmetric moment. The design of a control law for the free-flight model is nearing completion, and is to be added to the existing Departure Prevention System<sup>3</sup> already tested on HIRM1. The aim is to make the model roll about the velocity axis at high angles of attack near  $30^\circ$ , so the 'error' signal ( $r \cos \alpha - p \sin \alpha$ ) is being minimised, using differential flow rates to overcome the asymmetric forces and moments. The induced rolling moments are being controlled by the lateral control law for roll demand, and the induced pitching moment should be compensated by the pitch demand law. The control laws are being implemented on the digital computer developed for HIRM<sup>3</sup>.

## 5 DYNAMIC TESTS TO MEASURE AERO-DYNAMIC LAGS

One of the problems likely to cause difficulty in using actively-controlled vortices to generate forces and moments is that of aerodynamic lag, i.e. the total time taken for the vortices to move to a new position after the flow rates have been changed, and for the resulting change in pressure distribution on the aircraft. The current data acquisition system in the 13ft x 9ft tunnel is implemented digitally, and it was difficult to obtain analogue signals directly. However, it has been possible to test a simple missile-like model (Fig 3), made of the large forebody mounted on a cylindrical afterbody, in the RAE Farnborough 11ft Tunnel. The model had been made in order to investigate the effects of fixing transition on the control powers due to flow rates, and it had been shown that the levels of sideforce and yawing moment generated are comparable with those on HIRM1. Typical results are shown in Fig 11 for  $\alpha = 30^\circ$ ,  $V = 20$  m/s and 33 m/s, where reference area and

length are those of HIRM1. Further details of the static data are given in Ref 4.

It may be observed that the maximum control powers and the asymmetries at zero flow rate are similar for the two speeds, but the variations with flow rate are different, particularly for flow rate through the port hole. Extensive investigation was made of the 'kink' near  $C_q = 0.1$  on the port side, which is apparent at  $V = 33$  m/s, but not obvious at  $V = 20$  m/s. The magnitude of the discontinuity was affected by the length of the transition strips, but could not be eliminated, so these results are for the same transition strips as on HIRM1, which gave the minimum kink. The slope of  $C_n - v - C_q$  near zero  $C_n$  is also affected by tunnel speed, even though transition is fixed on the forebody.

The experimental technique used was to drive the needle valves differentially with a sinusoidal demand, over a range of frequencies, for a demand amplitude smaller than the limits indicated by the static tests, as shown in Fig 11. The relative phase of yawing moment and demand was measured with a differential analyser, and analogue records of demand, sideforce, yawing moment, nose chamber pressures, and actuator positions were taken. Separate bench tests were also conducted to obtain phases between demand and actuator positions, and between demand and pressures.

The servos which drive the actuators have nonlinear response characteristics, and analysis of the phase shifts between demand and servos shown in Fig 12 does not yield first or second-order lags. However, if the assumption is made that the response of yawing moment to flow rate is near-linear over the range of flow rates used, then the corresponding phase shift is the difference between those plotted in Fig 12. The port and starboard servos are moved differentially, so a mean phase shift,  $\delta_{ps}$ , between demand and servo has been chosen. The measured phase shifts between demand and yawing moment, at the two speeds of 20 m/s and 33 m/s, were unsteady, so about ten readings were taken at each frequency. Consecutive readings occasionally gave extreme maxima and minima, so were rejected, and the scatter in data is shown by the remaining maximum and minimum readings plotted in Fig 12. The mean variations of  $\delta_{DN}$  with frequency,  $f$ , at intervals of 0.5 Hz were chosen as shown, to derive the phase shift  $\delta_{NS} = \delta_{DN} - \delta_{ps}$  between yawing moment and servo position.

The variation of the parameter  $(f \cot \delta)$  with  $f^2$  indicates the order of the equation of motion (or transfer function); a constant value indicates a simple lag, and a linear variation indicates a second-order system. The results for  $V = 20$  m/s and 30 m/s are both remarkably linear (see Fig 13), but do not collapse with reduced frequency, where frequency has been expressed in radians/s,  $\omega = 2\pi f$ , and factored by  $\bar{c}/V$  to give reduced frequency. (Aerodynamic mean chord has been chosen as representative length). The damping and frequency of the second-order systems may be derived from these linear variations, to give the response equations for yawing moment,  $N$ , assuming that the response time of the strain-gauge balance is negligible

$$\ddot{N} + 33 \dot{N} + 790 N = F(Q_S - Q_P) \text{ for } V = 20 \text{ m/s}, \quad (3a)$$

$$\ddot{N} + 24 \dot{N} + 980 N = F(Q_S - Q_P) \text{ for } V = 33 \text{ m/s}, \quad (3b)$$

or, expressed in reduced time,  $tV/\bar{c}$ ,

$$\ddot{N}^* + 0.64 \dot{N}^* + 0.295 N^* = F(Q_S - Q_P) \text{ for } V = 20 \text{ m/s}, \quad (4a)$$

$$\ddot{N}^* + 0.28 \dot{N}^* + 0.135 N^* = F(Q_S - Q_P) \text{ for } V = 33 \text{ m/s}, \quad (4b)$$

The values of amplitude ratio obtained from these transfer functions agreed well with the experimental results at  $V = 33$  m/s, but the results at  $V = 20$  m/s were scattered, so were not so convincing.

The most likely cause of the results not collapsing with reduced frequency is the change of slope  $dC_n/dC_q$  noted in Fig 11, as this slope must be related to the frequency of the response. The ratio of reduced damping to reduced frequency is approximately the same,  $(0.64/0.295 = 0.28/0.135)$  in equation (4), as indicated by the intercept on the vertical axis on Fig 13, but it is difficult to interpret this generally. However, it is encouraging to note that both transfer functions indicate a 'lag' of less than 0.1 s in the responses to a step input, Fig 14, and this includes any lag of the strain-gauge balance. The smaller damping at the higher speed leads to a 28% overshoot, but both responses are within  $\pm 10\%$  of the final value by  $t = 0.16$  s.

The equivalent lag of about 0.1 s may be scaled for model size and tunnel speed by the factor  $V/\bar{c}$ , to give  $t^* \approx 6$  arosec for both 20 m/s and 33 m/s. This is comparable to the time taken for vortex breakdown over a slender wing to be overcome by suction through a probe placed in the vortex core ahead of the trailing edge, as measured by Parmenter and Rockwell<sup>7</sup>. The time taken to re-establish the vortex was dependent on suction level and probe position, varying between 2 arosec for very high suction rates to above 10 arosec for probe positions behind the wing.

It would seem sufficient to use a first-order lag in the generation of control powers for mathematical models of the aerodynamic forces and moments used for the design of flight control laws, since the frequencies are high. This lag is in addition to any lags introduced by the actuator system, which must be modelled separately.

## 6 CONCLUSIONS

The results from static and dynamic wind-tunnel tests on the use of suction at the nose to control forebody vortices are sufficiently encouraging to warrant an experiment in free flight using the existing HIRM1 drop model. The magnitudes of the maximum yawing moment and sideforce have been shown to be determined by forebody geometry (diameter and slenderness ratio for given apex angle), and appear to be independent of the wing/fin/tail configuration. The variation of control powers with flow rates is suitable for use in an active control law, although nonlinear, and the associated rolling and pitching moments should be alleviated by demand-type control laws in roll and pitch. The scaling of flow rates with model size determined from these tests indicate that control power is dependent on the nose geometry, so full-scale aircraft would require similar levels to those used on the models.

The wind-tunnel model of HIRM1 has been successfully controlled on a free-to-yaw rig, using angle of sideslip as feedback to a sideslip-demand control law. The flow rates are controlled by needle valves to give the required yawing moment to overcome the moment due to asymmetric flows or to move the model. A control law to maintain rolling about the velocity axis is being developed for the free-flight model, and will be added to the existing Departure Prevention System.

The aerodynamic lag of the yawing moment has been measured on a missile-like model, by driving the needle valves sinusoidally and taking analogue records of moment (and sideforce). The response of the moment appears to be second-order, with equivalent frequency and damping which do not scale directly with aerodynamic time ( $l/V\bar{c}$ ) for the two low speeds tested. However, the frequencies are high, so the responses to a step input at both speeds reach the steady-state value within 0.1 s, model scale.

Further work is planned on the free-flight model in the RAE Farnborough 24ft Tunnel and then in flight if possible.

**Table 1**  
**Dimensions of forebodies tested**

Name	Station of tip	Length	Max diameter	$l/d$
Original	0	246	116	2.1
Large	-366.7	612.7	156	3.9
Short	-128.7	374.7	100.5	3.7
Inter	-266.7	512.7	100.5	5.1
Long	-366.7	612.7	100.5	6.1
Free flight (4/9 factor)	-223	469	116	4.0

All dimensions are in mm, and those for the free-flight model have been factored by 4/9 to show the comparative size.

## REFERENCES

- Heydari, F.; 'Active yaw control of a generalised missile body at high angles of attack by means of nose suction'. RAE Technical Memorandum Aero 2140 (1988)
- Ross, A. Jean, Jefferies, E.B., Edwards, Geraldine F.; 'Control of forebody vortices by suction at the nose of the RAE High Incidence Research Model'. AGARD FDP Conference, October 1990, Paper 27 (RAE Technical Memorandum Aero 2172, January 1990)
- Naseem, M.A., Ross, A. Jean; 'Development and implementation of flight control system for a research drop model'. Seventh Bristol International Conference on Remotely Piloted Vehicles, September 1988 (BAe YAD 386)
- Ross, A. Jean, Jefferies, E.B., Edwards, Geraldine F.; 'Aerodynamic data for the effects of nose suction on the RAE High Incidence Research Model with a large forebody. With an Appendix by D.G. Mabey. RAE Technical Memorandum 2204, 1991
- Ross, A. Jean, Jefferies, E.B., Edwards, Geraldine F.; 'Static aerodynamic and dynamic data on the control by nose suction of the vortices on several forebodies on the RAE High Incidence Research Model. RAE Technical Memorandum Aero to be published, 1991
- Lamont, P.J., Hunt, B.L.; Prediction of aerodynamic out-of-plane forces on ogive-nosed circular cylinders. J. Spacecraft, Vol 14, No.1, January 1977
- Parmenter, K., Rockwell, D.; Transient response of leading-edge vortices to localized suction. AIAA Journal, Vol 28, No.6, June 1990

Copyright ©, Controller HMSO London, 1991

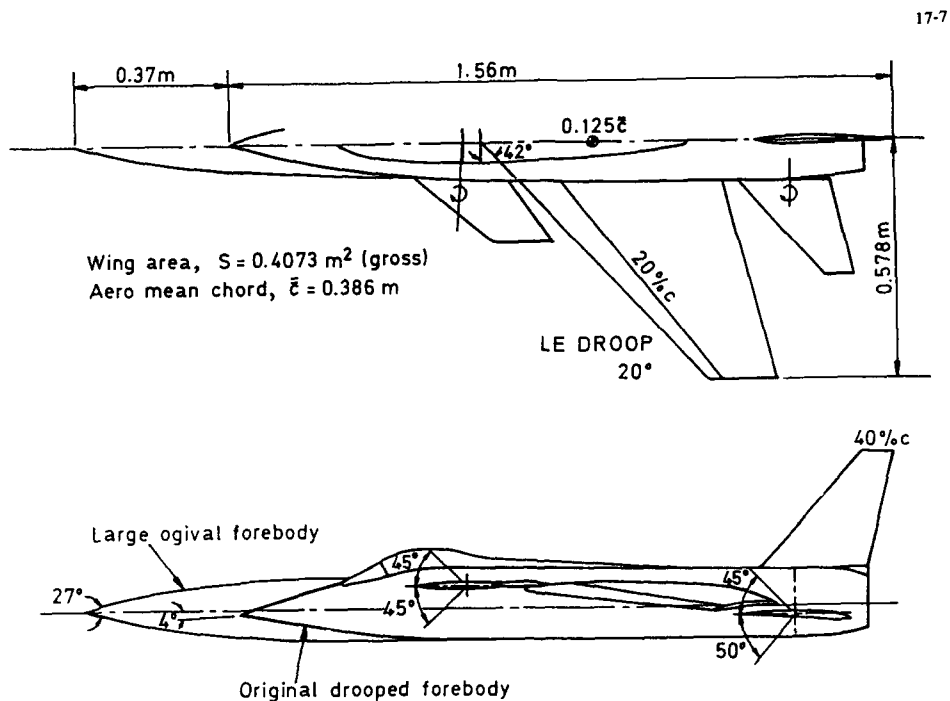


Fig 1 General arrangement of HIRM1 with original and large forebody

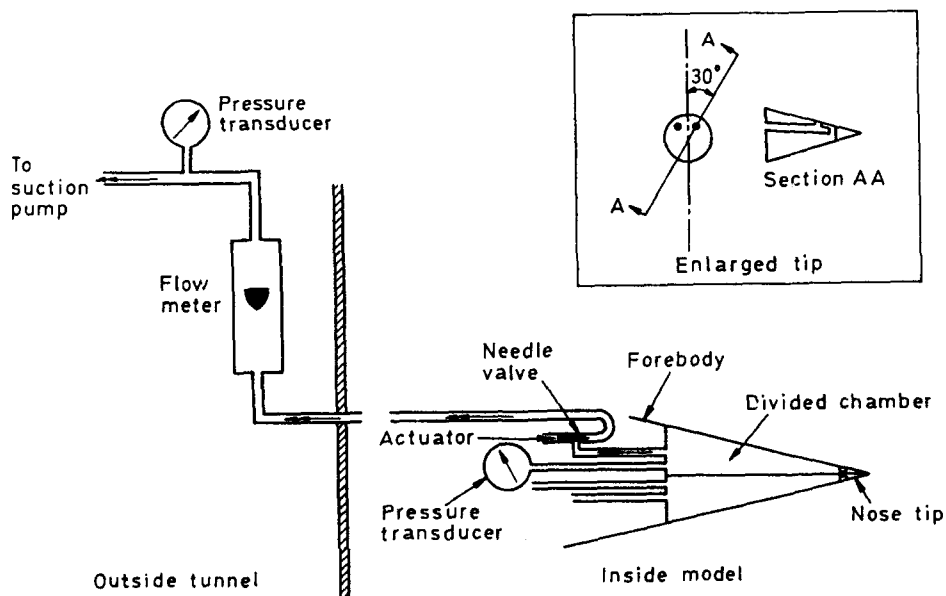


Fig 2 Sketch of suction system (port side only)

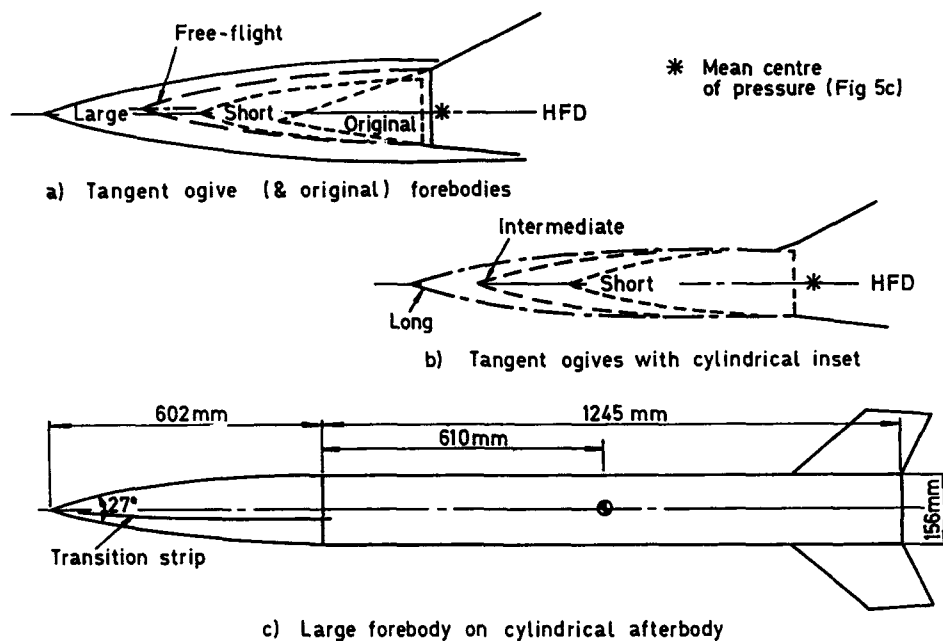


Fig 3 Various forebodies tested on HIRM1, and large forebody on a simple model

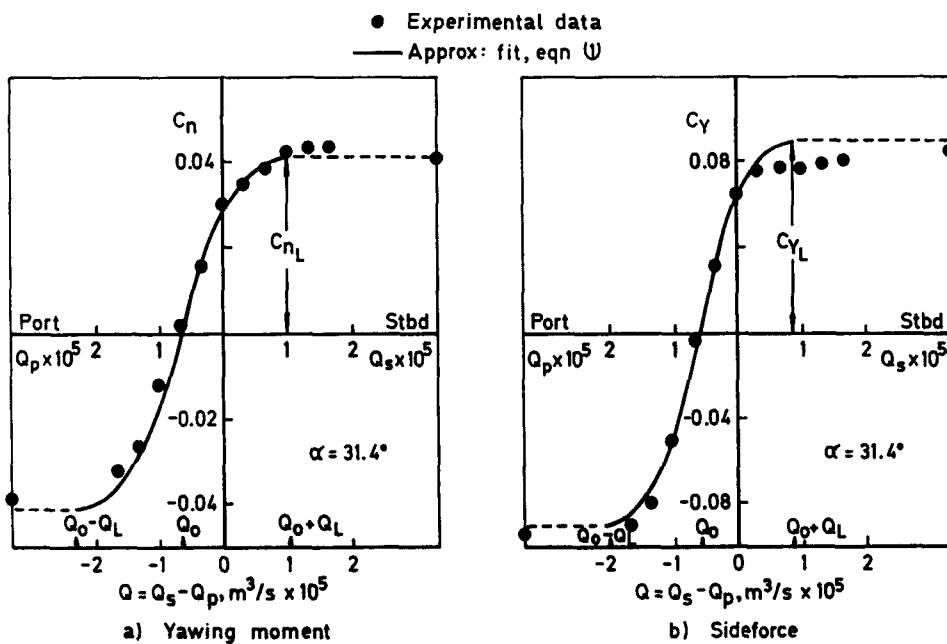


Fig 4 Empirical fits to yawing moment and sideforce due to flow rates

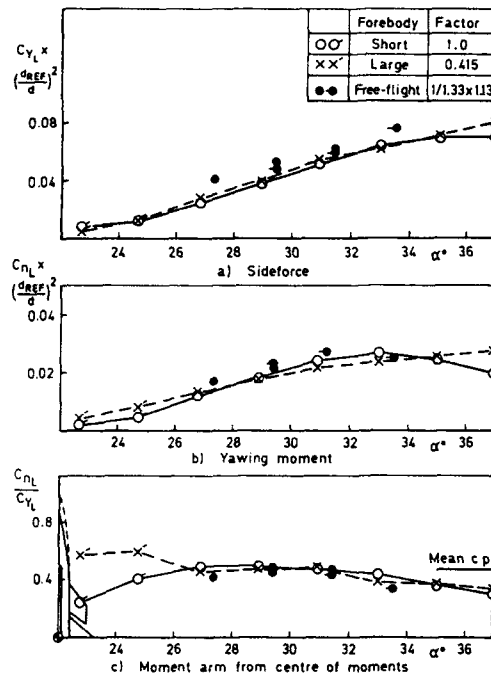


Fig 5 Scaling of maximum control powers with forebody diameter,  $l/d = 4.3$

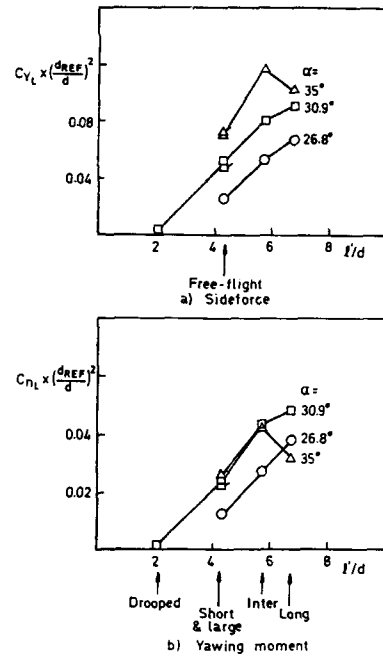


Fig 6 Scaling of maximum control powers with forebody slenderness ratio

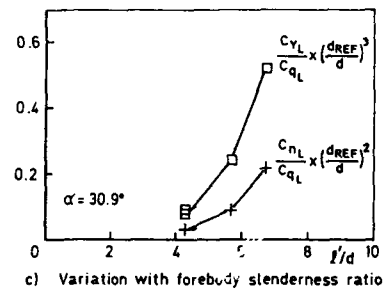
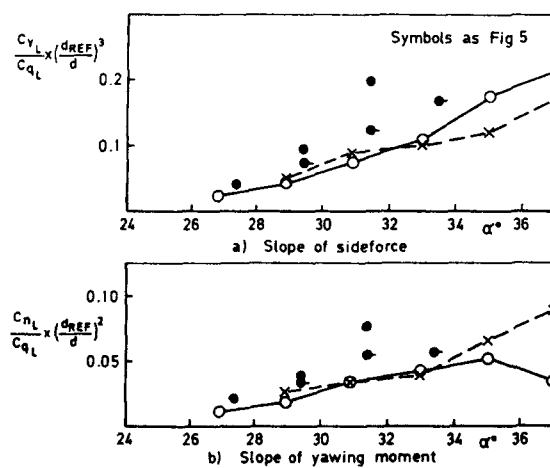


Fig 7 Scaling of slopes of control powers



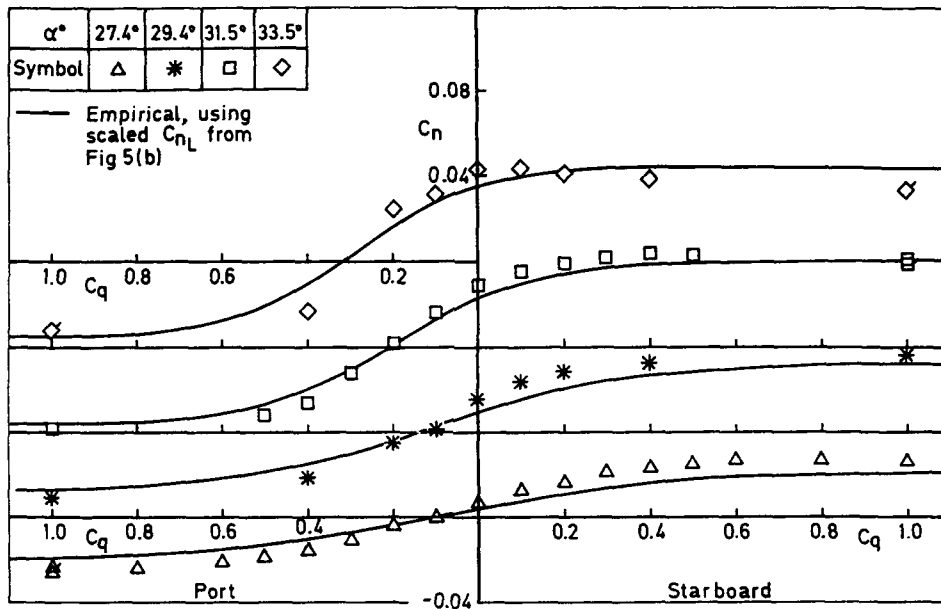


Fig 8 Comparison of measured and scaled yawing moment due to flow rates, free-flight forebody

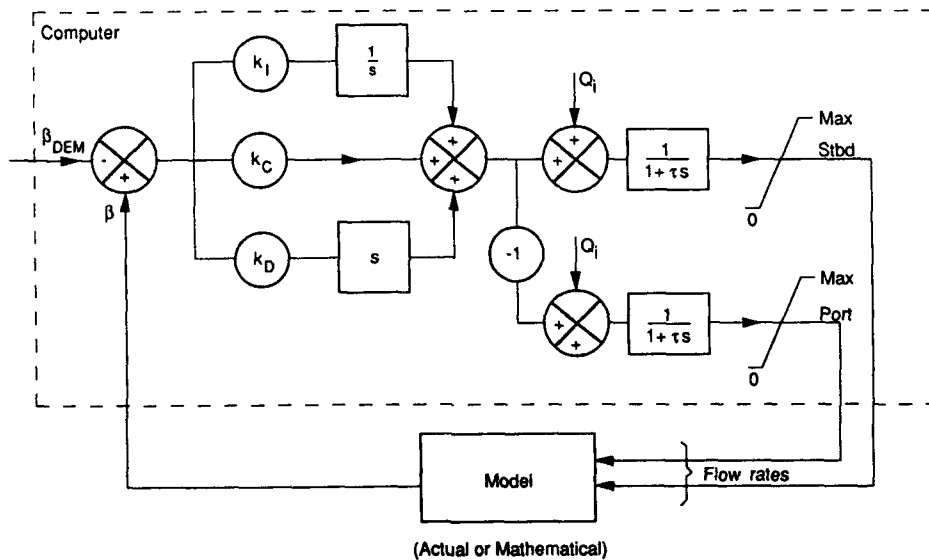


Fig 9 Block diagram of control system

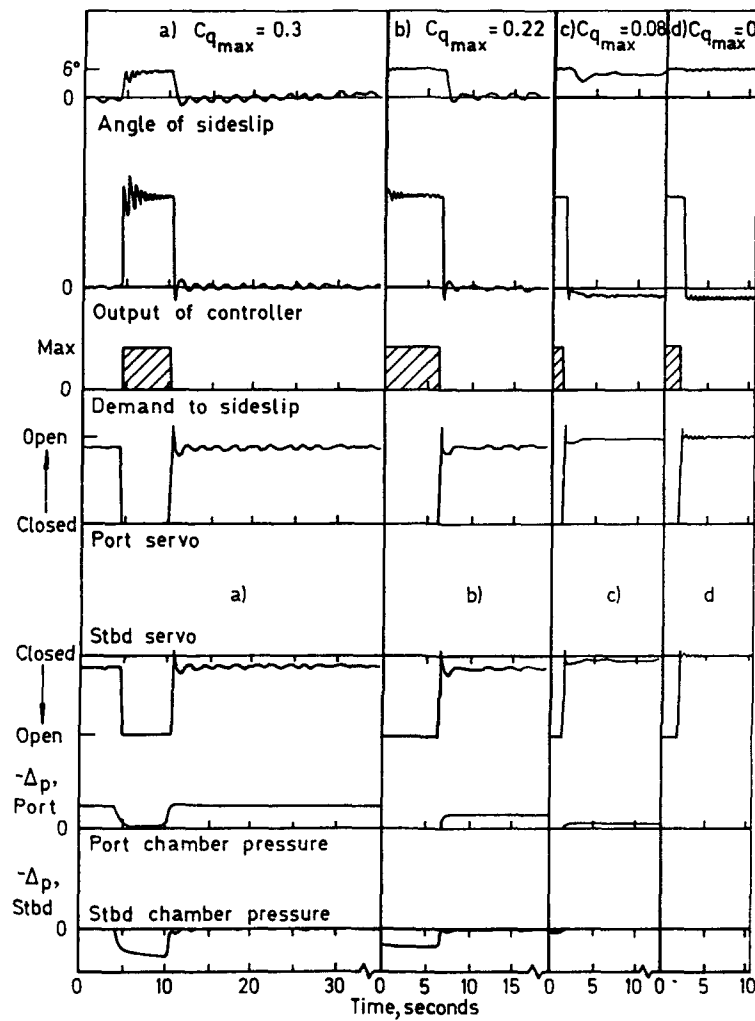


Fig 10 Responses of model with short forebody on free-to-yaw rig  
 $\alpha = 30^\circ$ ,  $V = 20$  m/s

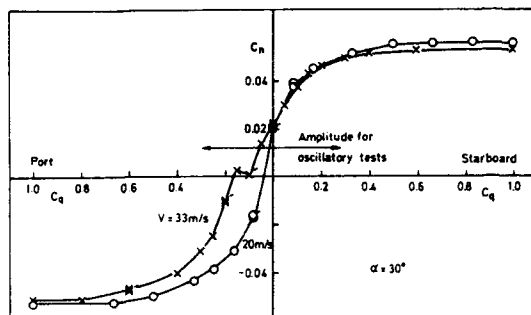


Fig 11 Yawing moment due to flow rates for large forebody on cylindrical afterbody

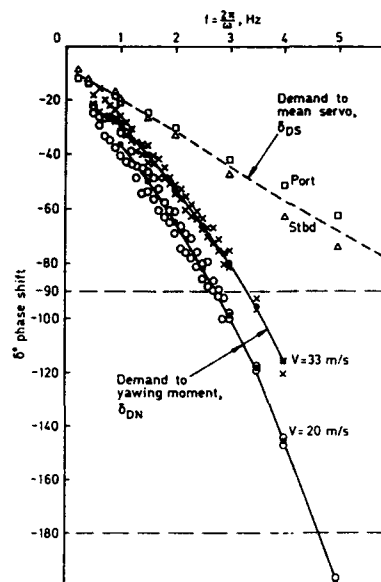


Fig 12 Measured phase shifts for sinusoidal input of flow rates

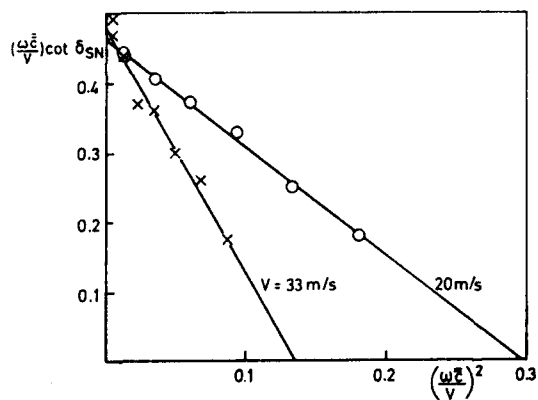
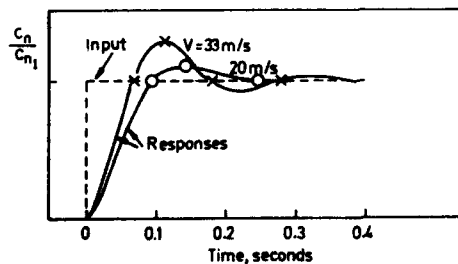


Fig 13 Analysis of phase shift: servo to moment

Fig 14 Response in yawing moment to step input



# Transformation of Flightmechanical Design Requirements for Modern Fighters into Aerodynamic Characteristics

Peter Mangold  
Dornier Luftfahrt GmbH  
Federal Republic of Germany  
P.O. Box 1303  
7990 Friedrichshafen 1

## 1. Summarizing Introduction

Ever since fighter aircraft have been designed and built the most important flightmechanical task has been to provide good and safe Flying Qualities. Sufficient margins for stability, adequate control power and trim capabilities in combination with acceptable control forces have always been regarded as key characteristics from which criteria for a proper sizing of stabilizers and control surfaces could be derived.

For stable unaugmented aircraft of the past the characteristic equations and transfer functions could mathematically be defined right from the start of a project. So the static and dynamic flightmechanical features of the aircraft to be developed, were directly linked to aerodynamic derivatives. The desired Handling Quality Standards could straight away be achieved by sizing and positioning of stabilizers and controllers. Scheduling of control surfaces for performance optimization, load alleviation, etc. was not feasible at that time and therefore the flightmechanical and aerodynamic design goals did not interfere too much.

The flightmechanical design of highly augmented aircraft with partly unstable basic characteristics is no longer straight forward. In addition to Handling Quality aspects, maneuverability and agility up to high angles of attack further design goals like optimum performance, observance of structural limits, Carefree Handling, etc. have to be considered within the flightmechanical evaluations. The task to integrate these requirements from various disciplines is focused on the Flight Control System. Unfortunately the exact capabilities of this system will not be defined prior to the development phase. So in contrary to unaugmented aircraft, for which the sizing of stabilizers and controllers could directly be done by consideration of Level-1 Handling Quality requirements, it is now necessary to design for the capabilities and technical inadequacies of a FCS which will be developed in a later phase.

In section 6 of AGARD Advisory Report 279 [Ref. 1] the members of FMP-Working Group 17 "Handling Qualities of Highly Augmented Unstable Aircraft" summarized their experience concerning "The Impact of Unstable Design and High Angle of Attack on the Requirements for the Aerodynamic Configuration". Their main conclusion was that, in order to maintain the chance to fulfil the challenging requirements for optimum performance and superior Handling Qualities it is necessary to define a set of flightmechanical criteria which translate the most important aspects derived from Handling, Agility and Safety points of view into aerodynamic requirements. These criteria have to generate the necessary link between the disciplines Control Law Design, Flightmechanics and Aerodynamics within the Pre-Development phases of modern fighter aircraft.

The publications referenced at the end of this paper, represent a certain (but uncomplete) scope of flightmechanical research which was done to settle usable recommendations for early design phases of modern fighters. Derived from these publications the following general criterion for a balanced aerodynamic design can be given:

"The basic unaugmented features of any aircraft have to be optimized in such a way that a realistic Flight Control System is able to convert the resulting dynamic characteristics into good Handling Qualities with sufficient stability margins by use of the control authorities and rates available from the primary controllers. Trim schedules resulting from Performance and/or Load Alleviation Requirements have to be taken into account and may introduce criteria of equivalent importance."

The paper in hand is a contribution of the AGARD Flightmechanics Panel to this aerodynamic specialist meeting, and it should form a basis for further discussion and research on a field which is of common interest for both disciplines. Therefore it contains a summary of the ideas in Ref. [9] and of joint activities of AGARD Working Group 17 [Ref. 1, Section 6].

In detail it is shown that the "Time to Double Amplitude  $T_d$ " of the basic aircraft may act as key characteristic which describes the problems associated with stabilization in Pitch. If related to the available Pitch Authority and Control Power Buildup Rate, limits for "Minimum permissible  $T_d$ " may be established. These limits are easily convertible into aerodynamic requirements and therefore applicable within the early design phases of modern fighter design.

At high angles of attack additional pitch down control power is needed to cancel the effects of inertial coupling due to roll maneuvers. The acceleration to be provided is dependent on angle of attack and attainable rollrate around the velocity vector.

As far as the lateral/directional axes are concerned the FCS is mainly used for stability augmentation and for optimum coordination of the control surfaces. Therefore the flightmechanical design still aims at stable basic characteristics. To achieve this design goal  $C_{L_{max}}$  is very often the only parameter which is used for optimization during windtunnel testing. Especially at high angles of attack stable static derivatives are not sufficient to maintain dynamic stability. The dynamic derivatives "roll and yaw damping" have to be considered as well and at least negative  $C_{L_p}$ 's and  $C_{L_r}$ 's are necessary to complete the listing of desired characteristics.

Agility around the velocity vector at higher angles of attack is mainly a matter of roll and yaw control power. As angle of attack increases the rudder effectiveness gets more and more important; if bank angle requirements deducted from MIL-Spec shall be performed in a well coordinated manner at high angles of attack, the body fixed yaw potential has to exceed the roll control power according to the inertia ratio  $(I_x/I_y)^{1/2}$  multiplied by  $\tan \alpha$ .

## 2. Flightmechanical Criteria for the Design of Unaugmented Stable Configurations

For stable unaugmented fighters of the past the flightmechanical task to provide good and safe Flying Qualities by ....

- .... adequate static and dynamic stability,
- .... sufficient control power for maneuvers and trim
- .... and acceptable control forces

could directly be transferred into criteria for a proper sizing of stabilizers and control surfaces. Ailerons, rudder and elevator were almost directly linked to the pilot by cables, rods and levers via stick and pedals in the cockpit. So right from the start of the design the transfer functions "Aircraft Behaviour due to Pilot or Gust Input" and the characteristic equations of the total system were analytically defined.

With respect to pitch axis most of the applicable criteria which can be deducted from the Handling Qualities document MIL-F-8785, turn out to form corner stones for the design for the horizontal tail (stabilizer and elevator). Fig. 1 for example summarizes dynamic requirements for the short period and phugoid characteristics and presents the relevant equations which define the relations to the aerodynamic derivatives. Parametric variations in size and position of the horizontal tail lead to continuous parameter changes. Together with other requirements like "Nose Wheel Lift-off at a certain airspeed 1.0  $V_0$ ", "Minimum Static Stability", etc. the main goal of horizontal tail design, to define and open a permissible centre-of-gravity range can be achieved straight away.

The same principles apply in lateral/directional axes as shown in Fig. 2. The correlations between the Handling Quality Requirements for Dutch Roll, Spiral-, Roll mode, etc. and the aerodynamic derivatives are again analytically linked by the characteristic equations and by relatively simple transfer functions. So particular variations of configuration details, as for example vertical tail size and/or position, will directly lead to changes in the dynamic behaviour of the aircraft and, with the Handling Quality Requirements under consideration, stabilizer, rudder and ailerons can be defined.

### 3. Design Criteria for modern Configurations with Unstable Characteristics in Pitch

The flightmechanical design of highly augmented aircraft with unstable basic characteristics is no longer straight forward. In addition to handling quality aspects, maneuverability and agility which have to be provided up to high angles of attack, further design goals like optimum point performance, observance of structural limits and carefree handling has to be integrated into the flightmechanical considerations. The task to integrate the requirements from different disciplines is transferred to a single "Black Box", that is to say on the Flight Control System. The various subtasks, which have to be managed by the FCS may roughly be split into two parts: One is related to the control of steady-state and instantaneous maneuvers which includes surface scheduling for different modes, optimum coordination of the available controllers and the surveillance of structural and physiological limitations. The other part covers the vital aspects of stabilization throughout the permissible flight envelope.

The summary in Fig. 3 shows in which direction the flightmechanical design aspects have to be changed if stability augmentation or artificial stabilisation is introduced: Sufficient static and dynamic stability and, at high angles of attack, acceptable departure characteristics have to be replaced by the limitation of basic dynamic instabilities. The provision of control potential for maneuvers and trim has to be supplemented by additional power for stabilization purposes and if required for control modes. Acceptable stick and pedal forces need no longer be taken into account within early design

phases. They can be treated separately and optimized in combination with the cockpit design. Horizontal/vertical tails, ailerons and rudder can no longer be treated as completely separate segments. They have to be considered as multi-functional, integrale stability and control units which are linked via FCS for optimized management of trim, maneuver and limitation tasks.

As the capabilities of any existing and future Flight Control System will be restricted by unavoidable technical inadequacies of realistic hardware and software, it is necessary to design for basic unaugmented characteristics which can be handled by the FCS even under adverse conditions. Therefore requirements which include the aspects of control law design have to be developed and prepared for use in the aerodynamic optimization process in order to restore the early link between Handling Qualities and Aerodynamics which has been broken by the FCS.

It has to be kept in mind that any criterion must be easily convertible into aerodynamic derivatives and coefficients which implies that considerable simplifications of the Control law aspects may be necessary. But even rough considerations are sufficient to enable the design team to define feasible aerodynamic instability levels and trim schedules which leave sufficient control power in pitch roll and yaw.

#### 3.1 Key Characteristics for Unstable Design in Pitch

From the very beginning all the design phases of "New Generation" fighter aircraft are dominated by the attempt to find an optimum balanced concept within the frame of maximum performance, defined mass figures and limited costs. Especially the field of performance encompasses aspects on at least three planes, which are defined by the headlines "Mission-, Point- and Manoeuvre Performance". Requirements derived from these different items are often rather contradicting.

A suitable and well known tool to overcome some of the contradicting requirements is the introduction of Unstable Design in Pitch which has remarkable effects on the trimmed polars as illustrated in Fig. 4. Relative to a conventionally stable aircraft maximum lift can be increased by roughly 25 % and induced drag at a typical lift coefficient for manoeuvre (say  $C_L = 0.7$ ) can be reduced by about 20 %.

This means that unstable configurations when designed for the same performance requirements and under the same flight mechanical constraints, will be remarkably smaller than their stable brothers.

A qualified parameter which indicates the potential for drag reduction and higher maximum lift is the static instability level (Static Margin).

$$SM = - \frac{\frac{\partial C_m}{\partial \alpha}}{\frac{\partial C_L}{\partial \alpha}} = - \frac{C_{m\alpha}}{C_{L\alpha}} = \frac{x_{ac} - x_{cg}}{c}$$

If only aerodynamic aspects had to be taken into account, it would make sense to increase the negative static margin to a point where the resulting trimmed flap schedule leads to optimum drag polars.

From the flight mechanical point of view a reasonable interpretation of SM is only possible in linear areas at smaller angles of attack. It defines nothing else than the lever arm of aerodynamic forces and is only useful for the flight mechanical design of unaugmented aircraft, which have to be equipped with a certain margin of static stability. As maximum lift is approached ( $C_{L\alpha} \rightarrow 0$ ) the physical evidence of SM ( $SM \rightarrow \infty$ ) is lost.

Aerodynamic parameters which allow a flightmechanical interpretation even at high angles of attack are summarized in Fig. 5 (flightmechanics specialists are talking of "Aerodynamic Key Characteristics" in this context). The typical  $C_m$  versus  $\alpha$  plots with curves for "zero" and "full nose down" controls point out that one limiting factor for unstable design will be given by the definition of a necessary pitch recovery moment which above all has to guarantee a safe return from high angle-of-attack manoeuvres.

The basic design instability is defined by the derivative  $C_{m\dot{\alpha}}$ . It will be chosen at low and medium angle of attack to cover the performance requirements. This instability has to be checked against the capabilities of the Flight Control System. The same applies to the allowable pitch-up  $C_{m\dot{\alpha}_{max}}$  at higher angles of attack in trimmed conditions.

Unfortunately neither the static instability SM nor the pitching moment derivative  $C_{m\dot{\alpha}}$  are sufficient to describe the dynamic problems associated with the stabilization of unstable configurations. According to the equations of Fig. 1 and 11 the highly dynamic short period motion of any aircraft is dependent on much more factors as for example moment of inertia, damping derivatives, wing area, mean aerodynamic chord and dynamic pressure. All these parameters contribute to a "Time to Double Amplitude"  $T_d$ , during which, with controls fixed, the aircraft will double a distortion in angle of attack. As the simplified schematic graph of Fig. 6 (pitching moment versus time) shows, it is essential to counteract this aperiodic movement by an appropriate control input. Build-up rate  $\dot{M}$  and magnitude  $M$  of the stabilizing moment must be large enough to stop and reverse the sign of pitch acceleration so that the aircraft returns to its original, trimmed condition. The Time Delay  $T_d$  between disturbance input and stabilizing control reaction can be identified as a further important parameter which will increase the problems of control law design if it exceeds certain values.

So the key characteristics for unstable design in pitch may be summarized, as done in Fig. 7:

- Static Margin SM or  $C_{m\dot{\alpha}}$  for the aerodynamicists
- Time to Double Amplitude  $T_d$ , Maximum Pitch Control Moment  $M$  and Build-up Rate  $\dot{M}$ , Time Delay  $T_d$  for the control law designers and flightmechanics people

As stated above it is necessary that control law people and aerodynamicists can communicate and understand each other in order to end up with a well balanced design. So once dynamic limits for  $T_d$  have been identified they have to be translated into aerodynamic characteristics. A good approximation for the transcendental relation between  $T_d$  and the aerodynamic derivatives is presented in Fig. 11.

As far as the control power is concerned it is necessary to sum-up the authority and control reaction available from all primary pitch controllers. This can be done by the following simple algebraic equations:

- Control Authority in terms of Pitch acceleration:

$$\pm \ddot{\theta} = \frac{a \cdot V^2 \cdot S \cdot C_{m\dot{\alpha}}}{2 \cdot m \cdot I_y} \cdot \sum_{i=1}^n \Delta C_{m_i} (\eta_i)_{max}$$

- Control Reaction:

$$\ddot{\theta} = \frac{a \cdot V^2 \cdot S \cdot C_{m\dot{\alpha}}}{2 \cdot m \cdot I_y} \cdot \sum_{i=1}^n |C_{m_i}| \cdot \eta_i$$

$n$  is the number of all reliable primary controllers; limitations due to hinge moments and load restrictions have to be considered.

### 3.2 Criterion for Maximum Dynamic Instability in Pitch

The discussion in the previous section has shown that criteria based on relationships between maximum permissible dynamic instabilities  $T_d$  and the required control authority and reaction could be helpful tools for the aerodynamic design even in very early design phases. Concrete steps which have to be taken in order to generate such boundaries are described in [Ref. 9]. Based on parametric attempts to optimize control law parameters for different dynamic instability levels the "T<sub>d</sub>-Criterion" shown in Fig. 8 was evaluated and proposed for use in the design and optimization process of unstable combat aircraft.

The procedure which lead to the boundaries in the two graphs considered simplified but realistic hardware assumptions including requirements and methods which are normally used within a thorough Control Law Design. In detail the following principles have been taken into account (for further information see section 4.2 of [Ref. 9]):

- Typical control law structure for fighter type aircraft providing a pitch rate command/attitude hold platform
- Hardware assumptions for sensors, actuators, filters etc.
- Level-1 Handling Quality requirements for Cat. A (i.e. Combat) flight phases
- Ride Quality aspects
- Criteria for sufficient stability margins of the Control law design
- Data bandwidth of modern fighters derived from the requirements for the European Fighter Aircraft (see Fig. 9 and 10).

Starting from general data of modern fighters represented by three different tail concepts, the relevant aerodynamic parameters, Machnumber and dynamic pressure have been varied in order to achieve different values in Time-to-Double Amplitude  $T_d$ . In a second step the control law parameters have been defined by optimizer strategy in accordance with the handling quality and stability requirements; simulated flights with test inputs have been performed in order to evaluate the required control authority and control reaction. The results in Fig. 8 confirm that it is possible to generate limiting functions "Recommended Minimum Pitch Authority" (i.e. Acceleration  $\ddot{\theta}$ ) and "Recommended Minimum Pitch Control Reaction" (i.e.  $\ddot{\theta}$ ) versus "Time to Double Amplitude  $T_d$ ".

As  $T_d$  decreases the required control authority and rate increases rapidly. Especially for smaller Mach-numbers the continuous lines are limited by sharp edges which mark the point where the safe stability margins (Phase and Gain margins) can no longer be achieved.

Differences found for the different tail concepts can be neglected. So the limits shown in the two diagrams should be valid for all modern fighter configurations with a mass density  $\mu_0 > 50$  and a control system with an equivalent overall time delay of  $T_c = 0.02$  s.

For larger time delays no increase in the required control power would be necessary if the overall time delay exceeds 0.02 s. The sharp edges for insufficient Phase and gain margins, however have then to be shifted towards higher  $T_d$  values.

A further analysis of Fig. 8 shows that configurations with Time-to-Double  $T_d < 0.2$  s may not be feasible for a production aircraft. Even a small unfavourable error concerning  $T_d$  (caused by aerodynamic uncertainties for example) would require excessive additional control power and/or would

hurt the necessary stability margins. This does not mean that such an aircraft cannot be realized or equipped with reasonable handling qualities (see for example X-29). But the statement does point out that such a high dynamic design instability introduces a lot of risk which does not pay-off and that during development and operation major difficulties with respect to safety and handling may be encountered.

### 3.3 Application of the $T_1$ -Criterion within the Aerodynamic Design Process, Range of Validity

In order to end up with concrete "application rules" for the  $T_1$ -Criterion, it is necessary to have a look on typical (aerodynamic) data of modern fighters and their influence on the basic dynamic behaviour of the aircraft.

In spite of the challenging requirements which have been formulated for future fighters based on the European Scenario, it is astonishing that solutions based on all tail concepts have been proposed. The configurations, which are roughly sketched in Fig. 9, are all equipped with relatively low aspect ratio wings ( $A < 3$ ) and the common understanding of the design teams has been that an unstable design together with a horizontal tail (aft-tail, vector nozzle, canard) is needed to achieve a high performance standard and agility.

The table of Fig. 10 summarizes typical data for these configurations including geometrical, aerodynamic and mass/inertia characteristics, which should be valid for a preliminary dynamic analysis in the subsonic region up to maximum lift. - The first line of the table shows that the design instabilities (static margin SM) of the tailed aircraft are considerably larger than that of the tailless configuration. This is due to requirements concerning the pitch recovery margin (section 3.4) which for tailless concept is hard to achieve together with an unstable design.

In order to get some deeper insight into the dynamic effects of the data presented, it is necessary to have a look at the equations which determine the location of the short period roots in the complex plane and the key parameter  $T_1$ . Fig. 11 illustrates that the positions of the two unstable roots are defined by two major parts: ( $C_{w_1}$ ) settles the line of symmetry from which the two aperiodic roots  $s_1$  and  $s_2$  will separate once static stability is lost. This first part is influenced by the lift curve slope  $C_{L\alpha}$  and by the dynamic derivatives but it is not dependent on the design instability. The shift of the roots on the Real Axis is dominated by the term  $w_1$  and therefore directly related to  $C_{w_1}$ .

If the data from Fig. 10 are analysed by the dynamic equations of Fig. 11 it gets evident that the relatively high mass density of the configurations  $\mu_1 > 70$  (50 for tailless aircraft) diminishes the influence of the dynamic aerodynamic derivatives and the lift curve slope considerably. This general trend is confirmed in Fig. 12 where starting from reference values parametric variations of the longitudinal derivatives and their influence on "Time to Double Amplitude" are investigated for a sample aircraft. Reference values and data bandwidth to be expected for the Low Speed region, are indicated.

So with respect to the aerodynamic derivatives the key parameter  $T_1$  will mainly be altered by  $C_{w_1}$ .  $C_{L\alpha}$  is of minor importance but should be considered. The bandwidth of the dynamic derivatives may in any case be neglected.

With these generic results in mind it is rather easy to involve the  $T_1$ -criterion into the normal aerodynamic design and optimisation process as shown in the diagrams Fig. 13 to 15. All information, needed for a first assessment of the flight-mechanical feasibility of a proposed configuration in pitch axis are ...

- ... a three view drawing with characteristic geometric data
- ... a typical combat mass including the radius of inertia
- ... rough (Datcom) estimates of the dynamic derivatives
- ... Static Lift and Pitching moment coefficients or derivatives versus angle of attack for different control settings (incl. maximum symmetric deflections)
- ... assumption of attainable deflection rates

As most of the data (Fig. 13) is required anyway in order to fix the basic static instability-level and to optimize the trim schedules for performance purposes in a first step, the amount of additional work to be done to check the dynamic instability levels is small. Via the static derivatives  $C_{w_1}$  and  $C_{w_2}$  in trimmed flight conditions and the Pitch (Down i.e. most Critical) Control Power available from all primary controllers it is possible to compute  $T_1$  and the pitch acceleration capability  $\ddot{\theta}$  by the equations given in Fig. 8 and 11. A comparison with the boundaries of the criterion (Fig. 14) identifies problematic areas and recommendations for further improvement of the configurations may be given as indicated. The same procedure is applicable for the required pitch control reaction (Fig. 15) which can be computed via the pitch control effectiveness (derivatives in trimmed conditions) of all primary controllers.

As already stated in section 3.2, the boundaries of the  $T_1$ -criterion presented in Fig. 8 are only verified for

- ... fighter type aircraft with a data bandwidth shown in Fig. 10,
- ... Combat Flight Phases,
- ... and a Pitch Rate Command/Attitude Hold type control system with the hardware assumptions described in [Ref. 9].

For other aircraft, flight phases and control systems it is necessary to examine the validity of the specific numbers. But nevertheless it is worthwhile to rerun the procedure for the evaluation of the criterion described in [Ref. 9] and a modification of the boundaries, tuned to updated requirements should be as easy as the application of the criterion itself.

### 3.4 Margins for Pitch Recovery from High Angles of Attack

The minimum pitch recovery control power which has to be installed at high angles-of-attack near  $C_{Lmax}$  cannot only be defined by sufficient nose down acceleration which has to provide a safe return from maneuvers near stall. A more detailed analysis of the problem leads to the conclusion that the required nose down control power can roughly be split into two parts (Fig. 16):

- 1) basic demand for stabilization, for counteracting gusts and for sufficient pitch handling qualities during high angle-of-attack maneuvers
- 2) additional control power for increased agility at high angles-of-attack.

The basic demand, which has to be provided in the nose-up as well as in the nose-down direction, could probably be defined by appropriate  $T_1$ -design charts. The criterion presented in Fig. 8, however

is based on handling quality requirements of CAT.A flight phases, which are not applicable for high angle of attack maneuvers. So the whole criterion has to be recalculated on a modified basis which has not been done up to now.

As a rule of thumb the required pitch acceleration could be fixed at about  $\ddot{\theta} = \pm 0.3 \text{ rad/s}^2$ . This margin which should be designed for in any case, is supported by several simulation studies and recent work within several fighter projects. Additional pitch control power for increased agility at high angles-of-attack is directly combined with the requirements for maximum roll rate in this region. The sketch on the lefthand side of Fig. 16 shows that any roll rate around the velocity vector is combined with a pitch-up moment. The aircraft acts like a dumb-bell and the resulting inertial coupling produces a nose-up acceleration which is given by:

$$\ddot{\theta}_{IC} = \frac{1}{2} p_V^2 \cdot \sin 2\alpha$$

So beneath the basic recovery margin additional pitch down control power is needed to counteract the inertial coupling during roll maneuvers. As soon as the angle-of-attack for maximum lift (i.e. roughly the location of minimum nose down control power) is known it is possible to draw a design chart of required pitch down acceleration versus roll rate, as shown on the righthand side of Fig. 16. The fix of a roll rate requirement at a certain calibrated airspeed leads us straight forward towards the nose down recovery margin in terms of  $\theta$  or pitching moment coefficient  $\Delta C_{mRec}$  which has to be installed. It is important to point out that a certain loss in pitching moment due to differential flaps has to be taken into account; this leads to the slightly transverse line in the design chart if the recovery moment is defined to be derived from the configuration with all pitch controls deflected fully down.

### 3.5 Design Criteria for Lateral/Directional Stability

Considerations about requirements for the lateral-/directional basic characteristics have to start with the evidence that an unstable design in roll/yaw will not lead to such remarkable gains in performance as a destabilization in pitch. Furthermore a dynamically unstable aircraft in pitch and yaw may multiply the complexity of the flight control system and hence is not very likely to pay off.

The consequence is that at low as well as at high angles-of-attack the design should aim towards coefficients and derivatives which produce at least indifferent roots in the dynamic analysis (slightly unstable spiral mode excluded).

The critical area for low angle-of-attack characteristics may be found at high supersonic Mach numbers. In the region of maximum dynamic pressure the elastic factors usually diminish the stabilizing contribution of the vertical tail.

For the low speed/high angle-of-attack region stable directional/lateral derivatives ( $+C_{n\dot{\beta}}$ ,  $-C_{y\dot{\beta}}$ ) with smooth behaviour versus sideslip, avoidance of yaw and roll departure tendencies, sufficient margin for spin resistance and effective rudder/roll control power highlight the optimization goals.

To assess departure and spin resistance, the "Dynamic Directional Stability Parameter"  $C_{n\dot{\beta}dyn}$  and the "Lateral Control Departure Parameter"  $C_{LCP}$  have been proposed as a prediction method by Weisman (see Ref. 2,3,4). The resulting Weisman Criterion (taken from [Ref. 3]) in Fig. 17 specifies regions of stable and unstable behaviour in the  $C_{n\dot{\beta}dyn}$ - $C_{LCP}$  plane.  $C_{n\dot{\beta}dyn}$  itself has been derived from the characteristic equation as it is summarized in Fig. 18, using the experience that

divergence usually occurs if the C-coefficient becomes negative. As shown in [Ref. 7] many of the terms, contained in C are usually small enough to be neglected. The result of the evaluation leads to the conclusion that directional divergence is likely to occur, if

$$C_{n\dot{\beta}dyn} = C_{n\dot{\beta}} \cdot \cos \alpha - \left(\frac{1}{2} \frac{\dot{\alpha}}{V}\right) \cdot C_{L\dot{\beta}} \cdot \sin \alpha$$

approaches zero or gets negative. This tendency was checked against the behaviour of several combat aircraft and the correlation turned out to be fairly good. So it has become common use for preliminary design to set a certain minimum positive margin for  $C_{n\dot{\beta}dyn}$  to make sure that spin tendency at high angles-of-attack is excluded.

Meanwhile many papers have been published (see for example [Ref. 4 and 6]) where the clear evidence was pronounced that some key phenomena of modern fighters are not covered by the criterion. In examining the data used by Weisman it was found in [Ref. 4] that some important design features have changed since the criterion was developed. Especially maximum lift and usable angle of attack have shifted to considerably higher values ( $\alpha_{CL_{max}}: 20^\circ \rightarrow 30^\circ$ ) which implies that the static and dynamic lateral/directional derivatives are now dominated by forebody vortices from nose, strakes or canard.

For the older aircraft the dynamic data were of minor influence and the departure characteristics in Weisman's correlation were dominated by the static derivatives. - High angle of attack characteristics of modern aircraft are more dependent on the dynamic derivatives which are heavily influenced by forebody geometry.

In spite of the fact that configurations and usable flight envelopes have changed the characteristic equation of Fig. 18 is still valid:

Stable behaviour may be expected if all the coefficients B, C, D and E are positive and if the Routh-discriminant  $(C \cdot B - D) \cdot D - E^2$  keeps larger than zero.

A rough estimation shows that according to the geometric, mass and inertia figures of typical modern fighters (Fig. 10 with radius of inertia  $i_x = 1.5$ ,  $i_z = 3.4$ ; span = 10 m) the following characteristic values may be assumed (see Fig. 19):

- mass density:  $\mu_s > 80$
- inertia ratios:  $K_x = 0.1 < K_z = 0.5$
- flightmechanical time:  $t_f < 0.1 \mu_s$

Furthermore the results of various windtunnel tests show that ...

...  $C_{y\dot{\beta}}$  will always stay negative

...  $C_{L\dot{\beta}}$  will always stay positive  
( $C_{L\dot{\beta}} - C_L, C_{L\dot{\beta}} > 1.0$  at  $C_{L_{max}}$ )

Keeping these assumptions in mind the DESIGN RULES for the aerodynamicists are straight forward (Fig. 19 bottom):

- Avoid autorotation tendency ( $C_{L\dot{\beta}} < 0$ ) and maintain yaw damping ( $C_{n\dot{\beta}} < 0$ ) in order to keep the B-coefficient of the characteristic equation greater than "zero".
- $C_{n\dot{\beta}dyn}$  must be kept larger than zero as this parameter dominates the C-coefficient.
- Close to maximum lift, where  $C_{L\dot{\beta}}$  is considerably larger than 1.0, it is essential to maintain  $C_{n\dot{\beta}dyn} > 0$  with negative  $C_{y\dot{\beta}}$  and only slightly positive  $C_{n\dot{\beta}}$  ( $= +0.1$ ).



In addition to these design guidelines it is important to emphasize that ...

- Nonlinearities and Hysteresis Effects versus sideslip have to be avoided.

This is necessary, because the sideslip sensors will not be very accurate, especially at higher angles of attack. In consequence it is extremely difficult or even impossible to schedule the control laws in order to cope with such aerodynamic inadequacies.

The fundamental evidence of this section however is the need, to include the dynamic derivatives into the design considerations for modern fighters as early as possible by adequate dynamic windtunnel tests.

### 3.6 Design Rules for Lateral/Directional Controllers

The essential factors which influence the control power requirements in roll and yaw may directly be deducted from MIL-Spec., as for example from requirements for "Time to Bank", Engine failure during Take-off and "Take-off/Landing in Crosswind". Control power for stabilization or stability augmentation of the lateral/directional axis is dependent on the chosen basic stability characteristics, as discussed above. But as long as no excessive instability in roll or yaw has to be covered, the control power defined by the conventional criteria should be sufficient.

The capability to initiate and maintain coordinated rolls at high angles-of-attack represents a major point of interest especially for future fighter aircraft with high agility in this part of the flight envelope. Already during preliminary design phases these aspects may be covered. Fig. 20 illustrates within three sketches in the time domain the essential parameters:

The desired roll performance of an aircraft may be sufficiently described by the Roll Time Constant  $T_R$ , the Maximum Roll Rate  $p_{MAX}$  and a "Time to Bank to  $\theta$  degrees". Most of the control law designs try to avoid sideslip and therefore prefer a well coordinated roll around the velocity vector.

So the "pitch recovery margin" which has to be provided according to the discussion in chapter 3.4 sets the first corner stone by defining the maximum permissible roll rate  $p_{VMAX}$  (roll rate around the velocity vector) due to inertial coupling compensation.

From the applicable Handling Quality Documents (f.e. MIL-F-8785C) recommended "Level-1"-values for "Time-to-Bank" and "Rolltime-Constants" may be depicted for the essential flight conditions. These characteristics are linked by the simple equation

$$\phi(t) = p_{V_{max}} \cdot (t - T_R (1 - e^{-t/T_R}))$$

and so the "required"  $p_{V_{max}}$  may be checked against the "permissible" defined by the pitch recovery margin installed.

In a second step the required angular acceleration around the velocity vector which is necessary to initiate the coordinated roll maneuver may simply be defined as:

$$\dot{p}_{VO} = \frac{p_{V_{max}}}{T_{R_{Req}}}$$

Fig. 21 points out how the roll acceleration requirement has to be transferred into body axes. The definition of angle-of-attack and calibrated airspeed/dynamic pressure, where the agility is required, leads to the deduction of the body fixed roll and yaw control power requirements. Some further analysis shows that for any coordinated roll maneuver onset the relation

$$C_{no} = C_{l0} \cdot \frac{i_z^2}{I_x^2} \cdot \tan \alpha$$

must be satisfied. Because of  $i_z > i_x$  good roll performance at high angles may only be achieved if sufficient yaw control power can be provided.

The summary of all the discussions above is presented in Fig. 22 showing a possible "design chart" for yaw and roll controllers at high angles-of-attack. The diagram (body fixed yawing moment versus body fixed rolling moment) contains the line of coordination (defined by the equation above) and an arbitrary minimum requirement for  $C_n$  and  $C_l$  (deducted from Fig. 21). The example assumes that the aileron and/or flaperons at high angles-of-attack produce an adverse yaw/roll characteristic. Starting from this characteristic it is now necessary to meet the coordination line above the requirement by providing the appropriate yaw control power. It gets evident that this does not only require a certain yawing moment  $C_n$  but also an  $C_n-C_l$  characteristic of the yaw controller. Once the yaw/roll control behaviour is fixed by configuration details it is of no use to increase the yaw potential beyond the "line of coordination". The capabilities for a well coordinated roll maneuver will not improve.

### 4. Conclusions

Recent experience in the design of highly augmented modern fighter aircraft with basically unstable characteristics in pitch has shown, that the early integration of flightmechanical requirements into the aerodynamic optimization process is mandatory. Maximum allowable instabilities and control power requirements, will set remarkable constraints to the freedom of aerodynamic design and influence essential components of the aircraft. Because of the complex aerodynamic effects at high angles-of-attack it will be necessary to approach the "basic configuration" by some optimization loops. During the whole process specialists from flightmechanics, aerodynamics and overall design departments have to form a close team in order to end up with an excellent well-balanced design.

Furthermore the discussions have shown that the requirements, presented in the sections above, are up to now not finally settled and they may not be applicable for other aircraft projects without previous examination. The specific boundaries and numbers within the criteria will have to be individually tuned to the design goals of the project under consideration. Especially the diagrams of the  $T_R$ -Criterion can easily be updated and revised if the procedure in [Ref. 9] is run with Handling/Ride Quality and Stability Requirements of current interest.

It is proven, however, that a set of criteria which represents a platform of common discussion for the specialist groups "Aerodynamicists", "Flightmechanics" and "Control-Law Designers" within early phases of a new fighter project can be and must be established in order to avoid unexpected, time consuming and costly difficulties in later design phases.

### 7. Nomenclature

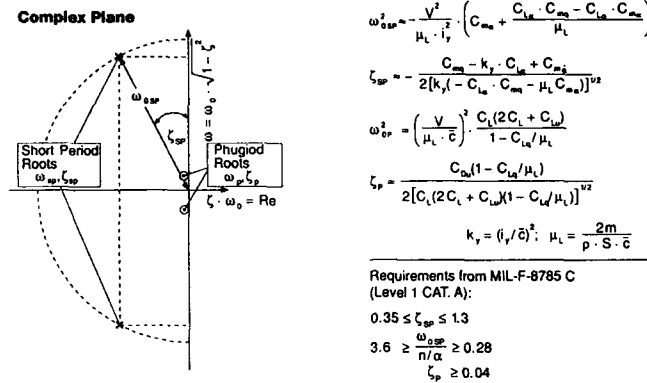
B, C, D, E	Coefficients of characteristic equation, see Fig. 18
b	Wing span
$C_D$	Drag Coefficient
$\bar{c}$	Mean Aerodynamic Chord
$C_L$	Lift Coefficient
$C_{L\eta}$	Lift due to Deflection of Pitch Controller
$C_{L\dot{\alpha}}$	Lift Curve Slope
$C_{L\dot{\alpha}}^A$	Lift due to Angle of Attack Rate
$C_{L\dot{\alpha}}$	Lift due to Pitch Rate

$C_l$	[rad <sup>-1</sup> ]	Rolling Moment Coefficient (Body Fixed)
$C_{l\beta}$	[rad <sup>-1</sup> ]	Rolling Moment due to Sideslip
$C_{l\dot{\alpha}}$	[rad <sup>-1</sup> ]	Rudder efficiency
$C_{l\dot{p}}$	[rad <sup>-1</sup> ]	Rolling Moment due to Roll Rate
$C_{l\dot{r}}$	[rad <sup>-1</sup> ]	Rolling Moment due to Yaw Rate
$C_m$	[-]	Pitching Moment Coefficient
$C_{m\dot{\alpha}}$	[rad <sup>-1</sup> ]	Efficiency of Pitch Controller
$C_{m\dot{\alpha}}$	[rad <sup>-1</sup> ]	Pitching Moment derivative
$C_{m\dot{\alpha}}$	[rad <sup>-1</sup> ]	Pitching Moment due to Angle of Attack Rate
$C_{m\dot{q}}$	[rad <sup>-1</sup> ]	Pitching Moment due to Pitch Rate
$C_n$	[-]	Yawing Moment Coefficient (Body Fixed)
$C_{n\beta}$	[rad <sup>-1</sup> ]	Directional Stability
$C_{n\dot{\beta}}$	[rad <sup>-1</sup> ]	Spin Resistance Parameter (Def. see Fig. 17)
$C_{n\dot{p}}$	[rad <sup>-1</sup> ]	Yawing Moment due to Roll Rate
$C_{n\dot{r}}$	[rad <sup>-1</sup> ]	Yawing Moment due to Yaw Rate
$C_{n\dot{\alpha}}$	[rad <sup>-1</sup> ]	Rudder efficiency
$C_{y\dot{\alpha}}$	[-]	Sideforce coefficient (Body Fixed)
$C_{y\dot{\beta}}$	[rad <sup>-1</sup> ]	Sideforce due to Sideslip
$C_{y\dot{p}}$	[rad <sup>-1</sup> ]	Sideforce due to Roll Rate
$C_{y\dot{r}}$	[rad <sup>-1</sup> ]	Sideforce due to Yaw Rate
$H$	[m]	Altitude
$I_x$	[m]	Radius of Inertia (Body Fixed)
$I_y$	[m]	
$I_z$	[m]	
$I_{xy}$	[-]	
$I_{yz}$	[-]	
$I_{xz}$	[-]	
$LCDP$	[-]	Ratios of Inertia (see Fig. 11/18)
$M$	[m]	Lateral Control Departure Parameter (see Fig. 17)
$\dot{M}$	[Nm/s]	Pitching Moment
$\dot{M}_a$	[-]	Pitching Moment Build-up Rate
$m$	[kg]	Mach Number
$p$	[deg/s]	Mass
$q$	[deg/s]	Roll Rate
$r$	[deg/s]	Pitch Rate Body Fixed
$s$	[deg/s]	Yaw Rate
$S$	[m <sup>2</sup> ]	Reference Area
$s$	[m]	Half Span
$s_{1,2}$	[s <sup>-1</sup> ]	Short Period Roots
$SM$	[%]	Static Margin
$t_p$	[s]	Flightmechanical Time (Fig. 18)
$T_d$	[s]	Time-to-Double Amplitude
$T_R$	[s]	Roll Time Constant
$t_d$	[s]	Time Delay
$t_t$	[s]	Time
$V$	[m/s]	Airspeed
$x_{c.g.}$	[%]	Centre of gravity
$x_{a.c.}$	[%]	Aerodynamic centre
$\alpha$	[deg]	Angle of Attack
$\beta$	[deg]	Angle of Sideslip
$\zeta$	[-]	Damping Ratio
$\delta$	[deg]	Rudder Deflection
$\eta$	[deg]	Deflection of Pitch Controller
$\theta$	[deg]	Pitch Attitude
$\ddot{\theta}$	[rad/s <sup>2</sup> ]	Pitch Acceleration
$\ddot{\theta}$	[rad/s <sup>2</sup> ]	Pitch Control Reaction (see Fig. 8)
$\phi$	[deg]	Bank Angle
$\mu_L$	[-]	Mass Density (see Fig. 11)
$\mu_s$	[-]	Mass Density (see Fig. 18)
$\rho$	[kg/m <sup>3</sup> ]	Density
$\omega$	[rad/s]	Frequency
$\omega_d$	[rad/s]	Undamped Frequency

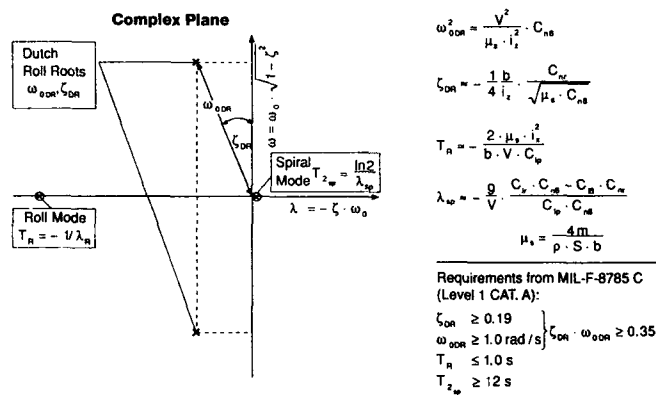
## 8. References

- [Ref. 1] H. Wünnenberg et al.  
Handling Qualities of Highly Augmented Unstable Aircraft  
AGARD Advisory Report AR-279
- [Ref. 2] Weisman Robert  
Criteria for Predicting Spin Susceptibility of Fighter Type Aircraft  
ASD-TR-72-48, June 1972
- [Ref. 3] Beaufre, H.  
Flight Plan Development for a Joint NASA/Navy High Angle of Attack Flight Test Program  
Grumman Contract No. NASA 2965  
March 1983
- [Ref. 4] J.R. Chody, J. Houghkinson, A. Skow  
Combat Aircraft Control Requirements for Agility  
AGARD Symposium "Aerodynamics of Combat Aircraft..."  
Madrid, 2. - 5.10.1989, CP 465
- [Ref. 5] Military Specifications  
Flying Qualities of Piloted Air Vehicles MIL-F-8785C
- [Ref. 6] P. Mangold, G. Wedekind  
Integration of Aerodynamic, Performance, Stability and Control Requirements into the Design Process of Modern Fighter Aircraft Configurations  
AGARD, LS 153
- [Ref. 7] H.D. Greer  
Summary of Directional Divergence Characteristics of Several High Performance Aircraft Configurations  
NASA-TN D-6993, Nov. 1972
- [Ref. 8] P. Mangold/G. Wedekind  
"Inflight Thrust Vectoring" a Further Degree of Freedom in the Aerodynamic/Flightmechanical Design of Modern Fighter Aircraft  
AGARD CP 465, Madrid 1989
- [Ref. 9] P. Mangold  
Integration of Handling Quality Aspects into the Aerodynamic Design of Modern Unstable Fighters  
FMP-Symposium AGARD: Flying Qualities Quebec, 15. - 18.10.1990

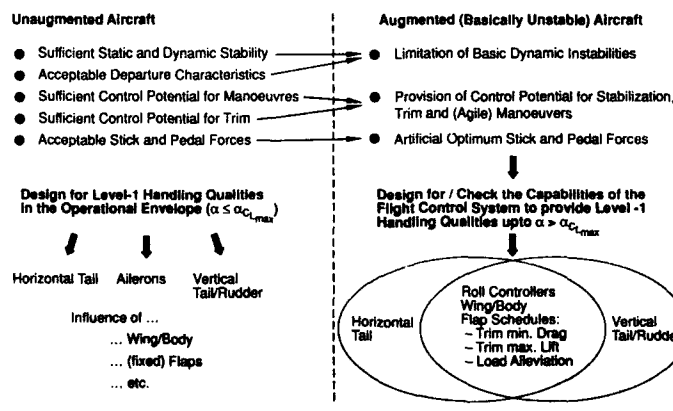
**Fig. 1 Correlations between Handling Quality Requirements and Aerodynamic Parameters for an Unaugmented Aircraft (Pitch Axis)**



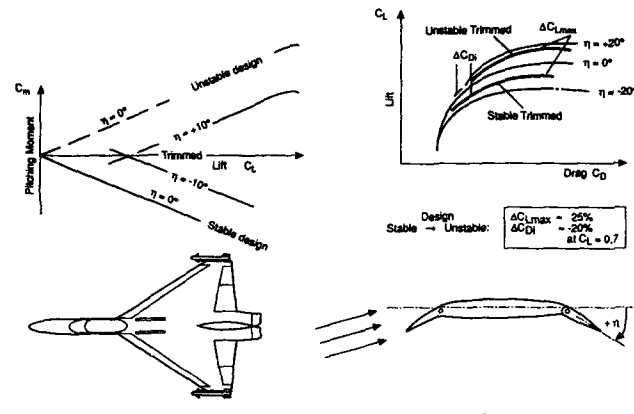
**Fig. 2 Correlation between Handling Quality Requirements and Aerodynamic Parameters for Unaugmented Aircraft (Lat./Dir. Axes)**



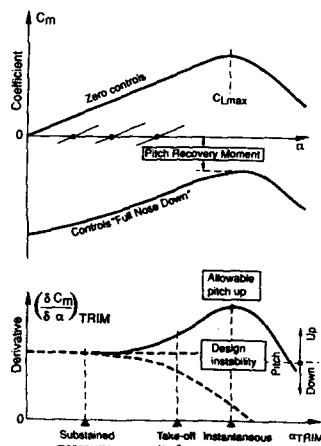
**Fig. 3 Flightmechanical Design Aspects**



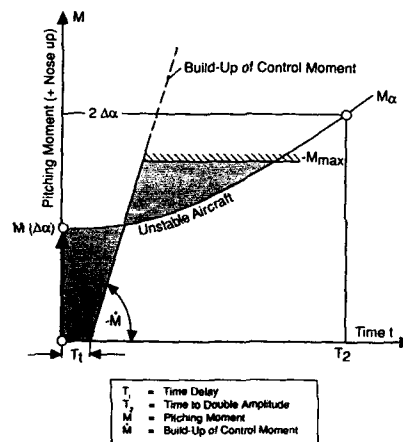
**Fig. 4 Key Characteristics for the Aerodynamicists  
Effect of Destabilization on Performance**



**Fig. 5 Key Characteristics for the Aerodynamicists  
Pitching Moment versus Angle of Attack**

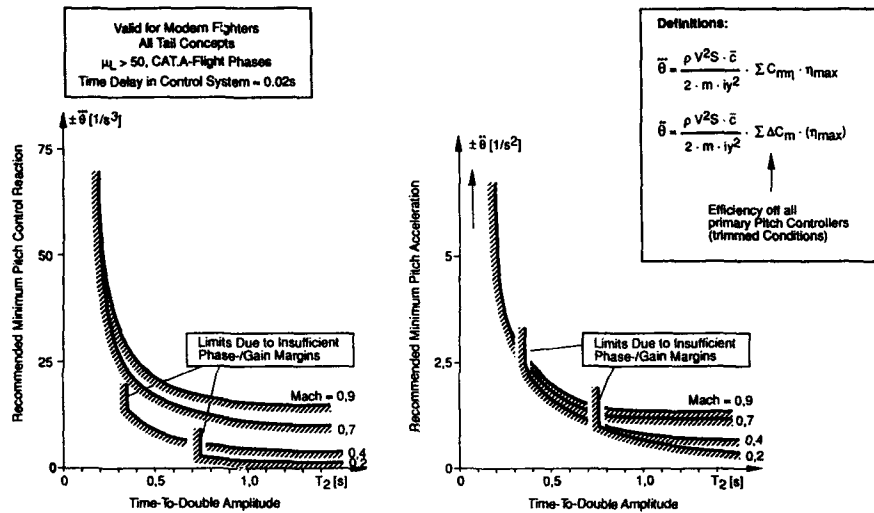
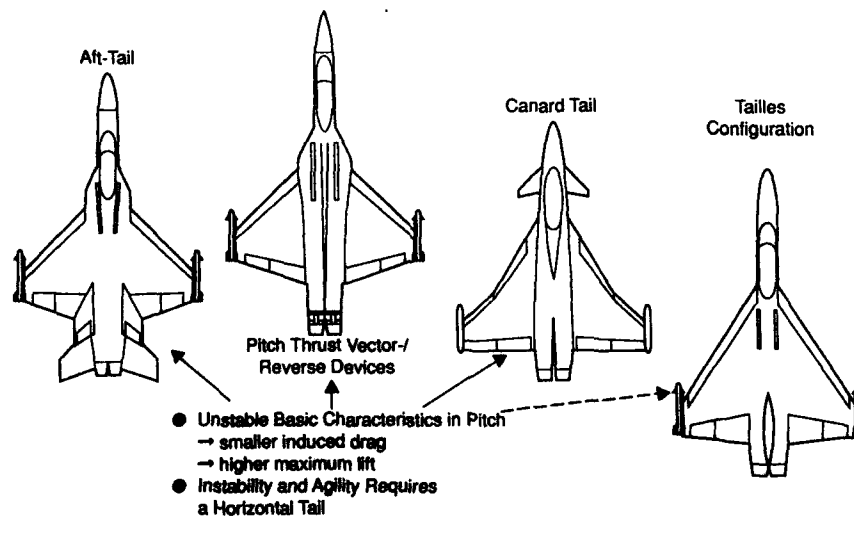


**Fig. 6 Principle Problems of (Pitch) Stabilization**



**Fig. 7 Key Characteristics of Unstable Design in Pitch**

Parameter	Remarks
Static Margin $SM = -\frac{\delta C_m}{\delta C_L} = \frac{x_{ac} - x_{cg}}{\bar{c}}$	<ul style="list-style-type: none"> <li>● Aerodynamic Characteristic of Instability</li> <li>● Lever Arm of Aerodynamic Forces</li> <li>● Indicates Potential for Drag Reduction</li> <li>● Indicates Potential for Higher Max. Lift</li> <li>● Flightmechanical Design Criterion for stable Unaugmented Aircraft</li> <li>● No Indication for Higher Agility</li> </ul>
Time to Double Amplitude $T_2$	<ul style="list-style-type: none"> <li>● Quantification of Dynamic Problems</li> <li>→ Stabilization</li> <li>→ Optimization of Flying Qualities</li> </ul>
Maximum Pitch Control Power $\pm \dot{M}_{max}$ Rate of Control Power Build-up $\pm \ddot{M}_{max}$	<ul style="list-style-type: none"> <li>● Defines Potential to Solve Problems</li> </ul>

**Fig. 8 T<sub>2</sub>-Criterion for Unstable Fighter Aircraft****Fig. 9 Typical Modern Fighter Configurations  
(Designed for European Mission and Manoeuvre Requirements)**

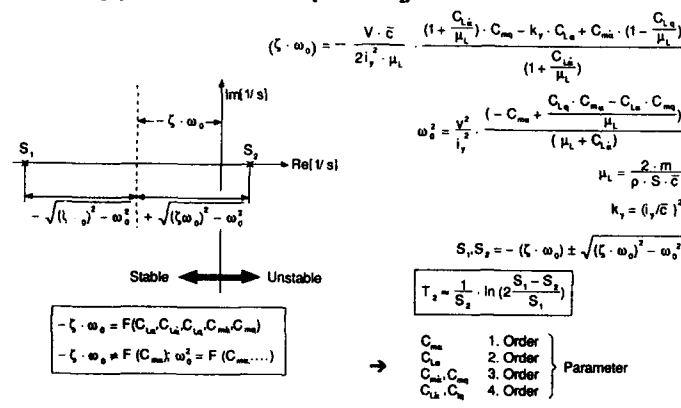
**Fig. 10 Typical Data of Modern Fighter Aircraft in the Subsonic Region (Longitudinal Motion);**

Parameter	Aft-Tail	Horizontal Tail Arrangement		
		Vector Nozzle	Canard	Tailless
Static Instability Margin (small $\alpha$ )	SM $\approx -10\%$	SM $\approx -8\%$	SM $\approx -8\%$	SM $\approx 0\%$
Medium Combat Mass m	ca. 12500 kg	ca. 12500 kg	ca. 12500 kg	ca. 12500 kg
Reference Wing Area S	45 m <sup>2</sup>	45 m <sup>2</sup>	50 m <sup>2</sup>	60 m <sup>2</sup>
Mean Aerodynamic Chord $\bar{c}$	5.4 m	5.4 m	5.7 m	6.7 m
$C_{L\alpha}$	+0.4 12 0.0	0.28 12 0.35 12 0.0	0.26 12 0.5 12 0.0	0.0 12 0.2 12 0.0
$C_{L\alpha}$	+4.0 12 0.0	+3.5 12 0.0	+3.3 12 0.0	2.6 12 0.0
$C_{m\alpha}$	-1.5 12 -2.5	-0.5 12 -1.0	-0.5 12 -1.0	-0.4 12 -0.8
$C_{L\alpha}$	+1.6 12 +2.0	+1.0 12 +1.5	1.2 12 +1.9	+1.2 12 +1.9
$C_{m\alpha}$	-1.0 12 -1.0	+0.1 12 +0.2	-0.1 12 0.0	-0.1 12 0.0
$C_{L\alpha}$	+0.8 12 +2.5	+0.6 12 +1.5	+0.7 12 +1.5	+0.7 12 +1.5
$C_{m\alpha} / \alpha_{CL_{max}}$ (Low Speed)	1.50/30°	1.50/30°	1.35/30°	+1.15/30°
Tail Efficiency $C_{L\alpha}/C_{m\alpha}$	+0.45/-0.5	$\dot{\alpha}_{max} = \pm 2.0 \text{ rad/s}^2$	+0.03/0.12°	-/-
Flap Efficiency $C_{L\alpha}/C_{m\alpha}$	+0.63/-0.13**	+1.0/-0.30	+1.15/-0.35	+1.15/-0.35
Mass Density $\rho$	84	84	72	50
Radius of Inertia $I_y$	3.4 m	3.3 m	3.0 m	3.2 m

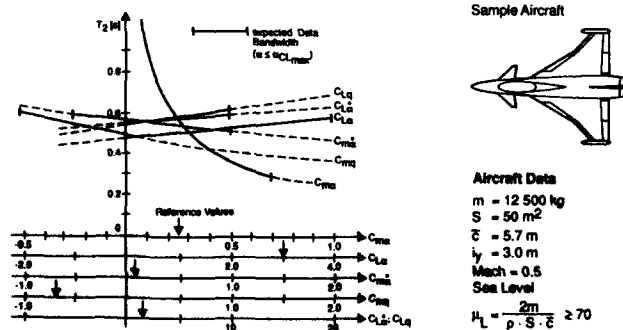
\* incl. Wing Interference  
 \*\* incl. Tail Interference

$$\mu_L = \frac{2m}{\rho \cdot S \cdot \bar{c}}$$

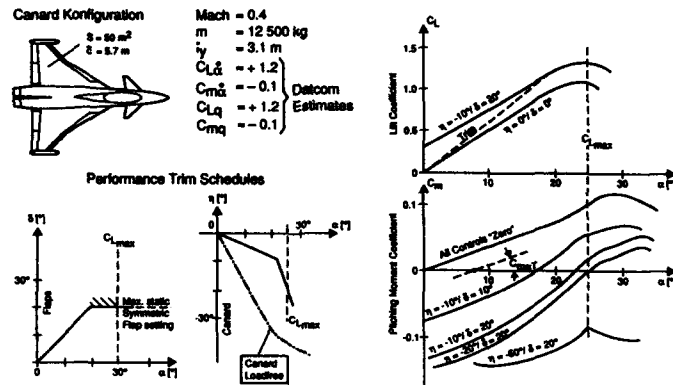
**Fig. 11 Correlations between Aerodynamic Derivates and Dynamic Instability (Time to Double Amplitude  $T_2$ )**



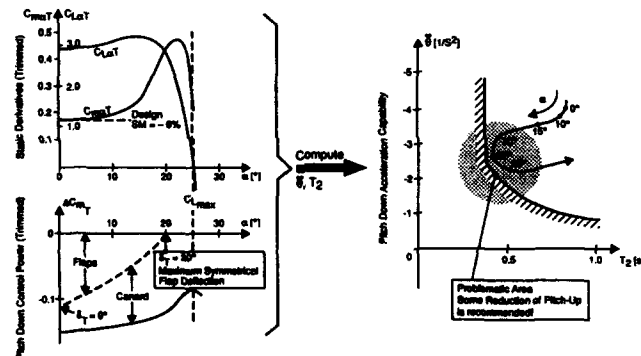
**Fig. 12 Influence of Static and Dynamic Derivatives on Time-to-Double Amplitude  $T_2$**



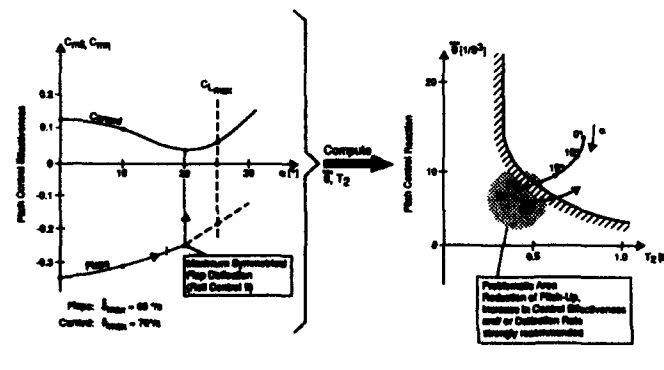
**Fig. 13 Example for Application of the T<sub>2</sub>-Criterion within the Aerodynamic Design Process**



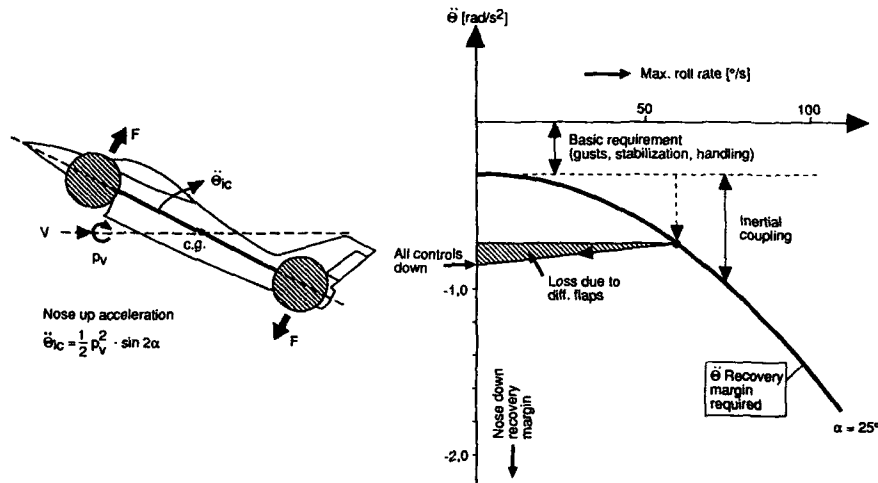
**Fig. 14 Application of T<sub>2</sub>-Criterion within the Aerodynamic Design Process (Ctd.)**



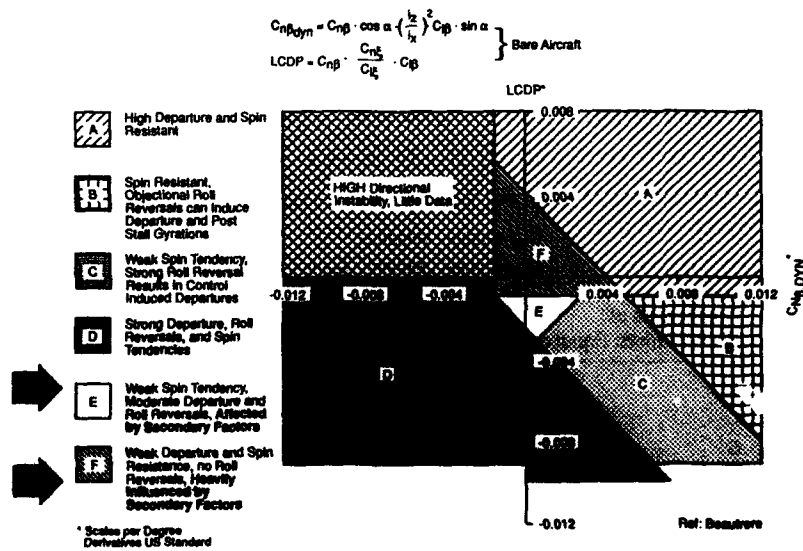
**Fig. 15 Application of T<sub>2</sub>-Criterion within the Aerodynamic Design Process (Ctd.)**



**Fig.16 Definition of Pitch Recovery Margin at High Angles of Attack by Roll Rate Requirement**



**Fig.17 Weissmann Criterion for Lateral/Directional Stability**





**Fig. 18 Characteristic Equation of Lateral/ Directional Motion (Derivatives in Body Axes)**

$$\lambda^4 + B\lambda^3 + C\lambda^2 + D\lambda + E = 0$$

Stable if:  $B, C, D, E > 0$  And  $(C \cdot B - D) D - EB^2 > 0$

$$B = -\frac{1}{t_f \cdot K_x \cdot K_z} \cdot (K_x \cdot C_{\dot{w}} + K_z \cdot C_{\dot{p}} + K_x K_z \cdot C_{\dot{r}})$$

$$C = \frac{1}{t_f^2 \cdot K_x \cdot K_z} (\mu_s \cdot k_x \cdot C_{\dot{w}} \cdot \cos \alpha - \mu_s \cdot K_z \cdot C_{\dot{w}} \cdot \sin \alpha + C_{\dot{p}} \cdot C_{\dot{w}} - C_{\dot{r}} \cdot C_{\dot{p}} \\ + k_x \cdot C_{\dot{r}} \cdot C_{\dot{p}} - K_z \cdot C_{\dot{r}} \cdot C_{\dot{w}} + K_x \cdot C_{\dot{r}} \cdot C_{\dot{w}} - K_x \cdot C_{\dot{p}} \cdot C_{\dot{w}})$$

$$D = \frac{1}{t_f^3 \cdot K_x \cdot K_z} \cdot [\mu_s \cdot (C_{\dot{w}} \cdot C_{\dot{p}} \cdot \cos \alpha - C_{\dot{w}} \cdot C_{\dot{p}} \cdot \cos \alpha + C_{\dot{w}} \cdot C_{\dot{r}} \sin \alpha - C_{\dot{w}} \cdot C_{\dot{r}} \sin \alpha) \\ + t_f^2 \cdot \frac{g}{s} \cdot (-k_x \cdot C_{\dot{w}} \cos \alpha - K_z \cdot C_{\dot{w}} \sin \alpha) \\ + C_{\dot{p}} \cdot C_{\dot{r}} \cdot C_{\dot{w}} + C_{\dot{w}} \cdot C_{\dot{p}} \cdot C_{\dot{r}} + C_{\dot{w}} \cdot C_{\dot{p}} \cdot C_{\dot{r}} - C_{\dot{w}} \cdot C_{\dot{p}} \cdot C_{\dot{r}} - C_{\dot{w}} \cdot C_{\dot{p}} \cdot C_{\dot{r}}]$$

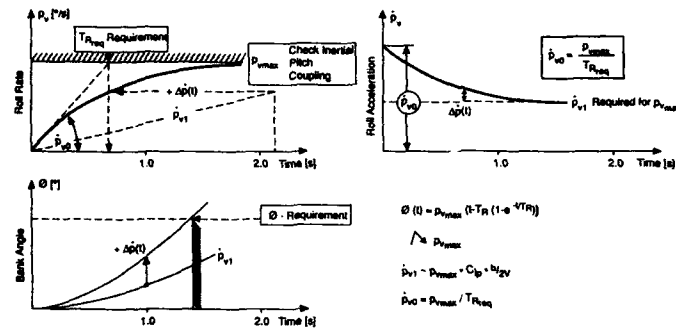
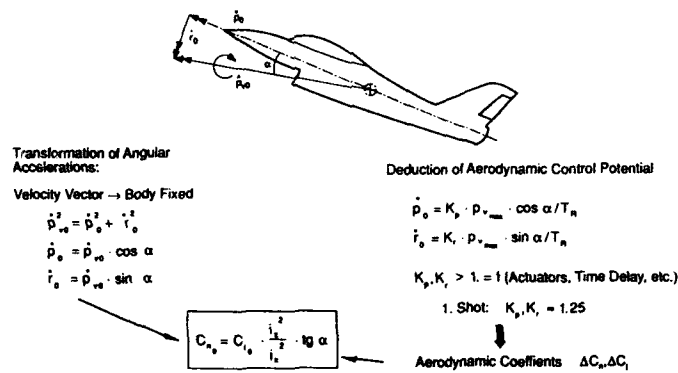
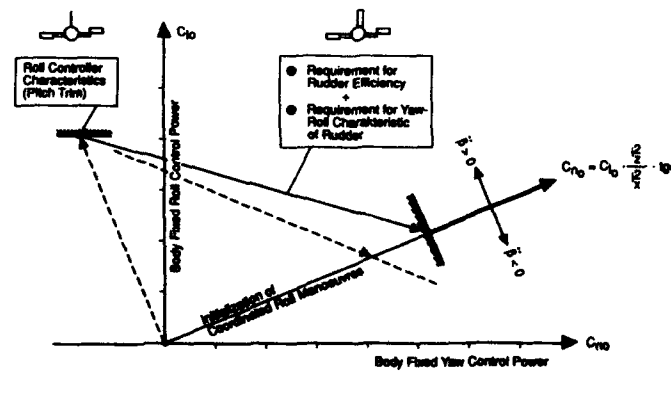
$$E = \frac{g}{t_f^2 \cdot s \cdot K_x \cdot K_z} (C_{\dot{w}} \cdot C_{\dot{r}} \cdot \cos \alpha - C_{\dot{w}} \cdot C_{\dot{r}} \cdot \sin \alpha + C_{\dot{w}} \cdot C_{\dot{p}} \sin \alpha - C_{\dot{w}} \cdot C_{\dot{p}} \cdot \cos \alpha)$$

$$\mu_s = \frac{4m}{\rho \cdot S \cdot b} \quad t_f = \frac{2m}{\rho V \cdot S} \quad k_x = \left( \frac{2i_x}{b} \right) \quad k_z = \left( \frac{2i_z}{b} \right) \quad s = \text{Half Span}$$

**Fig. 19 Design Criteria for Lateral/Directional Characteristics (at High Angles of Attack)**

- **Assumptions:**  $\mu_s \gg 0$  (typical values  $\geq 80$ )  
 $K_x > K_z$  ( $K_x \approx 0.1$ ,  $K_z = 0.5 + 0.8$ )  
 $\mu_s \gg t_f$  ( $\mu_s = \frac{2V}{b} \cdot t_f$ ;  $\mu_s > 10t_f$ )  
 $C_{\dot{r}}$  always negative  
 $C_{\dot{w}}$  always positive ( $C_{\dot{w}} = C_{\dot{z}}$ ,  $C_{\dot{w}} \geq 1.0$  at  $C_{L_{max}}$ )

Coefficients of Characteristic Equation	Design Rules for Dominating Parameters		
B	Avoid Autorotation	⇒	$C_{\dot{p}} < 0$
	Maintain Yaw Damping	⇒	$C_{\dot{r}} < 0$
C	Dominated by $\mu_s \cdot K_x \cdot C_{\dot{w}} \cdot \cos \alpha$	⇒	$C_{\dot{w}} > 0$
D, E	Avoid Large Positive Directional Stability	⇒	$C_{\dot{w}} = +0$
	Maintain $C_{\dot{w}} > 0$ by Lateral Stability	⇒	$C_{\dot{p}} < 0$
$(C \cdot B - D) D - EB^2$	Keep C Larger Than D	⇒	$C_{\dot{w}} > 0.1$ with slightly positive $C_{\dot{w}}$

**Fig. 20 Definition of Roll Control Power by Roll Performance Requirements****Fig. 21 Definition of Body Fixed Roll and Yaw Control Power (Coordinated Rolls at High Angles of Attack)****Fig. 22 Design Diagram for Yaw and Roll Control Power at High Angles of Attack**

# **AEROSERVOELASTIC STABILITY OF AIRCRAFT AT HIGH INCIDENCE**

by  
Juergen Becker

MBB GmbH FE273  
P.O. Box 80 11 60  
D-8000 München 80

## **SUMMARY**

The aeroservoelastic stability of a fighter type aircraft is investigated at high angle of attack. The effects of nonlinear, incidence dependent unsteady aerodynamic forces of elastic modes and of control surface deflections on the structural coupling are demonstrated for low and high subsonic speeds for different incidences. The difference of open loop frequency response functions calculated with linear and with high angle of attack unsteady aerodynamics documents the necessity of introduction of high incidence effects for aeroservoelastic stability calculations. Nonlinear effects are introduced using unsteady pressures of windtunnel experiments on an oscillating model by correcting of theoretical pressures.

## **1. INTRODUCTION**

This contribution describes a possible way to predict the aeroservoelastic stability of an aircraft at high incidence including nonlinear aerodynamic effects. The design of flight control laws for modern aircraft is very much influenced by aeroservoelastic members to alleviate structural coupling effects. Notch filters or active feedbacks of local elastic accelerations or rates have to be optimized in order to give minimum structural coupling together with minimum acceptable effects on aircraft handling and on flutter phase and gain margins without violating required stability limits. The design of the notch filters or of the active feedback control laws is in general based on an analytical dynamic model which includes the description of flight and structural dynamics together with unsteady aerodynamic forces of the elastic vibration modes and of control surface deflections. A specific problem area concerning layout of filters or control loops arises especially at high incidence, high dynamic pressure flight conditions since the unsteady aerodynamic forces which especially in case of unstable aircraft configurations play an important role for the stability margins of elastic modes compared to those on ground conditions.

The problem stems from the fact that theoretical unsteady aerodynamics from linear theory which have anyhow to be applied do not include high incidence aerodynamic effects, effects of flow separation or related nonlinear aerodynamic behaviour. The investigation is performed on a typical Delta Canard fighter aircraft similar to the configuration shown in Fig. 1.

## **2. STABILITY CRITERIA**

For stability assessments of the aircraft with Flight Control System (FCS) criteria from the following MIL-Specs are applied:

- 1) FLIGHT CONTROL SYSTEM, MIL-F-9490D(USAF)
- 2) AIRPLANE STRENGTH AND RIGIDITY VIBRATION FLUTTER AND DIVERGENCE, MIL-A-8870B(AS)

The military specifications for aircraft with FCS contain gain and phase margin requirements for the open loop frequency responses for the rigid dynamics in the frequency range of the modes  $M$  from  $0.06 \leq f_n < f_{n1}$  first aeroelastic mode which are in the range of minimum to maximum operational speed 6 dB gain and 45 degree phase margin and at limit airspeed  $V_L$  4.5 dB gain and 30 degree phase margin. MIL-F-9490D requires for the mode frequencies  $f_n > f_{n1}$  first elastic mode 8 dB and 60 degrees phase margin in the operational range and 6 dB and 45 degrees phase margin for  $V_L$ .

Special requirements for mode frequencies  $f_n > f_{n1}$  first elastic mode may be formulated which take into account uncertainties in the prediction of unsteady aerodynamic forces at extreme flight conditions. Especially if actively controlled configurations are concerned, which are unstable. For these configurations the flight clearance has to be based upon prediction for open loop response functions, since in flight testing cannot be the basis.

The aeroservoelastic stability requirements defined for flutter in MIL-A-8870B shall be met as well. A minimum required flutter margin boundary of 15% in  $V_D$  at constant altitudes and at constant Mach numbers is defined there. The damping coefficient  $g$  for any flutter mode shall be at least three percent.

The requirements are demonstrated in fig. 2.

### 3. DESCRIPTION OF THE STRUCTURAL COUPLING PROBLEM

The structural coupling problem described here is specific for military aircraft with heavy underwing tanks where at low frequencies down to about 4 Hz wing bending modes are present due to the high mass condition. These low frequency wing bending modes, shown for the configuration analysed in fig. 3, produce counteracting fuselage modes which are mainly rigid fuselage pitch oscillations.

These rigid fuselage modes create a coupling problem which is in contrast to the general well known structural coupling problem caused by the first elastic bending mode of the fuselage and the feedback of its elastic fuselage pitch rate signal through the gyros to the control surfaces, fig. 3 fifth mode. The structural coupling effects caused by the first fuselage bending mode can easily be reduced by putting the gyros in a position of zero elastic mode pitch angle or rate. In addition strong notch filtering can be introduced in the feedback loop to avoid coupling.

The feedback signal of the gyro in the frequency of the low frequency wing bending modes however cannot be influenced and alleviated by gyro positioning. In addition the frequency of the first elastic mode is so low that the normally used notch filter technique to reduce structural coupling cannot be applied fully. The stability criteria for handling would be affected by loss of phase at around the short period mode frequency due to effects of the notch filtering. Therefore the low frequency mode shall be shown as a phase stable mode. If this mode cannot be phase stabilized configuration changes or active control means would be helpful. A typical behaviour of the structural coupling effect in the low frequency mode is the increase of the frequency response in flight due to unsteady aerodynamic excitation by the control surfaces. (This effect was not experienced in the structural coupling signal of the first fuselage bending mode of other fighter aircraft where the problem was always found for on ground conditions and in flight aerodynamic mode damping caused lower coupling.)

Therefore the aerodynamic excitation forces of the low frequency mode and its aerodynamic damping is of prime interest for the stability of the heavy tank aircraft configuration. The effects of unsteady aerodynamic forces at high angle of attack have to be considered carefully.

### 4. ANALYTICAL MODELLING

The calculation of open loop frequency response functions has to be based on an analytical model which represents the rigid aircraft dynamics and contains the dynamic equations of the control laws, the sensor, computer and actuators transfer functions. This rigid aircraft dynamic model is coupled to the structural dynamic aircraft model which represent the dynamic behaviour of the elastic aircraft including unsteady aerodynamic forces of the elastic modes and of the control surfaces (generalized aerodynamic forces of elastic modes and generalized efficiencies of inboard, outboard and foreplane rotations). The structural dynamic equations are formulated for unsteady aerodynamic forces which are function of the angle of attack.

$$\begin{aligned}
 & - \omega^2 N_r q_r + N_r \omega_r^2 q_r (1 + i g_r) + \frac{1}{2} A_{r,1} (\alpha_0, M_\infty, \omega) q_1 (\omega) \\
 & + [A_r (\alpha_0, M_\infty, \omega)_{11/b} \delta_{1/b} + K_{1/b} + A_r (\alpha_0, M_\infty, \omega)_{10/b} \delta_{0/b} + A_r (\alpha_0, M_\infty, \omega)_{1p} \delta_{pp} + K_{pp}] \\
 & + [N_{r11/b} \delta_{1/b} + K_{1/b} + N_{r10/b} \delta_{0/b} + K_{0/b} + N_{r1pp} \delta_{pp} + K_{pp}] \\
 & F_{ACTUATOR}(i\omega) * F_{GYRO}(i\omega) * F_{PHASE ADVANCE}(i\omega)
 \end{aligned}$$

where

$q_r$	generalized coordinate
$\omega_r$	mode frequencies
$M_r$	generalized masses
$\omega_r^2 M_r$	generalized stiffnesses
$A_{r,j}(\alpha_0, Ma)$	generalized unsteady aerodynamic forces of the modes
$A_{r,i/b}(\alpha_0, Ma)$	generalized unsteady aerodynamic efficiency of inboard flap
$A_{r,o/b}(\alpha_0, Ma)$	generalized unsteady aerodynamic efficiency of outboard flap
$A_{r,fp}(\alpha_0, Ma)$	generalized unsteady aerodynamic efficiency of foreplane
$M_{r,i/b}$	generalized inertia coupling term for inboard flap
$M_{r,o/b}$	generalized inertia coupling term for outboard flap
$M_{r,fp}$	generalized inertia coupling term for foreplane deflection
$F_{FACTOR}(i\omega)$	Actuator impedance function
$F_{GYRO}(i\omega)$	Sensor transfer function
$F_{PHASE ADV}(i\omega)$	Advance filter characteristic
$K_{i/b}, K_{o/b}, K_{fp}$	Control loop gains

The unsteady aerodynamic forces  $A_{r,j}$ ,  $A_{r,i/b}$ ,  $A_{r,o/b}$ ,  $A_{r,fp}$  can be calculated by computer programs for the derivation of linear unsteady aerodynamic forces for the case of small angles of attack and for high angle of attack with the procedure as described in the following chapter.

## 5. PREDICTION OF UNSTEADY AERODYNAMIC FORCES AT HIGH INCIDENCE

Aeroservoelastic and flutter calculations with the inclusions of flight control effects are normally performed for level flight conditions using linear unsteady aerodynamic theory. The results of these calculations could be in error for manoeuvring conditions of military aircraft from medium up to high incidences, since the applied linear theories do not account for effects of leading edge vortices at higher incidences and effects of locally separated flow are not included in the calculation of motion induced unsteady aerodynamic forces. These effects may be introduced into the aeroservoelastic analysis using a correction method as described in ref. 1, 2, 3 and measured unsteady pressure distributions on a windtunnel model for only one rigid mode.

### 5.1 DESCRIPTION OF THE CORRECTION METHOD

The correction method as developed in ref. 1 is applied for the update of generalized forces used in the analytical model for aeroservoelastic calculations.

The calculation of the generalized aerodynamic motion dependent forces  $A_{r,j}(\alpha_0, Ma, k)$  is performed by a modification of linear unsteady aerodynamic theory, the 3D Doublet lattice method, or the collocation method using both measured steady pressure distributions and the measured unsteady pressure distribution of a wing oscillation. The problem consists here mainly in the prediction of the diagonal terms  $A_{r,r}$  and of the coupling terms  $A_{r,j}$  at separated flow condition if only one measured mode is available.

The corrected generalised aerodynamic motion dependent forces  $A_{r,j}(\alpha_0, Ma, k)$  are calculated as follows for given Machnumber  $Ma$  and reduced frequency  $k$ .

$$A_{r,j} = \iint_S \{ \dot{\Delta C_{p,r}}(\alpha_0, k) + [\dot{\Delta C_{p,i/c}}(\alpha_0, k) - \dot{\Delta C_{p,i}}(\alpha_0, k)] \} u_j dS$$

The corrected unsteady pressure distribution  $\dot{\Delta C_{p,i}}$  of the measured vibration mode  $u_i(x,y)$  is calculated by using a modified kinematic boundary condition.

$$\dot{\Delta C_{p,i}} = [D' + i D'']^{-1} \alpha'$$

where

$D' + iD''$  is the matrix of aerodynamic influence coefficients.

$$\alpha' = \frac{U_\infty + \bar{u}_0}{U_\infty} \frac{\partial u}{\partial x} + i k \bar{u}_i$$

The local velocity  $U_\infty + u_0$  is calculated from local Machnumber and speed of sound.

$$U_\infty + \bar{u}_0(x, y) = a(x, y) Ma(x, y)$$

$$Ma(x, y) = \left\{ \frac{2}{k-1} \left[ \frac{1 + \frac{k-1}{2} M_\infty^2}{\left(1 + \frac{k-1}{2} M_\infty^2\right) c_p} \right] \right\}^{1/2}$$

The local speed of sound  $a(x, y) = \sqrt{kRT}$  is derived from adiabatic compression.

from the difference between measured and corrected unsteady pressure distribution of the measured vibration mode an additive correction term

$$\{\Delta c_{pi} - \Delta c_{pi}'\}$$

is known, which for the formulation of arbitrary vibration modes is assumed to be independent of the mode.

The corrected pressure distribution for arbitrary mode shapes  $u_j$  are then calculated by

$$\Delta c_{pj} = [D' + iD'']^{-1} \alpha_j' + \{\Delta c_{pic} + \Delta c_{pi}'\}$$

In general the measured motion induced pressure contains a contribution of the fluctuating pressure at the reduced frequency of the harmonic oscillation  $k$ . The contribution  $\Delta c_{pi}'(k)$  may be approximatively extracted from the static measurement. Therefore the measured unsteady pressure can be corrected.

$$\Delta c_{pic}(k) = \{\Delta c_{pi}(k) + \Delta c_{pi}'(k)\} - \Delta c_{p0}(k)$$

## 5.2 WINDTUNNEL MODEL DESCRIPTION

The windtunnel tests were performed on a 1/7 scaled half model of a tactical fighter type aircraft. The model configuration included a delta wing, a foreplane and half a fuselage installed at the windtunnel wall (fig. 4). The wing and foreplane were very stiff, machined out of steel.

The fuselage was fixed to the turn table by means of a large rigid cylindrical part locked when incidence was reached by a set of hydraulic brakes (fig. 5). The fuselage contained two hydraulic rotating actuators. The first one aligned with the foreplane axis, allowed to give static foreplane deflections while the second one aligned with the fuselage center line provided roll excitation of the wing.

The different measurements performed were: steady and unsteady pressure fields, steady and unsteady roll moment, accelerations on the wing. The model was equipped with 67 pressure pick-ups, 67 steady pressure tappings, 7 accelerometers, 3 strain gauge bridges. The steady and unsteady pressure pick-ups pairs were distributed along four wing sections on the upper surface and, in a smaller number, along three wing sections on the lower surface.

Tests were performed using sinusoidal wing roll excitation. After conditioning and switching, amplifying and filtering at a cut-off frequency choosen between once and twice the excitation frequency, the signals were digitalized at a sampling rate of eight times the excitation frequency. Fourier analysis was performed, modulus and phase of each signal, normalized to the amplitude of the roll oscillation were computed at the excitation frequency, giving unsteady pressure coefficients.

Tests were performed for different Mach numbers and angles of attack including buffeting situations. The Mach number ranged from 0.3 to 0.95, incidence ranged from 0 to 40 degrees, decreasing as Mach number increased: 40 degrees at  $M = 0.3$ , 10 degrees at  $M = 0.85$  and 0.9, 8 degrees at  $M = 0.95$ .

## 5.3 MEASURED QUASISTEADY PRESSURE DISTRIBUTIONS

The quasisteady pressure distributions are demonstrated for some characteristic conditions in fig. 7 for the upper and lower wing surface separately. There are 7 spanwise sections shown for upper and lower side, 5 are corresponding to real measurement sections. The values at  $y/s = 0.3$  and 0.15 are interpolated.

Mach 0.8, zero incidence

The pressure distribution at upper and lower side shown in fig. 7 above is typical for subsonic flow, upper and lower side pressures are similar in amplitude, no transonic effects are apparent. The applicability of linear subsonic theory may be reasonable for this condition.

Mach 0.9, zero incidence

The pressure distribution at the wing upper side is characterised by transonic effects, visible in the spanwise sections  $y/s = 0.5, 0.75, 0.9, 0.95$ , possibly due to a shock located at about midchord.

The lower side shows less effects and is similar to the  $M = 0.8$  results.

Mach 0.8,  $\alpha = 8.0$  deg.

Strong changes can be observed in the upper side pressure distribution if the static incidence is increased from 0 to 8.0 degrees indicating a strong nonlinear behaviour of the quasisteady forces with incidence. High effects due to a leading edge vortex are present for the inner wing resulting in high pressure peaks, even changes in pressure sign are observed at  $y/s = 0.5$ .

The lower side pressures are less effected, especially for inner wing sections, however outer wing sections show a decrease in amplitude compared to zero incidence results.

Similar strong leading edge vortex effects are observed also at Mach 0.9 at inner wing sections in the upper side pressure distribution.

The strong increase of the outer wing trailing edge pressures compared to zero incidence results observed at  $\alpha = 8.0$  deg. upper side gives an indication of an increase in mode excitation if the behaviour is extrapolated to pressure for outboard flap rotation.

Conclusions from quasisteady pressures:

- A very strong nonlinear behaviour of quasisteady pressure distributions at wing upper side with static incidence is observed both for Mach 0.8 and Mach 0.9. The lower side pressures are less affected by static incidence and remain almost unaffected from 6.5 degrees on.

- Outer wing trailing edge pressures show an increase compared to zero incidence results, indicating higher excitation forces if extrapolated for instance to outboard flap rotation both for  $M = 0.8$  and  $M = 0.9$  and incidences greater than zero.

5.4 DESCRIPTION OF MEASURED UNSTEADY PRESSURE DISTRIBUTION DUE TO HARMONIC WING ROLL OSCILLATIONS5.4.1 MACH 0.8 RESULTS

The pressure distributions due to harmonic wing roll are demonstrated for the upper and lower side of the wing in real and imaginary part of the unsteady pressure upper side in fig. 8.

$$c_{pu}(x, y, k) = c_{pu}(x, y, k) + i c_{pi}(x, y, k)$$

( $\cdot$ )' and ( $\cdot$ )'' for real and imaginary part  
 $k = 2\pi f s/V$  reduced frequency ( $s = 0.821$  m)  
 $f = 10$  Hz.

Static incidence 8.0 degrees

Strong nonlinear effects with incidence are found in general for the inner upper wing leading edge corresponding to leading edge vortex effects and also for the outer wing sections strong  $\alpha$  dependent effects occur in the real and imaginary part of the unsteady pressures. The lower side pressure distributions are less influenced. Only one example is demonstrated here for 8.0 degrees and Mach 0.8.

Conclusions of the unsteady results

- Similar strong nonlinear effects with static incidence as observed for quasisteady pressures are present in unsteady upper side pressures due to harmonic wing roll oscillations. The modulus of the unsteady pressures is increased at incidences 3.5 to 8.0 degrees at the inner wing leading edge region and at the trailing edge outer wing region in real and imaginary part. The lower side unsteady pressures are less affected by static incidence.

#### 5.4.2 MACH 0.3 RESULTS

The unsteady pressure distributions due to the wing roll oscillation were evaluated for different static incidences from  $\alpha = 12.5$  up to 40 degrees and roll motion frequencies 6, 12 and 18 Hz for the clean wing configuration for wing upper and lower side. Some results are shown in fig. 8 and 9 for 12.5 degrees and 25 degrees.

##### Influence of frequency

The imaginary part of the upper side pressure distribution changes almost linearly with frequency in the measured frequency range 6 - 18 Hz. All typical leading edge vortex effects are repeated with different frequency for different high static incidences.

##### Influence of static incidences

The increase in the amplitude of the upper side outer wing imaginary parts of the pressure distribution at high incidence compared to zero incidence or linear theory gives indication of an increase in elastic model damping at least for the first wing elastic bending mode.

There is also the indication that the aerodynamic damping of elastic modes will be present up to 40 degrees of incidence, since all imaginary parts of the pressure distribution for all high  $\alpha$  conditions up to 40 degrees are of significant amplitude and increase linearly with frequency. Therefore no loss of damping may be expected also for other modes than the rigid wing roll mode.

But higher mode excitation due to an inboard / outboard flap rotation might be expected due to the increase of trailing edge real and imaginary pressures found at all high incidences.

#### 5.6 GENERALIZED AERODYNAMIC FORCES AT HIGH INCIDENCE

Two aerodynamic magnitudes are essential for the aeroservoelastic stability namely:

1. The generalized control surface efficiencies
2. The aerodynamic mode damping

For the structural configuration treated the generalized aerodynamic damping of the low frequency elastic total aircraft modes and the generalized inboard and outboard flap/aileron unsteady efficiencies will cause the most interesting coupling effects in flight.

In order to clarify the influence of the static incidence on the control surface efficiencies and mode dampings comparisons are demonstrated in tables 2 to 17 showing theoretical values indicated by ( $\alpha = 0$  deg) and corresponding corrected values for  $\alpha = 25$  degrees at Mach 0.4 and for Mach 0.8 and 0.9 at  $\alpha = 6.5$  and 8 degrees.

##### Control surface efficiencies:

For Mach 0.4 both for the inboard and outboard flap the correction causes in general an increase in the magnitude of the real part of the control surface efficiencies of about 10% - 48% of the theoretical value depending on the normal mode, see table 2 to 4. The unsteady hinge moments of outboard flap is strongly increased by about 35%. The imaginary parts of the efficiencies are also strongly changed.

The effects on unsteady outboard efficiencies are even higher at Mach 0.8  $\alpha = 6.5$  and 8 degrees as demonstrated in table 7 to 10. Factors up to 1.7 are present depending on the mode. The effects are smaller at Mach 0.9  $\alpha = 7.5$  deg, factors up to 1.35 are found compared to linear theory, see table 16.

##### Aerodynamic mode damping

Comparison of corrected and theoretical generalized forces for the first and second elastic mode are shown in table 5, 6 for Mach 0.4, in table 11, 12, 13 and 14 for Mach 0.8 and in table 15, 16, 17 for Mach 0.9.



At Mach 0.4, 25 deg the imaginary part of the second elastic mode is increased by a factor of 1.25.

At Mach 0.8, 6.5 degrees the imaginary part of the second elastic mode is increased by a factor of 1.7 (table 13), at Mach 0.8, 8 degrees the factor is also 1.7 (table 14).

At Mach 0.9, 7.5 degrees the imaginary part of the second elastic mode is increased by a factor of 1.3.

It is noted that the aerodynamic mode damping is proportional to the imaginary part of the generalized force.

## 6. PROOF OF THE PREDICTION METHOD

The validation of the prediction method has been performed earlier in ref. 2 and 3 using windtunnel measurements on a trapezoidal wing.

The corrected pressure distribution  $\Delta \bar{c}_p$  of a not measured mode  $j$  is predicted from a measured mode  $i$  according to chapter 5.1

$$\Delta \bar{c}_p(i\omega)_j = \Delta c_p(i\omega)_{th} + \{\Delta c_{p_i}(i\omega) - \Delta c_{p_i}(i\omega)\} \frac{\alpha_j(i\omega)}{\alpha_i(i\omega)}$$

where

- $\Delta c_p(i\omega)_j$  pure theoretical pressure of the not measured mode  $j$
- $\Delta c_p(i\omega)_i$  pure theoretical pressure of the measured mode  $i$
- $\Delta c_p(i\omega)_{exp}$  experimental pressure of the measured mode  $i$
- $\alpha_j(x, y, i\omega)$  incidence distribution of the not measured mode  $j$
- $\alpha_i(x, y, i\omega)$  incidence distribution of the measured mode  $i$
- $\Delta \bar{c}_p(i\omega)_j$  corrected pressure distribution of the not measured mode  $j$

The windtunnel measurements on the trapezoidal wing have been performed for a pitch and roll motion, see fig. 11.

For instance the corrected (predicted) pressure distribution of a pitch oscillation from a roll oscillation is

$$\begin{aligned} \Delta \bar{c}_{p_{pitch}}(i\omega) &= \Delta c_{p_{pitch}}(i\omega) + \Delta c_{p_{D1}}(i\omega) \frac{1+ik(x-x_D)}{iky} \\ \Delta c_{p_{D1}} &= \Delta c_{p_{roll}}_{exp} - \Delta c_{p_{roll}} \end{aligned}$$

or the corrected pressure distribution of a roll oscillation from a pitch oscillation is

$$\begin{aligned} \Delta \bar{c}_{p_{roll}}(i\omega) &= \Delta c_{p_{roll}}(i\omega) + \Delta c_{p_{D2}}(i\omega) \frac{iky}{1+ik(x-x_D)} \\ \Delta c_{p_{D2}} &= \Delta c_{p_{pitch}}_{exp} - \Delta c_{p_{pitch}} \end{aligned}$$

Fig. 11 demonstrates the comparison between theoretical and measured results of a wing roll motion with predicted pressures from wing pitch motion pressures. The result fully validates the correction method for subsonic speeds.

$$\begin{aligned} \Delta \bar{c}_p &= [D' + iD'']^{-1} \alpha_j^* - \Delta c_{p_i} - \Delta c_{p_i}^* \\ \alpha_j^* &= \frac{U_\infty + u}{U_\infty} \frac{f_j}{x} + ikf_j + \frac{v_\infty}{U_\infty} \frac{f_j}{y} \end{aligned}$$

is simplified because the influences of local velocity components were shown to be of minor influence for low subsonic flow.

The validation the method using transsonic model results could not be performed in a consistent manner for high subsonic speeds since only one vibration mode, wing roll was tested.

In order to check the prediction at high Machnumber quasisteady results have been applied in order to predict unsteady pressures from TRF wing roll measurements.

Using quasisteady pressures for the prediction of transonic model unsteady wing roll results was based on a reduced formula

$$\Delta c_{p_{roll}}(\alpha, \kappa) = \Delta c_{p_{roll}}^{Theory} + [\Delta c_{p_{exp}}(\alpha, \kappa = 0) - \Delta c_{p_{exp}}^{Theory}(\kappa = 0)] * i\kappa$$

where

$\Delta c_{p_{exp}}(\alpha, \kappa = 0)$  = measured quasisteady pressure distribution

$\Delta c_{p_{exp}}^{Theory}(\kappa = 0)$  = theoretical pressure distribution

The comparison of measured unsteady pressures of the transonic model wing roll motion with this prediction at Mach 0.8 and Mach 0.9 also demonstrated an improvement especially at the wing tip region.

## 7. OPEN LOOP FREQUENCY RESPONSE FUNCTIONS

The effects of high incidence unsteady aerodynamic forces on gain and phase margins are illustrated in fig. 12 and 13 for the open loop response function of the longitudinal controller of the Delta Canard fighter aircraft for Mach 0.4, 25 degrees and sea level.

Fig. 12 shows the Nichols diagram with and without corrected aerodynamics in the frequency range up to the third elastic mode. As expected from the aerodynamic forces in tables 1 to 6 there are small influences on the open loop gain and on the phase. The phase at around the second elastic mode is increased up to 15 degrees, gain difference up to 1.5 dB are observed.

The first elastic mode is shown to be phase stable, whereas the second mode at 4.5 Hz does not meet the stability requirements indicated by the shaded area.

The same frequency response functions are depicted in Bode diagrams in fig. 13 for frequencies up to 30 Hz. Depending on the elastic mode there are increases in the modulus up to 3 dB due to effects of high  $\alpha$  aerodynamics present.

In fig. 14 the results for Mach 0.8 and 8 degrees of incidence are illustrated without and with corrected unsteady aerodynamic forces in the Nichols diagram. For corrected and pure theoretical unsteady aerodynamic forces the results show a phase stable first and second elastic mode.

The third mode at 5.5 Hz does not meet the requirements with and without the effect of high incidence aerodynamics, but with incidence correction a reduction of the positive dB's is present. For higher elastic modes at 9 and 12 Hz the effect is about a 4 dB increase as demonstrated in the Bode diagram in fig. 15.

## 8. CONCLUSIONS

From the investigation of the aeroservoelastic behaviour of a Delta Canard configuration at high incidence the following conclusion can be drawn:

1. The structural coupling of low frequency elastic modes caused by pitch rate feedback can not be influenced by sensor positioning nor by notch filtering. The low frequency modes must be phase stable.
2. The effects of high incidence unsteady aerodynamics on the open loop characteristics of low frequency elastic modes are small, though the strong increases in the excitation caused by the unsteady control surface efficiencies are predicted (factors up to 1.7). The increase in aerodynamic elastic mode damping with incidence effects may have reduced the increase in mode excitation.
3. The effects of high incidence unsteady aerodynamics on higher frequency elastic modes are considerably big. Increases up to 4.5 dB in the open loop frequency response are possible.
4. The prediction method for high incidence unsteady aerodynamics is validated by windtunnel tests.
5. The validation of the prediction method by flight tests is outstanding.
6. High incidence aerodynamic effects have to be considered in aeroservoelastic stability predictions.

**9. REFERENCES**

1. J. Becker  
Bewegungsinduzierte Luftkräfte bei abgelöster Strömung und ihre Übertragung auf die Ermittlung der Strukturresponse  
1983
2. J. Becker , F. Weiß, U. Weitz  
Prediction of unsteady aerodynamic forces at static incidence  
MBB/LKE292/S/R/1570, March 1986
3. Zingel, H.  
Experimental Investigation and Semiempirical Prediction of a low Aspect Ratio Trapezoidal Wing Due to Flow Separation.  
AGARD-Specialists Meeting on Aircraft Dynamic Loads Due to Flow Separation  
Sorrento, Italy, 1990
4. J. Becker, A. Gravelle  
Some results of experimental and analytical buffeting investigations on a Delta wing.  
Second International Symposium on Aeroelasticity and Structural Dynamics  
April 1-3 1985, Aachen



FIG. 1 AIRCRAFT CONFIGURATION

TABLE 1: GAIN AND PHASE MARGIN REQUIREMENTS (DB, DEGREES)

Mode Frequency Hz	Winged	Below $V_{DMIN}$	$V_{DMIN}$ To $V_{DMAX}$	At Limit Angled ( $V_L$ )	At 1.15 $V_L$
$f_M < 0.06$		GM = +5.0 (No Phase Requirement Below $V_{DMIN}$ )	GM = +4.5 PM = +30	GM = +3.0 PM = +20	GM = 0 PM = 0 (Stable at Nominal Phase and Gain)
$0.06 \leq f_M < f_{M1}$	< First Aero-Elastic Mode		GM = +5.0 PM = +45	GM = +4.5 PM = +30	
$f_M > f_{M1}$	> First Aero-Elastic Mode		GM = +8.0 PM = +60	GM = +6.0 PM = +45	

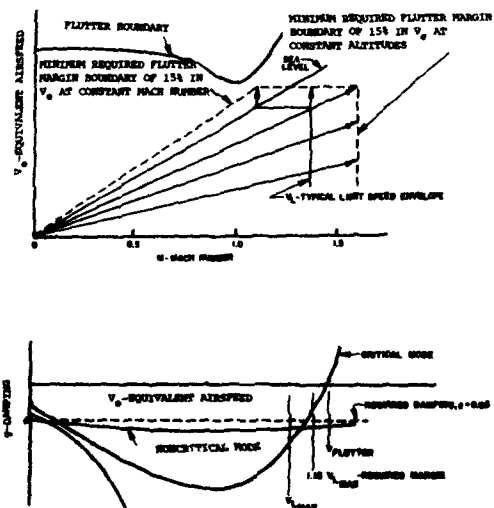
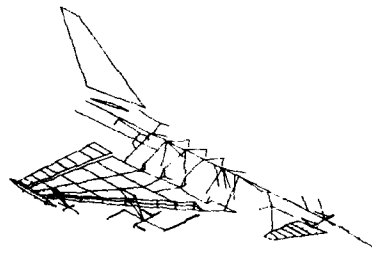
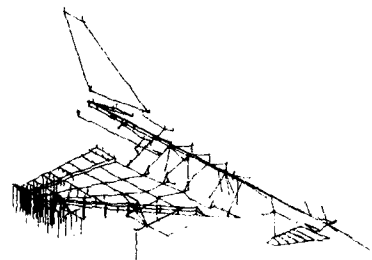


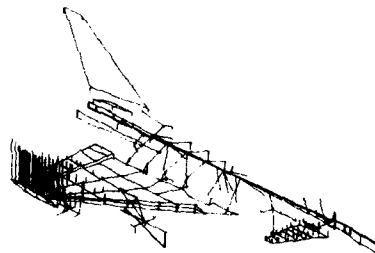
FIG. 2 MINIMUM REQUIRED FLUTTER MARGIN AND REQUIRED DAMPING



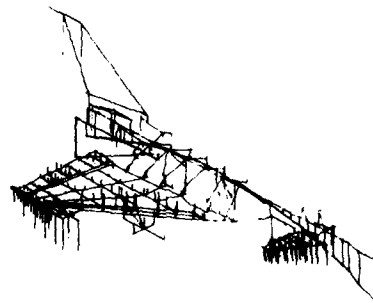
FIRST ELASTIC MODE: TANK YAW, 3.5 Hz



SECOND ELASTIC MODE: WING BENDING / TANK ROLL, 4.5 Hz

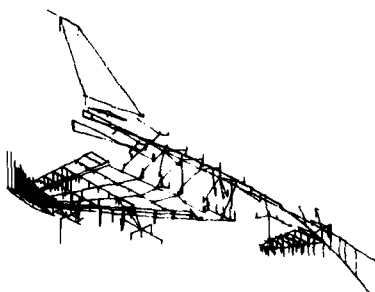


THIRD ELASTIC MODE: WING BENDING / TANK PITCH, 5.4 Hz



FOURTH ELASTIC MODE: FUSELAGE BENDING / ENGINE PITCH, 10.8 Hz

FIG. 3 NORMAL MODE SHAPES



FIFTH ELASTIC MODE, 14.0 Hz

FIG. 3 CONT'D.: NORMAL MODE SHAPES



FIG. 4 MODEL

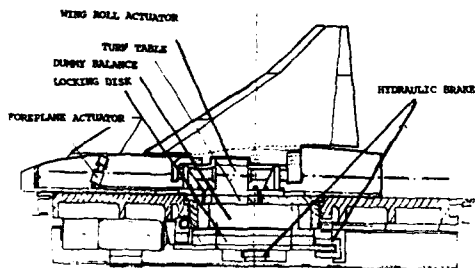


FIG. 5 MODEL SET UP

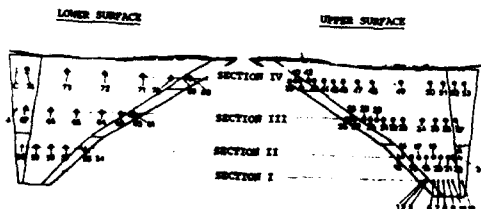
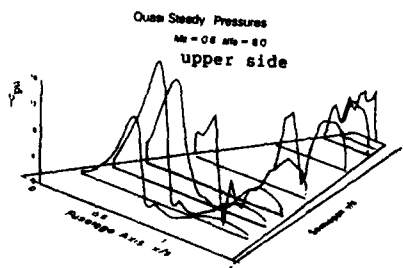
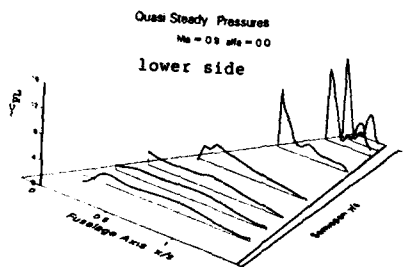
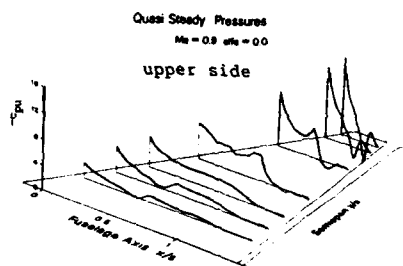
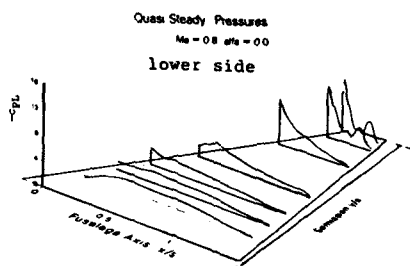
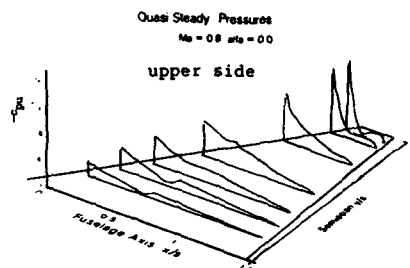


FIG. 6 PRESSURE PICK UP LOCATION

FIG. 7 QUASISTEADY PRESSURES AT UPPER AND LOWER SIDE, MACH 0.8, 0.9  
 $\alpha = 0$  deg,  $\alpha = 8$  deg

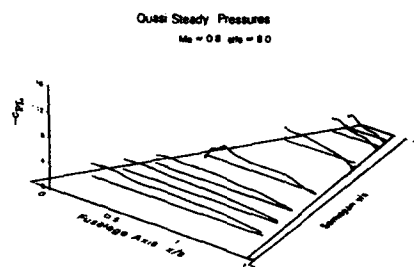


FIG. 7 CONTINUED

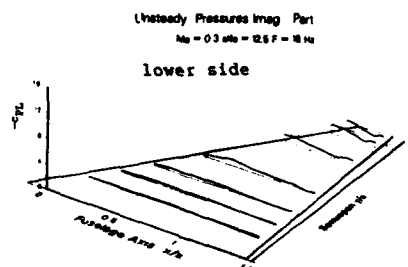
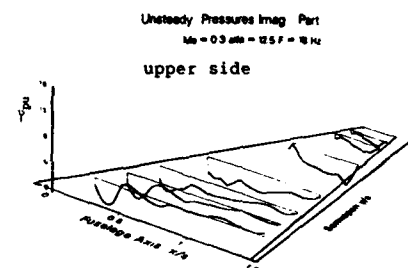
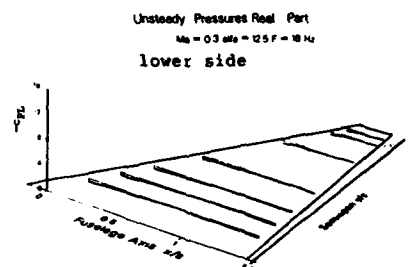
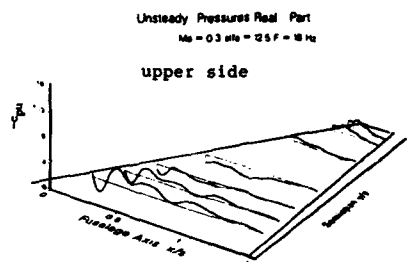
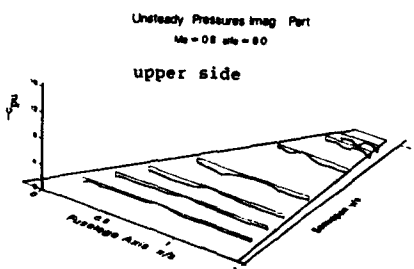
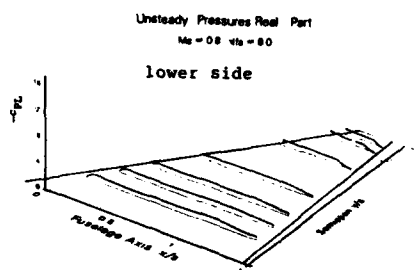
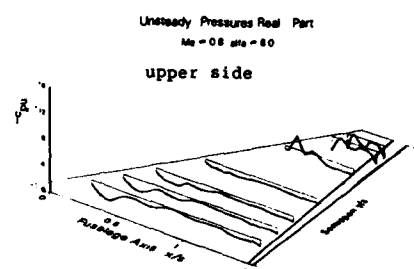


FIG. 8 UNSTEADY PRESSURES DUE TO HARMONIC WING ROLL MOTION AT UPPER AND LOWER SIDE,  $M_\infty = 0.8$ ,  $\alpha = 8.0$  DEG., REDUCED FREQUENCY  $k = 0.20$

FIG. 9 UNSTEADY PRESSURES DUE TO HARMONIC WING ROLL MOTION AT UPPER AND LOWER SIDE,  $M_\infty = 0.3$ ,  $\alpha = 12.5$  DEG., REDUCED FREQUENCY  $k = 0.94$

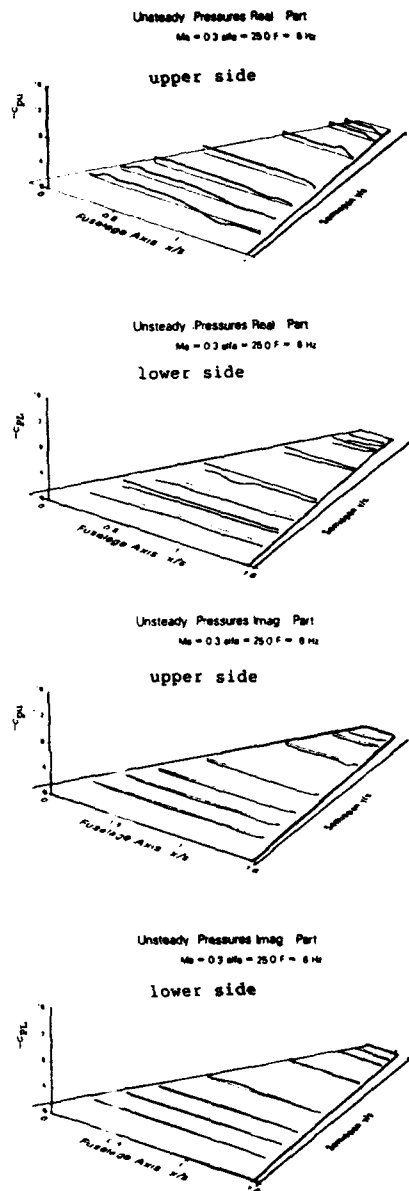


FIG. 10 UNSTEADY PRESSURES DUE TO HARMONIC WING ROLL MOTION AT UPPER AND LOWER SIDE,  $M_0 = 0.3$ ,  $\alpha = 25 \text{ DEG.}$ , REDUCED FREQUENCY  $k = 0.31$

$H = 0.4 \quad h = 0.5$

GENERALIZED EFFICIENCIES OF OUTBOARD FLAP

MODE $n^*$	REAL PART		IMAGINARY PART	
	$C'_{\alpha/\beta q_1} (\alpha = 0 \text{ deg})$	$C'_{\alpha/\beta q_1} (\alpha = 25 \text{ deg})$	$C''_{\alpha/\beta q_1} (\alpha = 0 \text{ deg})$	$C''_{\alpha/\beta q_1} (\alpha = 25 \text{ deg})$
1	-0.0008499	-0.0009568	0.0008781	0.001124
2	-0.01619	-0.01822	-0.001303	0.002527
3	0.03963	0.04537	0.001644	-0.00060
4	-0.02834	-0.03207	-0.0006112	0.004546
5	-0.01484	-0.01694	-0.0005380	0.003551
6	-0.03438	-0.03990	-0.002498	0.005612
7	0.009017	0.00975	-0.0004296	-0.001712
8	0.01971	0.02248	0.001071	-0.003454
9	-0.00908	-0.01031	0.0002790	0.001125
10	-0.02713	-0.03123	-0.002336	0.004791
$\bar{K}_{\alpha/\beta}$ (BENDING MOMENT)	0.003764	0.005056	0.0004353	-0.002454

TABLE 2 COMPARISON OF CORRELATED WITH THEORETICAL CORREL. EFFICIENCIES OF OUTBOARD FLAP

$H = 0.4 \quad h = 1.5$

GENERALIZED OUTBOARD FLAP EFFICIENCIES

MODE $n^*$	REAL PART		IMAGINARY PART	
	$C'_{\alpha/\beta q_1} (\alpha = 0 \text{ deg})$	$C'_{\alpha/\beta q_1} (\alpha = 25 \text{ deg})$	$C''_{\alpha/\beta q_1} (\alpha = 0 \text{ deg})$	$C''_{\alpha/\beta q_1} (\alpha = 25 \text{ deg})$
1	-0.000800	-0.000896	-0.0006435	0.0004604
2	-0.015294	-0.01753	-0.0038544	0.0084772
3	0.038190	0.04456	0.006633	-0.001311
4	-0.02682	-0.03096	-0.0037082	0.001360
5	-0.01422	-0.01656	-0.002371	0.000506
6	-0.03458	-0.03987	-0.000854	0.00125
7	0.008023	0.00868	0.001454	-0.001071
8	0.01916	0.02229	0.003847	-0.005162
9	-0.009011	-0.00942	-0.000525	0.000796
10	-0.02721	-0.03109	-0.006839	0.000037
$\bar{K}_{\alpha/\beta}$ (BENDING MOMENT)	0.003705	0.005263	0.001396	-0.001418

TABLE 3 COMPARISON OF CORRELATED WITH THEORETICAL GENERALIZED EFFICIENCIES OF OUTBOARD FLAP

$H = 0.4 \quad h = 0.5$

GENERALIZED EFFICIENCIES OF INBOARD FLAP

MODE $n^*$	REAL PART		IMAGINARY PART	
	$C'_{\beta/\alpha q_1} (\alpha = 0 \text{ deg})$	$C'_{\beta/\alpha q_1} (\alpha = 25 \text{ deg})$	$C''_{\beta/\alpha q_1} (\alpha = 0 \text{ deg})$	$C''_{\beta/\alpha q_1} (\alpha = 25 \text{ deg})$
1	-0.0002831	-0.0001365	0.00009735	-0.00006445
2	-0.005159	-0.004140	-0.001024	-0.0009053
3	0.01345	0.01530	-0.0006175	-0.001787
4	-0.006537	-0.003362	0.001938	-0.001289
5	-0.005928	-0.006617	-0.0003839	-0.0008754
6	-0.005234	-0.01025	-0.001458	-0.0003008
7	0.000637	0.007810	-0.001241	0.003484
8	0.01412	0.02093	0.0000039	0.00184
9	-0.01375	-0.01784	0.0002488	-0.001795
10	-0.03540	-0.06059	-0.004912	0.003575
$\bar{K}_{\beta/\alpha}$ (BENDING MOMENT)	0.003663	0.007671	0.001277	-0.005514

TABLE 4 COMPARISON OF CORRELATED WITH THEORETICAL CORREL. EFFICIENCIES OF INBOARD FLAP

$H = 0.4 \quad h = 0.5$

GENERALIZED AIRFOIL FORCES OF FIRST ELASTIC MODE

MODE $n^*$	REAL PART		IMAGINARY PART	
	$C'_{11} (\alpha = 0 \text{ deg})$	$C'_{11} (\alpha = 25 \text{ deg})$	$C''_{11} (\alpha = 0 \text{ deg})$	$C''_{11} (\alpha = 25 \text{ deg})$
1	-0.0001433	-0.0001360	0.00002274	0.00000050
2	-0.0001537	-0.0001716	0.00000082	0.00000041
3	0.0001892	0.0002074	-0.00000100	-0.00000046
4	-0.0003493	-0.0003744	0.00000429	0.00000463
5	-0.00009616	-0.0001288	0.000002141	0.000002049
6	0.0001343	0.0001706	-0.00000093	-0.000000757
7	0.0002138	0.0002540	-0.00000094	-0.000000711
8	0.0000945	0.0001280	0.000001851	-0.000002852
9	-0.0002498	-0.0003587	0.00000016	0.00000063
10	-0.00007518	-0.0001635	-0.00000049	-0.000000595

TABLE 5 COMPARISON OF CORRELATED WITH THEORETICAL GENERALIZED FORCES OF MODE 1



$H = 0.4 \quad h = 0.5$

GENERALIZED AIRFOIL FORCES OF 2ND ROW

ROW #	REAL PART		IMAGINARY PART	
	$C'_{x1} (\alpha = 0 \text{ deg})$	$C'_{x1} (\alpha = 25 \text{ deg})$	$C'_{y1} (\alpha = 0 \text{ deg})$	$C'_{y1} (\alpha = 25 \text{ deg})$
1	-0.0003953	-0.0003172	0.0005380	0.0006188
2	-0.0005247	-0.0004805	0.000267	0.000184
3	0.000979	0.000919	-0.001821	-0.001871
4	-0.0006367	-0.0006923	0.001117	0.001403
5	-0.0004031	-0.0004330	0.000426	0.000523
6	0.0001672	0.0001387	-0.0003934	-0.000602
7	0.0007172	0.000705	-0.0004710	-0.000451
8	0.0005312	0.0007595	-0.0003275	-0.000673
9	-0.0007878	-0.000668	0.000451	0.00036
10	-0.0005874	-0.001742	-0.0002293	0.000216

TABLE 6 COMPARISON OF COMPUTED AND THEORETICAL GENL. FORCES OF ROW 2

$H = 0.8 \quad h = 0.5$

GENERALIZED EFFICIENCIES OF OUTBOARD FLAP ( $\alpha = 6.5 \text{ deg}$ )

ROW # $e_1$	REAL PART		IMAGINARY PART	
	$C'_{xx/bq_1} (\alpha = 0 \text{ deg})$	$C'_{xx/bq_1} (\alpha = 6.5 \text{ deg})$	$C'_{xy/bq_1} (\alpha = 0 \text{ deg})$	$C'_{xy/bq_1} (\alpha = 6.5 \text{ deg})$
1	-0.0009317	-0.001067	0.0001101	-0.000565
2	-0.01875	-0.02213	0.000923	-0.01562
3	0.04882	0.05876	-0.0003468	0.04917
4	-0.03284	-0.03874	0.00138	-0.02867
5	-0.01815	-0.02203	0.0002494	-0.01849
6	-0.01978	-0.04491	-0.001938	0.05477
7	0.009150	0.01154	-0.002323	0.00637
8	0.02580	0.03235	0.0004247	0.02956
9	-0.01115	-0.01385	0.002040	-0.00594
10	-0.04002	-0.05068	-0.002449	-0.04942
$\bar{C}_{x/b}$ (REFERENCE)	0.005103	0.00997	0.00675	0.02952

TABLE 7 COMPARISON OF COMPUTED WITH THEORETICAL OUTBOARD FLAP GENERALIZED EFFICIENCIES

$H = 0.8 \quad h = 0.5$

GENERALIZED EFFICIENCIES OF OUTBOARD FLAP ( $\alpha = 8 \text{ deg}$ )

ROW # $e_1$	REAL PART		IMAGINARY PART	
	$C'_{xx/bq_1} (\alpha = 0 \text{ deg})$	$C'_{xx/bq_1} (\alpha = 8 \text{ deg})$	$C'_{xy/bq_1} (\alpha = 0 \text{ deg})$	$C'_{xy/bq_1} (\alpha = 8 \text{ deg})$
1	-0.0009317	-0.001363	0.0001101	-0.000651
2	-0.01875	-0.02937	0.000923	-0.01832
3	0.04882	0.07987	-0.0003468	0.05653
4	-0.03284	-0.05187	0.00138	-0.03309
5	-0.01815	-0.02990	0.0002494	-0.02132
6	-0.01978	-0.06651	-0.001938	-0.06235
7	0.009150	0.01490	-0.002323	0.00782
8	0.02580	0.04411	0.0004247	0.03420
9	-0.01115	-0.01628	0.002040	-0.007496
10	-0.04002	-0.06932	-0.002449	-0.05697
$\bar{C}_{x/b}$ (REFERENCE)	0.005103	0.01675	0.00675	0.03353

TABLE 8 COMPARISON OF COMPUTED WITH THEORETICAL OUTBOARD FLAP GENERALIZED EFFICIENCIES

$H = 0.8 \quad h = 1.5$

GENERALIZED EFFICIENCIES OF OUTBOARD FLAP ( $\alpha = 6.5 \text{ deg}$ )

ROW # $e_1$	REAL PART		IMAGINARY PART	
	$C'_{xx/bq_1} (\alpha = 0 \text{ deg})$	$C'_{xx/bq_1} (\alpha = 6.5 \text{ deg})$	$C'_{xy/bq_1} (\alpha = 0 \text{ deg})$	$C'_{xy/bq_1} (\alpha = 6.5 \text{ deg})$
1	-0.0007290	-0.0008999	0.0000683	-0.0008281
2	-0.01654	-0.02054	0.0000076	-0.01717
3	0.04639	0.05227	-0.000236	0.05252
4	-0.02914	-0.03256	-0.0007795	-0.03144
5	-0.01681	-0.01914	-0.0000574	-0.01977
6	-0.03706	-0.04370	-0.007280	-0.05908
7	0.00931	0.00948	-0.001640	0.00723
8	0.02519	0.02933	0.0006123	0.0303
9	-0.007004	-0.00908	0.002016	-0.00515
10	-0.04190	-0.04895	-0.000263	-0.04815
$\bar{C}_{x/b}$ (REFERENCE)	0.005103	0.007207	0.001325	0.02221

TABLE 9 COMPARISON OF COMPUTED WITH THEORETICAL OUTBOARD FLAP GENERALIZED EFFICIENCIES

$H = 0.8 \quad h = 1.5$

GENERALIZED EFFICIENCIES OF OUTWARD FLAP ( $\alpha = 8$  deg)

MODE $n_{e1}$	REAL PART		IMAGINARY PART	
	$C'_{1e/n_{e1}} (\alpha = 8 \text{ deg})$	$C'_{2e/n_{e1}} (\alpha = 8 \text{ deg})$	$C''_{1e/n_{e1}} (\alpha = 8 \text{ deg})$	$C''_{2e/n_{e1}} (\alpha = 8 \text{ deg})$
$j = 1$	-0.007290	-0.001899	0.0000663	-0.0007500
2	-0.01654	-0.02560	-0.0000076	-0.02024
3	0.04639	0.07282	0.002316	0.06155
4	-0.02914	-0.04537	-0.0007795	-0.03608
5	-0.01681	-0.02666	-0.0006574	-0.02325
6	-0.03706	-0.06474	-0.007280	-0.06412
7	0.005031	0.009737	-0.001640	0.00090
8	0.02519	0.04075	0.0006123	0.03598
9	-0.007806	-0.01221	0.003016	-0.00694
10	-0.04190	-0.06672	-0.000163	-0.05727
$\lambda_{e1}$ (EIGENVALUE)	0.005163	0.01472	0.001925	0.02595

TABLE 10 COMPARISON OF CORRECTED WITH THEORETICAL OUTWARD FLAP GENERALIZED EFFICIENCIES AT  $H = 0.8, h = 1.5, \alpha = 8$  DEG

$H = 0.8 \quad h = 0.5$

GENERALIZED AERODYN. FORCES OF FIRST ELASTIC MODE

MODE $n_{e1}$	REAL PART		IMAGINARY PART	
	$C'_{11} (\alpha = 8 \text{ deg})$	$C'_{21} (\alpha = 8.5 \text{ deg})$	$C''_{11} (\alpha = 8 \text{ deg})$	$C''_{21} (\alpha = 8.5 \text{ deg})$
$j = 1$	-0.0001568	-0.0002837	0.00003361	0.0001523
2	-0.0001703	-0.0002943	0.00002838	0.0001063
3	0.0002131	0.0004135	0.000009668	0.0000525
4	-0.0002758	-0.0004718	-0.00004727	-0.0001946
5	-0.0001079	-0.0002160	0.000004113	0.0000233
6	0.0001450	0.0001073	-0.000008699	-0.0000450
7	0.0002390	0.000344	-0.00004396	-0.0002962
8	0.0001117	-0.000170	0.00002989	0.0000067
9	-0.0002826	-0.0006443	0.00002951	0.000268
10	0.0000267	-0.0002553	-0.0001317	-0.000259

TABLE 11 COMPARISON OF GENERALIZED AERODYNAMIC FORCES OF FIRST ELASTIC MODE AT  $H = 0.8, h = 0.5, \alpha = 6.5$  DEG

$H = 0.8 \quad h = 0.5$

GENERALIZED AERODYN. FORCES OF FIRST ELASTIC MODE

MODE $n_{e1}$	REAL PART		IMAGINARY PART	
	$C'_{11} (\alpha = 8 \text{ deg})$	$C'_{21} (\alpha = 8 \text{ deg})$	$C''_{11} (\alpha = 8 \text{ deg})$	$C''_{21} (\alpha = 8 \text{ deg})$
$j = 1$	-0.0001568	-0.0002067	0.00003361	0.00005762
2	-0.0001703	-0.0002078	0.00003258	-0.00003112
3	0.0002131	0.0005179	0.000009668	0.000223
4	-0.0002758	-0.0002289	0.00004727	0.0001287
5	-0.0001079	-0.0001962	-0.000004113	-0.00005679
6	0.0001450	0.000133	-0.000008699	-0.0003974
7	0.0002390	0.0003955	-0.00004396	-0.0001993
8	0.0001117	-0.0004609	0.00002989	0.000232
9	-0.0001816	-0.0006454	0.00002951	0.0000414
10	0.0000267	-0.0001441	-0.0001317	-0.0000895

TABLE 12 COMPARISON OF GENERALIZED AERODYNAMIC FORCES OF FIRST ELASTIC MODE AT  $H = 0.8, h = 0.5, \alpha = 8$  DEG

$H = 0.8 \quad h = 0.5$

GENERALIZED AERODYN. FORCES OF 2ND ELASTIC MODE

MODE $n_{e1}$	REAL PART		IMAGINARY PART	
	$C'_{22} (\alpha = 8 \text{ deg})$	$C'_{32} (\alpha = 8.5 \text{ deg})$	$C''_{22} (\alpha = 8 \text{ deg})$	$C''_{32} (\alpha = 8.5 \text{ deg})$
$j = 1$	-0.0000483	-0.0000319	0.00000174	0.000113
2	-0.0005704	-0.000084	0.0007545	0.00120
3	0.0000205	0.0001933	-0.0001176	-0.00066
4	-0.0000070	-0.000187	0.001175	0.00223
5	-0.0000627	-0.000770	0.000459	0.000732
6	0.000030	-0.00144	-0.000933	-0.00137
7	0.0007285	0.000000	-0.000037	0.00134
8	0.0000479	0.001540	-0.0001064	-0.000319
9	-0.0000045	-0.000995	0.0007964	0.00130
10	-0.0000134	-0.000319	-0.0002091	-0.00068

TABLE 13 COMPARISON OF GENERALIZED AERODYNAMIC FORCES OF SECOND MODE AT  $H = 0.8, h = 0.5, \alpha = 6.5$  DEG

$$R = 0.8 \quad k = 0.5$$

## GENERALIZED AIRSOPH. FORCES OF 2nd ELASTIC NODE

NODE $H^*$	REAL PART		IMAGINARY PART	
	$C'_{12} (\alpha = 0 \text{ deg})$	$C'_{12} (\alpha = 8 \text{ deg})$	$C''_{12} (\alpha = 0 \text{ deg})$	$C''_{12} (\alpha = 8 \text{ deg})$
1	-0.00004183	-0.00004028	0.00006174	0.00009879
2	-0.0005784	-0.001182	0.0007545	0.001279
3	-0.001565	-0.003109	-0.001125	-0.002028
4	-0.0009078	-0.001864	0.001279	0.002335
5	-0.0004627	-0.001205	0.000459	0.0007689
6	0.000610	-0.001868	-0.000533	-0.0005377
7	0.0007200	0.0008453	-0.000627	-0.0008769
8	0.0006679	0.002208	-0.0003566	-0.0001753
9	-0.0008845	-0.00147	0.0007964	0.0006049
10	-0.0009144	-0.004424	-0.0003991	-0.001867

TABLE 14 COMPARISON OF CORRECTED WITH THEORETICAL GENERALIZED AIRSOPH. FORCES OF SECOND NODE

GENERALIZED AIRSOPH. FORCES OF FIRST ELASTIC NODE  
(CORRECTED BY QUASISTATIONARY REQUIRED PRESSURES AT  $\alpha = 7.5 \text{ deg}$ )

NODE $H^*$	REAL PART		IMAGINARY PART	
	$C'_{101} (\alpha = 0 \text{ deg})$	$C'_{101} (\alpha = 7.5 \text{ deg})$	$C''_{101} (\alpha = 0 \text{ deg})$	$C''_{101} (\alpha = 7.5 \text{ deg})$
1	-0.0000185	0.000010406	0.00000429	-0.00000164
2	-0.0001793	0.0001033	0.00003133	-0.0000382
3	0.0002345	-0.00006217	0.000002205	0.0000759
4	-0.0002895	0.0001380	0.00006146	-0.00003738
5	-0.0001167	0.0000293	0.000001226	-0.00002627
6	0.0001113	-0.000316	-0.0001167	-0.00000848
7	-0.0002459	-0.0000737	-0.00000618	-0.000005276
8	+0.00013138	0.00001303	0.0000378	0.00000654
9	0.0001019	0.0001374	0.00004608	-0.0000524
10	-0.00001428	-0.0003077	-0.0001696	-0.000125

TABLE 15 COMPARISON OF CORRECTED WITH THEORETICAL GENERALIZED AIRSOPH. FORCES OF FIRST ELASTIC NODE

$$R = 0.9 \quad k = 0.5$$

GENERALIZED EFFICIENCIES OF OUTBOARD FLAP ( $\alpha = 7.5 \text{ deg}$ )  
(CORRECTED USING QUASISTATIONARY REQUIRED PRESSURES)

NODE $H^*$	REAL PART		IMAGINARY PART	
	$C'_{10/002} (\alpha = 0 \text{ deg})$	$C'_{10/002} (\alpha = 7.5 \text{ deg})$	$C''_{10/002} (\alpha = 0 \text{ deg})$	$C''_{10/002} (\alpha = 7.5 \text{ deg})$
1	-0.000895	-0.001171	0.000197	0.0001922
2	-0.01995	-0.026177	0.002267	0.002137
3	0.00556	0.07291	-0.002913	-0.002549
4	-0.03495 32%	-0.04647	0.003499	0.003257
5	-0.02042	-0.02867	0.001394	0.001262
6	-0.04516	-0.0614	-0.003887	-0.004242
7	0.007931	0.00998	-0.003563	-0.003520
8	0.03099	0.03678	-0.001666	-0.001301
9	0.01098	0.01167	0.00408	0.004066
10	-0.0527	-0.06367	0.00101	0.0007798
$\bar{E}_{1/2}$ (RANK HYPOTH)	0.50852	-0.50866	0.000917	0.000938

TABLE 16 COMPARISON OF CORRECTED WITH THEORETICAL OUTBOARD FLAP CORR. EFFICIENCIES

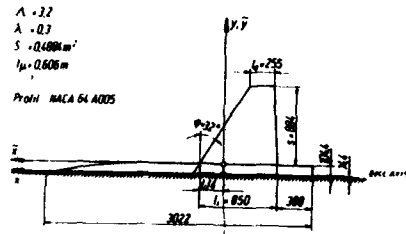
$$R = 0.9 \quad k = 0.5$$

GENERALIZED AIRSOPH. FORCES OF 2nd ELASTIC NODE  
(CORRECTED BY QUASISTATIONARY REQUIRED PRESSURES AT  $\alpha = 7.5 \text{ deg}$ )

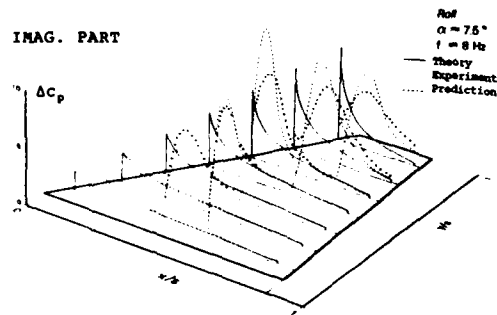
NODE $H^*$	REAL PART		IMAGINARY PART	
	$C'_{101} (\alpha = 0 \text{ deg})$	$C'_{101} (\alpha = 7.5 \text{ deg})$	$C''_{101} (\alpha = 0 \text{ deg})$	$C''_{101} (\alpha = 7.5 \text{ deg})$
1	-0.0000401	-0.0000399	0.0000681	0.000009514
2	-0.000590	-0.000748	0.000027	0.000111
3	-0.001190	-0.00237	-0.00117	-0.000456
4	-0.000918	-0.001227	0.001398	0.000360
5	-0.000498	-0.000846	0.000095	0.0002299
6	-0.0000688	-0.000458	-0.000025	0.000025
7	0.00044	0.000777	-0.000735	-0.000348
8	0.000733	0.001034	-0.000482	-0.000254
9	-0.000903	-0.000766	0.000917	-0.0000489
10	-0.001279	-0.00219	-0.000295	-0.000366

TABLE 17 COMPARISON OF CORRECTED WITH THEORETICAL CORR. AIRSOPH. FORCES OF 2nd ELASTIC NODE

19-18



IMAG. PART



REAL PART

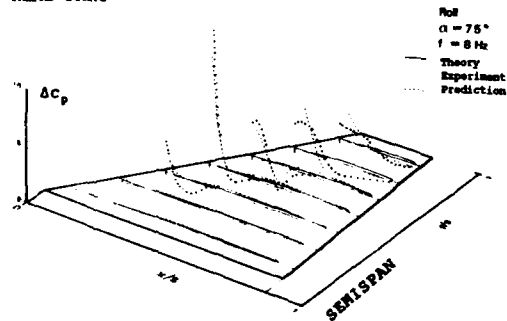
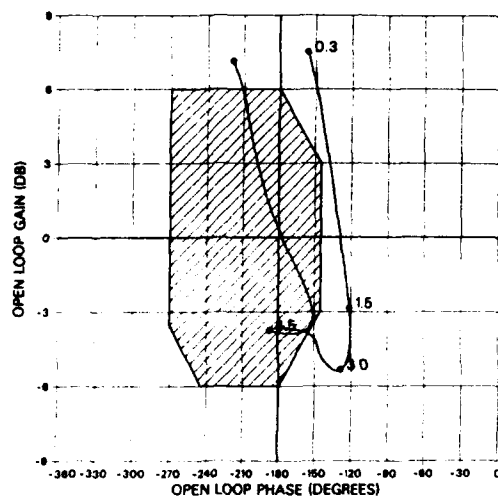
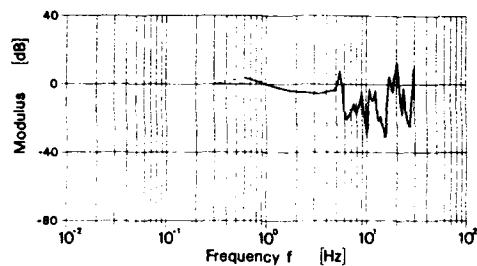


FIG. 11 VALIDATION OF THE CORRECTION  
 METHOD FOR HIGH INCIDENCE  
 DFL GÖTTINGEN TRAPEZOIDAL  
 WING WINDTUNNEL MEASUREMENT  
 OF UNSTEADY PRESSURES FOR WING  
 ROLL AND PITCH  
 - PREDICTION OF PRESSURES FROM  
 PITCH FOR ROLL

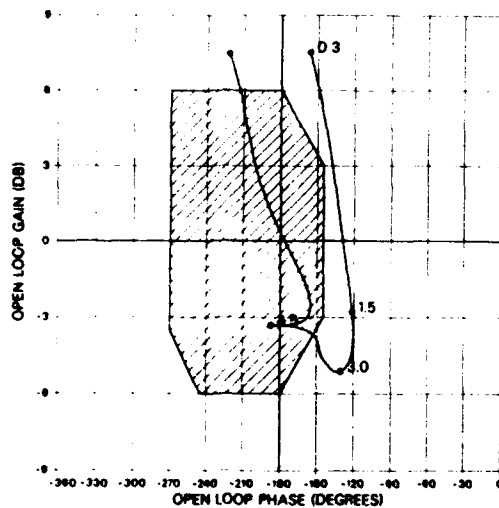
Altitude 0.m / Mach 0.4  
Theory



Altitude 0.m / Mach 0.4  
Theory



Plot No 2  
Altitude 0.m / Mach 0.4  
 $\alpha = 25 \text{ deg}$



Altitude 0.m / Mach 0.4  
 $\alpha = 25 \text{ deg}$

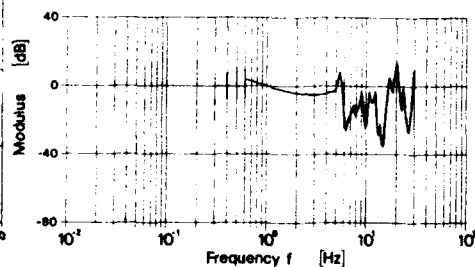


FIG. 12 NICHOLS DIAGRAM OF OPEN LOOP FREQUENCY RESPONSE  
COMPARISON OF RESULTS WITH AND WITHOUT (ABOVE) HIGH INCIDENCE AERODYN. EFFECTS  
MACH = 0.4,  $\alpha = 25 \text{ DEG}$ .

FIG. 13 BODE DIAGRAM OF OPEN LOOP FREQUENCY RESPONSE  
COMPARISON OF MODULUS WITH AND WITHOUT (ABOVE) HIGH INCIDENCE AERODYN. EFFECTS

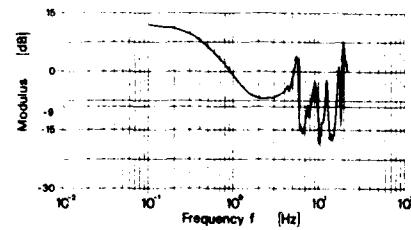
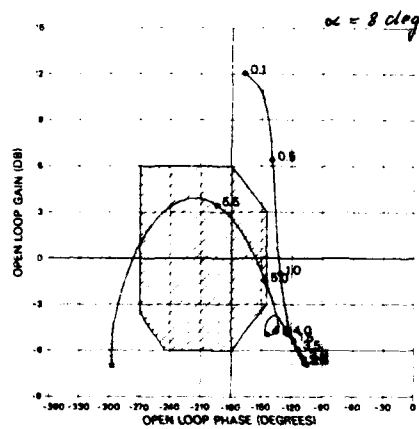
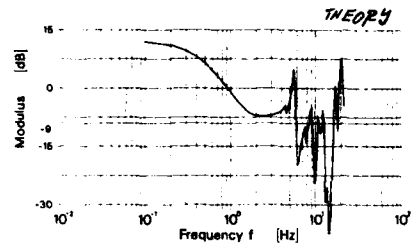
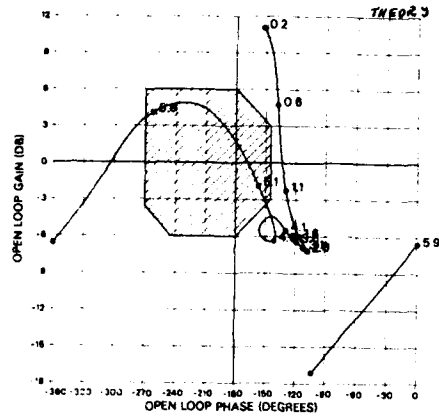


FIG. 14 NICHOLS DIAGRAM OF OPEN LOOP  
FREQUENCY RESPONSE  
COMPARISON OF RESULTS WITH AND  
WITHOUT (ABOVE) HIGH INCIDENCE  
ABSORPTION. EFFECTS  
NACH = 0.8,  $\alpha = 8$  deg

FIG. 15 BODE DIAGRAM OF OPEN LOOP  
FREQUENCY RESPONSE  
COMPARISON OF RESULTS WITH AND  
WITHOUT (ABOVE) HIGH INCIDENCE  
ABSORPTION. EFFECTS  
NACH = 0.8,  $\alpha = 8$  deg

## ROUND TABLE DISCUSSION

Dr. K.J. Orlik-Rückemann, Institute for Aerospace Research, Canada

As has become customary at FDP symposia, we will begin the round table discussion with the remarks of the Technical Evaluator. I would like to remind you that this is an exceptionally hard job to perform. The Technical Evaluator has to sit here for two days and try to absorb all the papers which are being presented. In this particular case, he has at the same time to present his own paper, and at the end of the two days he has to give us an assessment or whatever wise words he has for us more or less summarizing the meeting. It is a very tough act and I am very happy that Gerry Malcolm of Eidetics International has agreed to undertake this act. Without further ado I would like to ask him to tell us what his thoughts are about this meeting.

Mr. G.N. Malcolm, Eidetics International, USA

Probably what you would most like to hear is a suggestion that we just all go to dinner, but I have to earn my keep. When Kazik asked me to do this, I asked him what the requirements were and he was helpful but vague. I created my own job description which looks something like this. As Kazik said you have to (1) listen attentively to 19 papers in two days, (2) take copious notes, (3) remember all the key points, (4) condense all relevant facts into a 20 minute review, (5) don't leave anyone out, (6) stimulate discussion but don't offend anyone and (7) don't exceed your welcome and your time. The first two I have done, the middle four remain to be seen yet, and I to promise to take care of number 7.

The beginning of the Conference was opened with some very relevant comments by Kazik with regard to background and he suggested that we need to worry about a number of things related to flight at high angle of attack in non-zero sideslip, a flight regime that involves vortex flows, separated flows, and non-linear aerodynamics. We are talking about rapid angular motions which means time-lag effects, and dynamic effects that you have to be able to cope with, in terms of both measuring or estimating them. We must have an extended aero data base because of the fact that we now need to include dynamic terms as well as static terms. We must explore the potential need for enhanced aerodynamic controls where methods other than the conventional control systems will be required including thrust vectoring, forebody control, etc. He mentioned unorthodox configurations. I don't know if there are really any unorthodox configurations anymore, but we have three surface configurations, the X29 which is perhaps the most unorthodox with its forward swept wing, and many types of high fineness-ratio forebodies. Probably the bottom line is that we need to provide the means for better mathematical models, not only in terms of the experiments that we are performing, but how we integrate results from experiments into the math model for simulation and for the prediction of flight. We had papers grouped into three categories; five papers in the high angle of attack aerodynamics, eight papers under dynamic experiments where these two groups were quite closely related as you have seen and then five papers classified as stability and control oriented.

For my evaluation I attempted to do a couple of things. Since I don't consider myself to be a judge of any of the papers that have been presented, I thought I would try to stimulate an active Round Table Discussion and just show one or two comments from each of the papers that were presented, points that struck me as being of relative importance. These points may not be the same as what you consider to be important, but then at the end of my discussion I have a couple of pages of suggested topics and issues that you might want to discuss.

In the high angle of attack aerodynamics session we had essentially five papers, two of which were more or less combined dealing with the X31. We had one concerning large-amplitude motions on delta wings which was presented by Bob Nelson from Notre Dame dealing with some fundamental studies in a small-scale wind tunnel. Mr. Ferretti discussed methods for predicting aerodynamic phenomena and the limitations regarding aircraft manoeuvrability and Mr. Visintini presented a very nice study on parametric evaluations of effect of aircraft components on high alpha characteristics.

The points that I got out of these various discussions are as follows: With regard to the first paper on the X31, at high angles of attack approaching stall, the lateral directional stability and control degrades rapidly. The emphasis for agility is on an attained rather than sustained turn rate and also attained smaller turn radius. The degradation in directional and lateral stability obviates the need for yaw control power with increased angle of attack and increased ability to roll around the velocity vector. Thrust vectoring is, of course, one way to achieve this, and on the X31 that is one of the important parts of that airplane system for both pitch and yaw. Obviously, the X31 will provide a very good flight demonstration on post-stall technology, and we will all be anxious to see how this program progresses.

Paper number 2 deals with some fundamental work again by Bob Nelson where he looked at some simple wind tunnel experiments showing the importance of high amplitude unsteady aero effects both in pitch and roll high amplitude pitch and roll oscillations were studied including wing rock phenomena where he showed the importance of time lags and hysteresis and the particular importance of vortex breakdown and vortex position. It also illustrated the fundamental need for research on simple bodies in order to provide an understanding of the flow phenomena that we are dealing with. Paper number 3 was presented by Mr. Ferretti, and he emphasized the need to develop prediction techniques for a separated flow in the design stage, dealing both with conventional wing planforms and also highly swept planforms that are dominated by vortex flows.

Mr. Visintini from Aermachi discussed some of the work they have been doing looking at configuration-components contributions determined through model buildup wind tunnel tests with static and rotary-balance tests. He illustrated some of the difficulties including Reynolds number simulations with some very interesting results showing the effects of putting transition strips on the model, a topic that we will want to discuss a little bit more in the Round Table Discussion. Also, the coupling between the natural asymmetry that we see on these slender forebodies and the asymmetric flow conditions that are induced by non-zero sideslip and by rotation rate.

We had eight papers classified in the dynamic experiment session. We had a presentation by Gerry Jenkins and his co-author Ernest Hanff working on methods to represent non-linear airloads with a hypersurface model, which was really an analysis of the hypersurface approach in comparison to the indicial response in the time domain. This paper consists both of analytical work and some very important experiments that have gone on at IAR in Ottawa and will be continued in the SARL tunnel at Wright Patterson in the next month. We heard an interesting presentation by Cunningham from GD on some very detailed work that he has been doing with NLR looking at a pitching strake-wing model, measuring forces, pressures, and flow visualizations. It is a very detailed study looking at the combination of force and pressure data in conjunction with flow visualization. He had a unique display of the pressure and the flow visualization data which I think is very helpful in helping us to understand the nature of these dynamic flows. He also illustrated, as did a couple of other people, the phenomena of lift overshoots and undershoots.

Charles O'Leary presented some information on measuring acceleration derivatives both in heave and sideslip on an apparatus that he has developed at the RAE in Bedford. He is talking about considering whether we need to include alpha dot and beta dot effects at high angles of attack. His conclusion is that they can be quite large in the high angle of attack regime and that we cannot ignore them. He also showed, as Kazik mentioned in his remarks after that paper, that it was nice to see a good correlation between  $C_m$  alpha dot which was determined from oscillatory translation and  $C_m q$  plus  $C_m$  alpha dot which came from the forced oscillation in pitch and then a separate experiment for  $C_m q$  which was done with a whirling arm. The combination of those derivatives from different sources correlated quite well. The fourth paper also related to high-amplitude motions with a highly swept delta wing,  $60^\circ$  delta wing, and this was presented by Mr. Torlund from FAA in Sweden. He showed essentially normal-force and pitching-moment data with several different types of harmonic oscillations. He indicated that stepwise motions show very long time delays for vortex breakdown which we need to be concerned about. He also showed some comparisons between stepwise pitching and an unusual gust generator in the tunnel which allows you to evaluate alpha dot and  $q$  effects separately. The fifth paper in this session was presented by Mr. Rennier and dealt with unsteady aerodynamic phenomena at high angles of attack. He described a unique apparatus at Lille which I have had the pleasure of seeing. It is a rotary balance apparatus mounted in a spin tunnel that allows not only pure coning but also oscillatory coning experiments which no one else is really doing. He also described a new test facility which provides the capabilities for high-amplitude dynamic pitch or yaw motion. He then discussed some of the experiments they had done with sinusoidal and constant angular-rate motions at high rates.

The sixth paper was a presentation by David Thompson with his co-author Colin Martin from the Aeronautical Research Lab in Melbourne, Australia. They have been doing considerable work on the F/A-18 looking at the tail buffet problem from the standpoint of understanding the vortex flows by virtue of wind tunnel tests and water tunnel tests. They have looked at the effects of the Lex fence in water tunnel studies to try to understand what effect the fence has on the leading edge extension Lex vortices. They provided a correlation of the Lex vortex breakdown position with angle of attack looking at subscale models in the water tunnel, wind tunnel models and full-scale flight and showed a very good correlation that basically says that the vortex breakdown location is independent of Reynolds number. This is because of the sharp edge of the Lex. This correlation is encouraging to those of us that are doing a lot of studies in water tunnels for visualization as well as for quantitative measurements. He also showed the effect of inlet flow on the Lex burst location which several of us have also seen.

The seventh paper in this group was another presentation on the X-31 dealing primarily with the steady-state aerodynamics and rotary-derivative measurements. I just noted a few bullets here that I got from the conclusions. One was that the X-31 has positive pitching moment at all angles of attack below stall; it has good lateral directional static stability, well damped in roll and in yaw. Near stall, as you might expect, lateral stability is reduced, and it's propelling in roll without augmentation. However, the aileron control power can overcome the propelling rolling moment. Above  $45^\circ$  angle of attack, rudder is ineffective, and therefore one of the requirements to take care of this problem is thrust vectoring. They have identified only one spin mode, a flat spin at approximately  $86^\circ$  angle of attack which is well away from the operational envelope that they expect to fly; therefore, it doesn't appear to be a problem.

The last paper in this session was the presentation by Mr. Perkins on a parameter estimation technique that British Aerospace is using with an experimental airplane program which is called an equation error method. I couldn't follow the logic very closely, but apparently it has some advantages over the methods which are used by other people. The method is able to accommodate non-linear aerodynamic characteristics. It doesn't require a predefined aerodynamic math model. Part of the process of fitting flight test data is the determination of which coefficients are the important ones to keep. It does require extremely high accuracy flight test data. This is a requirement that is not peculiar to that method, but perhaps in some ways it is more important for this particular method.

We also had a session this afternoon on stability and control, and the first three papers in that session dealt with forebody vortex control. I discussed some of the work that Eidetics has been doing primarily on a generic fighter configuration and recent work on an FA-18 model looking at forebody strakes, blowing, and miniature rotatable tip strakes. Bob Guyton presented work that the Air Force has been involved in primarily on the X29A and the F16 and also a little bit of work on generic chine-shaped forebody configurations which are more appropriate perhaps for the next generation of airplanes.

Jean Ross presented a very nice paper on some work that she has done on forebody suction, again with the idea of controlling the forebody vortices and described a dynamic test technique which allows them to evaluate the suction technique in conjunction with the flight control system.

Finally, we had two invited papers which we just heard. One from Mr. Mangold in which he discussed how to transform flight mechanics requirements into aerodynamic coefficients and he discussed the need for departure criteria which not only include the usual static terms but some of the dynamic terms. We had some discussion here as you heard in terms of what should be included in those dynamic terms. Clearly, we need to include them at high angles of attack. The question is how do we determine what they are and



whether derivatives themselves are appropriate in view of the fact that we have large time-lag effects in some of the dynamic motions we discussed earlier. The last paper, by Mr. Becker, was on servoelectric stability of aircraft at high angles of attack. He discussed the method to predict the effects of non-linear incidence-dependent unsteady aero forces of the elastic modes of control surface deflections on structural couplings. A very complex subject and one which I am glad I am not involved in.

My final task was to attempt to keep track of some of the more interesting questions and try to generate a few of my own just based on discussions I have had with people here and with people before coming here. What I was going to suggest is that I just read through these. Kazik, do you want to lead off the Round Table Discussion once they have seen some of these questions on the viewgraph? They may not all create much discussion and some may create more than we want to have. One thing that was brought home with Livio Visintini's paper was the question of Reynolds number. Not that it is anything new, but we saw from some of the experiments in the wind tunnel at Aermacchi that he was trying to place transition on the forebody or on various places on the aircraft at high angles of attack in a meaningful way so that we have some assessment of the importance of Reynolds number and whether we can, in fact, try to create a high-Reynolds-number simulated condition with an obviously low-Reynolds-number test situation. It is not very clear to me that we know how to do that yet. I think many people would agree that what we have learned in the past on transition strips for wings, etc. at low angle of attack doesn't really apply all that well to some of the problems that we are faced with at high angles of attack. I believe there is a lot that needs to be learned yet about whether to try to create artificial transition with transition strips or whether we simply ignore transition effects and test at whatever Reynolds numbers we have.

Dr. Orlik-Rückemann

This is exactly what the Technical Evaluator should do; summarize very nicely the whole meeting and then start posing those kinds of questions. I would not like to lose this opportunity to have some discussion. If you bear with me, I would like to take the topics one at a time and ask if there are any questions or comments on this particular item. Let us start with the Reynolds number. Can we simulate it by transition strips; how do we do this; does it apply in dynamic situations, for instance? Is there anybody who wants to say anything about that?

Dr. A.M. Cunningham, General Dynamics, USA

I guess one of my concerns is that in most of our wind tunnel tests we are looking at forebodies that are in the region of about one half million cross-flow Reynolds number range which is the worst possible region to test in. Thus we need some way of stabilizing such flows through some kind of transition strip modelling. Also we need to consider how the Reynolds number effects at sub-critical Reynolds numbers, like we use in a water tunnel and low speed tests, influence forebody flow fields and how well do they match the supercritical flows with turbulent type separations like we have at full scale. I think that there are at least two different issues here.

Mr. Malcolm

I agree with your comment. I think that most people that have worked in the forebody flow area for a while have come to understand that a lot of the phenomena that you see at very low Reynolds number, where the flow is laminar, is very similar to what you see in the case where you have totally turbulent flow. Obviously the characteristics in the boundary layer are different, but the net results in terms of how the forebody vortices behave are very similar at very low Reynolds numbers and very high Reynolds numbers. Unfortunately many wind tunnel tests are run in this transitional range that you mentioned where you get very, very different results compared to either flight Reynolds number or in some of the lower Reynolds number facilities.

Dr. Orlik-Rückemann

You may recall that Bob Nelson, for instance, saw that very nice comparison of the wing rock characteristics of the very, very small, I believe 2 or 3 % model of the F18 in water (I assume it was in water) and compared it with full-scale F18, such as in HARV tests. This was a good example showing that very low Reynolds numbers in the subcritical range gave similar results to those which can be obtained in a fully supercritical situation. The point, however, to be remembered here is that there is no guarantee at all that the subcritical test will always give supercritical results, but they often come closer to the real thing than if you are in the bucket in between. I would like to sound a note of caution that one should not use the very low Reynolds numbers and hope that they will necessarily give you the full-scale results.

When it comes to transition strips in dynamic testing one has to remember that transition of course has a tendency to move and if you fix it, then again you do something that is really basically wrong.

Dr. D. Woodward, Royal Aerospace Establishment, UK

I think that the last point made by Kazik is a really significant one. It is all very well to fix transition, but we don't really know what we are trying to simulate yet. I think that the only way that we are going to get the right answer is to "bite on the bullet" and do dynamic tests in large pressurized facilities so that we can actually simulate varying Reynolds number at constant Mach number. We will then find out exactly what is going on with the change in the transition front, and get some really good data. Now that is easy to say and not very easy to fund, nor to do, but I suspect that if we spend a lot of time trying to fiddle around with transition strips at the end of all of that time, still not know what we have got hold of.

Ir A. Elsenaar, National Aerospace Laboratory NLR, Netherlands

I agree with David Woodward. But it still wouldn't solve all of the problems because even at the flight Reynolds number in the wind tunnel, the transition location might be different due to roughness and flow quality effects. I wonder a little bit if it would help, or if there is any experience, in putting on the nose sparsely distributed roughness grains to get an almost even roughness area, not too much or you will thicken the boundary layer too much, but sufficient to force the boundary layer turbulent wherever it is laminar without the grains and then do Reynolds number studies to see what a Reynolds number variation has for effect.

Dr. R.G. Bradley, Jr., General Dynamics, USA

Let me just add a little bit to the complexity and lack of understanding in this area. There was a time as a young engineer, I would have bet my paycheck that sharp leading edges are insensitive to Reynolds number. I have had some recent experiences that would make me doubt that somewhat. We actually tested very sharp leading-edge chines on a nose probe, for example, quite thoroughly both dynamically and in a wind tunnel, statically, and we were disappointed in flight tests and the effects that were noted. This is the case of a very sharp-edge vortex flow which influences the larger, developed vortex flow and perhaps the nose separation. It is a very, very complex problem and I am not sure that there is a simple solution.

Mr. Malcolm

I think that we all would agree with that.

We have had a lot of discussion about time-lag effects in this particular flight regime that we are in, both in terms of appropriate wind tunnel test techniques and also how we incorporate these into the aerodynamic math models. Probably as important, at least in the long term, can we measure these in flight? We have a number of high angle of attack, high manoeuvre rate flight programs, such as the F/A-18 HARV, the X-31; is there going to be some way to get feedback from these flight tests that will tell us more about the importance of the time-lag effects? It is not an easy problem and I am not a flight test engineer. Perhaps someone who is dealing with flight tests would like to make some comments either one way or another. Also, people who are having to deal with simulations obviously are faced with the problem of how to deal with the time-lag problem, how to put these coefficients in in terms of a time varying and a history dependent manner. Any comments from the floor?

Mr. J.E. Jenkins, Wright Patterson AFB, USA

With regard to the time effects, even in a linear sense, one possibility would be to pick up on an idea that Etkin proposed quite some time ago. That is, to treat the aerodynamic reaction as a transfer function. This would require dynamic tests in order to define these transfer functions, but you could handle in theory significant time-lags in that way. In the non-linear sense, including the history effects, I think we are forced to look at the hypersurface or indicial response type of models. That makes the problem much more difficult for the flight mechanics people because you can't use the small-perturbation equations of motion any longer.

Dr. Orlik-Rückemann

One of the reasons why we are obtaining dynamic derivatives is so that we can correctly formulate the various control laws and design control systems. An associated question is, "do we need to incorporate the various time-lag effects in our control laws and control systems?"

Dr. L. Visintini, AerMacchi, Italy

I have just a short comment. I think that the range of pitching rates shown in the various experiments is very wide, we have seen numbers up to .2 or .5 in  $g/c/v$ . In the recent AGARD FDP short course at NASA Langley Research Center we have seen that the most realistic values for manoeuvring aircraft are limited to something like .03 or .05. So, I think that lag effects that should be considered for modelling or manoeuvring prediction should be the ones coming from just those levels of pitch rate. Probably large pitch rates induce very large lags that may not be meaningful for manoeuvring aerodynamics.

Dr. Orlik Rückemann

Thank you for your comment, however, I would like to recall that the point was made during the meeting that these higher reduced rates are of interest when you discuss the dynamic behavior of control surfaces. So there is still some application of these rates.

Mr. Malcolm

For the next question we perhaps already know the answer, "Do we need to include alpha dot and beta dot effects?" I believe that there have been enough studies done already to show that they can be important, certainly Charles O'Leary's experiments have shown the importance. Probably the only reason that they haven't been included in the past is just the difficulty of actually determining what they are experimentally and certainly analytically. But perhaps with the addition of rigs such as Charles' and others who are beginning to look at the translational effects, we'll know more about the beta dot and alpha dot effects, in the future and they can be included in the simulation model. Any comments?

Mr. C.O. O'Leary, Royal Aerospace Establishment, UK

I got the impression, from the discussion with Kazik after his lecture, that Peter Mangold was saying that they weren't too significant because the aircraft control system was designed such that beta dot effects were suppressed. But this pre-supposes that the actual aerodynamic controls are working properly, and they can be effective, but what if the aerodynamic controls become ineffective in a particular situation, then you are going to get your betadot whether you like it or not. I wonder whether you have a comment on that.

Mr. Malcolm

Peter discussed the need for better criteria at high angle of attack and the need for incorporating dynamic derivatives or coefficients, as the case may be. The other problem is having to do an analysis in terms of, say for example, the departure criteria on an airplane that is unstable, you can't just do an analysis on the bare airframe, you have to somehow include the effects of flight control system which of course, in the early design stage hasn't been established yet. So, I think the criteria that are being used by aircraft designers,  $C_m$  beta dyn, and so forth, as he said, are really not adequate any more. We have to have a better understanding of what kind of terms to include and where we get them and how we determine them at that point in the aircraft design. Whether beta dot and alpha dot effects are important at the design stage or definition of control system, I do not know; I am not the right one to answer that. Peter wants to make a comment.

Mr. P. Mangold, Dornier Luftfahrt, Germany

Yes I want to make a comment on this question. Things which I have spoken about in my paper are the design criteria for the very early stage of an aircraft. So I didn't want to say that these alpha dot and beta dot effects shouldn't be included in the simulation model, which after all represents the real behavior of the augmented aircraft. In fact, we are using these alphas dot and betas dot derivatives if they are available. In longitudinal motion, for example, we have these alpha dot and q derivatives separated for the simulation model by an empirical method. We flight mechanics people would, of course, appreciate it if the aerodynamicist could provide us with more confident data.

So, in summary we are using these derivatives in simulation. Up to now the aerodynamicist did not come up with confident data. Due to my experience in the augmented fighter business, I must say, that the augmented system is not very sensitive to variations in these derivatives.

Of importance, however, are the time-lag effects. Here I am not sure if things that we are measuring now or you are measuring now, are of great importance for flight mechanics. Most of the tests seen during this meeting have been done with rotary movements. If you look at a real flight and to the maneuvers a pilot is doing, you see that he is initiating a maneuver and then he stops at an angle of attack. He flies for some time, then he is pitching down. Our Swedish colleague, Mr. Torlund, showed some results from such maneuvers. These maneuvers will be of interest to the flight mechanics people. The problem is, how to include these effects in the simulations because you know when you initiate your maneuver, but you don't know where you will stop it, so you cannot really model this effect because the magnitudes of dynamic forces and moments are dependent on the time histories of the whole movement in the past. It will be very difficult.

Dr. Orlik Rückemann

You are referring to the ramp-type maneuver, especially a very fast one. There are several rigs available now in the NATO community which can produce data showing very large time-lag effects which can be measured with those rigs. I would also like to make a comment regarding the effect of the dot derivatives on our ability to predict the dynamic behavior of aircraft. This does not necessarily mean departure or something like this, but just how would the aircraft react to various disturbances. It has been shown by several different organizations in the last 10 years or so, that the separation of the dot derivatives from their forced-oscillation counterpart is quite an essential requirement to make those predictions correctly. In other words, if you just use, for example, the q plus alpha dot derivative instead of the q derivative and then put the alpha dot derivative equal to zero, you get in many cases quite an incorrect prediction. For that, of course, you must be at an angle of attack high enough so that the dot derivatives are of a significant magnitude. Of course, as long as they are very small it does not make any difference.

Dr. Cunningham

Another thing that has always concerned me is if you have a g-limited aircraft and are conducting a dynamic maneuver, you will have a significant normal force overshoot, and your flight control system G-limiter must be able to recognize what is coming up before it gets there. This needs to be included in the flight control system for safety purposes.

Mr. Malcolm

Now I will go back to the one that we skipped. We have seen a lot of data in the last several years on the effects of dynamic lift on two-dimensional airfoils. We are beginning to see more and more experiments and analysis on very highly swept delta wings, 60° and greater. But I haven't seen very much about lower sweep. For a typical existing aircraft wing sweep, 25° to 45°. I wonder if there is very much research going on anywhere looking at the effects of the moderate sweep. Is there anyone who would care to comment on that?

Dr. Orlik Rückemann

There has been a NASA Langley investigation which included rectangular wings as well. It seems that the effect of dynamic lift was different, but still there.

Dr. Cunningham

I have been doing some work on lower sweep wings, but not as low as 45°. However, our strake-delta wing was 76°-40°. Looking at the more complex planforms with double sweep where two different types of vortical flow systems (low sweep and high sweep) interact you have an added problem. This is especially true for the F18 and the F16.

Mr. Malcolm

We need to have some feedback from flight tests. Will we be able to get some feedback from high rate maneuver flight tests that are going to be done in the near future to assess whether we are doing the right experiments, whether we are measuring the right quantities for simulation and flight test prediction? Will anyone comment, for the X31, on the type of data they expect to get that will shed some light on some of these time-lag problems at high-rate conditions and in full scale?

Dr. H. Ross, MBB, Germany

I think that we should wait about a year. Then we should be able to substantiate results with flight test data and we should be able and in a position to present facts rather than talking about speculations at this point in time.

Mr. Malcolm

I guess the point I was trying to get at is, "are we designing flight tests in such a way that we will be able to determine these kinds of effects?". We know that they exist at least in sub-scale experiments. The question is will we be able to measure those from full-scale flight tests in a way that we can learn something from that?

RTD-6

Dr. Bradley

I think we should, in answer to your question. We definitely should take more flight test data for these effects. I wanted to comment that what really turned Dr. Cunningham on to this area some time back was flight data from the F16. We recorded the hysteresis effect and have flight data. That was what tweaked our interest in doing some more research about six years ago.

Mr. Malcolm

I have another comment on this, and I don't think that anyone would disagree. I believe that AGARD should aggressively continue to promote technology exchange in this area. It is obviously an area which has a lot of interest, a lot of relevance to aircraft that are flying now and probably more importantly for future aircraft. I certainly, as an evaluator, would like to encourage AGARD to continue these kinds of meetings.

Dr. Orlik Rückemann

Very good point. Professor Slooff?

Prof. Ir. J.W. Slooff, National Aerospace Laboratory NLR, Netherlands

What I am going to say does not apply to any of the dots over there, but it may also apply to all of them. A point I was missing - it is not a question or issue that fits into the picture from your point of view - is the question to what extent can we expect to make use of CFD-type methods in this area, if not now, then perhaps in the more distant future. I have heard very little on that. Oh, I see I was too early. You address your point on your next viewfoil.

Mr. Malcolm

Obviously there are a lot of advances being made in computing steady flows with CFD methods. A lot of work is done at NASA Ames and NASA Langley, at least these are the ones I am most familiar with, but there is obviously some work going on in Europe in this area. They have been very successful in calculating forebody flows and extending that gradually back over the entire airplane. Obviously, doing this in a high rate maneuver is a different question. I don't know if there are any CFD people in the group here who want to comment on the problems involved in doing that and how soon we might expect to see people doing those kind of computations.

Dr. Orlik Rückemann

I think we have only recently started considering the possibility of running some rotary CFD calculations which by the nature of things are of a quasi-steady rather than of an unsteady type. As I understand it, no unsteady CFD calculations on complete configurations have yet been made.

Mr. E. Waggoner, NASA Langley, USA

I would like to make a comment. I think we have made essential progress during the last years to calculate high angle of attack cases in steady flow, the time has now come to attack the unsteady problems. I think this is possible, especially those maneuvers which have been mentioned here which are not really oscillatory, ramp-type maneuvers and so this can now be attacked with computational methods, for example, for delta wings etc. I would encourage our people to do this.

Dr. Orlik Rückemann

I am very happy to hear that. We have about 10 minutes left for the discussion, so could we press on please.

Dr. W.J. McCroskey, NASA Ames Research Center, USA

I just wanted to advertise a forthcoming conference by our sister panel, Structures and Materials. On 6 - 11 October in San Diego, will be a specialists meeting entitled "Unsteady Aerodynamics and Aeroelasticity". As you can guess from the title there is unsteady aerodynamics in that. It is aeroelasticity oriented, but it is my understanding that there will be some attempts to address the potential for CFD in this area, if not actual results presented at that meeting.

Mr. Malcolm

That is good to hear. We have several questions left. I am not sure what the priority ought to be. Why don't we just go through them one at a time and if someone wants to make a comment, they can, and if not, we'll go on. We have actually touched on the second one probably in the discussion we have had already in terms of how to include dynamics effects in preliminary design and what the penalties are if you don't. If anyone wants to comment on that they are welcome to. The third one actually as Peter Mangold mentioned a moment ago. Does the wind tunnel test community or does the aerodynamicist, in a sense, understand the needs of the aircraft designer, perhaps in terms of what are the important aerodynamic coefficients to include, particularly in the preliminary design stage. I don't know the answer to that. Perhaps there needs to be closer contacts between flight test people or the aero mechanics people and the aerodynamicist.

Dr. Orlik Rückemann

One of my main considerations when organizing these meetings has always been to do that in such a way that the specialists from the different walks of life have a chance to talk to each other, and I hope that we will continue doing it in this way. I think it was very interesting for us to hear Mr. Mangold's remarks this afternoon.

Mr. Malcolm

I have a couple of questions related to forebody vortex control. Most of the work that has been done to date has been on a more or less conventional forebodies, if you will, with circular and elliptical cross-sections, where you can have a high influence over the separation location by either blowing or using miniature strakes and so forth. One question is how applicable are some of these techniques to chine-shaped forebodies. We saw one comment on it today in Bob Guyton's talk, looking at a generic chine configuration where separation is relatively well fixed due to the sharp edge. I think that probably some of the techniques that we have been looking at will work and some will not on the next generation of forebodies. That is an important issue to keep in front of us, I believe. Also, is forebody vortex control in competition with thrust vectoring or is it considered to be complementary, particularly for yaw

control? Does anyone want to comment on that? My own view is that they can and probably will be complementary. One won't be used in place of the other. I believe that they both have a place. I believe that eventually on the HARV configuration, for example, you will see both of these in operation. As has been mentioned before, they are now in the beginning stages of flying HARV with the paddles for thrust vectoring and they are doing some full-scale wind tunnel tests at NASA Ames now to evaluate both blowing and also the Langley conformal strakes. It is planned to flight test with both of these systems in operation, eventually, so this may be an opportunity to see how these two unique controls effectors can be used in conjunction with one another.

Dr. Orlik Rückemann

I would like to add to this that the only reason why there were no specific papers addressing the question of thrust vectoring in this meeting is that, of course, the meeting was about aerodynamics of maneuvering aircraft. Certainly I agree with the rest of what you said. The two techniques most likely will become very complementary in nature. Also I would like to add that thrust vectoring is a technique which will be soon proven in flight, whereas forebody vortex control methods are being so far developed and looked into in a research environment only so far.

Mr. Malcolm

Related to that is the last bullet, and I will come back to the next to the last one in a moment, and that is the obvious need for understanding the effect of Reynolds number on forebody vortex control and also to evaluate it in non-steady conditions, either in high rate motions that might be produced by some of the high-rate pitch or yaw motions or in particular, on the rotary balance. We are going to be doing some experiments on a sub-scale F18 in the Ames 7 by 10 on a rotary balance to look at the effects of forebody blowing in the presence of a rotational motion. There is not a whole lot known yet about the dependency on that technique on rotation rates, so I think that we need to know more in that area. Finally, with the various flight programs that are on-going, including for a short time at least, the X29A at NASA Dryden and also the F18 HARV and the X31, the question arises as to how accessible is the flight data going to be to those of us who are trying to understand high angle of attack, high rate motion data. Hopefully, even though these are taking place in various organizations, we will have access to that data as it becomes available. It will help us to do our job better. Any other comments? I know that we are about to run out of time.

Dr. Cunningham

On your last bullet on the chart about the dynamic effects of forebody vortex control, it is interesting that when we fix our static stability problems by straightening up our forebody flow fields, we sometimes get into a dynamic problem. You can't fix everything, so I think it is good to emphasize that if forebody vortex control works statically it may not necessarily work dynamically or vice versa.

Mr. Malcolm

Well, we certainly need to know.

Dr. Bradley

I would just like to make one comment. We seem to have a propensity in the United States for mis-managing these flight programs. We develop special flight vehicles, the X29, X31 and APTI. By the time we get them in the air, we have spent all the money and we never have enough money to do the sufficient flight testing to get detailed data. I would just like to raise the flag here. You who have a lot of influence with the money sources should straighten that out.

Mr. Malcolm

I agree.

Dr. Orlik Rückemann

Let us close this discussion on this note. Let us be optimistic that we can really affect the powers that be in this direction. I would like now to thank very much our Technical Evaluator, Gerry Malcolm for a very well done job. I would like to thank all the authors who participated in this meeting for the careful preparation of their material and written versions of their papers. Finally, I would like to thank the session chairman who did a good job in keeping everything on course and on time. With this I would now like to call on the Panel Chairman to close the meeting.

Dr. McCroskey

The joy of being Panel Chairman is that you get in the last words. So I will take the prerogative to just amplify Dr. Bradley's comment. Often when the data are acquired there is no money left over to analyze them and disseminate them. According to the time table, and AGARD is renowned for keeping the schedule, it is all over and we are all on the bus. So, I will just make a few remarks that relate to our bus ride in. But first, thanks to Kazik, for his Herculean efforts in putting together this program and again a special thanks for Mr. Malcolm for sitting in as Technical Evaluator and doing such a fine job. I would like also to say on behalf of the Panel, we appreciate the contributions of Mr. Mangold of the Flight Mechanics Panel and Mr. Becker representing the Structures and Materials Panel. On behalf of the Panel I want to express again our appreciation to organizations and individuals here in France who made this all possible: The French AGARD Delegation, Sup'Aero, our host, Aerospatiale, Airbus Industrie, and ONERA, and in particular, Monsieur Sergeant who had the task of running up and down and keeping all of the audiovisual working. Again Mr. Bouquet and Monsieur and Madame Dujarric for their efforts.

One essential part of this meeting is the task of the translators, and I don't really know how they do it. Let us express our appreciation to Mademoiselle Celie, Madame Couedic and Monsieur de Liffiac. We do appreciate the job that you do. I particularly appreciate and understand probably better than most, the effort of our Panel Executive and his wife, Dr. and Mrs. Goodrich and our secretary, Mademoiselle Rivault.

As I said at the conclusion of the Specialists Meeting on Adverse Weather, please translate this warm feeling and applause into favorable comments back to your management about the value of AGARD. Now a peek at future attractions. I would like to show the viewgraph of our forthcoming meeting, that will be

RTD-8

the fall symposium on "Aerodynamic Engine Airframe Integration". I will just reiterate the fall meeting by the Structures and Materials Panel, 6 to 11 October 1991, on "Unsteady Aerodynamics and Aeroelasticity". Then we have two symposia next year on Hypersonics in Torino, on High Lift System Aerodynamics in Canada, and two special courses that will be put on in connection with the von Karman Institute. Finally, I would like to just show you a quick video about the meeting in Fort Worth.

REPORT DOCUMENTATION PAGE			
1. Recipient's Reference	2. Originator's Reference	3. Further Reference	4. Security Classification of Document
	AGARD-CP-497	ISBN 92-835-0643-X	UNCLASSIFIED
5. Originator	Advisory Group for Aerospace Research and Development North Atlantic Treaty Organization 7 rue Ancelle, 92200 Neuilly sur Seine, France		
6. Title	MANOEUVRING AERODYNAMICS		
7. Presented at	the Fluid Dynamics Panel Specialists' Meeting held in Toulouse, France 1st—2nd May 1991.		
8. Author(s)/Editor(s)	Various		9. Date November 1991
10. Author's/Editor's Address	Various		11. Pages 292
12. Distribution Statement	This document is distributed in accordance with AGARD policies and regulations, which are outlined on the back covers of all AGARD publications.		
13. Keywords/Descriptors	<div style="display: flex; justify-content: space-between;"> <div style="width: 45%;"> <p>* <i>Fluid dynamics,</i></p> <p>* <i>Flight maneuvers,</i></p> <p><i>Flight characteristics,</i></p> <p><i>Angle of attack</i></p> <p>* <i>Aerodynamics</i></p> <p><i>Aerodynamic forces,</i></p> </div> <div style="width: 45%;"> <p><i>Flight control,</i></p> <p><i>Flight tests,</i></p> <p><i>Unsteady flow,</i></p> <p><i>Vortices,</i></p> <p><i>France,</i></p> <p><i>NATO.</i></p> </div> </div>		
14. Abstract	<p>→ This volume contains the 17 papers presented at the AGARD Fluid Dynamics Panel (FDP) Specialists' Meeting on "Manoeuvring Aerodynamics" held 1st—2nd May 1991 in Toulouse, France. In addition to these papers, the general discussion held at the end of the meeting and the Technical Evaluation Report are included in this document.</p> <p>This FDP sponsored meeting and document reflect the growing interest in rapid, large-amplitude manoeuvres of aircraft at high angles of attack and highlights the importance of the unsteady, separated, vortical and often non-linear characteristics of the aerodynamic flows that exist under such conditions. Developments in pertinent experimental techniques, relevant aerodynamic data and their applications to flight behaviour predictions, importance of time lags, methods for forebody vortex control, and flight tests of the X-31A aircraft are among the topics discussed.</p> <p style="text-align: right;">(25)</p>		

<p>AGARD Conference Proceedings 497 Advisory Group for Aerospace Research and Development, NATO MANOEUVRING AERODYNAMICS Published November 1991 292 pages</p> <p>This volume contains the 17 papers presented at the AGARD Fluid Dynamics Panel (FDP) Specialists' Meeting on "Manoeuvring Aerodynamics" held 1st-2nd May 1991 in Toulouse, France. In addition to these papers, the general discussion held at the end of the meeting and the Technical Evaluation Report are included in this document.</p> <p>PT.O.</p>	<p>AGARD-CP-497</p> <p>Flight maneuvers Flight characteristics Angle of attack Aerodynamics Aerodynamic forces Flight control Flight tests Unsteady flow Vortices</p>	<p>AGARD Conference Proceedings 497 Advisory Group for Aerospace Research and Development, NATO MANOEUVRING AERODYNAMICS Published November 1991 292 pages</p> <p>This volume contains the 17 papers presented at the AGARD Fluid Dynamics Panel (FDP) Specialists' Meeting on "Manoeuvring Aerodynamics" held 1st-2nd May 1991 in Toulouse, France. In addition to these papers, the general discussion held at the end of the meeting and the Technical Evaluation Report are included in this document.</p> <p>PT.O.</p>	<p>AGARD-CP-497</p> <p>Flight maneuvers Flight characteristics Angle of attack Aerodynamics Aerodynamic forces Flight control Flight tests Unsteady flow Vortices</p>
<p>AGARD Conference Proceedings 497 Advisory Group for Aerospace Research and Development, NATO MANOEUVRING AERODYNAMICS Published November 1991 292 pages</p> <p>This volume contains the 17 papers presented at the AGARD Fluid Dynamics Panel (FDP) Specialists' Meeting on "Manoeuvring Aerodynamics" held 1st-2nd May 1991 in Toulouse, France. In addition to these papers, the general discussion held at the end of the meeting and the Technical Evaluation Report are included in this document.</p> <p>PT.O.</p>	<p>AGARD-CP-497</p> <p>Flight maneuvers Flight characteristics Angle of attack Aerodynamics Aerodynamic forces Flight control Flight tests Unsteady flow Vortices</p>	<p>AGARD Conference Proceedings 497 Advisory Group for Aerospace Research and Development, NATO MANOEUVRING AERODYNAMICS Published November 1991 292 pages</p> <p>This volume contains the 17 papers presented at the AGARD Fluid Dynamics Panel (FDP) Specialists' Meeting on "Manoeuvring Aerodynamics" held 1st-2nd May 1991 in Toulouse, France. In addition to these papers, the general discussion held at the end of the meeting and the Technical Evaluation Report are included in this document.</p> <p>PT.O.</p>	<p>AGARD-CP-497</p> <p>Flight maneuvers Flight characteristics Angle of attack Aerodynamics Aerodynamic forces Flight control Flight tests Unsteady flow Vortices</p>



<p>This FDP sponsored meeting and document reflect the growing interest in rapid, large-amplitude manoeuvres of aircraft at high angles of attack and highlights the importance of the unsteady, separated, vortical and often non-linear characteristics of the aerodynamic flows that exist under such conditions. Developments in pertinent experimental techniques, relevant aerodynamic data and their applications to flight behaviour predictions, importance of time lags, methods for forebody vortex control, and flight tests of the X-31A aircraft are among the topics discussed.</p> <p>ISBN 92-835-0643-X</p>	<p>This FDP sponsored meeting and document reflect the growing interest in rapid, large-amplitude manoeuvres of aircraft at high angles of attack and highlights the importance of the unsteady, separated, vortical and often non-linear characteristics of the aerodynamic flows that exist under such conditions. Developments in pertinent experimental techniques, relevant aerodynamic data and their applications to flight behaviour predictions, importance of time lags, methods for forebody vortex control, and flight tests of the X-31A aircraft are among the topics discussed.</p> <p>ISBN 92-835-0643-X</p>
<p>This FDP sponsored meeting and document reflect the growing interest in rapid, large-amplitude manoeuvres of aircraft at high angles of attack and highlights the importance of the unsteady, separated, vortical and often non-linear characteristics of the aerodynamic flows that exist under such conditions. Developments in pertinent experimental techniques, relevant aerodynamic data and their applications to flight behaviour predictions, importance of time lags, methods for forebody vortex control, and flight tests of the X-31A aircraft are among the topics discussed.</p> <p>ISBN 92-835-0643-X</p>	<p>This FDP sponsored meeting and document reflect the growing interest in rapid, large-amplitude manoeuvres of aircraft at high angles of attack and highlights the importance of the unsteady, separated, vortical and often non-linear characteristics of the aerodynamic flows that exist under such conditions. Developments in pertinent experimental techniques, relevant aerodynamic data and their applications to flight behaviour predictions, importance of time lags, methods for forebody vortex control, and flight tests of the X-31A aircraft are among the topics discussed.</p> <p>ISBN 92-835-0643-X</p>

**AGARD**

NATO  OTAN

7 RUE ANCELLE · 92200 NEUILLY-SUR-SEINE  
FRANCE

Téléphone (1)47.38.57.00 · Téléc 610 176

Télexcopie (1)47.38.57.99

**DIFFUSION DES PUBLICATIONS**

**AGARD NON CLASSIFIEES**

L'AGARD ne détient pas de stocks de ses publications, dans un but de distribution générale à l'adresse ci-dessus. La diffusion initiale des publications de l'AGARD est effectuée auprès des pays membres de cette organisation par l'intermédiaire des Centres Nationaux de Distribution suivants. A l'exception des Etats-Unis, ces centres disposent parfois d'exemplaires additionnels; dans les cas contraire, on peut se procurer ces exemplaires sous forme de microfiches ou de microcopies auprès des Agences de Vente dont la liste suit.

**CENTRES DE DIFFUSION NATIONAUX**

**ALLEMAGNE**

Fachinformationszentrum,  
Karlsruhe  
D-7514 Eggenstein-Leopoldshafen 2

**BELGIQUE**

Coordonnateur AGARD-VSL  
Etat-Major de la Force Aérienne  
Quartier Reine Elisabeth  
Rue d'Evere, 1140 Bruxelles

**CANADA**

Directeur du Service des Renseignements Scientifiques  
Ministère de la Défense Nationale  
Ottawa, Ontario K1A 0K2

**DANEMARK**

Danish Defence Research Board  
Ved Idraetsparken 4  
2100 Copenhagen Ø

**ESPAGNE**

INTA (AGARD Publications)  
Pintor Rosales 34  
28008 Madrid

**ETATS-UNIS**

National Aeronautics and Space Administration  
Langley Research Center  
M/S 180  
Hampton, Virginia 23665

**FRANCE**

O.N.E.R.A. (Direction)  
29, Avenue de la Division Leclerc  
92320, Châtillon sous Bagneux

**GRECE**

Hellenic Air Force  
Air War College  
Scientific and Technical Library  
Dekelia Air Force Base  
Dekelia, Athens TGA 1010

**ISLANDE**

Director of Aviation  
c/o Flugrad  
Reykjavik

**ITALIE**

Aeronautica Militare  
Ufficio del Delegato Nazionale all'AGARD  
Aeroporto Pratica di Mare  
00040 Pomezia (Roma)

**LUXEMBOURG**

Voir Belgique

**NORVEGE**

Norwegian Defence Research Establishment  
Attn: Biblioteket  
P.O. Box 25  
N-2007 Kjeller

**PAYS-BAS**

Netherlands Delegation to AGARD  
National Aerospace Laboratory NLR  
Kluuyverweg 1  
2629 HS Delft

**PORTUGAL**

Portuguese National Coordinator to AGARD  
Gabinete de Estudos e Programas  
CLAFIA  
Base de Alfragide  
Alfragide  
2700 Amadora

**ROYAUME UNI**

Defence Research Information Centre  
Kentigern House  
65 Brown Street  
Glasgow G2 8EX

**TURQUIE**

Milli Savunma Bakanligi (MSB)  
ARGE Daire Bakanligi (ARGE)  
Ankara

LE CENTRE NATIONAL DE DISTRIBUTION DES ETATS-UNIS (NASA) NE DETIENT PAS DE STOCKS  
DES PUBLICATIONS AGARD ET LES DEMANDES D'EXEMPLAIRES DOIVENT ETRE ADRESSEES DIRECTEMENT  
AU SERVICE NATIONAL TECHNIQUE DE L'INFORMATION (NTIS) DONT L'ADRESSE SUIT.

**AGENCES DE VENTE**

National Technical Information Service  
(NTIS)  
5285 Port Royal Road  
Springfield, Virginia 22161  
Etats-Unis

ESA/Information Retrieval Service  
European Space Agency  
10, rue Mario Nikis  
75015 Paris  
France

The British Library  
Document Supply Division  
Boston Spa, Wetherby  
West Yorkshire LS23 7BQ  
Royaume Uni

Les demandes de microfiches ou de photocopies de documents AGARD (y compris les demandes faites auprès du NTIS) doivent comporter la dénomination AGARD, ainsi que le numéro de série de l'AGARD (par exemple AGARD-AG-315). Des informations analogues, telles que le titre et la date de publication sont souhaitables. Veuillez noter qu'il y a lieu de spécifier AGARD-R-nnn et AGARD-AR-nnn lors de la commande de rapports AGARD et des rapports consultatifs AGARD respectivement. Des références bibliographiques complètes ainsi que des résumés des publications AGARD figurent dans les journaux suivants:

Scientific and Technical Aerospace Reports (STAR)  
publié par la NASA Scientific and Technical  
Information Division  
NASA Headquarters (NTT)  
Washington D.C. 20546  
Etats-Unis

Government Reports Announcements and Index (GRA&I)  
publié par le National Technical Information Service  
Springfield  
Virginia 22161  
Etats-Unis

(accessible également en mode interactif dans la base de  
données bibliographiques en ligne de NTIS, et sur CD-ROM)

Imprimé par Specialised Printing Services Limited  
40 Chigwell Lane, Lougham, Essex IG10 3TZ

AGARD

NATO OTAN

7 RUE ANCELLE • 92200 NEUILLY-SUR-SEINE  
FRANCE

Telephone (1)47.38.57.00 • Telex 610 176  
Telefax (1)47.38.57.99

**DISTRIBUTION OF UNCLASSIFIED  
AGARD PUBLICATIONS**

AGARD does NOT hold stocks of AGARD publications at the above address for general distribution. Initial distribution of AGARD publications is made to AGARD Member Nations through the following National Distribution Centres. Further copies are sometimes available from these Centres (except in the United States), but if not may be purchased in Microfiche or Photocopy form from the Sales Agencies listed below.

**NATIONAL DISTRIBUTION CENTRES**

**BELGIUM**

Coordonnateur AGARD — VSL  
Etat-Major de la Force Aérienne

**LUXEMBOURG**

See Belgium

**CAN**

**NASA**

National Aeronautics and  
Space Administration

Postage and Fees Paid  
National Aeronautics and  
Space Administration  
NASA-451

Official Business  
Penalty for Private Use \$300



ARD  
NLR

**DEN**

Washington, D.C. **SPECIAL FOURTH CLASS MAIL**  
20546 **BOOK**

Establishment

**FRAN**

L2 001 AGARDCP497920109S002672D  
DEPT OF DEFENSE  
DEFENSE TECHNICAL INFORMATION CENTER  
ATTN : DTIC-FDAB/JOYCE CHIRAS  
CAMERON STATION BLDG 5  
ALEXANDRIA VA 223046145

or to AGARD  
as

**GRI**

Scientific and Technical Library  
Dekelia Air Force Base  
Dekelia, Athens TGA 1010

Milli Savunma Başkanlığı (MSB)  
ARGE Daire Başkanlığı (ARGE)  
Ankara

**ICELAND**

Director of Aviation  
c/o Flugrad  
Reykjavik

**UNITED KINGDOM**

Defence Research Information Centre  
Kentigern House  
65 Brown Street  
Glasgow G2 8EX

**ITALY**

Aeronautica Militare  
Ufficio del Delegato Nazionale all'AGARD  
Aeroporto Pratica di Mare  
00050 Pomezia (Roma)

**UNITED STATES**

National Aeronautics and Space Administration (NASA)  
Langley Research Center  
M/S 180  
Hampton, Virginia 23665

THE UNITED STATES NATIONAL DISTRIBUTION CENTRE (NASA) DOES NOT HOLD  
STOCKS OF AGARD PUBLICATIONS, AND APPLICATIONS FOR COPIES SHOULD BE MADE  
DIRECT TO THE NATIONAL TECHNICAL INFORMATION SERVICE (NTIS) AT THE ADDRESS BELOW.

**SALES AGENCIES**

National Technical  
Information Service (NTIS)  
5285 Port Royal Road  
Springfield, Virginia 22161  
United States

ESA/Information Retrieval Service  
European Space Agency  
10, rue Mario Nikis  
75015 Paris  
France

The British Library  
Document Supply Centre  
Boston Spa, Wetherby  
West Yorkshire LS23 7BQ  
United Kingdom

Requests for microfiches or photocopies of AGARD documents (including requests to NTIS) should include the word 'AGARD' and the AGARD serial number (for example AGARD-AG-315). Collateral information such as title and publication date is desirable. Note that AGARD Reports and Advisory Reports should be specified as AGARD-R-nnn and AGARD-AR-nnn, respectively. Full bibliographical references and abstracts of AGARD publications are given in the following journals:

Scientific and Technical Aerospace Reports (STAR)  
published by NASA Scientific and Technical  
Information Division  
NASA Headquarters (NTT)  
Washington D.C. 20546  
United States

Government Reports Announcements and Index (GRA&I)  
published by the National Technical Information Service  
Springfield  
Virginia 22161  
United States  
(also available online in the NTIS Bibliographic  
Database or on CD-ROM)



Printed by Specialised Printing Services Limited  
40 Chigwell Lane, Loughton, Essex IG10 3TZ

ISBN 92-835-0643-X